An experimental study of sonic and supersonic nozzles and their application to high pressure ejectors for aircraft attitude control

Miller, P.

Award date:
1988

Awarding institution:
University of Bath

AN EXPERIMENTAL STUDY OF SONIC AND SUPERSONIC NOZZLES AND THEIR APPLICATION TO HIGH PRESSURE EJECTORS FOR AIRCRAFT ATTITUDE CONTROL

submitted by P Miller
for the degree of PhD
of the University of Bath
1988

ProQuest LLC
789 East Eisenhower Parkway
P.O. Box 1346
Ann Arbor, MI 48106-1346

SUMMARY

A study has been conducted of reaction controls for VSTOL aircraft using thrust augmenting ejector techniques.

Rapid mixing nozzles have been developed for high pressure ejectors. Mass flow increases for sonic nozzles of up to 50% at x/D=8 were recorded, compared with plain circular nozzles. Their use was found to improve the thrust performance of a simple ejector by 9%, and larger increases are believed possible.

Results from an ejector performance prediction model were successfully compared with experimental data. The use of rapid mixing nozzles in a practical ejector design has been assessed. It is predicted that a maximum thrust increment of 20% could be achieved, compared with a simple fully expanded jet flow.

Acknowledgements

I would firstly like to thank sincerely my supervisor Dr. P J Wingham for his consistent advice and help throughout the period of my research. Many other people at Bath University have also provided me with support and encouragement but I would like to especially thank the technicians Mr. J G Butt and Mr. T J Keston for their friendship and help with the experimental work.

I am grateful to Mr. S F Stapleton and Mr. C L Bore of British Aerospace Kingston for their decision to allow the programme to be undertaken and for many hours of helpful discussion.

Finally I wish to express my gratitude to my parents for their continued encouragement during the long period of writing-up.

CONTENTS

Contents contd.

Contents contd.

Contents contd.

Contents contd.

Contents contd.

Contents contd.

LIST OF TABLES

LIST OF FIGURES

List of Figures contd.

List of Figures contd.

List of Figures contd.

List of Figures contd.

List of Figures contd.

List of Figures contd.

List of Figures contd.

List of Figures contd.

NOTATION

CHAPTER 2

A	Area normal to flow direction
A	Hypermixing nozzle segment width
B	Hypermixing nozzle segment length
D	Diameter
F	Ejector total thrust
k	Turbulent kinetic energy
L_M	Ejector mixing length
L_D	Diffuser length
M	Mach number
p	Gauge static pressure
p_o	Absolute total pressure
P_o	Absolute total pressure
R	Radius
T_o	Absolute total temperature
u	Local time averaged velocity
β	Incompressible momentum skewness $\overline{u^2} / \bar{u}^2$
Φ	Thrust augmentation ratio, see text for definition
ρ	Static density

Subscripts

o	Stagnation conditions
1	Injection plane of single stage ejector Inlet of first stage secondary flow in multi-stage ejector
2	End of parallel mixing section of single stage ejector Inlet of second stage secondary flow in multi-stage ejector
3	End of diffuser of single stage ejector End of second stage in multi-stage ejector
4	End of first stage in multi-stage ejector
a	Ambient
e	End of parallel mixing section
m	Location of secondary flow minimum area
p	Primary

Notation contd.

s Secondary

∞ Ambient

Superscript

* Primary throat condition

CHAPTER 3

M Mach number

CHAPTER 4

A Area
M Mach number
r Cylindrical polar radial direction
R Specific gas constant
T_o Absolute stagnation temperature
V Streamwise velocity magnitude
z Cylindrical polar axial direction

γ Ratio of specific heats
ϕ Flow angle from z direction
μ Mach angle
ν Prandtl-Meyer angle

Superscript

* Throat condition

Notation contd.

CHAPTER 5

D Nozzle throat diameter
M Mach number
p Absolute static pressure
p_o { Gauge jet reservoir pressure / Absolute pitot pressure
p_{ot} Absolute total pressure
r Radial position from jet axis
R Specific gas constant
T Absolute static temperature
T_o Absolute total temperature
v Time averaged velocity
x Axial distance from nozzle exit plane

γ Ratio of specific heats
δ Jet divergence angle
ν Prandtl-Meyer angle
ρ Static density

Subscripts

ex Exit of nozzle
FE Fully expanded
M Nozzle Mach number

∞ Ambient

CHAPTER 6

A Area
D Diameter
k Jet dependent constant
$\dot{m}$ Mass flow
M Mach number
p Absolute static pressure

Notation contd.

P_o	Gauge jet reservoir pressure Absolute pitot pressure
P	Momentum
r	Radial position from jet axis
R	Jet radius
R	Specific gas constant
T_o	Absolute total temperature
v	Time averaged velocity
x	Axial distance from nozzle exit plane
γ	Ratio of specific heats
ρ	Static density

CHAPTER 7

A	Area
A_R	Area ratio
D	Diameter
l	Ejector duct half-width
M	Mach number
p	Absolute static pressure
p_o	Gauge jet reservoir pressure Total pressure, absolute and gauge
Q	Half-volume flow rate in ejector duct
T	Thrust
u	Cartesian velocity in x direction
v	Cartesian velocity in y direction
w	Transformed domain $\phi + j\psi$
x	Cartesian flow direction Axial distance from nozzle exit plane
y	Cartesian transverse direction Spanwise vertical distance from ejector axis
z	Spanwise horizontal distance from ejector axis Geometric domain $x + jy$

Notation contd.

γ Ratio of specific heats
ϕ Velocity potential
Φ Thrust augmentation ratio: relative to specified primary Mach number thrust
Φ_t Thrust augmentation ratio: relative to fully expanded Mach number thrust
ψ Stream function

Subscripts

s Secondary
i Ideal

∞ Ambient

Superscript

* Throat condition

CHAPTER 8 and APPENDIX G

a Elemental area
A Area
A_d Diffuser area ratio
A_{SR} Ejector cross-section aspect ratio
A_R Nominal ejector area ratio
A_{RT} Actual ejector area ratio
C_F Skin friction coefficient
C_p Specific heat capacity at constant pressure
C_{Pd} Diffuser pressure coefficient
D Nozzle exit diameter
D^* Full scale single nozzle diameter
$F_2(M)$ Mass flow function $M(\rho/\rho_o)(t/T)^{1/2}$
$F_3(M)$ Momentum function $(p/P)(1+\gamma M^2)$
L Length of ejector mixing duct
$\dot{m}$ Mass flow

Notation contd.

M	Mach number
p	Absolute static pressure
p_o	Gauge reservoir stagnation pressure
P	Absolute total pressure
P_a	Ambient pressure
P_d	Diffuser pressure factor
P_e	Ejector exit static pressure factor
R	Specific gas constant
t	Absolute static temperature
T	Absolute stagnation temperature
u	Streamwise time averaged velocity
U	Streamwise time and area averaged velocity
W	Width of ejector mixing duct
x	Distance from nozzle exit plane
α	Mass flow skewness $\int \frac{\rho}{\bar{\rho}} \frac{u}{U} d(a/A)$
β	Momentum skewness $\int \frac{\rho}{\bar{\rho}} \frac{u^2}{U^2} d(a/A)$
γ	Ratio of specific heats
δ	Energy skewness $\int \frac{\rho}{\bar{\rho}} \frac{u^3}{U^3} d(a/A)$
ϵ	Energy skewness $\int \frac{\rho}{\bar{\rho}} \frac{u}{U} \frac{t}{\bar{t}} d(a/A)$
κ	Temperature function (see Appendix G)
ξ_o	Primary nozzle total pressure loss
ξ_i	Inlet total pressure loss
ξ_f	Friction loss in ejector duct (see Appendix G)
π	Pressure ratio P_{RES} / P_a
ρ	Static density
ρ_o	Stagnation density
Φ_t	Thrust augmentation ratio: relative to fully expanded Mach number thrust

Notation contd.

Subscripts

2 Ejector exit plane

ISEN Expanded to isentropic conditions
p Primary
RES Reservoir conditions
s Secondary
WALL Condition on ejector duct surface

APPENDIX C

a Sonic velocity
M Mach number
p Static pressure
r Cylindrical polar radial direction
u Cartesian velocity in x direction
v Cartesian velocity in y direction
v_r Velocity in cylindrical polar radial direction
v_ϕ Velocity in cylindrical polar circumferential direction
V Velocity vector
w Cartesian velocity in z direction
w Velocity in cylindrical polar axial direction
x Cartesian direction
y Cartesian direction
z Cartesian direction
z Cylindrical polar axial direction

ϕ Cylindrical polar circumferential direction
μ Mach angle
ρ Static density
ϕ Flow angle from z direction

Notation contd.

APPENDIX D

D Nozzle diameter
D Pitot tube external diameter
D_i Pitot tube internal diameter
M Mach number
p Gauge static pressure
r Radial distance from jet axis
v Time averaged velocity in mean flow direction
v_x Turbulent velocity in x direcion
v_y Turbulent velocity in y direcion
v_z Turbulent velocity in z direcion
x Axial distance from nozzle exit plane

δ Effective probe displacement
ρ Static density

APPENDIX E

k Turbulent kinetic energy
M Mach number

ϵ Rate of dissipation of k

APPENDIX F

D Nozzle diameter
x Axial distance from nozzle exit plane

APPENDIX G see NOTATION for CHAPTER 8

1. INTRODUCTION

Thrust augmenting ejectors have been considered to have potential application in VSTOL aircraft for many years, either as a means of increasing engine thrust or, in the case discussed here, for attitude control purposes.

At the low speeds encountered in jet-borne flight conventional control surfaces are ineffective. Two different methods that have been considered to overcome this problem are:-

1) Vectoring and modulating the main jet thrust to maintain control, additional to the vectoring needed for transition from jet-borne to wing-borne flight.

2) Using air bled from the engine compressor and supplied to a separate control system.

From the earliest days the latter option has been the favoured choice because of the ease of controlling such systems. However, the first method is gaining in popularity due to the increasing ability to automatically govern aircraft stability. Military aircraft design in this country still follows the separate control system approach, as exemplified by the British Aerospace Harrier.

This programme of work is related to the design of British Aerospace's next generation STOVL (Short Take-off Vertical Landing) fighter/attack aircraft. The need for increased control power has been identified in this project. Utilising engine compressor air for control is an inherently wasteful process and leads to an immediate reduction in available propulsive thrust. The need for increasing the thrust available for control is obvious.

Background to the use of ejectors in aircraft

All earlier aircraft-related work on thrust augmenting ejectors has been carried out with the alternative objective of enhancing engine thrust. However the specific aim, for VSTOL purposes, has always been to develop a system for use only in the take-off/landing and

transition phases of flight.

Combat aircraft engines are sized to cater for maximum take-off weight, minimum take-off run, specific excess power in combat, and in the case of STOVL aircraft, landing weight. All of these criteria involve running at or near full power, when engine performance is markedly different to that required for cruising. Consequently a full power augmentation system cannot be expected to work at all in the cruise unless major variable geometry features are added. Dedicated cruise augmentation has been used in a few conventional aircraft, eg. Saab Viggen and Lockheed SR-71A, to improve range performance by admitting secondary air to the jet pipe. Combat augmentation has not been attempted due to the impossibly severe inflow/outflow conditions experienced as the aircraft manoeuvres. There could also be adverse effects of the transient entrained flow over aircraft surfaces.

This only leaves the take-off and landing condition amenable to augmentation, but even this area has met with failure. The Lockheed XV-4A Hummingbird was a bold attempt to augment thrust in VTOL flight stages. It's lack of success was due to the paucity of ejector experience in the 1950's and 1960's. Much more effort was put into the Rockwell XFV-12A project of the late 1970's. This aircraft failed to become airborne, which highlighted the extreme difficulty of translating a promising laboratory ejector into real hardware. Severe flow separation problems at the ejector inlet were experienced which mitigated against good performance.

The scope of this research

The aim of this programme of work was to contribute to the development of a useful thrust augmenting ejector for controlling purposes. It was apparent that a control system ejector would have to operate at a design point very different to that at which previous ejectors have operated. Engine bleed air would by necessity be at both high pressure and temperature. A thorough literature survey of the entire field of aircraft ejectors was conducted and the findings are described in Chapter 2. It became clear that the severe nature of the specification excluded the use of most existing

ejector techniques, and so a unique approach was necessary.

All ejectors have a basic need to achieve good mixing between the two flow-streams. From the literature survey there was a lack of previous experience in the interaction of high pressure jets and their surroundings in the context of ejectors. It was therefore reasonable to base the project on a study of high pressure jet mixing. The work evolved into a largely experimental exercise for two reasons.

1) The need to acquire a mass of jet data in an area devoid of it at the present time. This would allow prediction methods of jet and ejector behaviour to be evaluated at a later date.

2) The extreme difficulty of producing accurate theoretical models of the macroscopic characteristics of complete high speed jets. It is sufficient at this stage to note that even the field of incompressible jet modelling is still the subject of vigorous debate. As a supersonic jet is bounded by subsonic regions, where the viscous mixing occurs, the difficulty of patching a complete solution can be appreciated. There are no computational simulation packages yet available which adequately address the whole problem. In the current exercise, where the jet mixing is the primary concern, it was felt best to avoid a full theoretical analysis of this uncertain area of jet prediction.

Notwithstanding the two reasons just stated some effort was expended in using an existing commercial flow simulation package for one aspect of the work. A global prediction of the behaviour of various high speed jet flows was attempted, more to ascertain the applicability of non-specialised models than for comparison with the experimental results.

Specification for the control ejector

A typical Harrier reaction control nozzle has an area of approximately 5800 mm^2 and is required to deliver about 6000 N of thrust. The air supply currently used has an engine bleed pressure of about 17.6 bar gauge (255 psig), giving a total pressure

available at the nozzle of less than 13.8 bar gauge, (200 psig). Air total temperature does not exceed 600 K.

Future ASTOVL aircraft will require control power at least 100% greater than has the Harrier family. A graphic statement of the detrimental effects of such a bleed demand on aircraft take-off weight is given in Bore, Williams and Riddlestone (1983). The proposed engine for the ASTOVL machine will provide higher pressure air, say greater than 20 bar, at temperatures above 750 K. Precise figures are sensitive but can be found in Bore (1984). For the purpose of this investigation it is acceptable to work on the basis of at least 15 bar, 750 K being available at the reaction control nozzle.

Space and weight considerations are of prime concern; the only comment suitable in the specification would be "as small and light as possible". Approximate target dimensions are given in Miller (1987a), as are the performance goals.

In the final installed form the control ejector must be capable of precise thrust modulation, preferably not in a manner which wastes engine bleed, eg. control by spoiling the diffuser effectiveness is pointless. The ability to maintain operation with up to 150 knots (80 m/s) flow across the ejector is also essential.

Principles of thrust augmentation

The basic principles of thrust augmentation can be described as follows. An air jet (the primary flow) is used to entrain secondary air by the process of viscous mixing in a duct system. Figure 2.1 is a simple outline of an ejector with the component parts identified. The device is designed so that the secondary flow passes over an upstream facing surface of the duct, thereby producing a sub-atmospheric pressure on that surface. This area of reduced pressure provides a net thrust force additional to the normal stream thrust of the primary jet.

As a first approximation a thrust augmentation factor can be conceived as the ratio of primary plus secondary thrusts to primary

thrust alone. Values of augmentation ratio of 1.6 would be quite satisfactory for proposed aircraft if they were achievable in both static and forward flight conditions. A lower limit to useful augmentation ratio exists where the weight and installation penalties are not compensated for by enough additional thrust.

The structure of this report

A summary of the findings of the literature survey and the directional influence given by earlier work is presented in Chapter 2. The complete experimental facility used in the tests in described in Chapter 3, with the theoretical process used to design the primary nozzles following in Chapter 4.

The major experimental activities of the research are reported in Chapters 5, 6 and 7. A detailed study was made of the behaviour of free sonic and supersonic jets as they mix with the surrounding air. Various scale notches were then machined around the nozzles to try to improve the mixing. These notches created a previously undiscovered mixing mechanism. The results from the free jet tests were very encouraging, with large improvements in jet mass flow downstream of the nozzle.

The nozzles were then re-tested when situated inside a square duct device constituting the fundamental features of a thrust augmenting ejector. No attempt was made to optimise the geometry of this ejector, but the increased mixing evident with certain nozzles produced corresponding increases in ejector performance.

Included in Chapter 5 is a brief discussion on the applicability of a commercial finite difference code in predicting the properties of an underexpanded free jet flow.

Chapter 8 discusses the ejector performance achieved in Chapter 7 in context with previous work. An attempt is then made to apply all that has been learnt in the course of this research to the design of a high pressure ejector configuration suitable for controlling VSTOL aircraft. The Conclusions and Recommendations are finally presented as Chapters 9 and 10.

2. THE LITERATURE SURVEY

2.1 Introduction

The purposes of this chapter are twofold. Firstly the work uncovered on the thrust augmenting ejector by a comprehensive literature search is presented, including related topics such as mixing processes and diffuser design. Secondly the features of ejector design which appear to possess the greatest chances of development are highlighted and the particular direction chosen for this research programme is detailed.

2.2 Literature survey of ejectors and confined jet mixing

This literature search initially identifies the early roots of ejector research, and then describes the progress made in ejector technology during the last twenty years. Lastly the topic of confined jet mixing is examined as it was essential to gain an appreciation of the physics of the ejector flowfield.

The majority of thrust augmenting ejector research has been conducted in the United States under funding from military agencies. Almost all of this research has been aimed at augmenting main engine thrust for the take-off/landing condition. No work has been reported on ejectors suitable for operating at the conditions present in an attitude control system.

A comprehensive presentation of a literature survey having the same terms of reference as this chapter is presented as a British Aerospace report, Miller (1987b). The report considers the subject in far more detail than is needed here, and contains references to papers which were not known to the author at the time the research was being conducted. In some respects therefore, the remainder of this chapter is a précis of Miller (1987b).

2.2.1 The early work and basic principles

The earliest useful recorded comments on thrust augmenting ejectors applicable to aircraft appear to stem from research performed in

Germany in World War Two. Von Kármán produced a paper soon after the war, von Kármán (1949), in which he states the basic concepts of ejector augmentors and proposes simple means of analysing their performance using only momentum considerations. Even though quite simple in style this paper laid a solid foundation for all subsequent ejector work and it is instructive to summarise the analysis. Figure 2.1 will be used throughout this chapter as an example of simple ejector configurations, and is suitable for explaining the methods of von Kármán if the diffuser is ignored. Assuming incompressible and inviscid flow, the continuity and momentum equations for the device are respectively:

$$A_s u_s + A_p u_p = (A_s + A_p) u_2 \tag{2.1}$$

$$A_s \left(u_s^2 + \frac{p_1}{\rho} \right) + A_p \left(u_p^2 + \frac{p_1}{\rho} \right) = (A_s + A_p) u_2^2 \tag{2.2}$$

These two equations assume uniform inlet conditions at station '1' and uniform, ie. mixed, flow at '2'. The static pressure at '2' is taken as atmospheric. Using Bernoulli's equation (2.1) and (2.2) can be manipulated to a quadratic in u_2/u_p. The equation can be simplified if A_s/A_p is large to the form,

$$\frac{u_2}{u_p} = -\frac{A_p}{A_s} + \sqrt{2 \frac{A_p}{A_s}} \tag{2.3}$$

The total thrust, F, of the device is equal to the exit momentum at station '2'.

$$F = \rho (A_p + A_s) u_2^2 \tag{2.4}$$

Von Kármán (1949) defines the thrust augmentation ratio Φ as,

$$\Phi = \frac{F}{\rho A_p u_p^2} \tag{2.5}$$

so

$$\Phi = \left(1 + \frac{A_s}{A_p} \right) \left(\frac{u_2}{u_p} \right)^2 \tag{2.6}$$

Thus Φ is shown to be a unique function of the primary to secondary area ratio. In fact von Kármán's definition of Φ is not based on very rigorous arguments and it would be wise to discard equation (2.5) in future analysis. However, substituting (2.3) into (2.6) produces the classical result that Φ increases with area ratio and has a limiting value of 2.0 . Von Kármán does not consider the use of diffusers but includes an interesting comment on the effect of deliberate skewness in the quantity u_s. In the context of ejector flows the skewness β is defined as

$$\beta = \frac{\overline{u^2}}{\overline{u}^2} \qquad (2.7)$$

across a section where u varies. It is shown that by increasing β the same process that produced equation (2.6) would lead to a higher value of Φ at a given A_s/A_p . This analysis and application is described further in Section 2.2.3 .

The work of Kohlman (1980) presents a simple analysis for a diffuser-ejector, where the same equations are solved as von Kármán (1949) but also included is a diffuser area ratio such that Figure 2.1 is a complete representation of the problem. The final velocity u_3 is again assumed to be uniform. The result of the analysis is an equation for u_3/u_p in terms of the three areas. Adding a perfect diffuser improves performance due to a reduction in the exit kinetic energy of the system. The simple arguments about optimising geometries are well explained using graphs of Φ against area ratios. It is useful to emphasise two very fundamental points at this stage.

1) Both von Kármán and Kohlman assume complete mixing of the primary and secondary streams. This assumption has little practical significance unless either special steps are taken to accelerate the mixing, or a long mixing length is acceptable. It will become apparent throughout the remainder of this chapter that the achievement of complete mixing is the main difficulty for ejector designers.

2) The excess thrust achieved by an ejector is manifested as a suction force on the ejector secondary inlet; this thrust is

equivalent to the inlet secondary momentum. If the primary mass flow is not limited it is possible to achieve an additional increment in primary thrust due to the reduced exit pressure at the primary injection plane.

2.2.2 The 1970's work by the U.S.A.F. on lift augmentation

Throughout the period of the 1950's to 1970's most of the major U.S. aircraft manufacturers considered thrust augmenting ejectors to be worthy of inclusion in their research programmes. Most of the ideas that were generated never progressed beyond the project office, and those concepts which were the subject of more detailed investigation carried security restriction. This lack of information is not a great handicap to the researchers of today because nothing worthy of development was achieved in the research laboratories. As mentioned in Chapter 1, there was one moderately successful ejector lift aircraft, the Lockheed XV-4A Hummingbird. This machine proved that ejectors could be installed in a dedicated airframe but the weight and space limitations made the aircraft all but useless operationally.

The starting point for this survey was therefore chosen to be the work in hand through most of the 1970's at the United States Air Force Energy Conversion Research Laboratories (E.C.R.L.). The precise application for this work has never been made clear, but most probably it was conceived to form a broad base of information for a late 1970's advanced VSTOL fighter aircraft.

The configuration of Fancher (1970), Figure 2.2, is a good example of early low pressure E.C.R.L. work. The primary air is brought to two plenum chambers and then directed out through a series of lobed nozzles. Performance does not exceed $\Phi = 1.75$ with Φ defined as

$$\Phi = \frac{\text{Total ejector thrust}}{\text{Isentropic thrust of primary mass flux}}$$

Fancher (1972) and Quinn (1972a) develop the configuration of Fancher (1970) but with the addition of a geometric modification to

the nozzle, Figure 2.3 . The 'hypermixing' nozzle, as it has since become known, is first described by Eastlake (1971) and the two types under development are shown in Figures 2.4 and 2.5 . By imparting opposing transverse velocities to adjacent portions of the primary jet a streamwise vortex is created at the boundary of the two streams. The additional vortex increases the entrainment capability of the jet.

Fancher (1972) develops an analysis method which has become known as a 'one-dimensional' model. The continuity, momentum and energy equations are combined in a manner not dissimilar to that of von Kármán and solved for u_s and u_3 from Figure 2.1 . Quinn (1972a) further improves the hardware and analysis of Fancher with the addition of a much more complex primary injection system. The maximum Φ achieved is approximately 1.65 and performance is shown to be independent of injection velocity at low pressure.

Quinn (1972b) proposes another incremental improvement in hypermixing ejector technology by making minor modifications to the wall jet blowing geometry. It is shown that keeping the flows attached throughout the ejector is of prime importance. The paper also considers the effect of plausible ejector losses on the thrust performance.

The problem of optimising the ejector mixing length is the subject of Quinn (1973a). Free jet entrainment techniques are developed to predict when mixing will be complete. It is demonstrated that such methods are applicable to confined jet predictions.

Campbell and Quinn (1973) and Brown and Murphy (1974) describe experiments in which the designs of Quinn and others are scaled up (and sometimes simplified) to enable installation in a representative wing. The two reports have rather different conclusions. The former suggests that direct scaling up has validated the use of small scale models for laboratory tests, whereas Brown and Murphy show that it is easy to introduce severe losses with minor engineering modifications.

Yet another 'one-dimensional' model and some validating experiments are detailed by Bevilaqua (1974). The effect of hypermixing nozzle aspect ratio is investigated and an optimum aspect ratio of 8 is discovered, see Figure 2.4 . The presence of an optimum is attributed to interference between adjacent vortices if the hypermixing segments are too short.

Bevilaqua (1976) describes more hypermixing experiments but the main interest is the use of a finite-difference code. The downstream behaviour of a free hypermixing jet is well predicted but it is unclear if the nearfield region is sufficiently accurate for ejector use. The model uses an additional Reynolds stress to represent the hypermixing vortex, but the size of this stress needs prior knowledge of the vorticity created by the nozzle.

All the analysis of the E.C.R.L. so far reported has been low speed and incompressible. Nagaraja, Hammond and Graetch (1973) present a compressible 'one-dimensional' flow model. The equations are far more complex than low pressure methods, and it is shown that performance should decrease with a pressure increase.

Quinn (1975), (1976), (1977) and Rosjford and Toms (1975) all cover various aspects of the same high pressure ejector programme. A 'one-dimensional' model is presented for a compressible solution of a simple axisymmetric ejector with no diffusion. Performance of an experimental device is well predicted but the aeroacoustic phenomenon of screech is present which causes accelerated mixing. It appears that acoustic resonance will fix the shear layer vortex frequency and strengthen the vortices ability to entrain flow. The passage of the jet vortices through the shock system is itself the cause of the screech tones, so the process is self-sustaining at certain conditions. The overall performance of high pressure ejectors is shown to be much worse than low pressure devices, but the occurrence of resonance can dramatically improve the thrust of short ejectors.

2.2.3 The remaining literature on low pressure ejectors

This section provides a summary of all other relevant ejector literature on the restricted subject of low pressure devices. The layout will cover papers written since 1969 in approximately chronological order.

The ejector wing developed and flown by De Havilland Canada on the Buffalo/Spey Jet-STOL Research aircraft is described in Whittley (1972). Most of the ejector design was carried out in the late 1960's, and the final configuration was a single Coanda surface device functioning in a similar way to a blown flap.

Alperin, Harris and Smith (1969) test a Coanda type ejector in which the Coanda surface is replaced by a series of aerofoil sections. Entrained air is allowed to join the primary jet by passing over the aerofoils and thereby generating additional lift. Figure 2.6 shows a sample geometry of this very unusual technique.

Jones (1975) furthers the discussion started by von Kármán concerning secondary flow skewness, and again concludes that skewness would be beneficial. Jones is the most valuable source of definitions pertaining to ejectors discovered in the search, but no new theories or experiments are presented.

Skoblenick and Hill (1977) run an axisymmetric ejector at conditions just sufficient to choke the primary jet, the main purpose being to provide a validating case for a finite-difference code. The prediction program needs separate prescription of the eddy viscocity in the many parts of the flowfield that are identified. With the inclusion of this prior knowledge (taken from a whole range of fluid flow experience) the method produces accurate values of wall pressure and wall shear stress. The results suggest that codes of this type do have applications to simple ejectors.

DeJoode and Patanker (1978) also use a finite-difference code but with a k-ε turbulence model. The problem is solved as a three-dimensional parabolic case, but the geometry, see Figure 2.7, is rather different to any previously reported. The overall flowfield from the nozzle is well predicted, and it is interesting to see that the level of inlet turbulent kinetic energy is shown to be unimportant in relation to the turbulence generated in the mixing process.

Seiler and Schum (1978) describe the optimisation process for the diffuser used in the Rockwell XFV-12A technology demonstrator. The philosophy behind the augmentor wing programme and the operational characteristics of the XFV-12A are fully detailed in Janes All The World's Aircraft 1979-80 (Taylor (1979)). Seiler and Schum use a geometry similar to DeJoode and Patanker (1978) in the tests, see Figure 2.7. The conclusion is that a trumpet shape diffuser is better than a conventional straight wall type of the same area ratio. The reason proposed is that the shape imparts enough streamline curvature at exit to allow further compression (ie. diffusion) to occur outside the diffuser. Crucial to this process is the need to keep the primary flow attached to the trumpet walls, achieved in this case by considerable secondary wall blowing. The proposal of such a mechanism is very interesting because the ejector hardware can be kept very short if diffusion is occurring outside the bounds of the geometry. It is important to note that everywhere across the diffuser exit plane the flow is subsonic, the Mach number typically not exceeding 0.3 .

Viets (1975) and (1981) combine to provide a summary of augmentors which achieve rapid mixing by introducing an unsteady component into the primary flow. The imposition of time dependence introduces a mixing mechanism based on normal stresses as the pressure pulses pass through the flowfield. Such normal stresses are considered more efficient at causing mixing than the usual shear mechanisms.

The flapping nozzles, see Figure 2.8, work by scooping part of the primary flow from the side of attached flow and feeding it upstream.

This transmission of low pressure fluid causes the whole jet to switch attachment to the other surface. The nozzles are shown to be effective at improving the thrust of very short ejectors.

Binder and Didelle (1981) also introduce unsteadiness but this time by an independent switching signal. Again the benefits are readily apparent. Binder and Didelle also contains a refreshing view of ejector principles and highlights the difficulty of defining Φ for the unsteady case.

A review of ejectors applicable to aircraft propulsion was presented by Quinn to the 1981 AGARD conference on VSTOL Aerodynamics. The one major mechanism to improve jet mixing discussed in Quinn (1981) but not yet covered in the present literature search is that of external acoustic stimulation. For subsonic jets rapid increases in mixing can occur in the early stages of the jet development, but the sound power level required can be very large, values up to 38 dB over the ambient noise level are discussed.

Quinn (1981) concludes that the inability of analytical models to predict ejector performance is due to the lack of information about the turbulent stresses inside the mixing duct. If such data could be incorporated in the thermodynamically exact flow equations then all aspects of the flow would be specified and solution would be solely a computational problem.

The most exciting progress in low pressure ejector design for many years is discussed by Alperin and Wu (1981). This work is rather unique in that the authors attempt to apply a potential flow model in a way which optimises the ejector geometry. Once again the application is at a low pressure ratio of 1.25, but important results are achieved which are relevant to higher pressure work.

The earliest reported geometry is shown in Figure 2.9 . The primary flow is injected from two plenum chambers rather remote from the shroud, but the main feature of the device is the absence of a parallel mixing section. The extremely large area ratio diffuser is

used as a mixing section, but is only made effective by the addition of substantial wall blowing in the region of the throat. The endwall also has a blowing slot, not shown on Figure 2.9, but augmentation is only achieved in quantity if sizeable endplate extensions are fitted to protrude beneath the device.

The wall blowing is such that a thin sheet of air is ejected from the entire periphery of the diffuser exit, thereby acting as a boundary inside which the flow continues to diffuse. This process is based upon similar ideas to those of Seiler and Schum (1978). Values of Φ up to 2.18 are achieved by this jet-diffuser ejector. The ability of the jet sheet to sustain transverse static pressure gradients is crucial to this 'free-space' diffusing. If the endwall extensions are absent it appears that the endwall jet sheet is unable to bear the required pressure differential, and the device behaves as if only the solid diffuser is operating.

Alperin and Wu (1981) then describe an ingenious theoretical method for designing an improved three-dimensional diffuser-mixer using potential flow theory. A complex vortex ring is constructed at the ejector throat which produces the correct throat flowfield. The diffuser walls are then successively modified until the maximum predetermined streamwise pressure gradient is achieved. This method produces a very complex curved diffuser shape with $\Phi = 2.12$, but the overall diffuser length is far less than before, and there is no need for the endwall extensions.

A further exercise conducted by Alperin and Wu (1981) is the optimisation of the primary nozzle type and location, as shown in Figure 2.10 . The resulting design injects the primary flow from a series of separate round nozzles mounted on the shroud and inclined at 30° to the ejector thrust axis. The inclined jets appear to entrain more secondary air than would result from axial injection; a similar basic feature is found with inclined jets in cross-flow. It is shown that to avoid secondary flow separations the primary nozzle mounting has to be designed with great care.

2.2.4 The remaining literature on high pressure ejectors

This section discusses work on ejectors operating with choked primary jets and high speed secondary flows. A fundamental change in the nature of the high pressure work will be apparent. Very little thought has been given to real ejector geometries suitable for use in a propulsion or control system. This is in contrast to the low pressure work when achieving a practical device is usually the driving factor in the design.

Chow and Addy (1964) present a detailed attempt to understand the complicated flow patterns in an axisymmetric supersonic ejector. Figure 2.11 represents the problem which is seen to differ from that shown in Figure 2.1 by the significant expansion of the primary jet on leaving the nozzle. Figure 2.11 shows a convergent-divergent primary nozzle but the theory presented allows the nozzle exit pressure and Mach number to be set independently. The work is not an easy report to interpret as it contains many concepts which were only just becoming understood at the time of publication. Its main purpose is to construct a theoretical model that will predict ejector flow parameters with a choking secondary stream, and the necessary conditions for such a flow are discussed. A further complication is that the theory allows the secondary air to be drawn from a reservoir at a pressure different from ambient. The more usual case of ambient stagnation conditions is covered but it is difficult to extract the information. All the theories and experiments are evaluated at very low area ratios in order to achieve secondary flow choking, an area ratio of 3.1 being typical.

The flow model developed uses an axisymmetric characteristic process for the primary jet structure. The solution for the underexpanded jet results in a certain minimum flow area for the secondary air. Isentropic relationships are used to calculate the pressure existing at this point of minimum area. The characteristic procedure is then repeated with the primary jet expanding to the new pressure. The whole process is iterated until the secondary flow is found to choke.

The reference Chow and Addy (1964) identifies conditions when it is essential to take into account the viscous interaction between the two streams as well as the inviscid process described above. The proposed viscous procedure uses an integral mixing method to solve the flow parameters at the boundaries of the two streams.

For the case of unchoked secondary flow the high pressure analysis is reduced to little more than a 'one-dimensional' scheme. All the theories presented by Chow and Addy accurately predict the experimental validating cases, but it should be emphasized that considerable thought is needed to identify the correct part of the theoretical model for the regime in question. The model is certainly not a unified ejector theory.

Benson and Eustace (1973) is an extension of Chow and Addy (1964) with the discussion presented in a clearer form. The geometry is changed from axisymmetric to two-dimensional plane ejectors. A similar primary-characteristic / secondary-isentropic process is performed to predict the conditions of secondary flow choking but the model is restricted to the far more common case of ambient secondary air. A similar viscous model is used to account for the secondary flow entrainment.

The theoretical predictions clearly show that the viscous correction is only important at very low secondary flows, ie. when the primary jet expands to fill almost the entire duct. The results of the characteristic predictions are interesting in their own right because the ducted jet is shown to behave in a rather different fashion to an equivalent free jet. This is due to the longitudinal external pressure field changing the way in which the shock waves are reflected at the jet boundary.

The theory is tested against a very long two-dimensional ejector equipped with wall static pressure tappings and allowing optical visualization of the primary and secondary streams. Both schlieren and Mach-Zhender interferometer images are presented which show that the theory predicts the flow patterns very well. It must be remembered however that the theory has no means of predicting or

accounting for shock waves. Consequently the method is only applicable for situations where weak shock waves are present, therefore severely underexpanded primary jets cannot be modelled.

The critical discussion included after the paper of Benson and Eustace (1973) is valuable. The merits of using convergent-divergent nozzles and the prediction the optimum ejector length are examined. The difficulties of adapting the model to include wave effects are also highlighted.

A useful summary of the basic performance of a simple supersonic axisymmetric ejector is provided by Cheng and Wang (1973). The experimental apparatus can be represented by Figure 2.1 without the diffusor. Cheng and Wang use a very simple flow model to predict the jet growth from a convergent nozzle, thereby predicting duct diameter and length. However, the basis for this model appears unsound. Subsonic free jet data are used to predict the angle of divergence of the jet plume, with the justifying argument that "in slightly supersonic flow the similarity condition is expected to hold". This is unlikely to be true because the pressure ratio range of the tests is 3.0 to 5.0, making the jet severely underexpanded. It is possible that well downstream of the nozzle, of the order of 8 diameters, the primary flow might behave in a self-similar fashion, but the ejectors under investigation are in fact short devices.

The report does, however, provide good experimental data. It is shown that increasing the shroud diameter (the area ratio A_s/A_p) improves the thrust, and that, whereas a maximum thrust is reached at a mixing length of 5 injection diameters further extension of mixing length has no effect.

The variation of the axial injection position in relation to the start of the mixing duct is an interesting parameter because of the lack of research from other sources. Unfortunately it is not clear from the notation exactly where the datum for longitudinal measurement is taken. However, it appears that withdrawing the nozzle 2-3 diameters upstream provides most thrust. This must be due to the underexpanded jet needing to expand closer to ambient

pressure before any large scale entrainment occurs.

Throndson (1973) is one of the few high pressure experiments which concentrates on geometric optimisation, and so is a very useful reference. Figure 2.12 shows four of the Coanda configurations tested at pressure ratios between 1.5 and 3.2 .

It is shown that conventional opposing Coanda surfaces work best, and diffusion is possible immediately after the inlet region. The most important result from Throndson (1973) is that quite severely underexpanded jets can be made to turn through 90° by tight Coanda surfaces without separation. The overall performance of Throndson's ejector is very creditable (Φ up to 1.4), considering that the ejector length never exceeds 4 times the cylinder spacing.

Gilbert and Hill (1975) use a finite difference scheme incorporating a mixing length model that requires separate prescription in all the different flow regimes. The work is similar to Skoblenick and Hill but the test cases are run at higher pressure. Very close agreement between computed and measured wall static pressures are observed. In addition traverse runs at various axial stations show good agreement. Sensible variations in the prescription of the mixing length, and therefore eddy viscosity, are shown to have very little effect on the computational results.

Miller and Whittaker (1983) provide a description of some experiments conducted in the early stages of the British Aerospace reaction control augmentation programme. Two Coanda blown cylinders are set between endplates with a 'separator' strip mounted under the cylinders to detach the Coanda jets, see Figure 2.13 . Variables tested include cylinder gap and injection angle at constant primary pressure ratio of 3.0 . The performance is recorded by traversing the ejector exit plane with pitot-static tubes.

Unfortunately the accuracy of the measurements is not high, but it is shown that blowing at large angles to the ejector axis increases

thrust whereas varying the cylinder gap (area ratios in the range 6 - 17 are tested) has no consistent effect. An instability is noted at narrow gaps whereby the flow separates from one wall; this being attributed to the over-rapid diffusion ratio created with the cylinders close together.

An earlier exercise using the same test rig, recorded by Smith and Bollands (1982), measures only the mass entrainment. Values of secondary to primary mass flow ratio up to 1.75 are recorded.

The topic of supersonic ejectors for aircraft cruise is the subject of a series of papers by Alperin and Wu. The first publication, Alperin and Wu (1983a), identifies the particular difficulties encountered when the ejector is translating forward at speeds up to $M = 2.0$. The energy, mass and momentum equations are solved in a compressible form for the Mach number at the end of the mixing section, effectively just another 'one-dimensional' solution process. Alperin and Wu (1983a) assume uniform jet properties and lossless fully mixing flows. It is shown that the exit Mach number equation is a quadratic; one solution being subsonic and the other a uniform supersonic value which is given the title 'second solution'. It should be noted that the description of the flow phenomena adopted by Chow and Addy (1964) of 'supersonic' and 'mixed' is rather different because they only consider flow properties close to the injection plane.

The analysis of Alperin and Wu is conducted over a range of secondary throat Mach numbers, the effects on the flow pressures and Mach numbers in the duct being recorded. It is indeed possible to produce a theoretical device operating in the 'second solution', albeit highly constrained by the need not to violate the second law of thermodynamics. From this theoretical data can be ascertained whether the ejector will need convergent, divergent or convergent-divergent inlets and outlets. All combinations of these inlet/outlet geometries are useful in some part of the operating envelope. It should be emphasized that 'first solution' ejectors are not restricted to conventional configurations with convergent inlets and divergent diffusers. Having established the existence of the two

regimes Alperin and Wu (1983a) continues to concentrate only on the 'first solution' type of device.

By careful selection of the inlet and diffuser the ideal performance of the 'first solution' ejectors is shown to be very good but the attention given to loss mechanisms appears to be less than adequate. However it is possible to deduce certain important results from this work.

1) Performance declines rapidly with increasing injection pressure at static conditions.

2) High temperatures associated with high pressures produce acceptable thrust performance.

3) Forward motion of the ejector generally reduces performance but compression effects in the inlet can sometimes be beneficial.

Alperin and Wu (1983b) contains a similar theoretical investigation of supersonic ejector design to that of Alperin and Wu (1983a) but the emphasis is moved to 'second solution' devices. Once again the authors predict performance up to a flight speed of $M = 2.0$, primary pressure ratios up to 20, and temperatures up to 3000°C.

At zero forward speed the 'second solution' is shown to be useful only at pressures ratios less than 5.0, and moderate temperatures. If the ejector is translating forward at $M = 2.0$ the maximum augmentations achieved are much lower than at zero speed. In addition, if comparison is made with Alperin and Wu (1983a) then the equivalent 'first solution' device works better.

Alperin and Wu (1983b) then address the more practical side of supersonic ejector design with consideration given to the ejector outlets. Crude variable geometry is theoretically effective at coping with a similar starting shock wave problem to that encountered in supersonic wind tunnels.

These two papers of Alperin and Wu put forward some radical ideas for high pressure ejectors, albeit an entirely theoretical proposal, and it was essential to establish whether the proposed benefits could be realised in practice, this being the purpose of Wu (1986).

The difficulty of rigorously testing a 'second solution' device is well outlined in Wu (1986). All of the tests are run at a high subsonic 'flight' Mach number, M = 0.5 - 0.8, which is achieved by injecting the secondary air at the requisite pressure. It is rather unfortunate that no runs are made at zero forward speed because, although the second solution is hardly beneficial, they would provide good datum cases.

Having attempted to show that 'second solution' devices are useful it is clear that Wu (1986) presents a unconvincing case. It is true that the 'second solution' can be made to occur, but the performance at these flight speeds is little better than the optimum 'first solution' answer. The variable geometry outlet required to start the ejector presents large losses, as do the inlet wave effects. Theory predicts an increase in thrust with temperature but Wu (1986) fails to prove this in practice.

Abdel-Fattah (1984) is a rather isolated piece of research into very high pressure ejectors which contains a lot of interest. The author specializes in analysing two stage ejectors, see Figure 2.14, at pressure ratios up to 50. With the range of pressures and temperatures under consideration the theoretical ejectors could obviously run in the 'second solution'. This problem is deliberately avoided by only considering large area ratios so that $M_4 < 1$ and $M_3 < 1$. The analysis proves that such large pressures need very large area ratios for conventional operation. Values such as $A_3/A^* = 800$ are applicable.

The results of Abdel-Fattah show quite conclusively that multi-staging is not useful at these very high pressures and temperatures. The report clearly states the algorithm needed for solution of the governing equations.

2.2.5 Confined jet mixing

Further references covering the mixing phenomena have been studied. Other topics, such as diffuser design, are also widely covered in the literature but the applications are not specific enough for consideration in ejectors.

Rajaratnam (1976) contains a large section on ducted jets, which includes clear statements of the continuity and momentum equations applicable to axisymmetric and plane incompressible jets in ducts. A comprehensive comparison of methods is presented and two solution techniques are evaluated; similarity, and the solution of the integral forms of the flow equations by numerical means. It would appear that the integral methods are superior for predicting the flows because they cope well with the large number of possible flow regimes which could occur in the general case. Solution of the differential forms of the momentum equations is not considered.

Hill (1965) is an attempt to predict ducted jet behaviour using jet growth data gathered from free jet tests. Integral solutions are developed which are based upon the self-preserving nature of the free jet circumstances. The technique is shown to be acceptable for certain ranges of primary to secondary velocity ratio, hence ducted flows can be self-preserving. Even regions of recirculation are successfully evaluated using the assumption of constant static pressure in these zones. Although real ejectors have been shown, Quinn (1972b), to be susceptible to wall friction, Hill (1965) ignores this feature.

Curtet and Ricou (1964) and Barchilon and Curtet (1964) are papers concerned with establishing how applicable self-preserving assumptions are for jets in ducts. These two references have become a classical part of the literature because they introduce parameters that allow classification of the flow regimes. There is agreement between Curtet and Ricou (1964) and Hill (1965) that the

mean velocities obey similarity rules, but the former reference shows that the unsteady velocity component distributions are not of a self-similar form.

Barchilon and Curtet (1964) allow the ducted flow to contain a recirculating region. The phenomenon of recirculation occurs under certain conditions when the secondary flow is fully consumed by the primary jet before the primary jet spreads to reach the duct wall. Difficulties are encountered in measuring the reversed flows in the experimental exercise. However it is found that the analysis of Curtet and Ricou is not suitable for such recirculating flows.

Razinsky and Brighton (1971) provides an extensive collection of experimental data, including turbulence quantities, in a mixing duct. The pressure recorded on the duct wall is shown initially to rise with longitudinal distance from the injection plane as the viscous mixing process results in a drop of mean kinetic energy. A maximum is then reached before the pressure falls as the high velocity flow adjacent to the wall causes increased wall friction. It is shown that the two streams are not fully mixed at the point of maximum pressure.

Tyler and Williamson (1980) use the data of Razinsky and Brighton (1971) to evaluate an empirical model of an incompressible axisymmetric ducted jet configuration. The approach adopted in Tyler (1980) is rather different to those previously discussed for it uses ideas more relevant to ejector design. The skewness factor is incorporated and an empirical model is developed for the way in which the skewness changes along the duct.

The final paper to be considered, Tabakoff and Hosny (1972), covers the case of incompressible eccentric injection of a round jet in a round duct. It is proposed that the primary jet can be treated as having a self-similar profile, with a simple cut-off used when the jet hits one side of the duct. The analysis compares well with some simple experiments in terms of mean velocity profiles.

2.2.6 Summary of literature survey

Three points are worthy of emphasis in summarising the E.C.R.L. research work.

1) E.C.R.L. have conducted sufficient work to allow the construction of an efficient low pressure device based on hypermixers. The resulting ejector would be relatively compact, though quite complex, achieving a performance of $\Phi \simeq 1.8 - 2.0$.

2) The second area of the E.C.R.L.'s work, that of high pressure ejectors, did not progress beyond simple laboratory configurations. The screech tone phenomenon appears to produce substantial performance improvements, but would prove difficult to rely on in practice as controllable ejectors need smooth thrust modulation. The absolute thrust performance of high pressure devices is shown to be appreciably worse than low pressure augmentors. The effect of temperature is less easy to define, but the results show relatively small augmentation changes over large temperature ranges.

3) Very little thought has been given to thrust modulation other than by varying the primary pressure.

The work undertaken independently of the E.C.R.L. has only recently suggested sensible designs which could be installed in an airframe. In particular the work of Alperin and Wu (1981) has provided an idea for a device which has benefits over the U.S.A.F. programmes in terms of both reduced complexity and reduced length. There has been suprisingly little research conducted outside the U.S.A. on such a potentially useful propulsion concept.

The papers presented on high pressure augmentor research have shown an uncoordinated effort with widely varying goals. The work of Throndson (1973), and also Miller and Whittaker (1983) are the only exercises where the configuration design is addressed. It is not clear whether or not works like Chow and Addy (1964) and Alperin and Wu (1983a) and (1983b) have helped to achieve high performance

devices. Ejectors with supersonic secondary flows are very interesting mathematically with rather complex maxima and parameter dependences but there appears little hope for their use in VSTOL aircraft. For situations where ejector cross-sectional area is not of great importance Coanda style devices can be made to work. No practical high pressure devices which do not use the Coanda effect have been reported from sources other than the E.C.R.L.

2.3 Conclusions from literature survey

About 45 papers have been reviewed in this survey presented here. It is apparent that the flow mechanisms present in low pressure ejectors are well understood, even though full three-dimensional representation of the turbulent flowfield is not yet possible. Conversely, the rules governing high pressure ejectors are both more complicated and less defined. There has been a tendency for some authors to regard underexpanded primary jets as a simple extension of low pressure configurations, but the works such as Benson and Eustace (1973) and Alperin and Wu (1983a) show that this is incorrect. Not only can the jet structure affect the performance but the jet property changes can be considerable. The full compressible solution should be used, even if the resulting mixed stream is intended to be subsonic.

The construction of "one-dimensional" models involve large amounts of complex algebra, but the problem becomes trivial when coded into a suitable computer algorithm. It is this writers belief that well developed "one-dimensional" models, with empirical inputs, still present a necessary solution technique. The alternative philosophy of a computational fluids approach, with full regard taken of viscous mixing through a turbulence model, is also to be recommended. However the latter approach is more suited to those fully competent in the physics of turbulent flows. The use of the more classical techniques of integral equation solution have been explored and little more would be gained by further investigation of them.

2.4 The approach taken to thrust augmentation for the control ejector problem

At the start of this research exercise there were no constraints as to what form the programme should follow. The control problem specification was known, but the manner of solution certainly was not.

At the conclusion of the literature search a solid understanding of the state of ejector research had been achieved. The most obvious ommission is the lack of an existing suitable ejector to operate with the necessary high pressures. Indeed a large gap exists in ejector technology throughout the entire high pressure domain. One possible solution might have been the development of one of the high performance low pressure devices for operation at high pressure. However, on examining each of the previous ejector concepts there appeared to be good reasons not to proceed with this idea. A summary of the alternative ejector configurations and their expected characteristics at high pressure is now given.

1) Coanda devices always appear attractive because of the skewness they introduce into the secondary flow velocity profile. However Coanda ejector geometries require inlets that are long in one cross-stream dimension to provide uninterrupted Coanda surfaces, yet small in the other spanwise dimension to provide a suitable area ratio relationship. Consequently the aspect ratio of such augmentors will be high. This is acceptable if the application is main lift augmentation when a wing trailing edge provides the location, but control ejectors can be engineered into a design far better if the aspect ratio is close to 1.0 .

2) Introducing unsteadiness into the flow results in complex devices possibly including moving parts. However the use of very hot, high pressure air suggests the avoidance of deliberate complexity. In addition it would not be known if a fluidic switch type of unsteadiness could be introduced into sonic or supersonic flow.

3) The use of external noise to stimulate jet growth is quite impossible. Not only will the reaction control jets be a source of extreme noise themselves (Harrier nozzles produce about 165 dB) but the whole airframe is the source of many acoustic signals. It is indeed possible that previous ejectors have failed to operate in real aircraft environments due to substantial acoustic interference.

4) The use of the well proven hypermixer nozzles certainly appears hopeful, but the augmentor configurations finally developed by the E.C.R.L. are very complex with numerous flow paths. The construction of the nozzles themselves would have to be substantially modified to take the large increase in primary pressure.

The previous high pressure ejector research had provided little configurational help for ejector design. The 'second solution' type ejectors of Alperin and Wu are suitable only for a specific cruise condition, and the achievement of realistic length has yet to be realised. The use of a two stage device is implausible for the same volumetric reasons.

The most promising configuration appeared to be some form of high pressure hypermixers integrated in the low pressure jet-diffuser scheme of Alperin and Wu (1981), Figure 2.10 . Numerous configurations were considered which fulfilled the geometric constraints of the specification but would only operate if rapid mixing was occurring. At an early stage it became apparent that geometric optimisation of a complete high pressure ejector would be premature because the state of high pressure mixing is not sufficiently advanced. In addition it was decided that an axisymmetric design was unlikely to be of use, due to the difficulty of integrating and manufacturing a shroud plenum chamber.

The achievement of rapid mixing is certainly the hardest part of the design concept to fulfill. Various ideas relating to increasing the primary jet surface area were considered, including some taken from recent work on bypass/core turbofan mixers, but it transpired that the answer lay with a return to hypermixer technology. In low speed

hypermixers streamwise vortices are created by directing adjacent jets at incidence to each other. The idea then arose to use the natural desire of an underexpanded jet boundary to diverge substantially from the thrust line on leaving the nozzle. If some part of the flow could be made to diverge before an adjacent section then possibly a streamwise vortex would form at the meeting of the two streams. The easiest means to effect such an interaction appeared to be by cutting a series of notches around the primary nozzle exit plane. An optimum form for such cut-outs was not known and no prior work was available to aid the design process. A study of the effects of changing the nozzle exit geometry was therefore identified as being a valid exercise.

The selection of the primary nozzle geometry for investigation immediately directed the whole exercise towards a study of high pressure jet entrainment, although the precise requirements for such a study were not obvious at the start. It was decided to initiate an experimental programme to examine free jet entrainment, leaving the more distant aims of the research programme initially undefined. A considerable effort was therefore put into developing a high pressure free jet facility.

Predicting theoretically the behaviour of the high pressure jet plumes was also desirable because the literature survey had revealed no prior work applying finite-difference methods to severely underexpanded jets. Unfortunately the predictive aspects which could be studied were limited by time to the brief evaluation of an existing finite-difference scheme.

The idea of developing a 'one-dimensional' model was discarded as being unlikely to involve any original work. Some of the previous 'one-dimensional' models have been well documented, making it an easy task to extract particular predictions for comparison with the experimental data.

3. THE EXPERIMENTAL FACILITY

3.1 Introduction

The aim of the experimental programme was to develop an understanding of high speed jet flows, with special emphasis being placed on entrainment properties and the behaviour of a jet in an ejector. A completely new rig was designed and built to allow this study to be performed.

3.2 General description of test rig

A major factor governing the type of tests possible was the state of the air supply available. As previously discussed real ejectors will have to use clean air (not exhaust products) at pressures up to 15 bar and temperatures of 750 K. It was not feasible to provide hot air for tests and the pressure was limited to about 7 bar gauge. The University of Bath high pressure system consisted of a 27 cubic metre reservoir at 29 bar gauge, with suitable pipe runs into a laboratory. The 7 bar limit was imposed by the use of an existing constant pressure control valve. The reservoir was charged by two Reavell two stage reciprocating compressors which passed the air through a carbon filter followed by an alumina dryer. Total charging time was of the order of two hours, whereas only a few minutes were needed to empty the reservoir.

The rig was designed to include, in order downstream from the constant pressure valve: a venturi to monitor mass flow; a settling chamber; an open test section and finally a large duct to capture the jet. Figure 3.1 shows the major features incorporated. Effectively the rig was therefore a blow down device with the air jet entering the room before being directed away as waste. The major design constraint concerned the working section which had to provide good access for an optical system and standard pressure measuring devices. Figures 3.2 - 3.4 provide overall views of the test rig.

The design point for rig operation was chosen as 6.9 bar gauge (100 psi) which then dictated certain features of the nozzle design. An arbitrary throat area of 950 mm^2 was fixed for all subsequent test

nozzles which (at 6.9 bar) gave a mass flow of about 1.8 kg/sec. At this mass flow the air reservoir lasted about six minutes before the constant pressure valve ceased to operate satisfactorily. It was also possible to run the rig at lower values of stagnation pressure.

The air disturbance in the laboratory was minimal with the open jet arrangement, the only environmental problem being noise. Comprehensive sound-proofing was incorporated which included placing a barrier between the working section and the rig control position, and covering the ceiling and some walls with sound absorbing material.

3.2.1 The venturi

Unfortunately it was impossible to install the venturi in accordance with a relevant standard ie. BS 1042, due to space constraints, so the venturi was calibrated against a simple choked orifice. Emptying the air reservoir at the chosen rate caused a marked decrease in stagnation temperature with time. This in turn affected the local sonic velocity at the orifice and also the air density. The result of these changes was an increase in mass flow during a run, which was catered for in the calibration.

3.2.2 The settling chamber and working section

Upstream of the working section was a short length of parallel pipe emerging from the settling chamber to which the various nozzles under test were fixed. The settling chamber contained baffles to ensure that the flow entering did not tend to penetrate to the exit without slowing down sufficiently for the stagnation properties to be determined. Both stagnation pressure and stagnation temperature were continuously recorded by the data acquisition system described later.

The nozzles were attached to the exit pipe by simple screw collets. However because of the difference in size and shape between a M = 1.0 and a M = 2.0 nozzle various intermediate rings were used to ensure that the upstream nozzle face was always at the same axial station. This ensured standard entry conditions for all nozzles.

Figure 3.5 portrays the geometry of the test section when used for free jet runs, and Figure 3.6 illustrates a selection of the nozzles and collets used.

When the rig was being used to determine jet behaviour in a duct an additional extension piece had to be inserted downstream of the settling chamber for reasons of geometry. This was found to have negligible effect on the flow losses.

The test section contained a traversing mechanism which allowed a single automated degree of movement laterally. Axial motion was also allowed but had to be manually set between runs. For further larger axial changes in position it was possible to move the whole traversing gear. The automated operation of the traverse equipment will be described in the later section on data acquisition. Probes used with the traversing gear were of three types:- pitot pressure, static pressure and conical nose angle. Height adjustment of the probes was catered for but all free jet runs were made with the probes on the jet centreline.

3.3 Traverse probe design

Sonic and supersonic jets contain areas of rapidly accelerating and decelerating flow which drastically reduce the effectiveness of normal pitot-static tubes, and so slightly unconventional probes were designed for use in this work. It was necessary to employ probes with stems of 12.7 mm diameter steel to reduce stem bending to acceptable levels. Fortunately the drag forces on the axial portion was still quite small allowing fine tubes to be utilised for these parts.

It was essential to study photographs of the jet structure before trying to use the pressure probes because it was impossible to gain accurate pressure readings close to the severe shock systems.

3.3.1 Static pressure probes

Figure 3.7 shows two of the static tubes used in the tests. Measuring static pressures in supersonic flows has always presented

difficulties and much effort has been put into static probe design, see Ower and Pankhurst (1977) and Pope and Goin (1965), however even the best probes devised were not ideally suited to this particular problem. Existing supersonic static pressure tubes usually operate in a constant lateral pressure field and only a slowly changing longitudinal one. However, in jet work none of these conditions apply. Very strong lateral static pressure variations exist in the jet edge; Mach discs occur at regular axial positions; and some large areas of flow divergence and convergence occur. A further complication was that the probe had to operate in entirely subsonic flow as well. In Chapter 5 and Appendix D a detailed examination of the static probe accuracy is presented, but a brief summary of the design constraints is given here.

The lateral pressure gradient problem could only be met by making the probe as fine as possible, but still with four holes around the surface to take an average value. The minimum practical diameter was found to be 1.24 mm with an axial length of 39.5 mm i.e. a fineness ratio of 31.9 . Any higher values of fineness ratio produced serious vibration problems. The resulting lateral spatial resolution was of the order of 1 mm .

The second area of difficulty, that of longitudinal pressure gradients was harder to counter. Traditional subsonic static tubes have holes placed at the position where acceleration effects of the air passing over the tube nose are countered by the upstream effects of the stem. Fortunately quite long axial probes were possible as previously mentioned but a totally new phenomenon was encountered which dictated placing the holes near the nose of the probe. It was found impossible to place a probe such that it "punctured" a Mach disc without totally changing the flowfield. The problem appeared to be that the high pressure behind the disc was being transmitted forward along the probe boundary layer. Figures 3.8 and 3.9 explain the mechanism involved. It was found that even if a body as fine as a needle was placed through a Mach disc the same phenomenon occurred. All these conclusions were reached after studying schlieren photographs of the flows. As a result the static pressure could not be measured close to a normal (or oblique) shock. To mitigate this effect the distance from the probe nose to the holes

had to be reduced as much as possible. Obviously this then introduced the concern that in a fully supersonic stream the bow shock of the probe could be having an unduly large effect on the measured static pressure. Various static tubes were tried with noses ranging from fine points to hemispherical. Only small variations in pressures were actually recorded and indeed photographs of flows with and without probes showed very little difference to the jet structure around the position of the forward end of the probe; the reason being that the extreme fineness of the probes produced very weak shocks.

The problem of flow incidence to the probe was impossible to remedy because, even if the local flow angle could be independently found, mounting a static tube at incidence to the mean flow was not possible.

3.3.2 Total pressure probes

Measuring total pressure entailed none of the severe problems just described, although there were some very small areas of uncertainty close to strong discontinuities. Placing the very bluff pitot tube, see Figure 3.10, in the flow totally changed the jet structure but in a way which was known, through normal shock relationships.

3.3.3 Conical nose angle probes

The third type of probe used was that with a conical forward section to achieve an attached conical bow shock. Many probes were made with differing nose angle but all had strong 12.7 mm stems see Figure 3.11 .

3.4 Data acquisition system

The data acquisition problem posed by the jet experiments was not seen to be especially severe. Obviously some form of traversing through the jet and monitoring jet pressures was required together with frequent checks on the stagnation conditions. The previously mentioned need to find total and static pressures separately suggested that the approach should be that of storing all data after

each run. Data reduction would then follow later. However because of the need to use the available air supply as efficiently as possible it was necessary to employ a fully automated data gathering system. The problem was not to obtain extremely quick sampling and storing but rather that of coping with up to 500 data points in a few minutes whilst controlling the traversing probe position.

It was found possible to buy an 'off the shelf' unit which fulfilled this requirement with only slight modification. The selected system being the Mowlem Microsystems Autonomous Data Acquisition Unit Model 700. Using this as the basis a fully integrated traverse and record sequence was developed.

3.4.1 General description

The Mowlem unit controlled the actions of a single stepper motor which produced the desired intermittent motion required of the traverse gear. Simultaneously the unit was monitoring three pressure transducers and two thermocouple signals and recording them in time with the traverse motion. The Mowlem was itself running under the command of a BBC Model B microcomputer. Gathered data could be held in the Mowlem even when shut down or, more usually, sent straight to disc for future analysis.

The three pressures which were automatically scanned were the stagnation pressure in the settling chamber, the venturi pressure difference and the traverse pressure, either static or total. High quality strain gauge transducers, of both semi-conductor and conventional wire type, were used for the three channels. The two temperature signals were those of the main air bottle stagnation temperature and settling chamber stagnation temperature. The former was monitored for qualitative understanding of the prevailing conditions, not for future analysis. The block diagram of Figure 3.12 shows the overall system layout.

3.4.2 Data acquisition analogue inputs

Figure 3.13 shows the analogue inputs in simplified form. Four of the five analogue signals were brought directly to the Mowlem at

their source levels e.g. 5 to 30 mV . The Mowlem allowed for programmable gains and offsets for each channel, and so could immediately perform an A-D conversion and then store the results as a number of bits. Previous calibration was needed for each pressure channel to determined the number of bits per bar. The fifth channel, the venturi channel, required filtering before the signal was taken to the Mowlem. This was due to considerable low frequency noise which appeared to be generated as a real fluid phenomenon in the venturi. Mechanical damping was tried initially to cure this problem with some success but the electrical solution was eventually adopted.

The temperature signals were directly converted to units of Kelvins by the Mowlem with due regard to the thermocouple type, in this case T-type wire.

When the static pressure was being read on the traverse pressure transducer a difficulty arose because of the ability of the signal to be either positive or negative. This was countered by applying a large offset pressure to the positive side of the differential transducer and attaching the static line to the reference side. With due regard for the inverted nature of the signal this enabled static pressure to be read on a conventional "positive only" differential transducer.

The frequency with which each channel could be scanned was also programmable, to a limit of one second between readings. The actual period was a function of traverse position and will be discussed shortly. The Mowlem when commanded to read a channel would actually take 24 readings within a few milliseconds and digitally average to produce a result.

After a scan instruction had been issued all five results (as bits and Kelvins) were in fact sent back to the BBC computer and sorted into arrays. This continued until the completion of the test at which time these large arrays were manipulated into a more useful type of format, before being sent back to the Mowlem to reside in battery backed up memory. The BBC computer was now free to be used as a normal computer again with the data safely held elsewhere. The

next stage was, if required, to read the data back to the BBC and save it onto standard 5¼" disc. This sequence although rather complex was performed because the standard format of data files on the Mowlem was not compatible with future manipulation.

3.4.3 Data acquisition motor drive

As supplied the Mowlem unit produced a series of pulses on four separate digital outputs which could drive a low power stepper motor. For the required application however the current rating of this system was inadequate. The Mowlem unit was therefore modified to produce a succession of 5 volt pulses on one channel (when commanded). This signal was then taken through additional circuitry, including opto-isolators, before arriving at the CD20 Stepping Motor power unit. This device acted as both a power amplifier and sequencer, the output then being 50 volts at 1.8 amps., and directed along each of the stepper motor lines in turn. The motor drive circuitry is detailed in Figure 3.14 .

The data acquisition unit also contained a digital direction line which simply defined in which sense the motor should rotate. Microswitch end stops were provided which switched off the pulses from the Mowlem if contact was made by the traversing gear.

To initiate a traverse of the jet the Mowlem had to be given four pieces of information:

(1) The traverse direction

(2) The length of movement between readings

(3) The stationary time interval

(4) The total number of readings or movements required.

These parameters were entered into the BBC computer which was running the controlling software. The computer then altered the commands into a form understandable by the Mowlem unit and then passed them via the RS 423 link. From this information the BBC

computer also calculated the channel scanning instructions. In fact the scan command was issued after 0.8 of the stationary time interval. This allowed maximum settling time for the signals but still ensured all scanning was complete before the next motor movement.

Traverses were started from arbitrary transverse positions, so that accurate aligning of probes was therefore necessary to ensure that on successive runs the total and static tubes occupied the same spatial location. This process was aided by various fixtures and settling pieces which allowed positioning to within 0.25 mm .

3.4.4 Data acquisition software

The complete listing of the controlling program written to perform the one dimensional traverse and scan operations is shown in Appendix A. Hardcopy of the results of a single traverse could be obtained at any time.

3.4.5 Data reduction

The need to record static and total pressures separately dictated the data reduction procedure. With both total and static runs recorded on 5¼" magnetic disc a new program was loaded into the BBC computer which then retrieved all the data on disc. The ten signals now stored had to be treated in different ways according to their type.

The four supply condition pressure signals, two venturi and two settling chamber pressures were not needed for further analysis but were important to monitor. The former two gave the mass flow via the previous venturi calibration, the latter two gave a check on the steadiness of the stagnation pressure. The two reservoir stagnation temperatures were discarded, but previously they had provided a warning of impending icing of the traverse probes.

The remaining two temperatures were averaged at each step to produce an overall record of running stagnation temperature. The two final signals contained the total pressure and corresponding static

pressure which were then used to calculate jet properties together with the average stagnation temperature. The following quantities were then calculated by the computer using isentropic relationships and barometric pressure.

(1) Recorded pressure ratio

(2) Mach number

(3) True total pressure

(4) Density

(5) Velocity

The significance of these and other quantities calculated by the BBC computer will be discussed in Chapters 5, 6 and 7 . The data analysis program is listed in Appendix B.

There was no means by which the data stored in the BBC computer could be output graphically, this being achieved by a totally independent mainframe computer. However, to aid plotting the BBC data analysis program contained a routine to establish the jet centreline from the measured pressures.

3.5 Ducted jet apparatus

This set of experiments utilised the same hardware as the earlier free jet tests, except for the extensive modification of the working section.

The duct consisted of a square passage constructed of wooden horizontal surfaces and perspex vertical sides. The whole duct geometry could be set to one of two different square sections, these being equal to area ratios of 15 and 25 when related to the primary nozzle throat size. The inlet shape of the duct was derived using conformal transformations as described in Chapter 7 . Figure 3.15 shows a close up view of the duct system and its supports, and Figures 3.16 and 3.17 show the duct in relation to the rest of the

rig. The whole apparatus was suspended from a rigid framework using thin metal flexures. Strain gauge load cells were attached to these flexures allowing direct reading of the thrust on the duct.

3.5.1 Thrust measurement

The flexure size was calculated using the assumption that the secondary thrust would be of the same order as the primary thrust. The assumption that this thrust would achieve the maximum allowable strain of 0.05% in each flexure enabled the dimensions to be determined.

The longitudinal and transverse natural frequency of the hanging structure was calculated by Rayleighs method to be 873 Hz and 4350 Hz respectively. This appeared to be sufficiently high for satisfactory filtering. The structure was designed to allow easy calibration with a pulley and weight arrangement. Incorporated in the top of the duct supports was a mechanism for allowing axial movement of the whole device to keep the duct in a constant axial position relative to the nozzle exit for different length nozzles. The thrust measurement system was in fact calibrated at all different axial positions and both duct sizes. No recordable difference in calibration was found. A transverse load was also applied to find the susceptibility to this mode of movement. The results were of an order of magnitude less sensitive than the desired axial response.

3.5.2 Duct mass flow

For some of the duct tests the total duct mass flow was measured by traversing across the exit plane. A similar process to that described in the free jet tests was adopted except for the need to perform repeated traverses at various vertical positions by altering the probe heights. The original data analysis program was used after slight modification. Figure 3.18 shows a duct mass flow traverse.

3.6 Optical techniques

Both free and ducted experiments were conducted in such a manner

that shadowgraph and schlieren images could be obtained of the jets. Figure 3.19 shows a plan view of the optical equipment. A specialised argon arc spark generator was used to obtain photographs on Polaroid film, but a direct viewing of the images on a screen was also possible. The Polaroid film used was 4" x 5" Landpack Type 55, 50 ASA which produced both an instant print and a negative for future use.

The large distance of the light path, about 8 metres, dictated very accurate aligning of all components to make use of the available light. This was even more crucial when viewing ducted jets because the perspex reduced the illumination even further, but had no other effect on picture quality.

3.7 Flow visualisation techniques

Various uses were made of titanium dioxide flow visualisation paint but these will be described in the chapters on the jet experiments.

4. THE CALCULATION OF THE PRIMARY NOZZLE INTERNAL CONTOUR

4.1 Introduction

This chapter describes the axisymmetric characteristic procedure that was used to calculate the divergent portion of the supersonic nozzles used in the test programme. In an axisymmetric characteristic scheme the flow properties are described by differential equations which require a numerical differencing method for solution. Characteristics are more commonly employed in two-dimensional situations when the equations relating the flow properties and location of the characteristic lines can be solved in a simple algebraic manner. In both the two-dimensional and axisymmetric cases the characteristic lines are physically realised as Mach lines in the flowfield.

After the procedural algorithm for solving the flow was developed the whole characteristic solution was coded as a Fortran computer program. The software was written to allow the internal contour of any supersonic nozzle to be calculated.

Before embarking on the rigorous characteristic solution some experimental tests were conducted with nozzles designed using one-dimensional flow relationships. These simple nozzles produced flows containing unwanted compression waves which were believed could confuse the proposed study of the jet behaviour. However, it is interesting to note that supersonic jet research is often undertaken with nozzles having conical divergent portions.

Consideration was given to incorporating a boundary layer correction but was discounted when some simple analysis showed the thickness to be negligible. In fact boundary layers have very little effect on nozzle design, see ESDU Data Sheet 84029, because favourable pressure gradients suppress boundary layer growth in the convergent and divergent portions.

4.2 The application of characteristics to nozzle flows

With the emphasis in aircraft design always on minimum weight it is

essential that the nozzles are as short as practicable. Consequently so called "minimum length" nozzles are used which are considerably shorter than classical de Laval convergent-divergent nozzles. This shortening is accomplished by omitting the initial diverging portion of the nozzle where the value of the wall angle relative to the axis is increasing, thereby centering the expansion at the throat. The remaining portion of the divergent part is designed to cancel out all the expansion waves generated at the throat and hence produce uniform supersonic flow at the nozzle exit in the shortest possible distance.

The subsonic convergent portion of the nozzle contour is assumed to be a circular arc because the only criteria for this part is that the flow is parallel at the throat station.

Ferri (1949) and Anderson (1982) have discussed the use of axisymmetric characteristics for solving nozzle flows, but not in terms of actually producing a numerical solution. The philosophy of the method of characteristics and the derivation of the governing axisymmetric equations is detailed in Appendix C.

Figure 4.1 shows a longitudinal section of a nozzle and includes the co-ordinates and point numbering system adopted. The starting point in the characteristic procedure is the setting up of the expansion fan at the throat. The characteristic model generates its own grid as it marches spatially downstream. However the fineness of the grid is dependent only upon the number of finite expansion waves deemed to exist in the expansion fan. The choice of the number of waves is obviously an important parameter which can only be investigated after the solution codes are written because the actual effect could not be foreseen.

As previously explained the characteristic equations are fully derived and given in Appendix C, but it is necessary to consider the significance of one of the equations before the solution procedure can be commenced.

The slope of the characteristic lines can be expressed as:-

$$\frac{dr}{dz} = \tan(\phi \pm \mu) \qquad (4.1)$$

where ϕ is the flow angle
μ is the Mach angle
r is the radial direction
and z is the axial direction.

Both ϕ and μ are measured from the axial direction.

The position of the centre of the expansion fan is denoted as point 'A' in Figure 4.1 . Using the anti-clockwise/positive angle convention produces the result that the lines with slope tan (ϕ + μ) are known as left running waves and those with slope tan (ϕ - μ) are right running. The descriptions arise from the fact that if an observer is positioned in the flow stream looking in the predominant flow direction then some characteristics would appear to pass away from the observer going to the left and the others to the right.

Clearly the nozzle centreline is a line of symmetry, hence the solution has only to be obtained in half a meridian plane.

4.2.1 Initial procedure at throat

The expansion at the throat consists of a whole family of right running waves. The spatial location of the first right running wave is determined by the fineness parameter mentioned before. In reality this parameter is entered into the procedure as the flow deviation angle experienced by passing through any one of the expansion waves. In the case of the first wave this initial value of $\Delta\phi$ is equal to ν, the Prandtl-Meyer angle, because at the throat $\phi = 0$ and $M = 1.0$. Hence the Mach number after passing through this $\Delta\phi$ is found using the relation:-

$$\Delta\phi = \nu = \sqrt{\frac{\gamma+1}{\gamma-1}}\tan^{-1}\left(\sqrt{\frac{\gamma-1}{\gamma+1}}(M^2-1)\right) - \tan^{-1}\sqrt{M^2-1} \qquad (4.2)$$

Immediately the local Mach angle can be found from,

$$\mu = \sin^{-1} \frac{1}{M} \qquad (4.3)$$

Once both ϕ and μ are known at 'A' after this first wave then the spatial position of the wave is entirely defined by

$$\frac{dr}{dz} = \tan (\phi - \mu) \qquad (4.4)$$

It is important to note that this simple procedure is only valid at 'A' for the first wave because the flow is sonic and axial.

The intersection of this line from the throat with the centreline (r = 0) then gives the position of point '1'. In general the flow on the centreline is forced to be axial, as seems plausible, but for the first wave an exception is made. At point '1' the flow angle is still taken as $\Delta\phi$ to ease the start of the computation. In practice the value of $\Delta\phi$ used is very small and the effect on the final solution is negligible. An alternative technique is to create more nodes on the line between 'A' and '1' and force a decreasing value of $\Delta\phi$ at each node. This procedure was performed and though successful was unnecessarily complex for the small benefits which ensured.

4.2.2 General procedure for defining characteristics at throat

The second and subsequent right running characteristics are constructed in a different manner to the first. The right running compatibility equation is, from Appendix C, (C.12)

$$\frac{dV}{V} - \frac{\sin \mu \sin \phi \tan \mu}{\cos (\phi - \mu)} \frac{dz}{r} + d\phi \tan \mu = 0 \qquad (4.5)$$

Replacing the differential terms by small finite values gives:-

$$\frac{\Delta V}{V} = \frac{\sin \mu \sin \phi \tan \mu}{\cos (\phi - \mu)} \frac{\Delta z}{r} - \Delta\phi \tan \mu \qquad (4.6)$$

Consider the two right running characteristics, c_1 and c_2 shown in

Figure 4.2 . A left running characteristic can be generated at 'x' on c_1. This line will cross line c_2 at 'y' . If c_1 and c_2 are very close together (i.e. if there are many waves in the simulated fan) then the difference in the z direction of the positions of 'x' and 'y' tends to a very small quantity. This assumption can be utilised by making $\Delta z = 0$ in equation (4.6) . It is easier to appreciate the validity of this assumption if the final characteristic grids are studied, see Section 4.3.4 .

Equation (4.6) becomes,

$$\Delta V = -V \, \Delta\phi \tan \mu \qquad (4.7)$$

If the properties at 'A' on line c_2 in Figure 4.2 are being found then V and μ take the values of V_A and μ_A on c_1 . The local velocity can be readily obtained from the local μ if the stagnation temperature, T_o, is known. The value of $\Delta\phi$ is the same fixed number which was chosen to represent the flow deflection achieved by the first right running wave.

The value of ΔV thus found is added to V_A to produce a new V_A on the next characteristic. The local μ is then found from this velocity. The flow angle is simply the product of the wave number and $\Delta\phi$. Hence both properties, i.e. ϕ and μ, can be calculated at 'A' along all the characteristics.

4.2.3 Grid development

In the characteristic solution the grid points are not known a priori but they are rapidly self generating. At point '1', in Figure 4.1, there will exist a left running characteristic of slope $\tan(\phi + \mu)$ which will intersect with the second throat characteristic at point '2' . Continuing the process allows the right running line through '2' to be extrapolated to the axis to produce point '3' . The whole grid development can be seen to progress in this manner.

The procedure of generating each point can thus be summarised:-

(1) Deduce from where the two characteristics will emanate.

(2) Solve their intersection for position.

(3) Solve the compatibility equations to find the new properties.

It is possible to split the nodes into three separate types, refer to Figure 4.1 for examples.

(a) "Centreline" nodes where only one upstream characteristic is involved, points such as '1', '3', '6' etc.

(b) So called "overline" points '2', '5', '9' etc. where the effect of the special centreline point has to be accommodated.

(c) "Genpoint" nodes which are simple intersections of a left and right running characteristic. These are the most common in the solution.

Each of these types of nodes will be discussed in later Sections 4.2.4 to 4.2.6 .

It is interesting to note that this process will produce grids only dependent upon the initial increment, not upon the desired exit Mach number. Hence a grid for a M = 1.8 nozzle will contain all the points of a M = 1.4 nozzle. The grid generating procedure is stopped when the centreline Mach number has reached the desired exit value.

The above process does not imply that the initial diverging contour of a M = 1.4 and M = 1.8 nozzle would be the same as further factors influence the actual nozzle profile.

4.2.4 "Centreline" type nodes

The points which are on the nozzle centreline lie on only one upstream characteristic of the right running type. Figure 4.3 shows the situation where all the properties at 'B' are known and those at 'C' are to be found.

The location of 'C' is easily found by constructing the right running line from 'B' to the axis. It is assumed that if 'B' is close to the centreline then the variation of ϕ and μ between 'B' and 'C' can be neglected.

The compatibility equation invoked at 'B' is that of the right running type, i.e.

$$\frac{dV}{V_B} - \frac{\sin \mu_B \sin \phi_B \tan \mu_B}{\cos (\phi_B - \mu_B)} \frac{dz}{r_B} + d\phi \tan \mu_B = 0 \qquad (4.8)$$

so

$$\frac{\Delta V}{\Delta z}_{BC} = V_B \frac{\sin \mu_B \sin \phi_B \tan \mu_B}{\cos (\phi_B - \mu_B)} \frac{1}{r_B} - \frac{\Delta \phi}{\Delta z}_{BC} \tan \mu_B \qquad (4.9)$$

if 'B' and 'C' are close together.

The value of $(\Delta\phi/\Delta z)_{BC}$ is taken as the average flow direction variation from 'B' to 'C' . Hence, as $\phi_C = 0$,

$$\frac{\Delta \phi}{\Delta z}_{BC} = \frac{-\phi_B}{z - z_B} \qquad (4.10)$$

The value of $(\Delta V/\Delta z)_{BC}$ thus calculated is used to find the velocity at 'C' from:-

$$V_C = V_B + \frac{\Delta V}{\Delta z_{BC}} (z_C - z_B) \qquad (4.11)$$

The Mach angle at 'C', μ_C, is then calculated using,

$$\mu_C = \sin^{-1} \sqrt{\frac{\gamma R T_o}{V_C^2} + \frac{1-\gamma}{2}} \qquad (4.12)$$

4.2.5 "Overline" type nodes

These type of points are shown in Figure 4.4, where the flow

properties are known at 'B' and 'C' but need to be found at 'D' . It is not possible to use the normal left running characteristic equation at 'C' because r = 0 and the equation fails, so that approximations to the conditions there have to be made.

The spatial position of 'D' is easy to find however by solving the two slope equations of 'B' and 'C', i.e.

$$\left(\frac{dr}{dz}\right)_B = \tan(\phi_B - \mu_B) \tag{4.13}$$

and

$$\left(\frac{dr}{dz}\right)_C = \tan \mu_C \tag{4.14}$$

The right running characteristic equation can still be used at 'B'. The equation being,

$$\frac{dV}{V_B} - \frac{\sin \mu_B \sin \phi_B \tan \mu_B}{\cos(\phi_B - \mu_B)} \frac{dz}{r_B} + d\phi \tan \mu_B = 0 \tag{4.15}$$

But, as just stated, the left running equation cannot be used at 'C'. At 'D' however the left running equation must hold even though ϕ_D, μ_D, V_D are unknown.

Hence

$$\frac{dV}{V_D} - \frac{\sin \mu_D \sin \phi_D \tan \mu_D}{\cos(\phi_D + \mu_D)} \frac{dz}{r_D} - d\phi \tan \mu_D = 0 \tag{4.16}$$

Three assumptions now have to be made to proceed.

(1) ϕ_D is small, so $\sin \phi_D = \phi_D$

(2) $V_D \simeq V_C$

(3) $\mu_D \simeq \mu_C$

The first approximation is entirely valid in the circumstances. The other two statements are less easy to justify and the whole solution process is therefore repeated using average values as described shortly.

Writing equation (4.16) in terms of differences then produces,

$$\frac{\Delta V_{CD}}{V_C} - \frac{\phi_D \sin \mu_C \tan \mu_C}{\cos \mu_C} \frac{\Delta z_{CD}}{r_D} - \Delta\phi_{CD} \tan \mu_C = 0 \qquad (4.17)$$

Because $\phi_C = 0$ the flow angle $\phi_D = \Delta\phi_{CD}$.

Thus

$$\frac{\Delta V_{CD}}{V_C} - \Delta\phi_{CD} \tan^2 \mu_C \frac{\Delta z_{CD}}{r_D} - \Delta\phi_{CD} \tan \mu_C = 0 \qquad (4.18)$$

which has to be solved with

$$\frac{\Delta V_{BD}}{V_B} - \frac{\sin \mu_B \sin \phi_B \tan \mu_B}{\cos (\phi_B - \mu_B)} \frac{\Delta z_{BD}}{r_B} + \Delta\phi_{BD} \tan \mu_B = 0 \qquad (4.19)$$

Now $\Delta V_{CD} = V_D - V_C$ (4.20) and $\Delta V_{BD} = V_D - V_B$ (4.21)

so that $\Delta V_{BD} = \Delta V_{CD} + V_C - V_B$ (4.22)

similarly $\Delta\phi_{BD} = \Delta\phi_{CD} - \phi_B$ (4.23)

because $\phi_C = 0$.

Hence equation (4.19) becomes:-

$$\frac{\Delta V_{CD} + V_C - V_B}{V_B} - \frac{\sin\mu_B \sin\phi_B \tan\mu_B}{\cos (\phi_B - \mu_B)} \frac{\Delta z_{BD}}{r_B} + (\Delta\phi_{CD} - \phi_B) \tan\mu_B = 0 \qquad (4.24)$$

This equation is solved in conjunction with equation (4.18) to produce values of ΔV_{CD} and $\Delta\phi_{CD}$. The new velocity and flow angle at 'D' are then calculated, and then the local Mach angle is found from:-

$$\mu_D = \sin^{-1}\sqrt{\frac{\gamma RT_o}{V_D^2} + \frac{1-\gamma}{2}} \qquad (4.25)$$

Because the solution of "overline" points contain some numerical approximations the whole procedure is then repeated, including obtaining a revised location of point 'D' . This is achieved by using an average of the flow properties at both 'B' and 'D' with those at 'C' and 'D', in the slope equations. Similarly the compatibility equations are solved with average values of ϕ and μ .

The actual program written to solve "overline" type nodes cannot make use of the useful simplification that $\phi_C = 0$ because the program is used at point '2' . At this node, as explained, the previous left running point '1' has a non-zero value of ϕ_C . In most cases however, $\phi_C = 0$.

4.2.6 "Genpoint" type nodes

The most frequent node type occurs when two points remote from the centreline produce a third node at the intersection of their left and right running characteristics. Figure 4.5 details the situation.

The location of point 'D' is found by solving the two slope equations as before, i.e.

$$\left(\frac{dr}{dz}\right)_B = \tan(\phi_B - \mu_B) \qquad (4.26)$$

and

$$\left(\frac{dr}{dz}\right)_C = \tan(\phi_C + \mu_C) \qquad (4.27)$$

The two compatibility equations are used in their standard form:-

$$\frac{dV}{V_B} - \frac{\sin\mu_B \sin\phi_B \tan\mu_B}{\cos(\phi_B - \mu_B)}\frac{dz}{r_B} + d\phi \tan\mu_B = 0 \qquad (4.28)$$

and

$$\frac{dV}{V_C} - \frac{\sin \mu_C \sin \phi_C \tan \mu_C}{\cos (\phi_C + \mu_C)} \frac{dz}{r_C} - d\phi \tan \mu_C = 0 \qquad (4.29)$$

The velocity and flow relationships used in Section 4.2.5 are needed,

$$\Delta V_{BD} = \Delta V_{CD} + V_C - V_D \qquad (4.30)$$

and

$$\Delta \phi_{BD} = \Delta \phi_{CD} + \phi_C - \phi_D \qquad (4.31)$$

These four equations may be solved to produce values of ΔV_{CD} and $\Delta \phi_{CD}$ (or ΔV_{BD} and $\Delta \phi_{BD}$) . New values of velocity and flow angle at 'D' are thereby found, from which the Mach angle can be calculated.

The solution process is repeated using average values of the properties at the three points as explained in the section on "overline" points.

4.3 Description of the nozzle design computer program 'nozzle'

The complete nozzle design process was written in Fortran 77 as program 'nozzle' to run on a Honeywell Multics system. Included in 'nozzle' was the fan generation process described in Sections 4.2.1 and 4.2.2, whereas the solution of the actual characteristics were performed in three separate subroutines. These were named 'cenline', 'overline' and 'genpoint' to correspond to three different processes previously discussed. The nozzle contour was calculated in the 'nozzle' program after the characteristic grid had been produced and solved.

The first three right running waves from the throat were unique and so had to be solved individually. The fourth and subsequent waves were solved in a general fashion.

4.3.1 Inputs to 'nozzle'

Only two quantities needed to be entered into 'nozzle'. They were the desired exit Mach number and the grid fineness parameter. Other variables such as stagnation temperature and the air properties were coded into the program because all the nozzles were designed for I.S.A. operating conditions. The effect of grid fineness will be discussed later.

4.3.2 Nozzle contour calculation

Reference should be made to Figure 4.1. The nozzle contour is calculated from the flow properties along the last right running wave. The values of ϕ and μ do not change along each of the left running lines which pass through the nodes on the last right running wave. This invariance occurs because there are no waves of the opposite family in the region between the last right wave and the wall.

The initial divergence at the throat is set equal to the average of the final value of ϕ_A calculated by the procedure of section 4.2.2 and the flow angle at the first node on the last right wave. A point on the contour is generated where the initial divergence line intersects the left running line from the first node on the last wave.

The remaining contour points are formed by taking an average of the flow angles at successive nodes on the last right running wave, and constructing a line at this angle from the previous boundary point. The direction of the final part of the contour will be very close to axial because the flow angles of the last few points on the centreline will be very small. In this manner 'nozzle' calculates the entire expansion contour which then leads to a useful check on the accuracy of the whole solution. The entire nozzle design process is performed isentropically so the simple area relationship of supersonic flows should still apply. Making use of the last contour point the predicted exit area can be calculated and then compared with that given by the isentropic formula:-

$$\frac{A}{A^*} = \frac{1}{M}\left[\left(\frac{2}{\gamma+1}\right)\left(1 + \frac{\gamma-1}{2} M^2\right)\right]^{\gamma+1/2(\gamma-1)} \qquad (4.32)$$

The success of this comparison will be discussed in Section 4.3.4.

4.3.3 Output from 'nozzle'

'Nozzle' provides some options concerning the style of output desired. Field output can be selected which produces a complete record of ϕ, μ, r, z at all the node positions. Alternatively a reduced output provides only the data on the centreline. In addition graphics routines are included which plot all the node positions and also the nozzle contour.

4.3.4 Grid fineness and nozzle accuracy

Most test runs of the program have been made of M = 1.4 nozzles. Values of $0.04 \geqslant \Delta\phi \geqslant 0.0004$ were tried to deduce the effect of grid size on the nozzle contour. The major result of decreasing $\Delta\phi$ is to decrease the axial length of the nozzle expansion region. Over the range considered the node number varies from 45 to 3570 but with a decrease in nozzle length of 1% . This decrease is seen to be falling in size as the node number increases, i.e. there is convergence in the computation. For a M = 1.4 nozzle the optimum $\Delta\phi$ has been found to be about 0.0006 in terms of computation time and accuracy achieved. Figures 4.6 - 4.9 show the graphical output for three supersonic nozzles, produced with a range of values of $\Delta\phi$.

Table 4.1 shows the values of exit area/throat area achieved by the 'nozzle' program. Their agreement is generally good but consistently slightly lower than the isentropic prediction.

5. THE FREE JET TESTS PART I

5.1 Introduction

This chapter describes the first part of the experimental investigation into the mixing properties of a series of free round jets. Previous experimental work on free supersonic jets is used to explain the jet structures that are observed. There is also a discussion of some theoretical techniques for calculating the shock structure of underexpanded jets and the usefulness of a finite-difference method is discussed.

The effects of both the initial Mach number and nozzle exit geometry were investigated, special attention being given to the results of incorporating various scale notches around the nozzle exit planes as briefly described in Chapter 2 and shown in Figure 5.7. Nozzles with four different exit Mach numbers were tested. The methods of Chapter 4 were used to design M=1.4, 1.8 and 2.0 nozzles, and in addition a simple choked M=1.0 nozzle was utilised. The rig used for the experiment is fully detailed in Chapter 3.

The study involved recording both the jet static and total pressures at various axial stations, and taking schlieren and shadowgraph photographs of the flows. In this chapter the optical results will be fully discussed, followed by the first part of the pressure recording experiments. The test conditions and experimental errors encountered in all the free jet tests will be outlined and the results of an exercise to record the centreline properties of the M=1.4 flow are given.

Chapter 6 will contain a description of the second part of the free jet programme when the extensive set of transverse jet data are presented.

5.2 The extent of the free jet tests

The non-dimensional length scale used to determine axial position in the jet was chosen to be x/D, where x was the axial distance from the nozzle exit and D the throat diameter of all the nozzles, which

was 35 mm. The spanwise length scale was r/D, r being the local radial position.

Performing the traverse tests was time consuming due to the large amount of air used and the resulting long recharge period required. It was decided to investigate thoroughly all the different jet flows at one value of stagnation pressure rather than gather less rigorous data over a range of pressures. The pressure chosen was 6.9 bar gauge (100 psi), the highest attainable.

In Section 3.3.2 it was noted that supersonic jets contained certain regions inaccessible to total and static pressure probes. In order to identify these regions the first stage of this study was to take schlieren photographs of all the jets for about six diameters downstream of the nozzle exit. The details of the photographs will be discussed later in Section 5.7 but the salient points for the current purpose must be examined now.

At a stagnation pressure of 6.9 bar gauge Figures 5.8 and 5.9 show Mach discs to occur for both the M=1.0 and M=1.4 nozzles at an x/D downstream of the jet exit of about 1.8 . A much weaker shock system can be discerned at x/D≈3.5 . Further downstream no distinct structure can be determined in the highly turbulent jets. The M=1.8 and M=2.0 jets, Figures 5.11 and 5.12, are operating in the perfectly expanded or overexpanded regimes and so the oblique shocks present after the first cell are weak.

It was therefore considered sensible to traverse at x/D=4, and repeat at x/D=6 and 8. In fact the purpose of the centreline tests described in Section 5.9 was mainly to ascertain how reliable the proposed transverse tests of Chapter 6 were likely to be. In free jet experiment terms these traverse positions were still very much in the jet nearfield. The justification for considering jet structure only up to x/D=8 came from the desire to restrict this study to potentially aircraft applicable ejector geometries.

5.3 Air supply conditions and nozzle accuracy

Two supply parameters, the stagnation temperature and ambient pressures, were found to have a noticeable effect on the jet mass flow which therefore tended to disguise the jet entrainment properties. In addition small inaccuracies in the nozzles introduced slight difficulties in the data analysis. However, these uncertainties only became important when considering the overall entrainment characteristics of the jets. Consequently the manner in which these testing errors were countered is described in Chapter 6.

5.4 Jet and nozzle flow regimes

It was important to understand clearly the particular behaviour of the air in the nozzle at each of the Mach numbers and the chosen pressure ratio. Plots of theoretical static pressure against axial position in the nozzle were therefore produced to display the operating condition, and show readily the effect of changing the pressure ratio, p_{ex}/p_o . The latter becomes important for the ducted tests of Chapter 7. The plots for the M = 1.4 and M = 1.8 nozzles are presented as Figures 5.1 and 5.2 . Included on these figures is an indication of the relationship between the pressure ratio across the nozzle and the upstream stagnation pressure.

The plot for M = 2.0 is not included because this nozzle operated at the perfect expansion point at 6.9 bar upstream gauge stagnation pressure. Hence the operating condition was overexpanded at all lower values of testing pressure for this nozzle.

5.5 Castellated nozzles

The castellations were machined onto the exit plane of three of the different Mach number nozzles, the M = 2.0 nozzle being the exception. As discussed in Chapter 2 it was believed that the differential expansion mechanism would not work with perfectly expanded jets. To provide the castellations metal was actually removed from the supersonic effusers of the nozzles, or in the sonic nozzles case, from the convergent portion. Figure 5.3 shows sections through the three supersonic nozzles and Figures 5.4 to 5.7 show the

castellation geometries and a view of three of the nozzles tested.

It was hoped to investigate a broad range of castellated scales to provide an overall understanding of the castellation effect. The decision had however to be taken to restrict this study to regular geometries with equal lengths of tooth and space. Three parameters were needed to fully describe the proposed regular castellations.

(1) The tooth circumferential length

(2) The tooth depth

(3) The nozzle wall thickness.

The latter quantity was not a variable however, all nozzles being 2.25 mm thick at this point.

The stipulation that only regular geometries were being used made the tooth length dependent only upon the number of teeth present. It was useful to consider the tooth aspect ratio, this being defined as:-

$$\text{Tooth aspect ratio} = \frac{\text{Tooth depth}}{\text{Nozzle internal arc of one tooth}}$$

The desire to leave the nozzle expansion sections largely unaffected by the castellations machined on the exit led to keeping the tooth depth small and constant for all the tests.

A tooth depth of approximately 2 mm was chosen to be the original standard. From inspection of the nozzle contours of Chapter 4 it can be seen that removing 2 mm from the supersonic effusers would have no harmful effects on the exit Mach number generated. A reasonable starting assumption for the tooth shape would have been to use square profiles, i.e. an aspect ratio of 1.0 . If this were the case about 32 teeth could have been machined around a nozzle exit. After further consideration it was felt that the scale of the expansion mechanism generated by having this many teeth would be too small. A reduction was adopted and the initial tests were made with nozzles

having 16 and 8 teeth, i.e. aspect ratios of 0.5 and 0.25 respectively. Interesting results were immediately apparent which justified the choice of tooth number. After rigorous investigation of these castellated nozzles a further set were made and tested with only four teeth, i.e. aspect ratio 0.125 .

Because the nozzle exit area increased with increasing design Mach number, the tooth length (and therefore depth) did vary slightly from nozzle to nozzle. Table 5.1 contains the relevant dimensions of all the castellated nozzles.

It was unfortunate that the tooth depth parameter could not be investigated more thoroughly. However it was felt more important to concentrate the limited testing time on altering the number of teeth.

5.6 Data derived from observed pitot and static pressures

The data analysis program described in Section 3.4.5 was run after measurements of both the total and static pressures had been recorded. The software produced the local jet properties at each data point, and the overall mass flow and momentum if the data set constituted a complete diametral traverse. The description of the traverse analysis is included at the start of Chapter 6.

In the remainder of this discussion the quantity recorded by the total pressure tube will be referred to as the pitot pressure, whereas the true total pressure actually occurring at the point will be called the total pressure.

5.6.1 Local jet properties

1) From the ratio of local absolute pitot pressure to absolute static pressure the flow regime could be identified.

$$\text{If } \frac{p_o}{P} < 1.893 \quad \text{then flow subsonic}$$

If $\frac{p_o}{P} \geq 1.893$ then flow sonic or supersonic

2) For the subsonic case the local Mach number was found from the simple isentropic relationship:-

$$\frac{p_o}{P} = \left(1 + \frac{\gamma-1}{2} M^2\right)^{\gamma/\gamma-1}$$

3) For the sonic case obviously M=1.0, but for the supersonic condition the process was rather more complex due to the bow shock in front of the total pressure tube. In fact from isentropic and normal shock considerations it can be shown that the Mach number is a unique function of the pitot and static pressure ratio. From Massey (1979):-

$$\frac{p_o}{P} = \left(\frac{(M^2/2)^{\gamma}\ (\gamma+1)^{\gamma+1}}{(2\gamma M^2 - \gamma + 1)}\right)^{1/\gamma-1}$$

4) The true value of local total pressure can be found for the supersonic case:-

$$\frac{p_o}{p_{ot}} = \left(\frac{(\gamma+1)M^2}{2 + (\gamma-1)M^2}\right)^{\gamma/\gamma-1} \left(\frac{\gamma+1}{2\gamma M^2 - \gamma + 1}\right)^{1/\gamma-1}$$

p_{ot} is the true total pressure

5) Using the Mach number and the averaged (between the two runs) stagnation temperature allowed the local static temperature to be found for all regimes,

$$\frac{T_o}{T} = 1 + \frac{(\gamma-1)M^2}{2}$$

6) The local static air density was found using the equation of state,

$$\rho = p/RT$$

7) The local jet velocity was determined using the local sonic velocity value and the Mach number,

$$v = M\sqrt{\gamma RT}$$

5.6.2 Recorded data errors

Both the total pressure and the static pressure probes were expected to record slightly inaccurate values for a number of reasons. A thorough error analysis was therefore performed to discover how large these errors could be, and how great their effect on the derived jet data. The other parameters that were used in the data reduction, the air stagnation temperature and the transverse radial location, were expected to be recorded sufficiently accurately.

Appendix D contains the detailed error analysis and extends the discussion of Chapter 3 concerning pressure probe design.

Summarising the final results of the analysis of Appendix D produces three major points:-

(1) In supersonic regions the velocity could be found to within a few percent accuracy.

(2) For regions where the flow could be classed as high subsonic the predicted velocity would be of the order of 10% too high.

(3) For Mach numbers in the range 0.3 - 0.5 the reading could be up to 24% high, mainly caused by the unsteady velocity errors.

(4) Large uncertainty surrounded the small value velocities due to the strong dependence upon the signal conditioning accuracy and unsteady velocity effects.

The integrated effect of these velocity errors on the mass flow and momentum flux will not be considered here but where the flux quantities are presented in Chapter 6 . The velocity errors however do give a clear idea of how to interpret the free jet data.

5.7 The structure of the free jets close to the nozzle

Photographs were taken of the jet flows from each of the four plain nozzles before any pressure measurements were recorded. Schlieren photographs were also achieved of most of the castellated nozzle jet flows. Additional images were taken of conical probes immersed in some of the jets to provide comparisons with the pressure data. All of the following free jet photographs were obtained with a jet stagnation pressure of 6.9 bar gauge and a flash duration of about 10 microseconds.

5.7.1 Photographic results of plain jets

M=1.0

The schlieren image achieved for the M=1.0 plain nozzle jet flow is given in Figure 5.8 . The M=1.0 nozzle is just visible on the left of the picture with the jet emerging and flowing left to right across the photograph. In the bottom right of the image is a lozenge shape which reoccurs in many of the photographs. This device is used to help scale the photographs and represents one reference (ie. throat) diameter along the horizontal length. The three prominant spots on the picture are due to extraneous material in the film holder and should be ignored.

Figure 5.8 contains much of interest and nine important points are discussed.

1) A completely opaque zone occurs for approximately one diameter downstream of the nozzle. This is an indication of the severely underexpanded nature of the M=1.0 flow. On exiting the nozzle the flow expands so rapidly that the density decrease is recorded as a continuous strong density gradient.

2) The jet diverges substantially on leaving the nozzle. From the photograph this divergence angle can be measured and compared with that expected from the Prandtl-Meyer function. This exercise was conducted and the results are discussed in Section 5.8 . At x/D=2 the jet is approximately two reference diameters across.

3) A strong Mach disc occurs at x/D=1.75 .

4) The incident shocks on the Mach disc are just visible as extremely fine lines leading to the triple point.

5) The reflected shocks are clearly visible progressing downstream from the triple point.

6) Downstream of the Mach disc exists a zone of low speed flow mixing rapidly with the higher speed flow surrounding it. A further zone of accelerating (and expanding) flow then follows and is visible as a dark trapezoidal patch.

7) Another very faint dark area at x/D≈4.5 signifies continuing but weak cycling of the flow between high and low pressure. Some weak oblique shocks are progressing downstream but basically the flow structure is difficult to appreciate.

8) The jet width is constant between x/D=2 and 4 but the jet edge structure has become of larger scale which signifies faster mixing. Downstream of x/D=4 the jet edge is hard to define but increasing mixing is visible. Even the internal structure is rather blurred which is not a photographic fault but an indication of the many superimposed turbulence scales.

9) A very interesting facet of high pressure jet flows can be seen in the photograph. Sound waves generated at the nozzle exit are radiating predominantly downstream. Some secondary sources, generated by the internal shock system, also cause weak sound waves to emerge from the side of the jet.

M=1.4

Figure 5.9 is the schlieren photograph of the M=1.4 plain jet. This image was produced with an earlier configuration of optical system which unfortunately produced pictures of lower quality. Nevertheless it is possible to gather important facts from the photograph. The pale stripe on the right of the figure is a photographic fault.

1) The dark zone downstream of the nozzle is present for the M=1.4 jet as it was for the M=1.0 flow. However a slight reduction in darkness immediately adjacent to the nozzle is due to the less underexpanded nature of the jet. There will always be a constant pressure zone before the expansion fan generated at the nozzle lip penetrates across the jet.

2) Jet divergence is less than the M=1.0 case.

3) The Mach disc is narrower and further downstream at x/D≈1.85 .

4) The incident shock is clearly visible, especially the lower wave.

The remainder of the qualitative comments made of the M=1.0 flow apply to the M=1.4 jet. Even the parallel portion up to x/D≈3.5 - 4.0 is repeated, with the jet mixing improving downstream.

A further picture of the M=1.4 jet is included as Figure 5.10 . This is a shadowgraph image of the same event as Figure 5.9 . The fact that it is easier to achieve a better shadowgraph than a schlieren is readily apparent. This is due to the lower light intensity requirement for shadowgraph. The most important additional feature displayed by Figure 5.10 are the vortices generated at the triple point as the low and high speed streams interact. Also of interest is that the shadowgraph gives a misleadingly narrow view of the jet width. This is because of the reduced sensitivity of shadowgraph which cannot distinguish the secondary air which has joined the jet from ambient free flowing air.

M=1.8

The schlieren photograph of the M=1.8 plain jet, Figure 5.11, shows clearly the different flow structure to that achieved with the M=1.0 and M=1.4 jets. At this pressure the M=1.8 jet is still underexpanded (when p_o=6.9 bar gauge) but not enough for a Mach disc to form. The expansion on exiting the nozzle is weak so that a series of oblique shock waves at x/D≈2.3 can recover the pressure

deficit.

Jet divergence is lower than for both the M=1.0 and 1.4 flows as expected. There are a number of Mach waves generated inside the nozzle which are visible in the first diameter. These are caused by roughness in the nozzle or imperfections in the contour shape, but they have no lasting effect on the jet structure. Even though the longitudinal pressure gradients are not severe there is still faint evidence of cycling of the pressure field with axial distance.

As with the M=1.0 and 1.4 jets there exists a region of almost parallel flow, up to x/D≈3 in this case. This is caused by the requirement of the jet to provide overall pressure continuity across the boundary. Conventional inviscid representations of underexpanded jets, eg. Dash and Wolf (1984), show an inward curvature of the boundary after the first cell, but in practice it appears that viscous effects dominate and the jet mixing counters this supposed contraction. The result is that a more or less parallel section occurs before the mixing process establishes itself as the predominant mechanism.

M=2.0

Figure 5.12 is a slightly blurred schlieren picture of the last plain jet flow. At 6.9 bar gauge stagnation pressure the M=2.0 flow was expected to be perfectly expanded, ie. exiting at ambient pressure. The jet indeed emerges parallel but there are a number of Mach waves contained within the jet. Some of these Mach lines appear to coalesce and form finite compression waves which are not normally associated with perfectly expanded flows.

The behaviour of the jet boundaries for the underexpanded flows (a parallel portion before the commencement of jet spreading) is not repeated in the M=2.0 case. The perfectly expanded jet begins to spread almost immediately on leaving the nozzle with a linear increase in jet width from x/D≈1.0 onwards. This behaviour is analagous to that of a subsonic round jet where the static pressure variations are negligibly small.

Summary

1) The lower Mach number jets diverge more rapidly on leaving the nozzle.

2) In the range of the photographs, approximately 5 diameters from the nozzle, the lower Mach number jets are wider at all stations. This result coincides with the traverse data of Chapter 6 taken further downstream. The increased width early in the jet life presents more circumference and therefore more potential mixing (other factors being unchanged).

3) The convergent-divergent nozzles produce undesirable Mach lines in the flow. The overall effect of these waves does not appear to be deleterious to the jet structure.

5.7.2 The structure of underexpanded free jets

Having presented the schlieren pictures of the plain jets in the previous section it is necessary to explain the complex flows present in underexpanded jets.

An underexpanded jet emerges from the nozzle at a pressure above the local ambient value. To increase the underexpansion of a jet can be achieved by either increasing the nozzle pressure ratio or by reducing the exit Mach number at a given pressure ratio.

All underexpanded jets will expand on leaving the nozzle, as clearly demonstrated by Figures 5.8 to 5.11. The expansion takes place through a Prandtl-Meyer fan centred at the nozzle tip. The fan expands the outer regions of the jet to atmospheric pressure but the fan on the opposing lip will interact and cause a substantial overexpansion of the air in the region of the jet centreline. Owen and Thornhill (1948) calculate the expansion process from an initially sonic orifice using the method of characteristics, and Johannesen and Meyer (1950) solve the potential equations describing the fan.

The expansion waves from the fan are reflected at the constant pressure boundary as compression waves. For a substantially underexpanded flow, i.e high pressure and low exit Mach number, this results in a well defined boundary curvature as the rate of jet growth has to slow as the air passing through the compression waves increases in pressure. In some cases it is possible to see these compression waves coalesce to form an 'intercepting' or 'barrel' shock, such as seen in Figure 5.9.

If the jet is only moderately underexpanded the intercepting shock reaches the jet centreline and is matched by a 'reflected' compression wave. This is the situation occurring with the M=1.8 jet at 6.9 bar gauge stagnation pressure, but it is difficult to see the intercepting and reflected shocks on Figure 5.11.

For the more underexpanded jets it is possible that a single reflected shock cannot turn the flow back to the axial direction. The result is a Mach reflection and the formation of a Mach disc with subsonic flow immediately downstream.

Figures 5.8 and 5.9 show that Mach discs occur at 6.9 bar gauge jet pressure for the M=1.0 and 1.4 flows. The point where the intercepting shock is met by the Mach disc and the reflected shock is known as the triple point. A discontinuity in velocity occurs at the triple point because the flow leaving the reflected shock will be supersonic whilst that leaving the normal shock is subsonic. The slip lines from the discontinuity are well shown in Figure 5.10.

The basic structure of an underexpanded jet will repeat downstream as the flow progressively over-expands then over-compresses, but of course this process will rapidly dissipate due to viscous mixing between the jet and the surroundings. In practise the viscous effects become important even before the end of the first shock cell because no contraction of the jet boundary is visible on any of the photographs.

Characteristic solutions like Owen and Thornhill's provide no means for predicting shock positions and any jet solution will be expanded indefinitely downstream. Other workers have developed suitable

techniques but it is clear that locating the Mach disc is not a trivial exercise. Adamson and Nicholls (1959) present a simplified prediction based on one-dimensional properties of the flow. The results are good at low pressures and Mach numbers but of little use with severely underexpanded jets. Abbett (1971) develops a useful iterative scheme for Mach disc prediction which uses characteristics for the initial supersonic portion of the jet. Downstream of a disc a one-dimensional scheme is used to compute the reacceleration of the flow. The nature of the problem is such that only one value of the disc location can satisfy the physical requirement of a finite pressure gradient leading to a rechoking of the flow after the disc. Unfortunately Abbett does not produce data in a form such that any jet conditions can be predicted. Fox (1974) uses Abbett's algorithm and presents plots of Mach disc location against nozzle conditions.

A point which is not widely appreciated is the nature of the flow before the first Mach disc in a well underexpanded stream. From Owen and Thornhill (1948) the Mach number of a M=1.0 6.9 bar gauge jet is predicted to be about 3.6 at the location of the Mach disc. Associated with this Mach number is a static pressure of 0.10 bar absolute and the local static temperature is approximately 80 K. These figures are substantiated by the conical probe data presented later in this chapter where a maximum Mach number of 3.05 is recorded. It was not possible to obtain a direct Mach number reading as close to the shock system as would have been desirable due to probe interference effects.

A further observation from the photographs is the difficulty of visualising any structure after the first cell. This appears to be because a well underexpanded jet has regions of strong shear behind the first shock system. Such mixing generates considerable turbulence which obscures the jet structure downstream.

5.7.3 M=1.0 castellated nozzle photographic results

M=1.0 16 tooth nozzle

Unfortunately a photograph of the M=1.0 16 tooth sonic jet flow was not obtained. The continuous viewing facility displayed a jet

structure falling somewhere between the plain and 8 tooth case presented below.

M=1.0 8 tooth nozzle

The initial five diameters of the 8 tooth flow are recorded in Figure 5.13 which should be compared with Figure 5.8, the plain case. The effect of the eight teeth around the M=1.0 nozzle is to change totally the jet structure throughout the flowfield. The major features are highlighted and compared with the plain case, Section 5.7.1 .

1) The opaque zone is still present but is marginally reduced in size.

2) The initial divergence angle is increased greatly compared with the plain case. The initial boundary is less well defined but the jet penetrates further sideways before curving around to the axial direction to maintain pressure continuity.

3) The Mach disc occurs at the same axial location but is slightly narrower which signifies a less severe shock wave.

4) After the first shock system the visible shock waves are poorly defined.

5) Downstream of x/D≈3 the jet boundary is impossible to locate precisely. However at x/D=4 the jet width is approximately 3.5 reference diameters, whereas from Figure 5.8 the plain jet is only 2.25 diameters wide at this point. These numbers are lower than those measured by the pitot and static tubes because the low speed flows are transparent to the schlieren system.

M=1.0 4 tooth nozzle

The four tooth nozzle flow, Figure 5.14, displays less early jet growth than the eight tooth flow, Figure 5.13 , but the divergence is still larger than the plain jet. The Mach disc and associated reflected shocks are similar in strength to those of Figure 5.13 ,

but in the current jet the incident shocks are also visible. The jet boundary is again difficult to locate, but as the jet leaves the picture the width is less than that of Figure 5.13 .

The four tooth nozzle was rotated through 22.5 degrees and the photographs repeated. The results are not presented because the change in flow pattern is barely discernable.

Summary

Introducing castellations around the sonic nozzles produces extremely large increases in jet mass flows. The eight tooth flow spreads far more rapidly in the first five diameters than the four tooth jet.

5.7.4 M=1.4 castellated nozzle photographic results

M=1.4 16 tooth nozzle

The 16 tooth nozzle jet flow, Figure 5.15, demonstrates clearly the effect on jet spreading of the castellations. The Mach disc occurs at the same location as the reference case, Figure 5.9, but the system is weaker, as evinced by the shorter reflected shock waves. The cyclic nature of the underexpanded flows shows well, with a region of expanding flow following the Mach disc.

M=1.4 8 tooth nozzle

Figure 5.16 is the schlieren image of the 8 tooth M=1.4 jet. The general jet structure is quite similar to the 16 tooth case. As with the M=1.0 jet flows however, using 8 teeth causes a reduction in jet boundary definition downstream of $x/D \simeq 4$. It is possible to discern from Figure 5.16 that the energetic core of the jet is much narrower than that of Figure 5.8 after the Mach disc.

M=1.4 4 tooth nozzle

No suitable photograph of the flow emanating from this nozzle can be presented.

Summary

Again, as for the M=1.0 nozzles, the castellations improve jet spreading and mixing. The jet widths achieved with M=1.4 are less than those obtained for the lower speed jets.

5.7.5 M=1.8 castellated nozzle photographic results

M=1.8 16 tooth nozzle

The 16 tooth flow, Figure 5.17, is difficult to distinguish from the plain case, Figure 5.11 . Unfortunately the quality of Figure 5.17 is poor with uneven tone. Also the schlieren effect is lighter than usual so visualisation of entrained flow is not easy. The only effect of any importance is the slighty improved mixing evident from $x/D \simeq 1$.

M=1.8 8 tooth nozzle

Figure 5.18 is the eight tooth jet and is of better quality than Figure 5.17 . The parallel portion evident from Figure 5.11 does not appear on Figure 5.18 , consequently the castellations are causing linear jet growth from the nozzle.

Summary

Castellations do not substantially improve the entrainment of the M=1.8 jets, a conclusion supported by the traverse tests.

5.8 Initial jet divergence

Examination of the photographic results of Section 5.7 suggested that a study should be made of the angles at which the jet boundaries initially diverge from the thrust line.

For an axisymmetric underexpanded jet flow there exists a simple isentropic relationship between pressure ratio, Mach number and the

jet divergence. It can be shown that the initial divergence of an axisymmetric jet is the same as a two-dimensional plane jet, Johannesen and Meyer (1950) and Adamson and Nicholls (1959). From the definition of the Prandtl-Meyer function it follows that the divergence, δ, can be found from:-

$$\delta = \nu_{FE} - \nu_M$$

where ν_{FE} = Prandtl-Meyer angle associated with fully expanded stream

and ν_M = Prandtl-Meyer angle of local stream at nozzle exit

The Prandtl-Meyer function itself can be written,

$$\nu = \frac{\gamma+1}{\gamma-1} \tan^{-1}\left(\frac{\gamma-1}{\gamma+1}(M^2-1)\right) - \tan^{-1}(M^2-1)$$

For the fully expanded case the Mach number, M_{FE}, to be used in the Prandtl-Meyer function is,

$$M_{FE} = \sqrt{\left(\left(\frac{p_o}{p_\infty}\right)^{(\gamma-1)/\gamma} - 1\right)\frac{2}{\gamma-1}}$$

where p_o/p_∞ = upstream stagnation to exit ambient pressure ratio

As all the current free jets were investigated at a fixed value of stagnation pressure, 6.9 bar gauge, it was a simple process to compute a table of exit deflection versus exit Mach number at this pressure ratio. The data are presented as Table 5.2 which also includes the values of flow deflection measured from the photographic results. In addition a graph of δ against M is given as Figure 5.19 .

Both the figure and the table show that the plain jets diverged substantially less than the Prandtl-Meyer prediction. This cannot be attributed to poor nozzle design, and incorrect Mach number, because the purely convergent nozzle flow also suffers the discrepancy. It

was felt that possibly the initial divergence angle was not being measured correctly from the photographs because immediately downstream of the nozzle the jet boundary will indeed reduce in inclination. This is due to the three dimensional relieving nature of axisymmetric flows. The actual shape of the boundary has been the subject of prior work, Adamson and Nicholls (1959). This source showed that an axisymmetric jet will very quickly behave differently to a plane jet.

Figure 5.19 also contains the divergence data from the castellated jets. The precise path of the boundary on leaving a castellated nozzle is even harder to determine than the plain case. The value of angle plotted on Figure 5.19 is actually the largest which could be measured from the photographs.

In an attempt to resolve some of the uncertainties of the schlieren photographs a further exercise in flow visualisation was conducted. A razor blade was cut to shape and mounted axially on the nozzle lip such that the jet expanded over the blade surface. Titanium dioxide flow visualisation solution was placed on the blade surface before starting the test run. The trace of the jet boundary was achieved where the jet completely removed the solution from the surface. This exercise was performed with the M=1.4 plain nozzle (at 6.9 bar gauge pressure), and also with the castellated nozzles of this Mach number. The blade securing device was constructed such that any circumferential location could be selected for observation. The blades were photographed after use and the divergence angle measured.

Figure 5.20 is a selection of the best results achieved with the flow visualisation technique, but the tests do not directly resolve any of the previously mentioned disagreements. The fan lines on Figure 5.20 are spaced at 10 degree increments. Inserting the razor blade into the jet has dramatically increased the divergence of all the flows in which the exercise was attempted. However the results of the flow visualisation tests are in themselves of interest because the information gleaned appears to be coherent and credible.

For the plain nozzle the flow visualisation trace, Figure 5.20a, clearly shows the boundary curvature. The initial flow divergence is of the order of 40 degrees, compared with 17.6 degrees from the Prandtl-Meyer prediction, but reduces to about 31 degrees by the end of the blade. These figures differ so markedly from the schlieren observations that inaccuracies in interpreting the results cannot be solely to blame. The insertion of the blade appears to create a phenomenon not unlike the actual castellation induced mechanism itself.

For the castellated flows it is not possible to compare the discreet photographs of Figure 5.20 with the schlieren photographs because the latter obviously smear the expansion effect around the nozzle circumference. However each of the series of three castellated photograph sets is an interesting representation of the circumferential variation of divergence. Figures 5.20 b, f and j show the 'tooth' divergence for the 16, 8 and 4 tooth nozzles respectively. The value of the angle is always less than the plain flow but there is a progressive increase in angle with a reduction in tooth number. Both Figures 5.20 b and f clearly show the entrainment streamlines. Figures 5.20 c, g and k, the 'gap' flows, show the opposite dependence ie. slightly reducing divergence with tooth number reduction. This is a most interesting result compared with the 'tooth' data. Also the 'gap' results are marginally larger than the plain flow. All six 'step/gap' and 'step/tooth' results show much the same result; itself quite strange because it would have been expected that the 'step/gap' result would be considerably larger than the 'step/tooth'. In addition all six plots portray the fact that 'step' results are always larger than the 'gap' divergences. This again implies that the razor blade is itself very important because the effect occurs with equal magnitude both sides of the blade and is not dominated by the tooth geometry immediately adjacent to the blade.

5.9 Conical probe photographs

Early in the test programme it became apparent that the pitot and static probes would not provide a universal means of determining local jet properties. Three different conical probes were used with

nose angles of 20, 40 and 60 degrees to achieve independent determination of Mach number. It was expected that the sharper probes would be needed at the lower Mach numbers to keep the bow shock attached.

Some random checks were made using a value of Mach number found from the optical experiments to compare with the traverse data. As an example Figure 5.21 shows a photograph taken of the 40 degree probe immersed in the plain M=1.4 jet at x/D=4 and r/D=0.343 . The bow shock included angle is 36.4 degrees which from ESDU Data Sheet 70008 gives a local Mach number M=2.13 . Figure 6.7 contains the Mach number derived from the traverse data for this case, and the value at r/D=0.343 is M=2.12 . This closely equivalent result is not untypical of properties well downstream of the nozzle.

Figure 5.22 shows the result of positioning the 40 degree probe on the centreline of the M=1.4 exit plane. There is some distortion of the bow wave but measurement of the available angle gives a Mach number of 1.38 . An investigation of the centreline Mach number for the M=1.4 plain case was made at 6.9 bar gauge, and the results compared with the pitot and static pressures at intervals of x/D=0.25, up to x/D=4 . The image at x/D=0.75 is shown by Figure 5.23 as an example of a better conical shock photograph. For this example the bow wave included angle is 36.3 degrees which gives a Mach number of 2.12 . The combination of pitot and static pressures at this point produces M=2.15 . However it would not be true to assume that all the traverse data was as accurate as this example would suggest.

Figure 5.24 shows the centreline Mach number variation, as measured from the schlieren photographs, and also the Mach number deduced from the pitot and static pressure data. The agreement between the two Mach numbers is very good in the zone x/D=0 to 1, which is more a vindication of the static pressure reading than any other factor. The Mach number derived from the pressures even shows the expected constant region immediately downstream of the nozzle (before the expansion fan penetrates to jet centreline). The schlieren Mach number increases steadily up to a value greater than 3.0 which agrees with data given by Owen and Thornhill (1948). The dramatic

fall in pressure derived Mach number at x/D=1 is due to the static pressure probe / Mach disc interaction discussed in Chapter 3. The Mach number in the region x/D=2 to 3 is much lower than the true value (which must at least be greater than 0.378, which is the minimum sustainable by a normal shock). This discrepancy is again due to shock wave / probe interactions. Between x/D=3 and 3.75 the results are credible but it was difficult to achieve schlieren images in this region due to a combination of fairly weak conical waves and highly turbulent structure. The second series of compression waves at x/D≈3.75 to 4 is depicted clearly. It is possible to deduce that this wave series does not contain a predominant normal shock as the flow does not go subsonic at any point.

Figure 5.25 shows the pressure data which was used to construct the pressure derived Mach number of Figure 5.24 . Up to x/D=1 both data sets are credible and indeed combining both to produce the true (without bow shock) total pressure gives a value within 5% of the jet stagnation pressure of 6.9 bar gauge. The true total pressure should be constant up to the Mach disc, across which a massive drop will occur. However the static pressure reading is highly corrupted and so smears the Mach disc. Below M=1.0 the total pressure reading should be quite accurate but again the static pressure reading is too high, giving the near zero Mach number of Figure 5.24 . The manner in which the pitot pressure starts to recover at x/D=2.5 is interesting as it shows the very rapid inward mixing of the higher energy air surrounding the core flow.

5.10 Finite-difference predictions of the M=1.0 jet flow

Use was made of a commercial flow simulation package as part of the ejector research programme. The main purpose was to evaluate whether the prediction technique was useful in a supersonic environment, rather than to optimise any part of the ejector. The code used was the finite-difference package PHOENICS supplied by CHAM Ltd. The code was used to simulate the 6.9 bar gauge M=1.0 axisymmetric jet investigated experimentally.

Some difficulties were experienced in setting the downstream boundary condition and CHAM published a report describing a similar exercise before any success was achieved.

Appendix E describes the results presented by CHAM and the comparisons they made with experimental data. It is apparent that finite-difference codes have limited value in predicting jet flows. This is due to both inadequacies in axisymmetric turbulence models and the inability of shock-capturing techniques to provide good resolution of the shock structure. In addition, the CPU time to achieve convergence was greater than 8 hours on the ICL 2980 at Bath University.

5.11 Summary of the early free jet experiments

The tests described in this chapter have shown that it is possible to discover the macroscopic properties of high pressure, high speed air jets close to the nozzle; an exercise which has received little previous attention due to severe experimental difficulties. The use of the shadowgraph and schlieren system has given a valuable insight into the jet structure. The specially designed total and static pressure probes have performed well but an appreciation of the jet shock structure is needed before their use.

The experiments described in this chapter have shown that the castellations do improve the jet entrainment properties, but the use of the razor blade flow visualisation technique has shown the mechanism to be much more complex than originally thought. A finite-difference code has been shown to capture the basic features of underexpanded flows but the detail of the shock structure is poorly represented.

6. THE FREE JET TESTS PART II

6.1 Introduction

This chapter describes the tests undertaken to record the transverse properties of the free jet flows previously discussed in Chapter 5. The jet mass and momentum fluxes were calculated from the traverse data at x/D=4, 6 and 8, which allowed the overall entrainment characteristics of all twelve jet flows to be examined.

Chapter 5 contains sections describing the free jet test procedure and the data errors encountered. However certain information is relevant only to the transverse tests. Section 6.2 contains details of the mass and momentum flux calculation procedure, and Section 6.3 describes the effect of the ambient conditions prevailing during the traverse runs.

The traverse results are presented in Sections 6.4 to 6.8 as plots of jet parameters with spanwise position, at various axial locations. Curves are not fitted through the finely spaced data points as this would lead to confusion between the different data-sets. For graphs that contain a large amount information there is sometimes an additional enlarged scale plot of interesting areas. The use of positive and negative r/D values on the plots has no real significance. It is purely a convenient means of differentiating between the two halves of the traverse.

Conducting total and static traverses for the twelve nozzles at the three axial positions entailed 72 traverse runs which would have created a large number of individual plots of the local jet properties. The number of interesting combinations of data was therefore large, and only a small proportion can be included here.

Section 6.9 presents the mass and momentum fluxes, and includes an analysis of the effect of the data errors.

In addition to the programmed 72 sets of data, various other runs were made to investigate more specific areas which later became apparent. Some additional traverses were made to ascertain whether

the traverse data varied with nozzle rotation and are presented in Section 6.10 .

6.2 Calculation of the mass flow and momentum flux

For a round jet the mass flow can be expressed as:-

$$\dot{m} = 2\pi \int_0^R \rho v r \, dr$$

where r = radial position in jet
and R = overall jet radius

For each data point the product of v and ρ could be found but r, the radius of the data point, depended upon the position of the jet centreline.

The centreline location was found by numerically integrating the pressure ratio curve, p_o/p , then halving the result and finding the radial position associated with this half area. It should be noted that even though the mass flow increases during a test run, no change in pressure should occur.

A further quantity of interest, the jet momentum, was calculated using a similar method, ie.

$$P = 2\pi \int_0^R \rho v^2 r \, dr$$

Both $\dot{m}$ and P were calculated by using Simpsons numerical integration rule on plots of ρvr and $\rho v^2 r$ against r respectively.

The jet boundary location, R, was calculated by extrapolating the ρvr line to the horizontal axis, for example see Figure 6.11 .

6.3 Air supply conditions and nozzle accuracy

Two supply parameters were found to have a noticeable effect on the jet mass flow which therefore tended to disguise the jet entrainment properties. The barometric pressure varied in the range 0.962 to 1.007 bar over the time period the free jet tests were conducted. In addition the average (mid-span) stagnation temperature of the air supply was found to vary from 265.5 K to 281.1 K .

Another parameter, the nozzle manufacturing error, had also to be included in the results analysis. The process described in Chapter 4 produced accurate nozzle profiles which had to be manufactured as full size nozzle templates for use on a copy lathe. The final results whilst good in terms of absolute accuracy produced quite large errors when misalignment between throat and exit was taken into account.

Use of the isentropic mass flow relationship,

$$\frac{\dot{m}\sqrt{T_o}}{A\,p_o} = \sqrt{\frac{\gamma}{R}}\;\frac{M}{\left(1 + \frac{\gamma-1}{2}M^2\right)^{(\gamma+1)/2(\gamma-1)}}$$

A = nozzle exit area.

enabled the predicted mass flow to be found at all the operating conditions. The range of barometric pressures and stagnation temperatures given above produced a variation in ideal mass flow of 1.833 kg/sec to 1.891 kg/sec, i.e. a 3.3% change. In addition, due to nozzle error the maximum difference between the various predicted mass flows was a further 2.3%.

These unfortunate additional sources of error were accounted for by calculating the mass flow for each nozzle that would theoretically emerge at I.S.A. conditions. The theoretical exit mass flow that was apparently emerging during each specific test was also calculated. The I.S.A. mass flow was then subtracted from the theoretical test mass flow thereby producing a correction which was applied to each integrated traverse mass flow. The theoretical mass flows for each

test are shown in Figures 6.1 to 6.4, and the mass and momentum fluxes are listed in Table 6.1 .

The previously calibrated venturi was not sufficiently accurate to record these slight changes in mass flow. The venturi did however provide a check that stagnation conditions were being maintained to within ±3%.

6.4 Plain nozzle traverse results at M=1.0, 1.4, 1.8 and 2.0

These results are presented as the basic reference set of the free jet runs with the stagnation pressure of 6.9 bar gauge. They highlight many of the fundamental characteristics of supersonic jets, and some of the difficulties encountered experimentally. The x/D=4 data are presented first, to be followed by that at x/D=6 and 8 .

6.4.1 Plain nozzle jet traverse results, x/D=4

Pitot pressure, Figure 6.5

A first impression given by this graph and most of the subsequent results is the symmetry of the data collected.

The most striking feature of each of the four different jets is the reduction in pressure in the central portion of the flow. This pressure deficit can be attributed to two separate phenomena. Firstly there can exist a real pressure loss in the jet due to the upstream series of powerful normal and oblique shocks. Secondly, the total pressure probe can record a significantly lower pressure than should exist because of the shock wave formed in front of the probe nose, as discussed in Section 5.6.1 .

The intrinsic jet pressure loss feature is present only in the lower exit Mach number jets because these are the flows which are underexpanded and contain the necessary structure. The initially sonic jet will be affected most by this pressure loss as it is the most underexpanded jet. The perfectly expanded M=2.0 jet can not suffer at all from this phenomenon, hence the pressure deficit in

this case should be entirely due to the probe bow shock. This conclusion is borne out when the Mach number distributions are studied.

The data shown enlarged in Figure 6.5 of the jet edge displays the very slight difference in jet widths at x/D = 4. The lower M jets have expanded, in inverse order of Mach number, to greater widths than the M = 2.0 jet. Remembering that all data is non-dimensionalised with respect to a constant diameter, but that the higher Mach number jets emerge from larger exit diameters, emphasizes this point further. Even at distances as close to the nozzles as four diameters the slower jets are presenting more surface area to the ambient air. This is an asset in providing good downstream entrainment.

Static pressure, Figure 6.6

Some care should be exercised when studying this figure because of the use of a large scale. In fact probe, transducer and conditioning errors alone on each reading are of the order of 0.02 bar, or about 1/10th of the vertical graduations. Actual plotting errors can add a further 1/25th vertical scale uncertainty.

All four jets have similar edge characteristics where the static pressure is sub-atmospheric. This depression is due to the influx of entrained flow at relatively low static pressure across the jet boundary. The same phenomenon is present in entirely subsonic jets, see Schetz (1980).

The core pressures displayed in Figure 6.6 do however differ considerably. The M = 1.0 nozzle appears to produce a jet with a very different central structure to the other three jets. This is because at x/D = 4 the flow has just passed through the series of shock waves, causing a large rise in local static pressure. The pressure increase here is associated with the pitot pressure reduction shown in Figure 6.5 .

The M = 1.4 and M = 1.8 jets also display a noticeable central static pressure rise but in these cases the affected transverse

portion of the jets is much less that the M = 1.0 flow. The regions of the rapid change in static pressure for the three underexpanded flows are an indication of the location of the shear zones where the lower energy core flow mixes with the higher energy air at r/D = ± 0.5 .

It might be expected that the M=2.0 jet would have a constant zero value static gauge pressure but in practice this cannot occur. The perfectly expanded jet will actually have a static pressure variation similar to that of subsonic jet with a lower pressure in the central regions. However there appears to be some interaction between the pressure field and Mach waves which are inadvertantly generated in the nozzle. It is possible that some weak compression waves are formed by this process. The presence of such waves in the flow is substantiated by the photograph of Figure 5.12.

Mach number, Figure 6.7

The pitot pressure deficit noted earlier in this section reappears in the current plot as a reduction in centreline Mach number for the M = 1.0, 1.4 and 1.8 jet flows. The fact that the M = 1.8 jet contains regions of faster flow than the other two streams is a random occurrence. If the traverses had been performed at slightly different axial locations the properties recorded could have been altered considerably. The apparently linear Mach number variation for the M = 1.8 jet in parts of the core is of no particular significance.

An important result can be seen for the M = 2.0 jet. The combination of the static and total pressures has resulted in a core Mach number of close to M = 2.0, as is expected for a perfectly expanded flow. A slight increase can be noticed for the region r/D = ± 0.3 which could be attributed to either static probe induced error or the mechanism just described under the static pressure heading.

The sensitivity of the derived Mach numbers in the jet edge to the recorded jet pressures is clearly shown by Figure 6.7 .

Total pressure, Figure 6.8

Figure 6.8 is the spanwise total pressure corrected for the probe bow shock effect. Its comparison with Figure 6.5 is interesting. It is impossible for the total pressure to exceed the reservoir stagnation value of 6.9 bar gauge. This incontrovertible law is largely obeyed, the M = 1.8 jet providing a small violation which must be ascribed to experimental error. The massive pressure deficit at the centreline for the lower Mach number nozzles is again emphasized.

Static temperature, Figure 6.9

The local static temperature of the air flow is of less interest than the other quantities plotted. It is included to provide some information as to how the stagnation temperature affected the flows. The plot is very similar to an inverted version of the Mach number variation but with a superimposed gradual decline from right to left. The initial temperatures at r/D=1.25 are the stagnation conditions prevailing at the start of the traverse. For this particular series of tests the figure shows the coldest initial temperature occurred for the M=2.0 run at 277 K, and the warmest of 286 K for the M=1.4 nozzle. The final temperatures at r/D=-1.25 show a general decrease of about 10 K during a run. The static temperature only equals the stagnation temperature at the jet boundary where the velocity tends to zero.

Velocity, Figure 6.10

The spanwise velocity variation is included for completeness. In comparison with Figure 6.7 the velocity is seen to have less vertical resolution in the central regions of the jet. This is due to the reduction in local sonic velocity in the colder parts of the flow.

Mass flow, Figure 6.11

The quantity ρvr is plotted against non-dimensional radius in Figure 6.11 . The total jet mass flows are calculated by numerically

integrating each curve with respect to the true radius. It is clear that the mass flow for the M=1.0 jet is the greatest due to the larger ρvr quantities outside of $r/D=\pm 0.5$. Assuming an average exit mass flow of approximately 1.85 kg/sec then in the order M=2.0, 1.8, 1.4 and 1.0 the percentage increases on the exit flow are 20.7%, 22.3%, 25.3% and 35.7% respectively.

In Section 3.2.1 it was noted that the jet mass flow increases during a test run due to the decrease in stagnation temperature, but the size of the increase is beyond definition on Figure 6.11 . It may be assumed that the instantaneous mass flow occurring after 1/4 of the elapsed duration of a test can be represented on a ρvr graph by the first half of the traverse. Equally the second leg of the traverse will represent the mass flow after 3/4 of the testing time. During the middle half of a test a typical temperature fall may be about 5 K, which would result in a mass flow increase of only 1% .

The form of the ρvr graph is very susceptible to the location of the jet centreline, but the integrated result is relatively independent of any centreline errors. Very small changes in its predicted location (calculated from the spanwise pressure ratio distribution) considerably alter the symmetry of ρvr. However it may be shown that these asymmetric graphs when integrated produce mass flows almost identical to the original symmetric results. Thus it should be emphasized that Figure 6.11 contains information in which the shape of the ρvr line is of interest but the individual data points should not be relied upon to any high degree.

Momentum, Figure 6.12

The final graph presented in this series is that of $\rho v^2 r$ against non-dimensional radius as Figure 6.12 . The area under each of the lines is an indication of the momentum flux at the x/D=4 station. The arguments of the preceeding section concerning centreline position error apply equally to the $\rho v^2 r$ plot. The momentum flux could be expected to be independent of the axial position at x/D=4 because the static pressure distribution shows no substantial pressure forces to be present. Indeed from Figure 6.12 it can be seen that all four momentum fluxes are of similar size.

6.4.2 Plain nozzle jet traverse results, x/D=6

Most of the remarks of Section 6.4.1 concerning experimental techniques also apply to these results at x/D=6. In addition the following features of the jet structure need to be discussed.

Pitot pressure, Figure 6.13

The pronounced core pressure deficit occurring at x/D=4 for the M=1.0 and M=1.4 flows is still evident at x/D=6. In underexpanded jets the strength of the first shock system is much greater than that of the succeeding systems due to the severe viscous effects which modify the flow. Consequently the core pitot pressure appears to be recovering faster than the relatively weak recurring shocks are able to reduce it.

The M=1.8 jet contains regions of substantially higher pitot pressure than the M=2.0 jet. When the total pressure plot is studied later the situation can be seen to be reversed.

The jet edge structure at x/D=6 is also similar to that at x/D=4, with the M=1.0 jet still having the slightly greater width, but the M=1.8 and M=2.0 results now fall very closely to each other.

Static pressure, Figure 6.14

The jet edge behaviour is very similar to that of Figure 6.13 but as with the x/D=4 plot the central static pressures display some unusual features. In the distance of two diameters from the previous traverse it could be expected that a further shock series would occur. This assumption is based on the knowledge that the first two Mach discs occur at approximately 1.8 and 3.5 diameters downstream for the lower speed jets. If use is made of normal shock relationships it can be seen that the static pressure rise across normal shocks is larger, as a percentage of the upstream value, than the total pressure decrease. Consequently it can be expected that the static pressure results will display more streamwise variation than the total pressure results.

It should be noted that the static pressures presented in this chapter are not plotted to the same scale due to their wide spread in magnitude.

Mach number, Figure 6.15

The greater width of the M=1.0 jet shows clearly on the Mach number plot at x/D=6 . The perfectly expanded jet has core Mach numbers close to the expected values of M=2.0 but the lower M jets continue to exhibit reductions in central Mach number.

Total pressure, Figure 6.16

As with Figure 6.8 the plotted pressures do not generally exceed the limit of 6.9 bar gauge. It is not possible for any particular jet at x/D=6 to contain a maximum total pressure higher than that at x/D=4. This statement is obeyed by the experimental results.

Mass flow, Figure 6.17

The mass flow plot, Figure 6.17, shows increased ρvr values on the jet edge for the M=1.0 and 1.4 flows compared with those at x/D=4. Conversely there is a noticeable deficit of ρvr in the region r/D=0 to ± 0.5 . The mass flow increases, in the order M=2.0 to M=1.0, above the nozzle exit flow are 35.9%, 39.6%, 38.8% and 46.8% for the four jets at x/D=6. As in the x/D=4 case the M=1.0 nozzle produces flows markedly different to the other three in this respect.

6.4.3 Plain nozzle jet traverse results, x/D=8

The total pressure variation is given in Figure 6.18 and the static pressure in Figure 6.19 for the x/D=8 station. The overall reduction of total pressure in the central regions can be seen to continue in Figure 6.18 . However, the total pressures in the jet edges at x/D=8 are similar for all four jets. The enlarged scale portion of Figure 6.18 is produced to the same scale as that of the pitot pressure at x/D=6 in Figure 6.13 . Comparison reveals a wider jet at x/D=8 but that the earlier plot displays rather larger differences between the

various jets in the boundary region.

The static pressure in the jet boundaries also tend to be similar, see Figure 6.19, except that the M=1.0 jet is rather wider.

It may be supposed that this less well defined edge region is due to unsteady velocity components. This proposal is corroborated by the photographs of the plain jets, see Figures 5.8 to 5.12 . Furthermore, it would appear that the blurred and unsteady nature of the boundaries give an indication of the strength of the entraining processes.

The data shown in Figures 6.18 and 6.19 suggest that at x/D=8 the M=1.4, 1.8 and 2.0 jet boundaries are tending to behave in a similar manner. In addition it might be supposed that at some point downstream the M=1.0 jet will also exhibit similar properties. The deduction then made is that at large distances from the nozzles the jets become independent of the type of nozzle employed..

This supposition is supported if use is made of Figure 6.20 where the Mach number distribution at x/D=8 is plotted. The core Mach numbers are tending to coalesce to a value approaching M=2.0 . Again the edge regions show that only the M=1.0 jet differs to any noticeable degree from the others.

The final plot of this section is Figure 6.21 which shows how ρvr varies at x/D=8 for the plain nozzles. The mass flow increases are 55.1%, 52.7%, 54.0% and 64.6% over the exit flow for the M=2.0, 1.8, 1.4 and 1.0 cases respectively.

6.4.4 Axial variation of plain nozzles

The reference data of the preceeding three sections are now plotted for each of the nozzles in turn with all three axial traverses on the same graph.

M=1.0 nozzle

Figure 6.22 shows the spanwise total pressure for the sonic jet at x/D=4, 6 and 8. The recovery of the centreline total pressure as the jet progresses downstream is an obvious feature. This recovery occurs through the process of mixing between the high energy air at the r/D=±0.5 location with the less energetic core air. The jet growth can be seen by the increasing values of total pressure in the zones r/D=±0.75 to ±1.5 .

The static pressure in Figure 6.23 of the M=1.0 jet displays even more clearly the sideways jet spreading phenomenon. The static pressure distribution at x/D=8 appears to be that of a well developed flow with little internal shock structure. This is not necessarily the case due to the random relation between traverse position and the jet structure.

The combination of the total and static pressures form the Mach number results shown in Figure 6.24 . The figure most clearly shows how the jet structure changes downstream with an increasing central Mach number and jet growth. The rate of this growth is increasing slightly with downstream distance, suggesting that this jet has not yet reached the full entraining potential.

The final plot presented for the sonic nozzle is that of the $\rho v r$ variation downstream in Figure 6.25 . The manner in which the peak Mach number reduces and the edge values increase is shown to good effect. The symmetry of this plot is also worthy of note.

M=1.4 nozzle

The Mach number plot for the unmodified M=1.4 nozzle is shown by Figure 6.26 . Generally the Mach numbers at the three stations can be seen to be closer to the Mach number associated with an expansion to ambient pressure than those for the initially sonic case.

A slight anomaly is apparent in the region r/D=±0.25 where the Mach number at x/D=6 is higher than at x/D=8. This feature can probably be accounted for by the axial static pressure fluctuations.

In addition there is a lack of symmetry at all three axial locations outside of the lines r/D=±1.0 .The results suggest a wider jet on the 'positive' leg of the traverse. There is no obvious explanation for this occurrence in terms of any of the jet properties discussed so far. A possible argument concerning entrainment dependence on temperature will be outlined at the end of this section.

M=1.8 nozzle

The development of the M=1.8 jet can be summarised by studying the Mach number distribution, Figure 6.27 . The rather extreme behaviour of the core flow at x/D=4 has evolved to an almost uniform profile by x/D=8. The asymmetry mentioned in the preceeding paragraph for the M=1.4 nozzle tests is also evident for the M=1.8 case.

M=2.0 nozzle

The perfectly expanded jet variation of Mach number is given in Figure 6.28 . The behaviour of the centre of the stream is quite constant with a Mach number close to 2.0 . The jet boundary is spreading at a constant rate over the short axial distance under investigation.

Summarising the results of the plain nozzle jet experiments produces four major points.

1) The initial spreading of the lower M jets is larger, but by x/D=8 the differences are becoming less important.

2) The rate of jet growth at x/D=8 is nearly equal for all four jets.

3) The severe effects of the early shock systems are soon dissipated downstream for the underexpanded flows.

4) All four jets display slight asymmetry in the outer regions with the first leg traversed always producing higher Mach numbers. This suprising discovery is not due to any misalignment in the

traverse geometry but a real fluid phenomenon. There is no stagnation pressure drift during a test run, but of course the air total temperature does fall. In Section 6.4.1 the bulk effect of temperature on mass flow was investigated and rejected as being inconsequential, but it appears that locally the mean and turbulent jet structure is temperature dependent. The turbulent kinetic energy of the stream does depend upon the local static temperature just as the steady flow energy equation relates mean properties. Previous work, eg. Ing (1985), displayed similar asymmetries and Quinn (1976) discussed the effect of temperature on complete ejector performance but with special attention to mixing. The work of Quinn did conclude that higher temperatures (leading to more vigorous turbulence) will cause higher mixing rates.

6.5 Castellated M=1.0 nozzle traverse results

The traverse data recorded at x/D=4, 6 and 8 will be presented for the four M=1.0 castellated nozzles. The plots of castellated traverse data will often also contain the corresponding plain nozzle case for comparison purposes.

As with the plain jet tests all the castellated runs were made with p_o=6.9 bar gauge.

6.5.1 M=1.0, 16 tooth nozzle

x/D=4

The pitot pressure recorded at x/D=4 for the 16 tooth sonic nozzle is presented as Figure 6.29 . The castellations have made a large change to the pressure distribution. The peak pressure attained is substantially less than the plain case, this reduction extending outwards to r/D=$\pm$0.8 . However outside of r/D=$\pm$0.8 the castellated jet contains much higher pressures. In fact up to 100% increases in gauge pressure can be observed. Also the jet width is markedly greater.

The most obvious feature is the increased centreline pressure but this is not of prime importance. The castellations appear to have a diluting effect on the jet and so cause a reduction in some of the extreme properties of the plain case. In particular the first Mach disc is noticeably weaker, hence less total pressure is lost in the shock systems.

The smaller pitot pressure loss of Figure 6.29 is matched by a smaller central static pressure rise in Figure 6.30 . The large drop in jet edge static pressure is also a strong indication of faster flows in the this region. The combination of recorded static and total pressures produces, by the usual process, the Mach number plot of Figure 6.31 . This figure shows the drastically modified Mach number profile and much wider jet. The quantity of air in motion appears to be much larger for the castellated nozzle flow. The mass flow plot, Figure 6.32, amply demonstrates this fact. The integration of this figure produces a mass flow for the 16 tooth nozzle 15% greater than the plain case.

The momentum plots for the M=1.0 16 tooth and plain nozzles, Figure 6.33, are noteworthy because the areas under the two curves differ by only 2%.

x/D = 6

The pitot pressure variation of the sonic 16 tooth nozzle flow at x/D = 6, Figure 6.34 behaves in a very similar manner to that at x/D = 4. Changes in both scales are made to facilitate future comparisons between various nozzles. The jet boundary at both x/D = 4 and 6 is approximately 30% further from the centreline than the plain case. Hence the jet produced by this castellated nozzle is not growing at an increasing rate after the initial four diameters from the nozzle.

The static pressure, Figure 6.35, shows less difference at x/D = 6 between the toothed and plain nozzles than at x/D = 4. However the Mach number plot, Figure 6.36, displays the re-distribution of the flow from the peak velocity regions to new flow zones outside of the original jet. The mass flow increase is 18% over the reference plain

case for the 16 tooth nozzle at the station x/D = 6. The jet momentum value at x/D = 6 is similar to that at x/D = 4.

x/D = 8

At x/D = 8 Figure 6.37 shows the pitot pressue of the 16 tooth flow. Smaller changes from the plain case are noticeable than at the previous traverse locations. The castellated jet still exhibits a slightly higher centreline pressure than the plain case because of the more benign nature of the flow.

The equivalent static pressure plot, Figure 6.38, features again the susceptibility of static pressure to both nozzle type and axial location. It is difficult to make a jet edge comparison from this figure but the Mach·number variation, Figure 6.39, shows clearly the small movement outwards of the boundary. The modified nozzle produces a jet only 10% wider at x/D = 8, far less than the value of 30% quoted earlier for traverses further upstream. The mass flow increase has fallen to 10% at x/D = 8.

Axial variation

A plot of the Mach number variation for the M=1.0 16 tooth nozzle flow at the three axial stations is presented as Figure 6.40. The figure shows that the castellated jet growth is slowing down with downstream distance. However Figure 6.24, in comparison, shows that the plain jet is growing at a constant rate between x/D = 4 and 8. The effect of the castellations therefore appears to be dissipating quite early in the jet life.

6.5.2 M=1.0, 8 tooth nozzle

The next nozzle to be discussed is the eight tooth sonic case. The nozzles were in fact tested in the sequence 16 tooth, 8 tooth then 4 tooth. Having discovered interesting features of the castellations of the previous nozzle, some surprise was evinced when the even more unusual results of nozzles with fewer teeth were revealed.

x/D=4

The different jet behaviour obtained by having eight teeth is apparent immediately the pitot pressure plot, Figure 6.41, is studied. At x/D=4 the central jet structure is largely unaffected but relatively massive 'humps' of total pressure are visible outside of r/D=±1.0 . The static pressure graph, Figure 6.42, has an equivalent feature with large regions of low pressure. The jet width has increased to a figure 63% greater than the plain case.

The core static pressures of Figure 6.42 defy obvious explanation as they appear even higher than the plain case. A possible theory is that 8 teeth slightly displace the jet shock structure in the axial direction and thereby the static probe is removed from close proximity to the discontinuities.

The extreme nature of the results of Figures 6.41 and 6.42 prompted some thoughts as to whether nozzle rotational position is a factor. To investigate this theory some more tests were performed in addition to the originally planned series. In Section 6.6 the results of the M=1.4 tests are presented. The same phenomenon is also evident in the M=1.4 runs, and so it was with the M=1.4 nozzles that the additional traverses were made. The tests performed will be described in Section 6.10, after completion of the main jet flow discussion. It will suffice to say that there is some dependence on nozzle rotation at x/D=4, but that for other reasons the results portrayed here do have sigificance.

The combination of large total and large negative static pressures causes extremely large Mach numbers as shown by Figure 6.43 . A striking feature is the manner in which at r/D=±1.0 the Mach number profile changes in form. The outer region appears to consist mainly of entrained flow if the mass flow variation, Figure 6.44, is studied. Some slight asymmetry can also be seen on this graph but this is due to extreme sensitivity to centreline position. The mass flow increase is 53% over the plain nozzle flow.

The momentum plot, Figure 6.45, displays similar flanking areas to the main jet flow. The integrated result of the two sets of data

differ by 12%.

X/D=6

The pitot pressure at x/D=6 for the 8 tooth sonic nozzle, Figure 6.46, has returned to the usual form after the unusual behaviour at x/D=4. Comparison with the similar plot for the M=1.0 16 tooth nozzle flow does still show, however, increased jet width and higher edge pressures for the 8 tooth case. The same comments can be made about the static pressure, Figure 6.47. In addition the core static pressure has altered little from that at x/D=4.

The Mach number plot, Figure 6.48, shows how the new regions of flow are becoming more settled at x/D=6 than at x/D=4. The whole edge region is tending to attain the normal distribution commonly found in turbulent mixing flows. A phenomenon has previously been discussed whereby the castellations initially make the flow more benign by reducing the strength of the early shock waves. This in turn raises the centreline Mach number. Now an opposing feature is becoming apparent where the core speed is reduced due to more rapid mixing.

At x/D=6 the mass flow plot, Figure 6.49, conveys the manner in which smoothing of the jet properties occurs. For this station there is 47% more air in motion than the plain case. Comparison with the equivalent figure for x/D=4 reveals that the 8 tooth jet growth is slowing slightly from the initially high value.

x/D=8

The results at the last traverse location, x/D=8, for the 8 tooth nozzle show clearly how rapidly some of the castellation effects diminish. The pitot pressure graph, Figure 6.50, portrays the re-distribution, to the outer regions, of jet pressure. The core area is markedly slimmer, more so than that of the 16 tooth nozzle at the same position.

The static pressure is not presented but takes a form very similar to that of the castellated flow in Figure 6.47 .

Figure 6.51, the Mach number plot, clearly shows the beneficial effects of eight teeth as compared with the sixteen of Figure 6.39 . However the former graph also shows how the form of the jet mixing region is evolving back to the style of the plain flow.

Axial variation

Figure 6.52 is a plot of the Mach number variation for the 8 tooth initially sonic flow. A very interesting point can be seen when $r/D=\pm 1.25$. At $x/D=4$ the flow is faster than at the later locations. This could be attributed to the large unsteady flows dying away. The core behaves in exactly the same manner as that of the 16 tooth nozzle flow, Figure 6.40 .

6.5.3 M=1.0 4 tooth nozzle

x/D=4

Figure 6.53, the pitot pressure variation of the 4 tooth nozzle shows closer similarity to that of the 8 tooth nozzle, Figure 6.41, than the 16 tooth flow, Figure 6.29 . The peak pressures are reduced over both previous cases, and the edge regions are not as energetic as the eight tooth nozzle flow. Hence this figure does not provide many definite clues as to the relative benefits of four or 8 teeth. The only conclusion possible is that fewer teeth continue to dilute the jet strength.

Rather more asymmetry is present than has occurred in any of the results displayed so far. It is probable that misalignment occurred when the nozzle was set in the collet. The traverse then took place along a diameter slightly skewed with respect to a 'step' diameter.

The static pressure equivalent of the previous plot is given as Figure 6.54 . The boundary areas behave in quite the same way as Figure 6.42, the 8 tooth case. This broadly agrees with the observations of the preceeding paragraphs. However problems are created in attempting to justify the reduction in core static pressures because of the disparity with the eight tooth results.

When discussing the M=1.0 16 tooth data in Section 6.5.1 the dilution phenomenon was proposed to explain the static pressure reduction, but unfortunately the 8 tooth case, Figure 6.42, largely disobeys this trend. Notwithstanding this exception it is felt that the predominant mechanism at work is this dilution effect.

The Mach number, Figure 6.55, continues to display the remarkable Mach number variation discovered with the 8 tooth nozzle. In addition though, the more benign core expected of the castellated flow is visible. Not surprisingly the mass flow graph, Figure 6.56 is extremely similar to the eight tooth flow at x/D=4, Figure 6.44. In fact however, the integrated areas of the castellated flows presented in Figure 6.44 and 6.56 differ by 17%. The nozzle with fewer teeth is producing the lesser result. The momentum flux with 4 teeth is still close to the plain value at x/D=4.

x/D=6

Considering first the pitot pressure, Figure 6.57, other than the continuing asymmetry the most noticeable point is the manner in which the jet edge still contains regions of high total pressure. This result is different to that for the 8 tooth nozzle, Section 6.5.2, where the strange behaviour at x/D=4 had largely disappeared at x/D=6. The four tooth nozzle flow therefore does not seem to be susceptible to the rapid dissipation of the castellation effect.

Figure 6.58, the static pressure at x/D=6, also displays more static pressure magnitude in the boundary zone than either of the 16 or 8 tooth flows, Figures 6.35 and 6.47 . The core pressures are similar to those of the plain and 16 tooth cases. The skewed nature of the flow is apparent in Figure 6.59, the Mach number plot, as is some scatter especially on the negative leg of the traverse. Both the pitot and static pressure plots, Figures 6.57 and 6.58, contain this fluctuating condition. Looking back to the x/D=4 results, similar irregularities are evident. This leads credence to the supposition of nozzle misalignment. The mass flow for the four tooth nozzle at x/D=6 is 57% higher than the corresponding plain case. The comparison of the ρvr graph, Figure 6.60, with that for the 8 tooth flow, Figure 6.49, does indeed show a large difference in structure.

The four tooth flow shows no sign of the slowing in growth that was apparent with the larger number of castellations.

x/D=8

At x/D=8 the 4 tooth nozzle pitot pressure plot, Figure 6.61, does not display the boundary features of the 8 or 16 tooth flows. More precisely the jet contains continuing energetic boundary areas, in fact only slightly less energetic than at x/D=6, Figure 6.57 . This is a major result because with four teeth the castellation effect is not reducing with downstream distance. The core pressures are generally lower than those of either of the other test nozzles.

The static pressure distribution also has regions of low boundary pressure matching those of the total pressure in Figure 6.61. Otherwise the similarity with Figure 6.38 obviates the need to present it here.

Figure 6.62 is the Mach number plot for the x/D=8 station. Comparison with Figures 6.39 and 6.51 again shows the totally different form of the earlier results. In fact the 4 tooth case shows more resemblance to a flow at x/D=4 than to one at x/D=8. The large regions of additional flow in Figure 6.62 obviously translate to the strange shape on the ρvr graph, Figure 6.63. The data on this plot is probably the most scattered of all the results found from any of the free jet tests. The asymmetry unfortunately shows clearly but again it should be emphasized that on this graph the centreline position has a biasing effect on the results. The mass flow increase over the plain flow is a massive 78% but also a disturbing discrepancy in the momentum value is to be found.

All momentum results so far discussed have been quite similar, leading credence to the traverse procedure. The momentum for the 4 tooth nozzle however is 29% higher than the datum case. The only explanation for this present disparity is that the flow is of such an unsteady nature that the pressure readings may be highly corrupted. This leads to the conclusion that the mass flow is not as high as just deduced but the true value is certainly a marked increase over the uncastellated flow value.

Axial variation

Figure 6.64 is a plot of the Mach number variation at the three axial stations for the 4 tooth initially sonic flow. The core behaviour is almost identical to that of the 16 and 8 tooth flows, Figure 6.40 and 6.52 . The jet edge structure for 4 teeth is much more distinct however, with continuing jet growth clearly visible. If further traverses had been performed downstream a smoothing of the Mach number profile would most probably occur (as happened earlier for the 8 tooth flow).

6.5.4 Axial variation of all M=1.0 nozzle flows

The final presentation for the M=1.0 jets compares jet properties for all four nozzles at each particular location.

x/D=4

Figure 6.65 shows the Mach number profiles for the initially sonic flows at x/D=4. Note the change in symbols. The core Mach numbers display noticeable differences but no order is apparent in the variation. The only definite result is that the plain jet has the lower Mach number. The region of r/D=±0.5 to ±0.9 shows very close agreement between all four jets.

At this x/D the widest jet is clearly that from the 8 tooth nozzle. Both this and the 4 tooth result show the strange step at r/D=±1.0, which has already been commented upon.

The other plot given is that of ρvr, in Figure 6.66 . All three castellated flows display a similar maximum value of ρvr, that are considerably less than the plain jet. This reflects the more benign central regions of the modified jets. The progressive decay in steadiness of the ρvr values in the boundary regions with decreasing tooth number is noteworthy.

x/D=6

Figure 6.67 is a graph showing the Mach number at x/D=6 for the sonic flows. Here the 4 tooth nozzle flow is generally more energetic in the border zones than the eight tooth jet. This is reversed from the situation at x/D=4, but in fact the actual boundary position is very similar for both 4 and 8 teeth at x/D=6. The skew nature of the 4 tooth jet is quite noticeable. Again, as with Figure 6.65, the core displays no obvious dependence on tooth number.

The mass flow graph, Figure 6.68, summarises well the large effect of the castellations.

x/D=8

At x/D=8 the Mach number distribution, Figure 6.69, shows similar trends to those at x/D=6. The 16 tooth nozzle has little effect on jet behaviour whereas the 4 and 8 tooth nozzles certainly improve the jet width. Figure 6.70 is the final plot dealing with M=1.0 nozzles and shows the ρvr variation at x/D=8.

6.5.5 Summary of M=1.0 castellated nozzle results

Some important conclusions can be drawn.

(1) 16 teeth, of the described geometry, on a sonic nozzle causes small but consistent increases in mass flow at locations close to the nozzle. The effect has largely disappeared by x/D=8.

(2) Eight teeth causes remarkable changes to the jet structure and almost steady jet growth in the region x/D=4 to 8 .

(3) Four tooth flows initially grow slower than those produced by eight tooth nozzles. At about x/D=6 however, the 4 tooth jet has reached a similar width to that emanating from the 8 tooth nozzles. This phenomenon occurs again at x/D=8 but the jet produced by the nozzle with fewer teeth has a much more energetic structure.

(4) If good entrainment in the nearfield is desired, up to x/D=4 say, it would appear that an eight tooth nozzle would be appropriate. For distances greater than x/D=6 (up to an undetermined maximum) the nozzle with 4 teeth would be most effective in entraining secondary flow.

6.6 Castellated M=1.4 nozzle traverse results

The next type of nozzle considered is that with an exit Mach number of 1.4 . The results obtained with M=1.4 are, as may be seen, less remarkable than the earlier series. Consequently slightly less detail is given in the presentation. In particular the static pressure plots are omitted because of the unreliability of the visual clues they give.

6.6.1 M=1.4, 16 tooth nozzle

x/D=4

Sixteen teeth have a noticeable effect on the pitot pressure for the M=1.4 nozzle flow as shown by Figure 6.71 . Note should be taken of the more benign nature of the flow because of the change to a M=1.4 nozzle. Analysis of the r/D=±1.0 location in fact shows larger percentage increases in gauge total pressure for the M=1.4 flow than for the initially sonic case. The Mach number plot, Figure 6.72, is also very similar to that for the M=1.0 16 tooth nozzle. The mechanism by which the jet core extreme behaviour is reduced is amply demonstrated. Jet width is about 37% greater than the plain flow.

The ρvr graph for this test is very close in form to that of Figure 6.32 and is not presented. The mass flow increase over the plain case for the flow considered here is 22%. This is a larger increase than that recorded for the M=1.0 flow.

x/D=6

At the x/D=6 location the pitot pressure is given by Figure 6.73 . Increased jet width over the reference case is still apparent, but most instructive is a comparison with Figure 6.34, the equivalent plot for the M=1.0 nozzle. Having 16 teeth with the higher Mach number flow does actually produce larger increases in pitot pressure in the boundary areas, e.g. at r/D=±1.0.

The Mach number graph, Figure 6.74 shows no surprising features. The mass flow increase is 20% over the reference plain M=1.4 flow at x/D=6.

x/D=8

The 16 tooth flow at x/D=8 continues to show quite large increases in jet edge pitot pressure, Figure 6.75. In the Mach number plot, Figure 6.76, the castellated jet can be seen to be about 19% wider than the plain flow. This compares with the value of 10% found for the equivalent M=1.0 nozzle, Figure 6.39 . The central Mach number has reached the perfectly expanded value of 2.0, a sign that 16 teeth can quickly remove the harsh features of underexpanded jets.

Axial variation

The spanwise Mach number variation at the three axial locations is given in Figure 6.77 . The rate of jet growth appears to be slowing, a feature also discovered for the 16 tooth M=1.0 jet flow. Comparison with the earlier plot, Figure 6.40, also reveals the real width benefits obtained by using M=1.0 nozzles.

6.6.2 M=1.4, 8 tooth nozzle

x/D=4

The pitot pressure for the M=1.4 8 tooth jet, Figure 6.78, shows much larger flanking pressures than for the 16 tooth case. The behaviour is even more radical than that found in Section 6.5.2 at x/D=4 for the M=1.0 flow in terms of pressure magnitude. However the

lower M jet appears to have traded this feature for an increase in width in the affected areas.

The pressure 'humps' again translate to large boundary zones of high Mach number, see Figure 6.79, the results being of the same type as those in Figure 6.43. Comparison with the schlieren image for this jet, Figure 5.16, shows the flanking regions of low speed air to good effect. There is quite low data scatter on the mass flow graph, Figure 6.80 . The mass flow increase of this figure over the plain set of data is 49%, but there is a decline of 10% if the area is compared with that of Figure 6.44 .

x/D=6

The statements of the preceding section concerning the pitot pressure plot in relation to previous results apply equally well to the situation at x/D=6, shown in Figure 6.81 . The jet appears to be very slightly more energetic in the region of r/D=±1.0 than the equivalent M=1.0 jet. The actual jet width is however smaller.

When considering the Mach number variation, Figure 6.82, the first major discrepancy between the M=1.0 and M=1.4 results is apparent. For the lower M jet at x/D=6, Figure 6.48, the flow can be seen to behave in a distinctly different manner outside of r/D=±1.0. For the current jet this distinction has disappeared and the Mach number profile is quite a smooth curve. This feature is an indication that castellation effectiveness is dissipating and the flow is resorting to a conventional mixing distribution.

The mass flow plot of ρvr against r/D, Figure 6.83, confirms this with an almost linear variation in the boundary region. Consequently the 8 tooth nozzle is producing a flow pattern not dissimilar in form to that from the 16 tooth nozzle by x/D=6.

x/D=8

Figure 6.84 is the variation of pitot pressure at the last axial location, x/D=8. The boundary region behaviour is unexceptional, but the core area shows a large drop in pitot pressure over the

plain case. This largely disappears if the total pressure is plotted. Consequently the Mach number graph, Figure 6.85, has a peak of M=2.0, just as did the 16 tooth M=1.4 flow at x/D=8. The ρvr variation has not been plotted as it contains nothing of interest.

Axial variation

The spanwise Mach variation, Figure 6.86, is given as the summary of jet behaviour with axial position. The figure bears marked similarity to Figure 6.52, the same plot for the M=1.0 flow. Even the strange behaviour at r/D=±1.25 is repeated. Jet growth is sensibly constant over the short distance considered.

6.6.3 M=1.4, 4 tooth nozzle

x/D=4

Far less energetic boundary regions, in comparison to the 8 tooth case, is the prime feature of Figure 6.87, the pitot pressure at x/D=4. This agrees with the observations of the M = 1.0 nozzle. Also apparent is some slight asymmetry which seems to prove that flows from nozzles with four teeth are extremely susceptible to nozzle alignment. The Mach number plot, Figure 6.88, should be compared with both Figure 6.79, the M = 1.4 8 tooth flow, and Figure 6.55, the M = 1.0 4 tooth flow. Comparison with the former shows considerable reduction in jet width, but there is none of the scatter that was a feature of the latter plot.

The mass flow plots are not included in this section as many previous plots are good substitutes. In this case Figure 6.80 is quite representative of the ρvr variation for the current nozzle under consideration. The mass flow increase is only 21% over the plain flow, or 19% down on the 8 tooth flow.

x/D=6

Figure 6.89, the pitot pressure at x/D=6, displays continuing regions of high boundary pressure. This is distinct from the eight

tooth plot, Figure 6.81, where the pressure had declined from previous upstream levels. This feature again agrees with the findings of the initially sonic jets. The Mach number, Figure 6.90, shows slightly less asymmetry than at x/D=4. This would be expected as the distance from the misalignment increases. The flanking zones are not as well pronounced as those for the sonic jet, Figure 6.59 .

The mass flow at x/D=6 is 37% above the plain nozzle level, but this is still just less in absolute terms than that for the M=1.4 eight tooth flow.

x/D=8

The behaviour of the pitot pressure at x/D=8, Figure 6.91, is remarkably similar to the equivalent M=1.0 flow, Figure 6.61 . Consequently the comments of Section 6.5.3 at x/D=8 concerning continued jet growth apply equally to this case. When the effects of static pressure are considered the apparent core pressure deficit in Figure 6.91 largely disappears.

The Mach number plot, Figure 6.92, is a less exaggerated version of Figure 6.62, the M=1.0 graph. The close approach to a maximum M=2.0 Mach number is again a feature of all the castellated flows at x/D=8. The mass flow is 48% higher than the unmodified flow, however the momentum found from integrating the $\rho v^2 r$ graph is again substantially higher than expected. This was also found with the M=1.0 4 tooth flow at x/D=8.

Axial variation

The rate of jet growth over the distance x/D=4 to 8 can be seen to be constant from Figure 6.93, the Mach number variation. The negative leg of the traverse has considerably more scatter than the positive leg. It is possible that this problem is due to partial probe icing. During a long traverse run the probe tip temperature fell markedly. Usually the probes could be seen to ice after the run terminated when moist ambient air passed over the cold areas. The air used for blowing was thoroughly dried after compression, which probably delayed icing until the latter stages of the tests.

The Mach number behaviour in the central zone is quite consistent with previous circumstances eg. Figures 6.86 and 6.64 .

6.6.4 Axial variation of all M=1.4 nozzle flows

As for the M=1.0 flows the 1.4 Mach number jets will be compared at each axial station.

x/D=4

The Mach number distributions at x/D=4 are given by Figure 6.94 . The most important feature is the manner in which the 16 and 4 tooth results fall on each other (they are quite hard to distinguish) and that the eight tooth nozzle produces the largest jet. The peak properties are always reduced by using castellations, also found for the M=1.0 flows, Section 6.5.4, at x/D=4.

x/D=6

At x/D=6 the Mach number plot is Figure 6.95 . The core region displays no helpful order in the variation of Mach number but again the outer regions are very instructive. It is now the nozzles with 4 and 8 teeth which produce very similar results, with the 16 tooth nozzle flow being rather narrower. This result again agrees with that from the M=1.0 jets at x/D=6.

x/D=8

The final M=1.4 figure presented is that for the Mach number at x/D=8, Figure 6.96. The 4 and 8 tooth flows are of very similar overall width but the former jet has a considerably higher mass flow. The jet emanating from the 16 tooth nozzle is somewhat wider than the reference plain case.

6.6.5 Summary of M=1.4 castellated nozzle results

The four conclusions drawn from the M=1.0 results apply also to the M=1.4 runs, see Section 6.5.5 . Conclusions concerning the choice of

nozzle Mach number will be made later in Section 6.8 .

6.7 Castellated M=1.8 nozzle traverse results

The final nozzle type to undergo the castellation exercise was that with an exit Mach number of 1.8 .The test programme was terminated early when (largely as expected) the castellations were found to be having minimal effect. For this reason a 4 tooth M=1.8 nozzle was not tested. Also, in view of the poor results achieved, the presentation will be given in less detail than either of the M=1.0 or M=1.4 series.

6.7.1 M=1.8, 16 tooth and 8 tooth nozzles

x/D=4

The pitot pressure for both the castellated nozzle flows at x/D=4, Figure 6.97, displays how the teeth have very little effect. Only slight increases in the pressures above the plain case at r/D=±0.8 are evident for the modified jets. The 8 tooth nozzle does in fact produce a slightly more energetic jet at this location, which was also a feature of M=1.0 and M=1.4 jets. The static pressure plot (not shown) also has a very similar variation between the castellated and unmodified flows.

When manipulated to represent the Mach number, Figure 6.98, the core regions again show only slight reduction in jet M, but with some increases of M in the jet edge zone. No particular advantage of 8 tooth nozzles over those with 16 teeth is visible. This feature is not apparent with lower M jets and is caused by the weak nature of the castellation phenomenon when M=1.8 . The mass flow increase for these cases are a mere 9% and 12% respectively above the plain reference nozzle set.

x/D=6

At six diameters from the nozzle exit the pitot pressures measured from the modified nozzles are hard to distinguish from the plain case, Figure 6.99 . Consequently, as with the M=1.0 and M=1.4 jets,

the 16 tooth flow from the M=1.8 nozzle is rapidly returning to the form of the unmodified nozzle, but in addition the M=1.8 8 tooth flow is behaving in a similar fashion.

Due to the slight reduction in the centreline static pressure the Mach number plot, Figure 6.100, displays a moderate increase in jet core speed. This is again a realisation of the diluting effect of the castellations.

x/D=8

At x/D=8 the 16 tooth jet profile of pitot pressure falls closely on the plain reference case but the 8 tooth curve is marginally different, Figure 6.101. The different behaviour of the 8 tooth flow also features on the Mach number graph, Figure 6.102, as a width increase for the lower tooth number nozzle. At this axial distance the 8 tooth nozzle is having some effect on the entraining processes. However the major result is that the M=1.8 jets are not improved by castellations, as can be seen by comparing Figure 6.102 and Figures 6.69 and 6.96 . The mass flow for the 8 tooth jet is 14% over the datum case, and 4% higher for the 16 tooth nozzle.

Axial variation

The rate of axial growth of the sixteen tooth flow, Figure 6.103, appears to be quite constant. The overall similarity of this figure and the Mach number variation of the plain nozzle, Figure 6.27, is noteworthy.

Figure 6.104 is the equivalent Mach number variation for the eight tooth flow. Again the rate of growth is constant over the three stations that have been investigated. The only notable distinction between this figure and Figure 6.103 is the slightly better spread of data in the mixing region for the flow emanating from the 8 tooth nozzle.

6.7.2 Summary of M=1.8 castellated nozzle results

It was previously found that the M=1.0 and M=1.4 results could be summarised by the same set of comments. However the M=1.8 results do not quite reveal the same effects. Two major features can be identified.

1) At both x/D=4 and 6 very little difference can be found between 8 and 16 teeth. Compared to the plain jet both the 8 and 16 tooth flows do contain slightly more air.

2) At x/D=8 the 8 tooth jet is larger than the 16 tooth flow, but the latter is only marginally more energetic than the reference flow.

6.8 Summary of basic traverse results

This section will provide a summary of the traverse results previously presented but will exclude discussion of the actual mass flow and momentum flux values. In Section 6.9 the flux quantities are presented.

The following is a list of the most important conclusions from the free jet tests. A nozzle which produces a jet with good entraining characteristics is described as performing well.

1) Applying any of the castellations always improves the jet entrainment properties.

2) It was possible to test only a small number of castellation geometries but the results have suggested that other configurations might also improve the entrainment properties. In particular irregular shapes with few teeth could be beneficial.

3) Of the three castellation geometries tested, the 16 tooth jet always entrains less than the other two.

4) If the best nozzle for each Mach number is selected then, at a given station, the M=1.0 jet has the highest mass flow, and the

order of decreasing mass flow is then M=1.4, M=1.8 (and M=2.0).

5) Notwithstanding 4), if comparing similar geometry nozzles ie. M=1.0 16 tooth and M=1.4 16 tooth the percentage increase over the reference plain case does not necessarily favour the M=1.0 jet.

6) The choice of either the eight or the four tooth nozzles would depend upon the axial mixing length available. Generally eight tooth flows behave better up to six nozzle diameters.

These conclusions provide a very specific set of rules which allow the prediction with reasonable confidence of the performance of new configurations. None of the six observations is particularly noteworthy in itself, but what is noteworthy is the consistent manner in which the various results recurred.

6.9 Mass and momentum flux of basic traverse results

The error analysis of Section 5.6.2 and Appendix D will now be extended to the mass flow and momentum quantities. The actual flux values will then be presented with due regard to their uncertainty.

6.9.1 Accumulated errors in mass flow and momentum

In Appendix D the error analysis was restricted to the velocity uncertainties given in Table D.3 . The typical 'narrow' jet discussed in the earlier section can now best be identified as the M=1.8 x/D=6 plain jet. The effect of the tabulated errors in velocity are calculated for this particular case.

Figure 6.105 shows the calculated Mach number profile over a part of the traverse. The velocity errors of Table D.3 are translated to Mach numbers and the points plotted on Figure 6.105 with suitable lines joining the data. The behaviour of the error about the point M=1.0 is difficult to sensibly predict but a simple average of the two available errors is plotted. The errors in the supersonic regions are so small as to be insignificant and so are not plotted. Figure 6.106 is the same data but plotted for the ρvr case. The uncertainty in the extreme jet edges is considerable in terms of the

ρvr value but when the whole curve is integrated the effects diminish. The predicted zero velocity point is subject to an uncertainty of about ±5% in radial position, whereas the integrated areas of the two extreme lines differ from the mean by +1.4% and -4.8%. This implies the calculated values of mass flow could be up to 5.1% high or 1.4% low. The momentum flux graph, $\rho v^2 r$, is not plotted but the equivalent figures are 4.0% high to 1.1% low.

It is appropriate to reconsider the nature of the causes of the errors. It will be recalled from Appendix D that at low speed one of the main causes of error was the conditioning problem, whereas at high speed the unsteady velocities were the cause of the errors. The former error is fundamentally a random occurence but the unsteady effects are known to exist (and produce high readings). The problem with the unsteady effects is that their magnitude is difficult to determine. In addition throughout the speed range the yaw uncertainty is effectively a random occurrence because no independent means was available to determine whether yaw was present.

Bearing the nature of the errors in mind it is suggested that probably the mass flow is 2% high but with an uncertainty of ±3% on the resulting value. For the momentum flux these numbers would also be 2% high ±3%. In the remainder of this section the errors attributable to the inaccuracies in the data will be referred to as the 'velocity' errors.

For jets with wider mixing regions, for example a heavily entraining castellated jet flow, the 'velocity' errors will be different. An example calculation for a 'wide' jet (M=1.0 8 tooth x/D=6) showed the mass flow reading to be further in error than the 'narrow' case. For this jet the mass flow would be approximately 5% high ±7%, and 4% high ±6% for the momentum.

In addition an 'intermediate' jet class can be visualised which would have errors halfway between those for the 'narrow' and 'wide' cases.

6.9.2 The mass flow results from the free jet tests

Table 6.2 contains the mass flow data found from integrating the ρvr curves for all of the free jet traverses. Two values of mass flow are associated with each particular test case. The first number is the integrated result of the ρvr versus r graph when the effects of normalising the mass flow for ambient variations are included. The variation in the ambient conditions was discussed in Section 6.3 . The second value includes the effect of reducing the mass flow by the 'velocity' error factors given in the previous section. The key presented with this table shows into which class of jet (narrow, intermediate or wide) the data was placed, and consequently which correction has been applied.

Figure 6.107 is the mass flow variation with axial distance, corrected for all errors, for all four plain nozzles ie. M=1.0, 1.4, 1.8 and 2.0 . Note that the mass flows away from the nozzle are the measured values, whereas the exit mass flow is that estimated for the particular nozzle. The mass flow results for the M=1.0 nozzle are consistently higher, by approximately 10%, than the other three, but all results are increasing almost linearly with axial distance. These results accord with the simple subsonic rule for self-preserving jets from Ricou and Spalding (1961),

that $$\dot{m} = kx$$

where $\dot{m}$ = mass flow
k = jet dependent constant
x = axial distance from nozzle

However, for a complex supersonic flow close to the jet origin there is no such simple continuity or momentum condition which would alone force a supersonic jet to grow in the linear manner discovered.

The sonic jet is subject to a higher uncertainty in mass flow, due to the more vigorous and wider mixing region, than the other three jets. Consequently if the mass flow is plotted when not corrected for the 'velocity' errors there is a lower degree of coalescence between the four data sets. However, when plotted to the scale of

Figure 6.107 there is a barely visible distinction.

Figure 6.108 shows the axial mass flow variation for all the M=1.0 nozzle flows corrected for all the errors. Both the 16 and 8 tooth nozzles considerably increase the jet mass flow at all stations and no decay of the enhanced entrainment is apparent with axial distance. The four tooth nozzle behaves in quite a different manner however. The mass flow at x/D=8 for the 4 tooth flow is nearly 3 times the nozzle exit mass flow. The effect of the 'velocity' error correction is to reduce the more extreme results, but the castellation dependent trends are much in evidence.

For the M=1.4 nozzle the mass flow plot is shown in Figure 6.109 . The similarities with the M=1.0 graph, Figures 6.108, are very striking although most features are reduced in magnitude. The most important result is that again the 4 tooth nozzle initially entrains less than the 8 tooth but when x/D≃6 the two jets reverse in magnitude.

The M=1.8 jet data is plotted, Figure 6.110, for the fully corrected case. At M=1.8 the error corrections affect all points by a similar margin. The mass flows increase almost linearly with axial distance and the 8 tooth jet has consistently the largest flux.

The summary figure of the plain flows, Figure 6.107, contains all the data for the M=2.0 case.

6.9.3 The momentum results from the free jet tests

Table 6.3 contains the momentum values corresponding to those of mass flow in Table 6.2 . Following the previous procedure there are two numbers for each data point. It should be emphasized that the momentum presented is the conventional flux of momentum including only the velocity terms. The total momentum or stream force would in addition include the integrated effects of the local static pressure field, which accounts for the apparent non-conservation of momentum.

Figure 6.111 is the final corrected momentum flux for all the plain jets. The perfectly expanded jet should display conserved axial

momentum because there is ideally no pressure difference between the nozzle and any downstream station. This supposition is amply supported by Figure 6.111 which, completely independently, shows very good agreement between the integrated traverse results and the estimated nozzle exit momentum. In fact all four sets of momentum data agree closely over the range of measurement x/D=4 to 8. This also supports the previous assertion that the plain jet results have a high confidence level. On Figure 6.111 there is shown a line joining the x/D=0 and x/D=4 stations but this should not be taken as a prediction of the momentum distribution in this region.

Figure 6.112 is the corrected plot for all four M=1.0 jets, which shows a startling momentum disparity between the four tooth result and the other flows. The 16 tooth and the plain jets have very similar momentum flux quantities which are plausible because of the more reliable nature of the traverse data for these nozzles. The unfortunate discrepancies of the 4 tooth and some of the 8 tooth results suggests a direct correlation between having few teeth and producing unreliable data. The discrepancy cannot be explained by accepting that a momentum increase does occur for some cases, as this violates simple conservation laws. There is also no evidence of a large static pressure contribution which would allow the momentum flux to be dependent upon the axial position.

The cause of this supposed correlation must take the form of a very large unsteady flow structure which is even more vigorous than that allowed for in Appendix D. An additional inexplicable point is the flux at x/D=4 for the 8 tooth case which defies even this correlation because the momentum downstream behaves well.

Having just identified a powerful unsteady mechanism as the probable cause of the momentum irregularities makes the momentum variation without the 'velocity' error corrections applied of interest. However the plot of momentum flux just 'corrected to ambient' shows such little worsening of the momentum disparity that it is not necessary to include it.

The 'corrected for errors' streamwise momentum variation for the M=1.4 flows is given by Figure 6.113 . The similarity with the M=1.0

plot, Figure 6.112, is remarkable even to the extent of the 8 tooth x/D=4 point misbehaving.

For the M=1.8 jet flows the final corrected momentum is given by Figure 6.114 . Agreement is generally good between the three data sets, but as with the lower speed jets the 8 tooth results are slightly more erratic.

6.10 Traverse dependence upon nozzle angular position

In Section 6.5.3, when gathering data at x/D=4 with the four tooth M=1.0 nozzle, the extreme features recorded in the jet edge and some apparent skewness prompted concern as to whether the nozzle rotational position affected the traverse results. When conducting the same type of run with the equivalent M=1.4 nozzle these phenomena were also noticed. In this section are described the tests performed on the M=1.4 4 tooth nozzle to ascertain rotational effects.

Two additional traverses were made at x/D=4 along differing diameters. One was conducted from the centre of a tooth to the opposite tooth centre, and the other was from the centre of a gap to the opposing location. Effectively therefore the two traverses were made at ±22.5 degrees from the original traverse position. To ease identification in the following description the traverses will be labeled as 'tooth','gap' or 'step'.

The pitot pressure for the three traverses is given in the conventional presentation by Figure 6.115 . In the core region, r/D=0 to ±0.5, there is little difference between the three pressure variations. In the mixing zones however the results differ considerably from each other. The jet structure found from traversing a 'tooth' diameter is much narrower and has thin mixing regions. The 'gap' result has considerably greater width mixing zones than the previously recorded 'step' data set. The immediate conclusion from this plot is that the 'step' results could be a useful indication of the average jet properties, but quantification of this is impossible at this stage.

The static pressure, Figure 6.116, shows many of the same features in that the core pressures agree closely but behaviour in the mixing zone differs widely. It is not surprising that both the core pitot and static pressures are independent of nozzle rotation. The castellation induced mixing mechanism only directly affects the jet boundary so that if there is no active mixing, ie. velocity irregularity, in the core then it would be impossible to sustain circumferential pressure gradients.

From the Mach number plot, Figure 6.117, the 'tooth' traverse can be seen to be much slimmer than the other two. The predicted boundary points for 'gap' and 'step' traverses coincide quite closely which implies, not unreasonably, that the 'step' data tends to be heavily influenced by the vigorous 'gap' flow adjacent to it.

The most interesting features of Figure 6.117 are the additional regions of high speed flow found for the 'gap' traverse between $r/D=\pm 0.7$ and ± 1.1 . The mixing processes must be much stronger in the centre of a 'gap' to produce such a structure.

The final graph, that of the ρvr distribution Figure 6.118, demonstrates clearly the dependence on nozzle rotation. The strength of this dependence was an unexpected discovery. The flow regime at $x/D=4$ with 4 teeth is one of the hardest to record due to the magnitude of the unsteady velocities. This difficulty in recording manifests itself as asymmetry and scatter on Figure 6.118 .

The integration of the 'tooth' and 'gap' lines of Figure 6.118 has no direct significance because the integration is a circumferential exercise which assumes axisymmetry of the results. Indeed it can be argued that integrating the 'step' line may be an equally unrealistic exercise because the presence of axisymmetry has never been established. However if the mass flow for an imaginary axisymmetric jet having the 'tooth' properties is found and compared with the equivalent 'gap' result it is possible to deduce whether the integrated 'step' result produces a reasonable circumferential average. Table 6.4 contains such data for all three cases and also the average of the 'tooth' and 'gap' results. The 'velocity' error corrections are applied to the ambient corrected data as in the main

body of the flux presentations. Table 6.4 shows that both the mass flow and momentum differ considerably between 'tooth' and 'gap' but that the 'step' results are in close agreement with the average. The mass flow difference between the 'step' and the 'tooth/gap' average is only 1%, and the momentum difference is 7%. These results are no worse than the typical traverse cases.

A good means of portraying the extreme rotation dependence of the jet is a velocity contour plot, Figure 6.119 . This figure contains the velocity contours at x/D=4 of the M=1.4 4 tooth flow on the upper half, with the plain M=1.4, x/D=4 case below. It should be recalled that only three traverses were made of the castellated jet so Figure 6.119 contains some data assumed by reflection. The grossly distorted contours are a clear indication of the effect of the castellations but unfortunately no means is available to determine the velocity vectors around the contours.

The 100 m/s contour of the 'tooth' traverse occupies a similar radial location to that of the plain 100 m/s line. Even for the higher speed lines eg. the 400 m/s contour the 'tooth' results are similar to the plain case. However the 'step' results are of great interest. At low speeds the 'step' results are close to the 'gap' values but moving towards the core this association ceases and the 'tooth' and 'step' values are of equal size. This demonstrates clearly how the castellations create a disturbance in jet structure solely on the jet boundary but this effect progresses inwards as the jet moves downstream. By x/D=4 the 'gap' effect has reached the 400 m/s contour zone but the overall disturbance is small.

6.11 Summary of transverse free jet tests

The extensive pitot-static tests described in this chapter have established the entrainment characteristics of the plain and castellated jets. For the four plain jets the entrainment rates are all similar. In addition the data have shown that the four and eight tooth castellated jets entrain substantially more air in the first eight diameters when the nozzle Mach number is 1.0 or 1.4 . The castellating technique therefore is most effective on severely underexpanded jets, as initially predicted in Chapter 2. These

results are in accordance with those found from the photographic evidence of Chapter 5.

7. THE DUCTED JET TESTS

7.1 Introduction

This chapter describes the tests conducted on a simple augmentor-ejector to ascertain the performance dependence on primary nozzle design. The same twelve primary nozzles that have been detailed in Chapters 5 and 6 were used in the ducted jet programme.

The duct apparatus has been adequately described and illustrated in Chapter 3 with the exception of defining the intake contour. In Chapter 2 it was noted that previous work has highlighted the susceptibility of ejectors to inlet design. A simple two dimensional design process was therefore conducted using conformal transformations. Following the description of the inlet work in Section 7.2 this chapter will contain the results of the thrust measurements on the secondary shroud for all twelve nozzles tested. Some pitot and static pressure traverses across the exit plane of the ejector were also made and are presented in Section 7.4, with the optical results finally included in Section 7.5 .

7.2 Inlet design of ejector-duct

The purpose of this exercise was to design an efficient inlet which would allow the secondary flow to smoothly accelerate into the ejector. The approach adopted was to predict the streamline pattern into an ejector without an intake (as if it were a sink) and then construct an inlet shape to coincide with one of the streamlines. The constraints of the experimental exercise strongly suggested using a square duct cross-section. This choice suggested either restricting the inlet study to a purely two dimensional shape or developing a fully three dimensional solution. It did not appear to be a useful allocation of time to develop the latter option so the simple mathematical approach of conformal transformations was used.

Vallentine (1970) contains a section on conformal transformations restricted to potential two dimensional flows. Early in the planning of the test programme it became apparent that the proposed ejector would not operate in the fully supersonic 'second solution' regime.

This immediately avoided the problem of very high speed secondary flows. Indeed using an area ratio of 15 (based on primary throat area) the average secondary flow Mach number at the injection plane would not exceed 0.2 . Consequently the use of an incompressible solution was justified. The potential solution also neglected viscous effects. This was felt to be acceptable because the aim was to design an ideal device with no inlet separations. Intakes are often amenable to inviscid solutions because beneficial pressure gradients keep the accelerating flow attached to the inlet wall.

Figure 7.1 shows the flow pattern that was analysed. In physical terms it can best be visualised as a parallel two dimensional tube which is sucking free air. In the absence of viscous forces there is in theory no limit to the deflection sustainable by the flow entering the duct. The streamline pattern entering the duct is independent of the mass flow in the system. The general case of a flow of unit density is given by Vallentine as

$$z = \frac{l}{\pi}\left(e^{-(\pi/Q)w} - \frac{\pi}{Q} w \right) \qquad (7.1)$$

where l is the duct half width

Q is the half volume flow rate

z is the geometrical domain $\quad z = x + jy \qquad (7.2)$

w is the transformed domain $\quad w = \phi + j\psi \qquad (7.3)$

x and y are the cartesian dimensions, ϕ is the velocity potential and ψ the stream function.

By letting $l = Q = \pi$ equation (7.1) reduces to the equally useful form of :-

$$z = e^{-w} - w \qquad (7.4)$$

The streamline shapes would be entirely defined if x and y could be expressed in terms of ϕ and ψ.

Inserting (7.2) and (7.3) into (7.4) gives,

$$x + jy = e^{-\phi - j\psi} - (\phi + j\psi) \qquad (7.5)$$

Expanding $e^{-j\psi}$ and using the expansion of cos ψ gives, after equating real parts,

$$x = e^{-\phi} \cos \psi - \phi \qquad (7.6)$$

and

$$y = -e^{-\phi} \sin \psi - \psi \qquad (7.7)$$

Figure 7.2 shows the resulting streamlines and the velocity potentials. The x and y scales of Figure 7.2 are of course unimportant because of the non-dimensionality of the problem but the entrance to the two dimensional tube occurs at $x=-1$ and $y=\pm\pi$. From studying Figure 7.2 it was necessary to select the most appropriate streamline as the entry curve for the ejector shroud.

There were two stages in the selection process. Firstly an intuitive choice was made based on the conventional expectations of the intake geometry. Secondly a formal analysis of the intake pressure distribution around the various streamlines was calculated to justify the intuitive choice.

The intuitive criteria for selecting the shape were that the lateral (y) and axial (x) extents of the inlet curved sufaces would be approximately equivalent; that the shape would not contain any regions of large curvature which could produce flow separations in the viscous case; that the upstream end of the curve occurred at a large negative value of ϕ (ie. a low velocity). An example of a poor design would be the selection of $\psi=-0.5$ because the device would be extremely long and narrow, and the question of what form the far upstream shape should be is unanswered. The line having $\psi=-1.7$ was selected as the best compromise between having a high value of ϕ at a low upstream x, but with a sensible physical contour.

Determining the local pressures entailed calculating the velocity at discreet points on each streamline. The velocity components can be

found in terms of the complex variables via the complex velocity.

The complex velocity is given by

$$dw/dz = u - vj \qquad (7.8)$$

where u and v are the cartesian velocities in the x and y directions.

Now
$$\frac{dw}{dz} = - \frac{1}{e^{-W} + 1} \qquad (7.9)$$

So
$$u = R\left(\frac{-1}{e^{-W} + 1} \right) \qquad (7.10)$$

and
$$v = I\left(\frac{1}{e^{-W} + 1} \right) \qquad (7.11)$$

The local pressure was integrated along the streamline with respect to the projected axial area. A scaling factor had to be introduced to ensure that all cases investigated had the same final duct mass flow. In the extreme case of integrating between $\phi = -\infty$ and $\phi = \infty$ the resulting load would be the same whatever streamline is chosen. However by applying the dimensional constraints described in the above paragraph this process lead to a formal prediction of optimum shape. Curves with ψ=-1.7 produced the highest axial load between the limits ϕ=+∞ and ϕ=-1.0.

The practical ejector-shroud was constructed with an intake geometry based on ψ=$\pm$1.7 and an upstream limit of ϕ=-1.0 . No additional structure was incorporated to extend the lateral scope of the ejector inlet beyond ϕ=-1.0 . It was anticipated that an immediate performance penalty would be associated with this decision but as the purpose of the tests was to compare primary nozzle performance this degradation was acceptable. The lateral and axial length of the resulting intake was approximately three primary nozzle diameters.

7.3 Thrust measurements on secondary duct

The free jet tests were all conducted at a stagnation pressure of 6.9 bar gauge to provide a comparison of the nozzles under investigation. The ducted jet tests were also to be carried out to provide a comparison of nozzle performance as the primary aim. However the time required to determine the thrust generated on the ejector shroud was only of the order of a few seconds for each configuration. Consequently it was possible to investigate additional parameters during the ducted test phase.

The proposed application of the thrust augmenting ejector is to provide an aircraft with the ability to control itself whilst lacking forward speed. Such direct control of the aircraft by ejectors implies that the control characteristics of the actual ejector are of prime concern. The only available parameter which can be varied is the pressure supplied to the device. The opportunity was therefore taken to vary the stagnation pressure from 2.8 bar up to the maximum possible of 6.9 bar gauge.

The effect of varying the longitudinal position of the nozzle exit plane was not investigated as this would have entailed an exercise in geometrical optimisation. This is not to state that the injection location is unimportant, but that decisions as to which aspects to investigate had to be made.

The secondary thrust on the ejector shroud was read as a voltage offset across a Wheatstone bridge strain gauge circuit. Previous calibration of the ejector, using weights and pulleys, allowed quick determination of the thrust. In Chapter 2 the discussion of ejector principles lead to the definition of augmentation ratio as the ejector thrust divided by the isentropic primary thrust. However this conventional representation of ejector performance was not entirely appropriate because the main purpose of the tests was to evaluate different primary nozzles. Most of the comparative figures to be presented are of the secondary thrust relative to the theoretical thrust of the same Mach number plain nozzle.

For example for a Mach 1 nozzle:-

$$\Phi = \frac{T_s + T_{iM=1.0}}{T_{iM=1.0}} \qquad (7.12)$$

where T_s is the secondary thrust
and $T_{iM=1.0}$ is the ideal thrust of a M=1.0 nozzle

The ideal thrust, T_i, can be calculated for any nozzle, but it is easier to consider the non-dimensional thrust which is purely a function of nozzle Mach number and overall pressure ratio.

$$\frac{T_i}{p_o A^*} = \frac{1}{M}\left[\frac{2}{\gamma+1}\left(1 + \frac{\gamma-1}{2} M^2\right)\right]^{\frac{\gamma+1}{2(\gamma-1)}} \left[(1 + \gamma M^2)\left(1 + \frac{\gamma-1}{2} M^2\right)^{\frac{\gamma}{1-\gamma}} - \frac{p_\infty}{p_o}\right] \qquad (7.13)$$

where M is nozzle exit Mach number
A^* is the nozzle throat area
p_o is the upstream stagnation pressure
and p_∞ is the ambient pressure

This equation is, of course, only true if there is sufficient upstream pressure to ensure that the design exit Mach number of the nozzle is being achieved, a condition fulfilled in all the tests described.

In some cases the primary plus secondary thrust is compared to the continuously expanded isentropic thrust, as is more usually the case in ejector work. The thrust augmentation ratio is then denoted by Φ_t . Note should be taken however that the existing reaction control nozzles on the BAe Harrier use simple convergent nozzles which, having no secondary thrust, operate at a value of Φ_t considerably less than 1.0 .

As mentioned in Chapter 3 the duct was capable of being set with two alternative area ratios (A_R). The first area ratio was nominally 15 with respect to the nozzle throat area, and some further tests were made at the much larger area ratio of 25 . These nominal area

ratio values do not take into account the cross-sectional area occupied by the primary nozzle. In addition the nozzle wall thickness and, more importantly, the larger primary flow area of the supersonic nozzles also cause the secondary area to be less than the nominal value. Table 7.1 summarises the precise area ratios for each nozzle in relation to the nominal values. In the following text the nominal values will be used to identify the configuration.

The following sections describe the thrust runs in turn for all four Mach number nozzles at the two area ratios.

7.3.1 Secondary thrust performance with M=1.0 nozzles

The ejector was arranged such that the exit plane of the M=1.0 nozzles was positioned 6 throat diameters from the rear end of the duct. Each of the nozzles was run at seven different stagnation pressures and the thrust on the shroud recorded. A reasonable period was allowed for the supply pressure to settle and then the average value of the thrust over a five second span was recorded. Coincident with this process the Mowlem unit was recording the prevailing stagnation conditions. Every test was repeated at least once to improve the reliability of the data and additional runs were made with some of the castellated nozzles to check whether there was nozzle rotation dependence. From the repeatability tests the absolute thrust never varied by more than 0.5 N, which at the higher values represented 0.6% . Altogether 81 test runs were conducted with the A_R= 15, M=1.0 configuration, at nominal stagnation pressures of 2.76, 3.45, 4.14, 4.83, 5.52, 6.21 and 6.90 bar gauge. These pressures correspond to 40 to 100 psi in steps of 10 psi.

To determine a value of augmentation ratio the primary thrust was calculated for each nozzle at the relevant stagnation and ambient conditions for the test. Equation (7.13) can be simplified if the Mach number at the exit is known. For the M=1.0 nozzles there is no uncertainty about the exact exit Mach number and so equation (7.13) becomes,

$$\frac{T_j}{p_o A^*} = 1.2679 - \frac{p_\infty}{p_o} \qquad (7.14)$$

Area ratio = 15

The results of all the M=1.0 runs with an A_R = 15 duct are presented in Table 7.2 . The values for each test are the averaged result of the two test runs, and the value of Φ is that found from equation (7.12). The values of thrust augmentation achieved by the device are generally quite low, but the most important factor is the strong dependence of thrust on nozzle toothing. The maximum, Φ=1.098, is achieved by the M=1.0 eight tooth nozzle, whereas the plain nozzle thrusts are always close to zero. The recording of a negative secondary thrust has physical significance, either suggesting that the primary jet is impinging upon the duct or that a base drag is present. If the maximum Φ is presented in terms of the ideal isentropic thrust the value of Φ_t is 1.036 . This spread of data is an indication of the extremely poor design and performance of the ejector in conventional terms. Values of Φ_t less than 1.2 are usually considered to represent an unsatisfactory ejector, but for the purposes of nozzle comparison the results are very useful.

Figure 7.3 is a plot of the recorded secondary thrusts against stagnation pressure for all four M=1.0 nozzles. Included on the figure are the additional thrusts recorded at 6.9 bar gauge with the castellated nozzles rotated through a half tooth arc. Six points are revealed:

All the data appears credible, with a high degree of consistency in the thrust variations.

For all three castellated nozzles the thrust increases with pressure; and at high pressure the thrust increases almost linearly with pressure.

The eight tooth nozzle always has the highest performance, followed by the 4 tooth and the 16 tooth. The plain nozzle generally has the lowest performance.

At low pressures the effect on thrust of castellating the nozzles is greatly reduced.

The plain nozzle thrust curve suggests that a reduction of primary pressure below 2.8 bar gauge would improve the performance.

There is no dependence of thrust on nozzle rotation.

From the experimental observations given above it is possible to draw three conclusions.

1) The ducted jet performance is directly correlated to the free jet entrainment results of Chapter 6, with the 8 and 4 tooth nozzles performing best.

2) There is a strong dependence of secondary thrust upon primary pressure for the castellated nozzle, which suggests that the effectiveness of the castellations improves with pressure.

3) An additional factor appears to govern the plain nozzle results at low pressure. The nature of this phenomenon cannot be identified solely from the M=1.0 data.

The alternative means of presenting ejector performance is to plot Φ against nozzle pressure, Figure 7.4 . The results are broadly similar to Figure 7.3 but the gradient of the thrust lines appears to be falling slightly. This is because the secondary thrusts are small compared to the primary values so that equation (7.8) predominates in the value of Φ. However Figure 7.4 does show better the performance differences at low pressure with the four nozzles.

Figure 7.5 is the variation of Φ_t with pressure. A very interesting result can be seen where Φ_t increases with pressure for the eight tooth flow but consistently decreases for the other three nozzles. This result is solely due to the better performance of the 8 tooth nozzle.

Area ratio = 25

Table 7.3 contains the averaged results of the 69 runs made with the M=1.0 nozzles in the larger duct. The results are plotted as thrust

augmentation ratios on Figure 7.6 . Three points can be made.

The performance is considerably worse than the area ratio 15 tests, but again the results are very consistent.

The order of thrust variation ie. 8 tooth, 4 tooth, 16 tooth and plain nozzle is repeated exactly as for the narrower duct.

The plain nozzle again produces improved performance at the lower pressures.

The value of Φ_t is included in Table 7.3 to give an indication of the ejector performance in conventional terms, and is plotted against pressure in Figure 7.7 . The order of thrust variation is the same as for the A_R=15 runs. The overall decline in Φ_t is a fundamental feature of high pressure ejector design which will be discussed further in Chapter 8 .

7.3.2 Secondary thrust performance with M=1.4 nozzles

When using the longer M=1.4 nozzles the whole ejector shroud was positioned further downstream to ensure that injection still occurred six reference diameters from the rear end. All four nozzle types were tested at the seven stagnation pressures stated in Section 7.3.1 .

A thrust coefficient was calculated for each test run but it was not possible to present a simple equation like (7.14) to cover all the M=1.4 runs because of the slight geometrical variations in the nozzles noted in Chapter 5 .

Area ratio = 15

Sixty seven runs were conducted on the A_R=15, M=1.4 configuration and are summarised in Table 7.4 . The values of Φ_t are no longer included because the nozzle performance is adequately represented by the thrust and Φ. Figure 7.8 presents the secondary thrusts and Figure 7.9 the augmentation ratio. From the former the secondary thrust variation above 4.8 bar is seen to be of a similar form to

the M=1.0 tests, with the eight tooth jet producing the best result. However with the M=1.4 nozzle, the 16 tooth configuration is considerably better than the 4 tooth. Figure 7.8 contains two further important pieces of information which are crucial to the understanding of the behaviour of high pressure ejectors. The first of these concerns the three castellated nozzle thrust lines and the second deals with a previously identified duct flow phenomenon.

The first important result of Figure 7.8 is that the modified nozzle flows all show a well defined minimum thrust level. It is well established that the thrust performance of high pressure ejectors falls with increasing pressure, clearly demonstrated by Quinn (1976). It is possible to associate the thrust decay found between stagnation pressures of 2.8 and 3.6 bar gauge with this expected phenomenon. To account for the remaining part of the thrust curve it is necessary to restate that the M=1.4 nozzles are underexpanded over the complete span of pressures of interest. Indeed the perfect expansion pressure ratio for an M=1.4 nozzle is approximately 3.2, or a gauge stagnation pressure of about 2.2 bar on Figure 7.8 . The castellation technique was originally proposed to improve mixing when the nozzles are underexpanded, and, as has been demonstrated here and in Section 7.3.1, the performance does increase with pressure once the tooth dependent mixing mechanism has become established. Consequently the M=1.4 results show that the teeth do not become effective immediately the nozzle becomes underexpanded but are delayed by a pressure increment of about 1.5 bar. It may be conjectured that the M=1.0 results would have shown a similar trend if the rig could have been run at lower pressures.

The second major observation to come from Figure 7.8 concerns the plain nozzle thrust line. The strange behaviour of its thrust in the region of p_o = 3.0 - 5.0 bar is almost certainly due to an aeroacoustic interaction; the variation displays remarkable similarities to those shown by Quinn (1977), even though the geometries are widely different. It may be recalled from Chapter 2 that Quinn (1977) describes a phenomenon whereby noise generated internally by the shock structure reflects from the duct wall and promotes vortex growth in the jet mixing layer. The most important point, however, is that in the current experiments the castellated

flows are not at all susceptible to this acoustic mechanism, probably due to a markedly different vortex structure in the shear layer. Having ascribed the M=1.4 results to an aeroacoustic phenomenon it is possible to postulate that the previously unexplained behaviour of the plain M=1.0 flows at low pressure is occurring for the same reason.

Figure 7.8 also contains the results of the three runs conducted with the primary nozzle rotated through a half-tooth arc. As with the M=1.0 tests the nozzle rotation dependence is negligible.

Figure 7.9 also shows the M=1.4 behaviour at low pressures in a clearer form. The scale of this figure needs careful consideration in the low pressure region. The error in recording thrust produces a possible error of ± 0.0014 in Φ . This error does add some doubt to the precise variation of Φ.

Area ratio = 25

Figure 7.10 portrays the thrust augmentation ratios of the larger duct configuration. Seventy four runs with this layout were conducted, again with four nozzles at seven pressure ratios, and the results are listed in Table 7.5 . Figure 7.10 is plotted to the same scale as Figure 7.9 to ease comparison. The dependence of thrust on tooth number is very similar at A_R=25 as it was with an area ratio of 15, but the magnitudes of the thrusts are greatly reduced.

Notwithstanding the larger duct size, the plain flow still appears to be subject to a similar acoustic mechanism, but rather inexplicably, the castellated flows do not display the expected minima.

7.3.3 Secondary thrust performance with M=1.8 nozzles

The same procedure was adopted when testing the M=1.8 nozzles as used previously, but there were only three M=1.8 nozzles available.

Area ratio = 15

Table 7.6 contains all the small duct M=1.8 test results, 59 in total. The majority of the data was recorded as negative thrusts, an indication of the poor entrainment characteristics of the M=1.8 jets. Figure 7.11 is a plot of the secondary thrusts for these runs. There is some difficulty in interpreting the data. In Section 7.3.1 it was stated that the error recording each secondary thrust could be $\pm$ 0.5 N . If this uncertainty is included on Figure 7.11 it is still not possible to produce a smooth variation of the 16 tooth data. There is no obvious reason why only this line is behaving strangely but it could be an experimental fault in the strain measuring equipment. If some smoothing of the doubtful data is performed then the 16 tooth result follows quite closely the 8 tooth line.

Figure 7.11 certainly substantiates the observation of Section 7.3.2 concerning the apparent delay in the initiation of the improvement in mixing after the nozzle becomes underexpanded. For the M=1.8 case the nozzle will be perfectly expanded at a pressure ratio of approximately 5.75, or a stagnation pressure of 4.75 bar gauge. The two castellated flows display minima at a pressure increment of about 0.9 greater than the start of the underexpansion regime, whilst the plain nozzle thrust continues to fall. There is no evidence of an acoustic effect occurring with the M=1.8, A_R=15 configuration.

The tests with the primary nozzles rotated slightly are more difficult to interpret than at M=1.0 and M=1.4. The 16 tooth nozzle result when rotated coincides closely with the reference attitude value. However the 8 tooth nozzle displays more variation between the two rotation tests than the known inaccuracy of the measurements would account for. It was not felt necessary to establish the cause of the problems with the M=1.8 data because the overall performance of the ejector at this primary injection Mach number is so poor.

Area ratio = 25

Table 7.7 contains the results of the 46 runs attempted with the area ratio 25 duct. The plot of the secondary thrust data, Figure 7.12, shows clearly the steady decrease in thrust from the plain nozzle and also the minimum thrust location of the castellated flows.

7.3.4 Secondary thrust performance with M=2.0 nozzle

The plain M=2.0 nozzle was tested with both duct sizes over the same range of pressures as the lower speed jets.

Area ratio = 15

Twenty five runs were conducted on the A_R = 15 duct at pressures between 2.76 and 6.90 bar. Additional data were gathered at nominal pressures of 3.10, 3.79 and 4.48 bar gauge. The runs are tabulated in Table 7.8 and the secondary thrusts plotted in Figure 7.13, (as are also the A_R = 25 results). As with the M=1.8 results the absolute values of the thrusts are very poor but the most striking feature is the very particular variation with primary pressure. The discovery of this behaviour prompted rigorous investigation of the repeatability of the data and also the inclusion of more data points. The results of this further analysis were to wholly substantiate the data, and so, with the proviso that the thrusts are accurate to ± 0.5 N, the curve of Figure 7.13 is a true repesentation of the measured thrust variation.

The reason why the thrust varies so dramatically is undoubtably due to the occurrence of acoustic resonances. Unlike the M=1.0, 1.4 and 1.8 tests there was corroborating audible evidence when the M=2.0 nozzle was being run. As the jet stagnation pressure slowly rose through the pressure range a most distinct variation in noise frequency and intensity occurred. If the oscillatory nature of the thrust line is ignored then a gradual decline with pressure can be observed on Figure 7.13 .

Area ratio = 25

The final ducted runs performed to record secondary thrust are given in Table 7.9, and reference should be made to Figure 7.13 . The use of the large duct has noticeably changed the secondary thrust curve compared with the area ratio 15 arrangement. Distinct variations in audible tones were also present with the large duct, indeed the most unpleasant noise produced in any of the free or ducted test occurred between p_o = 4.8 and 5.5 bar gauge with the M=2.0, A_R=25 duct. The noise was noticeably less severe either side of this pressure band. It should be noted that the loudest noise does not coincide with a performance peak. The overall performance decline with pressure again occurs with this configuration.

7.3.5 Summary of the thrust measurements on the ejector-duct

1) Considering just the four plain nozzles at a given area ratio, and ignoring local aeroacoustic effects, the M=1.0 nozzle performs best in terms of secondary thrust, followed by the M=1.4 nozzle, with the M=1.8 and 2.0 nozzles performing worst. This result applies across the whole span of pressures investigated.

In the free jet tests of Chapters 5 and 6 there was no substantial difference between the entrainment rates of the four plain flows, but the M=1.0 jet was marginally better at entraining ambient air. This was ascribed to the overexpansion, and subsequently larger jet surface area, for the underexpanded flows on leaving the nozzle.

2) The plain nozzle flows are sometimes subjected to an aeroacoustic resonance which improves mixing at particular pressures. This mechanism does not exist with the castellated flows due to the change in shear layer structure. Both the M=1.0 and 1.4 plain nozzle flows are subject to the acoustic phenomenon at low pressures with both duct sizes; the M=1.8 nozzles are immune to the resonance effect whereas the M=2.0 flow suffers severely over most of the pressure band, in both of the ducts.

The selectivity of the occurrence of resonance suggests that the phenomenon is dependent on the acoustic spectrum of the jet as well as the physical geometry of the ejector.

The importance of acoustic effects in supersonic flows prompted an investigation of the literature on the subject. Appendix F contains a summary of the results found which are largely concerned with free jet situations.

3) In a given situation the castellation technique always improves the thrust performance over the plain case, except sometimes where the plain nozzles are subject to an extreme resonance.

4) The castellation mechanism only works effectively when the nozzles are substantially underexpanded.

5) Considering only the behaviour of the eight castellated nozzle flows, at a given pressure and geometry, the M=1.0 thrust results are far better than the M=1.4 results, which in turn exceed the M=1.8 data.

6) The eight tooth castellated nozzle always performs better than the four and sixteen tooth geometries at a given area ratio and pressure.

7) The area ratio = 15 results are invariably better than the area ratio = 25 data, unless a particular acoustic resonance is occurring.

7.4 Total and static pressure traverses across ejector exit

The secondary thrust measurements produced a clear picture of the effect of the castellated nozzles on each ejector tested, but it was apparent that further investigation of the flow behaviour in the duct would lead to a better appreciation of the ejector performance. In particular the mass flow of the combined streams was of great interest as this would give an indication whether the nozzles in the duct were entraining as effectively as the free cases. The mass flow was determined by conducting pitot and static pressure traverses

through the combined primary and secondary streams. It was not possible to use the existing total and static pressure tubes inside the duct confines, but it was a simple task to modify the traverse gear and software to record the exit plane properties, ie. at x/D=6 from the injection plane.

The choice of traverse resolution was rather difficult due to the unknown characteristics of a high speed round jet in a square duct. It was decided to be cautious and use a high resolution, so avoiding gathering unusable data. A consequence of this decision was that only two nozzle/duct configurations could be examined. The 'best' nozzle, ie. the M=1.0 8 tooth, was therefore investigated together with the corresponding reference case, the M=1.0 plain nozzle, in the A_R=15 duct. The nozzle pressure was chosen to be 6.9 bar gauge to provide a comparison with the free jet data.

The traverse took the form of scanning horizontally from one wall of the duct to a point just past the centreline, and then repeating the procedure at different vertical positions. Only a quarter of the duct exit was therefore traversed. The vertical distance between successive runs was 3 mm, the same as the horizontal step length. Twenty traverse runs were needed to record each of the static and total pressures, thereby producing 400 data points for the quadrant considered. Figure 7.14 is an illustration of the traverse resolution and procedure employed in the tests. The total elapsed time for one complete duct investigation was six working days. This prolonged testing period introduced unwanted uncertainty as to the behaviour of the atmospheric pressure and temperature during the test. A single value of the stagnation conditions was required, but fortunately the runs were conducted during a consistently warm and settled spell of weather, allowing a reasonable average to be calculated.

The jet properties were calculated at each data point using similar computer programs to those used in the free jet tests. Spanwise variations and contour plots of the flow properties at the exit plane were then constructed. The duct mass flow was simply found by summing the individual cell ρv products over the entire exit area.

M=1.0 plain nozzle, A_R=15 duct

Figure 7.15 shows six of the twenty spanwise variations of velocity in one quadrant of the plain nozzle case. To aid description of these results the spanwise horizontal distance from the duct centreline is called 'z', and is non-dimensionalised by the overall duct width, '2l'. Similarly the vertical distance from the centreline is labelled 'y/2l' . The six data sets correspond to traverses taken at y/2l = 0.0125, 0.0875, 0.1625, 0.2375, 0.3125 and 0.3875 . The velocity lines are all reasonably smooth and the data appears quite credible. No data is presented below about 20 m/s because the velocity cannot be resolved sufficiently accurately.

The y/2l = 0.0125 line corresponds quite closely to a traverse through a horizontal diameter of the primary jet, and as such provides interesting comparison with Figure 6.15 from the free jet tests. After allowing for the change to a Mach number scale, and the use of a different non-dimensional transverse quantity it is apparent that installing a duct around the jet changes the jet structure very little. The basic feature of the underexpanded M=1.0 jet at x/D=6, the reduction in core velocity due to severe shock structure, is still visible.

The axisymmetric nature of the core flow is shown clearly in the region where z/2l ≈ 0.1 . At this location the maximum velocities recorded for both y/2l = 0.0125 and 0.0875 are very similar, but the latter occurs at a position closer to the duct centreline, as expected.

The "centreline" traverse shows that the jet is very nearly reaching the duct wall by x/D=6. There is not a zone of constant velocity secondary flow visible, a point that will be discussed in Chapter 8.

Figure 7.16 is the velocity contour plot of the M=1.0 plain case. The basic symmetry of the flow is readily apparent, as is the fact that more than half the quadrant area contains an axial velocity of less than 50 m/s . The shaded zones of Figure 7.16 represent regions where the pitot pressure was equal to or less than the local ambient pressure. Of course it is possible for the potential unmixed

secondary flow to have a total pressure equal to ambient, and a sub-atmospheric static pressure. However the magnitude of the dynamic pressures in these regions is too small to show conclusively whether there is unmixed secondary flow, stagnant zones or even recirculating flow. Whichever is occurring will make very little difference to the calculation of the mass flux at the exit plane. The total mass flow passing through the exit plane of the device in this configuration is 2.60 kg/sec, compared to 2.68 kg/sec for the free M=1.0 jet at x/D=6.

M=1.0 8 tooth nozzle, A_R=15 duct

The contour plot for this case is shown in Figure 7.17 and the transverse velocity variation is Figure 7.18 . Referring first to Figure 7.18 there is considerably more scatter on the seven different traverses presented (a further line at y/2l = 0.4625 is included). The data in the region of z/2l = 0.35 is rather confusing but the most reasonable line through the data is plotted. To avoid giving misleading information no data is plotted below 50 m/s.

In comparison with Figure 7.15 the centreline data (y/2l = 0.0125) is reduced by about 5%, although it is similar in form to the free jet data for the eight tooth nozzle. However, the most dramatic differences occur at the larger value y/2l traverses; for example the velocity variation when y/2l = 0.3125 shows an increase across the whole span, with greatly increased values when z/2l > 0.2 . This is a direct manifestation of the increased mixing occurring with the castellated nozzle. A further interesting result is that the y/2l = 0.0125 and 0.0875 traverses show velocities of the order of 150 m/s within z/2l = 0.0125 (1.5 mm) of the duct wall. There is no uncertainty about the accuracy of the traverse position because all traverses were started with the probe initially set at 1.5 mm distance from the duct wall. The duct boundary layer is therefore extremely thin at x/D=6. The implication is that the jet is actually impinging on the duct wall before the end of the mixing length is reached. Any conventional secondary flow boundary layer that exists further upstream is being first compressed and then consumed by the jet flow. The conclusion to be reached from studying Figure 7.18 is

that the configuration could well be suffering from considerable skin friction drag. It will be recalled that obtaining the correct balance between mixing and friction is one of the toughest problems the ejector designer faces. Confirmatory evidence of the jet impinging on the duct was provided by an oil trace left on the perspex after prolonged running, the oil being contained in very small quantities in the air supply. The integrated mass flow for this case is 3.63 kg/sec, compared with 3.95 kg/sec for the corresponding free jet.

The contour plot of the castellated flow, Figure 7.17, demonstrates the remarkable effect of the nozzle teeth on the velocity field. It is not possible to construct the 50 m/s contour due to the considerable scatter of the data. There appears to be some asymmetry with the region of zero total pressure not occupying the exact corner of the duct. This is probably not due to a misalignment between the nozzle axis and the duct axis because the duct was left untouched between this run and the previous plain nozzle test. A slight circumferential error was noticed after the tests had been completed, ie. the nozzle 'step' diameter was not precisely aligned with the horizontal axis of the ejector. The 200 m/s contour clearly indicates that the two 'lobes' expected in the quadrant with eight teeth are not quite placed symmetrically.

From Figure 7.17 it might be supposed that orientating the primary nozzle so that a velocity lobe fills the duct corner would minimise drag and increase mixing. However the results of the thrust runs, Section 7.3, showed that no such effect is present, the thrust being independent of nozzle rotation.

Figure 7.19 is the mass flow variation of the free M=1.0 jets from Figure 6.108 with the two ducted results added. No corrections have been applied to the ducted runs and the free data is corrected solely for the ambient condition variations. The ducted mass flows are both lower than the corresponding free jet values but not substantially so. In Chapter 8 the duct mass flow data will be used to evaluate the ejector performance using some of the simple 'one-dimensional' ejector models described in the Chapter 2.

7.5 Schlieren images of ejector flows

Schlieren pictures of the A_R=15, M=1.0, 1.4 and 2.0 ejector configurations were obtained at 6.9 bar gauge stagnation pressure. The photographs cover the nozzle exit and most of the six diameters of the ejector length. The M=1.8 flow was not photographed because the M=1.8 case was considered to be of little importance. The flow patterns at each Mach number will be discussed in turn.

The four square silhouettes in the corners of the pictures are the supports for the perspex walls and the apparently irregular roof and floor of the ejector is caused by adhesive tape used to seal the duct corners.

7.5.1 M=1.0 A_R=15

The plain M=1.0 nozzle flow is shown by Figure 7.20 . The jet structure is very similar to the free case, Figure 5.8, throughout the flowfield. This is rather unexpected as the jet is emerging into a region of lower pressure than the free test cases. The primary jet mass flow should be unchanged but the divergence angle would be expected to be greater. The subsonic mixing mechanism is very hard to visualise but again there appears to be no substantial change in this region of the flow.

The reflection from the wall of some of the sound waves generated at the nozzle lip can just be seen. There is no visual evidence of the transverse resonance that was noticed in previous work, Quinn (1977), at this pressure.

The 16 tooth M=1.0 nozzle produces the flowfield of Figure 7.21. The increased jet spreading is evident but the behaviour of the jet at x/D=6, at the far right of the photograph, is not very clear. The next picture, Figure 7.22, is one of the more interesting photographs taken. Most of the events in the free and ducted tests were recorded by both shadowgraph and schlieren techniques but Figure 7.22 is the result of a very weak schlieren effect. The schlieren knife-edge was inadvertantly left just in the path of the light beam for an intended shadowgraph picture. Figure 7.22 is

positive evidence of the existence of streamwise vortices generated by the castellations. The occurrence of these vortices had previously been just speculation based on their formation with subsonic hypermixer nozzles. The vortices are visible until the region of the Mach disc, but their behaviour close to the nozzle is difficult to determine. It is possible that the vortices have a circumferential component to their paths until coalescence between adjacent vortices occurs.

The eight tooth nozzle photograph, Figure 7.23, displays less early jet growth than Figure 7.21 but by the end of the duct the jet is touching the wall. The four tooth jet, Figure 7.24, is similar in most respects to Figure 7.23 and also the free case Figure 5.14 .

7.5.2 M=1.4 A_R=15

Photographs were taken of all four M=1.4 jet flows, see Figures 7.25, 7.26, 7.27 and 7.28 . Yet again there is is very little difference between the ducted results and those taken earlier in the free jet series. The four tooth jet, Figure 7.28, shows much slower growth than the other castellated flows. This result correlates with the thrust measurements where the four tooth nozzle performed worse than the 16 and 8 tooth nozzles in the A_R=15 duct. Only the plain jet image contains visible sound waves and reflections.

7.5.3 M=2.0 A_R=15

The final photograph, Figure 7.29, is a clear picture of the strong penetration of the perfectly expanded jet. Suprisingly there are no sound waves observable in the duct although considerable audible evidence of resonances was noticed when measuring thrust. A very slight increase in the divergence angle can be seen if compared to Figure 5.12 .

7.5.4 Summary of evidence from schlieren photographs

The only two photographs in which sound waves are visible are those of the plain M=1.0 and M=1.4 flows, which substantiates the belief that only the plain nozzle flows are liable to aeroacoustic

resonance. Figure 7.22 shows clearly the streamwise vortices travelling along the perimeter of the jet for the M=1.0 16 tooth nozzle. Otherwise the results of the schlieren photographs are rather disappointing, not in terms of quality but the lack of noteworthy details. The reduction in exit pressure seems to have only a marginal effect on the initial jet divergence, but this is due to the low overall performance of the ejector configuration.

7.6 Conclusions from the ducted jet tests

The ducted jet tests have provided both a satisfactory extension and corroboration of the earlier free jet tests, and the existence of streamwise vortices from the castellated nozzles has been confirmed. The absolute performance of the ejector in conventional terms is very poor but the primary purpose of comparing nozzle characteristics has been adequately achieved.

The achievement of small values of secondary thrust is due to use of a very short mixing length and the omission of a diffuser.

The heavy entrainment of the free M=1.0 jets has been repeated in the smaller area ratio duct configuration; in addition the effect of the tooth number has produced the expected performance trends. The maximum thrust case, achieved with the M=1.0 eight tooth nozzle, can be attributed to the most complete mixing occurring with this configuration in the six diameters of the available ejector length. Eight teeth are most effective at entraining secondary flow in this length because the streamwise vortices are not interfering with each other before the end of the duct. If the duct had been longer it is probable that four tooth nozzles would have achieved the greatest performance.

A very important aeroacoustic effect has been highlighted but it has been shown only to influence the plain nozzles. However, the maximum realisation in terms of thrust was an order of magnitude smaller than that achievable by castellating the more underexpanded nozzles.

Selecting from these examples the most appropriate nozzles for use in an ejector is not a straightforward task. It is essential to recall that the perfectly expanded nozzle (the M=2.0) is delivering considerably more primary thrust than the M=1.0 nozzle at a given pressure ratio, see equation (7.13). Reference to the tabulated performance data provides most guidance in the selection process.

From Table 7.2 the M=1.0 eight nozzle is seen to produce a true thrust augmentation ratio of 1.034 at 6.9 bar pressure in the A_R=15 duct, whereas from Table 7.8 the value of Φ_t ($\Phi=\Phi_t$ when M=2.0) is 0.988 with the perfectly expanded nozzle. Therefore the castellations do indeed 'recover' more thrust than is lost by the use of a purely convergent nozzle. This result applies over the whole pressure span for the eight tooth nozzle.

Three further reasons can be proposed for using M=1.0 castellated nozzles in preference to convergent-divergent geometries.

Firstly, the supersonic effuser of a convergent-divergent nozzle is a large piece of structure in comparison to the convergent portion. Indeed for an M=2.0 nozzle the divergent part is approximately two throat diameters long, a distance which can barely be afforded in an ejector.

Secondly, the construction of a convergent-divergent nozzle is a far from trivial task.

Finally, the ducted tests were run at 6.9 bar gauge pressure which is about half the pressure available on the aircraft. The results have shown that Φ increases with pressure for the M=1.0 castellated nozzles in the crude ejector employed. This suggests that nozzle and ejector geometries exist which would have a performance at higher pressure far greater than that achievable by an ejector with perfectly expanded nozzles.

8. THE DESIGN AND PREDICTED PERFORMANCE OF A HIGH PRESSURE EJECTOR

8.1 Introduction

The free and ducted tests have identified the castellation technique of primary nozzles as a potentially useful idea for incorporation into high pressure ejectors. Chapter 7 showed that the M=1.0 nozzles were most amenable to castellating, and it is the aim of this chapter to propose a design for a high pressure augmenting ejector using M=1.0 castellated primary nozzles. In addition, a method for predicting the performance of such an ejector is detailed. In order to accomplish these tasks it is necessary to analyse in more detail the ejector performance revealed in Chapter 7.

The review of ejector technology presented in Chapter 2 discussed various prediction methods and that of Quinn (1976) is used here. Quinn's High Temperature and Pressure (HTP) model seemed well suited to the high pressures and high temperatures occurring in a reaction control system ejector.

8.2 Application of Quinn's HTP model to the ejector of Chapter 7

The HTP model was orginally developed in order to predict the performance of simple axi-symmetric ejectors operating with pressure ratios up to 6.0 and primary temperatures up to 800K. The method falls into the category of a "one-dimensional" scheme in which the continuity, momentum and energy equations are solved in the confines of the ejector mixing duct. The technique provides simple means for introducing nozzle, inlet, friction and mixing losses, but prior knowledge of these quantities is needed.

As with all one-dimensional ejector models the HTP method cannot forecast important phenomenon such as acoustic screech, or the effect of rapid mixing nozzles, without some prior knowledge of the efficacy of the mixing processes.

Appendix G summarises the HTP method without diffusion, and includes a modification to the form of the energy equation

contained in the Journal of Aircraft paper of Quinn (1976).

The HTP model is applied to the two M=1.0 A_R=15 test cases in which high resolution traverses were made across the exit plane. Four hundred readings were taken of the total and static pressures in one quarter of the exit area. From this data can be extracted the exit plane properties necessary to use the HTP model. The following data were common to both tests:-

Primary Mach No.	M_p	= 1.0
Primary Pressure	p_o	= 6.9 bar gauge
Nominal Area Ratio	A_R	= 15.0
Actual Area Ratio	A_{RT}	= 13.73
Nozzle Exit Diameter	D	= 35 mm
Ejector Mixing Length	L	= 6.0 D
Characteristic Width	W	= 3.8 D
Characteristic Length	L/W	$\simeq$ 1.6

8.2.1 The M=1.0 A_R=15 plain nozzle test

In Chapter 2 it was demonstrated that the skewness quantity β was very important in incompressible one-dimensional models. However, for a fully compressible model the situation is made far more complex with four skewness parameters α, β, δ and ϵ describing the flow, as defined in Appendix G.

The ejector exit traverses reveal the following values for the M=1.0 plain nozzle case:-

α = 1.194 β = 3.424 $\delta \simeq 7.0$ $\epsilon \simeq 1.0$

These figures are very interesting. Firstly, the three skewnesses parameters α, β and δ are all far higher than the values discussed by Quinn (1976). This leads to a low level of predicted augmentation ratio (borne out in practice). In addition, at such high values of skewness the relationships suggested by Quinn for calculating α and δ from β do not hold. The value of the energy skewness, ϵ, suggests that the static enthalpy across the

ejector is practically constant for a cold primary flow.

Using the corrected version of Quinn's energy equation, from Appendix G, the above skewnesses give the temperature function K as approximately equal to α . This results in the mean total temperature at the exit being very nearly equal to the primary flow total temperature. Thus for a cold ejector there is no need to use an energy equation if the primary and secondary temperatures are nearly equal. For the case under consideration this criterion was satisfied with the mean primary temperature being 291.8K and the ambient (secondary) temperature approximately 288K.

The iterative process of Quinn's HTP model results in three performance parameters of particular interest.

1) The secondary flow injection Mach number, M_s.

2) The ejector exit mean Mach number, $\bar{M}_2$.

3) The thrust augmentation ratio, $\bar{\Phi}_t$. This quantity is the same as that denoted by $\bar{\Phi}_t$ in Chapter 7 and is calculated from:-

$$\bar{\Phi}_t = \frac{\beta}{\alpha} \frac{\dot{m}_s}{\dot{m}_o} \frac{\bar{u}_2}{u_{ISEN}} \qquad (8.1)$$

For the case specified above and with zero inlet, nozzle and friction losses the following values are obtained:-

$$M_s = 0.137 \qquad \bar{M}_2 = 0.362 \qquad \bar{\Phi}_t = 0.966$$

The value of true thrust augmentation ratio actually measured in the thrust experiments of Chapter 7, see Table 7.2, was 0.945. The close agreement is encouraging but a number of other factors will have some small effects on the predicted $\bar{\Phi}_t$. Firstly, the exit plane traverse data did not have the pitot-static corrections applied that were discussed in Appendix D. The effect would be a very slight reduction in α and β , leading to a marginal reduction in augmentation ratio $\bar{\Phi}_t$. The nozzle, inlet and friction losses will in reality also tend to reduce $\bar{\Phi}_t$. According to Quinn, the friction loss, ξ_f , will be negligible because the

velocities close to the wall are very low. The nozzle efficiency, ξ_o, as defined in Appendix G, was calculated to be 0.973 by traversing the total pressure probe across the nozzle exit plane. The inlet efficiency was not measured but its effect was thought to be minimal due to the careful selection of the intake contour.

A repeat of the performance prediction, but with a primary nozzle efficiency of 97.3%, produces the following performance parameters:-

$$M_s = 0.139 \qquad \bar{M}_2 = 0.356 \qquad \bar{\Phi}_t = 0.962$$

Thus a 2.7% nozzle loss produces a 0.4% fall in the thrust augmentation. The secondary Mach number can actually increase because the device is effectively running at a lower primary nozzle pressure and so is more efficient, until of course, the energy lost in the nozzle is considered.

It is reasonable to assume that the slight overprediction of performance is due to the failure to incorporate the inlet loss in the equations. Consequently, by working back from the measured value it is possible to predict a value of inlet loss. This process leads to $\xi_i \simeq 0.99$, a plausible result. For completeness the three resulting performance parameters are:-

$$M_s = 0.136 \qquad \bar{M}_2 = 0.352 \qquad \bar{\Phi}_t = 0.942$$

Thus a 1% inlet loss has a 2% detrimental effect on $\bar{\Phi}_t$, considerably more effect than ξ_o.

All of the performance figures quoted above re-emphasise the conclusion of Chapter 7 that a 6.9 bar gauge, area ratio = 13.73 ejector of the type tested, produces no performance benefit over an unaugmented fully expanded jet flow. It is therefore of interest to evaluate the ejector model with an ideally mixed flow ie. setting $\alpha = \beta = \delta = \epsilon = 1.0$, and all other losses to zero.

An ideal 6.9 bar gauge, A_{RT}= 13.73 ejector produces:-

$$M_s = 0.711 \qquad \bar{M}_2 = 0.763 \qquad \bar{\Phi}_t = 1.258$$

The performance therefore increases dramatically in the ideal case, but it is apparent that even this ejector would barely meet the overall performance levels demanded from a reaction control system ejector. If however, a diffuser is incorporated it would be possible to boost the augmentation substantially, see Section 8.3.8.

A clear demonstration of the adverse effects of pressure ratio is provided if the incompressible (ie. low pressure) model of Fancher (1972) is applied to an area ratio = 13.73 ejector. In this case $\bar{\Phi}_t$= 1.566 for an ejector with no losses and no diffuser.

8.2.2 The M=1.0 A_R=15 8 tooth nozzle test

The second experimental test case provides an essential check on the apparently accurate method developed by Quinn.

The exit traverse data results in the following values of the two relevant skewnesses,

$$\alpha = 1.065 \qquad \beta = 1.530$$

Thus it can be seen that the castellated nozzle substantially reduces the skewness of the exit flow. The efficiency of the castellated nozzle was calculated to be identical to that of the M=1.0 plain nozzle ie. ξ_o = 0.973. This high efficiency was unexpected as previous work with subsonic hypermixing nozzles had shown considerable losses associated with the higher mixing rate designs, eg. see Eastlake (1971).

The friction loss, although increased over the plain nozzle ejector test, is still discarded as being negligible. The intake loss can be assumed to be the same as that calculated from the plain nozzle test case.

The HTP model results in the following predicted performance for the 8 tooth nozzle ejector, with $\xi_o = 0.973$ and $\xi_1 = 0.99$.

$$M_s = 0.358 \qquad \bar{M}_2 = 0.554 \qquad \bar{\Phi}_t = 1.042$$

Again the prediction is acceptably close to the measured value, from Table 7.2, of $\bar{\Phi}_t = 1.036$. It is clear that the castellations cause a large increase in the entrained flow Mach number, but the overall result in terms of augmentation ratio is a more modest increase.

An important point to note is that it is possible to extract from the free jet data of Chapter 6 values for the skewness parameters which would be quite accurate for the HTP model. Fancher (1972) discusses using free jet data and concludes that if the secondary velocity is a high fraction of the primary jet velocity then the ducted mixing rate will be less than the free case. However, in real ejectors with losses and with large area ratios (later shown to be necessary) the secondary velocity will be low. Thus it may well be sufficient to just conduct free jet surveys now that the HTP model is validated as a practical means of assessing ejector performance.

8.3 The major design variables of thrust augmenting ejectors

Having established that the HTP model is a useful method of assessing ejector performance, there are eight topics crucial to ejector design that merit discussion.

8.3.1 The effect of primary pressure ratio

The HTP model successfully predicts the conventionally expected fall in $\bar{\Phi}_t$ with an increase in primary pressure. This is partly due to the increasing disparity between choked nozzle thrust and fully expanded thrust as the primary pressure increases. In addition, with subsonic free jets it is found that entrainment rate decreases slightly as the pressure increases, see Ing (1985) and Fancher (1972). It is believed that high pressure jets contain a

relatively lower turbulence level which causes slower mixing.

Figure 8.1 shows the dependence upon pressure of an ideal ejector (no losses) having an area ratio = 13.73. It should again be noted that any pressure dependent mixing mechanisms (such as those caused by castellations) cannot be identified by the HTP model; this becomes apparent by comparing Figures 8.1 and 7.5, in which only the plain nozzle case on the latter plot follows the form of the curve on Figure 8.1.

Figure 8.1 does not contain data above a gauge pressure of 12 bar because at this point the secondary flow is predicted to choke. In certain circumstances the exit flow can be supersonic and the ejector can, in theory, be running in the so called 'second-solution' mode, see Section 2.2.4. In Section 8.4 more attention is given to high pressure ejectors at area ratios sufficiently large to avoid choking.

8.3.2 The effect of primary temperature

According to the discussion given by Quinn (1976) the effect of increasing the primary temperature is to improve the performance of short ejectors. This occurs because the higher viscosity of the primary fluid causes faster mixing and a reduction in skewness. Nagaraja et al (1973) also comment that at elevated temperatures the gas properties will alter (γ will fall slightly) and this will also lead to a small improvement in $\bar{\Phi}_t$. However, these observations disagree with a solution of the HTP model at high temperature, in which $\bar{\Phi}_t$ is found to fall slightly. The solution of the HTP model recognises an increase in temperature solely as an increase in injection velocity, and consequently $\bar{\Phi}_t$ falls in a manner similar to that found with an increase in pressure ratio.

The present experiments did not investigate hot primary flows and so it is not possible firmly to predict the effect of temperature. However, it appears that either a negligible or a small beneficial effect might be expected when the ejector is run at full temperature, 750K.

8.3.3 The effect of primary Mach number

It was established in Chapter 6 that all four plain nozzles (M=1.0, 1.4, 1.8 and 2.0) tested in the free jet programme produced similar jets at x/D=6 in terms of mass flow and overall diameter, see Figures 6.15 and 6.107. Thus the expansion occurring outside the nozzle of the various underexpanded cases seems closely to match that occurring in the nozzle of the perfectly expanded jet. It might therefore be expected that ejector performance (with plain nozzles) will be independent of the Mach number; this expectation is indeed fulfilled if the ducted jet tests of Chapter 7 are studied (acoustic phenomena excepted).

The discussion following the report of Benson and Eustace (1973) makes the rather misleading statement that expanding the flow in a convergent-divergent nozzle to ambient pressure will eliminate the blockage effects present when an underexpanded jet expands after leaving the nozzle. This is erroneous because the convergent-divergent nozzle itself will cause an equal amount of blockage but this may be 'hidden' in the choice of reference area. The notation employed in the current work leads to no such confusion and so Mach number effects are negligible for plain nozzles.

The only way in which blockage does enter the discussion is by its effect upon the quoted area ratio of the ejector. Thus it may be argued that the A_{RT} = 13.73, M = 1.0 ejector is actually an A_{RT} = 8 device. This helps to explain why high pressure ejectors have a poor performance at a given area ratio compared with low pressure devices. The HTP model can be used with supersonic primary flows but care must be exercised when defining the area ratio.

None of the foregoing should be confused with the certain benefits associated with M = 1.0 nozzles when attempting to improve the mixing rate by castellating. Thus M = 1.0 nozzles are the unequivocal choice for a high pressure ejector.

8.3.4 The effect of area ratio

The simple incompressible analysis of von Kármán (1949) shows that ejector performance should increase with an increase in area ratio. Application of the HTP model to an ideal high pressure ejector produces the same dependence, see Figure 8.2 with the 6.9 bar gauge case plotted. Also plotted are four experimental data points at area ratios of 13.73 and 23.73 showing the dramatic difference in the behaviour of the real ejector. Again, secondary flow choking provides a limit to the theoretical line; in this case choking occurs at area ratios less than 8.0.

In Section 8.2 it was shown how ejector exit flow skewness can have debilitating effects on the thrust augmentation. Using this knowledge it is possible to provide an explanation of the worse performance of the A_{RT} = 23.73 results compared with the area ratio = 13.73 data, as noted in Section 7.3.5. and shown by Figure 8.2.

A loss free ejector performance prediction for an A_{RT} = 23.73, 6.9 bar, M=1.0 augmentor shows that $\bar{\Phi}_t$ = 1.348, compared with an augmentation ratio $\bar{\Phi}_t$ = 1.258 for the A_{RT} = 13.73 duct, see Figure 8.2. However, changing to a larger duct does not automatically increase performance if substantial mixing losses (skewnesses) are present. By studying Figure 7.16, the M=1.0 plain nozzle exit velocity contour plot of the A_{RT} = 13.73 ejector, it is possible to observe that large areas of the duct are quiescent. It is quite plausible that the A_{RT} = 23.73 duct would contain even larger quiescent zones. The result would be an increase in each of the skewnesses α , β and δ . In the worst case it might be supposed that all the extra area of the larger duct would be quiescent, producing $\alpha \simeq 1.23$ and $\beta \simeq 5.91$, although, of course, no measurements were made to substantiate this. With these new values of skewness the predicted performance of the tested A_R = 25 plain nozzle ejector is:-

$$M_s \simeq 0.08 \qquad \bar{M}_2 \simeq 0.21 \qquad \bar{\Phi}_t \simeq 0.96$$

These figures clearly show that simply increasing the area ratio does not necessarily improve the performance of poorly mixed ejectors. The actual measured value of Φ_t is 0.940 from Table 7.3, thereby suggesting that considerable areas of the A_R = 25 ejectors were indeed quiescent.

8.3.5 The effect of mixing length

It is a fundamental feature of thrust augmenting ejectors that the thrust augmentation increases as the mixing process becomes more complete. Increasing the length available for mixing is thus a direct means of improving performance, but long mixing lengths are, of course, undesirable in an aircraft installation. A consequence of increasing the area ratio of an ejector is also to require a longer mixing length so that the flows can mix and fill the larger duct.

No direct investigation of the mixing length parameter was attempted in the ducted jet tests but the test results give a qualitative idea of the length necessary for good performance. The plain nozzle test in the A_{RT} = 13.73 duct produced very skewed flows, and it is clear that a substantial lengthening of the duct is necessary. For the 8 tooth test case the skewness was much reduced and only a small increase in mixing length would be necessary to make α and β close to 1.0. A more sensible step to improving the skewness would be to have a round mixing duct, thereby avoiding the quiescent zone shown on Figure 7.17.

The usual method of shortening the characteristic mixing length is to use multiple primary nozzles. This is discussed in Section 8.5. However, it is clear that castellated nozzles will always have an important role to play in reducing the mixing length of high pressure ejectors.

8.3.6 The effect of exit static pressure

Quinn's model for ejector performance makes the assumption that the static pressure across the ejector exit plane is atmospheric. However, due to the highly underexpanded flows in the current tests

it was doubtful whether the exit flows did differ substantially from ambient pressure, and whether this would affect the performance. A study of the M = 1.0, A_R = 15 plain nozzle ejector shows the mean static pressure to be 0.006 bar below ambient at exit. The local gauge static pressure did in fact vary between +0.089 and -0.035 bar; the higher figure occurring in the primary jet shock structure, and the sub-atmospheric pressure occurring in the regions of greatest shear. The effect of a non-atmospheric exit static pressure can be investigated by modifying Quinn's momentum equation. Equation G.10 thus becomes:-

$$F_3(M_s) = \left(1 + \frac{1}{A_{RT}}\right)\frac{\gamma(\beta + \xi_t)P_e}{\xi_1}\bar{M}_2^2 + \left(1 + \frac{1}{A_{RT}}\right)\frac{P_e}{\xi_1} - \frac{\pi}{A_{RT}}F_3(M_p)\frac{\xi_e}{\xi_1} \quad (8.1)$$

where P_e is defined as follows:- $P_e = \frac{\bar{p}_2}{P_a}$

$\bar{p}_2$ = mean static pressure
P_a = ambient pressure

In the current example P_e differs only marginally from 1.0, in fact P_e = 0.994.

Solving the iterative process, the equations of the HTP method produce values of M_s and $\bar{M}_2$ slightly higher than the case with P_e = 1.0. However, the effect is too small to be considered necessary to include in the performance method. The reason why the entrainment increases is that having a sub-atmospheric exit pressure causes the internal flows to expand to a higher Mach number, rather similar to the flow at the entrance to a diffuser. Of course the total exit thrust of the ejector will fall slightly because of the negative contribution of the exit static pressure, but the increased mass flow more than compensates and Φ_t can actually increase slightly.

In conclusion, it is adequate to assume uniform ambient static pressure for a diffuserless ejector, even at high primary pressures.

8.3.7 The effect of base drag

In the analysis of ejector performance it is important to consider the induced pressure forces on the ejector. It is a fundamental principal of ejector operation that the induced secondary momentum (measured at the primary injection plane) is exactly equivalent to the sum of the suction force on the ejector shroud and any losses present in the inlet, eg. friction. However, a question rarely addressed by ejector designers, but of significance in installation design, is that of the pressure forces on the downstream surface of the ejector, ie. base drag.

Base drag occurs in many aerodynamic applications when ambient fluid is entrained into an emerging jet, thereby creating suctions on the surface adjacent to the jet. The drag can be increased if the entrained fluid separates as it passes over the downstream surface; or conversely, careful design of a boat-tail or pen-nib fairing can reduce the base area close to the jet efflux.

If the downstream surface of the ejector is bluff, as in the ejector tested here, then base drag will be present. However, the base drag will not be substantially different in magnitude from the base drag occurring with a simple unaugmented nozzle arrangement. Consequently the reaction control nozzles on the Harrier also suffer from the adverse effects of base drag. The conclusion thus reached is that base drag cannot be solely linked to the utilisation of an ejector, but careful installation design can reduce base drag, for both ejectors and unaugmented cases.

8.3.8 The effect of diffusion

Diffusion can have significant beneficial effects on ejector performance, but unfortunately it is not possible to accurately predict the measure of thrust improvement obtained by adding a diffuser to an existing design. Fancher (1972) shows that diffusion will increase the secondary mass flow, but of course, the exit momentum can be reduced because the exit velocity will fall. Optimum Φ_t is thus shown to occur with diffusers operating between the points of maximum pressure recovery and maximum efficiency.

The augmentor technology summarised in Chapter 2 revealed that little work of practical use has been reported into diffuser design for ejectors. Even less work has been performed to analyse the effects of diffusers, except for presentations on loss-free ejector-diffusers at low pressures. The reason for the paucity of useful ejector-diffuser data is the uncertainty of the effects of diffusing highly skewed flows, as discussed by Quinn (1974).

The purpose of the following discussion is thus limited to the likely performance trends resulting from using the HTP model with diffusion. The high pressure ideal ejector (no losses) can be analysed with some confidence but the inclusion of losses, ie. skewness, makes the method very approximate.

Having no diffuser data available it is necessary to recourse to the most basic forms of diffuser representations. The conventional measure of diffuser performance is the pressure coefficient C_{Pd} :-

$$C_{Pd} = \frac{P_a - \bar{p}_2}{q_2} \qquad (8.2)$$

Where P_a is the ambient (exit) pressure; $\bar{p}_2$ the diffuser entrance static pressure and q_2 the dynamic pressure of the flow entering the diffuser. The HTP model assumes that the static pressure is constant across both the entrance and exit of the diffuser, and the discussion concerning transverse static pressure, presented in Section 8.3.6, substantiated this assumption. The definition of C_{Pd} also relies on the assumption of a constant static pressure at entrance $\bar{p}_2$, and a uniform ambient pressure at exit, P_a .

The reference pressure, q_2, introduces some difficulties because it will depend upon the overall diffuser-ejector combination effectiveness and will not be known a priori. However, it will not be an inordinate error to define q_2 as the dynamic pressure leaving the ejector without a diffuser present.

The quantity of prime interest in a diffuser-ejector is the static pressure at the end of the parallel mixing duct, $\bar{p}_2$. Rewriting equation (8.2),

$$\frac{\bar{p}_2}{p_a} = 1 - C_{Pd}\left(\frac{q_{12}}{p_a}\right) \tag{8.3}$$

and defining

$$q_{12} = \tfrac{1}{2}\gamma \bar{p}_2 \bar{M}_2^2 \tag{8.4}$$

gives

$$\frac{\bar{p}_2}{p_a} = \frac{1}{1 + \tfrac{1}{2}\gamma C_{Pd} \bar{M}_2^2} \tag{8.5}$$

For simplicity (and providing an ideal case) it can easily be shown that an incompressible analysis of a diffuser produces:-

$$C_{Pd} = 1 - \left(\frac{1}{A_d}\right)^2 \tag{8.6}$$

The compatibility equation of the HTP model is modified by the diffuser in an identical way to that of assuming a non-ambient exit static pressure, as in equation (8.1). Consequently the same notation of a pressure factor can be used, in this case it will be written:-

$$P_d = \frac{\bar{p}_2}{p_a} \tag{8.7}$$

Figure 8.3 displays how the ideal performance of a 6.9 bar gauge ejector is substantially improved with the addition of an area ratio $A_d = 2$ diffuser. This plot shows very similar trends to those presented at low pressures, eg. see Quinn (1972a) where at larger area ratios the effect of diffusion is increased. Secondary flow choking limits the lowest area ratio possible in the diffusion case to $A_{RT} \simeq 17$.

As previously mentioned it is unfortunately impossible to speculate about the effects of diffusion on the real test cases. However, it is apparent that diffusion of the M = 1.0 plain nozzle case, with the very large skewnesses present, would probably not be possible because of wall flow separation. The works of Quinn (1974) and Seiler and Schum (1978) have shown that slightly skewed flows can

be diffused but no quantitative data on the changes in skewness can be extracted for use in the HTP model. However, by studying the form of the equations of the HTP model, it is possible to conclude that real ejectors with losses will not respond as well to diffusion as the ideal cases shown in Figure 8.3.

To further elucidate this last point, Figure 8.4 is reproduced from the report of Nagaraja, Hammond and Graetch (1973). From Chapter 2 it may be recalled that Nagaraja et al develop a compressible one-dimensional model but the cases under study are all relatively low pressure. Thus Figure 8.4 shows a theoretical prediction of a 1.5 bar gauge (ie. choked) ejector of area ratio 15. In addition the primary temperature is 450K but this does not materially affect this use of the graph. The 'loss' case is not precisely defined but it includes the type of losses in the HTP model, in quantities expected to be realistic. It can be seen that diffusion is certainly less effective in real ejectors and that the optimum diffuser area ratios are lower because the diffuser stalls earlier.

From the above discussion it is apparent that the subject of diffuser design in both low and high pressure ejectors needs much more attention before firm predictions of diffuser effectiveness can be made. It is also clear, though, that a useful degree of diffusion is not directly linked to the primary pressure provided that the flow is well mixed before entering the diffuser, or alternatively, some additional means must be taken to ensure attached flow in the diffuser. The work of Alperin and Wu (1981) is a very important attempt to design a combined mixer-diffuser and any future work into high performance diffusers should take note of their ideas.

8.4 The extension of the HTP model to a 14 bar ejector

Quinn's HTP model has been shown to represent accurately the simple square duct ejector tested in the experimental programme. The next stage in the process of identifying a practical design is the application of the HTP model to an ejector at full pressure ratio, ie. 14 bar gauge primary pressure.

Figure 8.5 shows the performance dependence on area ratio for a 14 bar ejector. The ideal case shows that performance is poor at this high pressure and that large area ratios are essential. An example of diffusion is shown to produce substantial benefits, but secondary flow choking limits the diffuser effectiveness below area ratios of 25-30. The diffuser case should be treated with caution because of the uncertainties detailed in Section 8.3.8.

Nozzle and inlet losses, for a particular configuration, are usually considered to be independent of the operating condition, see Quinn (1976), so the data measured and calculated at 6.9 bar gauge can also be used in the 14 bar case. The result of adding these losses is to reduce Φ_t by about 2%.

The major performance penalty (and a source of uncertainty) is the level of skewness present in the real ejector. Increasing the pressure of a jet may produce slight increases in the skewness, see Ing (1985), but the free jet studies show that, at some distance from the nozzle, all plain (ie. not castellated) round jets of differing Mach number grow at similar rates and induce similar velocity fields, see Figure 6.107. Indeed, the results of Chapter 7 showed that the castellation-dependent mixing mechanism produced increased entrainment (decreased skewness) with a pressure increase. Hence it is conservative to use the 6.9 bar skewness data at 14 bar.

The best test case at 6.9 bar (the M = 1.0, 8 tooth, A_{RT} = 13.73 test) produced skewnesses α = 1.065 and β = 1.530. If the duct had been of circular section, instead of square, (to eliminate the small quiescent zones shown in Figures 7.16 and 7.17) then the skewness would reduce to $\alpha \simeq 1.06$ and $\beta \simeq 1.41$. Using these latter figures as the best attainable from an ejector having a characteristic length L/W $\simeq$ 1.6, (the geometry tested) the performance drops substantially, see Figure 8.5. It is clear that such an ejector would serve no practical purpose: it is therefore essential to have a skewness $\beta < 1.41$ and to incorporate diffusion.

The alternative means of predicting the performance is to extrapolate the thrust augmentation from the experimental 6.9 bar gauge data. A study of Figure 7.5 shows that it is not easy to predict Φ_t at 14 bar, but, assuming no unforeseen influences, the augmentation Φ_t is approximately 1.05. However, this value is much larger than the prediction shown on Figure 8.5 at A_{RT} = 13.73 and β = 1.41. Thus, it can be concluded that the skewness is reducing with pressure increase, and, at 14 bar pressure, the values of α and β in a simple axisymmetric ejector are possibly as low as 1.03 and 1.15 respectively. The simplest method of gaining an idea of the size of the skewness at 14 bar would be to conduct some free jet traverses at this pressure.

8.5 A practical 14 bar ejector design

Here follows a proposal for a high pressure ejector which takes account of all the performance experience presented in Chapter 8 and the overall understanding of ejectors gleaned from this research. The design should still be considered to be a broad proposal which would require substantial experimental investigation before a commitment is made to its use: there are still large areas of high pressure ejector design which are not fully understood.

Three parts of the proposal can be identified. Firstly the basic configuration will be selected, which is largely an intuitive choice based on ejector experience. Knowing the basic design allows the second phase, the ejector sizing, to be presented. Finally some more detailed aspects of the design are discussed, with an approximate performance prediction. Aspects such as installation design and the behaviour of the ejector in a cross-wind are not considered.

Whether or not a reaction control ejector is a viable proposition, given the low levels of performance attainable, is not discussed. The proposal presented is the best that can reasonably be hoped for, although it still contains a high speculative content.

8.5.1 Configuration selection

The application of the ejector to an ASTOVL reaction control system imposes certain geometric constraints. In particular a device having a mixing duct of rectangular planform, but not of excessive aspect ratio, is attractive as it can be accomodated in the rear fuselage/ tail structure. Multiple nozzles are, of course, useful in reducing the characteristic length of an ejector. Combining these two desirable features suggests an ejector having a planform aspect ratio, A_{SR} , of 4 and four primary nozzles. A design study trade-off exercise would be needed to finally optimise the aspect ratio question.

Figure 8.6 shows a suitable design having an A_{SR} = 4, and the various features will now be discussed.

The primary nozzles would be mounted in a similar fashion to that proposed by Alperin and Wu (1981) but with two nozzles fixed to each side of the inlet in a staggered arrangement. The inlet shrouds would themselves form the plenum chambers capable of containing the 14 bar pressure. Alperin et al also inject the primary flow at a small angle to the ejector axis. This apparently increases the entrainment rate (in the same manner that jets in cross-flow entrain) but a 'cosine-loss' is associated with this technique. It is probable that a small angle of injection could be found to be optimum at high pressure, but more work would be required to identify it quantitatively. Figure 8.6 shows a 15 degree angle of injection as a first choice.

The primary nozzles would be circular M = 1.0 nozzles with castellations. The characteristic length of the ejector would be greater than 1.6, hence the 4 tooth nozzle might be better than the 8 tooth. It is possible that future work will identify a nozzle having a better entrainment rate than those tested in Chapter 7, but currently the round 4 or 8 tooth nozzle must be selected.

It is crucial that the mixing duct design is matched to the flow system produced by the primary nozzles. The mixing flows must

occupy the entire cross-section at the ejector exit; it appears that this emphasis has been missed by many earlier ejector workers but the importance of a full duct has been demonstrated in Sections 8.2 - 8.4. Consequently it may be necessary to carefully contour the mixing duct walls.

It is proposed that a relatively short parallel section, about 30% of the available mixing length, should start at the injection plane, followed by a wide angle diffuser. The parallel section will allow the mixing process to commence without imposing an adverse pressure gradient. It is then essential that the mixing process continues in the diffuser, again as proposed by Alperin and Wu (1981). The diffuser will have a curved contour of either 'tulip' or 'trumpet' shape and will incorporate a substantial amount of wall blowing at the entrance plane. The wall blowing will be energetic enough to penetrate beyond the ejector exit, thereby making use of the ideas proposed by Seiler and Schum (1978) and Alperin and Wu (1981). The end walls will also diverge slightly and incorporate wall blowing. All the diffuser wall blowing will be supplied from the adjacent primary plenum chamber.

8.5.2 Basic sizing of ejector

A study of Figure 8.5 shows the limited envelope in which the ejector must be designed to operate. It is clear that the originally desired level of performance cannot be attained (the original target being $\bar{\Phi}_t \simeq 1.6$) and a device having useful performance will require a large area ratio. If good diffusion is achieved and nozzle and inlet losses are kept low then an area ratio 35 device might produce $\bar{\Phi}_t = 1.2 - 1.25$.

It is quite possible that future aircraft would be more amenable to a twin ejector installation replacing the more obvious single control. Each ejector would occupy half the planform area, but for simplicity the single large ejector will be the one discussed.

From geometric considerations it is apparent that to achieve a specified degree of skewness in a multiple nozzle ejector requires a shorter mixing length than that found in the single jet tests of

Chapter 7. Conversely, increasing the area ratio demands a larger mixing length. Figure 8.7 shows the geometries involved and it can be concluded that the A_R = 35, A_{SR} = 4 ejector needs a characteristic length L/W = 2.0 to achieve the same degree of mixing present in the simple square ejector.

It is now convenient to introduce full-scale absolute dimensions. A calculation of the thrust requirement shows that the single nozzle diameter necessary to produce the correct order of (unaugmented) thrust is approximately 90 mm (D^*). Thus the four nozzles of the ejector would each be 45 mm diameter ($D^*/2$) and the ejector throat dimensions would be $2.66D^*$ x $10.64D^*$ (240 mm x 960 mm). From the arguments of the preceeding paragraph it can be seen that a length of $5.3D^*$ (480 mm) is needed to achieve $\beta \simeq 1.4$. However the discussion of Section 8.4 suggested that β was far lower than 1.4 at 14 bar. If indeed β was 1.15 then, with the addition of angled primary injection, it might only need a mixing length of, say, $6.5D^*$ (585 mm) to achieve $\beta \simeq 1.0$.

It is fortunate that ejector length is less constrained by the installation design than the other ejector dimensions. Assuming the intake region takes up about $2D^*$ (180 mm) then the total ejector length becomes $8.5D^*$ (765 mm) which is acceptable. Following the arguments of Section 8.5.1, the duct would have a parallel portion about $2.1D^*$ long and a diffuser the remaining $4.4D^*$.

The specification of the diffuser area ratio (and its effect on performance) is the area of greatest doubt. It will probably be possible to achieve a mixer-diffuser operating efficiently with an area ratio of 2.0. Thus the exit width of the ejector will be about $5.3D^*$ (480 mm).

Figure 8.8 shows the ejector mounted in a suitable boom with the main representative dimensions included.

8.5.3 The high pressure ejector in detail

Having four nozzles protruding from the ejector shroud will increase the inlet loss ξ_1 above that calculated for the simple square duct ejector. Assuming no separations occur around the nozzles then all the ξ_1 loss comes from skin friction. Increasing the number of nozzles and changing to an $A_{SR} = 4$ duct will increase the wetted area by about 100%, thus $\xi_1 \simeq 0.98$. The inlet of the simple square ejector gave satisfactory performance, so it is believed that a rectangular hyperbola should provide the basis of the inlet contour in the proposed design. The more detailed aspects of inlet optimisation would provide a suitable case for investigation by CFD codes such as PHOENICS.

The primary nozzle efficiency, ξ_0, will only drop if the internal surface area of the nozzle array increases. Changing to four nozzles will thus double the ξ_0 loss to 0.95.

The form of diffuser wall blowing is not possible to define at this preliminary stage. A continuous nozzle around the diffuser entrance periphery is the most obvious technique but boundary layer excitation can be achieved more efficiently by using individual slot nozzles which create streamwise vorticity. These alternative schemes need to be thoroughly investigated because, of course, both have detrimental effects on the primary thrust available for injection.

The discussion of base drag in Section 8.3.7 highlighted the need to avoid large base (undersurface) areas. Therefore having the diffuser walls extending as strakes beneath the body could be useful, see Figure 8.8. The end walls would then have to be retractable to avoid drag in flight. Whether the ejector needs to be enclosed in forward flight is unclear but this is an area in which innovative folding doors and movable primary nozzles would be needed.

The final graph, Figure 8.9, shows the estimated performance of the ejector over a range of pressures. The plot is based on the following specification:-

Area Ratio $A_R = 35$ Aspect Ratio $A_{SR} = 4$

$\xi_o = 0.95$ $\xi_t = 0.98$ $\xi_f = 0.0$

The skewnesses are decreasing with increasing pressure (which accounts for the constant level of $\bar{\Phi}_t$) and are estimated from the 6.9 bar gauge test data. Examples are :-

6.9 bar: $\alpha = 1.05$ $\beta = 1.30$

10 bar: $\alpha = 1.03$ $\beta = 1.17$

14 bar: $\alpha = 1.015$ $\beta = 1.05$

The temperature is fixed at ambient, but as stated in Section 8.3.2 the effect of temperature is expected to be marginal.

The diffusion case has a diffuser of area ratio = 2. The performance with diffusion is very speculative, but the expected benefits are not optimistic.

The decrease in skewness with pressure increase is a useful feature as an almost constant level of $\bar{\Phi}_t$ simplifies the control mechanisms of the ejector air supply.

In concluding the discussion of ejector performance it must be stated that the performance predicted by Figure 8.9 is largely intelligent speculation, but it is probably the best that can be achieved. It is clear that augmented reaction controls are subject to large doubts about their viability at very high pressure. A change in the propulsion system to reduce the pressure available for the reaction controls will probably not produce improvements in the ejector performance because the duct flow skewness will increase.

A very important point also to consider is that a simple convergent 14 bar reaction control nozzle would be producing only 90% of the thrust of a fully expanded 14 bar jet: ie. an 'augmentation' ratio can be conceived such that Φ_t = 0.90 for a conventional reaction control nozzle. The percentage increase of the ejector reaction control therefore looks more encouraging, ie. Φ_t = 1.20 is a 33% increase over the unaugmented case.

9. CONCLUSIONS

Throughout this report on high pressure ejector systems specific conclusions have been given where appropriate. This chapter provides both a summary of these and a wider discussion of augmented reaction controls. The conclusions are given in a similar order to that of the thesis layout.

A comprehensive literature search revealed that although much work has been conducted to understand and design low pressure ejectors there is a large gap in knowledge relating to high pressure augmenting ejectors. The specification of the aircraft control requirement showed that an ejector would be supplied with high pressure air, up to 14 bar gauge pressure, making it clear that the ejector would have to be designed using innovative ideas. The literature also showed that the thrust performance of high pressure ejectors is relatively poor and that improvements to the jet mixing rate would be crucial.

The majority of this research was therefore concerned with developing high mixing rate nozzles for use in ejectors, and a comprehensive experimental programme was undertaken for this purpose. A test rig was built specifically for examining the large scale characteristics (mass flow, jet width etc.) of free and ducted jet flows emanating from choked nozzles.

9.1 The free jet tests

The results of the free jet experiments, undertaken to establish the relative entrainment characteristics of various nozzles, produced a series of conclusions concerning supersonic jets and nozzle design which are now presented. All the following points were revealed by tests of air jets at 6.9 bar gauge pressure and ambient temperature. The nozzles used were circular sonic (M=1.0) and supersonic (M=1.4, 1.8 and 2.0), with and without small notches incorporated at the exit plane to improve mixing rate. The notches, or castellations, were all of regular rectangular shape and the nozzles were identified as either 16, 8 or 4 tooth according to the number of castellations. The text containing the

relevant discussion is Chapters 5 and 6.

Experimental Techniques

1) Schlieren and shadowgraph short flash duration images of underexpanded and fully expanded jets have been achieved. The photographic technique produced high quality representations of the jets showing the shock structure and clearly defining the early development of the jet boundary. Downstream of x/D=4 the photographs show less well defined jets; due to both internal generation of vorticity and large unsteady processes on the jet edges. The addition of castellations to the nozzles produced changes which were clearly visualised by the schlieren photographs. Images of conical shock angle probes provided reliable means of determining the local Mach number in certain regions of the jets.

2) In regions free of shock waves the specially designed total and static pressure probes produced accurate data after due consideration of bow wave effects. The static tube was inaccurate when positioned close to shock waves because the bow wave, shock wave and the probe boundary layer interacted to corrupt the reading. It was essential to combine the visual data of the optical techniques with the pitot-static data before placing credence on the pressure readings.

3) Seven factors were identified which could adversely affect the total probe and static probe accuracies. These were investigated and corrective action established for the majority of the expected problems. The probe data were found to be of high accuracy at transonic onset Mach numbers and above. In the range M = 0.3 - 0.7 the unsteady velocities present in the stream caused a generally high reading (up to 24% in error). At lower speeds the unsteady velocity problem still occurred and the resolution of the recording system also added to the level of uncertainty of the data.

Jet Structures Close to the Nozzle

The following points were observed from the flow visualisation.

1) The flows emanating from M = 1.0, 1.4, 1.8 and 2.0 plain circular nozzles have been recorded in fine detail. Substantial changes in jet structure were apparent between the two extremes of M = 1.0 and M = 2.0, and the complex processes occurring in underexpanded flows have been described in detail. Methods extracted from the literature for predicting various parts of the structure of underexpanded jets are not well developed and no complete methodology for such predictions exist.

2) The incorporation of castellations substantially increases the mixing rate of all the cases tested. The shock strength in the castellated cases is reduced slightly, but this is an effect and not a cause of the more rapid mixing.

3) A detailed investigation of the initial divergence angle of some of the underexpanded jets revealed that plain jets were not expanding at the rate suggested by simple Prandtl-Meyer considerations. It was believed that the discrepancy was due to the difficulty of isolating the very early progress of the jet boundary from the later path when the Prandtl-Meyer prediction does not hold for axisymmetric jets. The divergence angle of the castellated jet flows was seen to be far larger than the plain cases for the underexpanded jets. An attempt to produce a trace of the jet boundary on a thin plate partially submerged in the jet produced divergence angles up to 75% larger than the case without the additional plate. Thus introducing the plate appeared to have an effect similar to that of the castellations themselves.

4) Many of the photographs recorded sound waves generated at the nozzle lip and by the internal shock structure. Sound waves have an important role in the mixing processes of supersonic jets; this is discussed further later.

Entrainment Characteristics of Free Jets

These conclusions resulted mainly from traversing through the jets and integrating the jet properties to find the mass flow and momentum at x/D = 4, 6 and 8.

1) High pressure jets are susceptible to anticipated variations in ambient pressure and temperature and consideration must be taken of these variations in a detailed study. The experimental errors in the traverse data must always be analysed.

2) The traverse data were credible and total pressures calculated from the pitot and static pressures were invariably less than the reservoir value. Calculated values of momentum were usually consistent with momentum conservation, see 3) below.

3) The transverse properties of the four plain jets (M = 1.0, 1.4, 1.8 and 2.0) close to the nozzle differ considerably but the results were always consistent with expectations from the photographic evidence. At x/D= 6 the M=1.4, 1.8 and 2.0 jets were indistinguishable, with the M=1.0 jet slightly wider. At x/D=8 the boundaries of the four jets were even more similar, but a study of the mass flow variation showed that the M = 1.0 jet was larger at all stations. The magnitude of the difference was small (not exceeding 10%) and for all practical purposes it can be assumed that plain jets at x/D=8 are largely independent of the initial Mach number in terms of diameter and mass flow. The momentum over the range x/D=4 to 8 for the plain nozzles was consistent at the stream force (static pressure + momentum) level at x/D=0, thereby improving confidence in the data.

4) The incorporation of castellations always increased the jet width and mass flow. The more underexpanded jets, the M = 1.0 series, were most improved by castellations, with the M = 1.8 jet least affected; thus the castellation-induced entrainment was dependent upon the excess static pressure at exit. Tests with a four-tooth nozzle showed that the jet had a regular but non-axisymmetric cross-section at x/D=4, but a method of taking average surveys of the jet sections was established. The increased

jet growth was caused by streamwise vortices formed at the sides of the notches. The existence of the vortices was confirmed by a photograph in the ducted jet test phase.

5) Sixteen teeth caused good entrainment in the early stages of the jet development but by x/D=8 the effects were rapidly diminishing. Eight teeth caused up to 47% more air to be in motion at x/D=6 compared with the plain case (for the M=1.0 nozzles). The four tooth nozzles showed slower early jet growth than the 8 tooth but by x/D=8 the 4 tooth jets were the largest entrainers. The observations clearly suggested that increasing the tooth number caused high initial jet growth but the closely spaced vortices soon interfered with each other; thus the 4 tooth nozzle produced the best entrainment far downstream. Some unexplained increases in jet momentum with 4 teeth at x/D=8 were recorded; otherwise the castellated jet momentum values were always close to the plain jet levels.

6) Exit plane traverses showed that the M=1.0 plain and 8 tooth nozzles had a similar total pressure efficiency of 97.3%. There is no reason why the results would be different for higher Mach number nozzles or for nozzles with more teeth; thus castellating introduces no worsening of nozzle efficiency.

7) As a consequence of momentum conservation the greatly improved mixing rates evident with some of the castellated nozzles produced jets with faster decaying centreline properties.

8) Due to being able to test only a limited number of castellation geometries it is quite probable that even better nozzle shapes exist. Some suggestions for more developed teeth shapes are contained in the Recommendations for Further Work, Chapter 10.

9) It has not been possible conclusively to identify the castellation-induced enhanced mixing mechanism. Streamwise vortices are formed as the jet stream that passes through the notches expands and interacts with the remaining jet flow. In addition, the circumferential vortex structure is severely

modified, thereby changing the aeroacoustic behaviour of castellated flows.

9.2 Ducted jet tests and ejector performance

A series of ducted tests followed the free jet programme. The existing nozzles were placed inside a square duct section to create the basic features of an ejector. The ejector had a short mixing section (six nozzle diameters long) and was constructed to allow area ratios of both 15 and 25 to be set. The conclusions from this phase of the work, described in Chapters 7 and 8, now follow.

Simple ejector tests

1) The simple square duct ejector produced credible and reliable thrust data over a pressure ratio range of 2.8 to 6.9 bar gauge, thereby allowing the primary aim of nozzle comparison to be achieved. The inlet design, a rectangular hyperbola section, showed no signs of inlet separation and operated at a high efficiency (about 1% total pressure loss). The incorporation of perspex side walls allowed visualisation of the flow in the ejector, an exercise apparently not previously attempted.

2) Schlieren and shadowgraph images of the ejector flows were achieved with most of the primary nozzles. The pictures revealed that the jets behaved in an almost indistinguishable manner to the equivalent free jets.

3) The plain nozzles, in both the area ratio 15 and area ratio 25 ducts always produced a falling augmentation ratio with a pressure increase, unless an aeroacoustic interaction was occurring, see 5) below. This accorded with ejector theory which predicts that injecting compressed primary fluid would worsen performance. In terms of secondary thrust the M = 1.0 nozzle always behaved best with performance decreasing with an increase in M. If considered in terms of true augmentation ratio the differences in performance level were negligible.

4) The values of thrust augmentation ratio observed for the plain nozzles were all close to 1.0. Thus no benefit ensued from using this ejector with plain nozzles. However, if the mixing duct had been eight instead of six diameters long the values of augmentation would have been better but the conclusions would have been the same.

5) The plain nozzles experienced acoustic resonance at certain pressures which lead to substantial improvements in mixing and hence thrust. The acoustic properties were not explored in detail because the castellation-induced phenomenon was more potent. The aeroacoustic interaction appeared to be caused by noise generated in the shock structure travelling upstream in the shear layer. The sound waves resonated in the duct confines and fixed the vortex frequency at the nozzle lip. The vortices were thus strengthened and more secondary air was entrained than in the non-resonance case. Sound waves were clearly visible in the plain nozzle ejector photographs, but were never evident in the castellated ejector photographs.

6) Incorporating castellated nozzles always improved the thrust performance compared with plain nozzles unless a particularly strong resonance was occurring. The largest comparable increase being 9% with the M=1.0 nozzles. Castellations had practically no effect at the lowest pressure tested (2.8 bar gauge) and only became effective after the nozzles became underexpanded. As with the free jet tests the improved entrainment occurred most with the M = 1.0 nozzle with eight teeth.

7) Rotating the castellated primary nozzles so that the primary jet occupied a different position relative to the duct had no effect on the augmentation.

8) Tests designed to record the mass flow and property distributions at the ejector exit plane were successfully conducted with total and static pressure tubes. A high level of skewness (the unevenness of the flow properties) was noted, especially with the plain nozzles. The high skewness was the cause of the poor performance noted in 4) above. The exit plane data showed that the

M = 1.0 8 tooth nozzle produced a substantial reduction in skewness compared with the plain case (from 3.42 plain to 1.53 castellated where unity represents a completely mixed flow).

9) The traverses across the ejector exit revealed that the property profiles were very similar to those of the free jet data at the same axial station. Thus placing a simple geometry ejector around a jet has little effect on the jet behaviour; so that free jet tests can have a role in establishing entrainment characteristics and likely ejector performance. Increasing the duct cross-section, but failing to increase the mixing length, will therefore not increase the thrust augmentation because the jet behaviour is largely unchanged and the skewness will increase.

10) It is apparent that good ejector design is fundamentally associated with the achievement of a nearly uniform property distribution across the ejector exit. Even small areas of reduced flow strength lead to thrust reductions. The tests have suggested that skewness may decrease with pressure increase as the nozzles become more underexpanded and the castellations are more effective.

Ejector performance prediction and high pressure ejector design

1) The 'one-dimensional' model from Quinn (1976) has been shown accurately to represent the performance of simple ejectors. The model solves the continuity, momentum and energy equations in the mixing duct, but requires a prescription of the degree of flow mixing and friction losses. For a 'cold' (ambient) primary temperature the model is simplified.

2) The ejector model enabled the effect of various parameters to be assessed, thereby allowing a good insight into features necessary in practical ejectors.

3) Ejectors at high pressures can suffer from secondary flow choking which provides a limitation on the operating envelope.

4) The prediction model did not adequately solve the problem of an ejector with a diffuser, thus predictions made of such cases should be treated with caution.

5) The effect of temperature has not been considered in the experimental programme but in a short ejector it is believed to be of little significance.

6) An extension of the model to represent a full pressure (14 bar) ejector has shown the absolute performance to be poor. It would be possible to achieve only a 1.2-1.25 level of augmentation if the area ratio is 35 and the ejector embodies an efficient diffuser.

7) Using the theoretical model an ejector concept has been designed to meet the reaction control system requirement described in Chapter 1. Its predicted performance is substantially lower than the original specification but is the best that could be achieved with a realistic size and weight. The proposal concept uses multiple (four) circular castellated primary nozzles injecting at a small angle into a rectangular duct. A high performance diffuser would be necessary, which requires wall blowing. The likely jet mixing rates in a very high pressure environment would be unknown but a decrease in skewness might be achieved, as noted in the simple duct experiments at lower pressure. This ejector is described in some detail in Chapter 8.

8) No substantial difficulties can be foreseen in manufacturing castellated nozzles and incorporating them in a design, the only area of concern being the acoustic fatigue characteristics of the primary nozzle teeth.

9.3 Computational methods utilised in the ejector studies

An axisymmetric characteristic solution technique was developed and coded as a Fortran program in order to define the divergent part of the supersonic nozzle contours. Good quality flow was achieved from the nozzles, validating the computational method. The characteristic techniques could form the basis of a solution of other supersonic axisymmetric flow fields.

The PHOENICS finite-difference fluid flow simulation code has been used to model a free sonic high pressure jet. The results were not accurate enough in terms of shock definition and nearfield centreline decay to allow the current version of PHOENICS to be recommended for similar problems. In its current state PHOENICS might be useful for predicting the larger scale aspects of high speed duct flows for ejector models, and topics such as low speed inlet design are currently addressable. However, computational fluid dynamics is a fast developing science and codes such as PHOENICS, or their successors, will eventually provide detailed information for all aspects of ejector flows.

9.4 Overall conclusion concerning viability of a reaction control ejector

An ejector of practical size cannot meet the original target performance level of $\bar{\Phi}_t$ = 1.6 at 14 bar pressure. The ejector described in Chapter 8 is confidently predicted to achieve an augmentation ratio of 1.2 if certain technological advances are made. Considering that a simple choked nozzle could only produce an 'augmentation' ratio of 0.9, compared to a fully expanded 14 bar flow, the 33% performance benefit associated with the use of the ejector would be significant. The approximate volume required for the ejector would be 1.3m long x 0.9m wide x 0.7m deep, which is substantial. The weight would be of the order of four times that of a single large choked nozzle. These space and weight penalties provide serious constraints on ejector viability, but are not enough to warrant rejection of augmented reaction controls.

The use of a simple convergent-divergent nozzle may also be considered to replace the simple choked reaction control as it would be a smaller and lighter means of attaining an 11% thrust increment.

It is considered that the ejector reaction control programme should be continued with the object of attaining a device with an augmentation ratio of 1.2 - 1.25. To meet this target requires considerably more work to be undertaken on the subject of augmented controls, as summarised in the final chapter.

10. RECOMMENDATIONS FOR FURTHER WORK

The following are seven areas on which the author believes effort should be expended. The order has significance: if at any stage it is found that a target is unattainable then the whole topic of ejector reaction controls should be reconsidered. Some of this development work has been recommended by the author for funding.

1) The jet mixing properties at 14 bar of castellated nozzles must be further investigated. The best levels of mixing skewness must then be used in a theoretical model to ascertain whether the performance is viable. This work can be conducted as a free jet programme. Further designs of castellations must be tested, possibly with the aim of making the streamwise vortices spiral around the jet. Non-circular exit nozzles should also be tested in order to increase the jet periphery. This work has been initiated.

2) An experimental investigation should be conducted into optimising the primary injection angle in a high pressure ejector.

3) The design and testing of an efficient mixer-diffuser must be attempted. It will be necessary to use a wide angle design with substantial wall blowing to keep the diffusing flow attached. Both a continuous slot nozzle and individual vortex nozzles should be investigated. This exercise is expected to be initiated shortly.

4) A theoretical study of diffuser performance, making use of data from 3) above, should be conducted with the aim of modelling how the flow skewness changes in the diffuser.

5) Several other topics relating to ejector design optimisation need to be addressed. Particular areas of concern are:- duct aspect ratio; number of primary nozzles; inlet design and nozzle installation.

6) A more distant aim would be to develop finite-difference codes to allow accurate prediction of the mixing processes. The flow skewness data could then be used in a 'one-dimensional' model.

7) Castellated nozzles may have applications outside the sphere of ejectors. Specifically they might be developed to reduce the ground 'footprint' of hovering VSTOL aircraft by making the propulsive jets more benign.

REFERENCES

Abbett M (1971):- "Mach Disk in Underexpanded Exhaust Plumes", A.I.A.A. Journal, Vol.9, No.3, March 1971

Abdel-Fattah A M (1984):- "A Theoretical Study of Two Stage Thrust Augmenting Ejectors", Australian Department of Defence, Aeronautical Research Laboratories, ARL-AERO-PROP-R-166, November 1984

Adamson T C and Nicholls J A (1959):- "On the Structure of Jets from Highly Underexpanded Nozzles into Still Air", Journal of Aero/Space Sciences, January 1959

Allen J M (1972):- "Pitot-Probe Displacement in a Supersonic Turbulent Boundary Layer", NASA TN D-6579, April 1972

Alperin M, Harris G L and Smith C A (1969):- "An Experimental Investigation of New Concepts in Ejector Thrust Augmentation for V/STOL", Flight Dynamics Research Corporation, U.S.A.F. Report AFFDL-TR-69-52, June 1969

Alperin M and Wu J-J (1981):- "Recent Development of a Jet-Diffuser Ejector", Journal of Aircraft, Vol.18, No.12, December 1981

Alperin M and Wu J-J (1983a):- "Thrust Augmenting Ejectors, Part I", A.I.A.A. Journal, Vol.21, No.10, October 1983

Alperin M and Wu J-J (1983b):- "Thrust Augmenting Ejectors, Part II", A.I.A.A. Journal, Vol.21, No.12, December 1983

Anderson J D (1982):- "Modern Compressible Flow: With Historical Perspective", McGraw-Hill, 1982

Barchilon M and Curtet R (1964):- "Some Details of the Structure of an Axisymmetric Confined Jet with Backflow", Journal of Basic Engineering, December 1964

References contd.

Benson R S and Eustace V A (1973):- "A Study of Two-Dimensional Supersonic Air Ejector Systems", Proc. Instn. Mechanical Engineers, Vol. 187 60/73

Bevilaqua P M (1974):- "Evaluation of Hypermixing for Thrust Augmenting Ejectors", Journal of Aircraft, Vol.11, No.6, June 1974

Bevilaqua P M (1976):- "Analytic Description of Hypermixing and Test of an Improved Nozzle", Journal of Aircraft, Vol.13, No.1, January 1976

Binder G and Didelle H (1981):- "Improvement of Ejector Thrust Augmentation by Pulsating or Flapping Jets", AGARD CP-308, Lisbon, November 1981

Bore C L, Williams R S and Riddlestone D (1983):- "Advanced Reaction Controls: Forces Required and Blowing Data", British Aerospace Report, BAe-KRS-N-GEN-285, November 1983

Bore C L (1984):- "Objectives of Controllable Ejector Research Programme", British Aerospace Report, BAe-KRS-N-306, October 1984

Brown S L and Murphy R D (1974):- "Design and Test of Ejector Thrust Augmentation Configurations", AGARD CP-143, April 1974

Campbell D R and Quinn B P (1973):- "Full-Scale Tests of an Augmentor VTOL Concept", A.I.A.A. Paper 73-1185, Propulsion Conference, Las Vegas, November 1973

Casale D L and Dickinson P W (1985):- "Effects of Shear Flow in Pitot Tubes", University of Bath, School of Engineering Report No.717, June 1985

Cheng D Y and Wang P (1973):- "Experimental Study on Optimization Parameters of a Supersonic Jet Ejector Augmentor", Journal of Aircraft, Vol.10, No.9, September 1973

References contd.

Chow W L and Addy A L (1964):- "Interaction between Primary and Secondary Streams of Supersonic Ejector Systems and their Performance Characteristics", A.I.A.A. Journal, Vol.2, No.4, April 1964

Curtet R and Ricou F P (1964):- "On the Tendency to Self-Preservation in Axisymmetric Ducted Jets", Journal of Basic Engineering, December 1964

Dash S M and Wolf D E (1984):- "Interactive Phenomena in Supersonic Jet Mixing Problems, Part I: Phenomenology and Numerical Modeling Techniques", A.I.A.A. Journal, Vol.22, No.7, July 1984

Davis M P, Ludwig J C and Rhodes N (1985):- "The Application of PHOENICS to Transonic Jets", CHAM Paper, First International PHOENICS Users Conference, 1985

DeJoode A D and Patankar S V (1978):- "Prediction of Three-Dimensional Turbulent Mixing in an Ejector", A.I.A.A. Journal, Vol.16, No.2, February 1978

Donaldson C D and Snedeker R S (1971):- "A Study of Free Jet Impingement. Part 1: Mean Properties of Free and Impinging Jets", Journal of Fluid Mechanics, Vol.45, Part 2, 1971

Eastlake C N (1971):- "The Macroscopic Characteristics of Some Subsonic Nozzles and the Three-Dimensional Turbulent Jets they Produce", Aerospace Research Laboratories U.S.A.F., ARL 71-0058, March 1971

Fancher R B (1970):- "A Compact Thrust Augmenting Ejector Experiment", Aerospace Research Laboratories U.S.A.F., ARL 70-0137, August 1970

Fancher R B (1972):- "Low Area Ratio, Thrust-Augmenting Ejectors", Journal of Aircraft, Vol.9, No.3, March 1972

References contd.

Ferri A (1949):- "Elements of Aerodynamics of Supersonic Flows", Macmillan, 1949

Fox J H (1974):- "On the Structure of Jet Plumes", A.I.A.A. Journal, Vol.12, No.1, January 1974

Gilbert G B and Hill P G (1975):- "Analysis and Testing of Two-Dimensional Slot Nozzle Ejectors with Variable Area Mixing Sections", Paper D3, Jet Pumps and Ejectors and Gas Lift Techniques Symposium, Cambridge, March 1975

Glass D R (1968):- "Effects of Acoustic Feedback on the Spread and Decay of Supersonic Jets", A.I.A.A. Journal, Vol.6, No.10, October 1968

Hammitt A G (1961):- "The Oscillation and Noise of an Overpressure Sonic Jet", Journal of the Aerospace Sciences, Vol.28, No.9, September 1961

Hill P G (1965):- "Turbulent Jets in Ducted Streams", Journal of Fluid Mechanics, Vol.22, Part 1,1965

Ing D N (1985):- "Effects of Nozzle Pressure Ratio on Free Jet Entrainment", British Aerospace Report, BAe-KAD-R-RES-3100, February 1985

Johannesen N H and Meyer R E (1950):- "Axially-Symmetrical Flow near the Centre of an Expansion", The Aeronautical Quarterly, Vol.II, August 1950

Jones C N (1975):- "The Effect of Secondary Flow Velocity Profile on the Static Performance of Low Speed Ejector Thrust Augmenters", Aeronautical Journal, November 1975

von Kármán (1949):- "Theoretical Remarks on Thrust Augmentation", Reissner Anniversary Volume Contributions to Applied Mechanics, Published by J W Edwards, Ann Arbor, Michigan, 1949

References contd.

Kohlman L (1980):- "Introduction to V/STOL Airplanes", Iowa State University Press, 1980

Malin M R and Rosten H I (1982):- "Turbulent Jet Issuing into a Freestream", CHAM Report, CHAM UK PDR 1, 1982

Massey B S (1979):- "Mechanics of Fluids", van Nostrand Reinhold, 4th Edition, 1979

Miller P (1987a):- "Salient Features of the Controllable Ejector Programme", Unpublished British Aerospace note, February 1987

Miller P (1987b):- "Ejectors-Augmentors: A Literature Survey", British Aerospace Report, BAe-KAD-N-GEN-3334, June 1987

Miller P and Whittaker E E (1983):- "Thrust Augmentation for Reaction Control Nozzles", University of Bath, School of Engineering Report No.619, June 1983

Nagaraja K S, Hammond D L and Graetch J E (1973):- "One-Dimensional Analysis of Compressible Ejector Flows Applicable to V/STOL Aircraft", U.S.A.F. Report AFFDL-73-250, November 1973

Owen P L and Thornhill C K (1948):- "The Flow in an Axially-Symmetric Supersonic Jet from a Nearly-Sonic Orifice into a Vacuum", Reports and Memoranda, R & M 2616, September 1948

Ower E and Pankhurst R C (1977):- "Measurement of Airflow", Permagon, 5th Edition, 1977

Pankhurst R C and Holder D W (1952):- "Wind-Tunnel Technique", Pitman, 1952

Pope A and Goin K L (1965):- "High-Speed Wind Tunnel Testing", Wiley, 1965

References contd.

Pope S B (1978):- "An Explanation of the Turbulent Round-Jet/ Plane-Jet Anomaly", A.I.A.A. Journal, Vol.16, No.3, March 1978

Quinn B P (1972a):- "Experiments with Hypermixing Nozzles in an Area Ratio 23 Ejector", Aerospace Research Laboratories U.S.A.F., ARL 72-0084, June 1972

Quinn B P (1972b):- "Recent Developments in Large Area Ratio Thrust Augmentors", A.I.A.A. Paper 72-1174, Joint Propulsion Specialist Conference, New Orleans, November 1972

Quinn B P (1973):- "A Simple Estimate of the Effect of Ejector Length on Thrust Augmentation", Journal of Aircraft, Vol.10, No.5, May 1973

Quinn B P (1974):- "The Decay of Highly Skewed Flows in Ducts", A.S.M.E. Paper 74-GT-55, Gas Turbine Conference, Zurich, April 1974

Quinn B P (1975):- "Effect of Aeroacoustic Interaction on Ejector Performance", Journal of Aircraft, Vol.12, No.11, November 1975

Quinn B P (1976):- "Ejector Performance at High Temperatures and Pressures", Journal of Aircraft, Vol.13, No.12, December 1976

Quinn B P (1977):- "Interactions between Screech Tones and Ejector Performance", Journal of Aircraft, Vol.14, No.5, May 1977

Quinn B P (1981):- "Thrust Augmenting Ejectors: A Review of the Application of Jet Mechanics to V/STOL Aircraft Propulsion", AGARD CP-308, Lisbon, November 1981

Rajaratnam N (1976):- "Turbulent Jets", Elsevier, 1976

Razinsky E and Brighton J A (1971):- "Confined Jet Mixing for Nonseparating Conditions", Journal of Basic Engineering, September 1971

References contd.

Ricou F P and Spalding D B (1961):- "Measurements of Entrainment by Axisymmetrical Turbulent Jets", Journal of Fluid Mechanics, Vol.11, Part 1, August 1961

Rosfjord T J and Toms H L (1975):- "Recent Observations Including Temperature Dependence of Axisymmetric Jet Screech", A.I.A.A. Journal, Vol.13, No.10, October 1975

Sanatian R and Adkins R (1988):- "Ejector Augmentor Technology Study: Use of the PHOENICS Computer Code for Predicting Mixer Length and Performance", Cranfield Institute of Technology, School of Mechanical Engineering Report, February 1988

Sarohia V (1978):- "Some Flight Simulation Experiments on Jet Noise from Supersonic Underexpanded Flows", A.I.A.A. Journal, Vol.16, No.7, July 1978

Schetz J A (1980):- "Injection and Mixing in Turbulent Flow", Progress in Astronautics and Aeronautics Vol.68, A.I.A.A.,1980

Seiler M R and Schum E F (1978):- "An Analytical and Experimental Investigation of Diffusers for VSTOL Thrust Augmenting Ejectors", A.I.A.A. Paper 78-1509, Aircraft Systems and Technology Conference, Los Angeles, August 1978

Shapiro A (1953):- "The Dynamics and Thermodynamics of Compressible Fluid Flow Vol.I", Ronald Press, New York, 1953

Skoblenick H R and Hill P G (1977):- "Experimental and Analytical Study of an Axisymmetric Thrust Augmentor", Journal of Aircraft, Vol.14, No.5, May 1977

Smith A G and Bollands K J (1982):- "Thrust Augmentation of Reaction Control Jets using Coanda Slots", University of Bath, School of Engineering Report No.566, June 1982

References contd.

Tabakoff W and Hosny W M (1972):- "Theoretical and Experimental Jet Mixing of an Eccentric Primary Jet in a Constant Area Duct", Journal of Aircraft, Vol.9, No.10, October 1972

Taylor J W R (1979):- "Janes All The World's Aircraft 1979-80", Janes Yearbooks, London 1979

Throndson L W (1973):- "Compound Ejector Thrust Augmenter Development", A.S.M.E. Paper 73-GT-67, Gas Turbine Conference, Washington D.C., April 1973

Tyler R A and Williamson R G (1980):- "Confined Jet Mixing of Coaxial Flows", National Research Council Canada, Aeronautical Report LR-602, October 1980

Vallentine H R (1970):- "Applied Hydrodynamics", Butterworths, 1970

Viets H (1975):- "Flip-Flop Jet Nozzle", A.I.A.A. Journal, Vol.13, No.10, October 1975

Viets H (1981):- "Unsteady Ejectors", AGARD CP-308, Lisbon, November 1981

Warsop C (1987):- "The Aerodynamic Loading on an Oscillating Aerofoil", University of Bath, School of Engineering PhD Thesis, 1987

Whittley D C (1972):- "The Buffalo/Spey Jet-STOL Research Aircraft", AGARD Paper, Flight Mechanics Panel on Military Applications of V/STOL Aircraft, October 1972

Wilson M (1988):- "The use of PHOENICS to Predict Underexpanded Jet Flows", Logico Systems Ltd./ Advanced Projects (UK) Report, to be published

References contd.

Wu J-J (1986):- "Experiments on High Speed Ejectors", Flight Dynamics Research Corporation, NASA Contractor Report, CR-177419, July 1986

Young A D and Maas J N (1936):- "The Behaviour of a Pitot Tube in a Transverse Total-Pressure Gradient", Reports and Memoranda, R & M 1770, September 1936

APPENDIX A :- DATA ACQUISITION PROGRAM

```
5       DIM ZL$(132),RE(10,132)
10      MS=0
12    REM SET RS423 LINKS
15      *FX5,2
20      *FX7,7
25      *FX8,7
30      GOTO 135
35      *FX3,7
40      RETURN
45      *FX2,1
50      *FX3,6
55      INPUT IP
60      *FX2,0
65      *FX3,6
70      RETURN
75      *FX2,1
80      *FX3,6
85      INPUT IP$
90      *FX2,0
95      *FX3,4
100     RETURN
105     *FX2,1
110     *FX3,6
115     INPUT NR,TS
120     *FX2,0
125     *FX3,4
130     RETURN
135     CLS
140     PRINT TAB(10) "ADU OPERATING PROGRAM"
145     PRINT TAB(10) "_____________________"
150     PRINT
155     PRINT "         1=RESET ADU:"PRINT
160     PRINT "         2=SET CHANNELS":PRINT
165     PRINT "         3=CALL CHANNEL READINGS":PRINT
170     PRINT "         4=RECALL ADU TEST READINGS":PRINT
175     PRINT "         5=LEAVE PROGRAM":PRINT
180     PRINT "         6=TRAVERSE PROCEDURE":PRINT
185     A$=INKEY$(0):IF A$="" THEN 185
190     IF VAL(A$)<1 OR VAL(A$)>6 THEN 185
195     ON VAL(A$) GOSUB 205,250,265,340,350,360
200     GOTO 135
202   REM RESET ENTIRE ADU
205     CLS:PRINT "RESET ADU OPTION":PRINT:PRINT:
        INPUT "ARE YOU SURE";A$:IF A$<>"Y" THEN RETURN
210     GOSUB 35:PRINT "RESET":GOSUB 75:PRINT IP$:
        INPUT "TIME HH MM SS ";T$
215     GOSUB 35;PRINT "TIME"+T$:GOSUB 75
220     INPUT "DATE DD MM YY ";D$
225     GOSUB 35:PRINT "DATE"+D$:GOSUB 75
230     GOSUB 35:PRINT "ERROR":GOSUB 75:IF IP$="O.K." THEN RETURN
235     PRINT:PRINT "ERROR= ";IP$
240     IF INKEY$(0)="" THEN 240
245     RETURN
247   REM INITIALISE TRANSDUCER CHANNELS
```

```
250     CLS:PRINT "SET ADU CHANNELS OPTION"
255     PRINT:PRINT "FAST SET ROUTINE"
260     GOSUB 2000:RETURN
262  REM DISPLAY SINGLE CHANNEL AVERAGE
265     CLS:PRINT "CALL CURRENT CHANNEL READING":PRINT:
        INPUT "ENTER CHANNEL ";CH
270     GOSUB 35:PRINT "ERROR":GOSUB 75:IF IP$="O.K." THEN 285
275     PRINT "ERROR= ";IP$
280     IF INKEY$(0)="" THEN 280
285     TY=0:SUM=0:CLS
290     GOSUB 35:PRINT "TODAY":GOSUB 75
295     PRINT TAB(0,0);IP$
300     PRINT:PRINT "CHANNEL ";CH;" READINGS":PRINT
305     GOSUB 35:PRINT "CALL",CH:GOSUB 75
310     TY=TY+1:PRINT;IP:SUM=IP+SUM:FOR HJ=1 TO 4000:NEXT:
        IF TY=6 GOTO 320
315     GOTO 305
320     AV=SUM/6
325     PRINT:PRINT "AVERAGE VALUE =",AV
330     IF INKEY$(0)="" THEN 330
335     RETURN
337  REM PRINT OUT ALL DATA HELD IN ADU
340     CLS:PRINT "RECALL ADU TEST READINGS"
345     GOSUB 1300:RETURN
350     CLS:PRINT "LEAVING PROGRAM"
355     END
360  REM SECTION CONTROLS MOTOR STEPPING AND DATA READING
362  REM CHECK INITIAL STATUS AND CHANGE IF REQUIRED
365     CLS:GOSUB 35:PRINT "MOTOR";2,0:GOSUB 45:MS=IP
370     IF MS=1 THEN PRINT "**":PRINT "MOTOR HOME":PRINT "**":GOTO 430
375     IF MS=2 THEN PRINT "**":PRINT "MOTOR AT HIGH LIMIT":
        PRINT "**":GOTO 385
380     PRINT "**":PRINT "MOTOR NOT HOME":PRINT "**":PRINT
385     INPUT "SHOULD MOTOR GO HOME Y/N";H$
390     IF H$="Y" THEN GOSUB 35:PRINT "MOTOR";2,-23000,4000:
        GOSUB 45:GOTO 400
395     GOTO 430
400     GOSUB 35:PRINT "MOTOR";2,0:GOSUB 45:MS=IP
405     IF MS<>1 GOTO 400
410     PRINT:PRINT "**":PRINT "MOTOR NOW AT HOME":PRINT "**":PRINT
415     PRINT:
        INPUT "DO YOU WANT TO CONTINUE TO ARRANGE A TEST Y/N";ANS$
420     IF ANS$="Y" GOTO 430
425     GOTO 630
427  REM ENTER TRAVERSE INFORMATION
430     PRINT:PRINT "NOW SET UP A TRAVERSE AND RECORDING OF DATA"
435     PRINT:PRINT"++++++++++++++++++++++++++++++":
        PRINT "TRAVERSE INFORMATION :-":PRINT
440     PRINT "1000 STEPS TAKES 4 SECONDS TO EXECUTE"
445     PRINT:PRINT "0.05 INCHES OF TRAVERSE REQUIRES 144 STEPS":
        PRINT
450     PRINT"++++++++++++++++++++++++++++++":PRINT
455     INPUT "ENTER HERE UP TO 80 CHARACTERS OF INFO ABOUT
        THIS TEST",TM$:GOSUB 35
460     PRINT:PRINT:INPUT "HOW MANY STEPS";NS:PRINT
465     TSTP=ABS(NS)*4/1000
470     IF MS=1 AND NS<0 THEN PRINT "ALREADY AT LOW LIMIT":GOTO 460
475     IF MS=2 AND NS>0 THEN PRINT "ALREADY AT HIGH LIMIT":GOTO 460
```

```
480     INPUT "HOW MANY REPETITIONS";REP:PRINT
485     INPUT "LENGTH OF PAUSE";PAUSE:PRINT:PRINT:BN$="Y"
490     INPUT "IS TEST STATIC (S) OR TOTAL (T) ";DSA$
495     IF BN$="Y" AND DSA$="S" SCAL1=142.95:SCAL2=2967.4:SCAL3=-618.3
500     IF BN$="Y" AND DSA$="T" SCAL1=142.95:SCAL2=2967.4:SCAL3=308.24
510     NR=REP:HALFPAUSE=PAUSE/2
515     GOSUB 35:PRINT "TODAY":GOSUB 75:SAS$=IP$
520     GOSUB 35:PRINT "WRITE":1,SAS$:GOSUB 75
525  REM SHORT DELAY BEFORE STARTING
528     TRAV=0
529     PRINT "READING":PRINT:GOSUB 1000
530     TIME=0:REPEAT:UNTIL TIME>(100*HALFPAUSE)
535     FOR TRAV=1 TO REP
540     GOSUB 35:PRINT "MOTOR";2,NS,4000:GOSUB 45
545     TIME=0
550     GOSUB 35:PRINT "MOTOR";2,0:GOSUB 45:MS=IP
555     IF MS=8 OR 9 THEN PRINT "MOTOR MOVING (";TRAV;")":PRINT
560     GOSUB 35:PRINT "MOTOR";2,0:GOSUB 45:MS=IP
565     IF MS=8 THEN GOTO 560
570     IF MS=9 THEN GOTO 560
575     IF MS=1 THEN PRINT "**":PRINT "MOTOR HOME":
        PRINT "**":GOTO 615
580     IF MS=2 THEN PRINT "**":PRINT "MOTOR AT HIGH LIMIT":
        PRINT "**":GOTO 615
585     ENDTIME=TIME
590     PRINT "MOTOR STOPPED":PRINT
595     REPEAT:UNTIL TIME>ENDTIME+(HALFPAUSE*1.8*100)
600     PRINT "READING":PRINT:GOSUB 1000
605     REPEAT:UNTIL TIME>ENDTIME+(HALFPAUSE*200)
610     NEXT TRAV
615     PRINT "###":PRINT:PRINT "SEQUENCE ENDED":PRINT:PRINT "###"
620     GOSUB 1600
625     IF INKEY$(0)="" THEN 625
630     RETURN
1000 REM SCAN ALL CHANNELS
1005    FOR CH=1 TO 3
1010    GOSUB 35:PRINT "CALL";CH:GOSUB 45
1015    RE(CH,TRAV+1)=IP
1020    NEXT CH
1025    FOR CH=9 TO 10
1030    GOSUB 35:PRINT "CALL";CH:GOSUB 45
1035    RE(CH,TRAV+1)=IP
1040    NEXT CH
1045    IF TRAV=0 GOTO 1055
1050    REPEAT:UNTIL TIME>ENDTIME+(HALFPAUSE*200)
1055    RETURN
1100 REM ERROR DETECTION LINES
1105    GOSUB 35:PRINT "ERROR":GOSUB 75:PRINT IP$:STOP
1200 REM TODAY COMMAND
1205    GOSUB 35:PRINT "TODAY":GOSUB 75:PRINT IP$:STOP
1300 REM OUTPUT DATA FROM NON-ALLOTED TEST
1305    *FX5,1
1310    *FX3,0
1315    VDU2
1320    PRINT:PRINT "CURRENT TEST IN ADU HAS FOLLOWING
        CHARACTERISTICS"
1325    GOSUB 35:PRINT "READ";1:GOSUB 75
1330    CB$=IP$
```

```
1335    GOSUB 35:PRINT "READ";0:GOSUB 75
1340    *FX5,1
1345    *FX3,0
1350    VDU2
1355    PRINT:PRINT CB$:PRINT
1360    PRINT:PRINT IP$:PRINT
1365    INPUT "HOW MANY READINGS IN TEST";REP
1370    PRINT:PRINT " CH 1          CH 2          CH 3
                CH 9           CH 10"
1375    PRINT "CHAMBER      VENTURI      TRAVERSE
          BOTTLE       CHAMBER"
1380    PRINT "PRESSURE     PRESSURE     PRESSURE
          TEMPERATURE  TEMPERATURE"
1385    PRINT " PSIG          PSIG          PSIG
             K             K"
1390    PRINT "_____________________________________
        _____________________"
1395    FOR J=1 TO REP
1400    IF REP=0 IP$="":GOTO 1410
1405    GOSUB 35:PRINT "READ";J+1:GOSUB 75
1410    *FX5,1
1415    *FX3,0
1420    VDU2
1425    PRINT IP$
1430    NEXT J
1435 REM SAVE DATA ON TO FLOPPY DISC
1440    PRINT:INPUT "SAVE RESULTS ON DISC Y/N ";XCV$
1445    IF XCV$="Y" GOTO 1480
1450    IF XCV$<>"N" GOTO 1440
1455    *FX5,2
1460    KKH=0:FR J=0 TO 120
1465    GOSUB 35:PRINT "WRITE";J,KKH:GOSUB 75
1470    NEXT J
1475    PRINT:PRINT "TEST DELETED":GOTO 1540
1480    IF DSA$="S" THEN VB=OPENOUT "TRESS"
1485    IF DSA$="T" THEN VB=OPENOUT "TREST"
1490    FOR K=0 TO REP+1
1495    GOSUB 35:PRINT "READ",K;GOSUB 75
1500    ZL$(K)=IP$
1505    PRINT #VB,ZL$(K)
1510    NEXT
1515    FOR K=REP+2 TO 750
1520    PRINT #VB,""
1525    NEXT K
1530    CLOSE #VB
1535    PRINT:PRINT "RESULTS ON DISC"
1540    VDU3
1545    IF INKEY$(0)="" THEN 1545
1550    RETURN
1600 REM PUT INFO INTO STRING FOR ADU
1605    FOR TRAV=1 TO REP+1
1610    FOR CH=1 TO 3
1615    IP=RE(CH,TRAV)
1620    IF CH=1 THEN IP=IP*1E5/SCAL1*1.4503E-4:GOSUB 1800
1625    IF CH=1 ML1$=ML$
1630    IF CH=2 THEN IP=IP*1E5/SCAL2*1.4503E-4:GOSUB 1800
1635    IF CH=2 ML2$=ML$
1640    IF CH=3 THEN IP=IP*1E5/SCAL3*1.4503E-4:GOSUB 1800
```

```
1645    IF CH=3 ML3$=ML$
1650    NEXT CH
1655    FOR CH=9 TO 10
1660    IP=RE(CH,TRAV)
1665    IP=IP+273.2:GOSUB 1900
1670    IF CH=9 ML9$=A$
1675    IF CH=10 ML10$=A$
1680    NEXT CH
1685    S$="       "
1690    ZL$(TRAV)=ML1$+S$+ML2+$S$+ML3$+S$+ML9$+S$+ML10$
1695    GOSUB 35:PRINT "WRITE";TRAV+1,ZL$(TRAV):GOSUB 75
1700    NEXT TRAV
1705    PRINT:PRINT "DATA NOW IN ADU"
1710    IF INKEY$(0)="" THEN 1710
1715    RETURN
1800 REM FORMAT PRESSURE DATA STRING FOR ADU
1805    IF IP>0 ML=IP+0.0005
1810    IF IP<0 ML=IP-0.0005
1815    IF IP=0 ML=IP
1820    @%=&01020814:ML$=STR$(ML):@%=10
1825    FOR I%=1 TO LEN(ML$)
1830    IF MID$(ML$,I%,1)="." THEN GOTO 1845
1835    NEXT I%
1840    ML$=ML$+".00"
1845    ML$=LEFT$(ML$,I%+3)
1850    RETURN
1900 REM FORMAT TEMPERATURE DATA STRING FOR ADU
1905    AAA=IP+.0005
1910    @%=&01020814
1915    A$=STR$(AAA)
1920    @%=10
1925    FOR I%=1 TO LEN(A$)
1930    IF MID$(A$,I%,1)="." THEN 1945
1935    NEXT
1940    A$=A$+".0"
1945    A$=LEFT$(A$,I%+1)
1950    RETURN
2000 REM ROUTINE FOR INITIALISING CHANNELS
2005    CLS:PRINT "IS TEST STATIC OR TOTAL S/T":INPUT DSA$
2010    GOSUB 35:PRINT "SETP",1,6,0:GOSUB 75
2015    GOSUB 35:PRINT "SETP",2,0,0:GOSUB 75
2020    IF DSA$="T" THEN GOSUB 35:PRINT "SETP",3,8,0:
        GOSUB 75:GOTO 2035
2025    IF DSA$="S" THEN GOSUB 35:PRINT "SETP",3,9,0:
        GOSUB 75:GOTO 2035
2030    PRINT "CHOOSE S OR T ":GOTO 2000
2035    GOSUB 35:PRINT "SETTTR",9:GOSUB 75
2040    GOSUB 35:PRINT "SETTTR",10:GOSUB 75
2045    SCAL1=142.95:SCAL2=2967.4
2050    IF DSA$="S" SCAL3=-618.3
2055    IF DSA$="T" SCAL3=308.24
2060    RETURN
```

APPENDIX B :- DATA ANALYSIS PROGRAM

```
5       DIM BT(132),CT(132),PC(132),PV(132),PO(132),PS(132),PR(132)
10      PRS(132),TTL(132),R(132),M(132),VEL(132),T(132),RHO(132),IN$(132)
15      ER=1:CD=0:CLS
20      INPUT "IS CENTRELINE LOCATION REQUIRED (Y/N) ?";CLOC$:PRINT
25      IF CLOC$="Y" THEN INPUT "SPACE BETWEEN READINGS ";XSPACE
30      CLS:INPUT "IS TEST STATIC (S) OR TOTAL (T) ";JH$
35      IF JH$="S" THEN VC=OPENIN "TRESS"
40      IF JH$="T" THEN VC=OPENIN "TREST"
42    REM READ IN ENTIRE FILE LINE BY LINE AS STRINGS
45      FOR DS=0 TO 132:INPUT #VC,IN$(DS):IF IN$(DS)="" GOTO 60
55      NEXT
60      CLOSE #VC
65      LS=DS-1
67    REM SPLIT DATA STRINGS INTO DATA COMPONENTS
70      FOR DS=2 TO LS
75      FOR I%=1 TO 10
80      IF MID$(IN$(DS),I%,1)=" " GOTO 90
85      NEXT I%
90      E%=I%-1
95      PC(DS)=VAL(MID$(IN$(DS),1,E%)):S%=E%+8
100     FOR I%=S% TO (S%+10)
105     IF MID$(IN$(DS),I%,1)=" " GOTO 115
110     NEXT I%
115     E%=I%-1
120     PV(DS)=VAL(MID$(IN$(DS),S%,E%)):S%=E%+8
125     FOR I%=S% TO (S%+10)
130     IF MID$(IN$(DS),I%,1)=" " GOTO 140
135     NEXT I%
140     E%=I%-1
145     IF JH$="S" THEN PS(DS)=VAL(MID$(IN$(DS),S%,E%)):GOTO 155
150     IF JH$="T" THEN PO(DS)=VAL(MID$(IN$(DS),S%,E%))
155     S%=E%+8
160     FOR I%=S% TO (S%+10)
165     IF MID$(IN$(DS),I%,1)=" " GOTO 175
170     NEXT I%
175     E%=I%-1
180     BT(DS)=VAL(MID$(IN$(DS),S%,E%)):S%=E%+8
185     FOR I%=S% TO (S%+10)
190     IF MID$(IN$(DS),I%,1)=" " GOTO 200
195     NEXT I%
200     E%=I%-1
205     CT(DS)=VAL(MID$(IN$(DS),S%,E%))
210     NEXT DS
212   REM IF SECOND OF PAIR GOTO MANIPULATION ELSE READ IN SECOND DISC
215     IF ER=2 GOTO 275
220     FOR DS=2 TO LS
225     T(DS)=BT(DS):RHO(DS)=CT(DS)
230     NEXT DS
232   REM EXTRACT HEADERS FROM TOP OF FILE
235     FIR$=IN$(0):SEC$=IN$(1)
240     IF JH$="S" QQ$="STATIC":QE$="TOTAL"
245     IF JH$="T" QQ$="TOTAL":QE$="STATIC"
250     PRINT:PRINT "THIS TEST WAS ";QQ$:PRINT:PRINT "NOW CHANGE
        DISC FOR CORRESPONDING ";QE$;" RESULTS"
```

```
255     PRINT:PRINT:PRINT:PRINT
260     INPUT "IS TEST STATIC (S) OR TOTAL (T) ";JH$
265     ER=2
267  REM REPEAT FOR THE SECOND DISC
270     GOTO 35
272  REM AVERAGE THE TEMPERATURES BETWEEN THE TWO TEST RUNS
275     FOR DS=2 TO LS
280     BT(DS)=(BT(DS)+T(DS))/2:CT(DS)=(CT(DS)+RHO(DS))/2
285     NEXT DS
287  REM INPUT ATMOSPHERIC PRESSURE FROM BAROMETER
290     PRINT:INPUT "ATMOSPHERIC PRESSURE= ";ATMOS:PRINT
292  REM CORRECT STATIC PRESSURE FOR ERROR AND CALCULATE PRESSURES
295     PRINT:INPUT "HOW MANY STATIC ERRORS 1 OR 2 ";O:PRINT:PRINT
300     IF O=1 THEN INPUT "STATIC ERROR =";STE:GOTO 315
305     IF O=2 THEN INPUT "TWO ERRORS ARE =";ST2;ST3:GOTO 315
310     GOTO 295
315     FOR I=2 TO LS
317     IF PO(I)<0.0 THEN PO(I)=0.0
320     PO(I)=(PO(I)*1.026)+ATMOS
325     IF O=2 AND I<12 PS(I)=PS(I)+ATMOS-ST2:GOTO 345
330     IF O=2 AND I<LS-10 PS(I)=PS(I)-((ST2+ST3)/2):GOTO 345
335     IF O=2 THEN PS(I)=PS(I)+ATMOS-ST3:GOTO 345
340     PS(I)=PS(I)+ATMOS-STE
345     PR(I)=PO(I)/PS(I)
350     NEXT I
352  REM CALCULATE POSITION OF CENTRELINE IF REQUIRED
355     IF CLOC$="Y" GOSUB 1000:GOSUB 1200
360  REM DECIDE ON MACH NUMBER PROCEDURE
365     FOR I=2 TO LS
370     IF PR(I)<=1.863 GOSUB 1400
375     IF PR(I)>1.863 GOSUB 1500
380     NEXT I
382  REM CALCULATE TRUE TOTAL PRESSURE,TEMPERATURE,DENSITY,VELOCITY
385     GOSUB 1600:GOSUB 1700:GOSUB 1800
390  REM OUTPUT RESULTS TO PRINTER AND SCREEN
400     *FX5,1
405     *FX3,0
410     VDU2
415     @%=&10
420     PRINT:PRINT "DATA HAS FOLLOWING CHARACTERISTICS":PRINT:
        PRINT:PRINT
425     PRINT FIR$:PRINT SEC$:PRINT:PRINT IN$(0):PRINT IN$(1)
430     PRINT:PRINT "ATMOS PRESS= ";ATMOS:PRINT
435     IF O=1 THEN PRINT:PRINT "STATIC ERROR= ";STE:PRINT
440     IF O=2 THEN PRINT:PRINT "STATIC ERRORS= ";ST2,ST3:PRINT
445     IF CLOC$="Y" THEN PRINT":PRINT "CENTRELINE LOCATION AT ";
        CLLOC-2:PRINT
450     IF CLOC$="Y" PRINT:PRINT "      M          PR         PO1
              T          RHO        VEL        RAD        RVR":
        PRINT "_____________________________________________________
        _____________________________":GOTO 465
455     PRINT:PRINT "      M          PR         PO1        T
           RHO        VEL        RVR"
460     PRINT "_____________________________________________________
        _____________________"
465     FOR I=2 TO LS
470     M(I)=(INT(1000*M(I)+.5))/1000
475     PR(I)=(INT(1000*PR(I)+.5))/1000
```

```
480     PO1(I)=(INT(1000*PO1(I)+.5))/1000
485     T(I)=(INT(10*T(I)+.5))/10
490     RHO(I)=(INT(1000*RHO(I)+.5))/1000
495     VEL(I)=(INT(10*VEL(I)+.5))/10
500     IF CLOC$="Y" THEN R(I)=R(I)*1000:R(I)=(INT(100*R(I)+.5))/100
505     IF CLOC$="Y" THEN
        RVR=(INT((1000*VEL(I)*RHO(I)*R(I)/1000)+.5))/1000:GOTO 515
510     RVR=(INT(100*VEL(I)*RHO(I)+0.5))/100:@%=&0002030A:GOTO 535
515     @%=&0002030A
520     IF CD=1 GOTO 530
525     IF I>NCL THEN PRINT"_._._._
```

```
1235    DWN=NCL
1240 REM DESCENDING RADS
1245    DWN=DWN-1
1250    FRAC=FRAC+XSPACE
1255    R(DWN)=FRAC
1260    IF DWN>1 GOTO 1245
1265 REM ASCENDING RADS
1270    UP=NCL+1
1275    FRACU=XSPACE-FRACS
1280    R(UP)=FRACU
1285    FRAC=FRACU
1290    FRAC=FRAC+XSPACE
1295    UP=UP+1
1300    R(UP)=FRAC
1305    IF UP<LS GOTO 1290
1310    RETURN
1400 REM CALCULATE SUBSONIC MACH NUMBER
1405    IF PR(I)<1 THEN PR(I)=1
1410    M6=((PR(I)^.2857)-1/.2
1415    M(I)=SQR(M6)
1420    RETURN
1500 REM CALCULATE SUPERSONIC MACH NUMBER
1505 REM FIRST GUESS THAT M=2 THEN ITERATE
1510    M2=4
1515    FIR=(((7*M2)-1)/6)^-2.5:SEC=(5/(6*M2))^-3.5:GPR=FIR*SEC
1520    RAT=GPR/PR(I)
1525    IF RAT>1.001 THEN M2=M2/RAT:GOTO 595
1530    IF RAT<0.999 THEN M2=M2/RAT:GOTO 595
1535    M(I)=SQR(M2)
1540    RETURN
1600 REM PO2/PO1 SECTION
1605    FOR I=2 TO LS
1610    IF PR(I)<=1.863 PO1(I)=PO(I)-ATMOS:GOTO 1630
1615    A=((6*(M(I)^2))/((M(I)^2)+5))^3.5
1620    B=(6/(7*M(I)^2)-1))^2.5:C=A*B
1625    PO1(I)=PO(I)/C-ATMOS
1630    NEXT I
1635    FOR I=2 TO LS
1640    IF PO1(I)<0 THEN PO1(I)=0
1645    NEXT I
1650    RETURN
1700 REM SECTION FOR TEMPS AND DENSITIES
1705    FOR I=2 TO 132:RHO(I)=0:T(I)=0:NEXT
1715    FOR I=2 TO LS
1720    T(I)=CT(I)/(1+(.2*(M(I)^2))):PMET=PS(I)*6895
1725    RHO(I)=PMET/(287*T(I))
1730    NEXT
1735    RETURN
1800 REM VELOCITY SECTION
1805    FOR I=2 TO LS
1810    SOV=SQR(1.4*287*T(I))
1815    VEL(I)=M(I)*SOV
1820    NEXT
1825    RETURN
1900 REM READ IN DATA DISCARD INFORMATION
1905    INPUT "IGNORE HOW MANY READINGS AT THE BEGINNING ";BEG
1910    INPUT "IGNORE HOW MANY READINGS AR THE END ";EGB
1915    IJ=BEG+2:IK=LS-EGB
```

```
1920    MUM=1
1925    GOSUB 2000
1930    PRINT:PRINT "AVERAGE AREA UNDER RVR CURVE IS= ";TTA/2
1935    MUM=2
1940    GOSUB 2000
1945    PRINT:PRINT "AVERAGE AREA UNDER RVVR CURVE IS= ";TTA/2
1950    RETURN
2000 REM INTEGRATION OF RVR AND RVVR CURVES
2005    ACRE=0
2010    FOR KJ=IJ TO IK
2015    RVR1=(INT((1000*VEL(KJ)*RHO(KJ)*R(KJ)/1000)+.5))/1000
2020    IF MUM=2 THEN RVR1=RVR1*VEL(KJ)
2025    RVR2=(INT((1000*VEL(KJ+1)*RHO(KJ+1)*R(KJ+1)/1000)+.5))/1000
2030    IF MUM=2 THEN RVR2=RVR2*VEL(KJ+1)
2035    ACRE=((RVR1+RVR2)/2)*XSPACE+ACRE
2040    TTA=ACRE
2045    NEXT KJ
2050    RETURN
```

APPENDIX C : AXISYMMETRIC CHARACTERISTIC EQUATIONS

C.1 Introduction

The aim is to deduce the special equations which describe the supersonic flowfield from the basic continuity and Euler equations. Vector notation is used to simplify the algebra.

C.2 Cylindrical continuity

For the special case considered here of axisymmetric flow the cylindrical continuity equation can be expressed as:-

$$0 = \rho\left(\frac{\partial v_r}{\partial r} + \frac{v_r}{r} + \frac{\partial w}{\partial z}\right) + v_r \frac{\partial \rho}{\partial r} + w \frac{\partial \rho}{\partial z} \qquad (C.1)$$

Figure C.1 displays the nomenclature and co-ordinate system used. The derivation of this equation is given in most fluid dynamic texts, for example see Shapiro (1953).

C.3 Euler equation

The momentum (or Euler) equation now has to be invoked. Expressed in non-conservation vector form it is,

$$\rho\,(\underline{V} \cdot \nabla)\,\underline{V} = -\nabla p \qquad (C.2)$$

if the flow is both steady and inviscid, and forces such as gravitational forces are neglected.

It is possible to derive a special form of Eulers equation which applies only to irrotational flow but is independent of the co-ordinate system. For clarity the derivation will be given in cartesian co-ordinates.

The cartesian velocity vector is $\underline{V} = u\underline{i} + v\underline{j} + w\underline{k}$ (C.3)

and

$$\nabla = \frac{\partial}{\partial x}\underline{i} + \frac{\partial}{\partial y}\underline{j} + \frac{\partial}{\partial z}\underline{k} \qquad (C.4)$$

combining gives

$$\underline{V}(\underline{V}\cdot\nabla) = \left(u\frac{\partial u}{\partial x} + v\frac{\partial u}{\partial y} + w\frac{\partial u}{\partial z}\right)\underline{i} + \left(u\frac{\partial v}{\partial x} + v\frac{\partial v}{\partial y} + w\frac{\partial v}{\partial z}\right)\underline{j} + \left(u\frac{\partial w}{\partial x} + v\frac{\partial w}{\partial y} + w\frac{\partial w}{\partial z}\right)\underline{k} \qquad (C.5)$$

Also

$$\nabla p = \frac{\partial p}{\partial x}\underline{i} + \frac{\partial p}{\partial y}\underline{j} + \frac{\partial p}{\partial z}\underline{k} \qquad (C.6)$$

Hence the momentum equation becomes:-

$$\left(u\frac{\partial u}{\partial x} + v\frac{\partial u}{\partial y} + w\frac{\partial u}{\partial z}\right)\underline{i} + \left(u\frac{\partial v}{\partial x} + v\frac{\partial v}{\partial y} + w\frac{\partial v}{\partial z}\right)\underline{j} + \left(u\frac{\partial w}{\partial x} + v\frac{\partial w}{\partial y} + w\frac{\partial w}{\partial z}\right)\underline{k} = -\frac{1}{\rho}\left(\frac{\partial p}{\partial x}\underline{i} + \frac{\partial p}{\partial y}\underline{j} + \frac{\partial p}{\partial z}\underline{k}\right) \qquad (C.7)$$

Extracting the terms for just one dimension, say the x direction, gives,

$$\rho\left(u\frac{\partial u}{\partial x} + v\frac{\partial u}{\partial y} + w\frac{\partial u}{\partial z}\right) = -\frac{\partial p}{\partial x} \qquad (C.8)$$

Use must now be made of the basic vector representation of an irrotational flow, i.e.

$$\nabla \times \underline{V} = 0 \qquad (C.9)$$

For the cartesian system considered the cross product is determined by matrix algebra.

$$\nabla \times \underline{V} = \begin{vmatrix} \underline{i} & \underline{j} & \underline{k} \\ \frac{\partial}{\partial x} & \frac{\partial}{\partial y} & \frac{\partial}{\partial z} \\ u & v & w \end{vmatrix} \qquad (C.10)$$

The determinant of this matrix is,

$$\underline{i}\left(\frac{\partial w}{\partial y} - \frac{\partial v}{\partial z}\right) - \underline{j}\left(\frac{\partial w}{\partial x} - \frac{\partial u}{\partial z}\right) + \underline{k}\left(\frac{\partial v}{\partial x} - \frac{\partial u}{\partial y}\right) \qquad (C.11)$$

For irrotational flow this must be zero. So for this to hold at every point then:-

$$\frac{\partial w}{\partial y} = \frac{\partial v}{\partial z} \qquad \frac{\partial w}{\partial x} = \frac{\partial u}{\partial z} \qquad \frac{\partial v}{\partial x} = \frac{\partial u}{\partial y} \qquad (C.12)$$

Returning to equation (C.8) it becomes,

$$\rho\left(u\frac{\partial u}{\partial x} + v\frac{\partial v}{\partial x} + w\frac{\partial w}{\partial x}\right) = -\frac{\partial p}{\partial x} \qquad (C.13)$$

or alternatively,

$$\rho\left(\frac{1}{2}\frac{\partial u^2}{\partial x}dx + \frac{1}{2}\frac{\partial v^2}{\partial x}dx + \frac{1}{2}\frac{\partial w^2}{\partial x}dx\right) = -\frac{\partial p}{\partial x}dx \qquad (C.14)$$

Also for the y and z dimensions

$$\rho\left(\frac{1}{2}\frac{\partial u^2}{\partial y}dy + \frac{1}{2}\frac{\partial v^2}{\partial y}dy + \frac{1}{2}\frac{\partial w^2}{\partial y}dy\right) = -\frac{\partial p}{\partial y}dy \qquad (C.15)$$

and

$$\rho\left(\frac{1}{2}\frac{\partial u^2}{\partial z}dz + \frac{1}{2}\frac{\partial v^2}{\partial z}dz + \frac{1}{2}\frac{\partial w^2}{\partial z}dz\right) = -\frac{\partial p}{\partial z}dz \qquad (C.16)$$

Now using the fact that $V^2 = u^2 + v^2 + w^2$ the three equations (C.14) - (C.16) can be written:-

$$\rho\left(\frac{1}{2}\frac{\partial V^2}{\partial x}\,dx\right) = -\frac{\partial p}{\partial x}\,dx \qquad (C.17)$$

$$\rho\left(\frac{1}{2}\frac{\partial V^2}{\partial y}\,dy\right) = -\frac{\partial p}{\partial y}\,dy \qquad (C.18)$$

$$\rho\left(\frac{1}{2}\frac{\partial V^2}{\partial z}\,dz\right) = -\frac{\partial p}{\partial z}\,dz \qquad (C.19)$$

Adding these gives,

$$\frac{\rho}{2}\left(\frac{\partial V^2}{\partial x}\,dx + \frac{\partial V^2}{\partial y}\,dy + \frac{\partial V^2}{\partial z}\,dz\right) = -\left(\frac{\partial p}{\partial x}\,dx + \frac{\partial p}{\partial y}\,dy + \frac{\partial p}{\partial z}\,dz\right) \qquad (C.20)$$

The form $\frac{\partial A}{\partial x}\,dx + \frac{\partial A}{\partial y}\,dy + \frac{\partial A}{\partial z}\,dz$

is the same as the total differential of A. Hence the Euler equation becomes,

$$\rho\left(\frac{1}{2}\,dV^2\right) = -dp \qquad (C.21)$$

Some points about this equation:-

(1) V is the velocity magnitude, not the velocity vector.

(2) It was derived using cartesian co-ordinates but it is now independent of any co-ordinate system. Hence it can immediately be used in cylindrical co-ordinates as the Euler equation.

Resorting now to the previously used cylindrical system where $V^2 = v_r^2 + v_\theta^2 + w^2$.

gives for axisymmetric flow $\qquad dp = -\frac{\rho}{2}\,d(v_r^2 + w^2) \qquad (C.22)$

For isentropic flow the pressure is related to the density by :-

$$\frac{dp}{d\rho} = a^2 \qquad (C.23)$$

where a is the local sonic velocity.

So that

$$a^2\, d\rho = -\rho\,(v_r\, dv_r + w\, dw) \qquad (C.24)$$

Replacing the total differentials with the form $dA = \frac{\partial A}{\partial r}\, dr + \frac{\partial A}{\partial z}\, dz$

produces two equations:-

$$\frac{\partial \rho}{\partial r} = -\frac{\rho}{a^2}\left(v_r \frac{\partial v_r}{\partial r} + w \frac{\partial w}{\partial r}\right) \qquad (C.25)$$

$$\frac{\partial \rho}{\partial z} = -\frac{\rho}{a^2}\left(v_r \frac{\partial v_r}{\partial z} + w \frac{\partial w}{\partial z}\right) \qquad (C.26)$$

C.4 Axisymmetric generalised flow equations

Equations (C.25) and (C.26) can now be inserted in the axisymmetric continuity equation (C.1) giving,

$$\rho\left(\frac{\partial v_r}{\partial r} + \frac{v_r}{r} + \frac{\partial w}{\partial z}\right) - \frac{v_r \rho}{a^2}\left(v_r \frac{\partial v_r}{\partial r} + w \frac{\partial w}{\partial r}\right) - \frac{w\rho}{a^2}\left(v_r \frac{\partial v_r}{\partial z} + w \frac{\partial w}{\partial z}\right) = 0 \qquad (C.27)$$

The density can be eliminated leaving:-

$$\frac{\partial v_r}{\partial r}\left(1 - \frac{v_r^2}{a^2}\right) - \frac{v_r w}{a^2}\frac{\partial v_r}{\partial z} - \frac{v_r w}{a^2}\frac{\partial w}{\partial r} + \frac{\partial w}{\partial z}\left(1 - \frac{w^2}{a^2}\right) = -\frac{v_r}{r} \qquad (C.28)$$

It is possible to define a system of cylindrical co-ordinates which are not based on transforming $\underline{i}$, $\underline{j}$, $\underline{k}$, Figure C2. The principal axes are now $\underline{e}_r$, $r\underline{e}_\theta$, $\underline{e}_z$.

For axisymmetric flow the velocity equation is $\underline{V} = v_r \underline{e}_r + w\underline{e}_z$.

Using again the irrotationality condition that $\nabla \times \underline{V} = 0$ gives,

$$\nabla \times \underline{V} = \begin{vmatrix} \underline{e}_r & r\underline{e}_\theta & \underline{e}_z \\ \dfrac{\partial}{\partial r} & 0 & \dfrac{\partial}{\partial z} \\ v_r & 0 & w \end{vmatrix} \qquad (C.29)$$

so that

$$r\underline{e}_\theta \left(- \frac{\partial w}{\partial r} + \frac{\partial v_r}{\partial z} \right) = 0 \qquad (C.30)$$

hence for irrotational flows, $\dfrac{\partial v_r}{\partial z} = \dfrac{\partial w}{\partial r}$ (C.31)

Equation (C.28) then becomes,

$$\frac{\partial v_r}{\partial r}\left(1 - \frac{v_r^2}{a^2}\right) - \frac{2wv_r}{a^2}\frac{\partial v_r}{\partial z} + \frac{\partial w}{\partial z}\left(1 - \frac{w^2}{a^2}\right) = \frac{-v_r}{r} \qquad (C.32)$$

Two further equations are available, ie. the total differentials of v_r and w . All three equations contain the variables $\partial v_r/\partial r$, $\partial v_r/\partial z$ and $\partial w/\partial z$, so writing them in the manner of the proposed solution produces:-

$$\left(1 - \frac{v_r^2}{a^2}\right)\frac{\partial v_r}{\partial r} - \frac{2wv_r}{a^2}\frac{\partial v_r}{\partial z} + \left(1 - \frac{w^2}{a^2}\right)\frac{\partial w}{\partial z} = \frac{-v_r}{r} \qquad (C.33)$$

$$dr\,\frac{\partial v_r}{\partial z} + dz\,\frac{\partial w}{\partial z} = dw \qquad (C.34)$$

$$dr\,\frac{\partial v_r}{\partial r} + dz\,\frac{\partial v_r}{\partial z} = dv_r \qquad (C.35)$$

Now a very significant result can be deduced from (C.32) . Suppose a solution of $\partial v_r/\partial r$ is desired then,

$$\frac{\partial v_r}{\partial r} = \frac{\frac{-v_r}{r} + \frac{2wv_r}{a^2}\frac{\partial v_r}{\partial z} - \left(1 - \frac{w^2}{a^2}\right)\frac{\partial w}{\partial z}}{1 - \frac{v_r^2}{a^2}} \qquad (C.36)$$

Refer now to Figure C3 . Assume that the flow is entirely defined at one point, say A, but the flowfield is only known in one direction at A, say the z direction. Hence $\partial v_r/\partial z$ and $\partial w/\partial z$ are known allowing a solution of (C.36) for $\partial v_r/\partial r$.

An interesting result occurs if $v_r = a$ because then $\partial v_r/\partial r$ becomes indeterminate.

From the geometry $\sin \mu = v_r/V$ (C.37)

but if $a = v_r$ then $\sin \mu = a/V$ (C.38)

but $a/V = 1/M$ (C.39)

where M is the Mach number.

Hence for this special choice of v_r the streamline direction is at the Mach angle to the z axis. So if one chooses a line to be at this particular angle then the value of $\partial v_r/\partial r$ is indeterminate. Mathematically these lines are called characteristic lines. The first sign of the unique nature of supersonic flows is now apparent. By letting $v_r = a$ it is forcing the velocity V to be always greater than or equal to the local sonic velocity. Hence the characteristic concept is only helpful if the stream is supersonic.

Fortunately it is possible to solve equations (C.33) - (C.35) to produce an indeterminate value of $\partial v_r/\partial r$, or either of $\partial v_r/\partial z$ and $\partial w/\partial z$.

Using Cramers Rule on (C.33), (C.34), (C.35) and solving for $\partial v_r/\partial z$ produces:-

$$\frac{\partial v_r}{\partial z} = \frac{\begin{vmatrix} 1 - \frac{v_r^2}{a^2} & -\frac{v_r}{a} & 1 - \frac{w^2}{a^2} \\ 0 & dw & dz \\ dr & dv_r & 0 \end{vmatrix}}{\begin{vmatrix} 1 - \frac{v_r^2}{a^2} & -\frac{2wv_r}{a^2} & 1 - \frac{w^2}{a^2} \\ 0 & dr & dz \\ dr & dz & 0 \end{vmatrix}} = \frac{N}{D} \qquad (C.40)$$

To make $\partial v_r/\partial r$ indeterminate but also finite, because it is known to exist, requires that N = D = 0.

C.5.1 Characteristic slope equation

First set D = 0

then $$0 = \left(\frac{dr}{dz}\right)^2 \left(1 - \frac{w^2}{a^2}\right) + \frac{dr}{dz}\frac{2wv_r}{a^2} + \left(1 - \frac{v_r^2}{a^2}\right) \qquad (C.41)$$

This is a quadratic in dr/dz where dr/dz is the gradient of the characteristic lines along which $\partial v_r/\partial r$ is indeterminate.

Solving gives,

$$\frac{dr}{dz} = \frac{\frac{-wv_r}{a^2} \pm \sqrt{\frac{w^2 + v_r^2}{a^2} - 1}}{1 - \frac{w^2}{a^2}} \qquad (C.42)$$

C.5.2 Compatibility Equation

Putting N = 0 gives

$$0 = \left(1 - \frac{v_r^2}{a^2}\right)(-dz\ dv_r) + \frac{v_r}{a}(-dr\ dz) + \left(1 - \frac{w^2}{a^2}\right)(-dr\ dw) \quad (C.43)$$

hence

$$\frac{dv_r}{dw} = \frac{1 - \frac{w^2}{a^2} + \frac{v_r}{r}\frac{dz}{dw}}{\frac{dz}{dr}\left(\frac{v_r^2}{a^2} - 1\right)} \quad (C.44)$$

but

$$\frac{dz}{dw} = \frac{dr}{dw}\frac{dz}{dr} \quad (C.45)$$

so that finally

$$\frac{dv_r}{dw} = \frac{dr}{dz}\left(\frac{1 - \frac{w^2}{a^2}}{\frac{v_r^2}{a^2} - 1}\right) + \frac{\frac{v_r}{r}\frac{dr}{dw}}{\left(\frac{v_r^2}{a^2} - 1\right)} \quad (C.46)$$

From the solution of D = 0 a relationship for dr/dz was found, equation (C.42). Substituting this gives:-

$$\frac{dv_r}{dw} = \frac{\frac{v_r}{r}\frac{dr}{dw} - \frac{wv_r}{a^2} \pm \sqrt{\frac{w^2 + v_r^2}{a^2} - 1}}{\frac{v_r^2}{a^2} - 1} \quad (C.47)$$

This equation is known as the compatibility equation.

C.6 Interpretation of the characteristic equations

Equation (C.42) directly gives the physical position of the axisymmetric characteristic lines. As can be seen it involves only the local velocity components.

Equation (C.47) however describes how the properties vary along the characteristic lines, but unfortunately it contains a differential term. This is why the solution procedure has to be numerical.

Equations (C.42) and (C.47) can be written in a more physically significant form.

From the velocity definition $V^2 = v_r^2 + w^2$ (C.48)

hence $$M^2 = \frac{w^2 + v_r^2}{a^2} \quad \text{(C.49)}$$

so (C.42) becomes,

$$\frac{dr}{dz} = \frac{\frac{-wv_r}{a^2} \pm \sqrt{M^2 - 1}}{1 - \frac{w^2}{a^2}} \quad \text{(C.50)}$$

This has real roots only if $M > 1$ hence again this reinforces the fact that the equations can only be solved in a useful fashion if the flow is supersonic.

It is now helpful to introduce a modified co-ordinate system, see Figure C4. The velocity vector is assumed to be directed at an angle ϕ to the predominant flow direction (in this case the z axis). Hence:-

$$v_r = V \sin \phi \qquad w = V \cos \phi \quad \text{(C.51)}$$

and $$M^2 = \frac{1}{\sin^2 \mu} \quad \text{(C.52)}$$

so that $$a^2 = V^2 \sin^2 \mu \quad \text{(C.53)}$$

Equation (C.50) then becomes

$$\frac{dr}{dz} = \frac{-\frac{\cos \phi \sin \phi}{\sin^2 \mu} \pm \sqrt{\frac{1}{\sin^2 \mu} - 1}}{1 - \frac{\cos^2 \phi}{\sin^2 \mu}} \quad \text{(C.54)}$$

but $$\frac{1}{\sin^2 \mu} - 1 = \cot^2 \mu \quad \text{(C.55)}$$

hence

$$\frac{dr}{dz} = \frac{-\frac{\cos\phi \sin\phi}{\sin^2\mu} \pm \cot\mu}{1 - \frac{\cos^2\phi}{\sin^2\mu}} \qquad (C.56)$$

This can be manipulated to

$$\frac{dr}{dz} = \tan(\phi \mp \mu) \qquad (C.57)$$

For the chosen co-ordinate system this equation defines the gradient of the two characteristic, or Mach lines, which pass through any point in the flowfield. The line with slope tan ($\phi + \mu$) is called the left running characteristic because to an observer facing downstream this line appears to pass away towards the left. The opposite argument applies to the right running line.

Similar processes can now be applied to equation (C.47) by using (C.51) to (C.53), in which case:-

$$\frac{dv_r}{dw} = \frac{\frac{V \sin\phi}{r}\frac{dr}{dw} - \frac{\cos\phi \sin\phi}{\sin^2\mu} \pm\sqrt{M^2 - 1}}{\frac{\sin^2\phi}{\sin^2\mu} - 1} \qquad (C.58)$$

Also from equation (C.51) $dv_r = dV \sin\phi + V \cos\phi \, d\phi$ (C.59)

and $dw = dV \cos\phi - V \sin\phi \, d\phi$ (C.60)

Multiplying (C.58) by (C.60), inserting (C.59) and collecting all the terms containing $d\phi$ together gives:-

$$\frac{V \sin^2\mu \, d\phi}{\sin^2\phi - \sin^2\mu}\left(-\cos\phi \pm\sqrt{M^2 - 1}\sin\phi\right) \qquad (C.61)$$

and the remaining terms are (after manipulation):-

$$\frac{\sin^2\mu}{\sin^2\phi - \sin^2\mu}\left[dV\left(\frac{-\sin\phi + \sin\phi\sin^2\mu}{\sin^2\mu} \pm\sqrt{M^2 - 1}\cos\phi\right) + \frac{V \sin\phi \, dr}{r}\right] \qquad (C.62)$$

Equating (C.61) and (C.62) produces:-

$$d\phi\ (-\cos\phi \pm \sqrt{M^2 - 1}\ \sin\phi) = \frac{dV}{V}\ (-\sin\phi\ \cot^2\mu \pm \sqrt{M^2 - 1}\ \cos\phi) + \frac{\sin\phi}{r}\ dr \tag{C.63}$$

but

$$\sqrt{M^2 - 1} = \cot\mu \tag{C.64}$$

hence

$$d\phi\ (-\cos\phi \pm \cot\mu\sin\phi) = \frac{dV}{V}(\mp\cot\mu)(\pm\sin\phi\cot\mu - \cos\phi) + \frac{\sin\phi}{r}\ dr \tag{C.65}$$

Finally

$$d\phi = \mp \cot\mu\ \frac{dV}{V} + \frac{1}{\pm \cot\mu - \cot\phi}\ \frac{dr}{r} \tag{C.66}$$

Equation (C.66) is thus the axisymmetric compatibility equation which has to be solved in conjunction with the slope equation (C.57).

Proceeding by looking at just one family of waves, say the left running gives:-

$$d\phi = \cot\mu\ \frac{dV}{V} - \frac{1}{\cot\phi + \cot\mu}\ \frac{dr}{r} \tag{C.67}$$

and

$$\frac{dr}{dz} = \tan(\phi + \mu) \tag{C.68}$$

Inserting (C.68) in (C.67) and rearranging gives,

$$\frac{dV}{V} - \frac{\tan\mu\ \tan(\phi + \mu)}{\cot\phi + \cot\mu}\ \frac{dz}{r} - d\phi\ \tan\mu = 0 \tag{C.69}$$

Consequently the final pair of equations which describe the left running family are:-

$$\frac{dV}{V} - \frac{\sin\mu \sin\phi \tan\mu}{\cos(\phi + \mu)} \frac{dz}{r} - d\phi \tan\mu = 0 \qquad (C.70)$$

$$\frac{dr}{dz} = \tan(\phi + \mu) \qquad (C.71)$$

Similar processes lead to these equations for the right running pair:-

$$\frac{dV}{V} - \frac{\sin\mu \sin\phi \tan\mu}{\cos(\phi - \mu)} \frac{dz}{r} + d\phi \tan\mu = 0 \qquad (C.72)$$

$$\frac{dr}{dz} = \tan(\phi - \mu) \qquad (C.73)$$

The two pairs of relationships above are the actual flow equations which are solved numerically in an axisymmetric characteristic problem.

If the case considered had been that of two dimensional plane flow the final equations would have been similar except for the absence of the differential term containing dz in the compatibility equations.

APPENDIX D : TOTAL AND STATIC PRESSURE DATA ERRORS

D.1 Introduction

This appendix describes the errors that were believed could influence the recording of the pressure data in the jet flow experiments. The precautions that were taken to alleviate the expected inaccuracies are discussed.

The pressure errors associated with the use of the 'High Speed Total' tube will be discussed first, with the performance of the specially designed 'High Speed Static' tube following. Some types of error affect the combined total-static result and these are presented separately. Finally a summary of the combined effects of all the errors on the predicted velocities are given. Both tubes are described in Chapter 3 and illustrated by Figures 3.7 and 3.10.

D.2 'High Speed Total' pressure tube errors

The causes of errors associated with the use of the total pressure tube can be classified as follows:-

a) Errors inherent with probe design in axial subsonic flow.

b) Transonic/supersonic behaviour.

c) Tube behaviour in inclined flow.

d) Tube behaviour in sheared flow.

e) Unsteady effects.

f) Transducer and recording errors.

g) Probe vibration.

In addition some of the above effects could occur simultaneously, leading to further uncertainty in the pressure reading.

a) Subsonic inherent inaccuracy The accuracy of standard pitot tubes should be independent of flow velocity, Pankhurst and Holder (1952). As the pitot tube used in the current exercise differed considerably from orthodox pitot tube design a calibration was performed over a limited speed range. This calibration was a simple comparison with a standard N.P.L. tube (modified ellipsoidal nose) at low speed. Over the range 3 to 16 m/s the 'High Speed Total' pressure tube consistently read 2.5% low. Consequently all gauge total pressure readings were multiplied by a calibration factor of 1.026 in the data reduction computer program.

The cause of the this error was due to the very fine hole employed in the nose of the tube (0.45 mm diameter). The choice of this small hole size was determined by the desire to achieve high spatial resolution, but it appeared to adversely affect the capture of the stagnation streamline.

b) Transonic/supersonic performance The 'High Speed Total' pressure tube was not calibrated at supersonic speeds because no particular difficulties were envisaged in this regime. The extreme bluntness of the probe nose would ensure that a detached shock would occur for all Mach numbers sensibly above 1.0 . In fact this slight concern for the total probe error at M = 1.0 proved unfounded because a study of the results obtained with the probe showed no inconsistency at or near predicted M = 1.0 speeds. The subsonic correction factor of 1.026 was also applied to the 'supersonic' results because the flow was subsonic at the probe tip.

c) Inclined flow The effect of inclined flow had to be considered separately for the subsonic and supersonic regimes. In subsonic flow a standard N.P.L. pitot-static tube was known to be quite insensitive to yaw angles, Ower and Pankhurst (1977). Up to 16 degrees yaw should not produce any unwanted discrepancy in the total pressure reading. From photographs of the free jets investigated, discussed in Chapter 5, it could be seen that, from x/D = 4 onwards, no subsonic portion of the jet would be inclined at this magnitude of angle to the jet axis. The highest yaw angle in the jet edge appeared to be of the order of a very few degrees. However to justify the readings in yawed flow the 'High Speed Total' pressure

tube was calibrated at incidence with respect to the N.P.L. standard tube. At flow angles up to 7-8 degrees no difference was recorded. Above this angle a slight drop in the reading from the custom tube was found. At 15 degrees incidence the custom tube was reading 1.2% below the N.P.L. tube. These results showed that no subsonic yaw correction was necessary.

Pope and Goin (1965) address the problem of inclined supersonic total pressure measurement. The 'High Speed Total' pressure tube utilised a measuring hole diameter to probe end diameter ratio of 0.167. The guide given by Pope and Goin suggested no error at angles up to 10 degrees yaw if a diameter ratio of 0.1 or above is used. The maximum flow angle in the supersonic regions of the jets would be extremely difficult to determine accurately. The most likely areas of inclined flow are close to the strong oblique shocks present in the severely underexpanded jets. Some rough approximations, assuming two dimensional flow, were made using the first series of shock waves as an extreme case. Further downstream, at x/D = 4 and beyond, the flowfield properties would be much less severe.

The most inclined shock occurred in the M = 1.0 flow, with an angle of 25 degrees to the axial direction. Use will now have to be made of some of the experimental results of Chapter 6. It was found that the underexpanded M = 1.0 jet would expand, on exiting the nozzle, up to a maximum speed of the order of M = 3.5. Assuming this speed and axial flow approaching the 25 degree shock can give a flow deflection of up to 9 degrees. Independent measurement of Mach number (using conical nose angle probes), in the region where the traverses were conducted, gave maximum Mach numbers of the order of M = 2.5. In this case the flow deflection would fall to 2 degrees. From these findings it was concluded that the supersonic incidence angle would not transgress the limit given by Pope and Goin.

d) Sheared flow All pitot tubes have long been known to record total pressure inaccurately in conditions of lateral pressure gradient. This error can be attributed to two phenomena. Firstly the presence of the probe can deflect the flow streamlines, and secondly the average pressure across the probe orifice might not be

the same as at the centre of the orifice. It was again necessary to consider subsonic and supersonic shearing flows separately.

For subsonic flows Ower and Pankhurst (1977) provided a summary of previous information on the effective geometric displacement of the recording position. Results of a more directly relevant nature were contained in the work of Young and Maas (1936). The investigation of Young and Maas used a design of pitot tube similar to the 'High Speed Total' pressure tube, but having a different diameter ratio. The experimental investigation, although not exhaustive, did show two points.

1) The displacement was independent of the mean total pressure.

2) The displacement was independent of the pressure gradient, provided the gradient was constant.

The displacement was found to obey the following rule,

$$\delta = 0.131D + 0.082D_1$$

δ = displacement (towards higher pressure)
D_1 = tube internal diameter
D = tube external diameter

The later work of Casale and Dickinson (1985) indentified a dependence on the velocity (or pressure) gradient. However their result applied to a flow in which the static pressure was constant across the nose of the pitot tube. In the current free jets it was possible to record velocity gradients as high as 22 (m/s / mm) which would cause substantial errors in velocity using Casale and Dickinson's theory. However Young and Maas's equation results in small displacements and so small velocity errors in all the flow regions. Young and Maas suggested that the velocity error would not exceed 9 m/s even in the regions of greatest shear. The work of Ower and Pankhurst (1977) stated that even the values produced by Young and Maas could be too high. No subsonic shear correction was actually applied to the present jet data.

Work on pitot tubes in supersonic shear flows has been limited to probe behaviour in wall flows such as described by Allen (1972). This report showed that probe displacement (towards the higher pressure) could be twice as large in supersonic than subsonic flows, but considered probe effects in relation to the probe/boundary layer thickness ratio. It was difficult to interpret the findings of Allen in terms of the current free jet tests due to the unknown thickness of the supersonic mixing regions. Due to the uncertainty detailed above, no supersonic shear correction could be applied.

e) Unsteady effects The effect of the perturbation velocities on the recorded total pressure was intrinsically part of the whole pitot-static turbulence problem. Consequently the turbulence discussion will be presented in a separate part, Section D.4 .

f) Transducer and recording errors The total pressure transducer had a specified repeatability accuracy of ± 0.1% on the gauge pressure readings. Calibrations demonstrated a linear response (to within the accuracy of the calibrating system) over the range 0 to 7 bar. The A-D conversion was performed by a high quality 12 bit converter. The specified conversion error would typically not exceed ± 0.5%.

From the equipment specification an accuracy of the order of ± 0.6% could have been expected but this was not necessarily the case due to the nature of the pressure being measured. If the recording system was allowed a 2 hour warm up time the converter would always produce readings to an accuracy of ± 1 bit. The equivalent of one bit accuracy on the A-D converter was approximately 0.0017 bar, which appeared to be within the range of the transducer repeatability error. On the lowest absolute pressure recorded, of the order of 1 bar, this error represented ± 0.17%. For pressures near to the full scale value the predicted error due to the A-D converter fell to an extremely low ± 0.02%. However for pressures much above the 1 bar case, say greater than 2 bar, it was more judicious to use the specified transducer error of ± 0.5%.

The very high levels of accuracy predicted in the previous paragraphs did reduce somewhat when combined with the static pressure errors.

A further factor, the dynamic response of the whole probe/tubing system, was a possible source of error. An analysis using the work of Warsop (1987) showed there would not be a problem with the large bore (3 mm) pipework employed.

g) Probe vibration The discussion of the problem of probe vibration was largely inspired by the work of Ower and Pankhurst (1977). This publication established probe vibration to be caused either by vortex shedding from the probe stem or a vibration caused elsewhere and transmitted to the probe tip. The following discussion applies equally to total and static pressure probe design.

The probe stem, see Figures 3.7 and 3.10, was calculated to have a natural frequency of approximately 400 Hz. The effect of flow velocity on shedding frequency could be found by using the Strouhal number of the stem. For the range of Reynolds number of interest the Strouhal number was found to be constant and equal to approximately 0.2. The flow velocity associated with a shedding frequency of 400 Hz, and a Strouhal number of 0.2, was found to be about 25 m/s. Obviously this value of velocity did lie in the range of possible results.

The actual problem of probe vibration was much harder to analyse than the above paragraph might suggest. If the probe tip was measuring a total (or static) pressure which predicted a local velocity of 25 m/s the probe stem could be subjected to a widely different velocity field.

Furthermore, the 25 m/s velocity line in the jet would be very close to the jet edge, in which case it could be argued that the stem would not be submerged in the jet at all. Assuming the vibrations were only a nuisance when the flow could be considered imcompressible, then Ower and Pankhurst (1977) gave a procedure for calculating the error in velocity arising from a pitot-static combination. At 25 m/s flow velocity and 1 mm probe amplitude

vibration, the error was 0.03%. If the amplitude increased to 2 mm the error rose to 0.1%.

The second type of vibration mentioned above, i.e. vibration transmission was not expected to occur. The pitot (or static) tube was very securely fixed to the traverse gear, which itself was a heavy and totally independent mounting. Even though the remainder of the rig was vibrating, no motion appeared to be transmitted to the traversing mechanism.

A useful check on the vibration phenomena was provided by the optical system. Any severe vibration present would be evident on photographs of probes in the jets. If stem bending was occurring this would translate to a rocking of the forward facing tube, (especially noticeable with the static tube). Assuming correct focus none of the schlieren photographs displayed any blurring of the probes. The only exception was when the static probe did vibrate when positioned through a Mach disc.

A summary of the possible error conditions for the 'High Speed Total' pressure tube shows that:-

a) Total tube inaccuracy in subsonic flow was found and a correction factor of 1.026 incorporated for all readings.

b) No problems were expected with the probe in transonic/supersonic flow.

c) No yaw corrections were applied.

d) No shear corrections were applied.

e) See Section D.4 for the unsteady analysis.

f) Conditioning errors were calculated and all readings were subject to the uncertainties specified above.

g) The uncertainty due to probe resonance was calculated and the effect will be discussed further in Section D.6 .

D.3 'High Speed Static' pressure tube errors

The same seven error sources affecting the total tube could also be expected to apply to the static pressure tube readings. Some of these errors will already have been discussed in Section D.2, to where reference should be made for the list of topics.

a) Subsonic inherent inaccuracy The major design constraint for the static pressure tube was the ability to behave satisfactorily close to shock systems, see Section 3.3.1. The tube used most frequently in the free jet tests therefore had the static holes placed 5.25 diameters from the probe nose. The stem to hole distance was about 27.0 diameters. From these figures Ower and Pankhurst (1977) suggested that the tube should read about 0.5% low. Due to the variation from standard design ideas employed by the 'High Speed Static' tube an uncertainty of up to -1.0% was felt to be more suitable.

No direct correction was applied to the static pressure readings because there would be some doubt as to whether the flow was locally subsonic or supersonic. The contribution of the -1.0% error will however be considered later in Section D.5 .

b) Transonic/supersonic performance This was discussed in Section 3.3.1. Ower and Pankhurst (1977) suggested a large uncertainty in static readings about the region of M = 1.0, but no evidence of this was found in the experimental results.

c) Inclined flow In subsonic inclined flow static pressure tubes generally behave worse than total tubes. Using the discussion of Section D.2 concerning likely incidence angles, and information from Ower and Pankhurst, lead to an uncertainty of -0.5% at 3 degrees being used with the 'High Speed Static' tube.

Tubes of similar design to the 'High Speed Static' pressure tube Ower and Pankhurst (1977), have been shown to produce errors in

supersonic flow of -1.0% at 3 degrees inclination.

d) Sheared flow No previous work has been found on static tube behaviour in lateral pressure gradients. The design of the 'High Speed Static' pressure probe with four very fine holes placed radially around the tube should help in producing a reasonable average pressure. The effect of streamline distortion could not be considered.

e) Unsteady effects The turbulence effects are presented in Section D.4 .

f) Transducer and recording errors The same transducer was used for measuring both total and static pressures. Consequently the earlier part of Section D.2 concerning signal conditioning errors also applied to the static errors except that the circuit gain was increased. A resolution of 1 bit for the A-D converter was equivalent to 0.0034 bar when reading static pressures.

At a nominal 1 bar absolute pressure the accuracy was therefore ± 0.34%. As the static pressure could fall well below atmospheric in the jet core the accuracy at the minimum pressure was also of interest. Hence the worst error possible was of the order of ± 0.68% at 0.5 bar absolute pressure.

g) Probe vibration The effect of probe vibration on recording performance was covered in Section D.2

Summarising the 'High Speed Static' tube error quantities produces the following list:

a) The tube was expected to read 1% low in subsonic axial flow.

b) No transonic/supersonic corrections were applied.

c) The static tube could be susceptible to yaw so an uncertainty of -0.5% at low speed rising to -1.0% at supersonic speeds was used.

d) No shear corrections were applied.

e) See Section D.4 for the unsteady analysis.

f) Signal conditioning uncertainty was calculated as specified above.

g) No further corrections for vibration were needed as the discussion for the 'High Speed Total' pressure tube covered the static pressure effects.

D.4 Unsteady velocity effects on experimental data

Much previous work has been performed on the theoretical effects of turbulence on pitot-static measurements. No helpful data on the unsteady aspects of the mixing of supersonic jets has been found however. No turbulence quantities were measured in the current exercise so that an accurate assessment of unsteady errors was impossible. What has been attempted is a modification of previous subsonic theory and experimental results to provide an approximate idea of the magnitude of the turbulent velocities in the jet mixing regions.

In turbulent flow a total pressure tube can be expected to read higher than the true mean pressure due to increased local velocities confronting the tube. From Ower and Pankhurst (1977) (this work summarised many classical theories) can be taken the conventional prediction that the total tube would read a value of pressure equal to:-

$$p + \tfrac{1}{2}\rho v^2 + \tfrac{1}{2}\rho \left(\overline{v_x^2} + \overline{v_y^2} + \overline{v_z^2} \right) \qquad (D.1)$$

where p = true static pressure

v = local mean flow velocity (in x direction)

and v_x, v_y and v_z are the turbulent velocities in the three cartesian axis directions

This equation applies only to incompressible flow but a compressibility correction is incorporated later in the analysis

allowing the use of (D.1) up to M=1.0 .

If the turbulence could be assumed isotropic then $\overline{v_x^2}$ would be of the same order of size as $\overline{v_y^2}$ and $\overline{v_z^2}$. Hence the tube would read,

$$p + \tfrac{1}{2}\rho \left(v^2 + 3\overline{v_x^2} \right) \qquad (D.2)$$

In unsteady flow the static tube would also read too high. In this case:-

$$p + \tfrac{1}{2}\rho \left(\tfrac{1}{2} \left(\overline{v_y^2} + \overline{v_x^2} \right) \right) \qquad (D.3)$$

Hence if the isotropic condition is made to apply then the static pressure would be,

$$p + \tfrac{1}{2}\rho\overline{v_x^2} \qquad (D.4)$$

Using conventional methods it is more convenient to combine (D.2) and (D.4) to produce the actual measured dynamic pressure.

$$\tfrac{1}{2}\rho v^2 \left(1 + \frac{2\overline{v_x^2}}{v^2} \right) \qquad (D.5)$$

The factor of 2 in this equation has been the subject of some debate, but Ower and Pankhurst conclude that it is as likely to be correct as any of the alternatives offered.

The value of $\overline{v_x^2}$ to fit into equation (D.5) is obviously dependent upon the flow conditions in the jet. Ower and Pankhurst only present data for large volume, constant pressure flows, i.e. windtunnels, so use was made of results given in Schetz (1980). The most applicable data in Schetz is an axisymmetric flow with an initial Mach number of 0.25. Unfortunately the turbulence data was collected far downstream (x/D=30) but other results in Rajaratnam (1976) suggested that this type of data could, if suitably non-dimensionalised, be independent of axial position.

The conventional representation of subsonic jet data makes use of some specialised scaling factors. In particular, the radial

location of the point of half maximum velocity has often been used as a length scale. This length is commonly known as the velocity half-width. The supersonic jets under discussion here are obviously not amenable to such descriptions. Consequently an approximate technique for transposing subsonic data onto the boundary of a supersonic jet is developed.

For this purpose it may be assumed that a typical velocity distribution can be drawn as Figure D.1 . If point 'B' represents the position of the sonic line on one side of the jet, then outside of 'B' there would exist the subsonic mixing region. The width of the mixing region depends on the efficacy of the mixing process, but typically the distance from 'B' to the jet edge varies between 0.8 and 1.7 r/D units. Figure D.1 is drawn to represent the narrower limit of this mixing width. The remainder of the explanation of the technique developed will be given in terms of the narrower limit, referred to as the 'narrow' jet.

The velocity half-width of solely the subsonic portion typically occurs at r/D = -1.0, point 'A' on Figure D.1 . The next step is to consider a fictitious jet with a velocity profile equal to the entire subsonic portion of the real supersonic jet. This was a major simplification because it ignored the axisymmetric nature of the real jet. Figure D.2 shows the imaginary jet, where 'B' now occurs at r/D = 0 and 'A', the velocity half-width, at r/D = -0.2 .

The data set previously chosen from Schetz (1980) is now used. A fourth order polynomial curve is fitted through the experimental data but with a transverse scale adapted to the conditions of the imaginary subsonic jet. Figure D.2 also shows this turbulent velocity profile superimposed, to a suitable scale, on the imaginary jet. It was now that the size of the possible turbulent velocities became apparent. Table D.1 gives some examples of the magnitude of these turbulent velocities.

The substitution of the turbulent velocities into equation (D.5) produces the percentage increase in the recorded value of the dynamic pressure.

Table D.1 contains these dynamic pressure errors and also the associated errors in final velocity after being corrected for compressibility effects. The errors are highest in the mid-velocity region of the imaginary jet because that is the area of greatest velocity gradient. The magnitude of the turbulent stresses are dependent upon the local transverse velocity gradient.

A typical 'wide' jet was also studied but when due consideration was given to the new radial scale the absolute velocity values at the relevant multiples of the velocity half-width locations were found to be so close to the 'narrow' case that a separate wide jet analysis was not warranted.

D.5 The accumulated errors in pressure measurement

The total pressure errors, from Section D.2, were only caused by conditioning inaccuracy. At a nominal 1 bar absolute pressure the error was therefore ± 0.17%. Alternatively at higher pressures, above 2 bar, this error was ± 0.5%.

The static pressure was subject to three sources of error:- normal probe inaccuracy; yaw inaccuracy and signal conditioning problems. The probe and yaw errors were calculated in Section D.3 as percentage errors on the gauge pressure readings. Consequently the combination of the three errors was not a simple process. However the worst error attributable to static pressure inaccuracy was +0.34% to -1.84% for the subsonic cases. In supersonic parts of the flow (for this purpose the approximation was made that total pressures greater than 2 bar constituted supersonic areas) this uncertainty increased to the range +0.68% to -2.68%.

Table D.2 shows how the pressure errors propagated through the data analysis into errors in the velocities. The nominal velocities used are the same as those for the unsteady procedure. At low speeds the signal conditioning inaccuracy lead to a wide variation in velocity, ie. the predicted velocity could be in the range of 15% too low, to 11% too high.

Table D.2 clearly shows the difficulty in recording the velocity in the jet edge. Indeed if a nominal pressure ratio of 1.0 was considered (i.e. the predicted jet boundary) then, using the calculated uncertainty, the pressure ratio could take any value between 1.0 and 1.005. At this higher value of pressure ratio the associated Mach number was 0.09, when, in truth, zero Mach number should have been deduced.

The data reduction software was written to provide a number of traps to avoid unnecessary errors in the jet edge. If the total pressure tube registered zero gauge pressure then all further readings outside of this point were discarded. Also if the static pressure reading was higher than the total pressure then the pressure ratio was set to 1.0.

D.6 Final accumulated errors in velocity prediction

Table D.3 contains the overall errors in velocity which combine the unsteady errors of Section D.4 and the pressure dependent errors of Section D.5. In addition the vibration problem, it may be recalled, was hard to quantify but a probe amplitude of 2 mm was found to produce a velocity error of ± 0.1%, which was not significant compared with the errors of Sections D.4 and D.5 .

APPENDIX E : THE USE OF PHOENICS TO PREDICT UNDEREXPANDED FREE JET FLOWS

E.1 Introduction

PHOENICS is a general purpose fluid flow simulation package which solves the conserved form of the Navier-Stokes equations. A finite-difference solution procedure is used in the package, with closure achieved by use of the k-ϵ turbulence model. The PHOENICS-81 code, supplied by CHAM Ltd, was implemented on the South West Universities ICL 2980 computer.

An attempt was made to use PHOENICS to simulate the initial development of an underexpanded free round jet. The progress in achieving a useful solution was slow and CHAM Ltd published a report describing a similar exercise before a successful prediction had been generated. The work at Bath using PHOENICS was therefore halted as it was not expected that any significant progress could be made beyond that achieved by CHAM.

A brief summary is given of the work completed at Bath and of the results achieved by CHAM.

E.2 The PHOENICS work at Bath University

CHAM supplied several demonstration exercises with PHOENICS so that new users could become familiar with the code. The most useful trial program was a single free round subsonic jet simulation reported by Malin and Rosten (1982). The boundary conditions of this case were modified to represent a real low speed round jet which was available for verification purposes. Excellent agreement between the computer prediction and the experimental data was achieved. However the closeness of this agreement was suprising because the k-ϵ model used in the code was expected to over-predict the jet spreading rate. The report of Pope (1978) explains the nature of the k-ϵ over-prediction phenomenon.

The next stage in the evaluation of the code was an attempt to model a high speed subsonic jet with an elliptical solution

procedure. All work prior to this stage had been solved using a parabolic method. With the elliptical solution it was apparent that the downstream outflow boundary was causing difficulties. This problem was not resolved until CHAM supplied details of a technique to falsely govern the mass flow through the last axial plane of cells. However, this technique was not used because it arrived after CHAM's own supersonic free jet results were published.

Before the 'last cell' problem had been resolved it was decided to apply the code to an underexpanded M=1.0 6.9 bar gauge jet. The results showed a very basic representation of the first shock system but the downstream difficulty meant that even after 8 hours CPU time the results had not converged.

E.3 The CHAM predictions of a free M=1.0 underexpanded jet

The CHAM report by Davis, Ludwig and Rhodes (1985) contains the results of a prediction of the experimental data of Donaldson and Snedeker (1971). An M=1.0 6.76 bar round jet is described by Donaldson and Snedeker, which is a similar jet to that utilised in the free jet experiments of Chapters 5 and 6.

Davis et al use the PHOENICS-81 code with the k-ϵ turbulence model corrected with axisymmetric jet modifications. Moderately good agreement with experiment is achieved but the simulation fails to identify the second shock system and the downstream velocity prediction is poor. With the incorporation of a compressibility correction and a change to the kinetic energy equations the results are improved. Figure E.1 is reproduced from Davis et al and shows the best results achieved by CHAM and also the Donaldson and Snedeker data. The manner in which the first shock is smeared by the numerical solution is demonstrated. All the corrections applied by CHAM are legitimate techniques well documented in the jet modelling literature.

Using PHOENICS to model less underexpanded jets produces results which are generally in closer agreement with experiment. Wilson (1988) shows the results of modelling a pressure ratio 2.5 sonic

jet with PHOENICS-84. Comparable experimental data are also contained in Donaldson and Snedeker's report. Figure E.2 shows that only the first two of the six shock cells are predicted by PHOENICS and all regions of supersonic velocity are under-predicted, but the downstream centreline properties are accurately presented.

E.4 Concluding remarks

It is apparent that finite-difference codes like PHOENICS are not capable of predicting the fine shock structure of supersonic jets due to smearing of the flow properties. The cause of this difficulty must lie in the numerical algorithm when applied to regions of very large fluid property gradients.

Recent work at Cranfield has shown some promising predictions of the wall static pressure rise in moderately underexpanded simple ejectors, Sanatian and Adkins (1988). Whether the jet structure is sufficiently modelled to enable ejector exit profiles to be predicted is not clear.

APPENDIX F : THE ACOUSTIC PROPERTIES OF SUPERSONIC JET FLOWS

It was not initially appreciated, either during the literature search into high pressure jets or whilst the free jet programme was underway, that the acoustic properties of high speed jets are a fundamental factor governing their interaction with quiescent air. Further searches of the literature later revealed many papers discussing aspects of jet acoustic noise and mixing. Some of the more pertinent papers are discussed here.

Hammitt (1961) discusses the oscillation of a two-dimensional underexpanded jet. The oscillatory nature of the jet is attributed to acoustic feedback, but it is unclear whether an axisymmetric jet would suffer the same effect. The shadowgraph images of Hammitt clearly show an unsteady mechanism, usually starting about 3 to 5 nozzle widths from the nozzle exit. The experimental results of the current exercise showed no such effects even though the first six diameters of the jet flows were photographed.

Hammitt shows that it is possible to stabilize the oscillating jets by placing sound absorbing material around the first shock cell so as not to interfere with the jet flow. In addition, shielding of the upstream surface from which the jet emanates has the same effect. Hammitt concludes that the sound waves generated downstream can dramatically affect the very early stages of jet development.

The acoustic feedback phenomenon is further explored by Glass (1968). The reverse situation to that described by Hammitt (1961) is encountered whereby a reflecting board close to the nozzle appears to accentuate the acoustic feedback mechanisms. Glass shows that it is possible to establish an audible screech condition and a coincident increase in jet mixing rate. No quantitative mass flows are given but by deliberately causing screech one can create a jet with a diameter of twice the no-screech case at x/D=20.

Glass concludes that the shock structure is the source of the screech but that the generation is a complex procedure. It is certain that the shock noise travels upstream both outside the jet and in the subsonic shear layer. Subjecting the emerging jet to

'external' noise creates undefined 'disturbances' which rapidly form into vortices spiralling around the jet surface. From the free jet results of Chapters 5 and 6 it is almost certain that screech was not present with a jet stagnation pressure of 6.9 bar gauge. This could be attributed to the lack of suitable nearby reflecting surfaces. However, at certain pressures below 6.9 bar the jets were producing definite tones audible above the overall jet noise. No prior work has been found that identifies the precise conditions necessary for jet screech.

Sarohia (1978) extends the discussion of underexpanded jet noise to the case of a jet with a coflowing stream. Specifically Sarohia considers the effect of jet noise in flight, but the results are also of interest in the context of ejectors. It is concluded that a coflowing stream can accentuate the spiralling vortices reported by Glass (1968) and produce improvements in jet mixing rate, although accompanied by an increase in the acoustic noise generated.

APPENDIX G: THE HTP EJECTOR PERFORMANCE MODEL

G.1 Introduction

This Appendix contains a derivation of the ejector performance model developed by Quinn and briefly described in the reference Quinn (1976). The HTP model solves the continuity, momentum and energy equations in the confines of the ejector mixing duct. Figure G.1 shows a representative ejector duct and the notation employed.

The main advantage of the HTP model is the concise manner in which the equations are formulated. Frequent use is made of the following two functions of Mach number:-

Mass flow function :
$$F_2(M) = M\left(\frac{\rho}{\rho_0}\right)\left(\frac{t}{T}\right)^{1/2} \qquad (G.1)$$

Momentum function :
$$F_3(M) = \frac{p}{\bar{p}}\left(1 + \gamma M^2\right) \qquad (G.2)$$

Use of these functions allows the mass flux and momentum to be quoted in terms of the Mach number, the total pressure and total temperature.

G.2 Continuity Equation

Applying the steady state continuity equation to the duct:-

$$\rho_p A_p u_p + \rho_s A_s u_s = \alpha \bar{\rho}_2 A_2 U_2 \qquad (G.3)$$

The quantity α is the mass flow skewness which is required because the product of two area mean values does not equal the mean of the product.

Thus,
$$\alpha = \int \frac{\rho}{\bar{\rho}} \cdot \frac{u}{U}\, d(a/A) \qquad (G.4)$$

where $\bar{\rho}$ and U are the mean values of the density and velocity across the area A.

Equation (G.3) can be rewritten in terms of stagnation values:-

$$A_p P_{RES} \xi_o F_2(M_p)\left(\frac{\gamma}{RT_p}\right)^{1/2} + A_s P_a \xi_1 F_2(M_s)\left(\frac{\gamma}{RT_s}\right)^{1/2} = \alpha A_2 \bar{P}_2 F_2(\bar{M}_2)\left(\frac{\gamma}{R\bar{T}_2}\right)^{1/2} \tag{G.5}$$

where ξ_o and ξ_1 are the nozzle and inlet total pressure loss fractions respectively.

Thus if $\pi = P_{RES}/P_a$,

$$\pi A_p \xi_o F_2(M_p)(T_p)^{-1/2} + A_s \xi_1 F_2(M_s)(T_s)^{-1/2} = \alpha A_2 \frac{\bar{P}_2}{P_a} F_2(\bar{M}_2)(\bar{T}_2)^{-1/2} \tag{G.6}$$

G.3 Momentum Equation

The steady state momentum equation applied to the duct is:-

$$(p_p + \rho_p u_p^2) A_p + (p_s + \rho_s u_s^2) A_s = \xi_f \bar{\rho}_2 U_2^2 A_2 + \bar{p}_2 A_2 + \beta \bar{\rho}_2 U_2^2 A_2 \tag{G.7}$$

where β is similar in form to α and represents the momentum skewness,

$$\beta = \int \frac{\rho}{\bar{\rho}} \cdot \frac{u^2}{U^2} \, d(a/A) \tag{G.8}$$

The friction loss ξ_f is defined arbitarily as a fraction of the exit dynamic pressure. Quinn suggests the following means of evaluating ξ_f :-

$$\xi_f = 2 C_F \left(\frac{L}{W}\right)\left(\frac{U_{WALL}}{U_2}\right)^2 \tag{G.9}$$

where $C_F \simeq 0.004$ and U_{WALL} and U_2 have to be estimated from the likely ejector flowfield.

Equation (G.7) finally becomes:-

$$\pi A_p \xi_0 F_3(M_p) + A_s \xi_1 F_3(M_s) = \frac{\bar{p}_2}{p_a} A_2 \left(1 + \gamma(\xi_f + \beta)\bar{M}_2^2\right) \qquad (G.10)$$

G.4 Continuity/Momentum Combination

Dividing Equation (G.6) into (G.10),

$$\frac{\pi A_p \xi_0 F_3(M_p) + A_s \xi_1 F_3(M_s)}{\pi A_p \xi_0 F_2(M_p)(T_p)^{-1/2} + A_s \xi_1 F_2(M_s)(T_s)^{-1/2}} = \frac{\bar{p}_2\left(1 + \gamma(\xi_f + \beta)\bar{M}_2^2\right)}{\propto \bar{P}_2 F_2(\bar{M}_2)(\bar{T}_2)^{-1/2}} \qquad (G.11)$$

and letting $A_R = A_s / A_p$ so

$$\frac{\pi F_3(M_p) + A_R F_3(M_s)(\xi_1/\xi_0)}{\pi F_2(M_p) + A_R F_2(M_s)(\xi_1/\xi_0) T_s^{-1/2} T_p^{1/2}} = \frac{\bar{p}_2}{\bar{P}_2} \frac{1}{F_2(\bar{M}_2)} \frac{1 + \gamma(\xi_f + \beta)\bar{M}_2^2}{\propto T_p^{1/2} \bar{T}_2^{-1/2}} \qquad (G.12)$$

Quinn defines the left hand side as F_4

ie.
$$F_4 = \frac{\pi F_3(M_p) + A_R F_3(M_s)(\xi_1/\xi_0)}{\left[\pi F_2(M_p) + A_R F_2(M_s)(\xi_1/\xi_0)(T_p/T_s)^{1/2}\right](\bar{T}_2/T_p)^{1/2}} \qquad (G.13)$$ ✓

So
$$F_4 = \frac{1 + \gamma(\xi_f + \beta)\bar{M}_2^2}{\propto} \frac{\bar{p}_2}{\bar{P}_2} \frac{1}{F_2(\bar{M}_2)} \qquad (G.14)$$

where
$$F_2(\bar{M}_2) = \bar{M}_2 \left(\frac{\bar{\rho}_2}{\rho_{o_2}}\right)\left(\frac{\bar{t}_2}{\bar{T}_2}\right)^{1/2} \qquad (G.15)$$

and
$$\frac{\bar{p}_2}{\bar{P}_2} \cdot \frac{\bar{\rho}_{o_2}}{\bar{\rho}_2} = \frac{\bar{t}_2}{\bar{T}_2} \qquad (G.16)$$

so that $$F_4 = \frac{1 + \gamma(\xi_f + \beta)\bar{M}_2^2}{\alpha \bar{M}_2} \left(\frac{\bar{T}_2}{\bar{T}_2}\right)^{1/2} \quad \text{(G.17)}$$

Also, $$\frac{\bar{T}_2}{\bar{T}_2} = \frac{1}{1 + \frac{\gamma-1}{2}\bar{M}_2^2} \quad \text{(G.18)}$$

Which gives $$\alpha \bar{M}_2 F_4 \left(1 + \frac{\gamma-1}{2}\bar{M}_2^2\right)^{1/2} = 1 + \gamma(\xi_f + \beta)\bar{M}_2^2 \quad \text{(G.19)}$$

Finally

$$\bar{M}_2^4 \left(F_4^2 \alpha^2 \left(\frac{\gamma-1}{2}\right) - \gamma^2 (\xi_f + \beta)^2\right) + \bar{M}_2^2 \left(F_4^2 \alpha^2 - 2\gamma(\xi_f + \beta)\right) - 1 = 0 \quad \text{(G.20)}$$

Equation (G.20) can be solved for $\bar{M}_2$ if F_4 can be calculated from (G.13) but there are two obstacles to this process:-

1/ M_s is not known.

2/ The value of $\bar{T}_2$ is unknown. If the primary stream is hot then an energy balance needs to be arranged in the mixing duct.

G.5 Energy Equation

The steady flow energy equation applied to the adiabatic process in the duct produces:-

$$\dot{m}_p T_p + \dot{m}_s T_s = \int_{A_2} \rho u T \, da \quad \text{(G.21)}$$

but $$T = t + u^2/2C_p \quad \text{(G.22)}$$

therefore $$\dot{m}_p T_p + \dot{m}_s T_s = \int_{A_2} \rho u t \, da + \int_{A_2} \frac{\rho u^3}{2C_p} da \quad \text{(G.23)}$$

Two new skewnesses need to be defined:-

$$\delta = \int \frac{\rho}{\bar{\rho}} \frac{u^3}{U^3} \, d(a/A) \qquad \text{(G.24)}$$

$$\epsilon = \int \frac{\rho}{\bar{\rho}} \frac{u}{U} \frac{t}{\bar{t}} \, d(a/A) \qquad \text{(G.25)}$$

Thus:- $$\dot{m}_p + \dot{m}_s \frac{T_s}{T_p} = \epsilon \bar{\rho}_2 U_2 \frac{\bar{t}_2}{T_p} A_2 + \frac{1}{2C_p T_p} \delta \bar{\rho}_2 U_2^3 A_2 \qquad \text{(G.26)}$$

Now from (G.4) $\dot{m}_2 = \alpha \bar{\rho}_2 U_2 A_2$ so:-

$$\frac{\alpha}{\epsilon} \left(\frac{\dot{m}_p + \dot{m}_s (T_s/T_p)}{\dot{m}_p + \dot{m}_s} \right) = \frac{1}{T_p} \left(\bar{t}_2 + \frac{U_2^2}{2C_p} \frac{\delta}{\epsilon} \right) \qquad \text{(G.27)}$$

The static temperature can be expressed,

$$\bar{t}_2 = \bar{\bar{T}}_2 - \bar{\bar{T}}_2 \left(1 - \frac{\bar{t}_2}{\bar{\bar{T}}_2} \right) \qquad \text{(G.28)}$$

and $$\frac{U_2^2}{2C_p} = \bar{\bar{T}}_2 \left(1 - \frac{\bar{t}_2}{\bar{\bar{T}}_2} \right) \qquad \text{(G.29)}$$

The energy balance becomes:-

$$\frac{\alpha}{\epsilon} \left(\frac{\dot{m}_p + \dot{m}_s (T_s/T_p)}{\dot{m}_p + \dot{m}_s} \right) \frac{T_p}{\bar{\bar{T}}_2} = 1 + \left(1 - \frac{\bar{t}_2}{\bar{\bar{T}}_2} \right) \left(\frac{\delta}{\epsilon} - 1 \right) \qquad \text{(G.30)}$$

Quinn defines the right hand side of equation (G.30) as the temperature function K . Quinn states that δ/ϵ rarely exceeds 1.5 so that K can comfortably be set to 1.0 with little error. However, this assumption can be incorrect: in the text of Chapter 8 the values $\delta \simeq 7.0$ and $\epsilon \simeq 1.0$ are noted for one of the test cases. Thus if the ejector flow is both hot and badly mixed the HTP method needs more information as to the value of $\bar{t}_2/\bar{\bar{T}}_2$. It is

suggested that trial calculations would have to be made with various values of $\bar{T}_1/\bar{T}_2$ to ascertain the models dependence on this parameter with poorly mixed heated flows.

Finally the energy equation becomes:-

$$\frac{\bar{T}_2}{T_p} = \frac{\alpha}{K\epsilon}\left(\frac{\dot{m}_p + \dot{m}_s(T_s/T_p)}{\dot{m}_p + \dot{m}_s}\right) \qquad \text{(G.31)}$$

This differs from Quinn's version in that K appears in the denominator. From equation (G.31) the value of $\bar{T}_2$ can be found and inserted in (G.13).

G.6 Concluding Remarks

The complete solution sequence thus needs the specification of the four skewnesses and the three ξ losses. If the primary and secondary streams are of the same temperature only two skewness parameters α and β are required.

A value of M_5 has to be estimated and used to find the quantity F_4 from (G.13) and then the exit Mach number $\bar{M}_2$ is calculated from (G.20). This value of $\bar{M}_2$ is then substituted back into either the continuity or momentum equations to find either $F_3(M_5)$ or $F_3(M_5)$. Thus M_5 can be calculated and the process repeated to convergence.

Initial Deflection $\Delta\phi$	Effuser Length mm	Exit Radius mm	Exit Area Throat Area	Resulting Mach No
0.0004	30.65	18.40	1.106	1.384
0.0008	30.68	18.40	1.106	1.384
0.0012	30.76	18.40	1.106	1.384
0.0016	30.86	18.41	1.107	1.386
0.0020	31.16	18.43	1.109	1.390
0.0024	31.11	18.43	1.109	1.390

Table 4.1 Effect of Grid Fineness on M=1.4 Nozzle Prediction

Nozzle	Tooth Aspect Ratio	Internal Arc Of One Tooth mm	Tooth Depth mm
M=1.0 16 Tooth	0.5	3.44	1.72
M=1.0 8 Tooth	0.25	6.87	1.72
M=1.0 4 Tooth	0.125	13.74	1.72
M=1.4 16 Tooth	0.5	3.63	1.81
M=1.4 8 Tooth	0.25	7.26	1.81
M=1.4 4 Tooth	0.125	14.51	1.81
M=1.8 16 Tooth	0.5	4.12	2.06
M=1.8 8 Tooth	0.25	8.24	2.06

Table 5.1 Castellated Nozzle Dimensions

Nozzle Type	Initial deflection from Prandtl-Meyer relation, degrees	Initial deflection from schlieren photographs, degrees
M=1.0 Plain	26.6	24.5
M=1.0 16 Tooth		——
M=1.0 8 Tooth		34.0
M=1.0 4 Tooth		35.0
M=1.4 Plain	17.6	16.5
M=1.4 16 Tooth		26.5
M=1.4 8 Tooth		31.0
M=1.4 4 Tooth		——
M=1.8 Plain	5.8	2.5
M=1.8 16 Tooth		7.0
M=1.8 8 Tooth		8.0
M=2.0 Plain	0.0	-0.5

Table 5.2 Theoretical and Observed Initial Jet Divergence

Nozzle Type	Exit Area / Throat Area	True Exit Mach No.	I.S.A. Reference Mass Flow kg/sec	I.S.A. Reference Momentum kg m/sec^2
M=1.0 Plain	1.0	1.0	1.820	565.2
M=1.0 16 Tooth	1.0	1.0	1.825	566.7
M=1.0 8 Tooth	1.0	1.0	1.821	565.5
M=1.0 4 Tooth	1.0	1.0	1.825	566.7
M=1.4 Plain	1.122	1.412	1.813	736.3
M=1.4 16 Tooth	1.114	1.398	1.831	738.3
M=1.4 8 Tooth	1.124	1.415	1.817	739.1
M=1.4 4 Tooth	1.129	1.424	1.809	739.1
M=1.8 Plain	1.431	1.792	1.837	873.8
M=1.8 16 Tooth	1.442	1.802	1.823	870.1
M=1.8 8 Tooth	1.441	1.801	1.830	873.2
M=2.0 Plain	1.721	2.024	1.796	916.8

Table 6.1 Reference Nozzle Properties, Mass Flow and Momentum

Nozzle Type	Jet Mass Flow kg/sec Two values:- Corrected for ambient variations & Corrected for all errors		
	x/D=4	x/D=6	x/D=8
M=1.0 Plain	2.473 N 2.424	2.681 I 2.590	3.006 I 2.904
M=1.0 16 Tooth	2.845 I 2.748	3.153 I 3.046	3.303 I 3.191
M=1.0 8 Tooth	3.779 W 3.598	3.949 W 3.759	4.307 W 4.100
M=1.0 4 Tooth	3.155 I 3.048	4.221 W 4.018	5.358 W 5.101
M=1.4 Plain	2.294 N 2.248	2.524 N 2.474	2.805 I 2.710
M=1.4 16 Tooth	2.801 I 2.706	3.037 I 2.934	3.236 I 3.126
M=1.4 8 Tooth	3.406 I 3.290	3.537 I 3.367	3.686 W 3.509
M=1.4 4 Tooth	2.785 I 2.690	3.504 I 3.417	4.168 W 3.968
M=1.8 Plain	2.228 N 2.183	2.544 N 2.494	2.790 N 2.734
M=1.8 16 Tooth	2.435 N 2.386	2.656 N 2.603	2.909 I 2.810
M=1.8 8 Tooth	2.500 N 2.450	2.760 N 2.705	3.173 I 3.065
M=2.0 Plain	2.191 N 2.147	2.472 N 2.423	2.811 N 2.755

N :- Narrow jet correction applied

I :- Intermediate jet correction applied

W :- Wide jet correction applied

Table 6.2 Free Jet Mass Flows at x/D=4, 6 and 8

Nozzle Type	Jet Momentum kg m/sec^2 Two values:- Corrected for ambient variations & Corrected for all errors		
	x/D=4	x/D=6	x/D=8
M=1.0 Plain	883.1 N 865.4	891.8 I 865.9	911.4 I 885.0
M=1.0 16 Tooth	865.9 I 840.8	879.2 I 853.7	885.5 I 859.8
M=1.0 8 Tooth	988.7 W 951.1	928.7 W 893.4	906.0 W 871.6
M=1.0 4 Tooth	882.5 I 856.9	1039.6 W 1000.1	1170.6 W 1126.1
M=1.4 Plain	946.8 N 927.9	940.1 N 921.3	935.5 I 908.4
M=1.4 16 Tooth	952.2 I 924.6	974.3 I 946.0	982.4 I 953.9
M=1.4 8 Tooth	1055.6 I 1025.0	1000.5 I 971.5	974.5 W 937.5
M=1.4 4 Tooth	949.5 I 922.0	1057.3 I 1027.1	1139.4 W 1096.1
M=1.8 Plain	964.4 N 945.1	956.6 N 937.5	945.3 N 926.4
M=1.8 16 Tooth	979.7 N 960.1	958.2 N 939.0	930.7 I 903.7
M=1.8 8 Tooth	1016.9 N 996.6	994.2 N 974.3	1026.1 I 996.3
M=2.0 Plain	919.3 N 900.9	948.2 N 929.2	967.4 N 948.1

N :- Narrow jet correction applied

I :- Intermediate jet correction applied

W :- Wide jet correction applied

Table 6.3 Free Jet Momentum Flux at x/D=4, 6 and 8

	Mass Flow kg/sec Two values:- Corrected for ambient variations & corrected for all errors	Momentum kg m/sec^2
Step Traverse	2.785	949.5
I	2.690	922.0
Gap Traverse	3.511	1290.3
I	3.392	1252.9
Tooth Traverse	1.977	734.8
N	1.937	720.1
Average of	2.744	1012.6
Tooth & Gap	2.665	986.5

N :- Narrow jet correction applied

I :- Intermediate jet correction applied

Table 6.4 Nozzle Rotation Dependence, M=1.4 4 Tooth, x/D=4

Nozzle Type	Nominal Area Ratio	Secondary Area / Nozzle Throat Area	Secondary Area / Primary Area
M=1.0	15	13.73	13.73
	25	23.73	23.73
M=1.4	15	13.60	12.20
	25	23.60	21.17
M=1.8	15	13.24	9.20
	25	23.24	16.15
M=2.0	15	12.96	7.68
	25	22.96	13.61

Table 7.1 Nominal and Actual Ejector Area Ratios

Nozzle Type	Total Press. bar gauge	Atmos. Press. bar abs.	Ideal Primary Thrust N	Secondary Thrust N	Thrust Aug. Ratio Φ	True Thrust Aug. Φ_t
Plain	2.786	0.994	365.35	5.45	1.015	0.999
"	3.470	0.994	450.50	0.25	1.001	0.981
"	4.145	0.994	531.30	0.15	1.001	0.969
"	4.833	0.998	615.35	-1.50	0.998	0.960
"	5.509	0.998	697.75	-0.75	0.999	0.954
"	6.199	0.998	781.95	-0.20	1.000	0.949
"	6.881	0.998	865.15	1.05	1.001	0.945
16 Tooth	2.802	0.994	367.45	1.55	1.004	0.989
"	3.454	0.994	447.05	4.20	1.009	0.986
"	4.129	0.994	529.30	7.25	1.014	0.983
"	4.831	1.003	615.10	10.80	1.018	0.979
"	5.531	1.003	700.50	15.90	1.023	0.977
"	6.199	1.003	782.05	20.65	1.027	0.974
"	6.907	1.003	868.40	28.05	1.033	0.973
16 T/Rot	6.881	1.003	865.25	29.45	1.034	0.976
8 Tooth	2.796	0.994	366.65	9.35	1.026	1.010
"	3.454	0.994	447.05	15.90	1.036	1.012
"	4.141	0.994	530.75	26.60	1.050	1.018
"	4.828	1.003	614.75	39.55	1.064	1.024
"	5.530	1.003	700.45	53.45	1.076	1.028
"	6.194	1.003	781.35	68.90	1.088	1.033
"	6.898	1.003	867.25	84.75	1.098	1.036
8 T/Rot	6.899	1.003	867.45	83.15	1.096	1.034
4 Tooth	2.768	0.994	363.30	6.90	1.019	1.004
"	3.481	0.994	451.25	10.25	1.023	0.999
"	4.143	0.994	531.90	12.80	1.024	0.992
"	4.816	1.003	613.30	17.00	1.028	0.989
"	5.558	1.003	703.80	22.55	1.033	0.986
"	6.203	1.003	782.50	27.55	1.035	0.983
"	6.875	1.003	864.50	33.45	1.039	0.980
4 T/Rot	6.915	1.003	869.40	32.30	1.037	0.979

Table 7.2 Thrusts and Augmentation Ratios from M=1.0 A_R=15 Tests

Nozzle Type	Total Press. bar gauge	Atmos. Press. bar abs.	Ideal Primary Thrust N	Secondary Thrust N	Thrust Aug. Ratio Φ	True Thrust Aug. Φ_t
Plain	2.784	1.000	365.45	1.30	1.004	0.986
"	3.451	1.000	446.70	0.65	1.002	0.978
"	4.123	1.000	528.70	-0.65	0.999	0.968
"	4.819	1.000	613.60	-2.50	0.996	0.958
"	5.506	1.000	697.45	-2.90	0.996	0.951
"	6.172	1.000	778.75	-3.25	0.996	0.946
"	6.898	1.000	867.25	-3.25	0.996	0.940
16 Tooth	2.752	1.000	361.55	-1.05	0.998	0.983
"	3.439	1.000	445.35	-0.55	0.999	0.976
"	4.129	1.000	529.45	0.00	1.000	0.969
"	4.822	1.000	614.00	0.30	1.001	0.963
"	5.513	1.000	698.00	1.25	1.002	0.957
"	6.203	1.000	782.50	2.60	1.004	0.952
"	6.892	1.000	866.40	4.70	1.005	0.948
16 T/Rot	6.888	1.000	866.00	4.60	1.006	0.948
8 Tooth	2.759	1.000	362.25	1.75	1.005	0.990
"	3.449	1.000	446.45	3.95	1.009	0.986
"	4.151	1.000	532.10	7.90	1.015	0.984
"	4.843	1.000	617.40	13.30	1.022	0.984
"	5.526	1.000	699.80	19.35	1.028	0.982
"	6.193	1.000	781.20	26.65	1.034	0.982
"	6.917	1.000	869.50	35.15	1.041	0.981
8 T/Rot	6.878	1.000	864.75	35.25	1.041	0.982
4 Tooth	2.753	1.000	361.60	0.55	1.002	0.987
"	3.434	1.000	444.60	2.15	1.005	0.982
"	4.138	1.000	530.50	4.50	1.009	0.978
"	4.801	1.000	611.40	6.15	1.010	0.972
"	5.507	1.000	697.60	8.60	1.013	0.967
"	6.177	1.000	779.30	10.65	1.014	0.962
"	6.890	1.000	866.30	13.70	1.016	0.958
4 T/Rot	6.886	1.000	865.70	12.95	1.015	0.958

Table 7.3 Thrusts and Augmentation Ratios from M=1.0 A_R=25 Tests

Nozzle Type	Total Press. bar gauge	Atmos. Press. bar abs.	Ideal Primary Thrust N	Secondary Thrust N	Thrust Aug. Ratio Φ
Plain	2.768	1.005	368.35	3.05	1.008
"	3.461	1.005	455.80	1.65	1.004
"	4.149	1.005	542.60	3.55	1.007
"	4.846	1.005	630.55	-4.15	0.994
"	5.533	1.005	717.25	-4.35	0.994
"	6.212	0.998	802.85	-4.90	0.994
"	6.881	0.998	887.30	-4.90	0.994
16 Tooth	2.788	0.998	370.75	0.70	1.002
"	3.470	0.998	456.80	-1.50	0.997
"	4.151	0.998	542.70	0.60	1.001
"	4.834	0.998	628.95	3.60	1.006
"	5.522	0.998	715.85	6.35	1.009
"	6.193	0.998	800.50	10.35	1.013
"	6.906	0.998	890.45	15.20	1.017
16 T/Rot	6.878	0.998	886.85	15.50	1.018
8 Tooth	2.780	0.998	369.75	1.00	1.003
"	3.456	0.998	455.05	-0.80	0.999
"	4.158	0.998	542.70	3.15	1.006
"	4.838	0.998	629.45	8.90	1.014
"	5.518	0.998	715.25	15.35	1.022
"	6.208	0.998	802.35	24.00	1.030
"	6.889	0.998	888.30	33.25	1.038
8 T/Rot	6.902	0.998	889.95	33.20	1.037
4 Tooth	2.790	0.994	370.90	3.25	1.009
"	3.458	0.994	455.15	-0.80	0.999
"	4.158	0.994	543.45	-1.20	0.998
"	4.825	0.994	627.75	-0.35	1.000
"	5.523	0.994	715.80	2.05	1.003
"	6.186	0.994	799.65	4.15	1.005
"	6.922	0.994	892.35	7.40	1.009
4 T/Rot	6.882	0.994	887.35	7.80	1.009

Table 7.4 Thrusts and Augmentation Ratios from M=1.4 A_R=15 Tests

Nozzle Type	Total Press. bar gauge	Atmos. Press. bar abs.	Ideal Primary Thrust N	Secondary Thrust N	Thrust Aug. Ratio Φ
Plain	2.804	0.999	372.75	-1.20	0.997
"	3.472	0.999	457.00	0.00	1.000
"	4.151	0.999	542.75	-1.00	0.999
"	4.815	0.999	626.55	-5.10	0.992
"	5.520	0.999	715.50	-4.60	0.994
"	6.181	0.999	799.00	-5.45	0.993
"	6.879	0.999	887.10	-6.60	0.993
16 Tooth	2.797	0.999	371.85	-1.20	0.997
"	3.451	0.999	454.40	-2.65	0.994
"	4.123	0.999	539.15	-2.25	0.996
"	4.824	0.999	627.25	-2.50	0.996
"	5.518	0.999	715.25	-2.75	0.996
"	6.184	0.999	799.40	-1.85	0.998
"	6.878	0.999	886.85	-1.20	0.999
16 T/Rot	6.883	0.999	887.45	-1.30	0.999
8 Tooth	2.802	0.999	372.50	-3.00	0.992
"	3.483	0.999	458.55	-2.70	0.994
"	4.131	0.999	540.20	-2.55	0.995
"	4.812	0.999	626.20	-0.80	0.999
"	5.524	0.999	716.05	1.65	1.002
"	6.181	0.999	798.90	4.35	1.006
"	6.885	0.999	887.75	8.40	1.010
8 T/Rot	6.876	0.999	886.55	8.20	1.009
4 Tooth	2.795	0.999	371.70	-1.70	0.996
"	3.490	0.999	459.40	-2.00	0.996
"	4.135	0.999	540.75	-1.75	0.997
"	4.828	0.999	628.15	-3.10	0.995
"	5.524	0.999	715.95	-2.75	0.997
"	6.181	0.999	799.00	-2.30	0.997
"	6.881	0.999	887.30	-1.55	0.999
4 T/Rot	6.908	0.999	890.70	-1.90	0.998

Table 7.5 Thrusts and Augmentation Ratios from M=1.4 A_R=25 Tests

Nozzle Type	Total Press. bar gauge	Atmos. Press. bar abs.	Ideal Primary Thrust N	Secondary Thrust N	Thrust Aug. Ratio Φ
Plain	2.766	0.999	363.95	3.70	1.011
"	3.452	0.999	455.45	-1.30	0.998
"	4.134	0.999	546.35	-5.05	0.991
"	4.830	0.999	639.25	-6.50	0.990
"	5.520	0.999	731.30	-7.80	0.990
"	6.189	0.999	820.50	-8.00	0.990
"	6.889	0.999	913.85	-8.50	0.991
16 Tooth	2.779	1.005	365.60	0.55	1.002
"	3.464	1.005	457.00	-2.20	0.996
"	4.134	1.005	546.35	-5.25	0.991
"	4.833	1.005	639.75	-5.20	0.992
"	5.535	1.005	733.25	-6.65	0.991
"	6.189	1.005	820.50	-5.95	0.993
"	6.894	1.005	914.60	-4.70	0.995
16 T/Rot	6.908	1.005	916.45	-4.55	0.995
8 Tooth	2.775	0.999	365.15	1.80	1.005
"	3.457	0.999	456.10	-1.30	0.997
"	4.139	0.999	547.05	-3.95	0.993
"	4.829	0.999	639.20	-5.45	0.992
"	5.528	0.999	732.40	-6.75	0.990
"	6.210	0.999	823.35	-6.30	0.992
"	6.901	0.999	915.55	-4.75	0.995
8 T/Rot	6.885	0.999	913.40	-5.40	0.994

Table 7.6 Thrusts and Augmentation Ratios from M=1.8 A_R=15 Tests

Nozzle Type	Total Press. bar gauge	Atmos. Press. bar abs.	Ideal Primary Thrust N	Secondary Thrust N	Thrust Aug. Ratio Φ
Plain	2.756	0.997	362.60	-3.10	0.992
"	3.479	0.997	458.95	-4.25	0.991
"	4.134	0.997	546.45	-5.40	0.990
"	4.832	0.997	639.00	-6.50	0.990
"	5.519	0.997	731.10	-7.10	0.990
"	6.180	0.997	819.35	-7.70	0.991
"	6.880	0.997	912.70	-8.40	0.991
16 Tooth	2.786	0.997	366.65	-3.00	0.992
"	3.472	0.997	458.00	-4.30	0.991
"	4.151	0.997	548.75	-5.40	0.991
"	4.816	0.997	637.40	-6.10	0.991
"	5.535	0.997	733.25	-6.90	0.991
"	6.180	0.997	819.30	-7.20	0.992
"	6.878	0.997	912.50	-6.70	0.993
16 T/Rot	6.894	0.997	914.50	-7.30	0.992
8 Tooth	2.777	0.997	365.35	-2.45	0.994
"	3.463	0.997	457.00	-3.65	0.992
"	4.151	0.997	548.60	-4.60	0.992
"	4.839	0.997	640.40	-5.55	0.991
"	5.514	0.997	730.50	-6.55	0.991
"	6.194	0.997	821.15	-6.95	0.992
"	6.876	0.997	912.05	-6.80	0.993
8 T/Rot	6.901	0.997	915.60	-7.00	0.992

Table 7.7 Thrusts and Augmentation Ratios from M=1.8 A_R=25 Tests

Nozzle Type	Total Press. bar gauge	Atmos. Press. bar abs.	Ideal Primary Thrust N	Secondary Thrust N	Thrust Aug. Ratio Φ
Plain	2.788	0.993	356.45	-2.65	0.993
"	3.093	0.993	398.40	1.95	1.005
"	3.478	0.993	451.00	4.30	1.010
"	4.138	0.993	541.40	-6.55	0.988
"	4.487	0.993	589.30	-2.00	0.997
"	4.816	0.993	634.30	-1.40	0.997
"	5.517	0.993	729.65	-8.00	0.989
"	6.187	0.993	820.95	-9.50	0.988
"	6.901	0.993	919.85	-10.70	0.988

Table 7.8 Thrusts and Augmentation Ratios from M=2.0 A_R=15 Tests

Nozzle Type	Total Press. bar gauge	Atmos. Press. bar abs.	Ideal Primary Thrust N	Secondary Thrust N	Thrust Aug. Ratio Φ
Plain	2.781	1.004	355.40	-3.40	0.991
"	3.476	1.004	450.60	-2.75	0.994
"	4.145	1.004	542.05	-1.05	0.999
"	4.826	1.004	635.30	-1.20	0.999
"	5.531	1.004	731.90	-3.65	0.995
"	6.171	1.004	819.55	-9.05	0.989
"	6.879	1.004	916.60	-9.50	0.990

Table 7.9 Thrusts and Augmentation Ratios from M=2.0 A_R=25 Tests

Imaginary Jet Radial Position r/D	Nominal Velocity m/s	Turbulent Velocity Factor $\sqrt{\overline{v_x^2}}/v$	Resultant rms Velocity m/s	% Increase On Recorded $\frac{1}{2}\rho v^2$	% Increase On Recorded Velocity
0.0	300	0.20	60	6.3	3.1
0.1	210	0.34	72	20.4	9.7
0.2	150	0.44	66	36.0	16.6
0.3	90	0.47	42	43.2	19.7
0.4	50	0.30	15	18.0	8.6

Table D.1 Imaginary Jet Turbulence Data

Nominal Velocity m/s	Significance of Nominal Jet Velocity	Velocity Errors from Pressure Readings
500	Any Supersonic Velocity	+ 1% - 0%
300	Sonic Velocity	+ 1% - 0%
210	Velocity at Half of 'Half-Width'	+ 1% - 1%
150	'Half-Width' Velocity	+ 1% - 2%
90	Velocity at 1.5 x 'Half-Width'	+ 4% - 4%
50	Velocity at 2.0 x 'Half-Width'	+ 11% - 15%

Table D.2 Velocity Errors due to Measurement of Pressure

Nominal Velocity m/s	Approximate Equivalent Mach Number	Velocity Error due to all Sources
500	All Supersonic Flows	+ 1% - 0%
300	1.0	+ 4% - 0%
210	0.7	+ 11% - 1%
150	0.5	+ 18% - 2%
90	0.3	+ 24% - 4%
50	0.17	+ 20% - 15%

Table D.3 Final Accumulated Velocity Errors

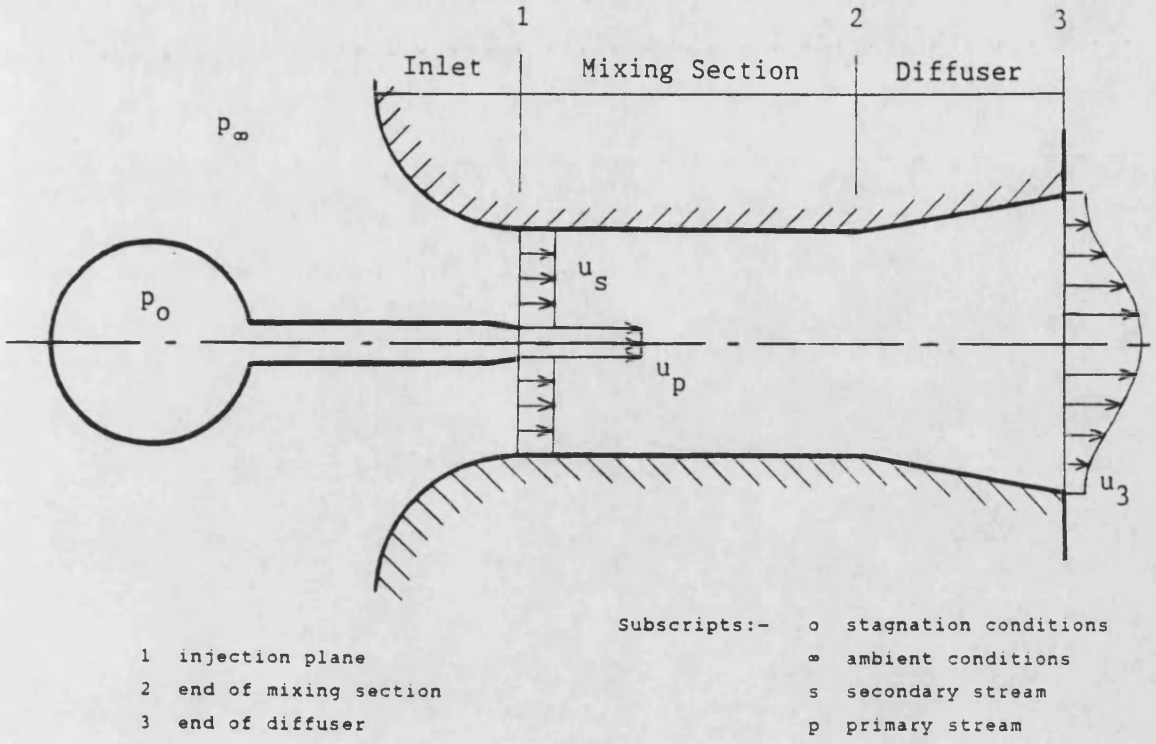

Figure 2.1 Generalised Ejector Layout

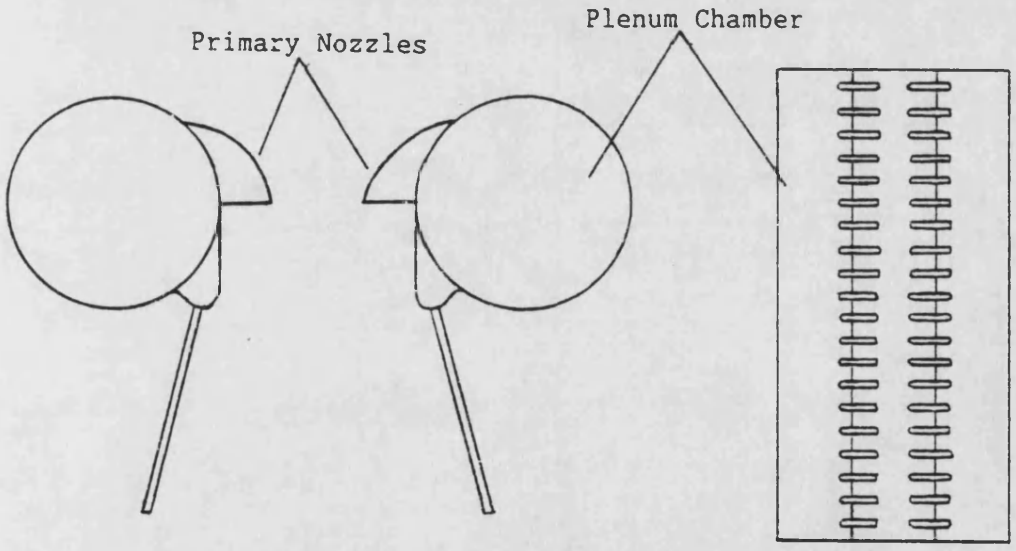

NOTE : Dissimilar Scales

Figure 2.2 Early Hypermixer Ejector tested by Fancher (1970)

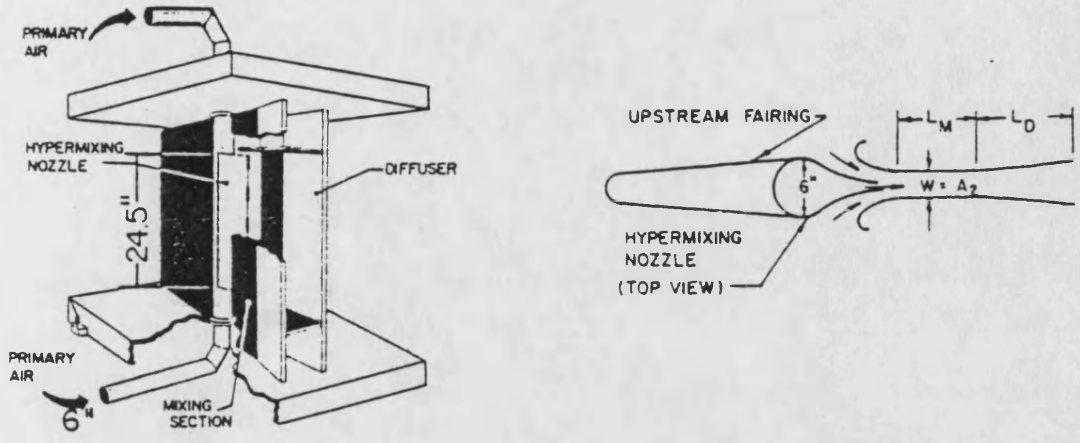

Figure 2.3 Hypermixing Ejector used by Fancher (1972)

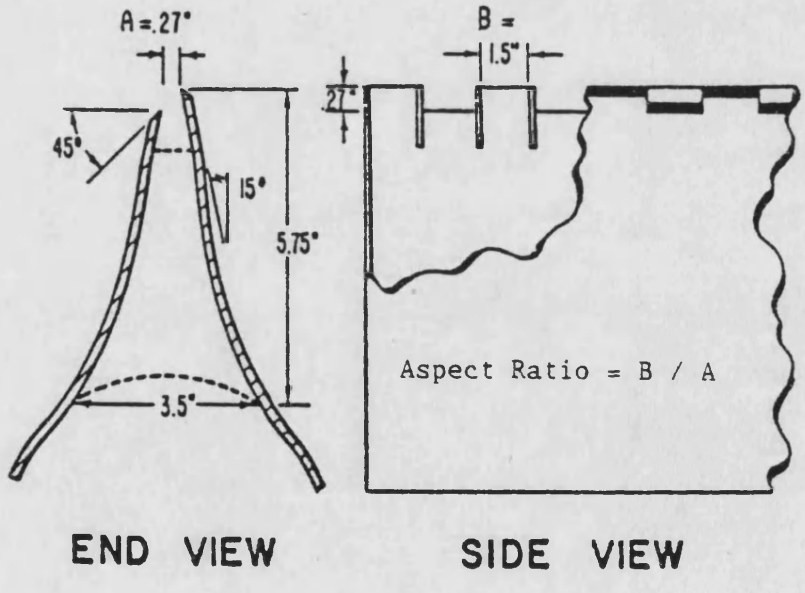

Figure 2.4 Typical Hypermixing Nozzle

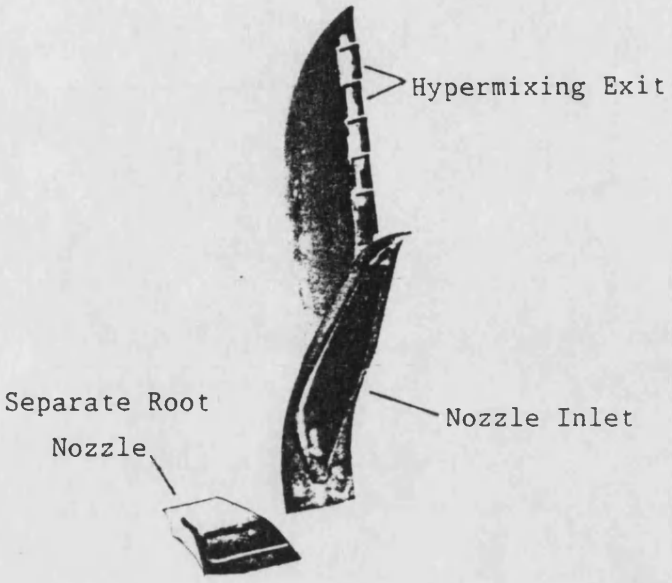

Figure 2.5 Cross-cylinder Hypermixing Nozzle from Quinn (1972a)

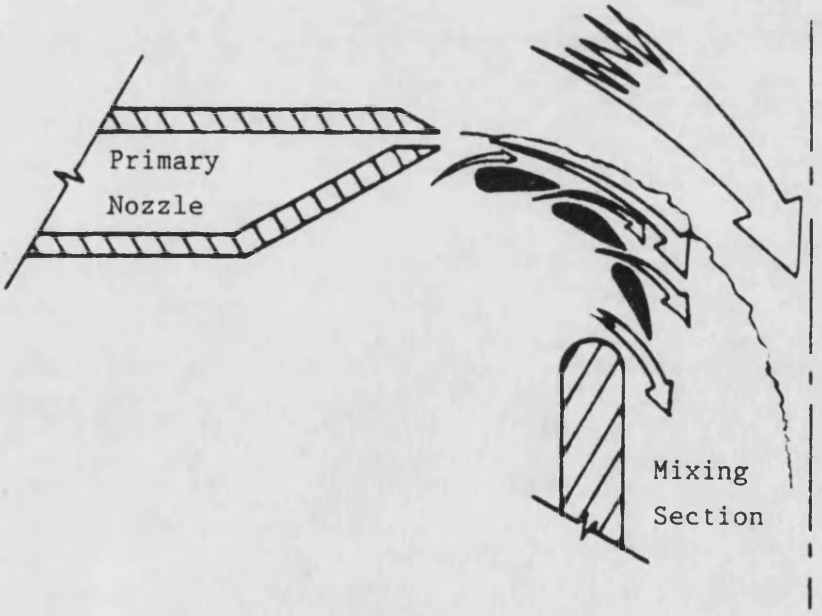

Figure 2.6 Half-section through 'Three-airfoil' Coanda Surface Ejector from Alperin, Harris and Smith (1969)

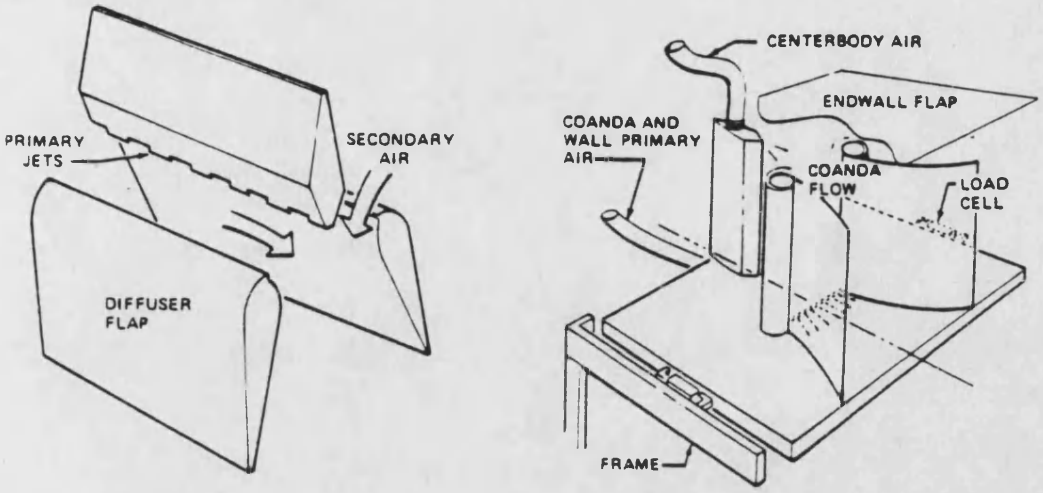

Simplified Ejector Layout

Sketch of Test Ejector

Figure 2.7 Ejector Investigated by DeJoode and Patanker (1978)

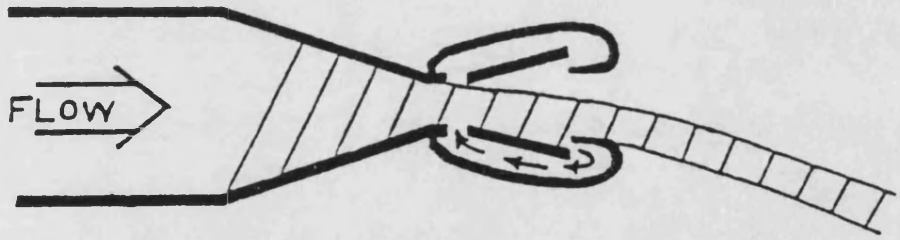

Figure 2.8 'Flapping' Nozzle Developed by Viets (1981)

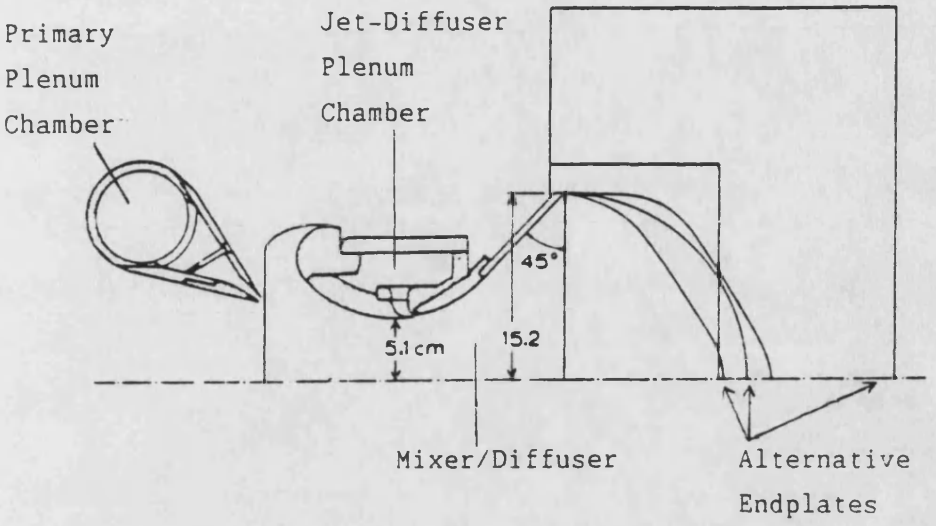

Figure 2.9 Half-section through early geometry reported in Alperin and Wu (1981)

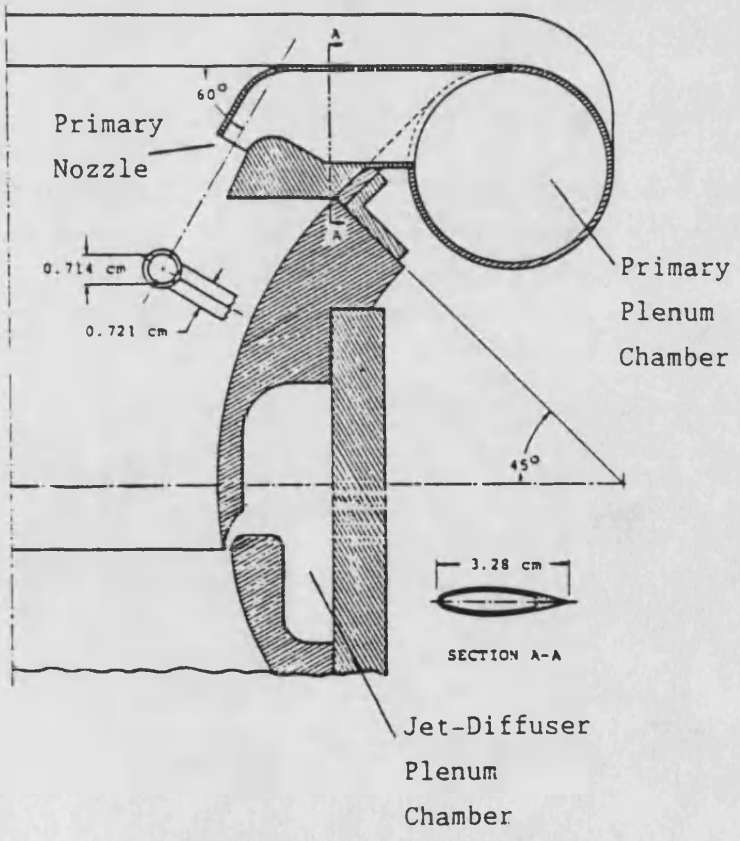

Figure 2.10 Half-section through late Jet-Diffuser Ejector from Alperin and Wu (1981)

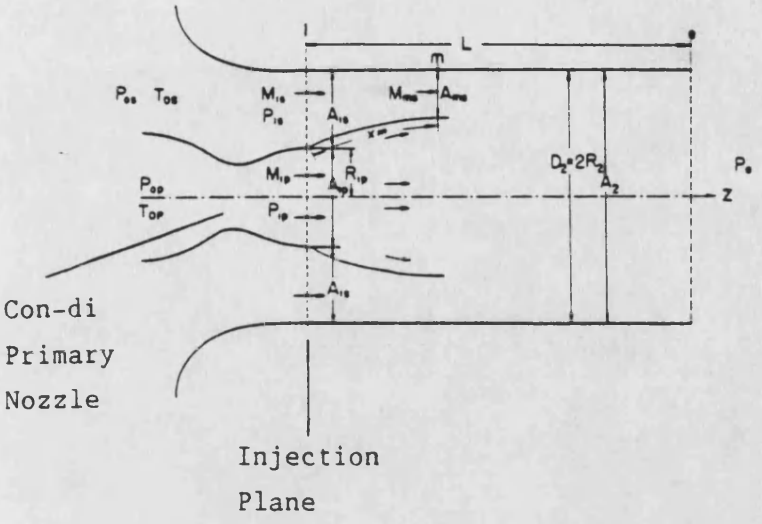

Figure 2.11 Theoretical Supersonic Ejector layout from Chow and Addy (1964)

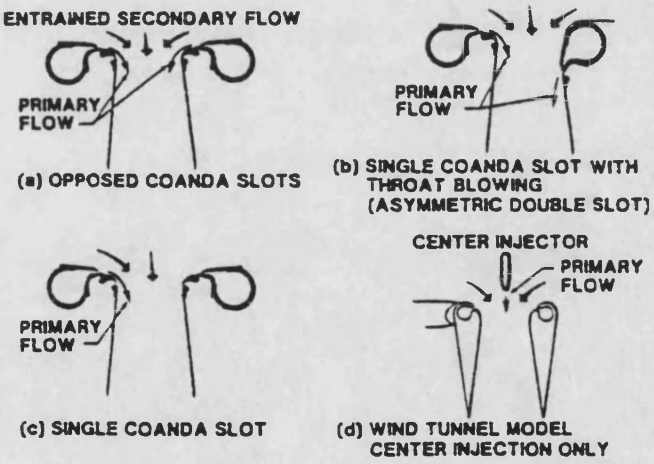

Figure 2.12 Four of the Coanda configurations tested by Throndson (1973)

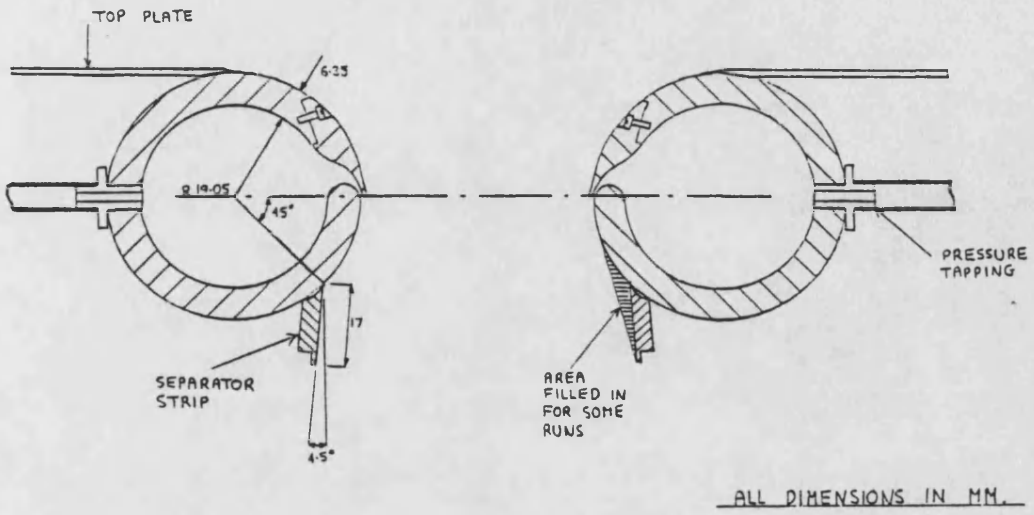

Figure 2.13 Short Coanda Ejector
tested by Miller and Whittaker (1983)

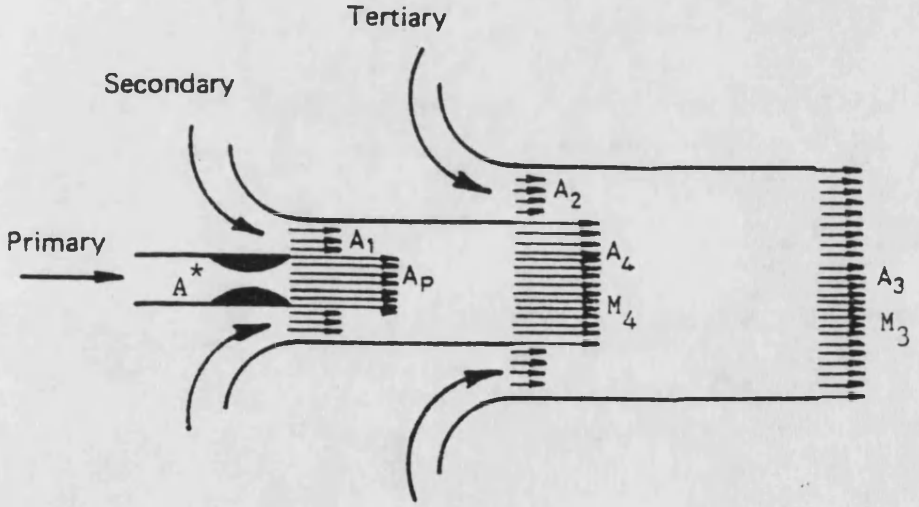

Figure 2.14 Schematic view of Two Stage Augmentor
of Abdel-Fattah (1984)

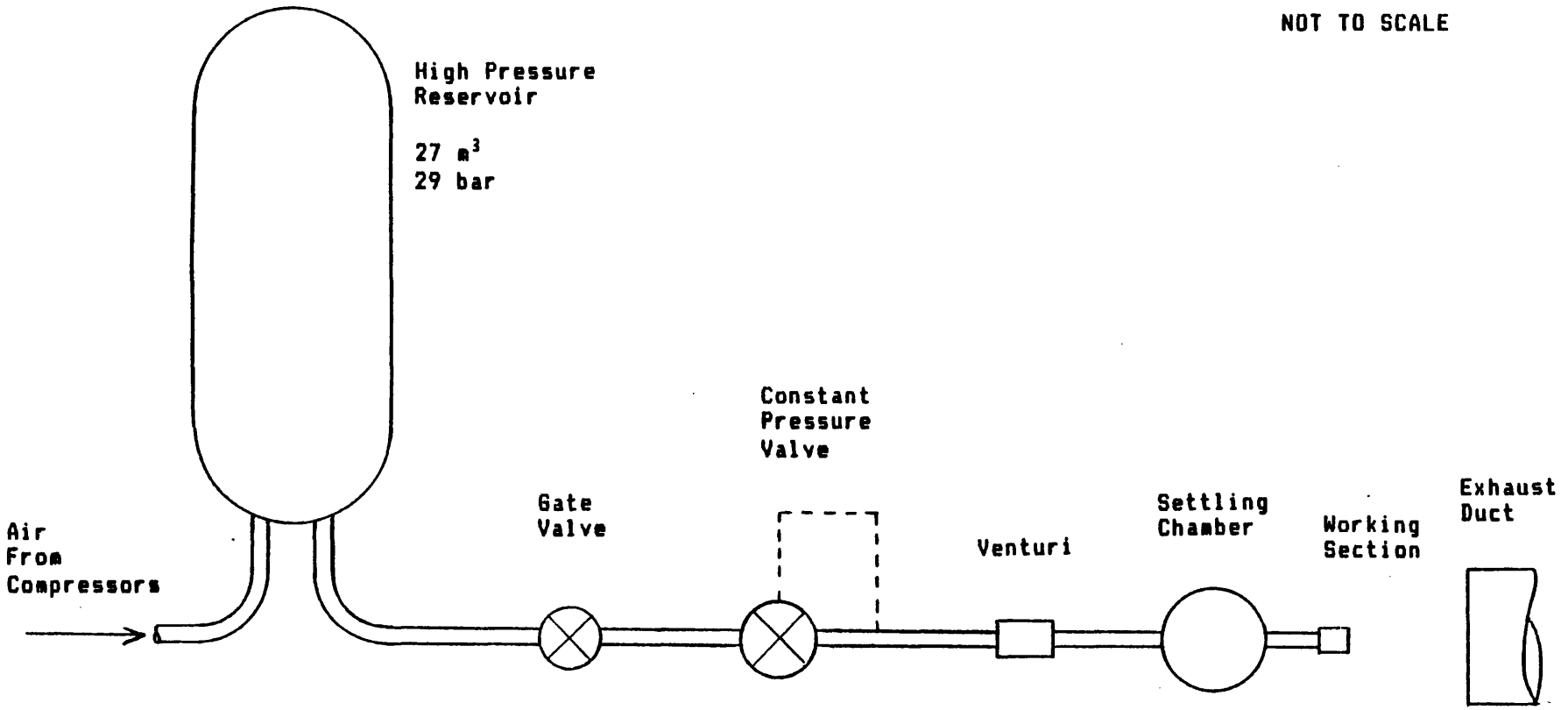

Figure 3.1 Schematic Layout Of Test Rig

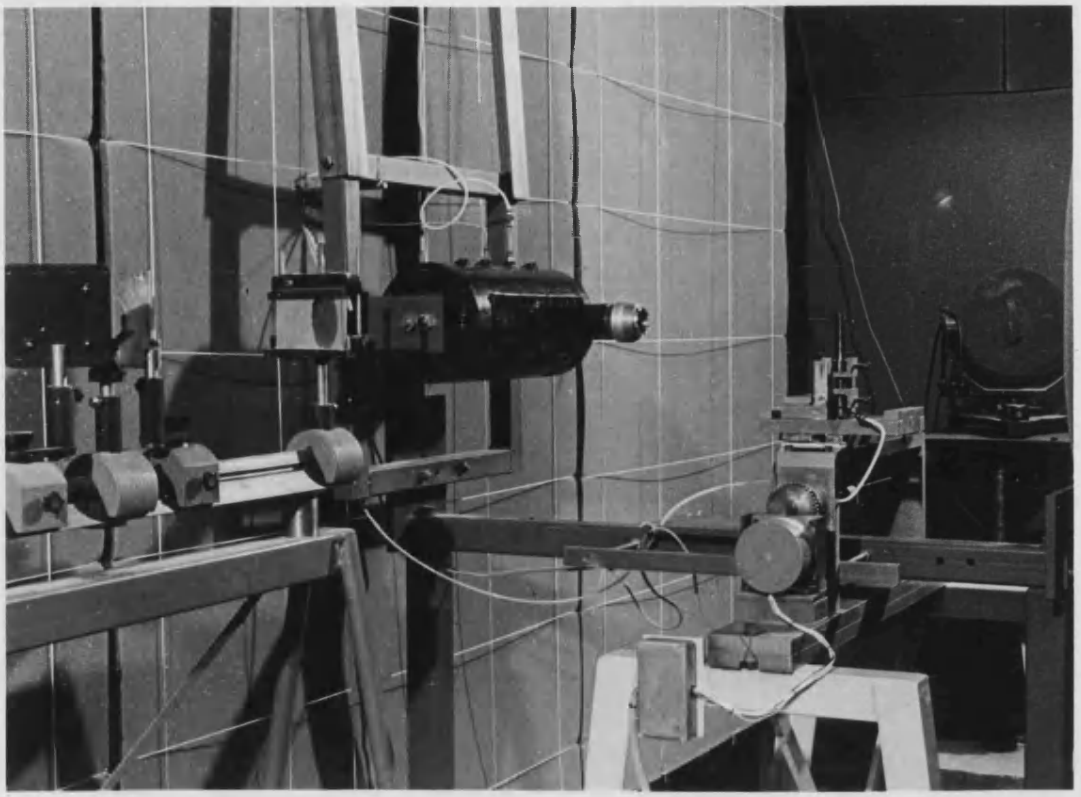

Figure 3.2 View Of Working Section

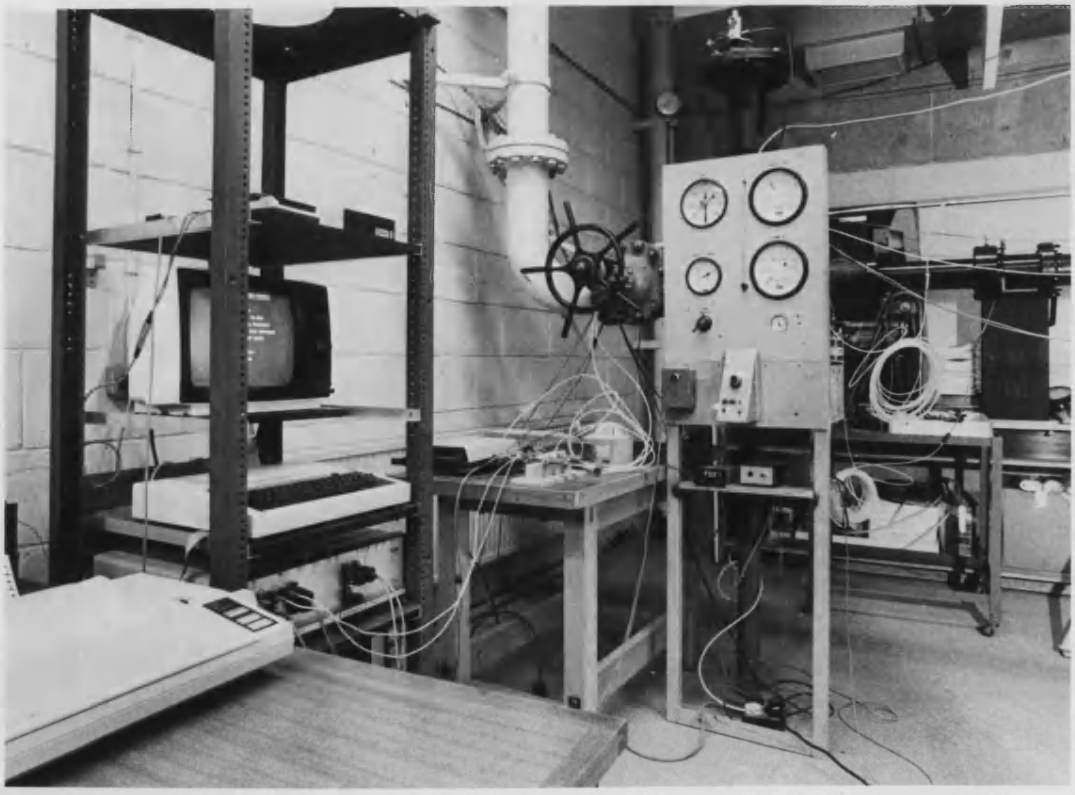

Figure 3.3 Control Position And Upstream Portion Of Rig

Figure 3.4 Downstream Portion Of Rig
Showing Settling Chamber And Exhaust Duct

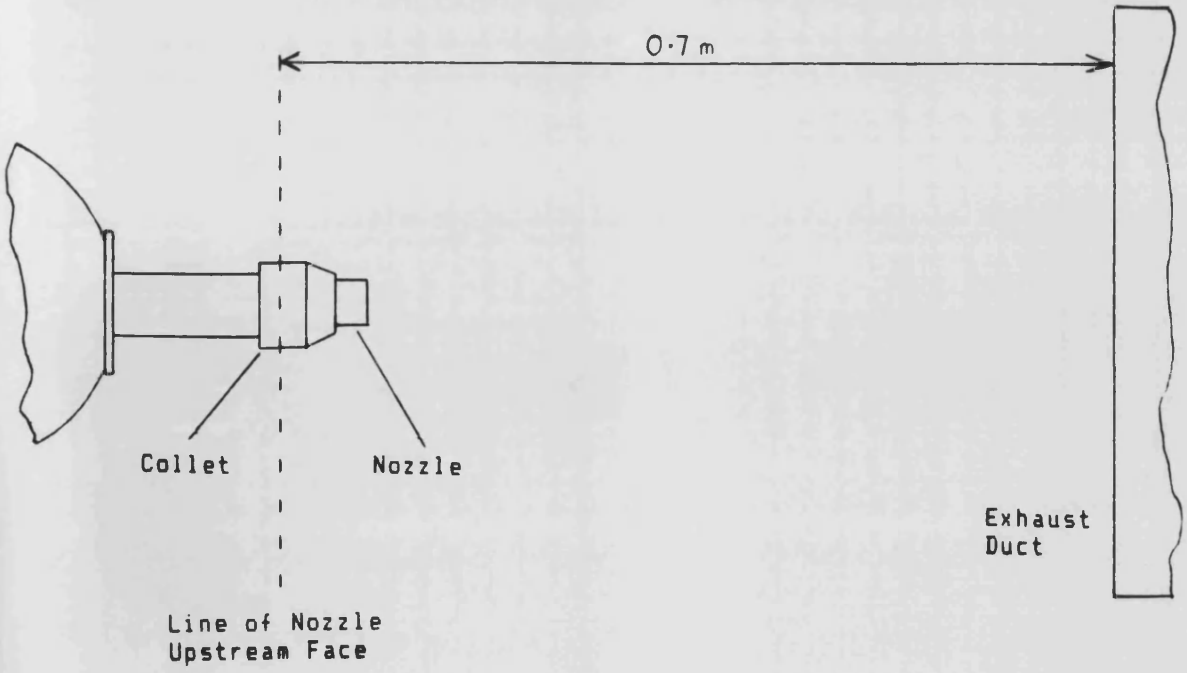

Figure 3.5 Geometry Of Test Section For Free Jet Tests
M = 1.4 Nozzle

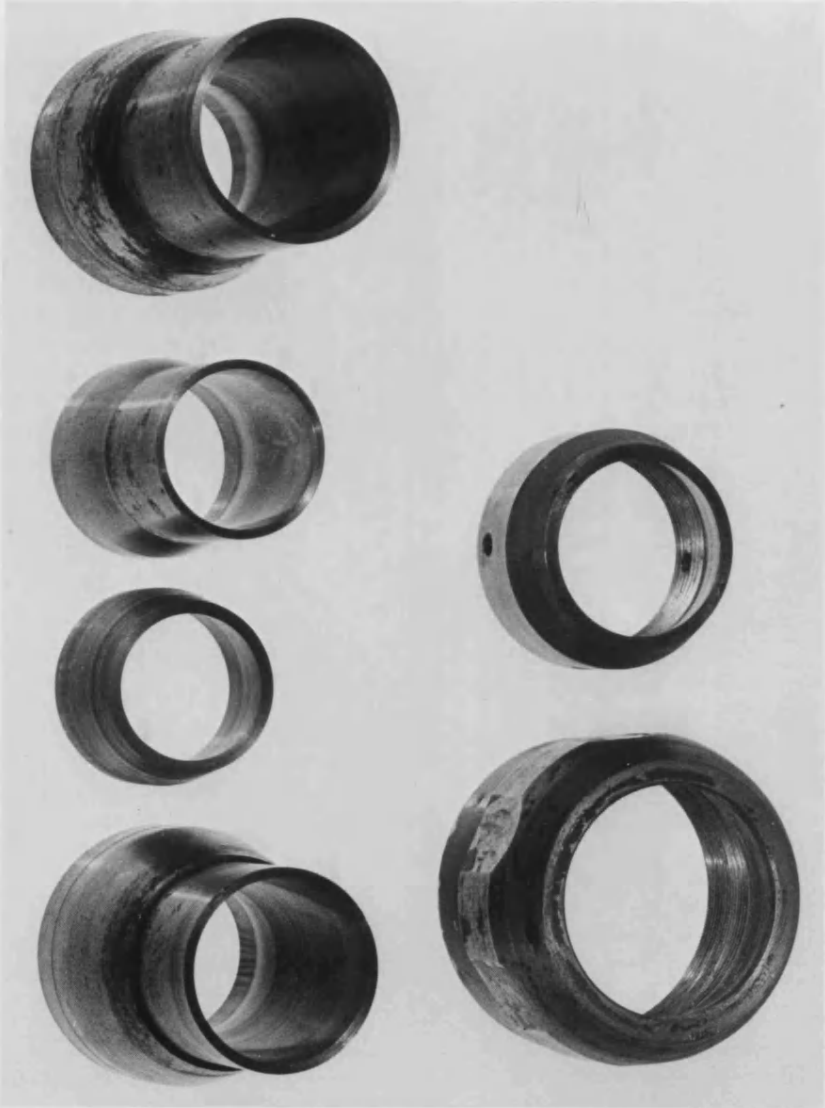

Figure 3.6 Selection Of Nozzles And Collets

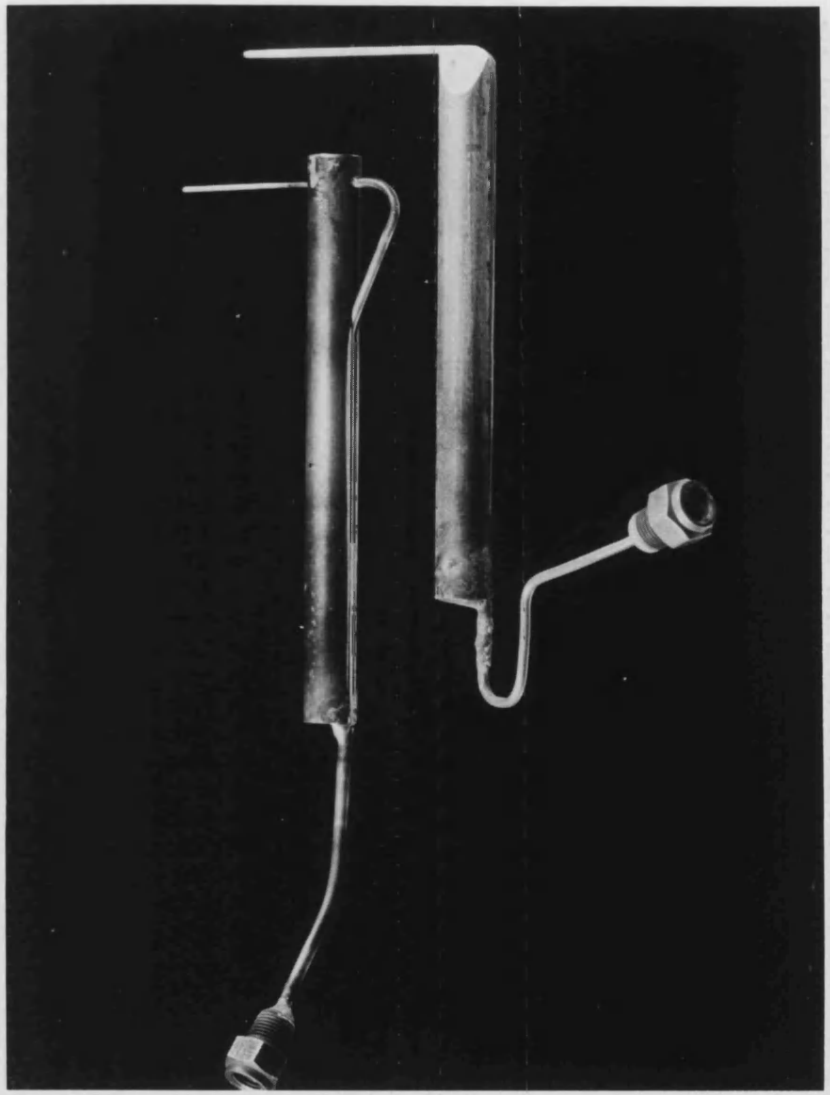

Figure 3.7 Two Static Pressure Probes

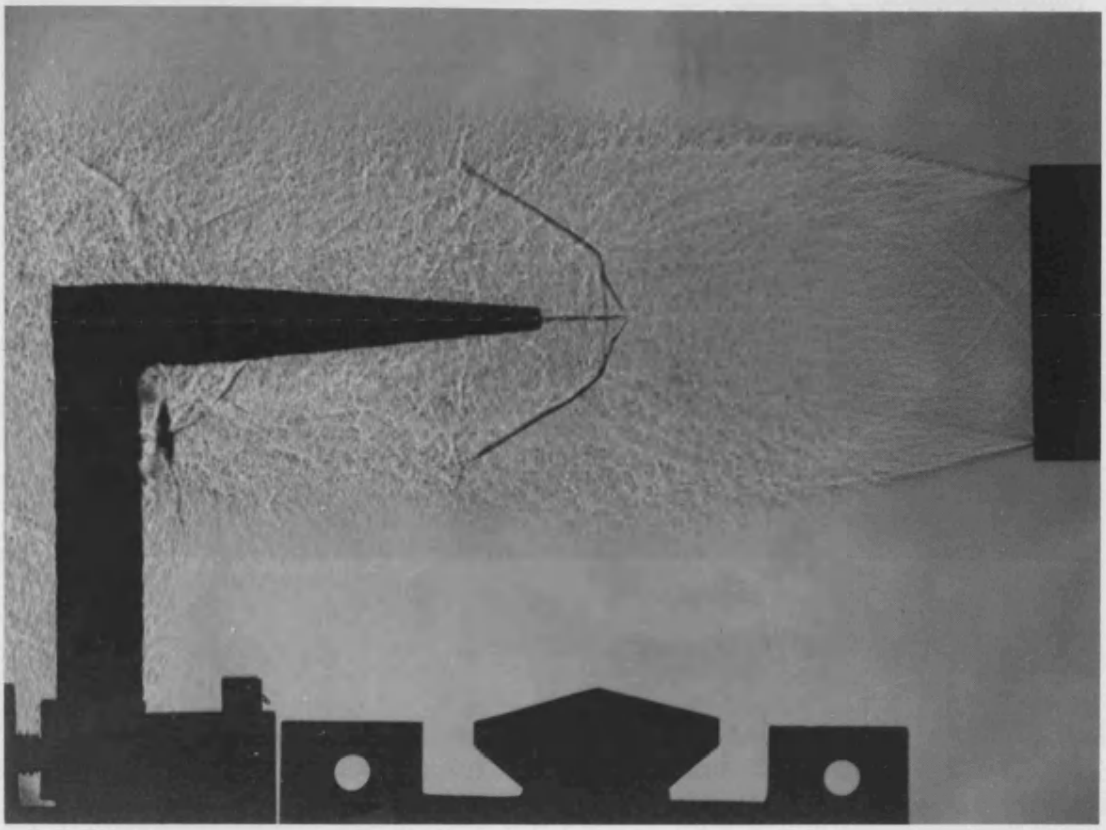

Figure 3.8 Schlieren Photograph Of Mach Disc ' Puncturing

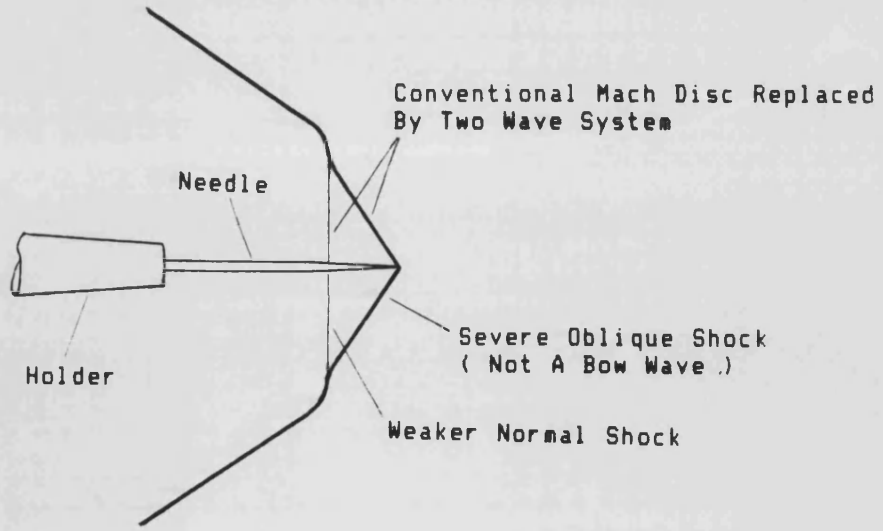

Figure 3.9 Mach Disc ' Puncturing ' Mechanism

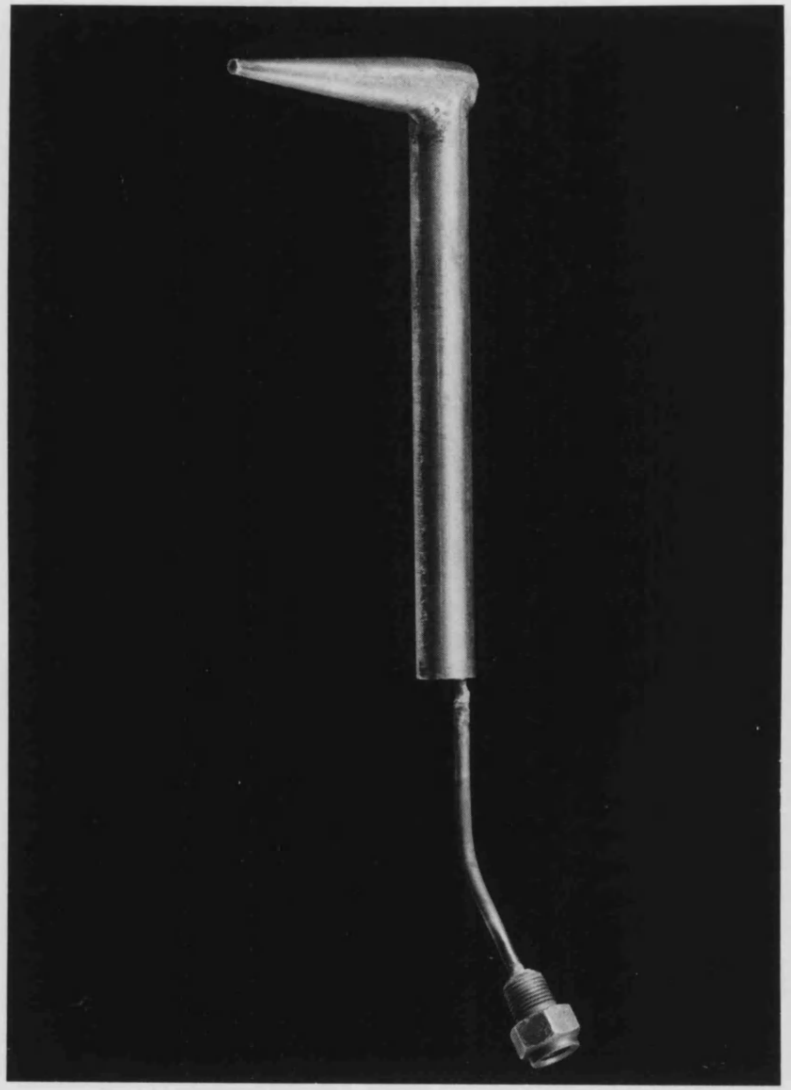

Figure 3.10 Total Pressure Probe

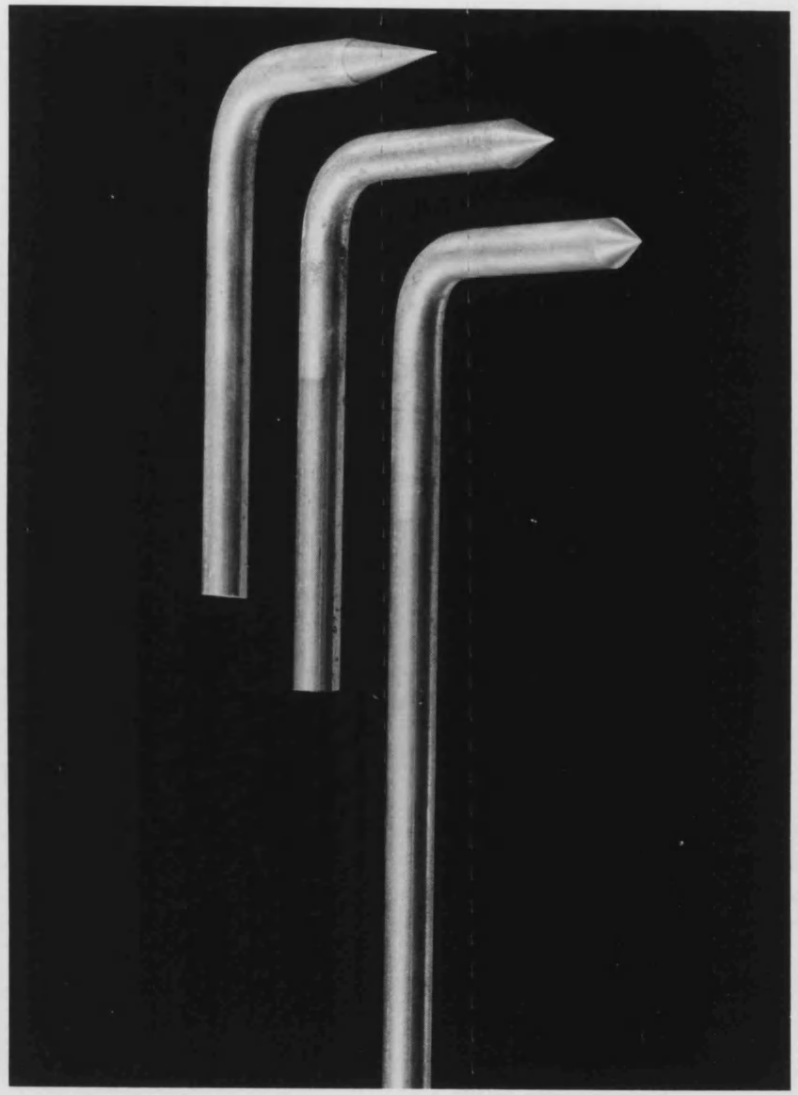

Figure 3.11 Shock Angle Probes

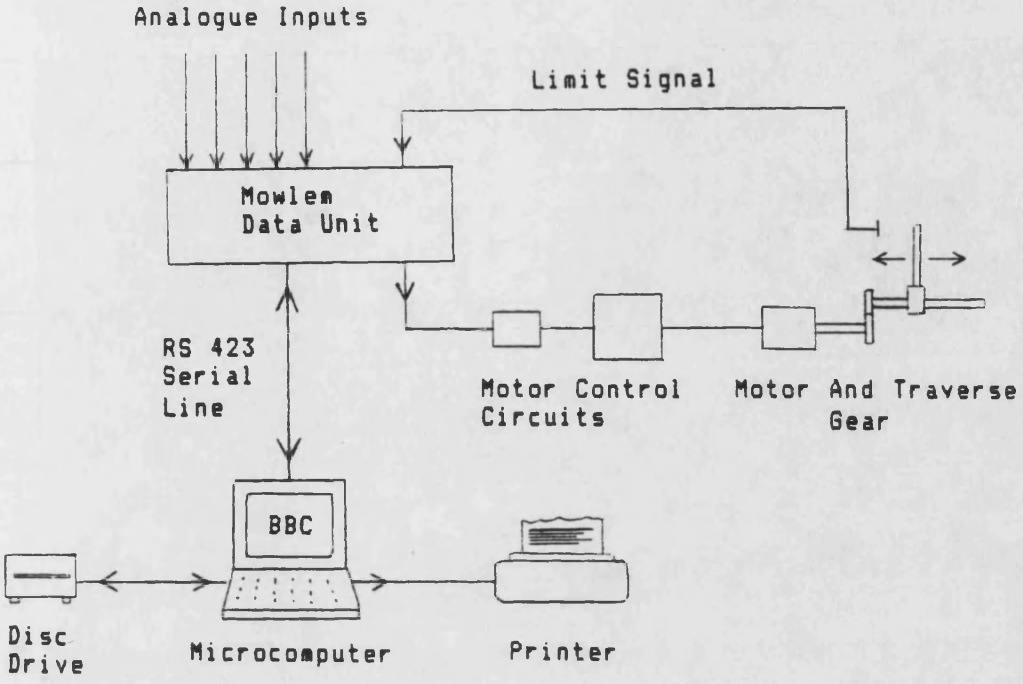

Figure 3.12 Data Acquisition System

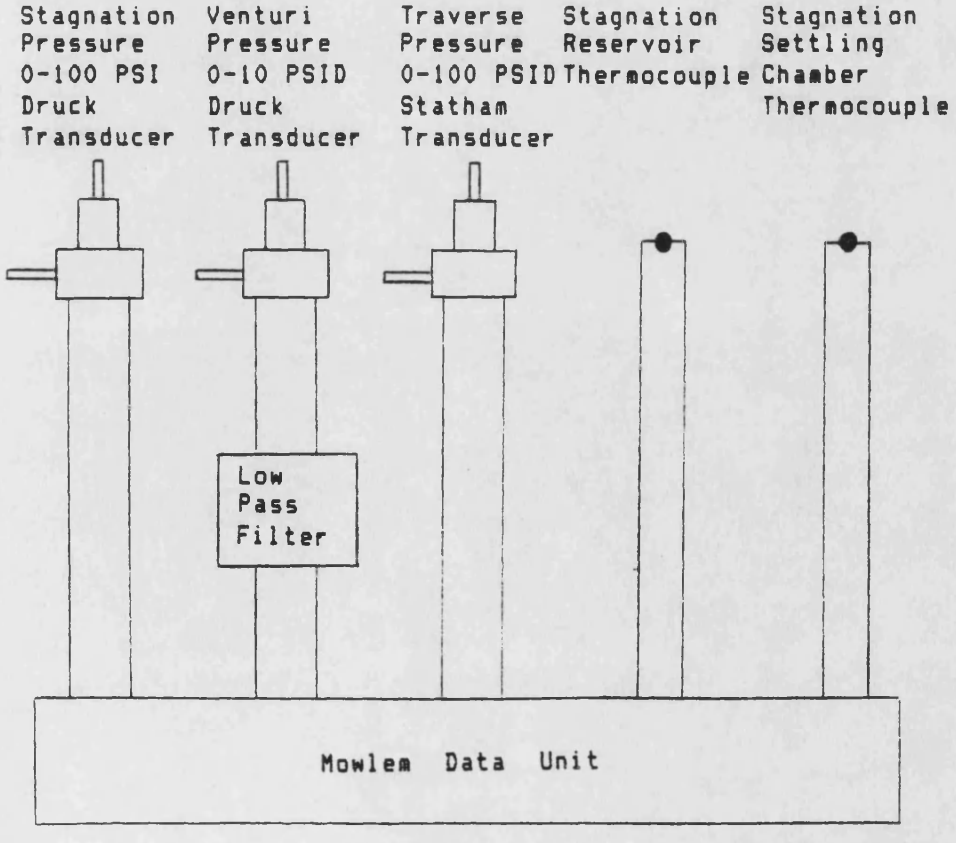

Figure 3.13 Analogue Inputs

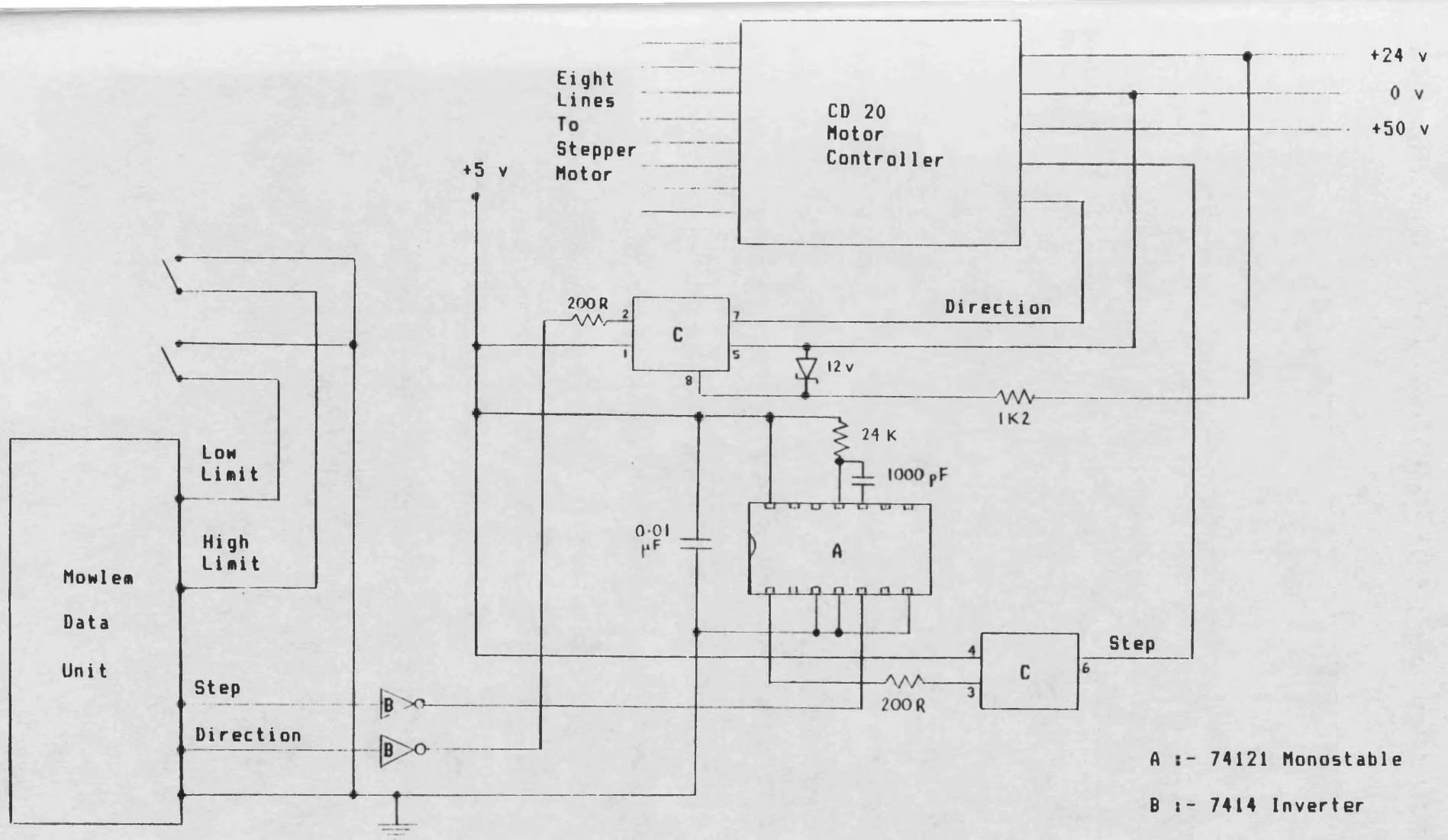

Figure 3.14 Motor Control Circuit

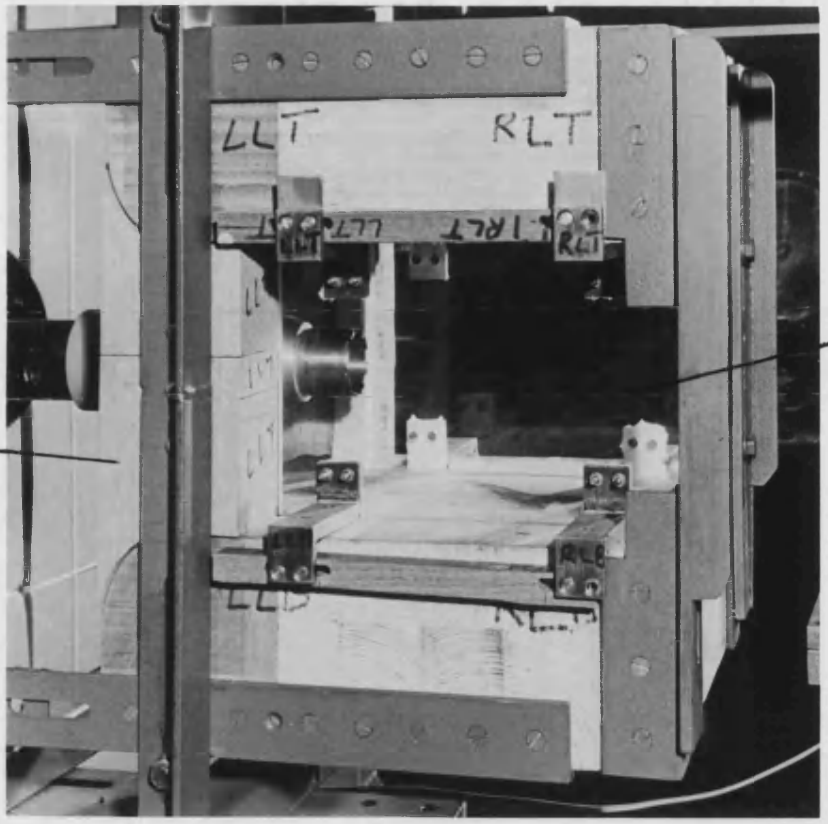

Figure 3.15 View Of Duct

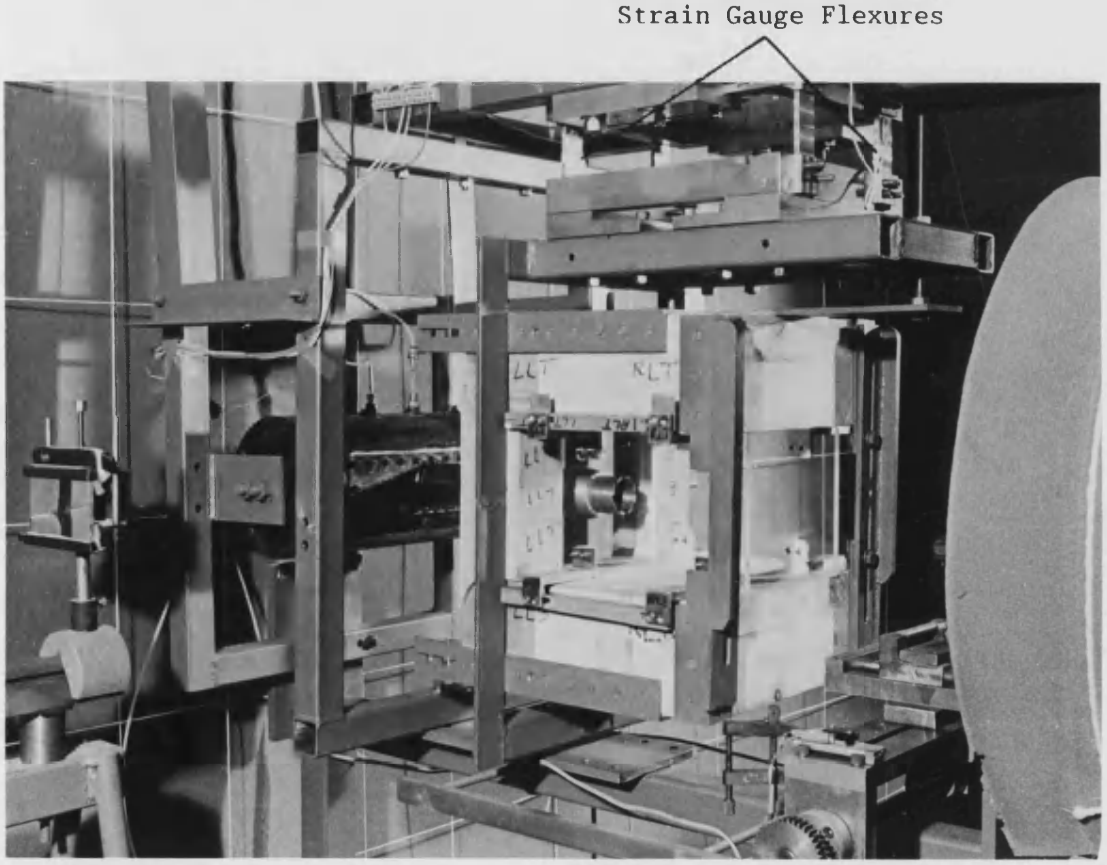

Figure 3.16 Working Section With Duct In Position

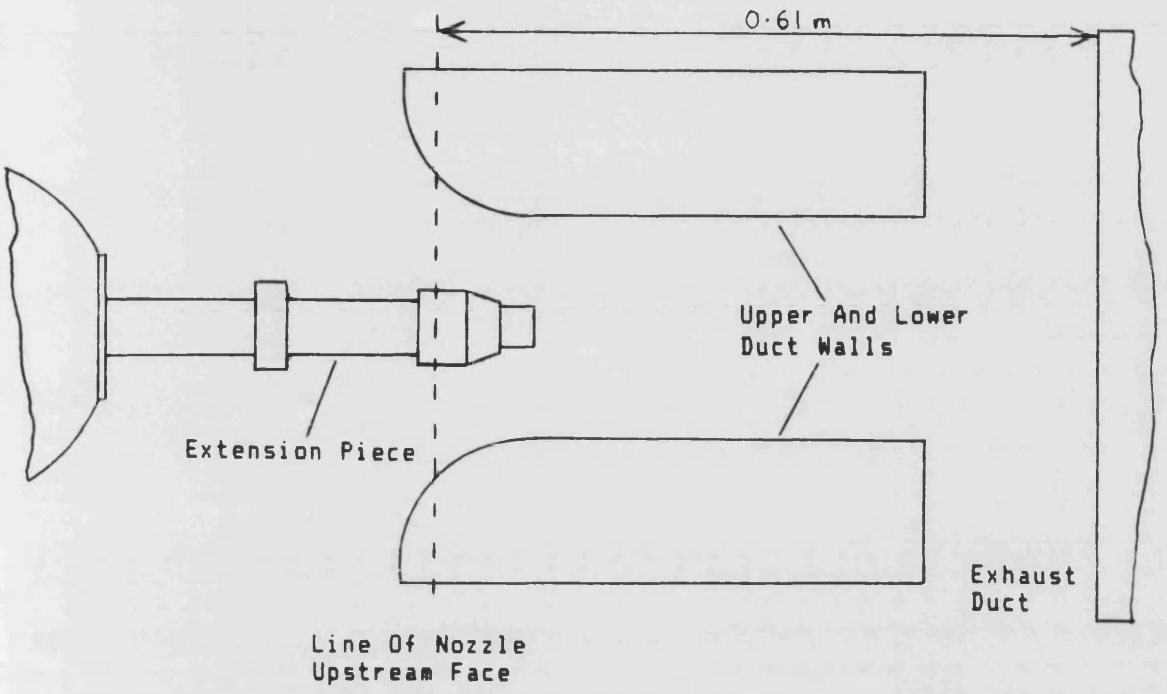

Figure 3.17 Geometry Of Test Section For Ducted Jet Tests
M = 1.4 Nozzle

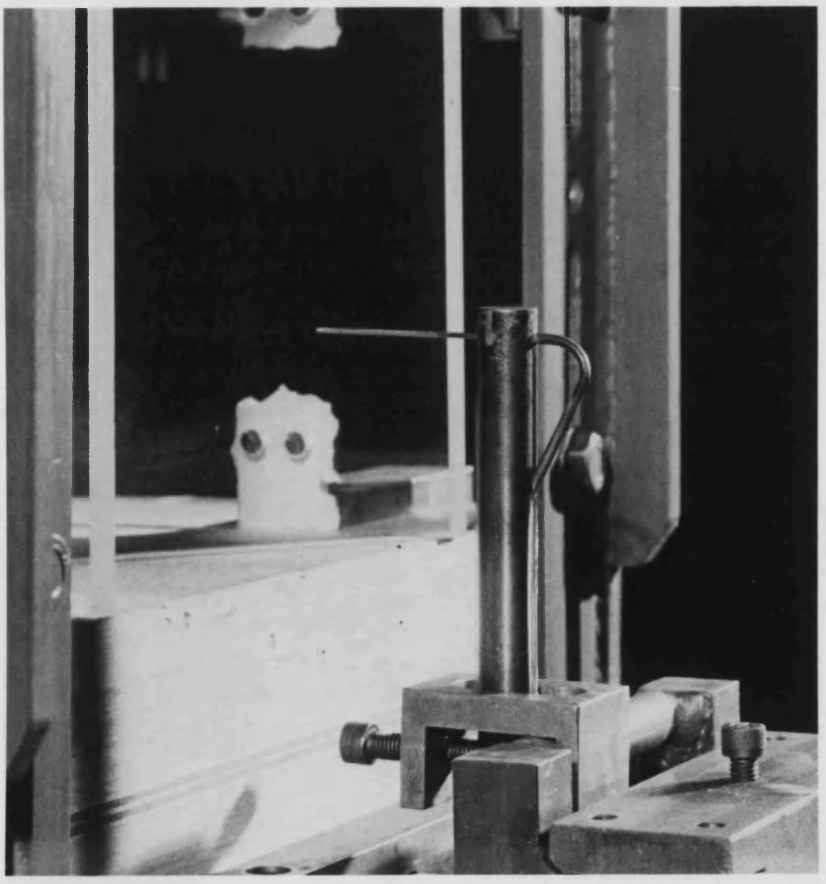

Figure 3.18 View Of Duct Exit Plane Traverse

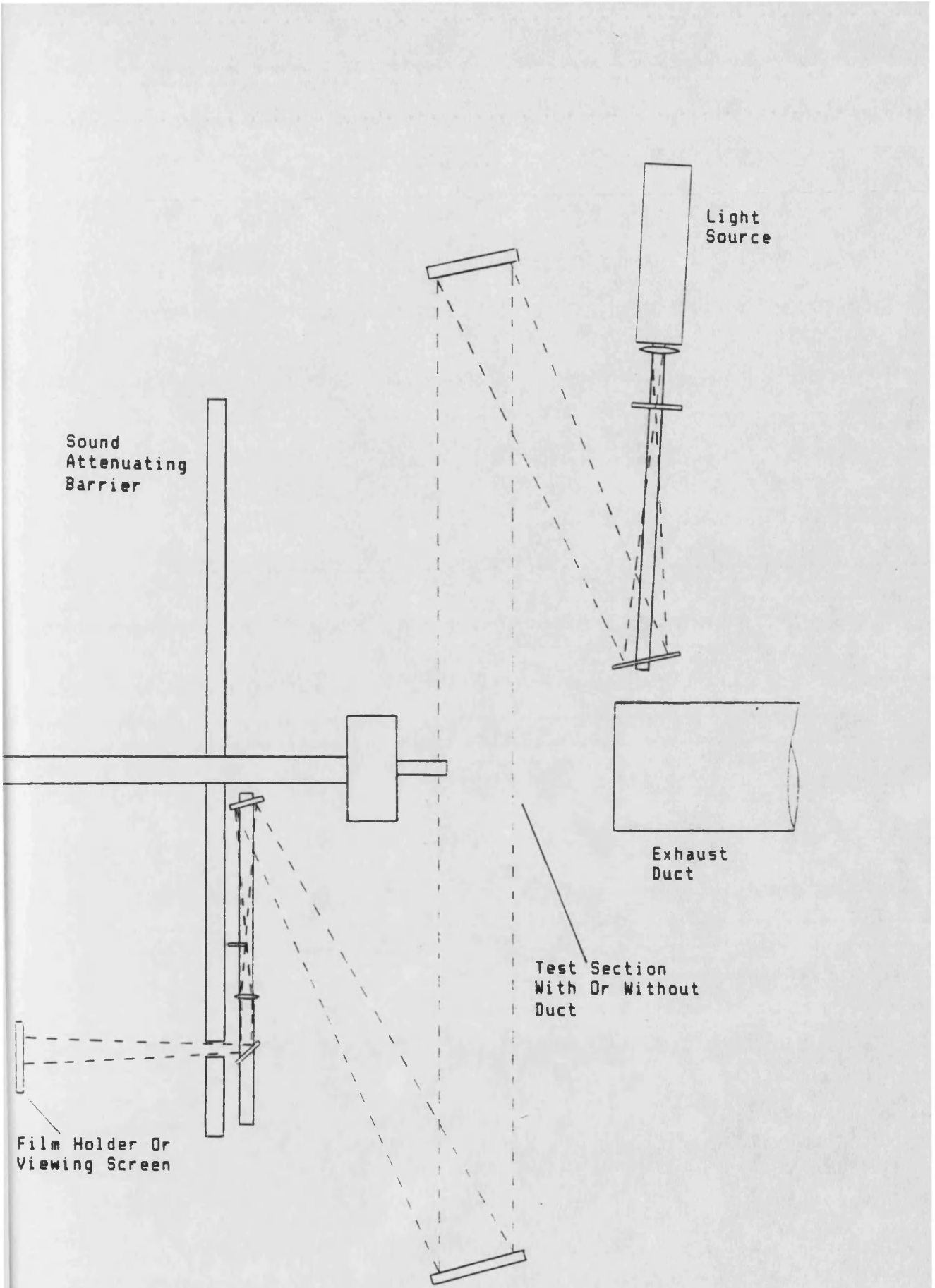

Figure 3.19 Plan Of Optical Equipment

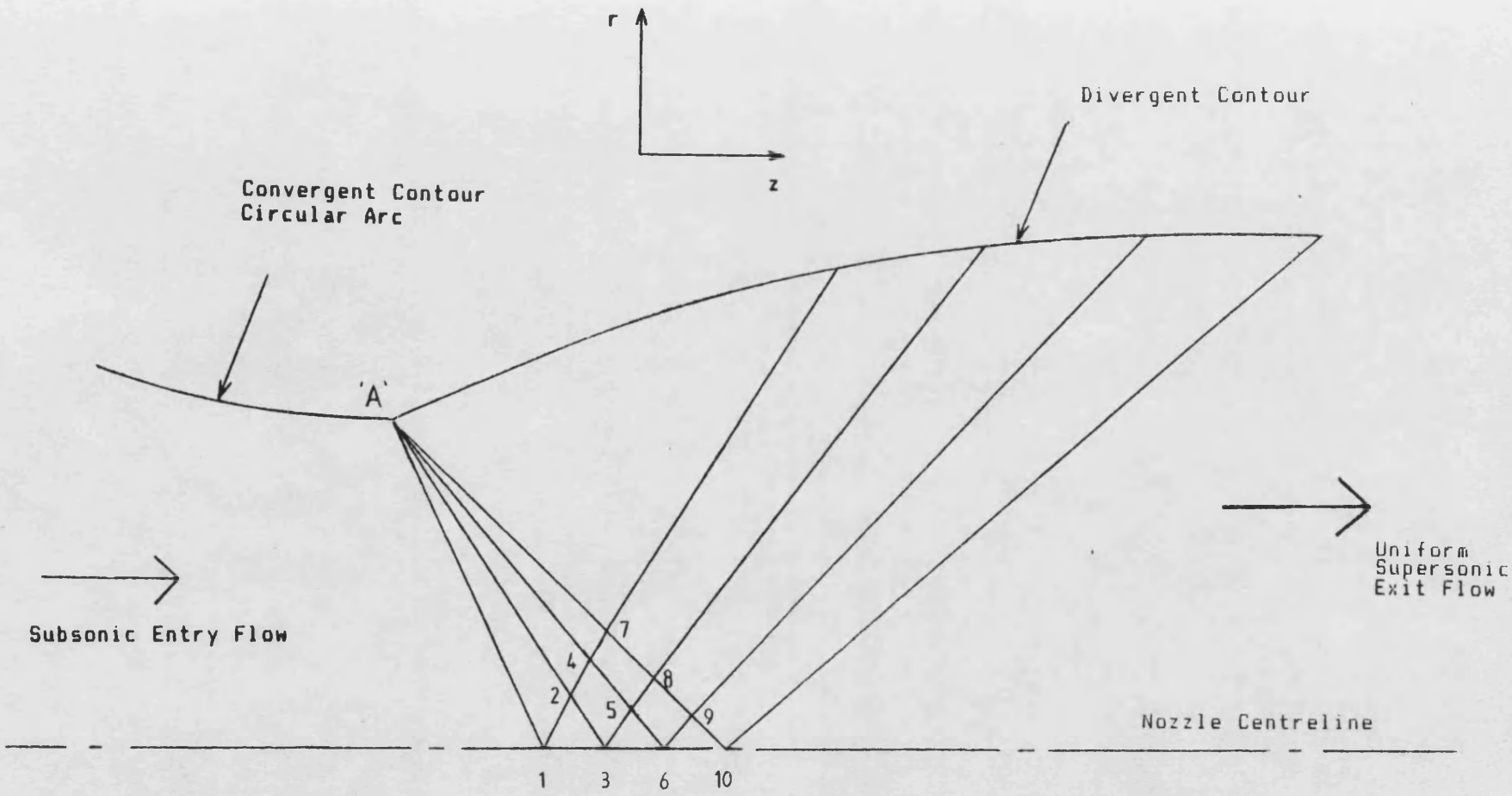

Figure 4.1 Longitudinal Section of Minimum Length Nozzle with Coarse Grid

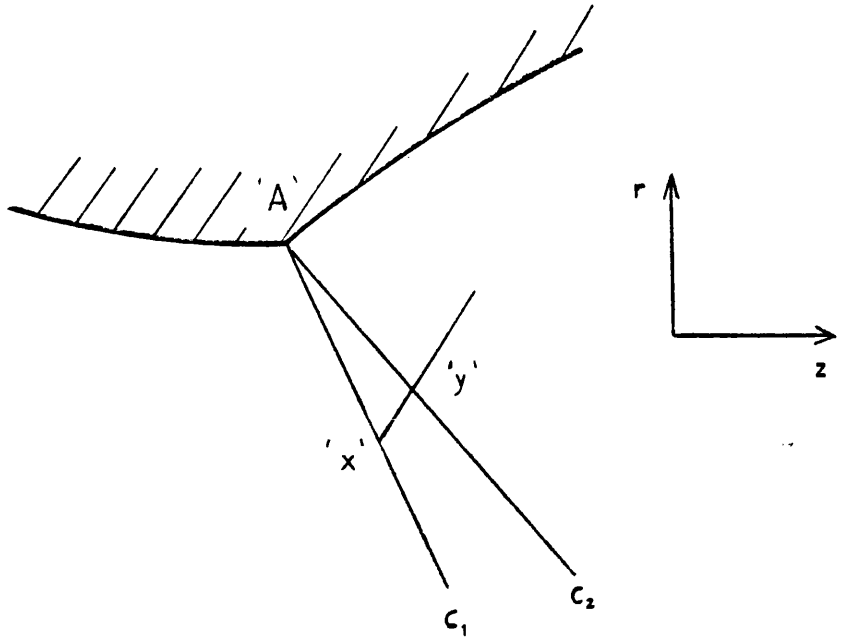

Figure 4.2 Characteristic procedure at Throat

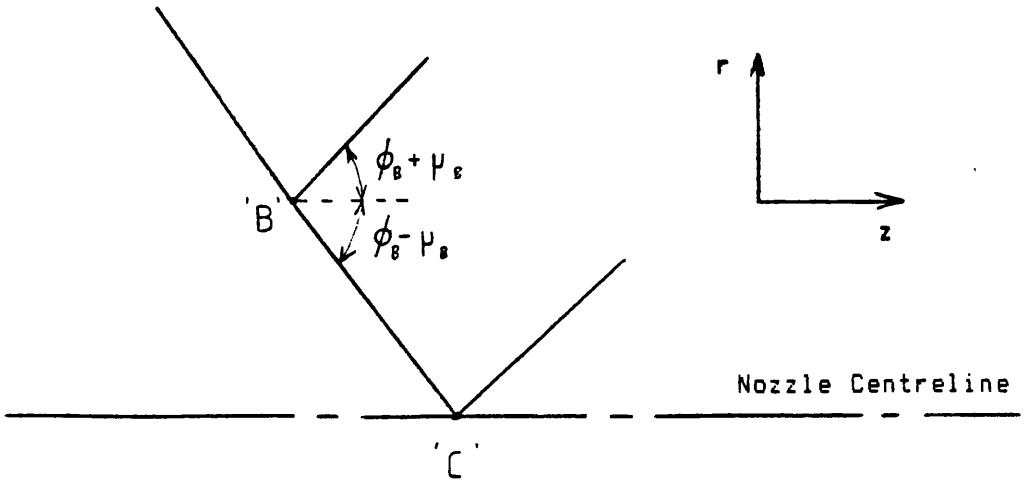

Figure 4.3 Characteristic procedure on Centreline

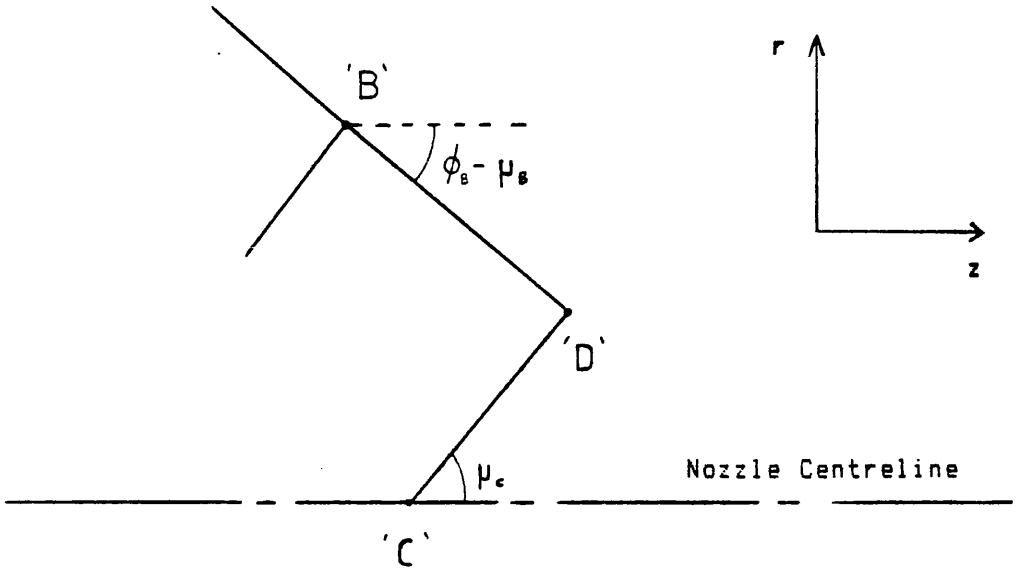

Figure 4.4 Characteristic procedure for point above Centreline

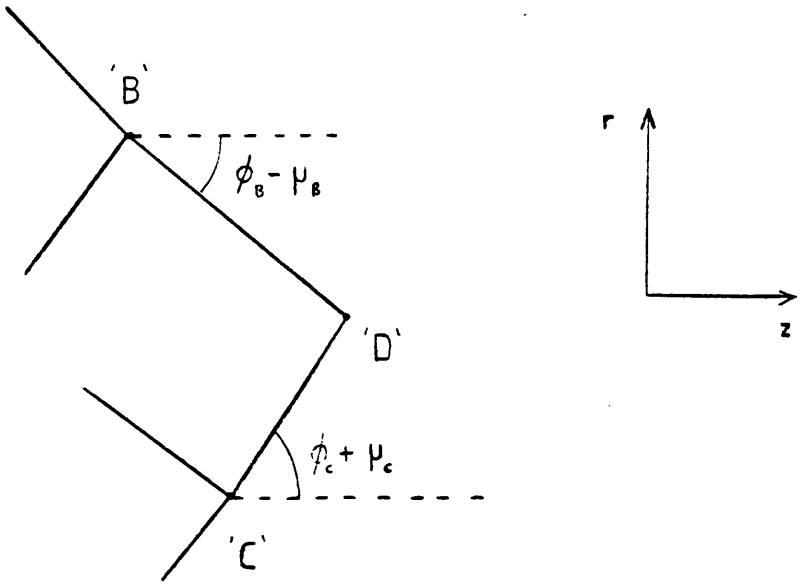

Figure 4.5 Characteristic procedure for General Node

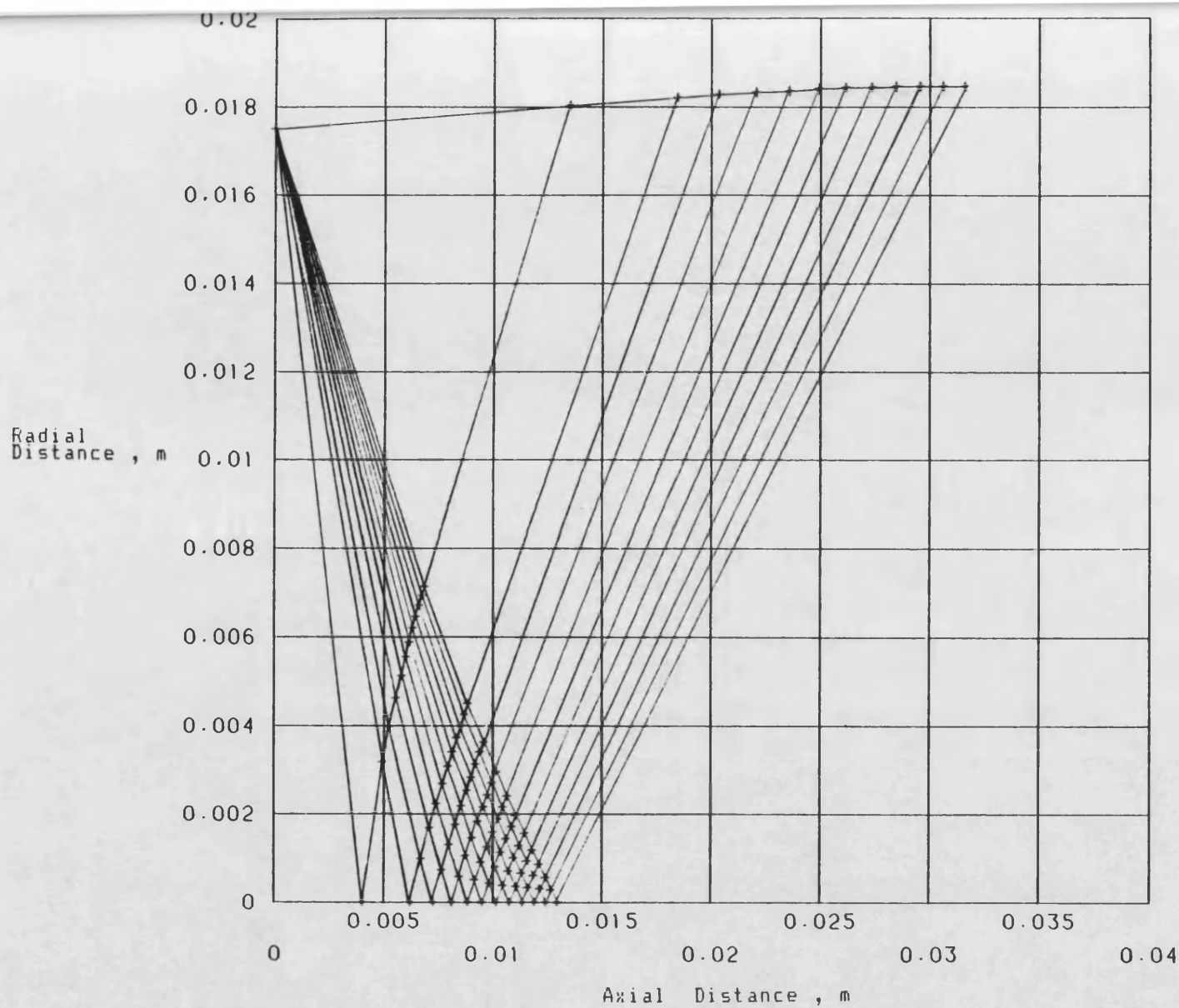

Figure 4.6 Characteristic Grid for M=1.4 Nozzle with $\Delta\phi$=0.003

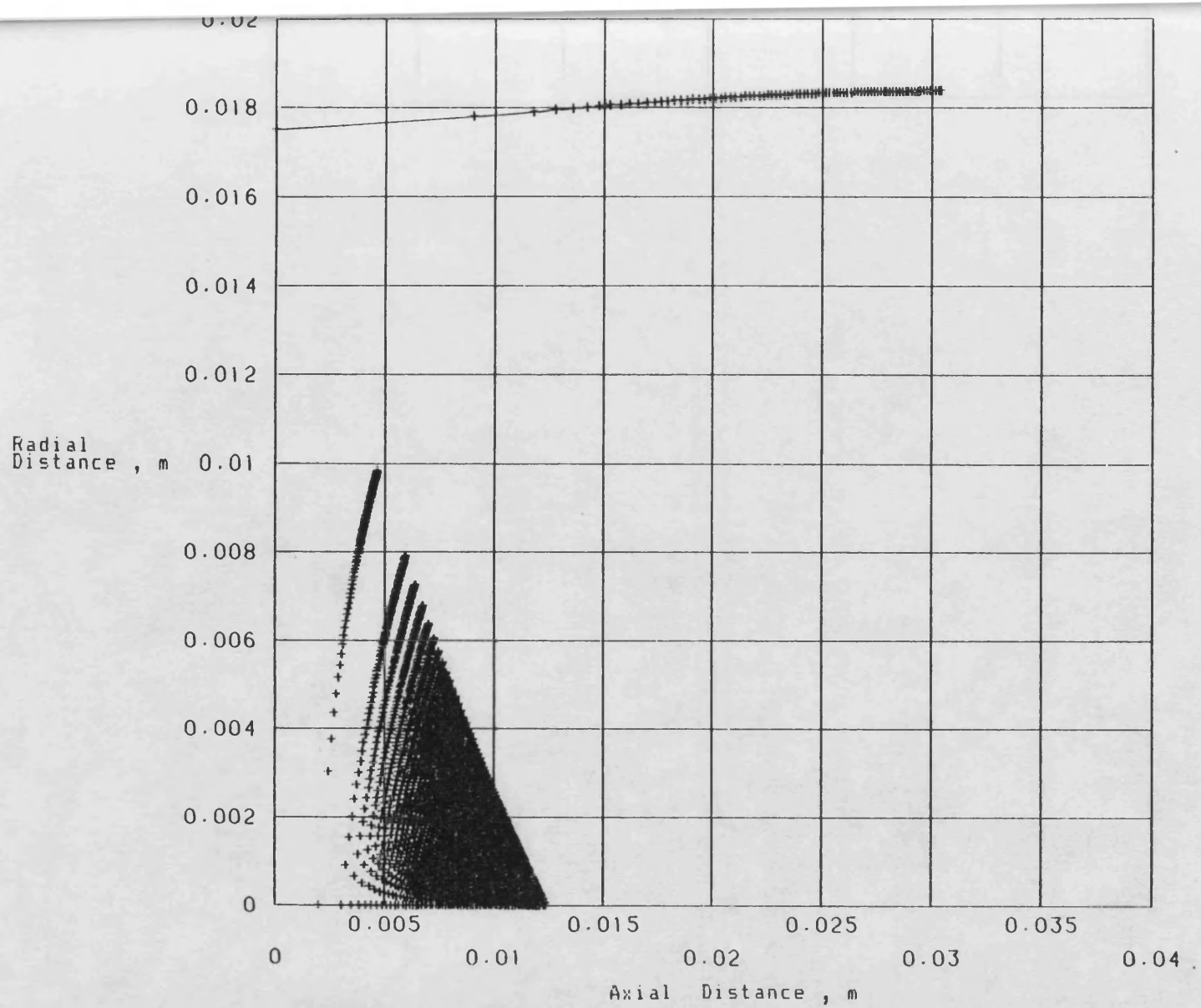

Figure 4.7 Characteristic Grid for M=1.4 Nozzle with $\Delta\phi$=0.0004

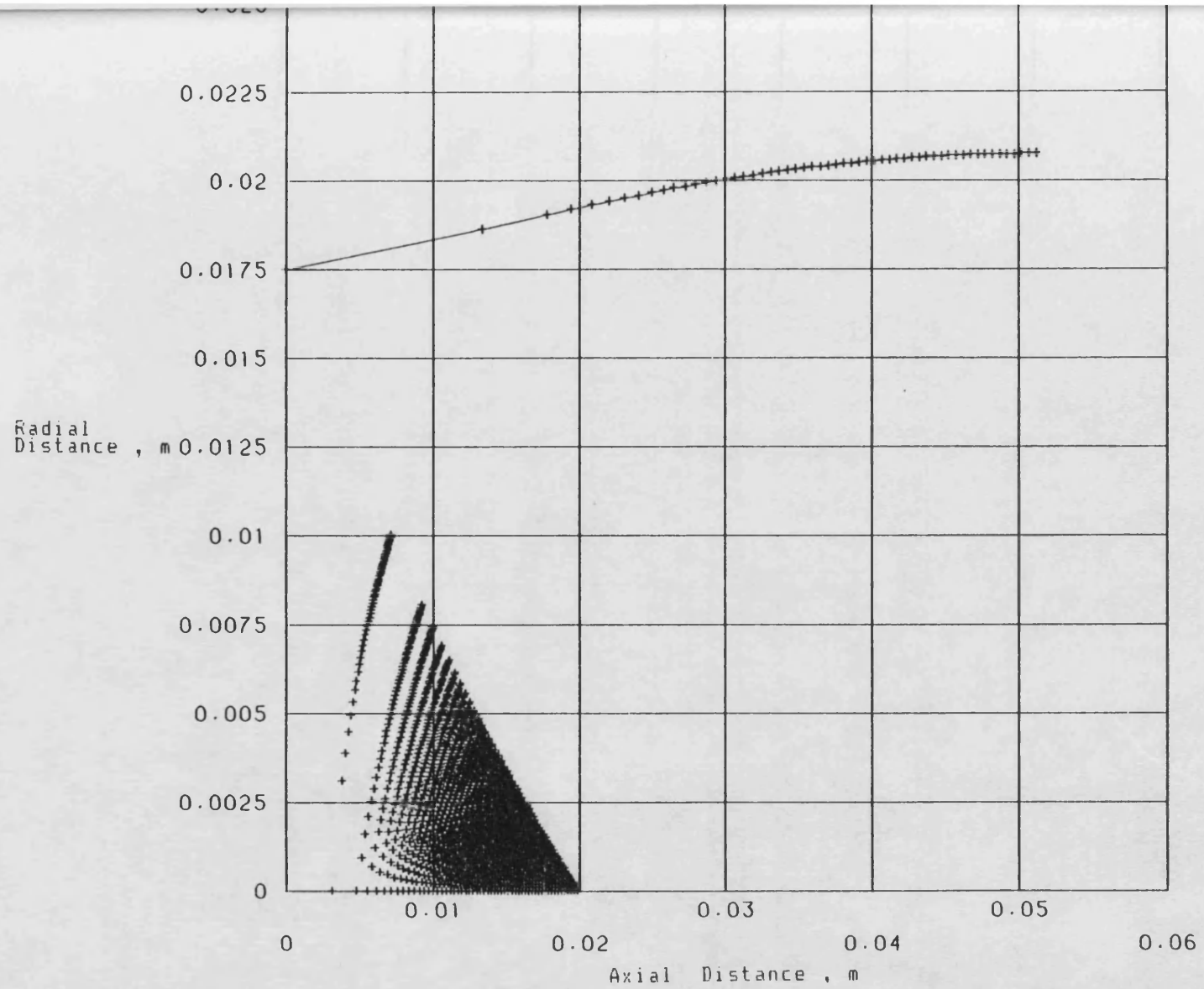

Figure 4.8 Characteristic Grid for M=1.8 Nozzle with $\Delta\phi$=0.0015

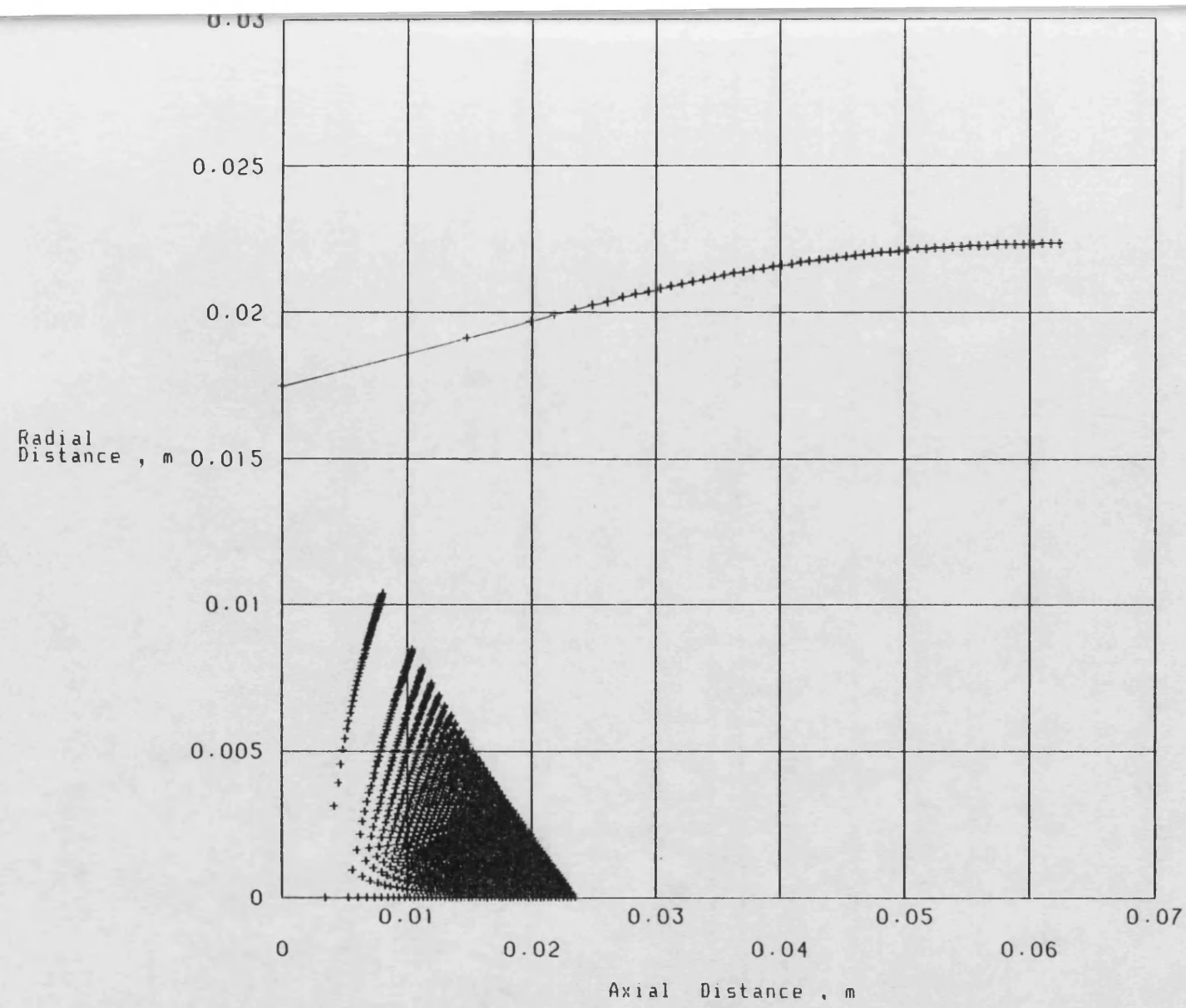

Figure 4.9 Characteristic Grid for M=2.0 Nozzle with $\Delta\phi$=0.002

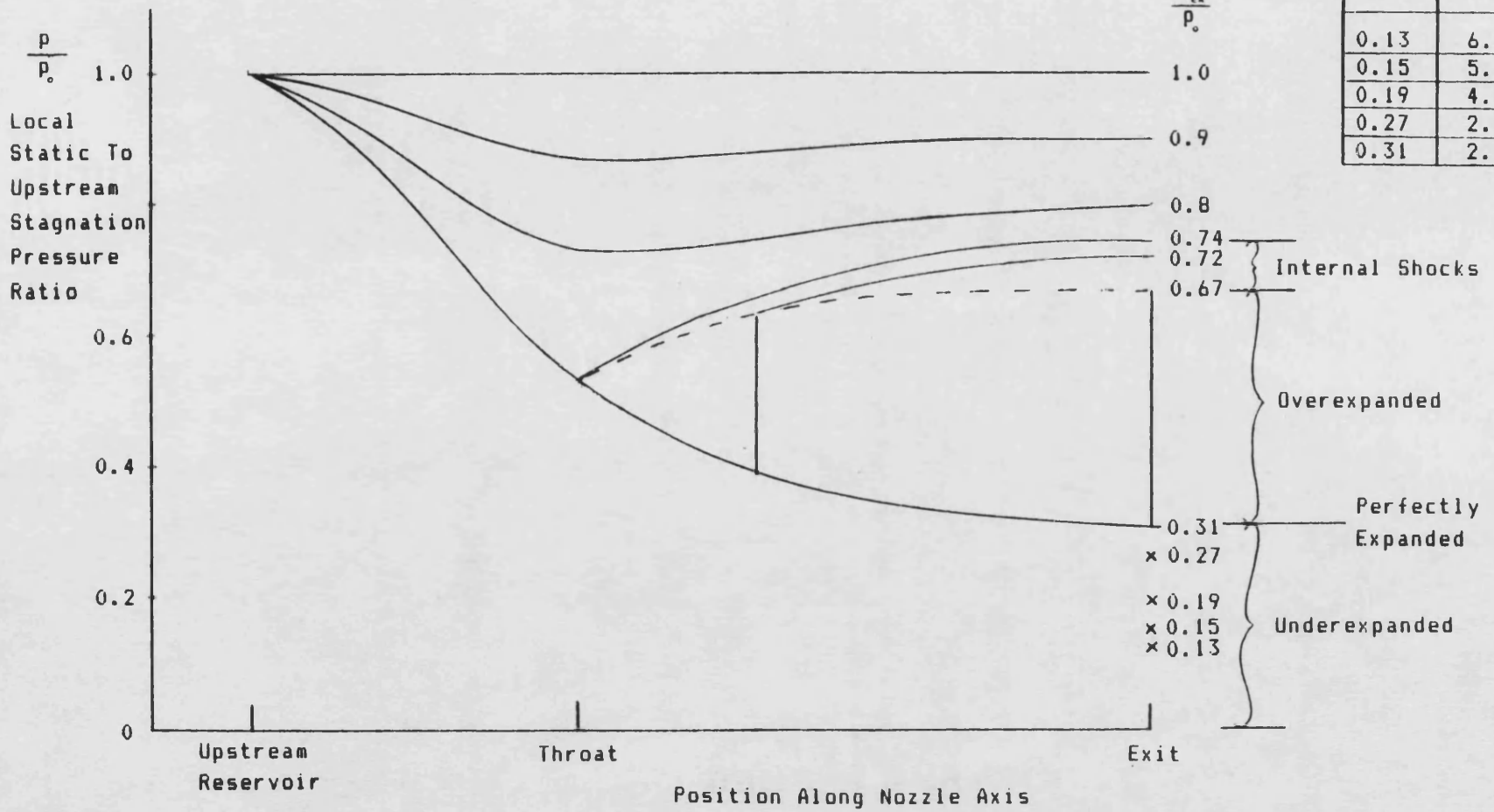

$\frac{p_{ex}}{p_0}$	p_0 bar	p_0 psi
0.13	6.9	100
0.15	5.5	80
0.19	4.1	60
0.27	2.8	40
0.31	2.1	32

Figure 5.1 Operating Regime for M = 1.4 Nozzles

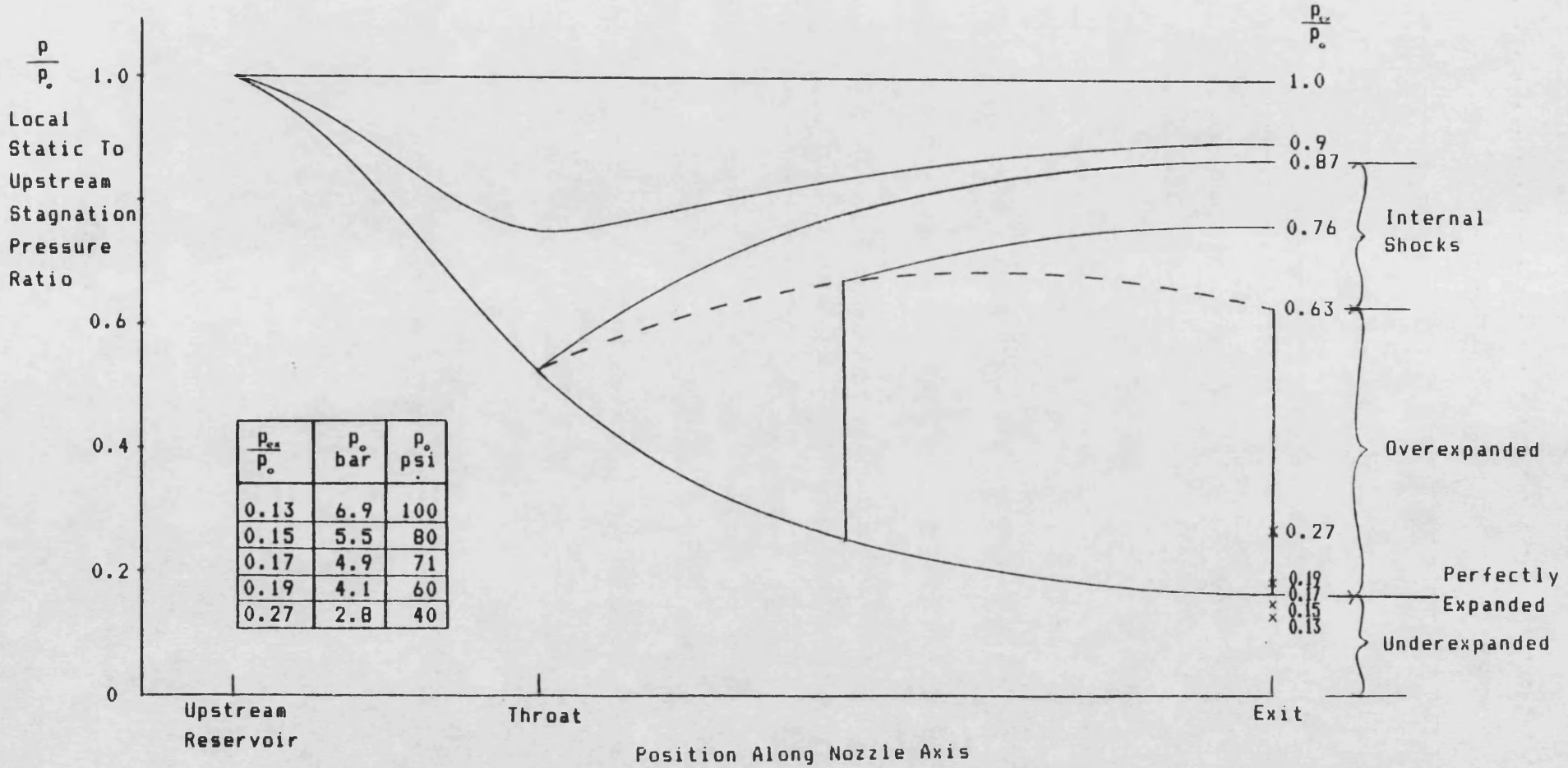

Figure 5.2 Operating Regime for M = 1.8 Nozzles

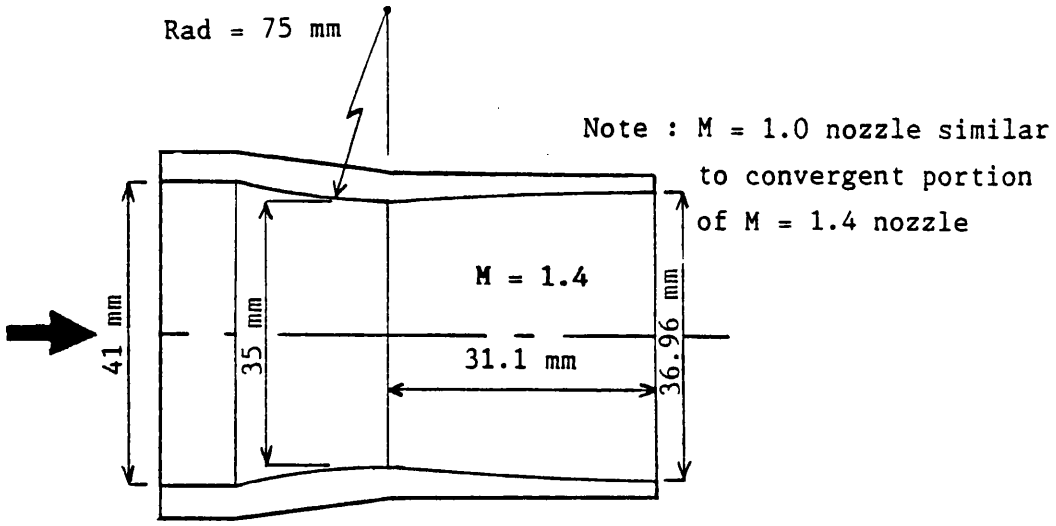

FULL-SCALE

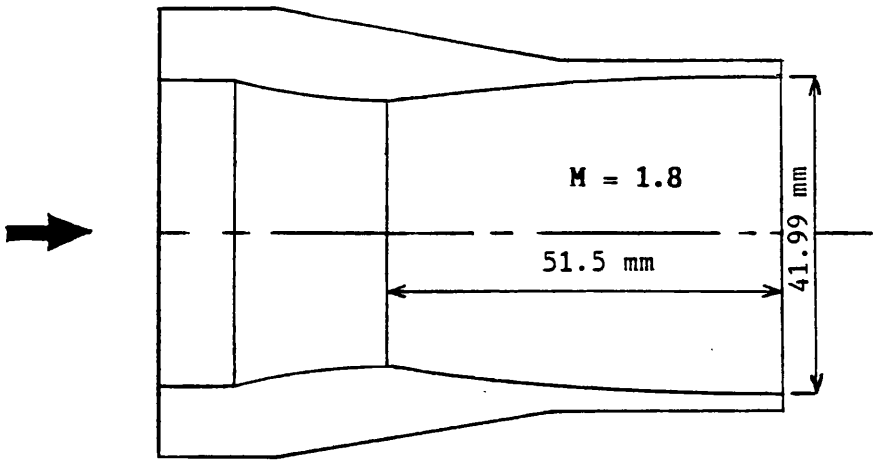

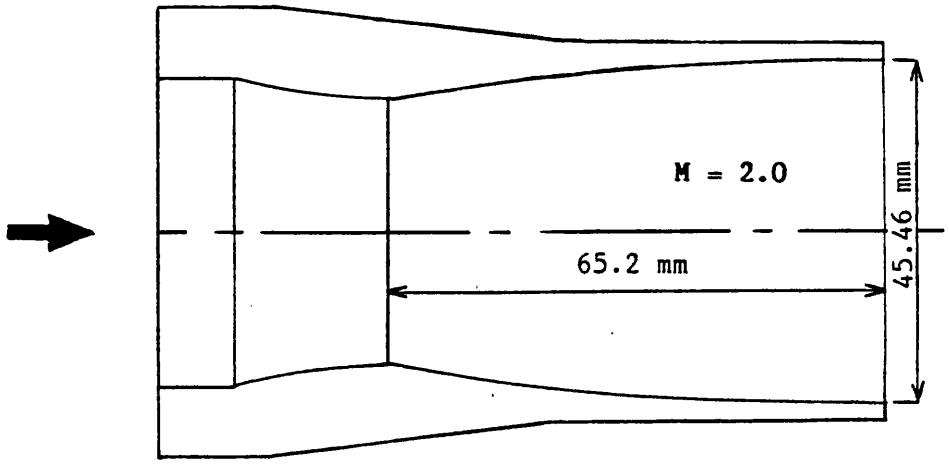

Figure 5.3 Sections through the three Supersonic Primary Nozzles

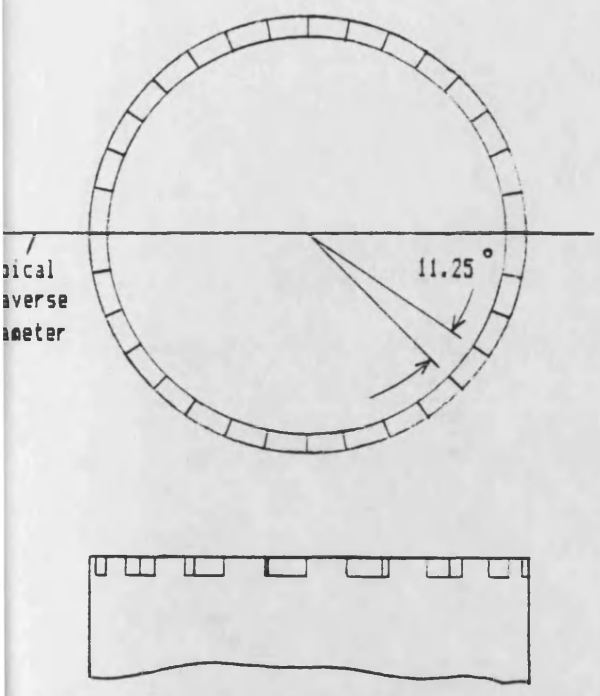

Figure 5.4 Sixteen Tooth Nozzle Exit Geometry

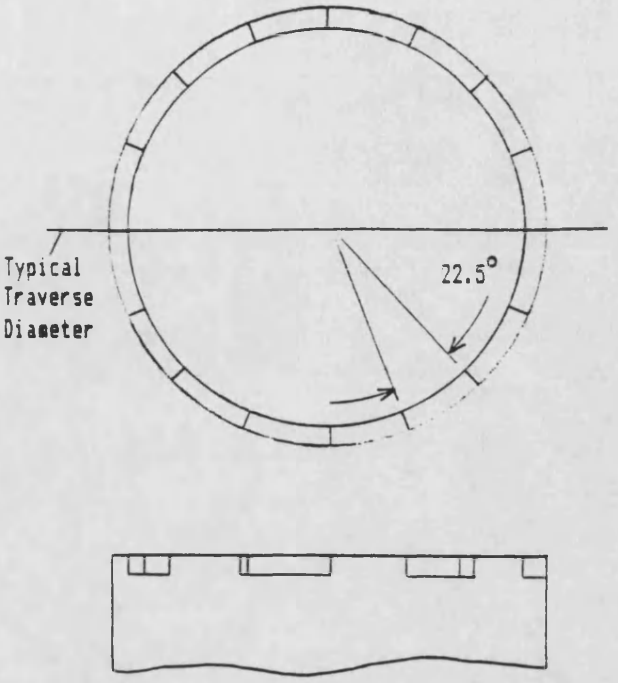

Figure 5.5 Eight Tooth Nozzle Exit Geometry

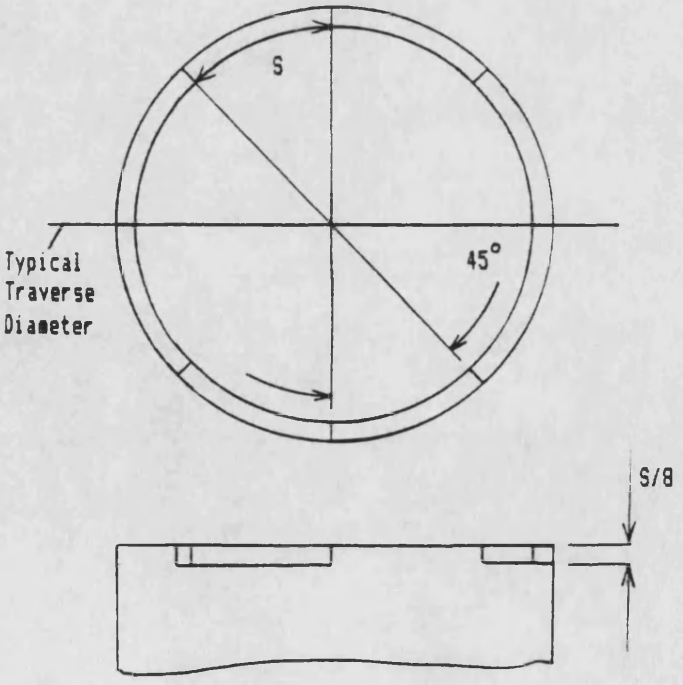

Figure 5.6 Four Tooth Nozzle Geometry

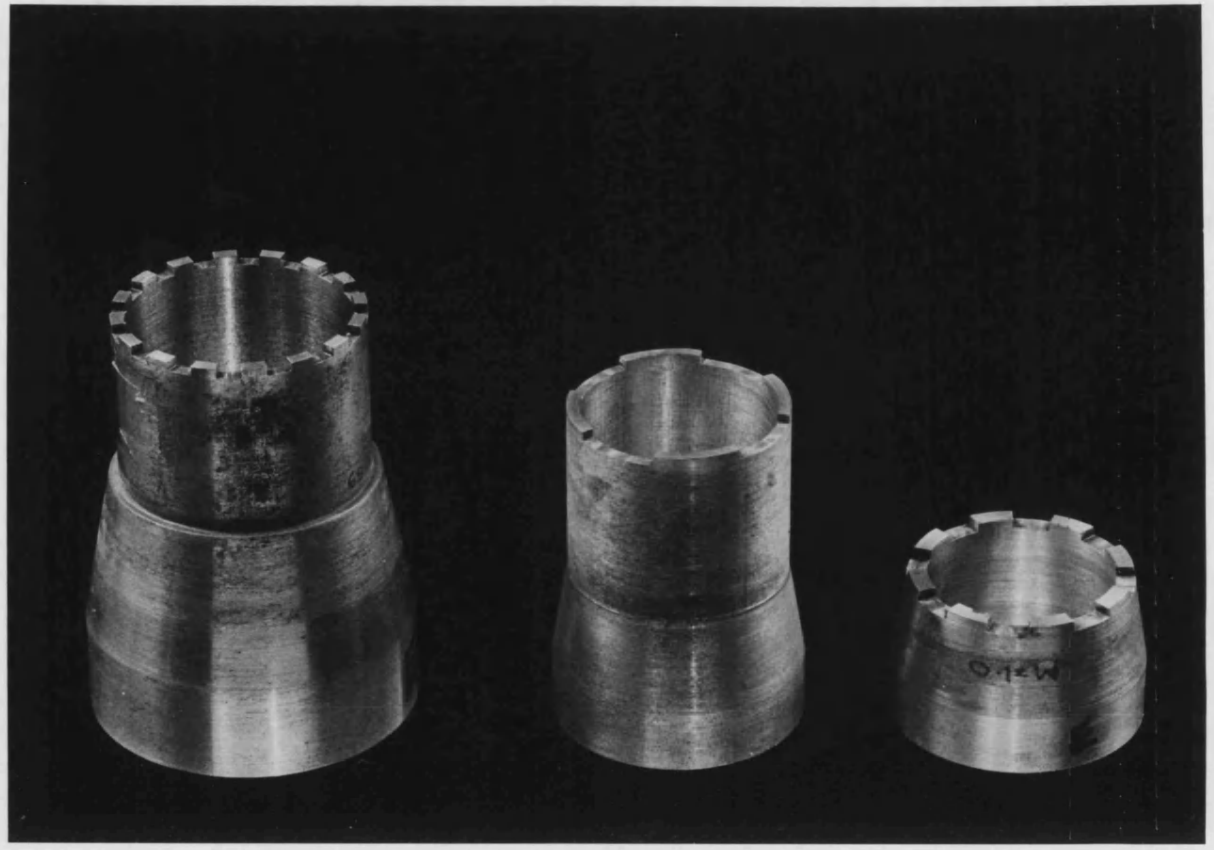

M=1.8 16 Tooth Nozzle M=1.4 4 Tooth Nozzle M=1.0 8 Tooth Nozzle

Figure 5.7 Selection of Castellated Nozzles

Figure 5.8 Free jet flow from M = 1.0 Plain Nozzle

Figure 5.9 Free jet flow from M = 1.4 Plain Nozzle

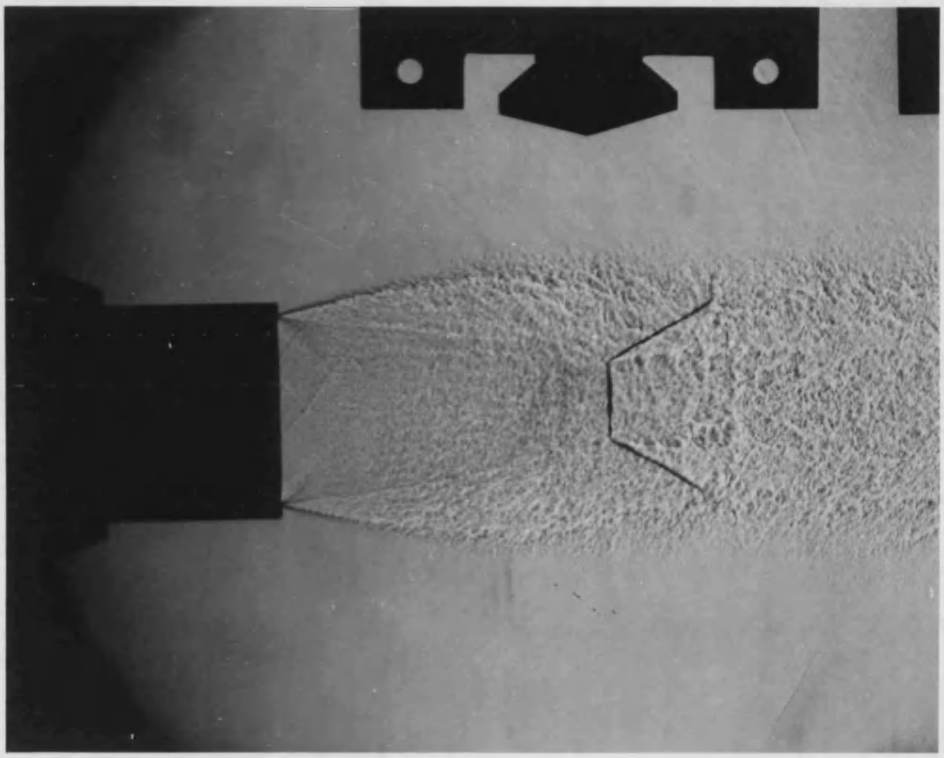

Figure 5.10 Shadowgraph of Free jet flow from M = 1.4 Plain Nozzle

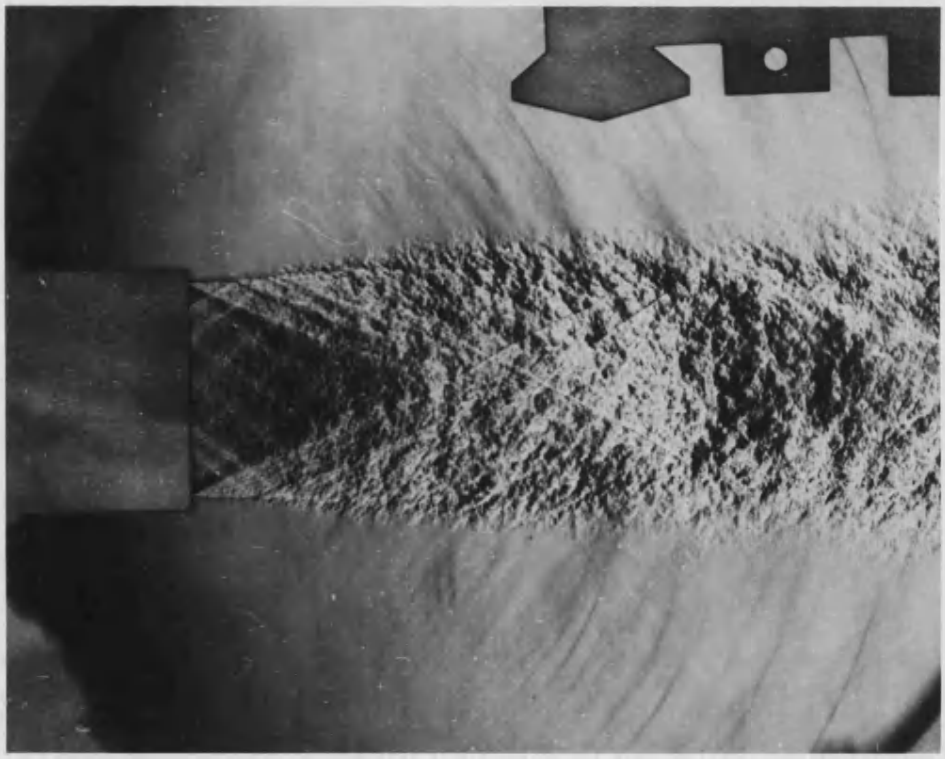

Figure 5.11 Free jet flow from M = 1.8 Plain Nozzle

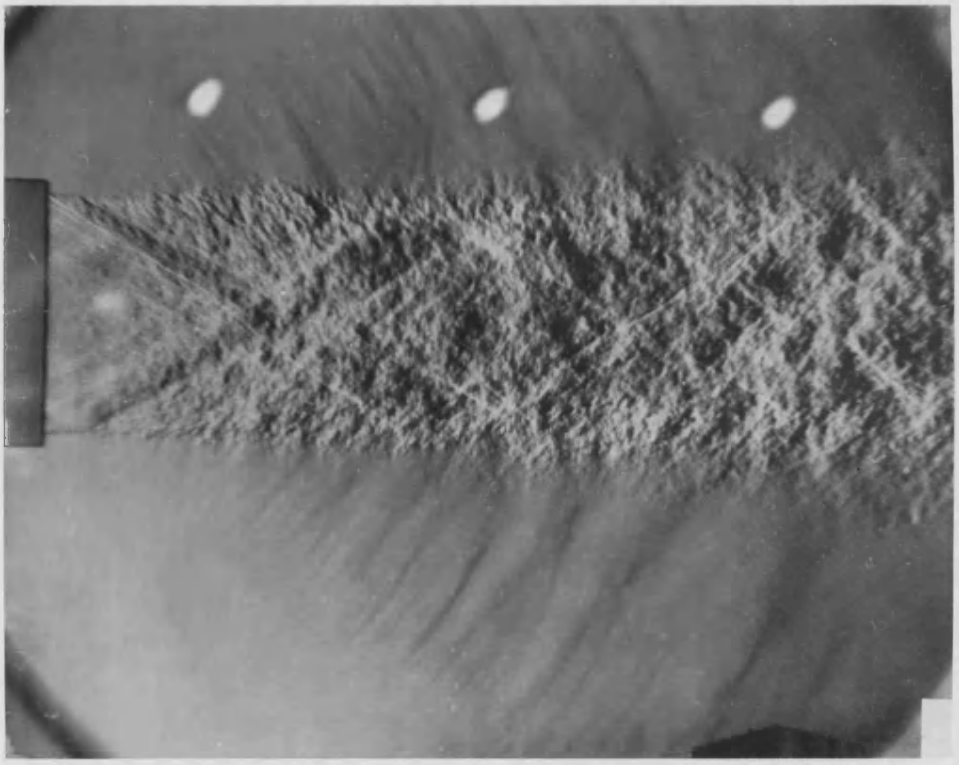

Figure 5.12 Free jet flow from M = 2.0 Plain Nozzle

Figure 5.13 Free jet flow from M = 1.0 Eight Tooth Nozzle

Figure 5.14 Free jet flow from M = 1.0 Four Tooth Nozzle

Figure 5.15 Free jet flow from M = 1.4 Sixteen Tooth Nozzle

Figure 5.16 Free jet flow from M = 1.4 Eight Tooth Nozzle

Figure 5.17 Free jet flow from M = 1.8 Sixteen Tooth Nozzle

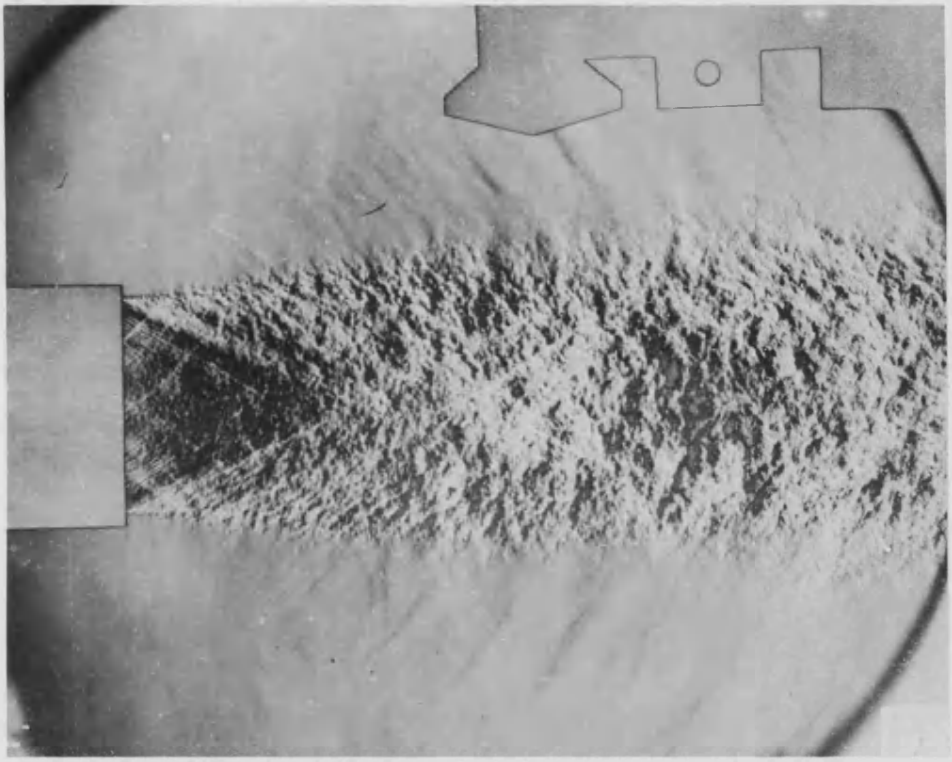

Figure 5.18 Free jet flow from M = 1.8 Eight Tooth Nozzle

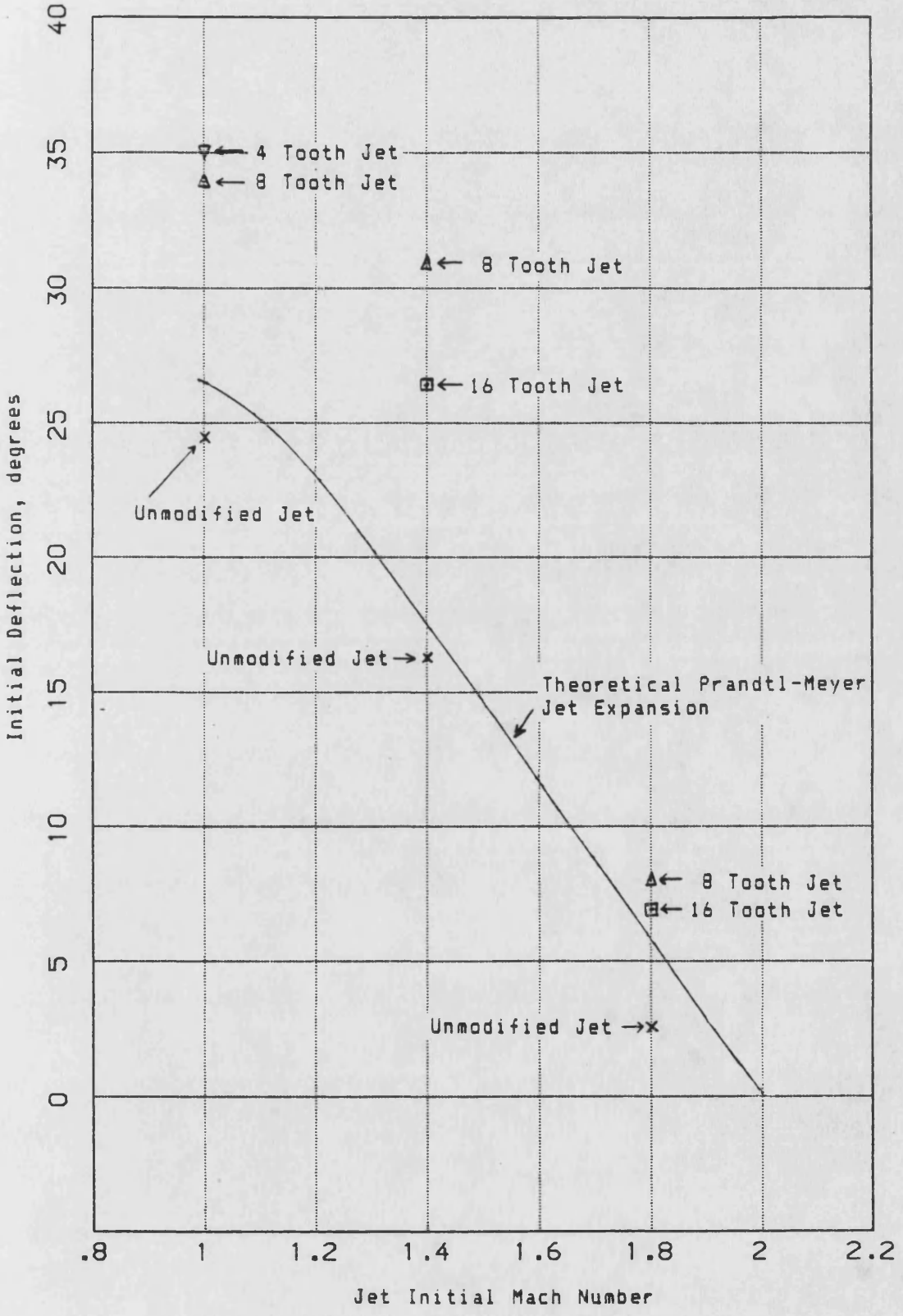

Figure 5.19 Theoretical and Observed Initial Expansion of Free Jets

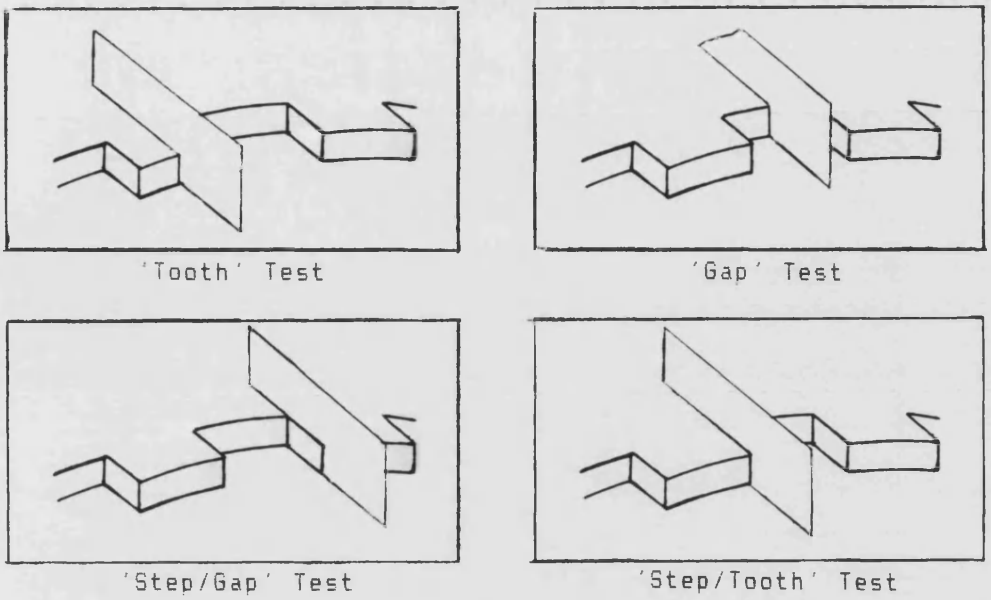

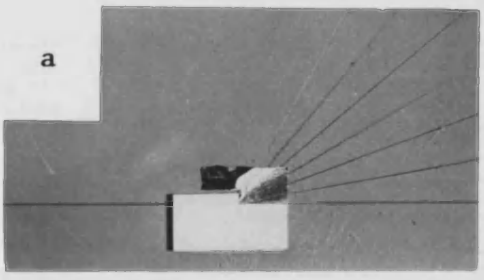

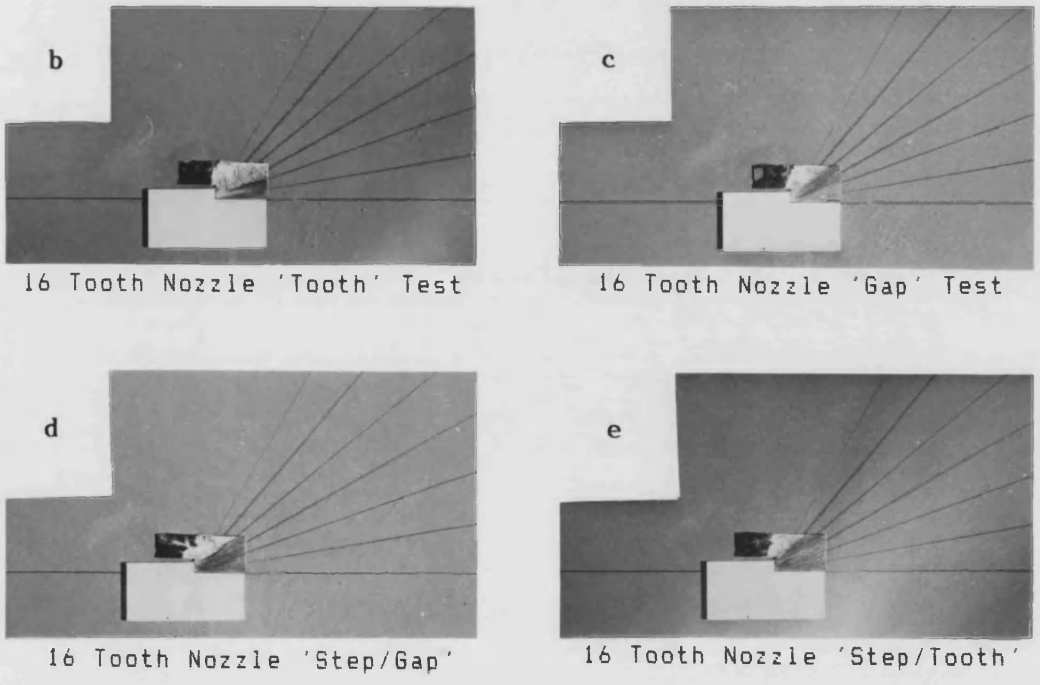

Figure 5.20 M = 1.4 Nozzle Flow Visualisation Tests

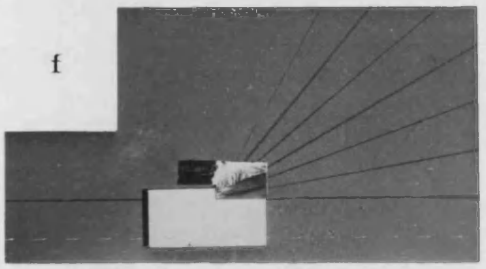

8 Tooth Nozzle 'Tooth' Test

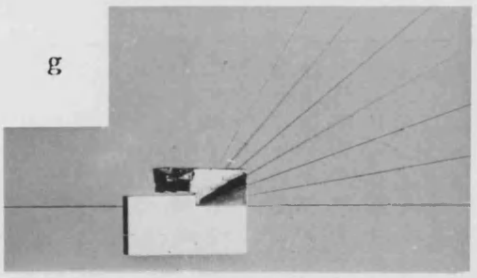

8 Tooth Nozzle 'Gap' Test

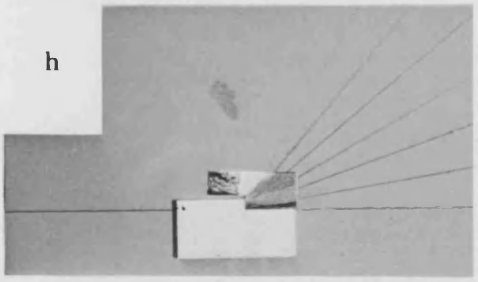

8 Tooth Nozzle 'Step/Gap'

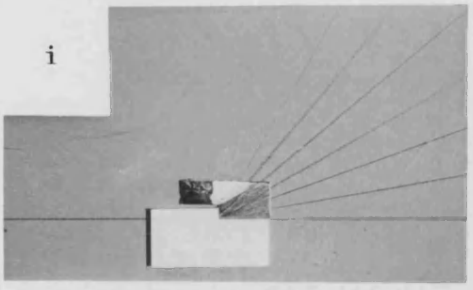

8 Tooth Nozzle 'Step/Tooth'

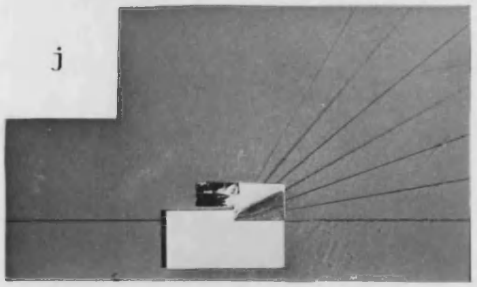

4 Tooth Nozzle 'Tooth' Test

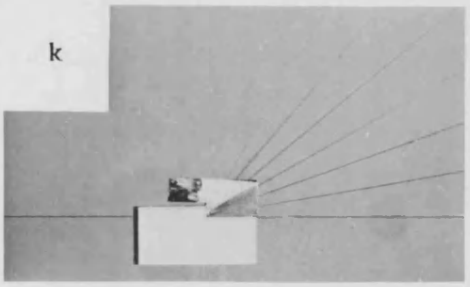

4 Tooth Nozzle 'Gap' Test

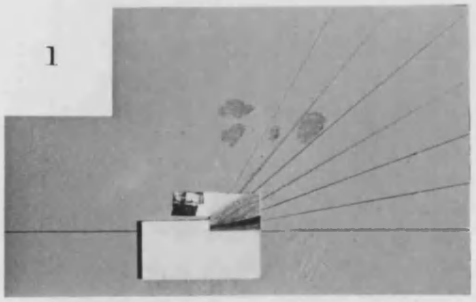

4 Tooth Nozzle 'Step/Gap'

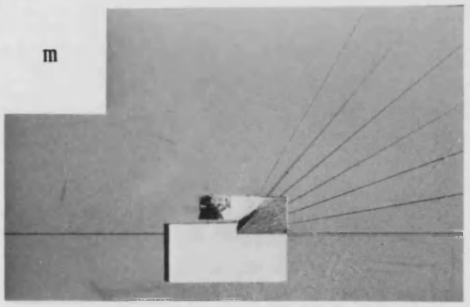

4 Tooth Nozzle 'Step/Tooth'

Figure 5.20 M = 1.4 Nozzle Flow Visualisation Tests, contd

Figure 5.21 M=1.4 jet, 40 degree shock probe, x/D=4, r/D=0.343

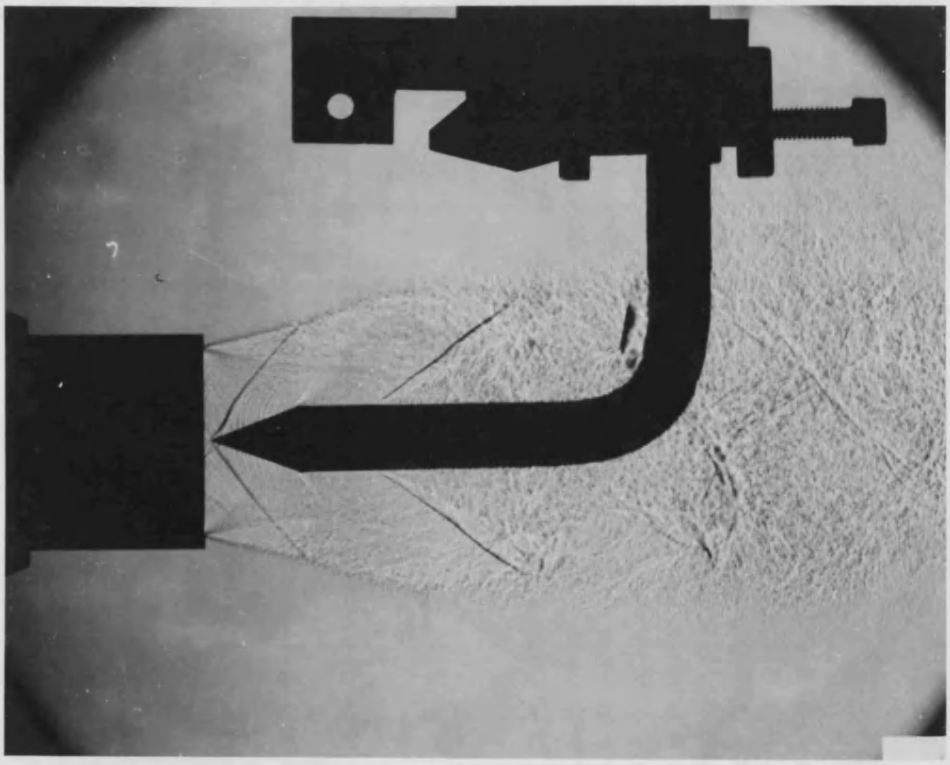

Figure 5.22 M=1.4 jet, 40 degree shock probe, x/D=0, r/D=0

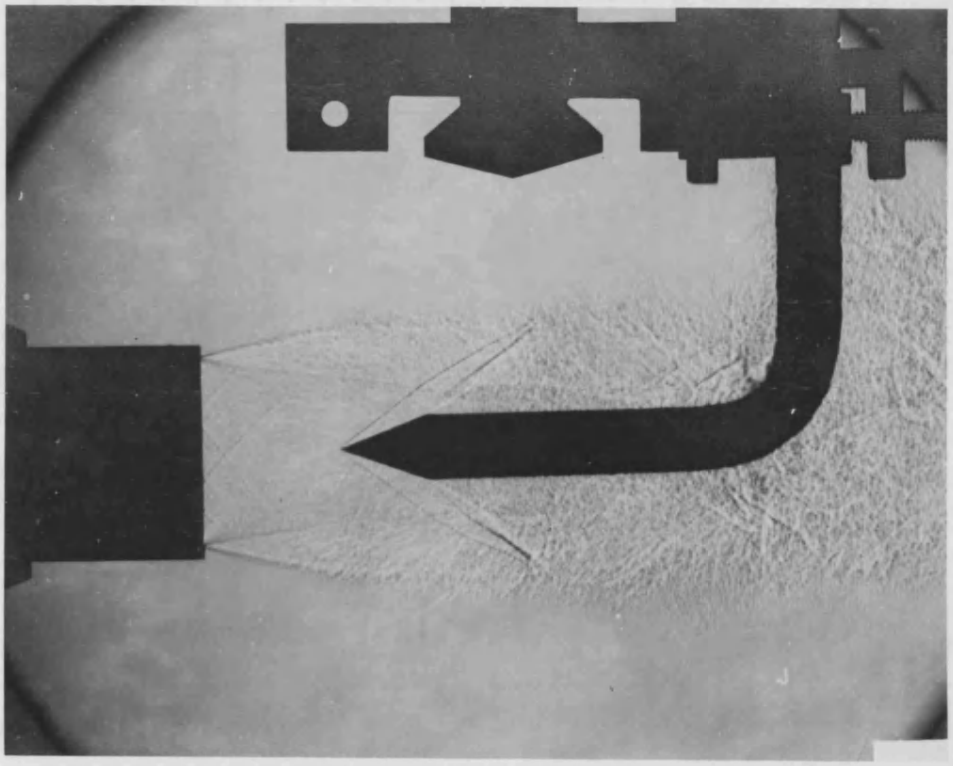

Figure 5.23 M=1.4 jet, 40 degree shock probe, x/D=0.75, r/D=0

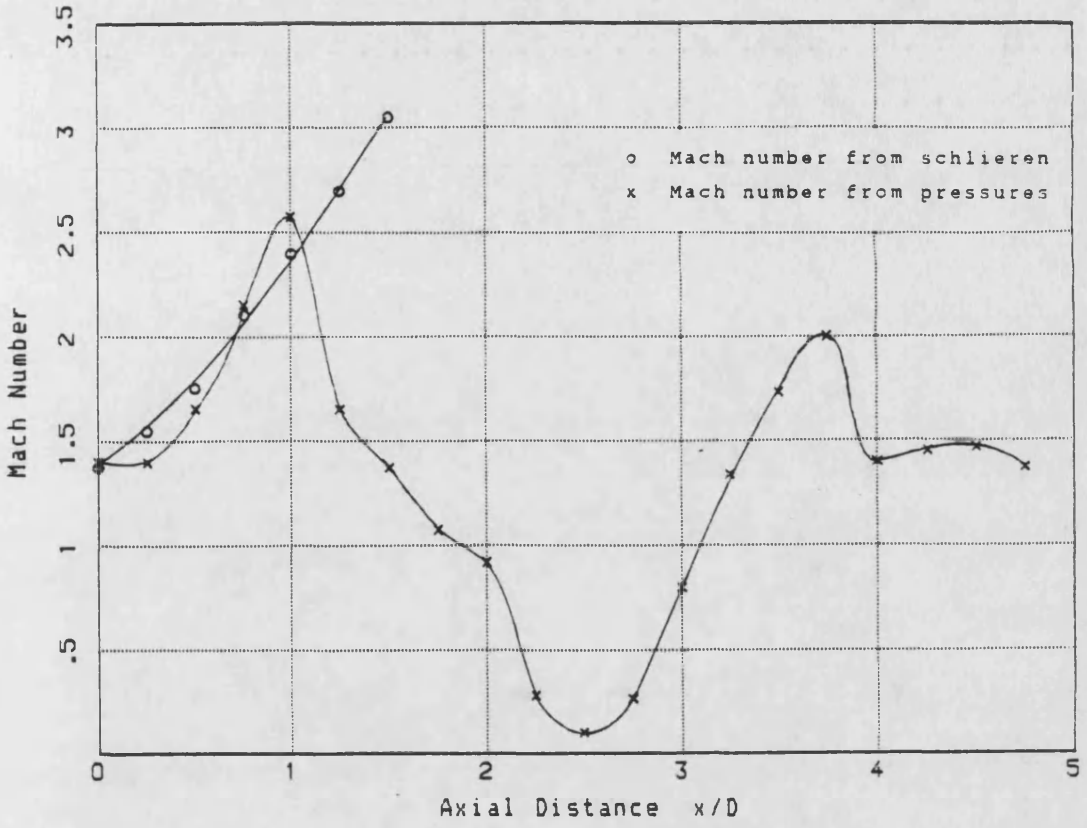

Figure 5.24 Centreline Mach number variation, M=1.4 Plain Jet

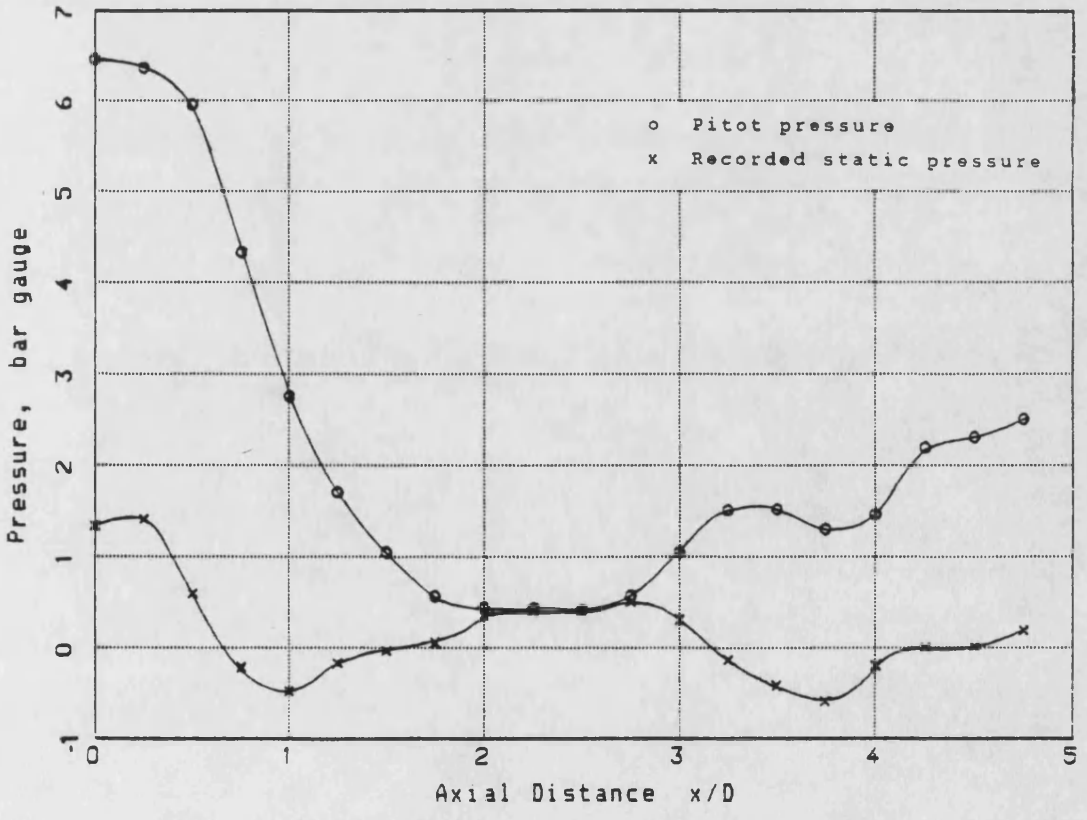

Figure 5.25 Centreline Pitot and Static Pressure variation, M=1.4 Plain Jet

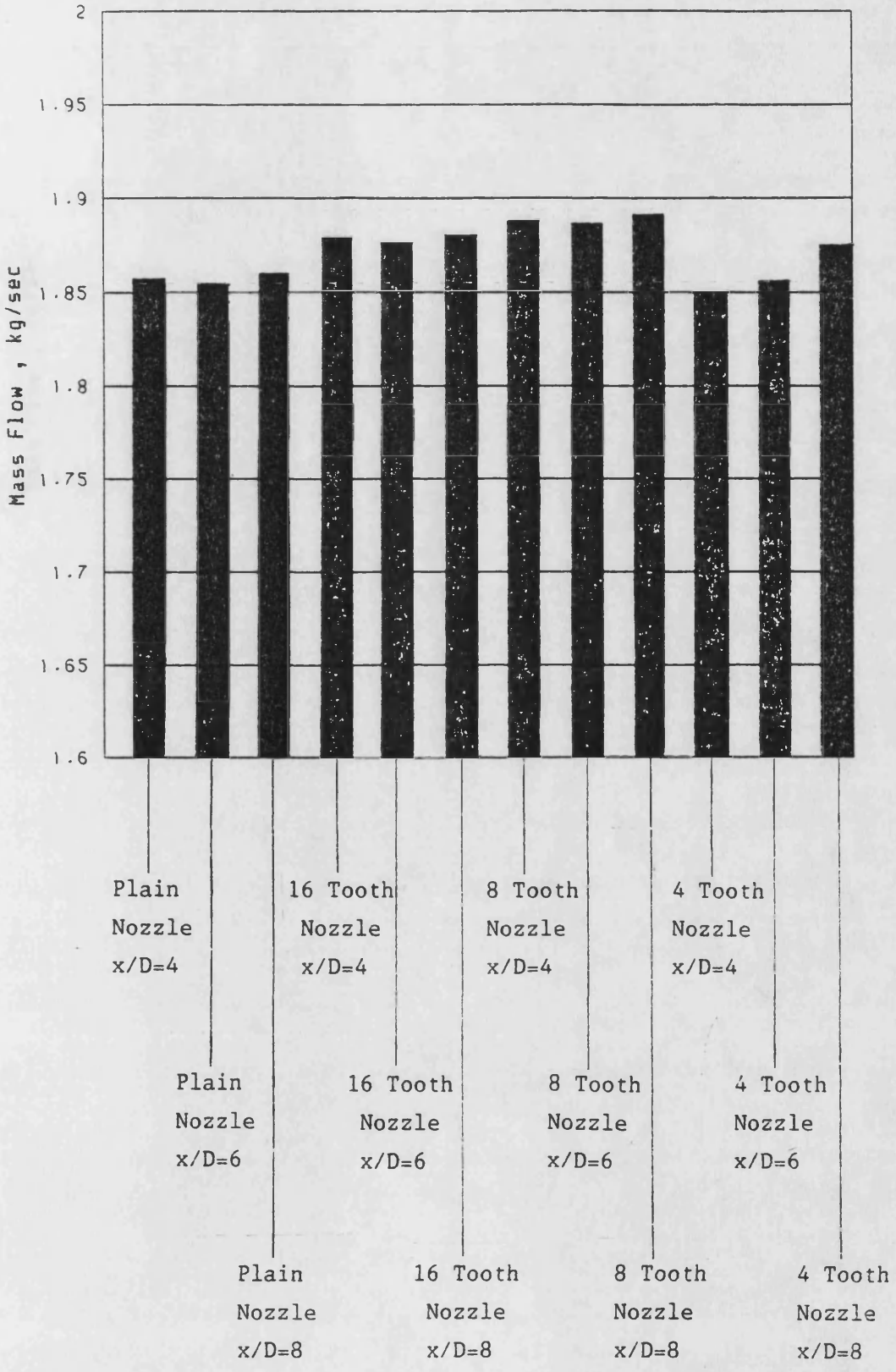

Figure 6.1 Nozzle Exit Mass Flow for all M=1.0 tests

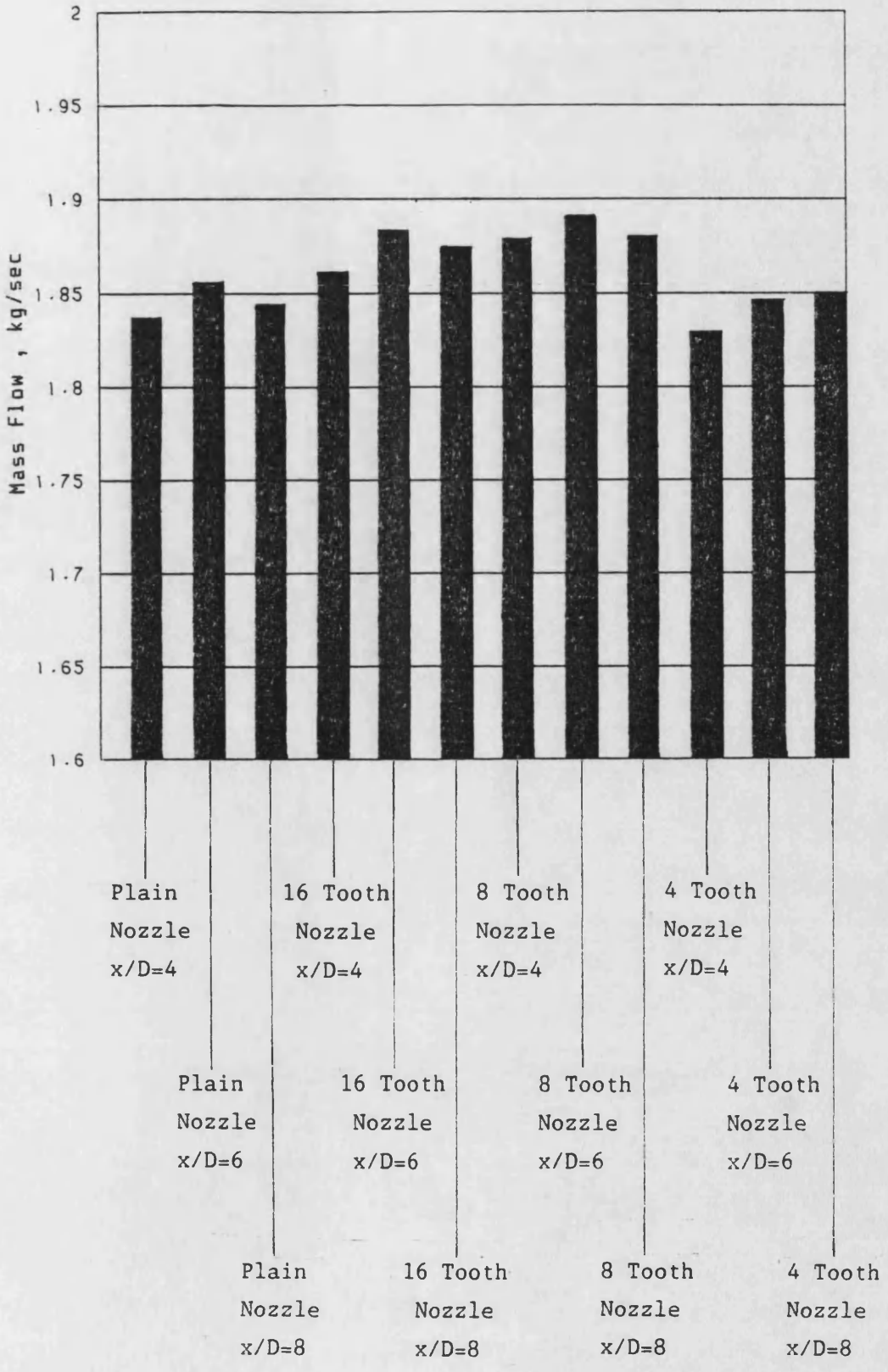

Figure 6.2 Nozzle Exit Mass Flow for all M=1.4 tests

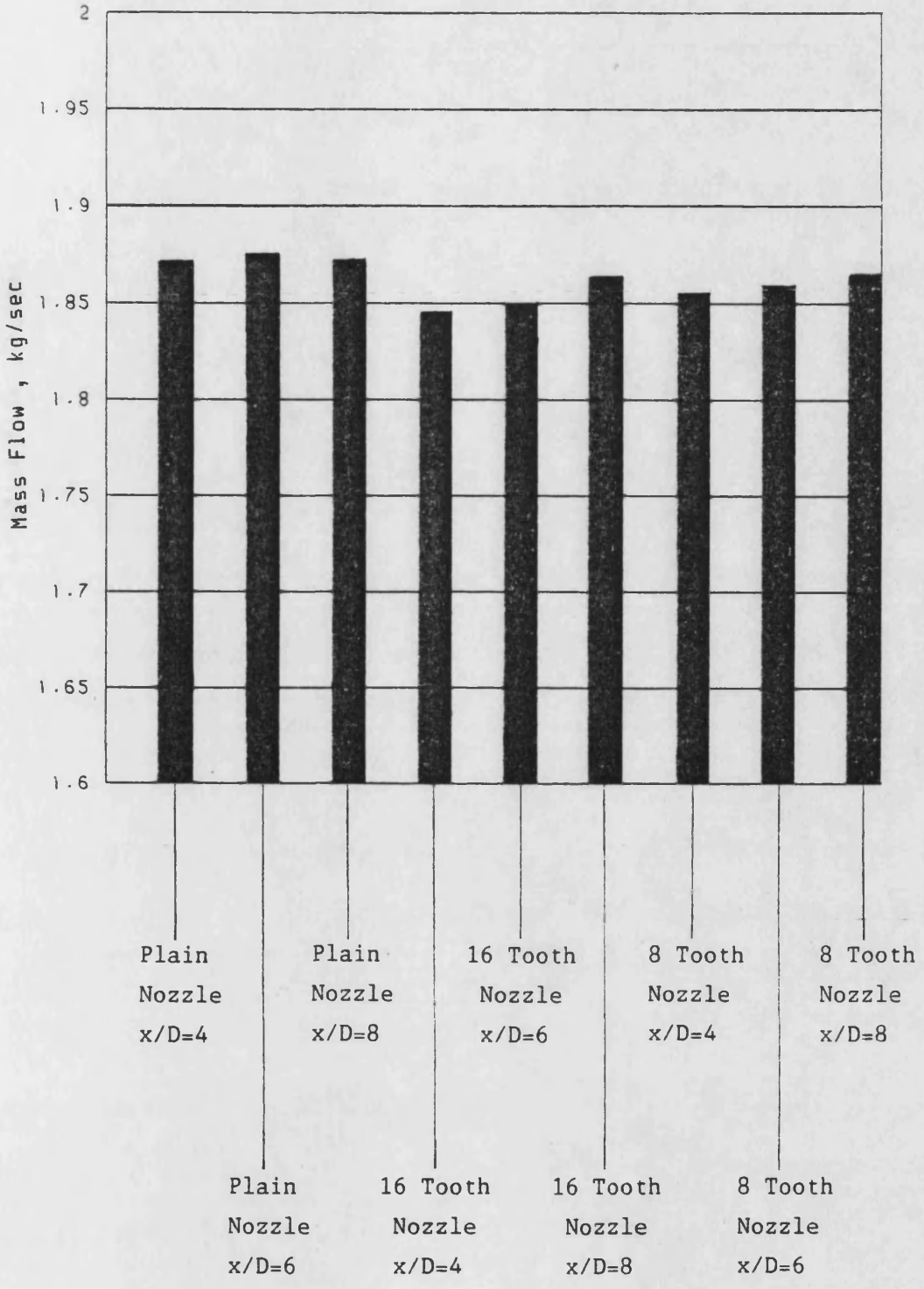

Figure 6.3 Nozzle Exit Mass Flow for all M=1.8 tests

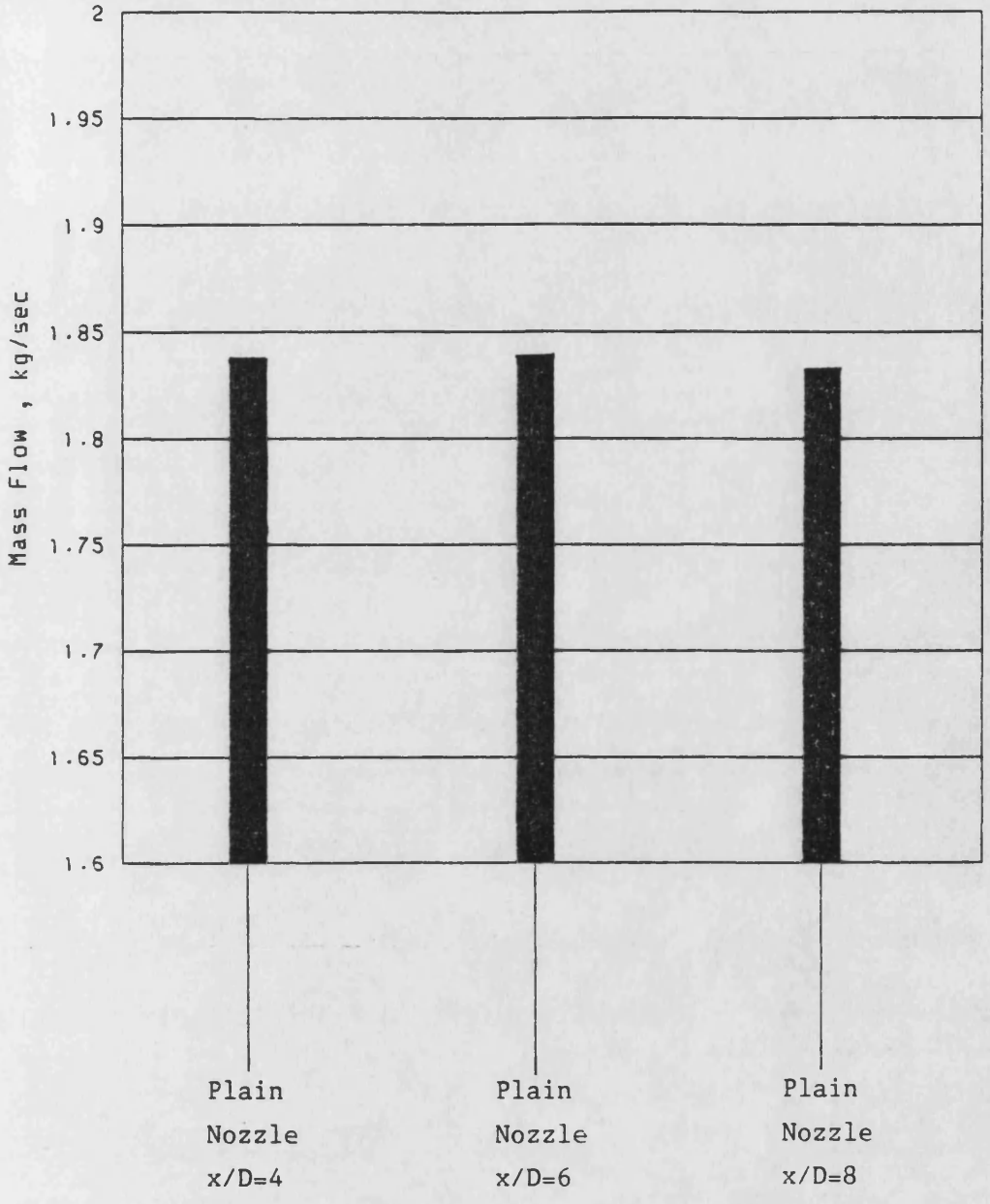

Figure 6.4 Nozzle Exit Mass Flow for all M=2.0 tests

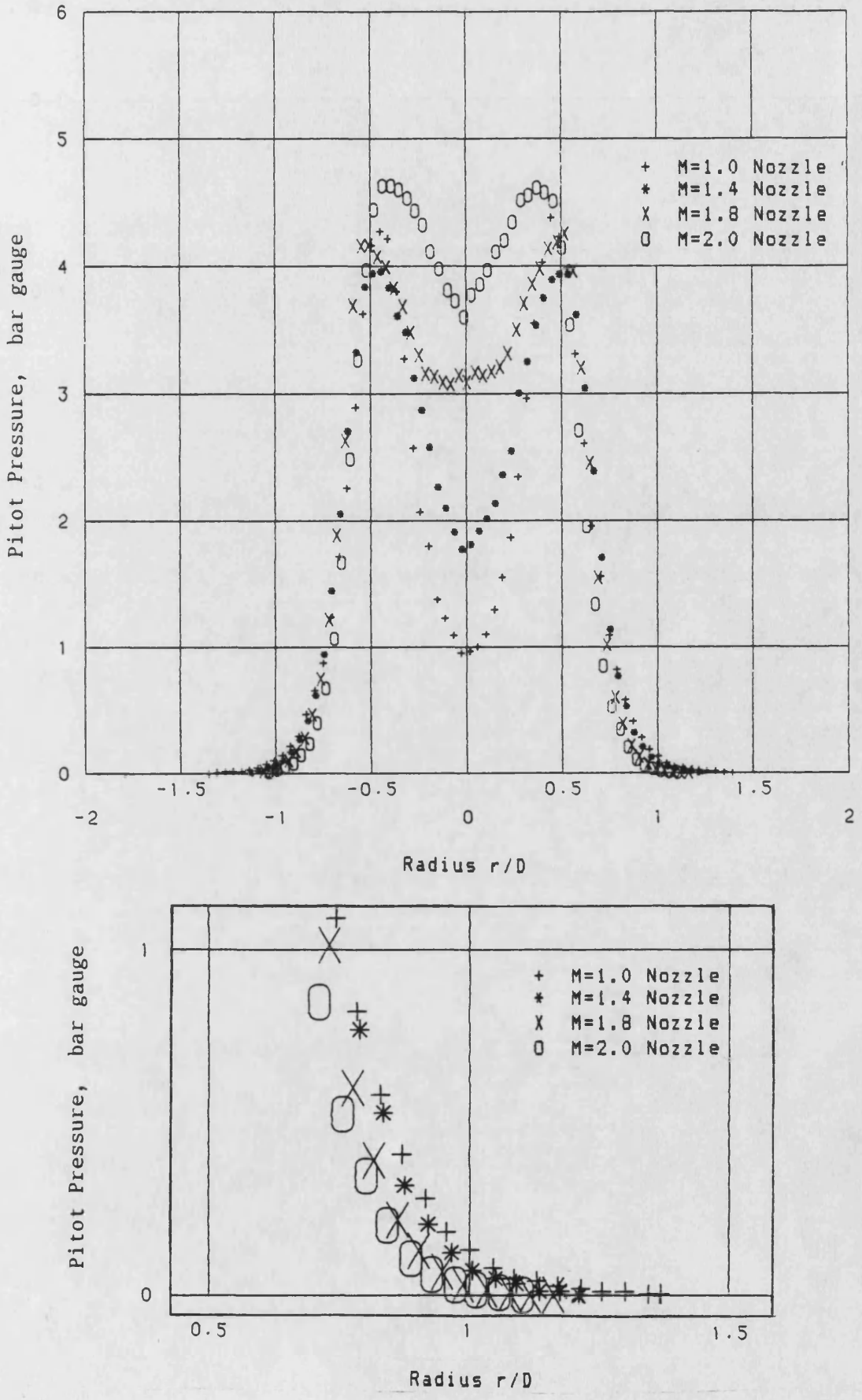

Figure 6.5 Pitot Pressure at x/D=4 for Plain Nozzles

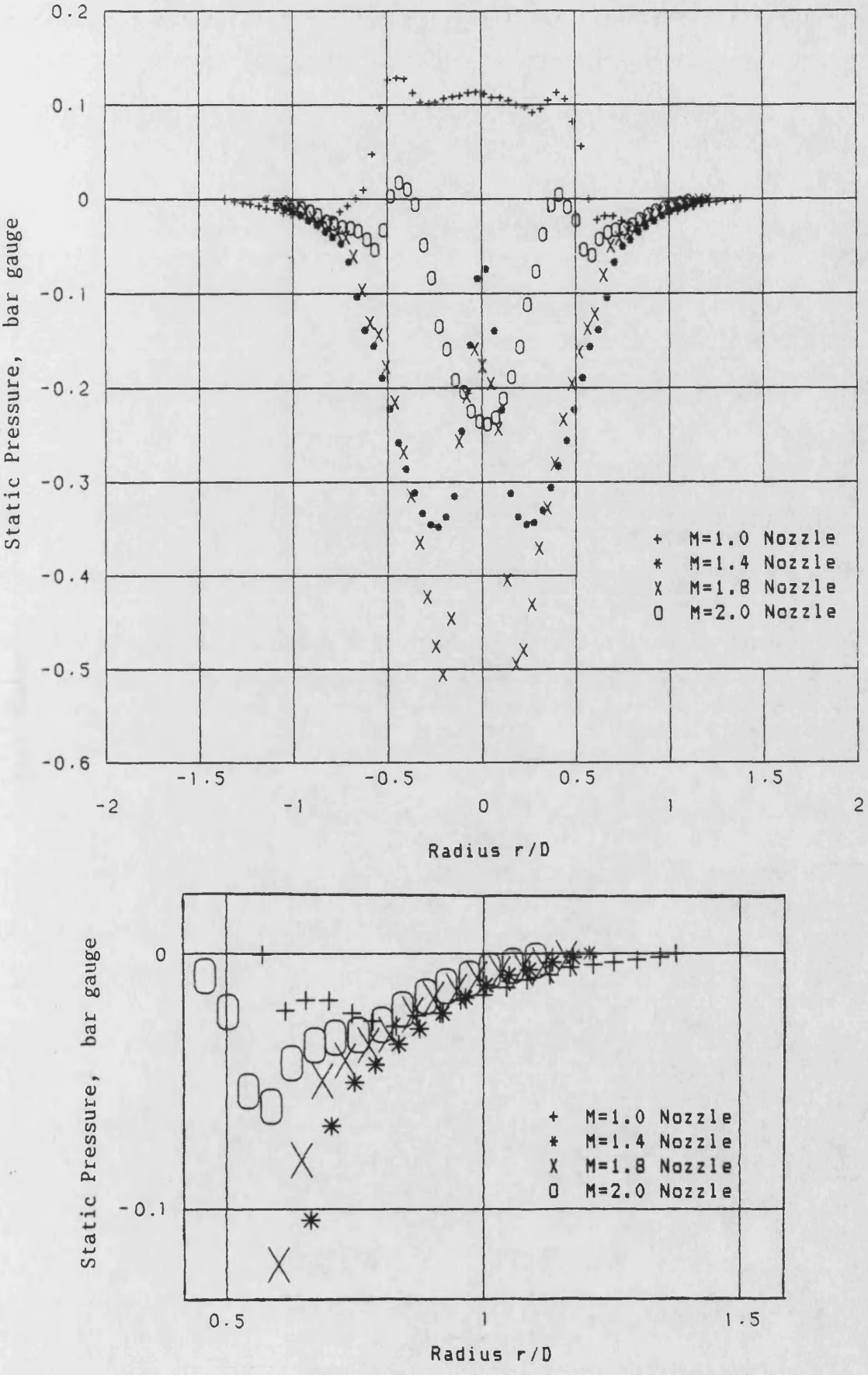

Figure 6.6 Static Pressure at x/D=4 for Plain Nozzles

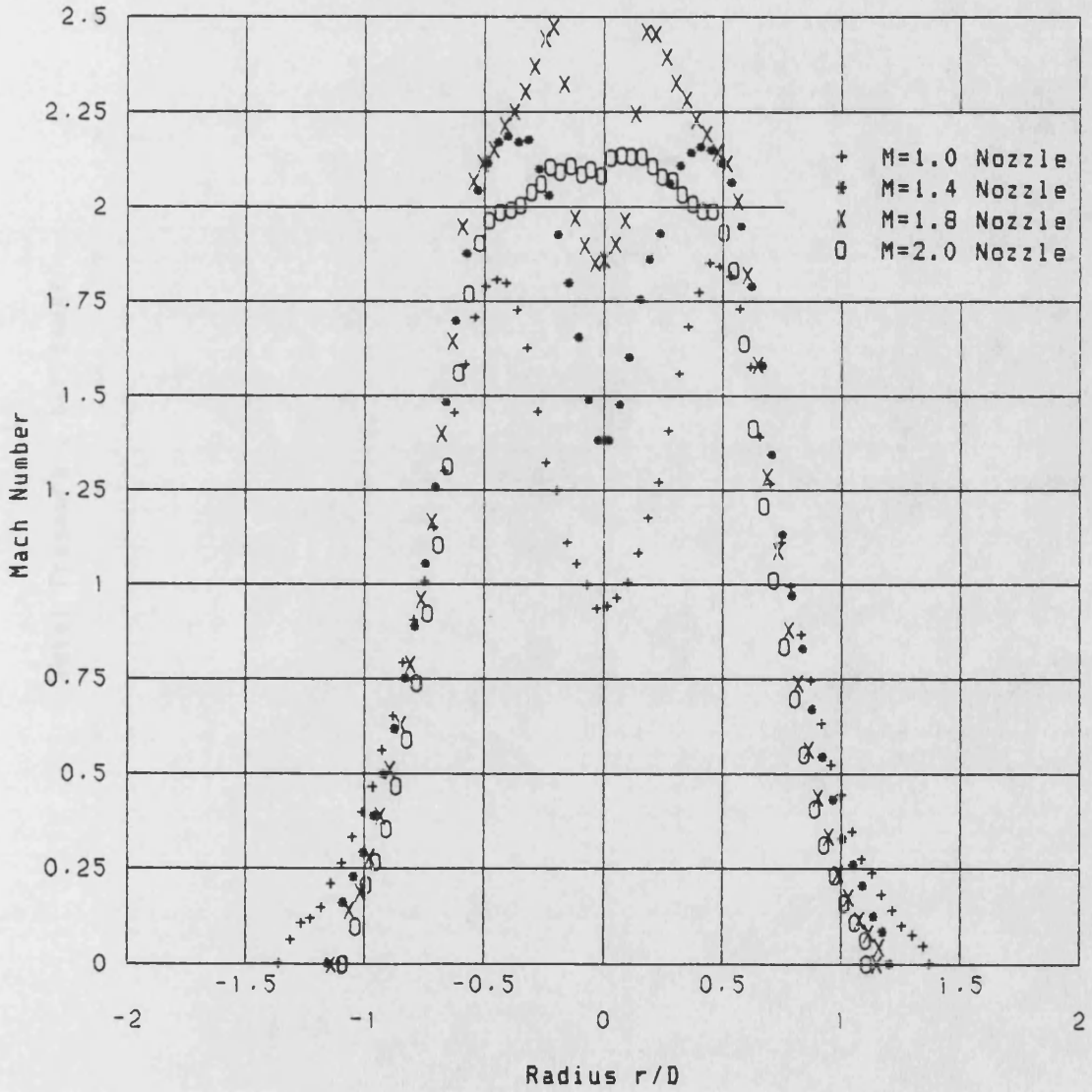

Figure 6.7 Mach Number at x/D=4 for Plain Nozzles

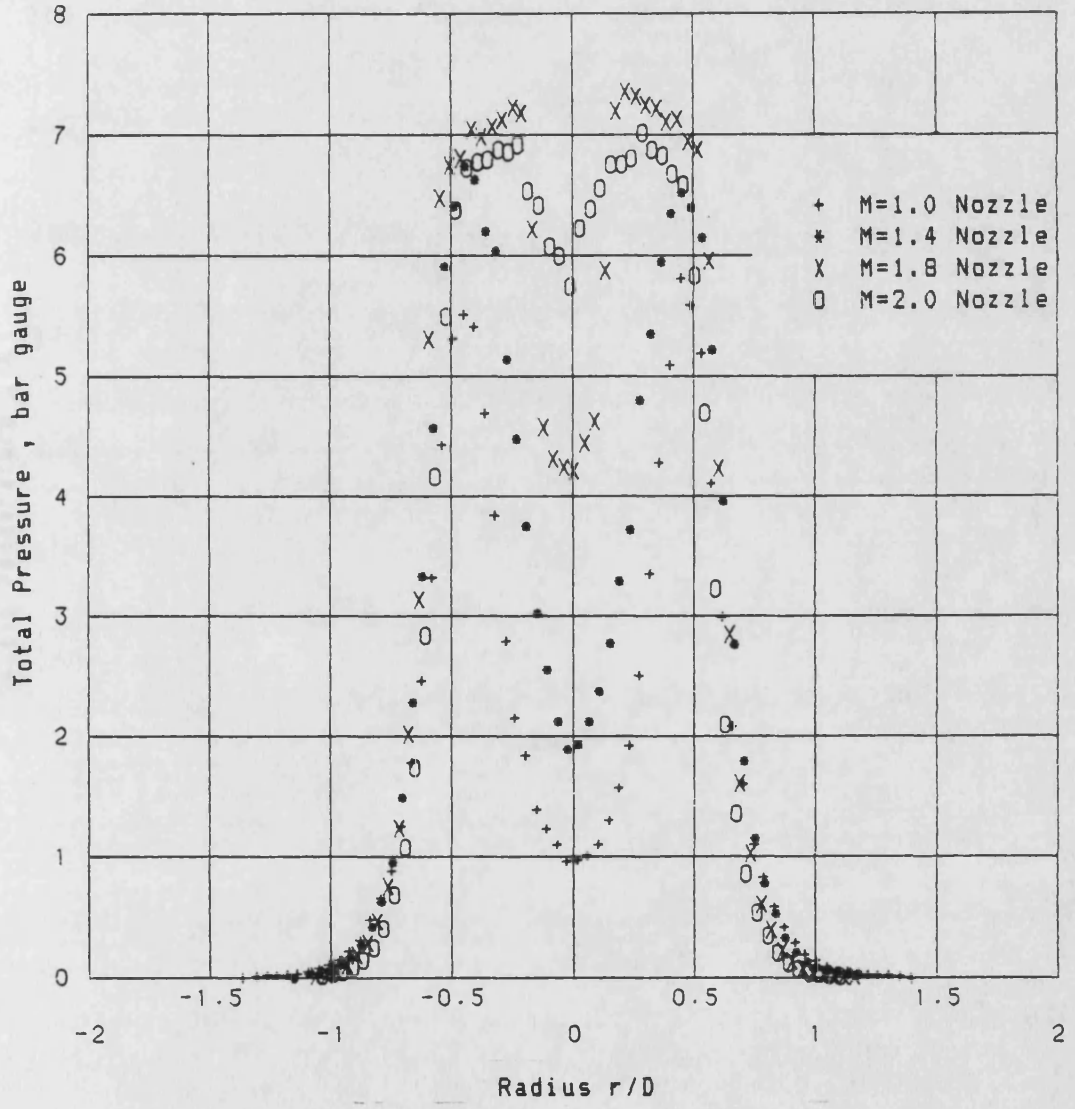

Figure 6.8 Total Pressure at x/D=4 for Plain Nozzles

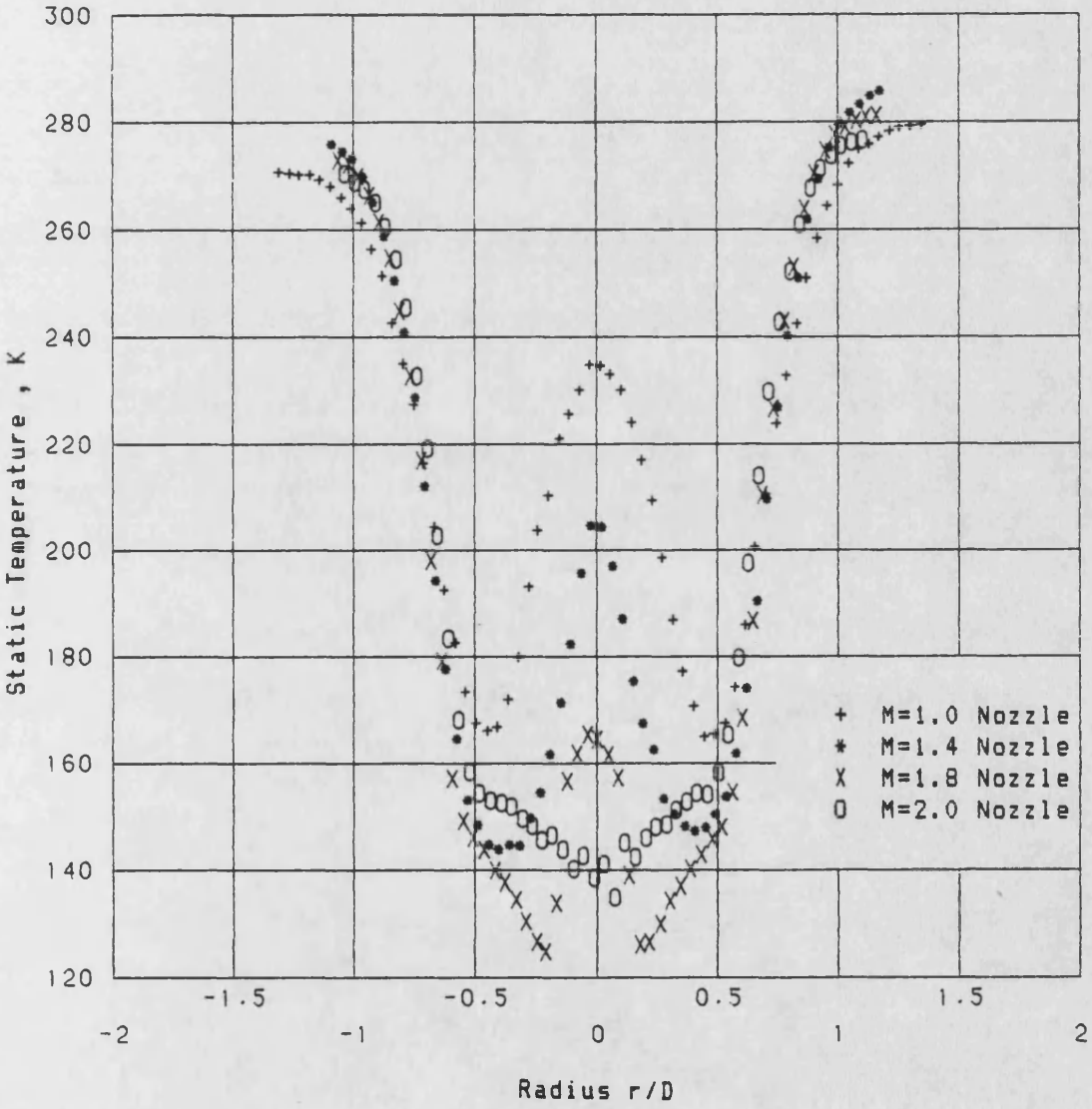

Figure 6.9 Static Temperature at x/D=4 for Plain Nozzles

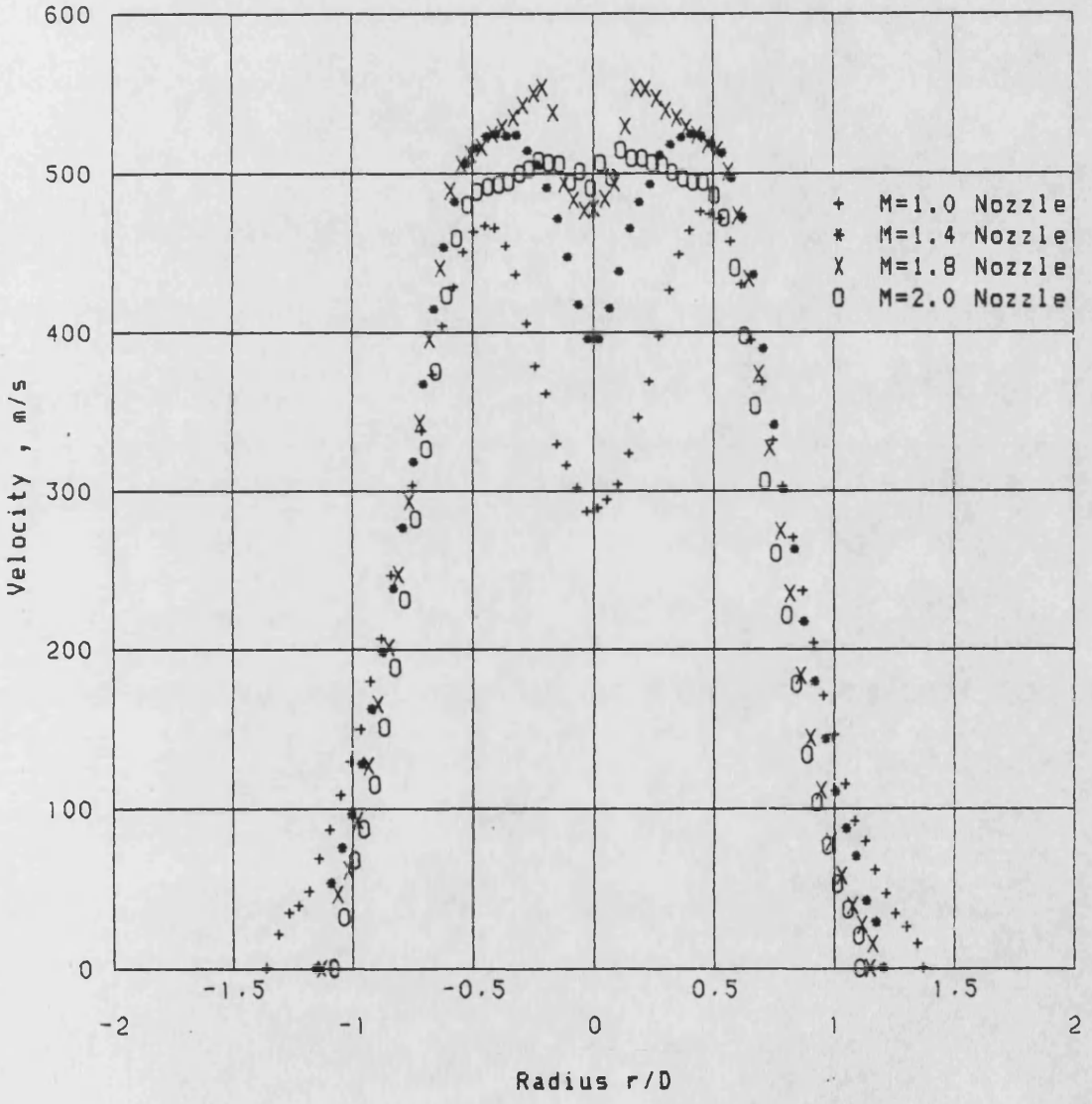

Figure 6.10 Velocity at x/D=4 for Plain Nozzles

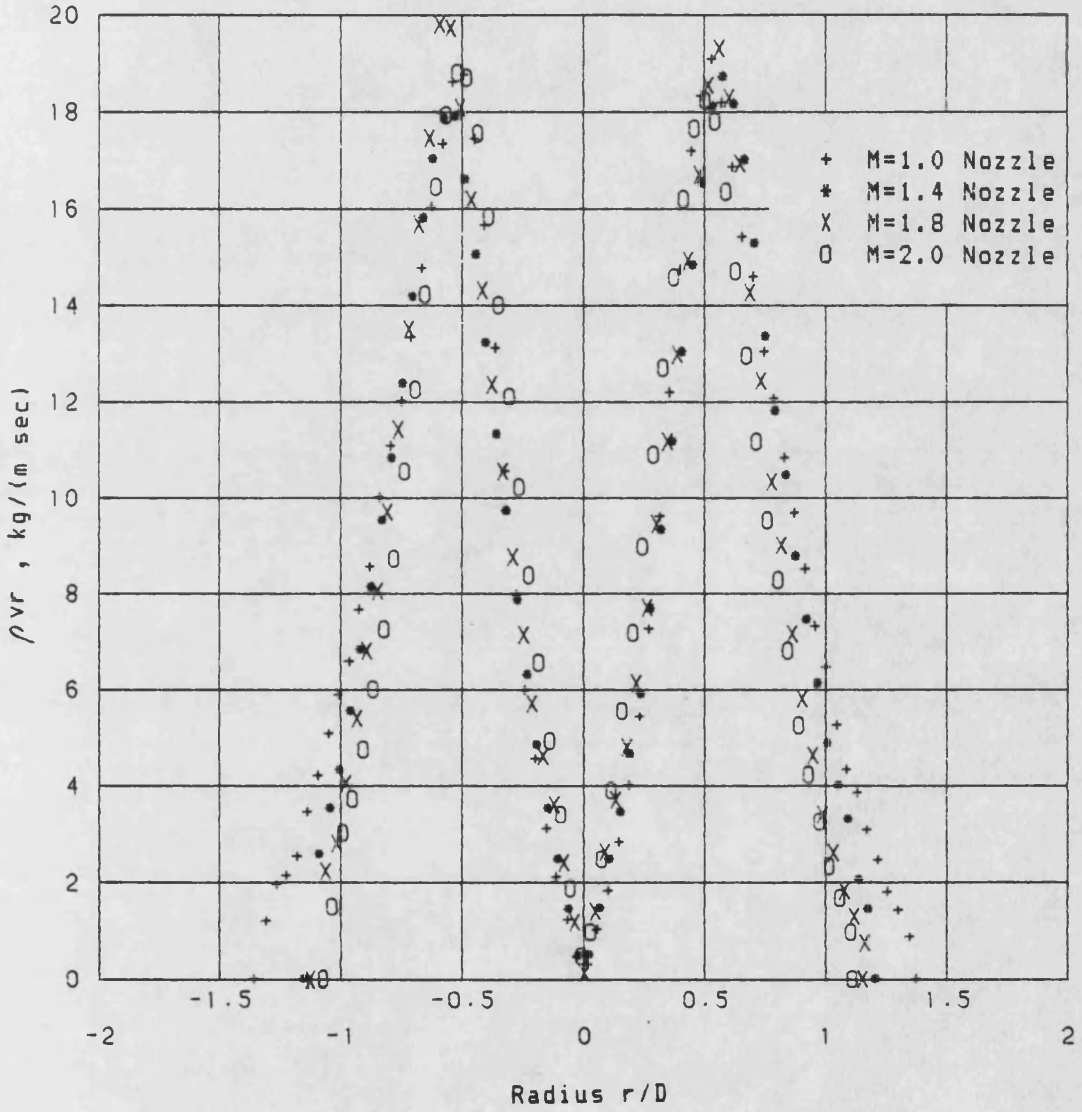

Figure 6.11 Mass Flow at x/D=4 for Plain Nozzles

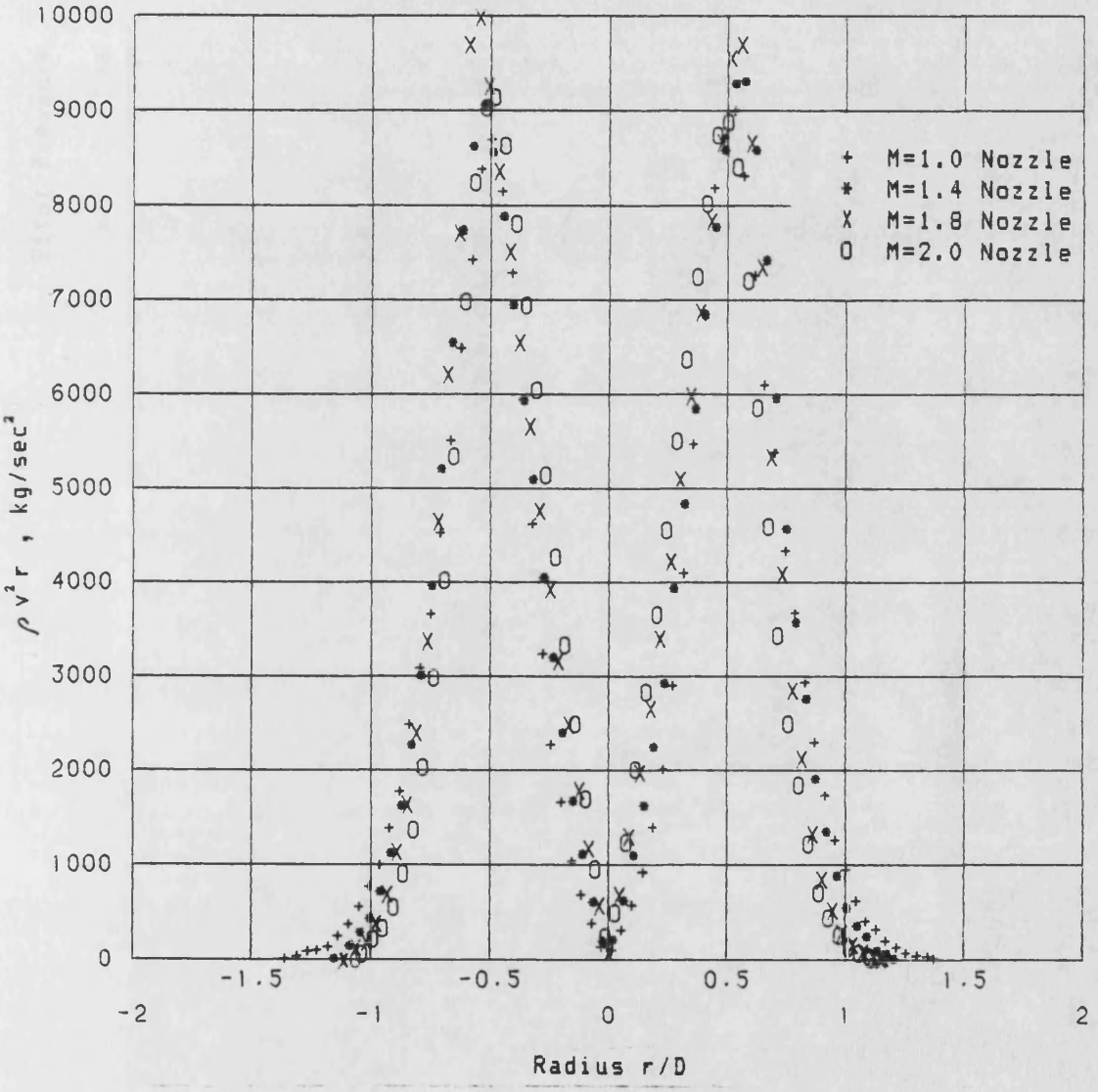

Figure 6.12 Momentum Flux at x/D=4 for Plain Nozzles

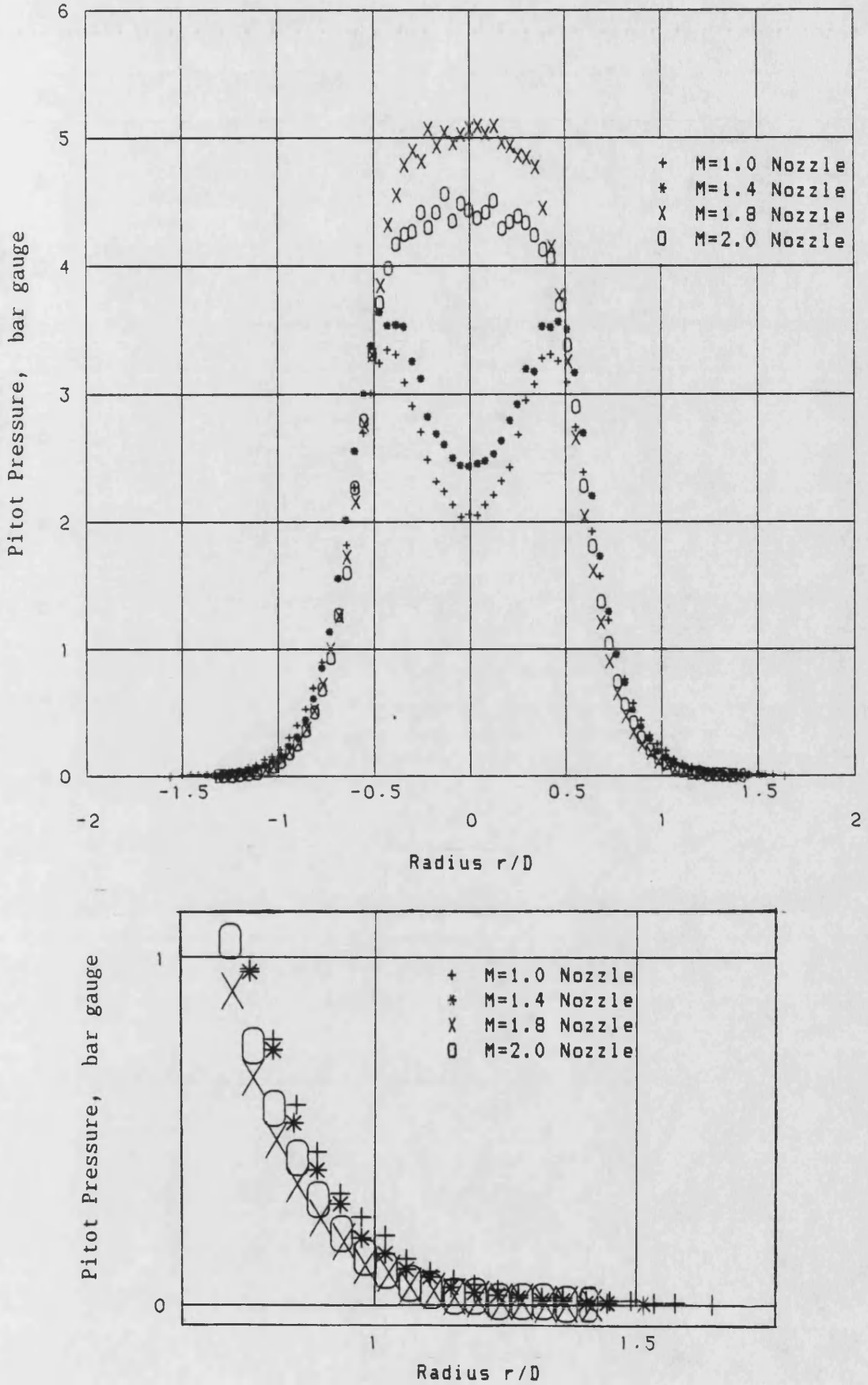

Figure 6.13 Pitot Pressure at x/D=6 for Plain Nozzles

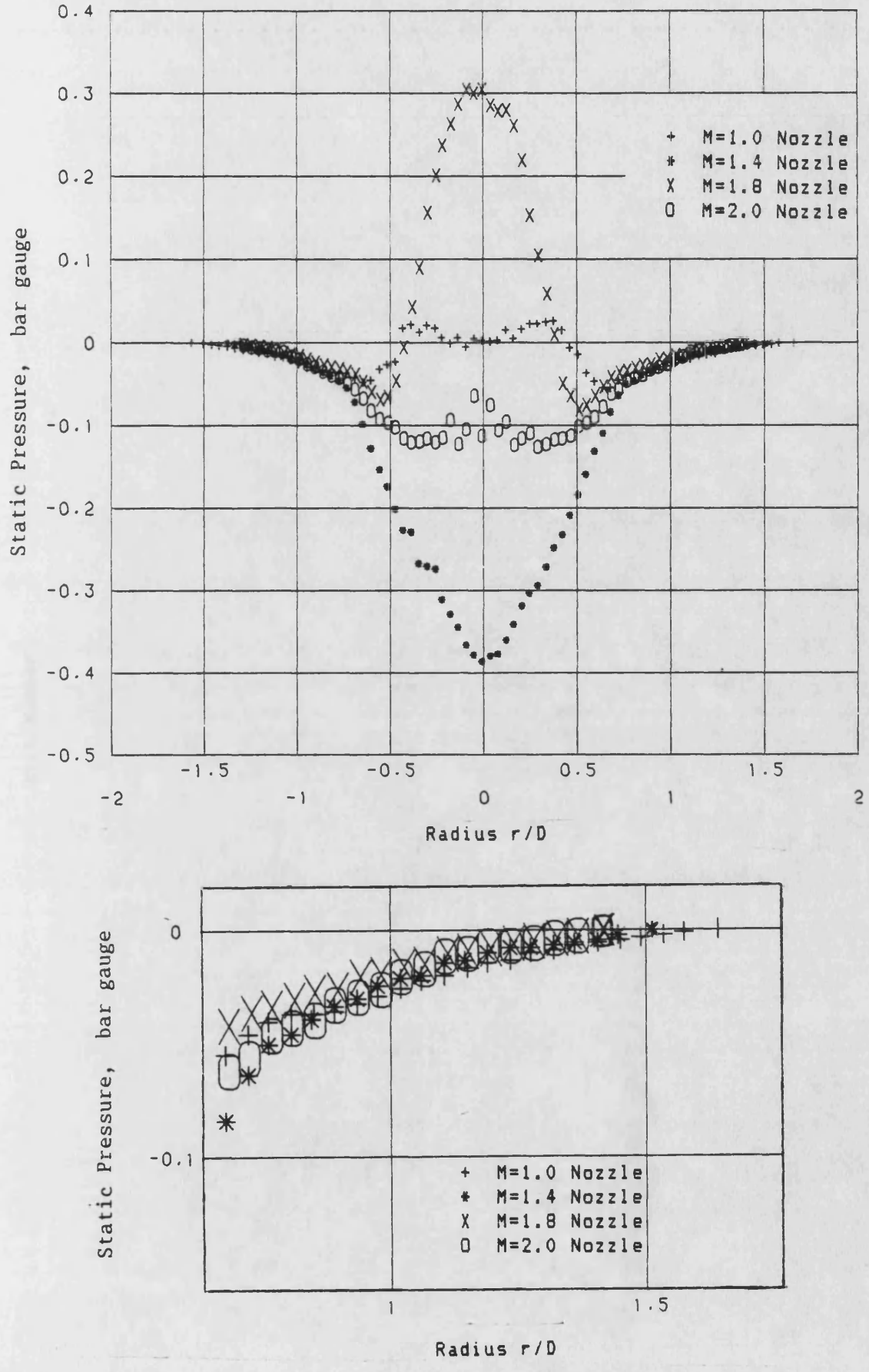

Figure 6.14 Static Pressure at x/D=6 for Plain Nozzles

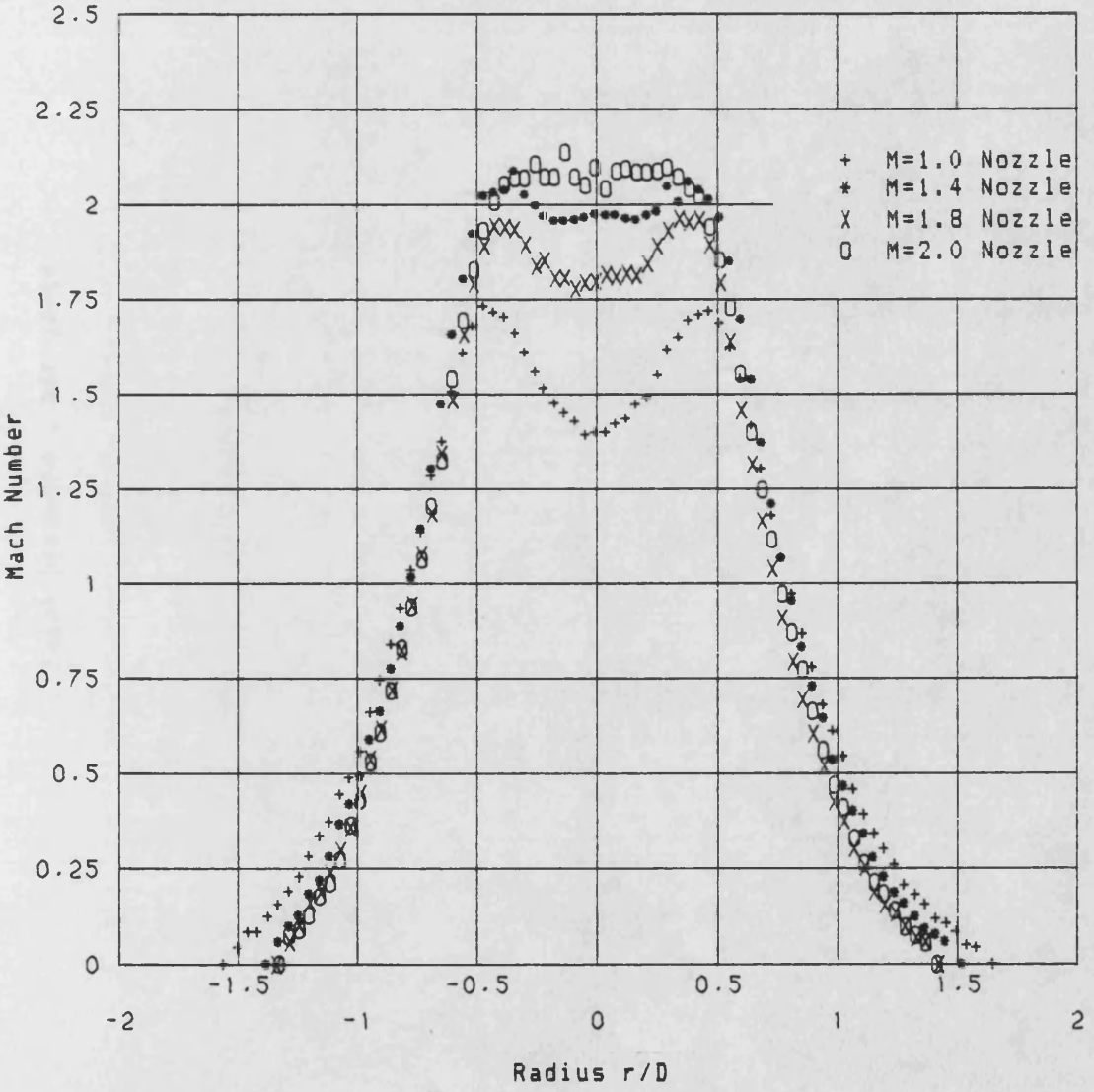

Figure 6.15 Mach Number at x/D=6 for Plain Nozzles

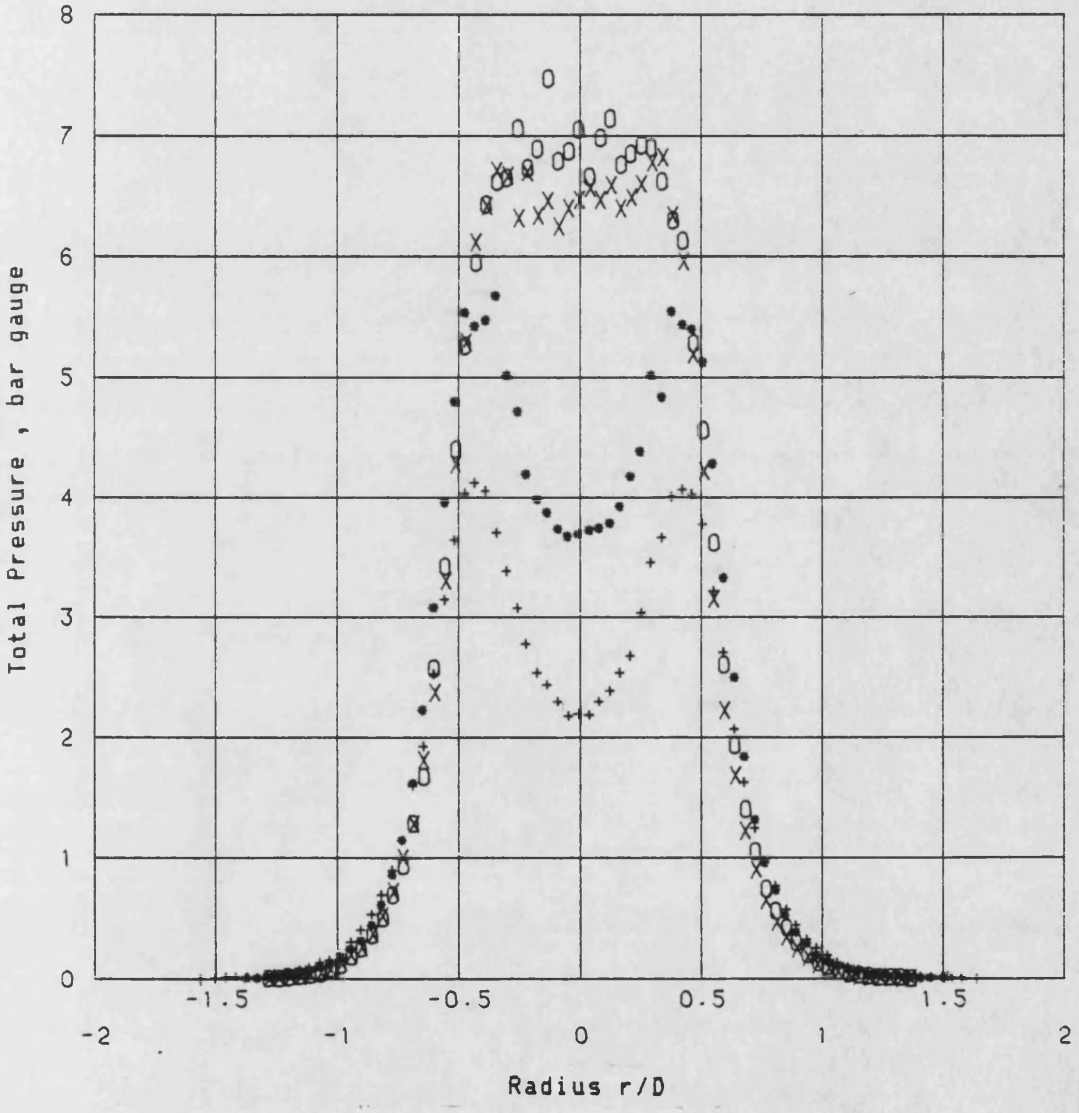

Figure 6.16 Total Pressure at x/D=6 for Plain Nozzles

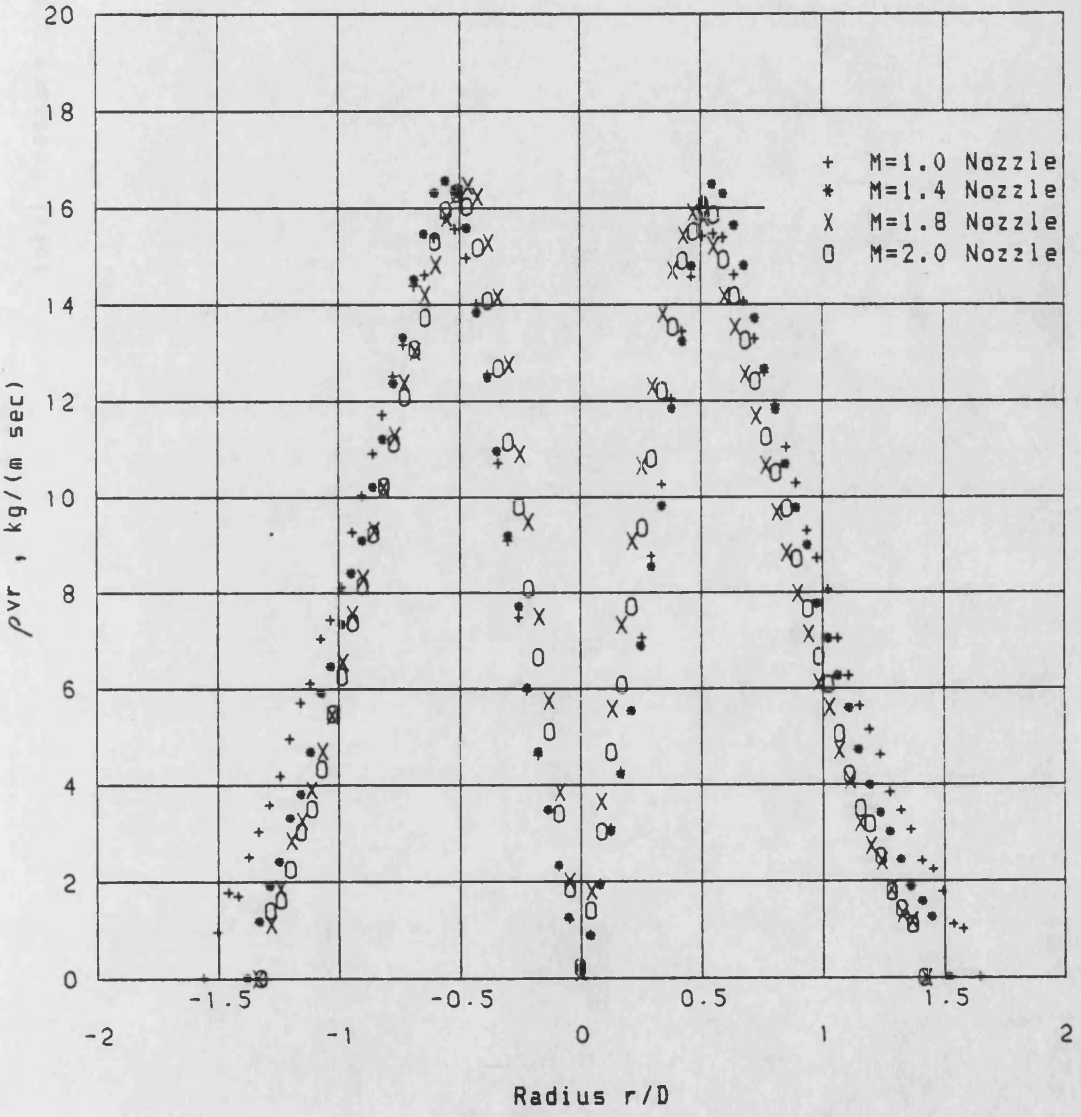

Figure 6.17 Mass Flow at x/D=6 for Plain Nozzles

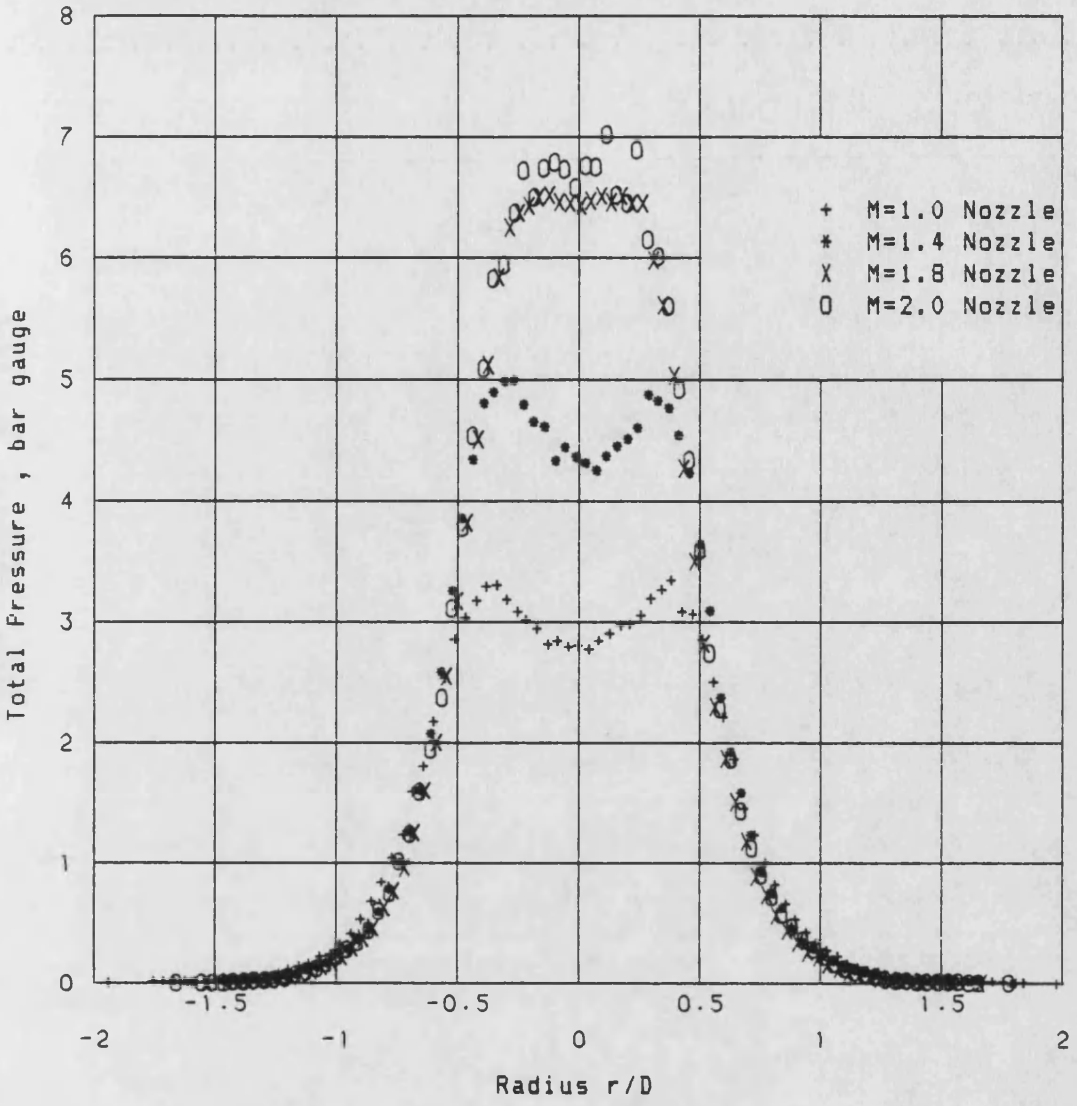

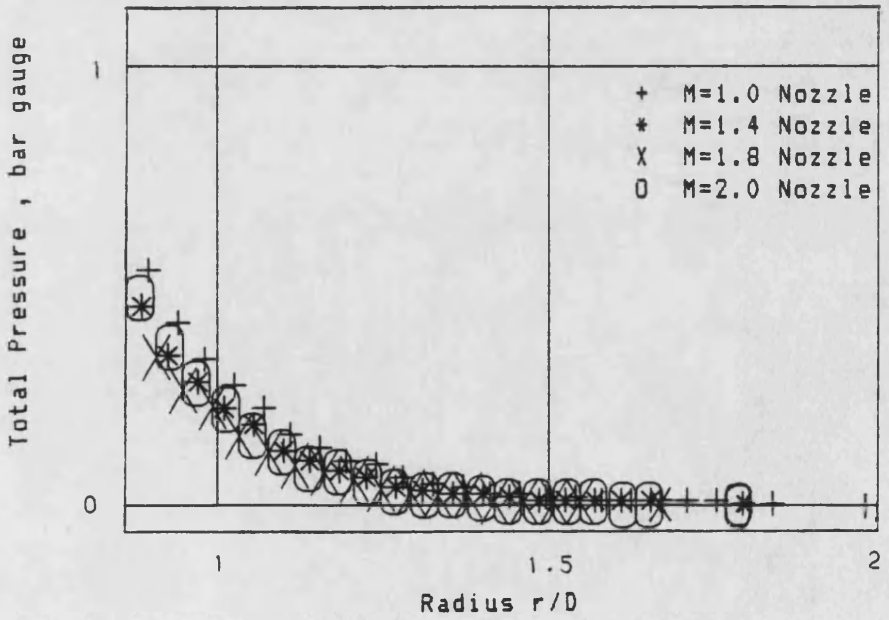

Figure 6.18 Total Pressure at x/D=8 for Plain Nozzles

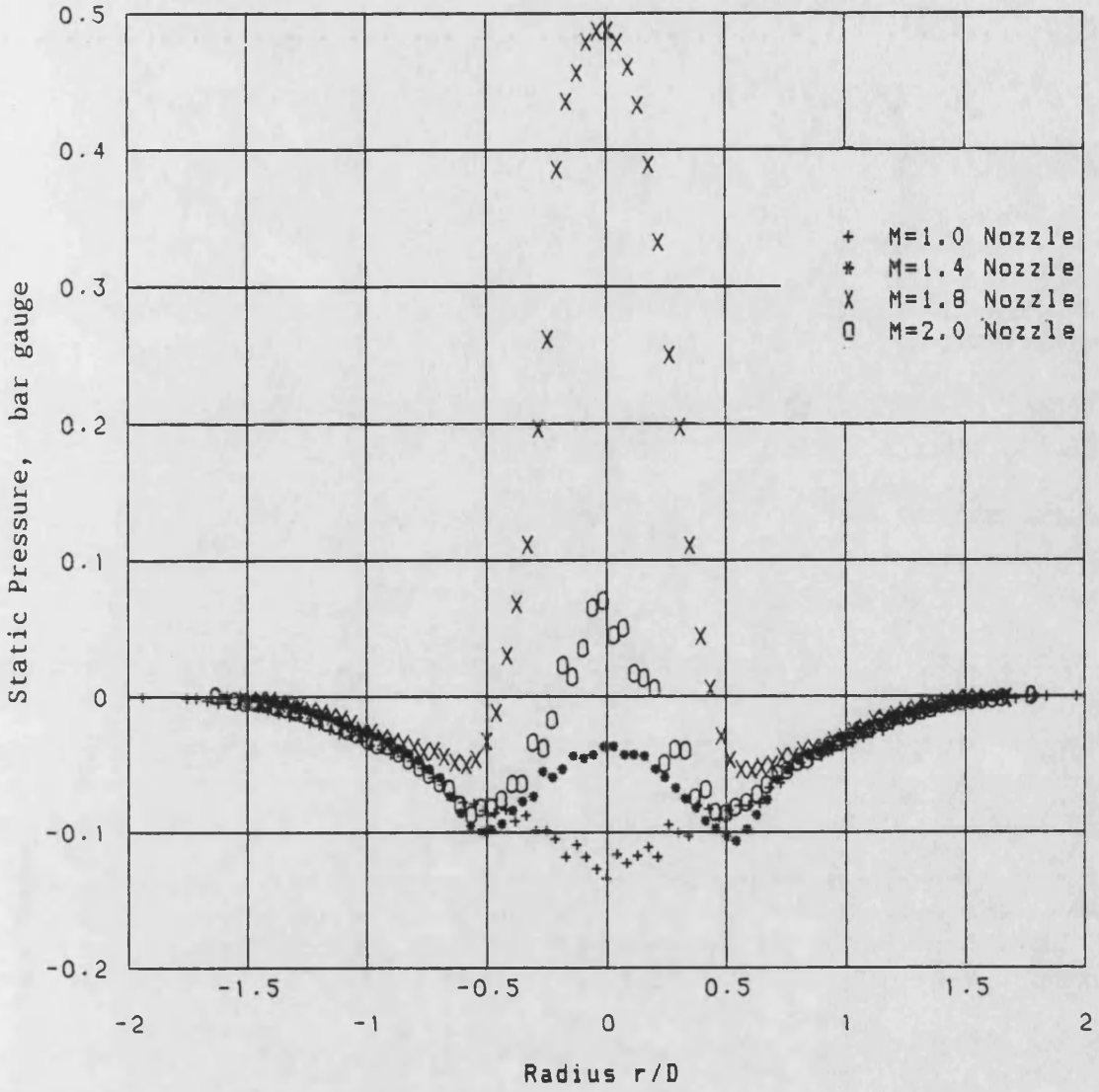

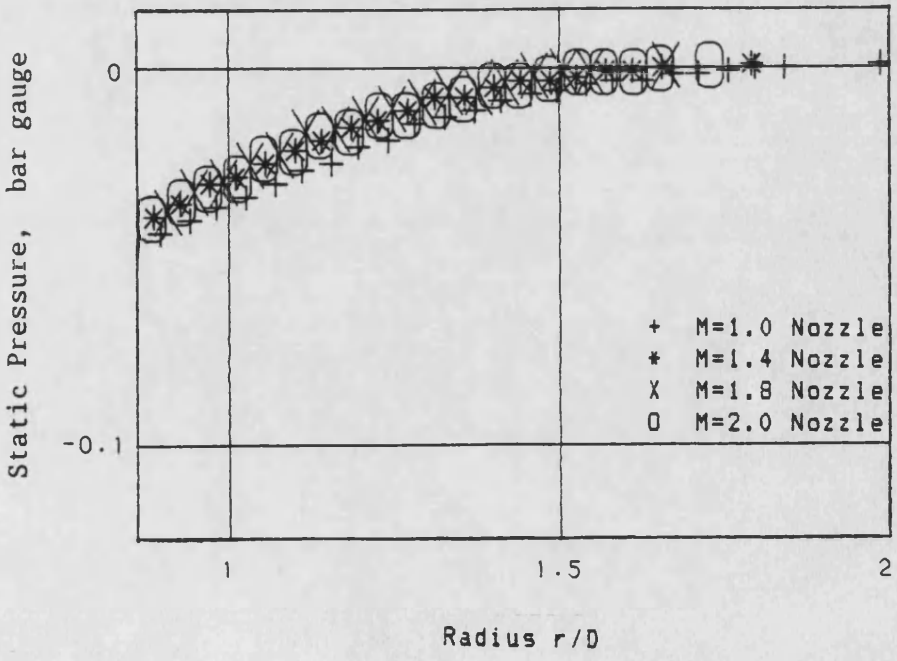

Figure 6.19 Static Pressure at x/D=8 for Plain Nozzles

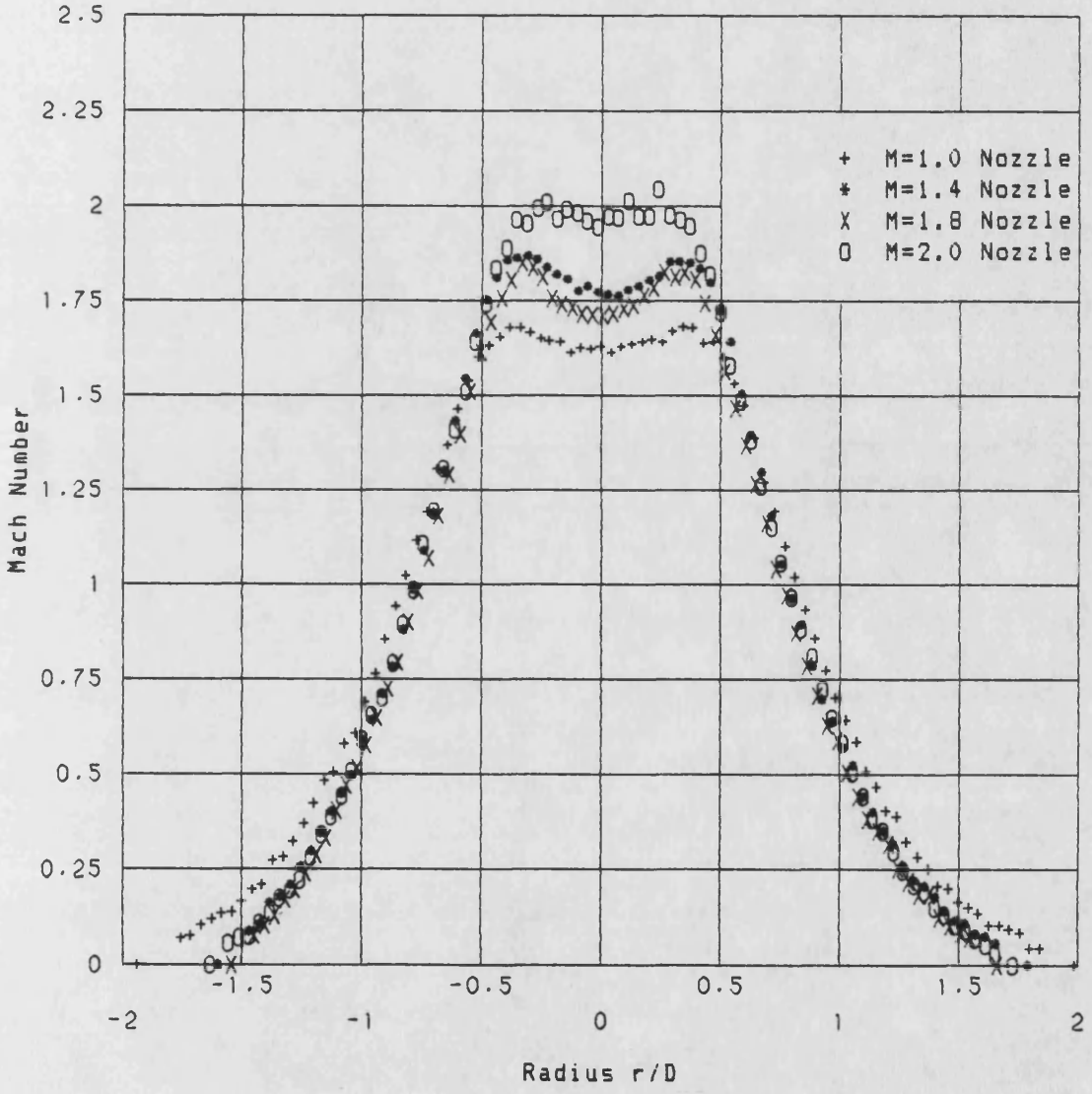

Figure 6.20 Mach Number at x/D=8 for Plain Nozzles

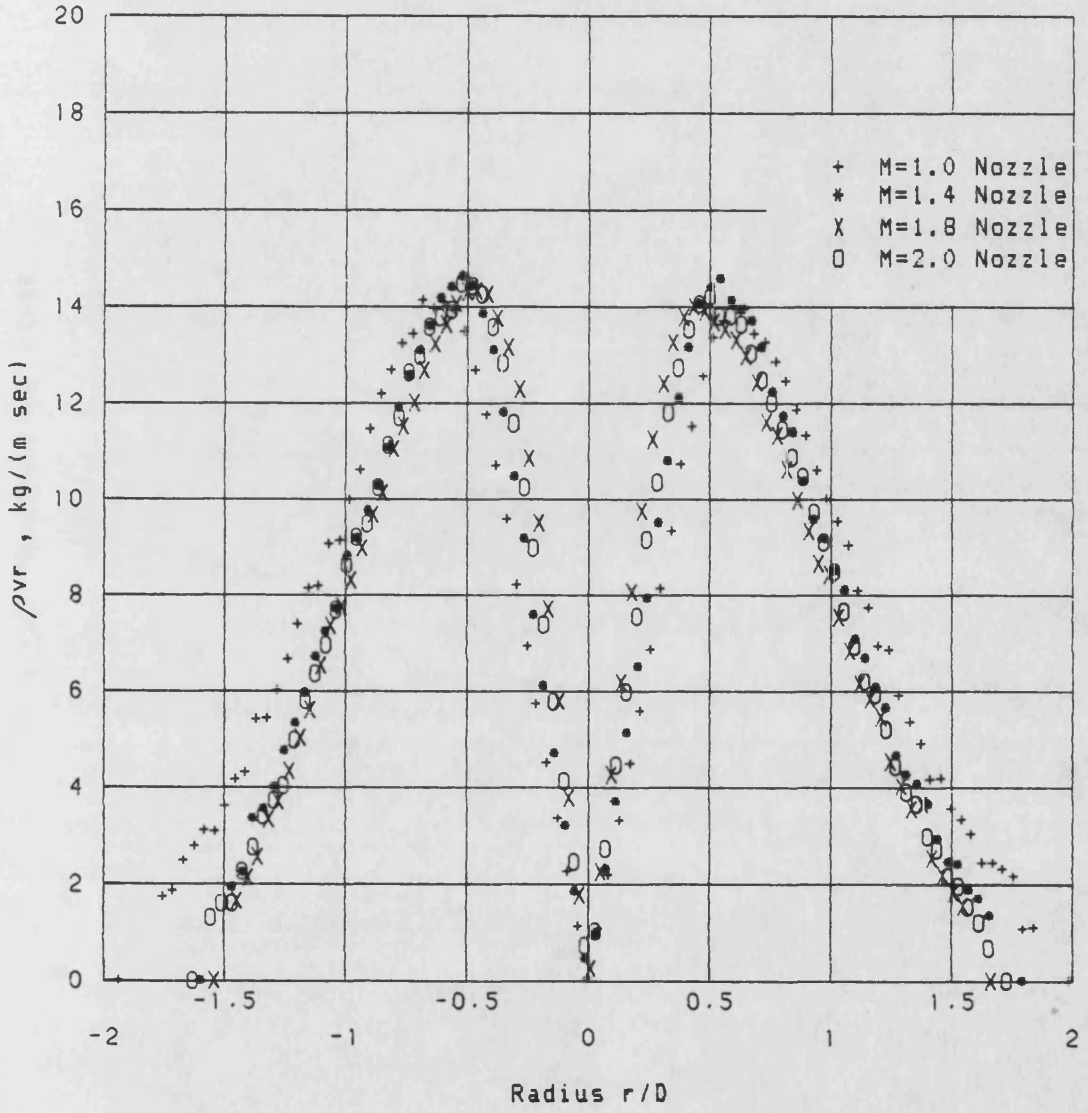

Figure 6.21 Mass Flow at x/D=8 for Plain Nozzles

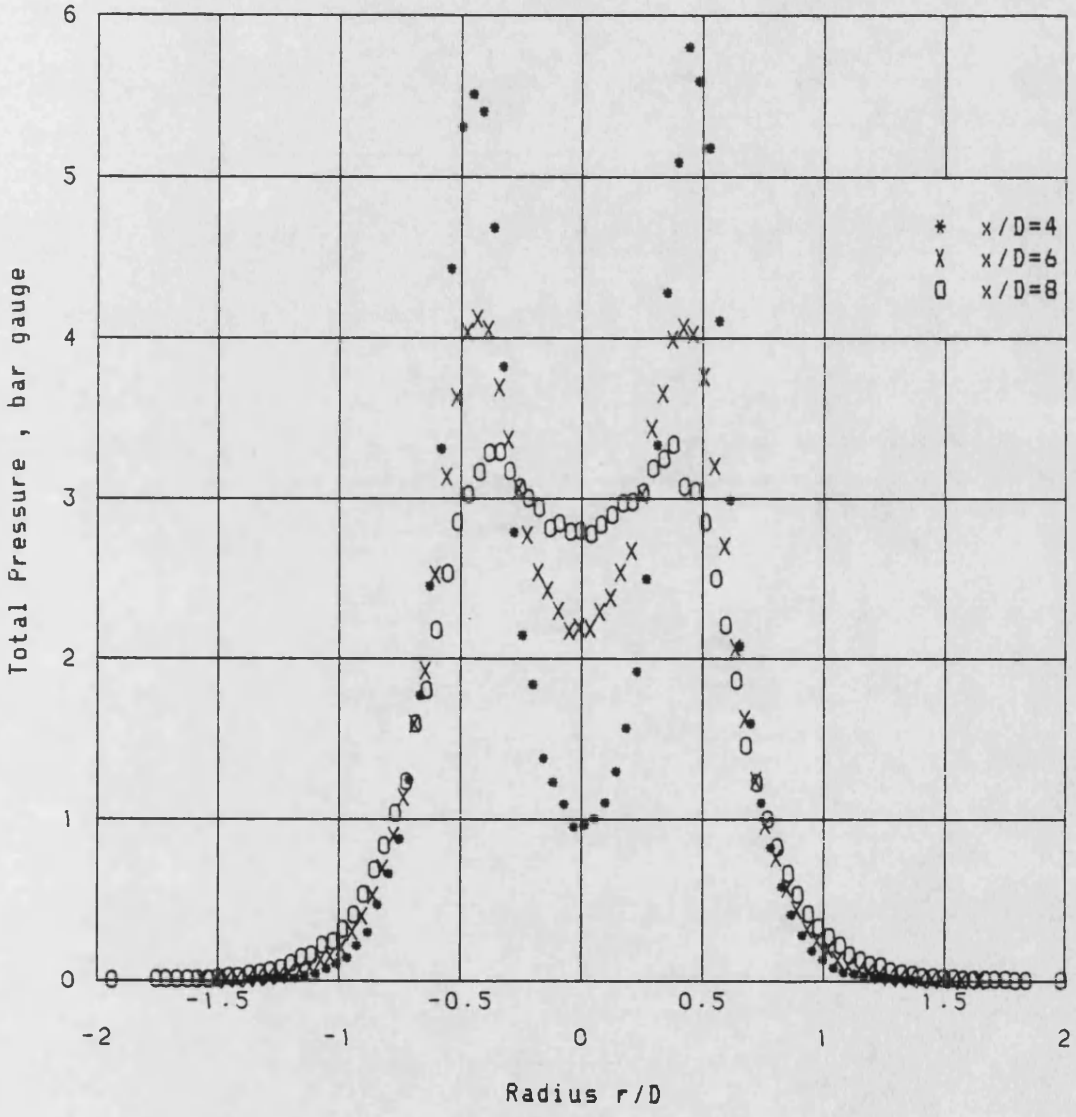

Figure 6.22 Axial variation of Total Pressure
for M=1.0 Plain Nozzles

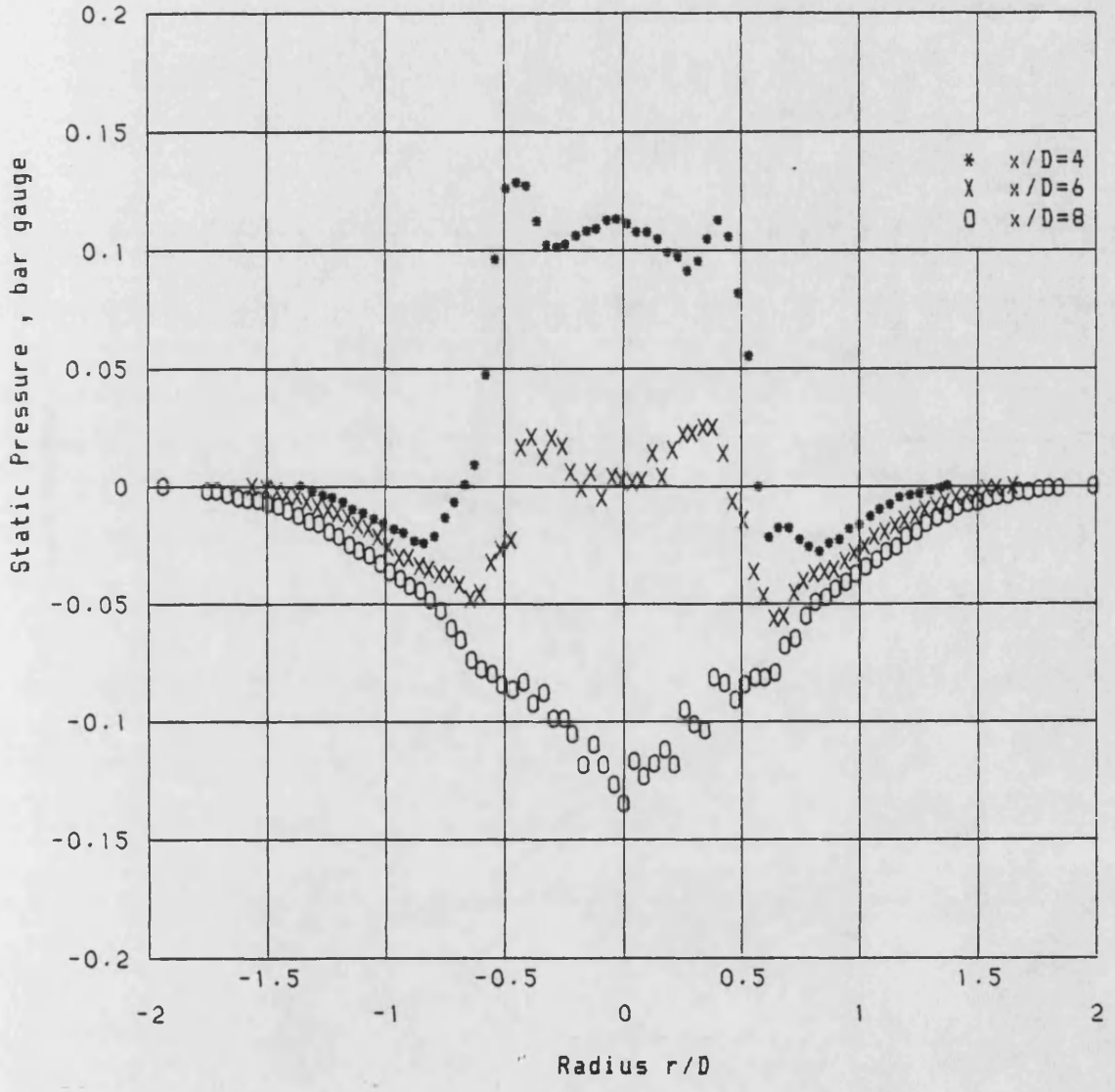

Figure 6.23 Axial variation of Static Pressure
for M=1.0 Plain Nozzles

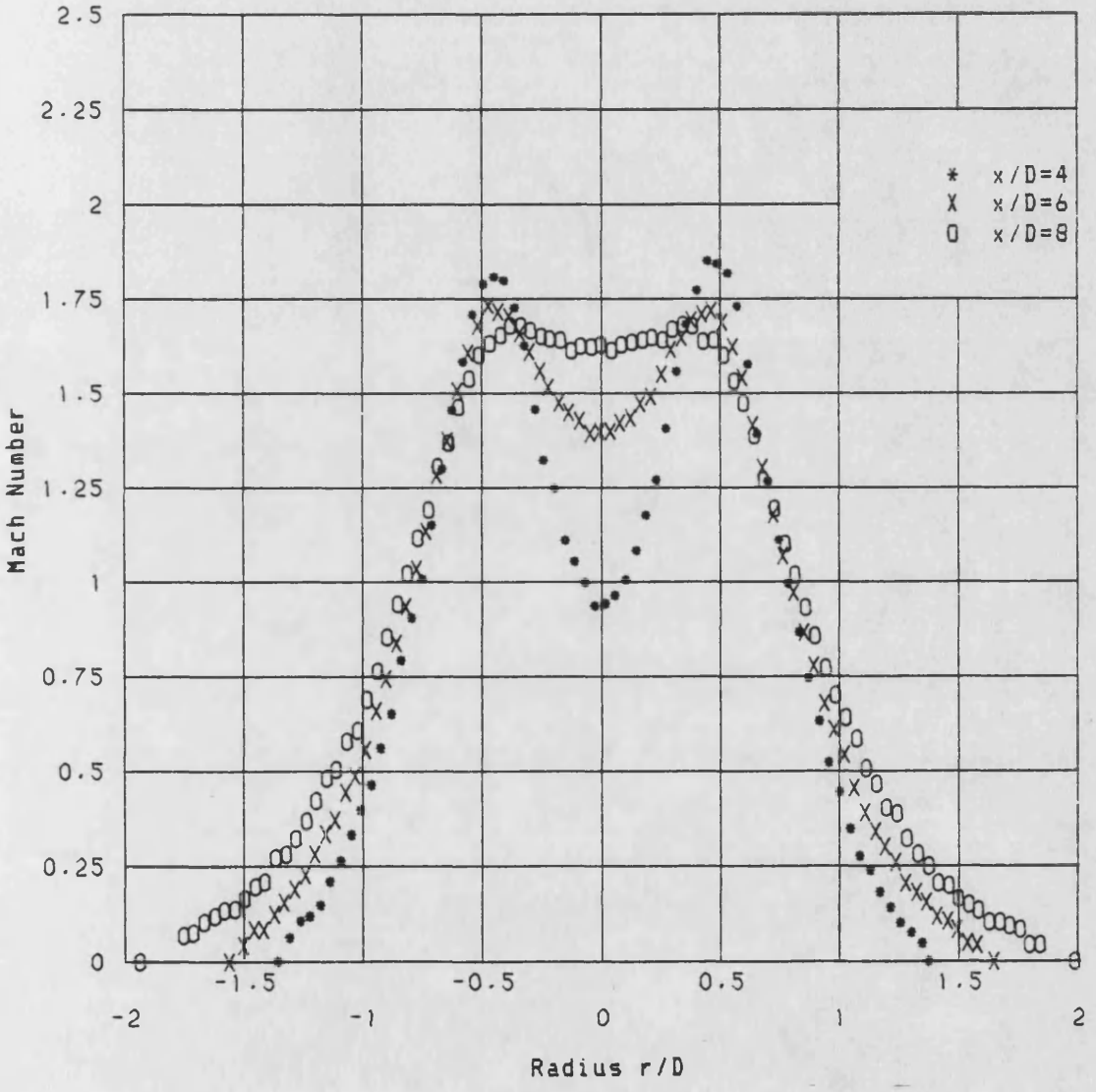

Figure 6.24 Axial variation of Mach Number
for M=1.0 Plain Nozzles

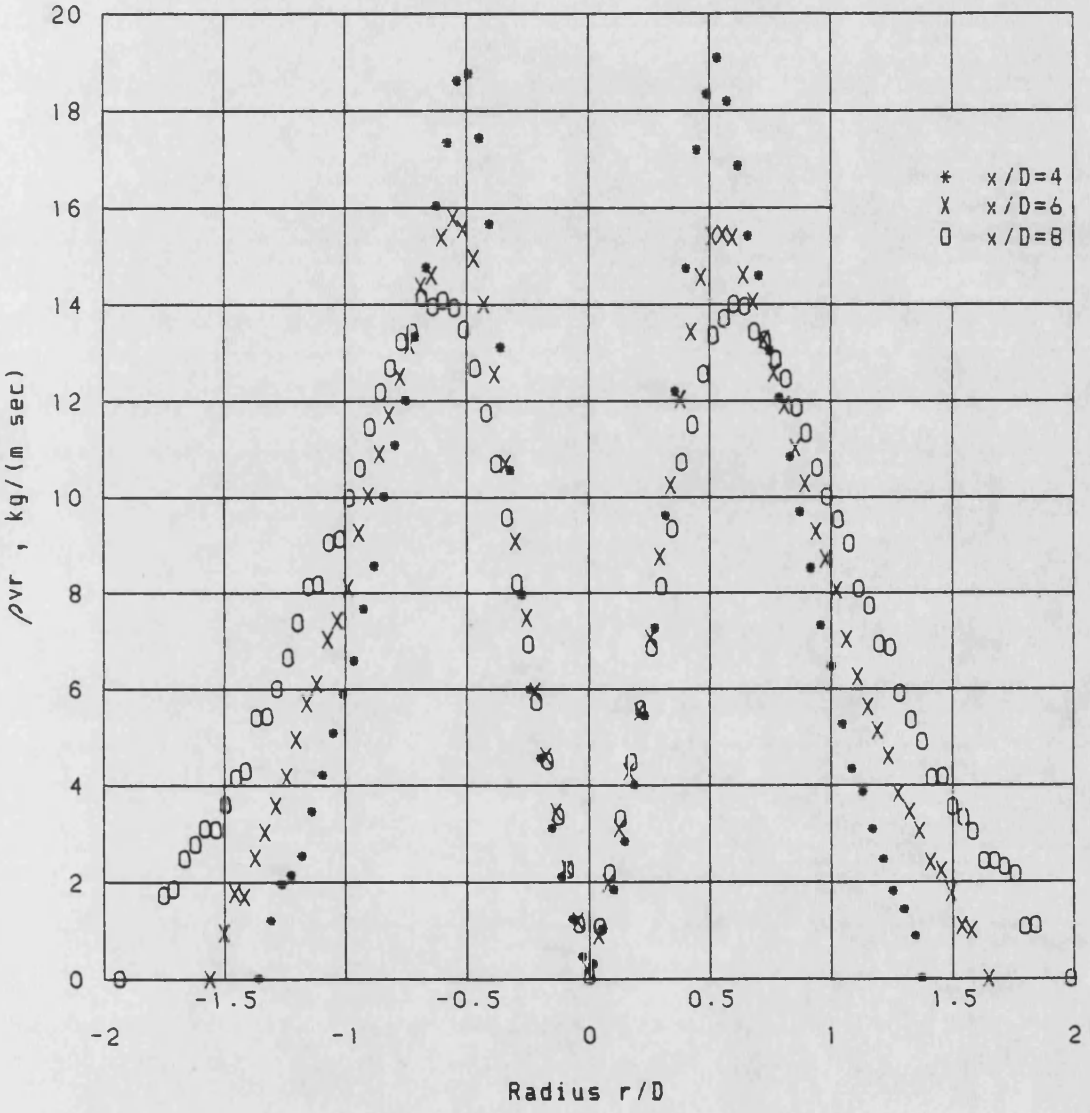

Figure 6.25 Axial variation of Mass Flow
for M=1.0 Plain Nozzles

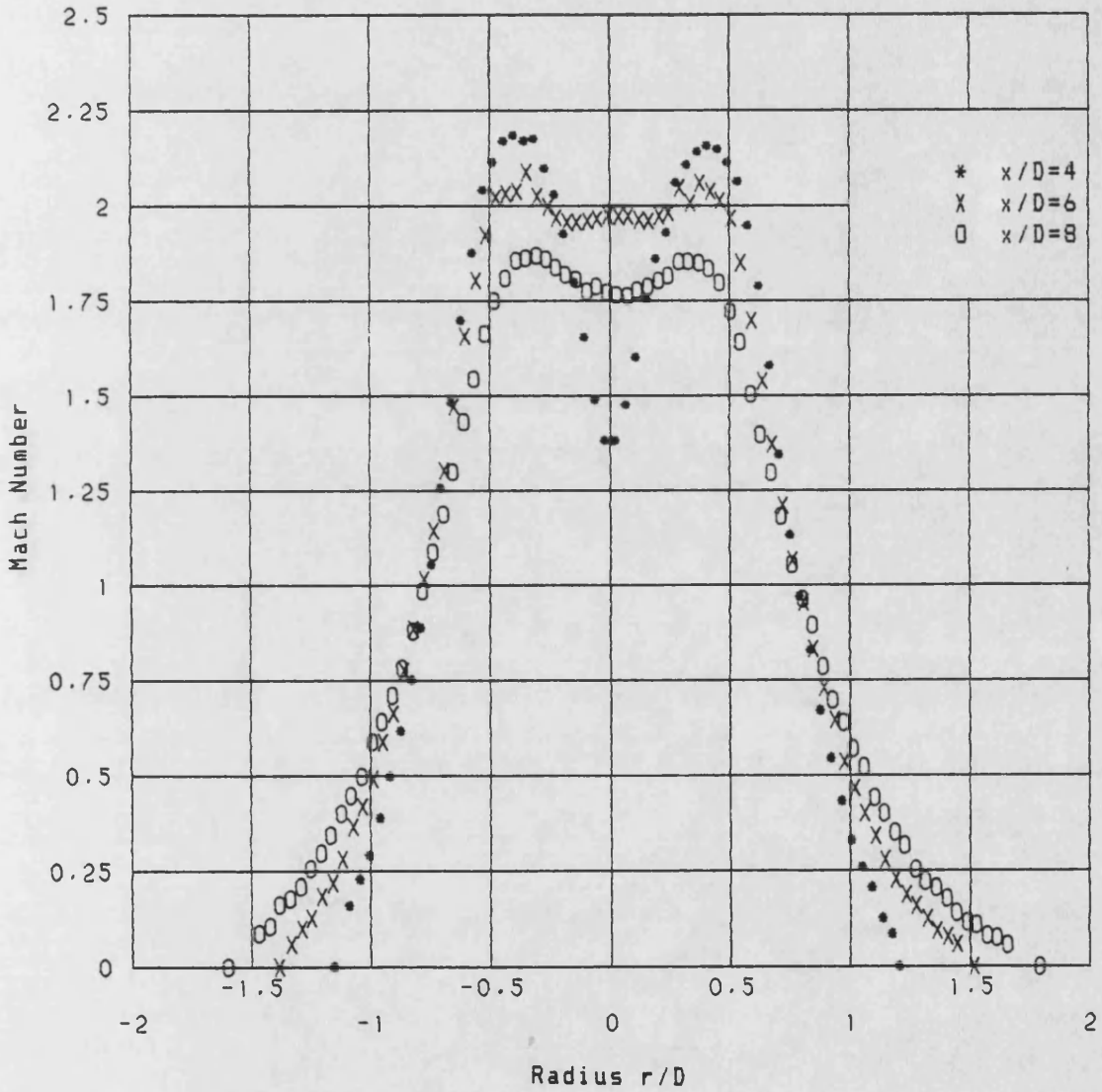

Figure 6.26 Axial variation of Mach Number
for M=1.4 Plain Nozzles

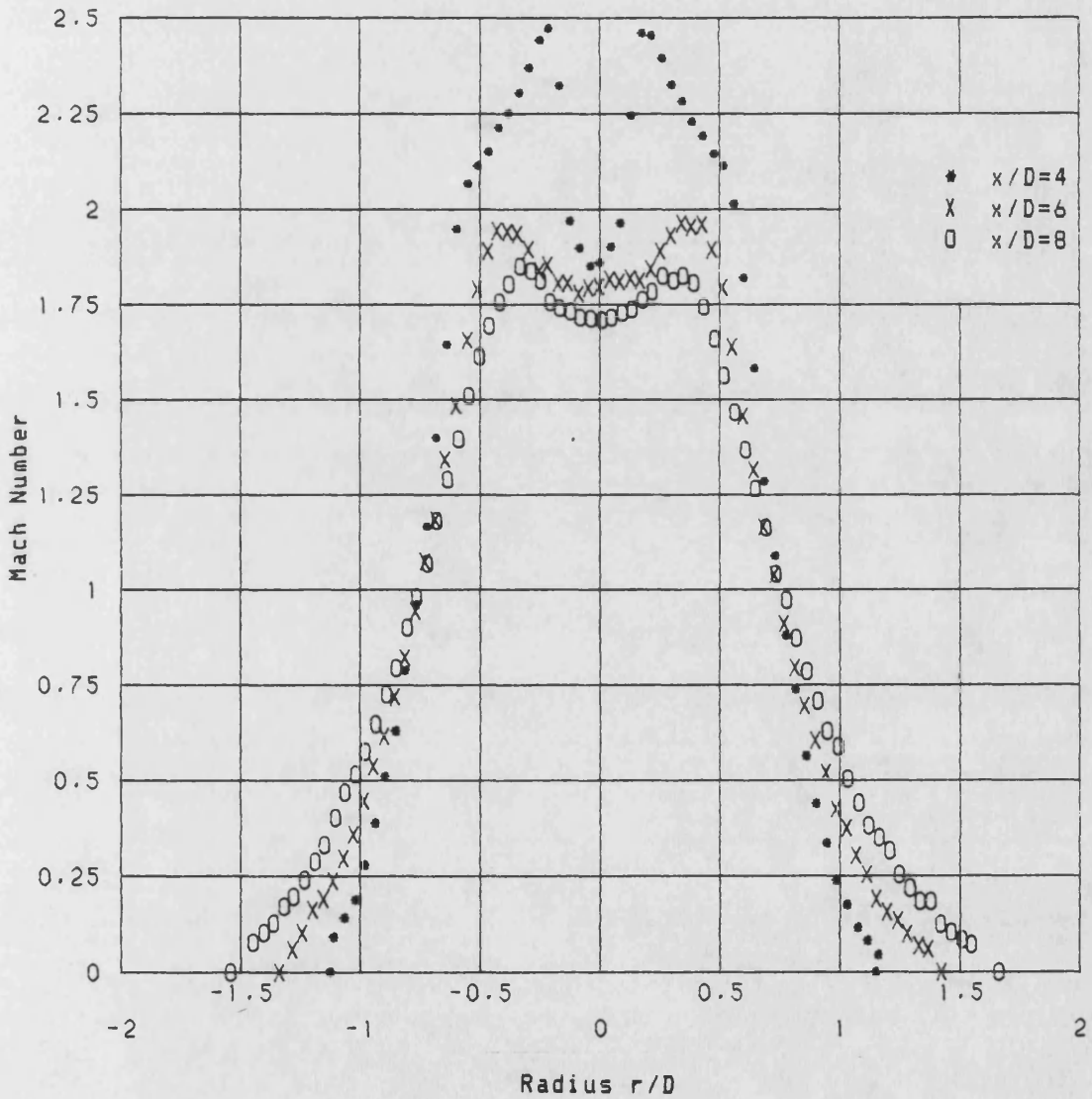

Figure 6.27 Axial variation of Mach Number
for M=1.8 Plain Nozzles

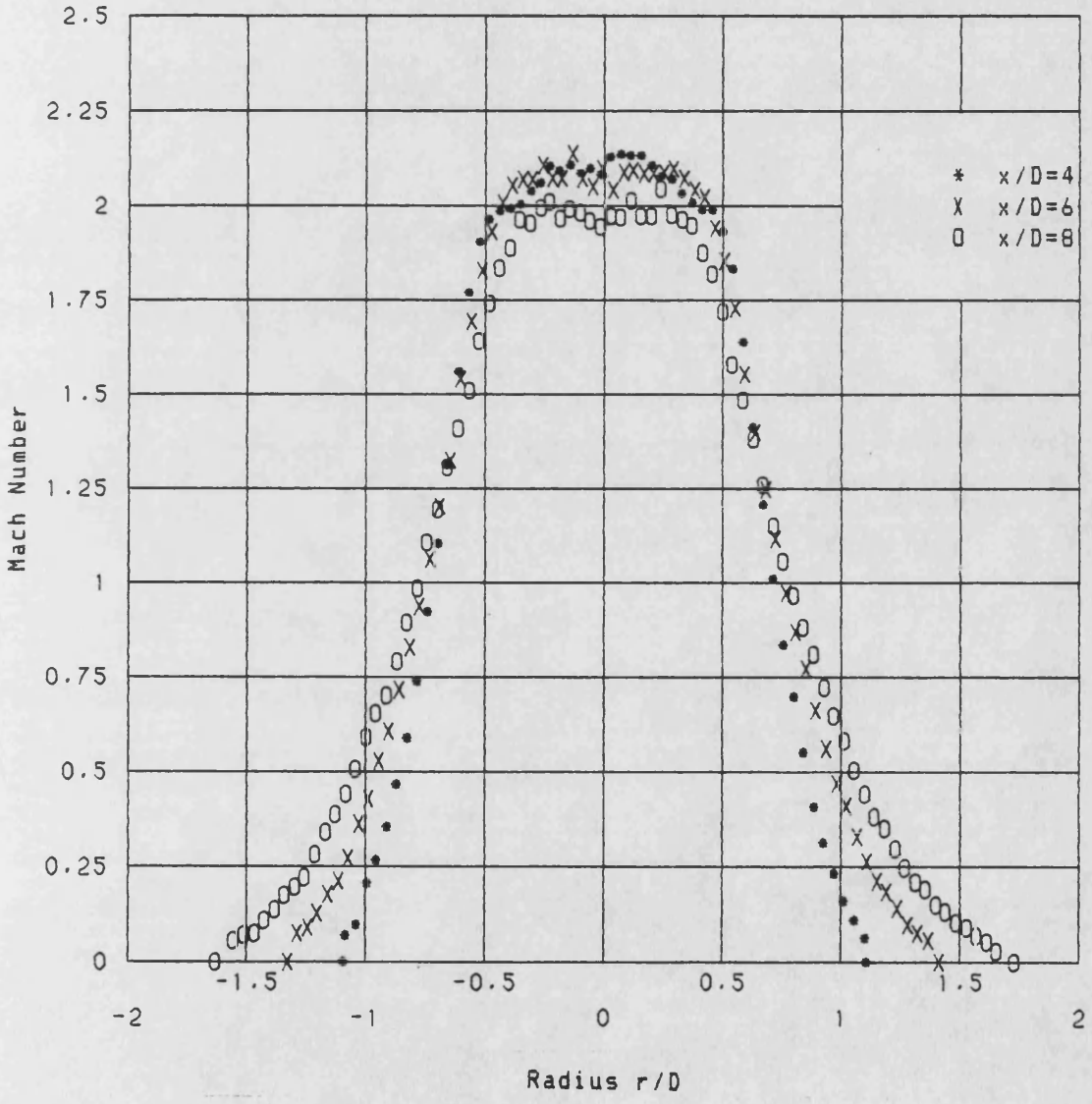

Figure 6.28 Axial variation of Mach Number
for M=2.0 Plain Nozzle

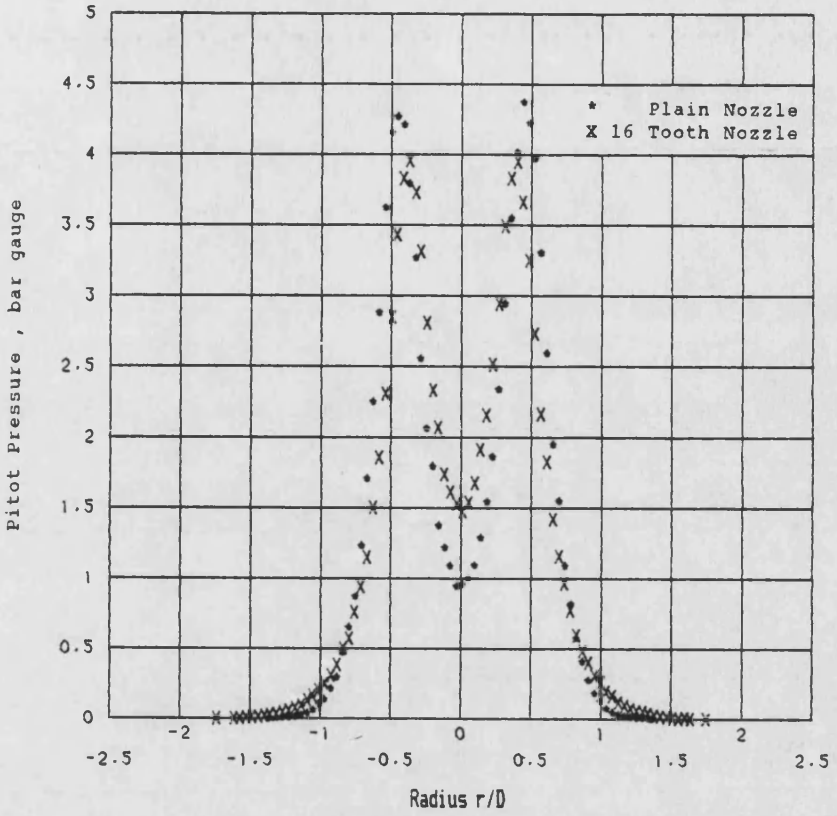

Figure 6.29 Pitot Pressure at x/D=4 for M=1.0
16 Tooth and Plain Nozzles

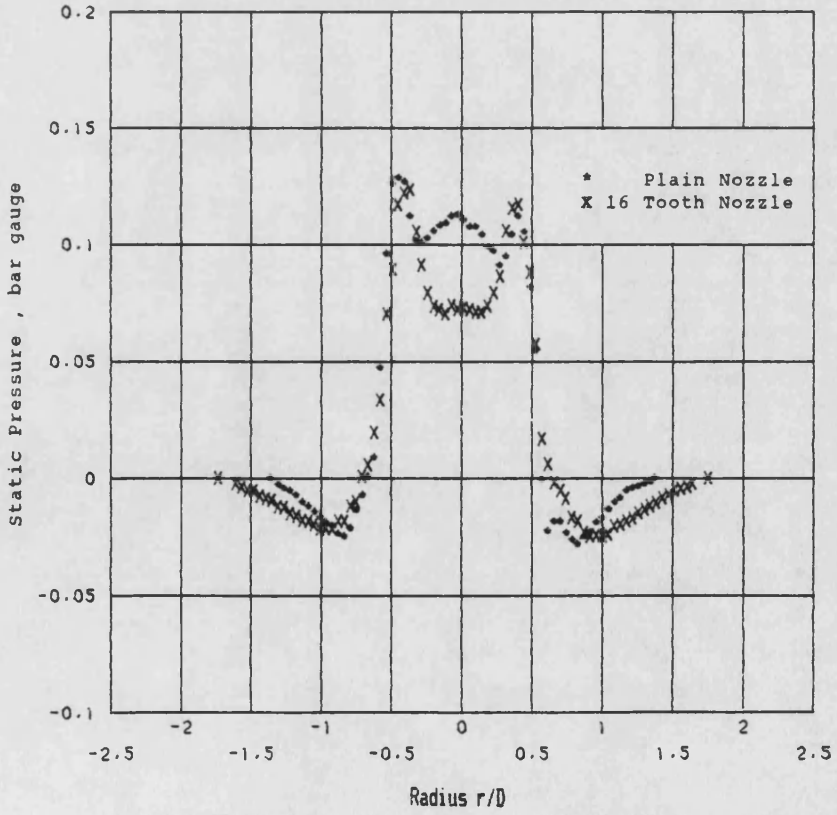

Figure 6.30 Static Pressure at x/D=4 for M=1.0
16 Tooth and Plain Nozzles

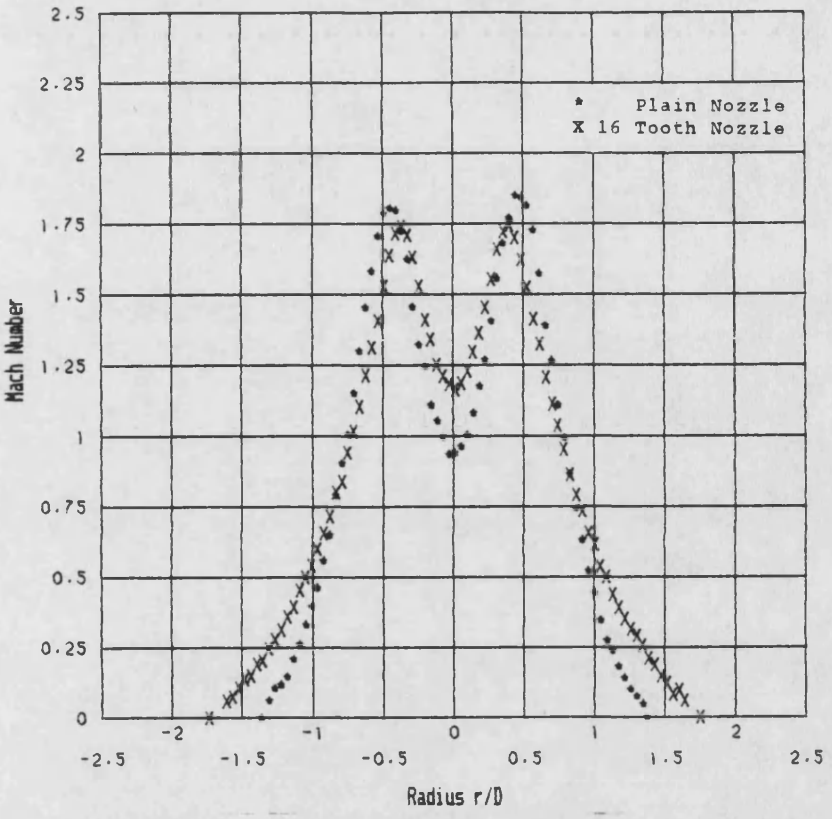

Figure 6.31 Mach Number at x/D=4 for M=1.0
16 Tooth and Plain Nozzles

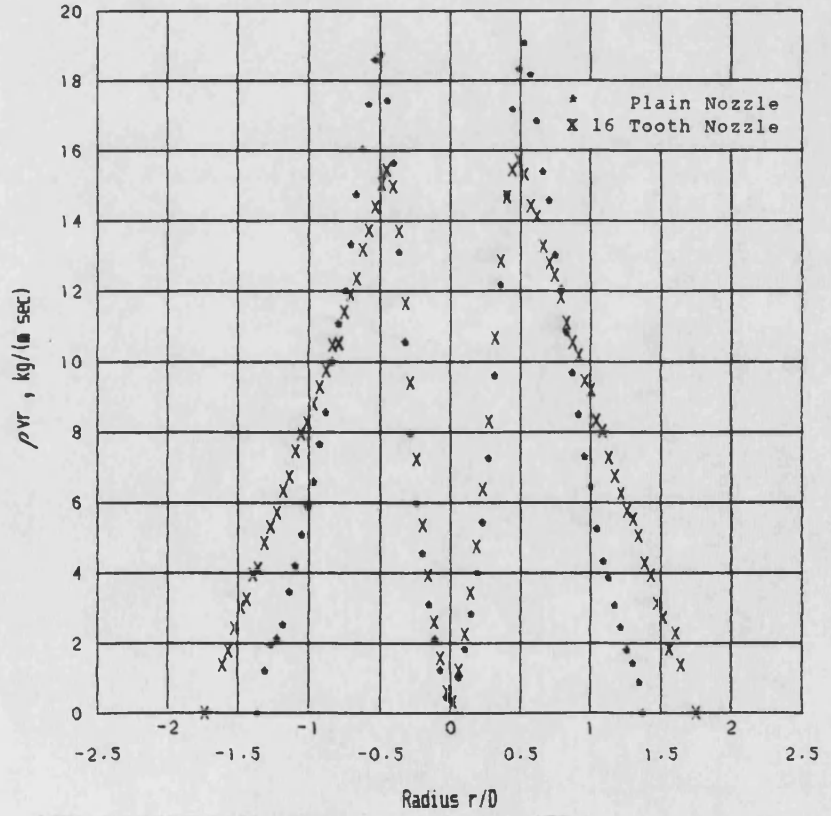

Figure 6.32 Mass Flow at x/D=4 for M=1.0
16 Tooth and Plain Nozzles

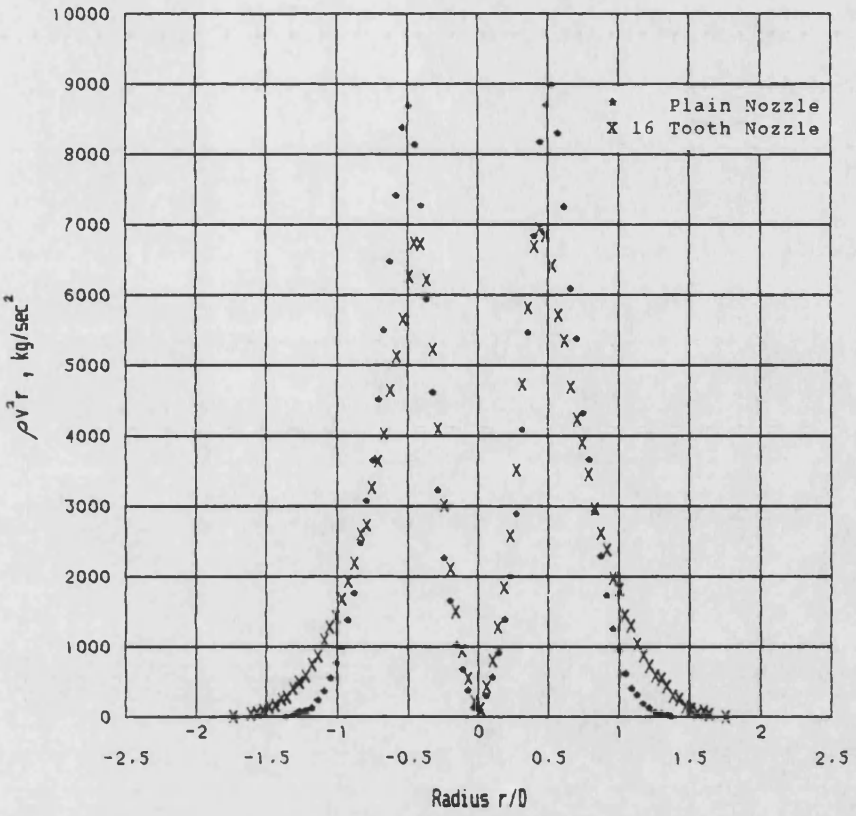

Figure 6.33 Momentum Flux at x/D=4 for M=1.0
16 Tooth and Plain Nozzles

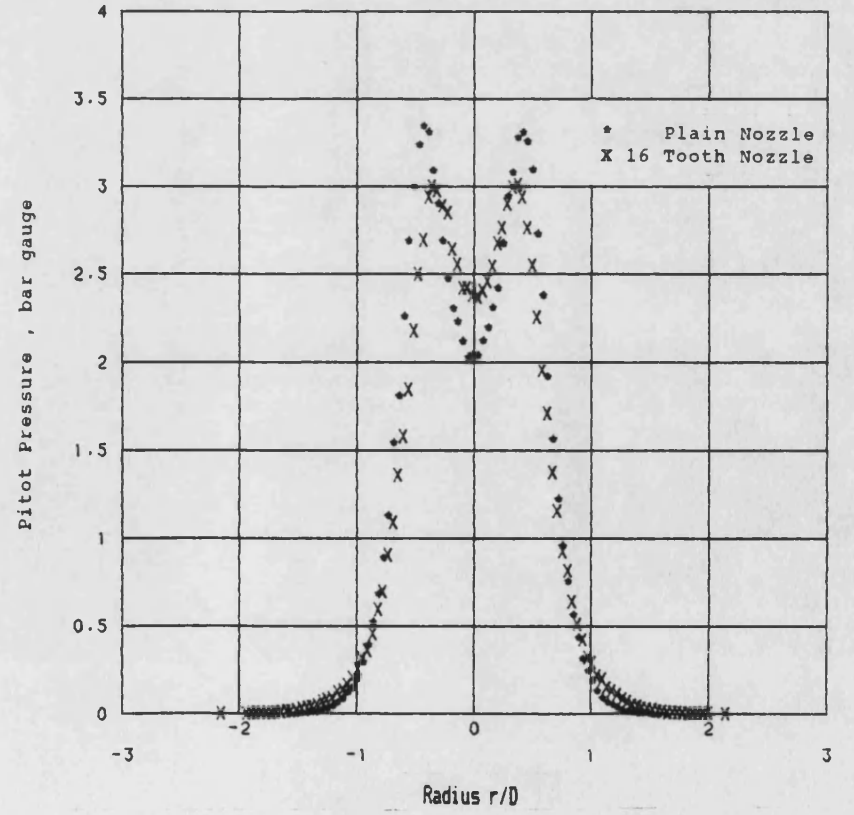

Figure 6.34 Pitot Pressure at x/D=6 for M=1.0
16 Tooth and Plain Nozzles

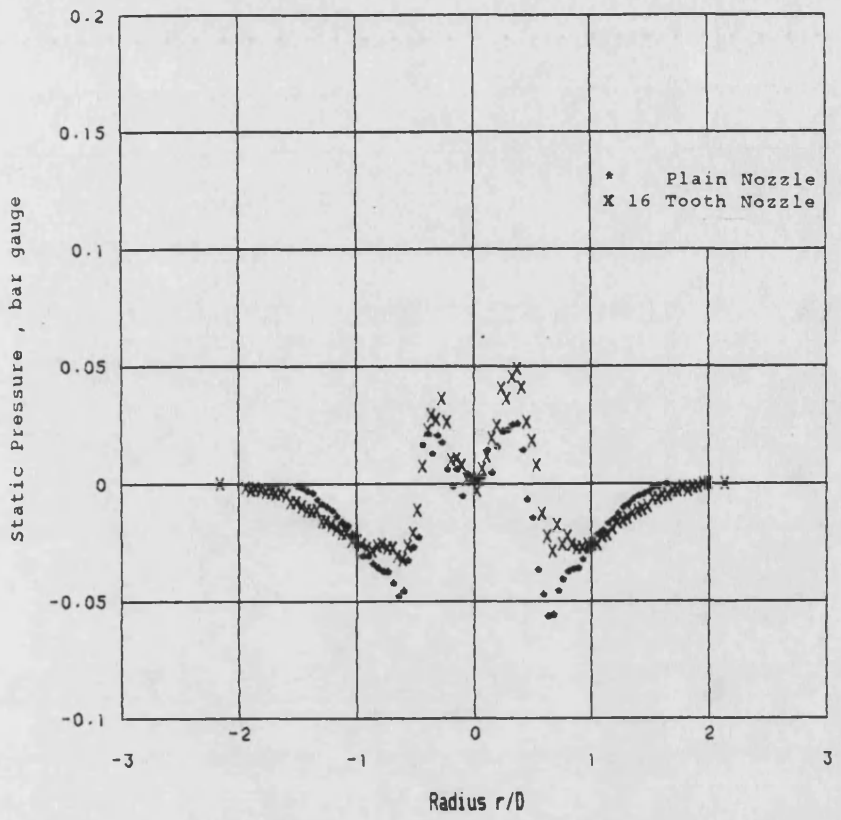

Figure 6.35 Static Pressure at x/D=6 for M=1.0
16 Tooth and Plain Nozzles

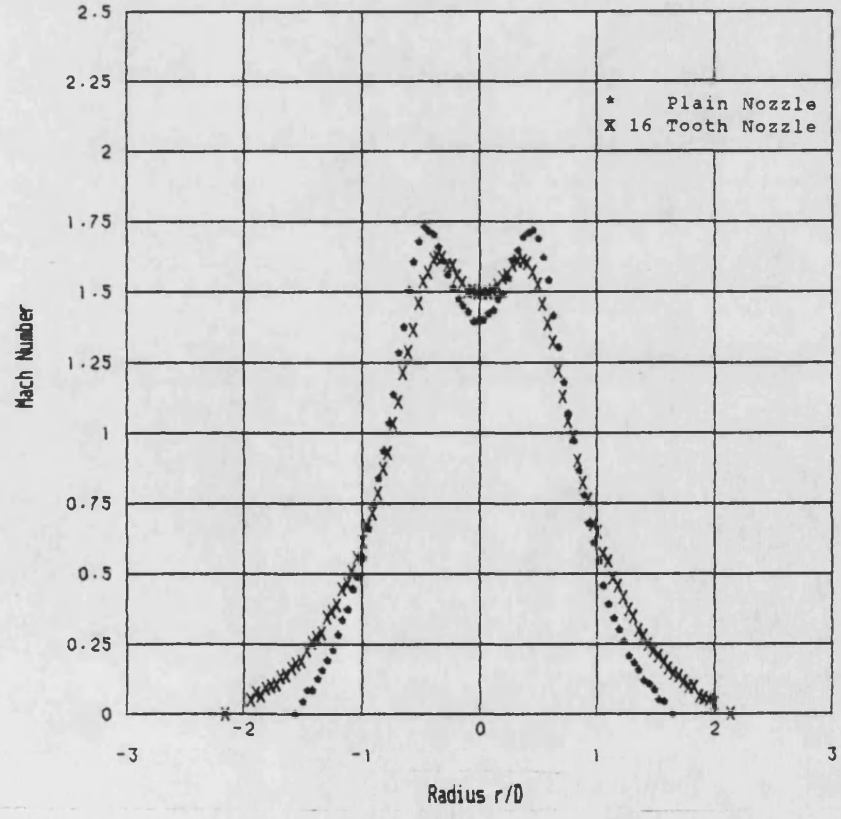

Figure 6.36 Mach Number at x/D=6 for M=1.0
16 Tooth and Plain Nozzles

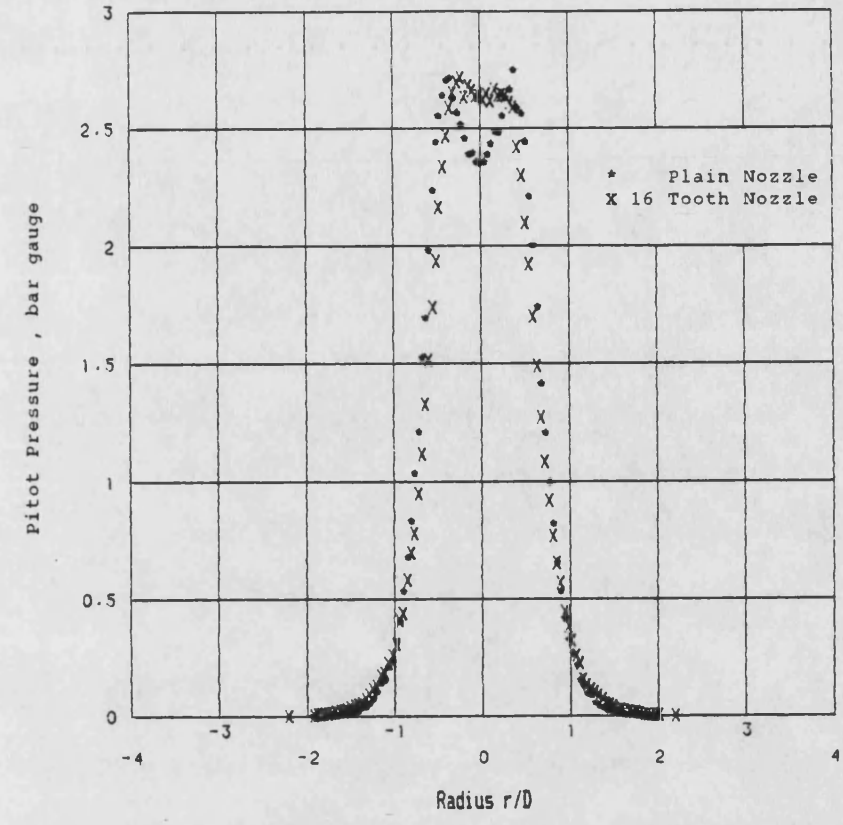

Figure 6.37 Pitot Pressure at x/D=8 for M=1.0
16 Tooth and Plain Nozzles

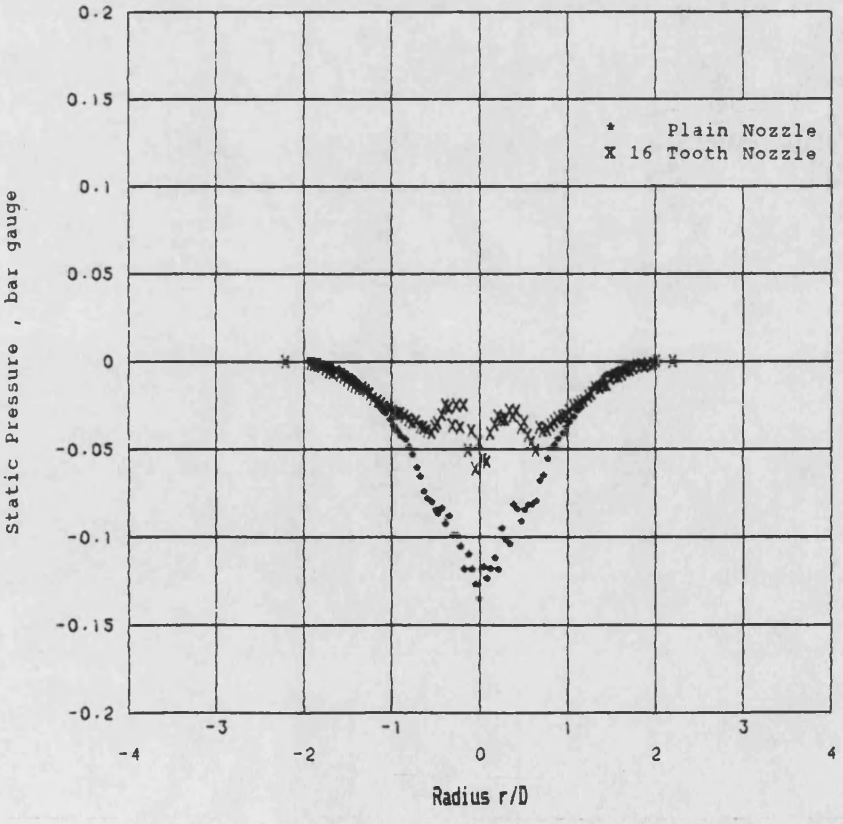

Figure 6.38 Static Pressure at x/D=8 for M=1.0
16 Tooth and Plain Nozzles

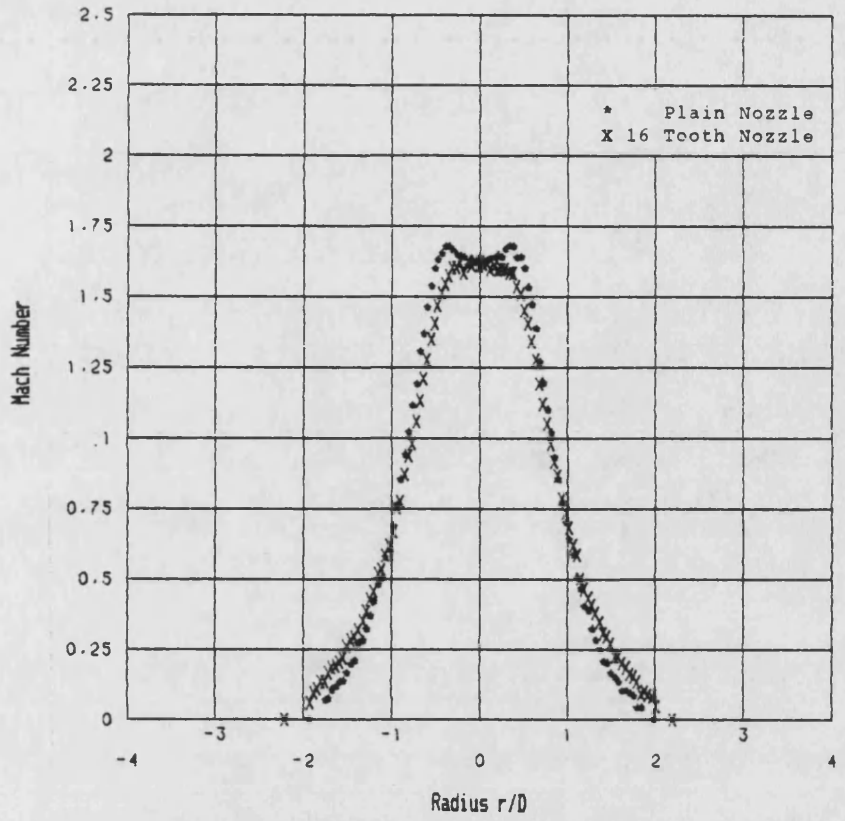

Figure 6.39 Mach Number at x/D=8 for M=1.0
16 Tooth and Plain Nozzles

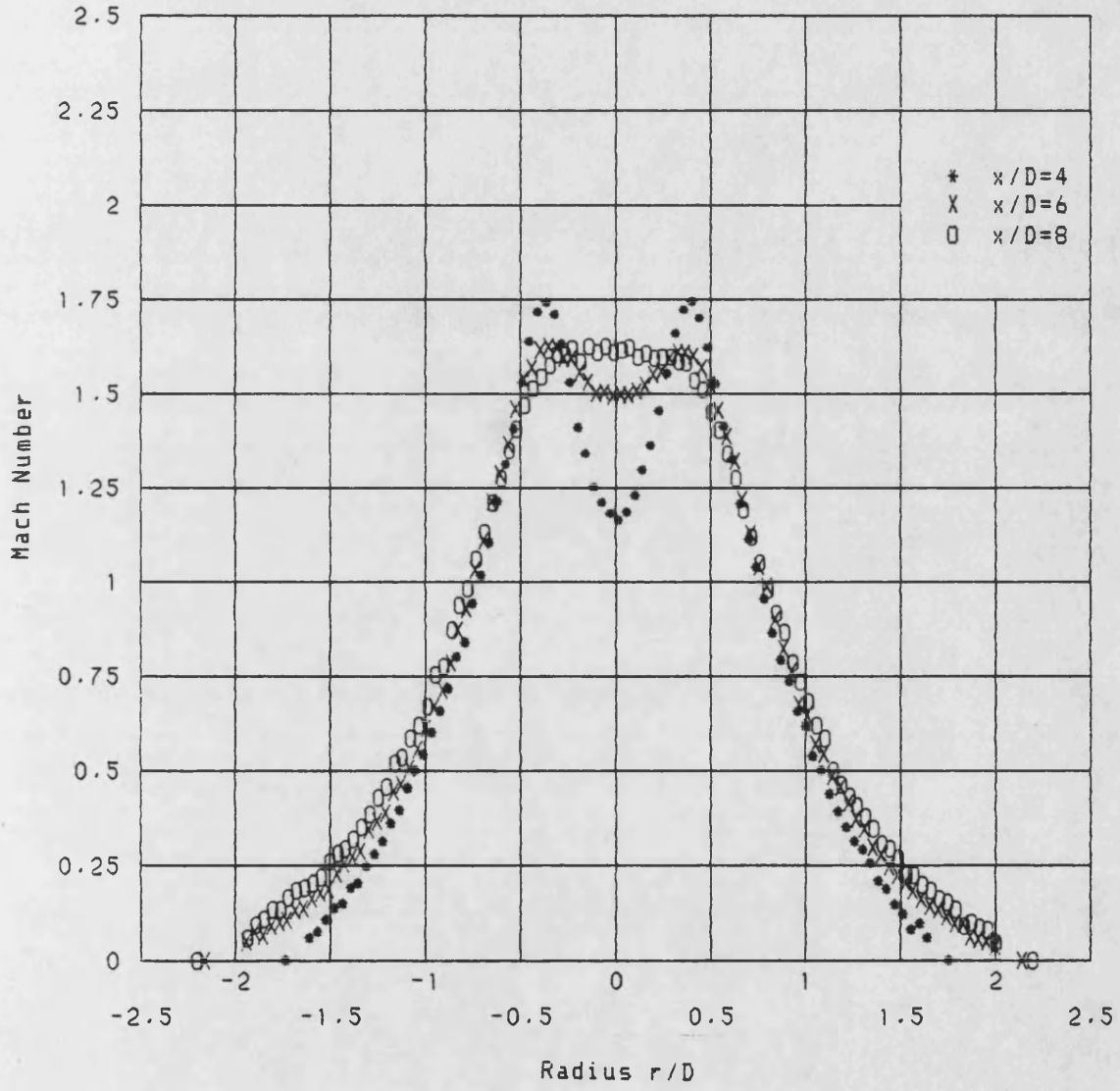

Figure 6.40 Axial variation of Mach Number for M=1.0 16 Tooth Nozzle

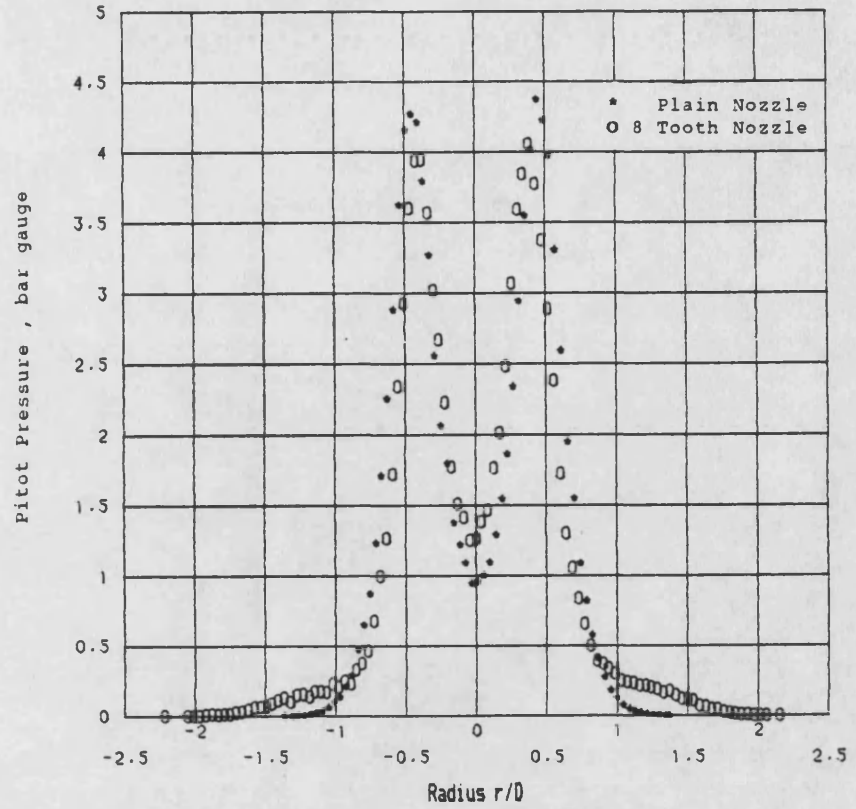

Figure 6.41 Pitot Pressure at x/D=4 for M=1.0
8 Tooth and Plain Nozzles

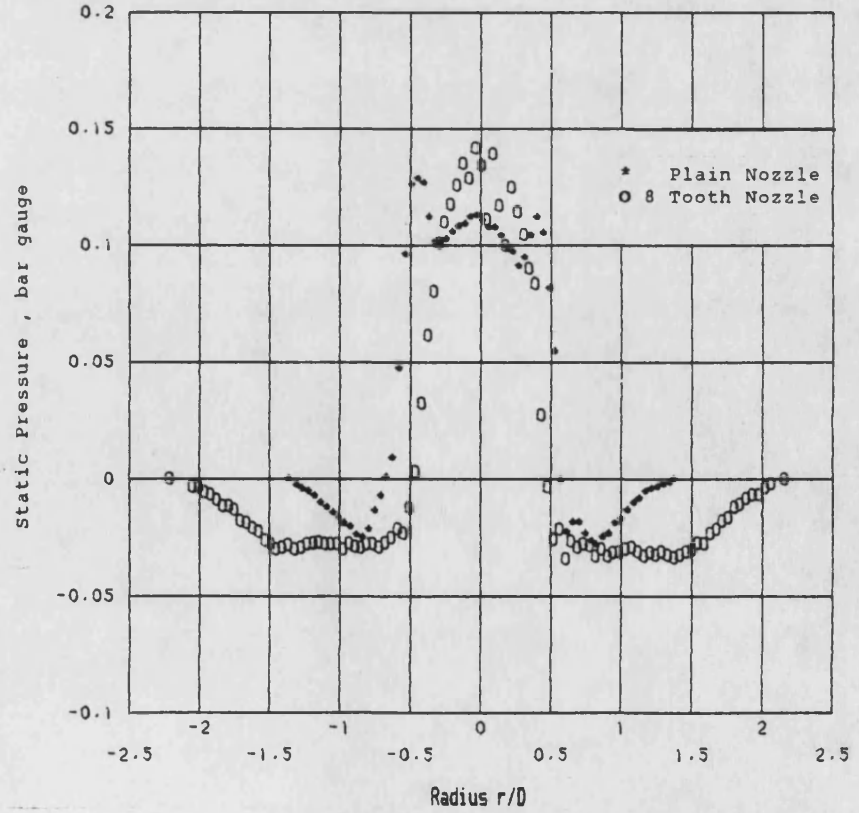

Figure 6.42 Static Pressure at x/D=4 for M=1.0
8 Tooth and Plain Nozzles

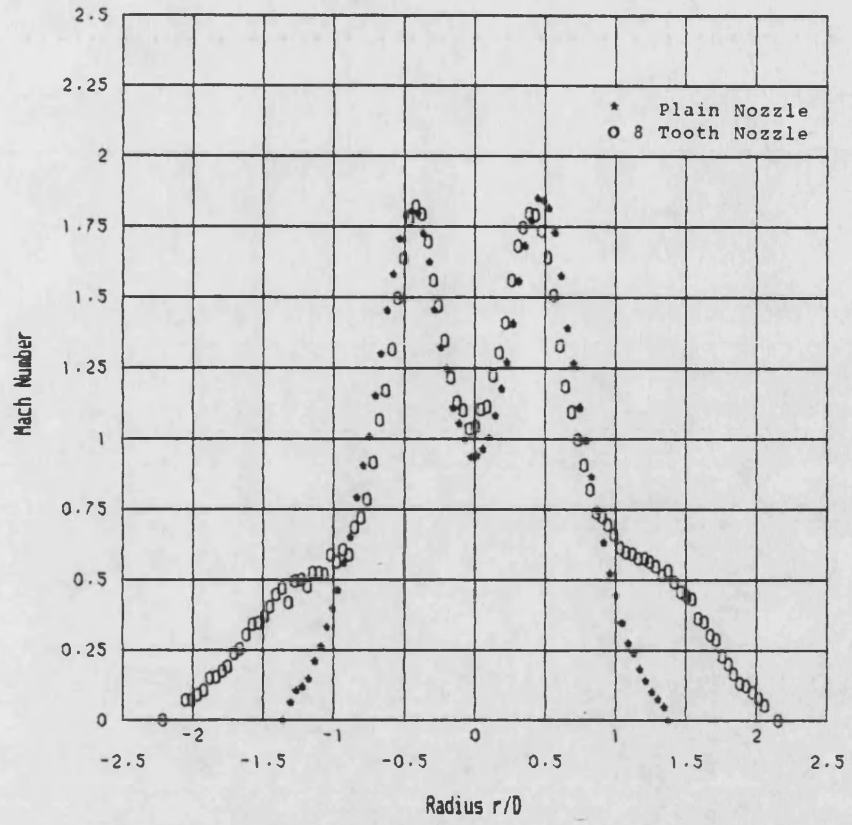

Figure 6.43 Mach Number at x/D=4 for M=1.0
8 Tooth and Plain Nozzles

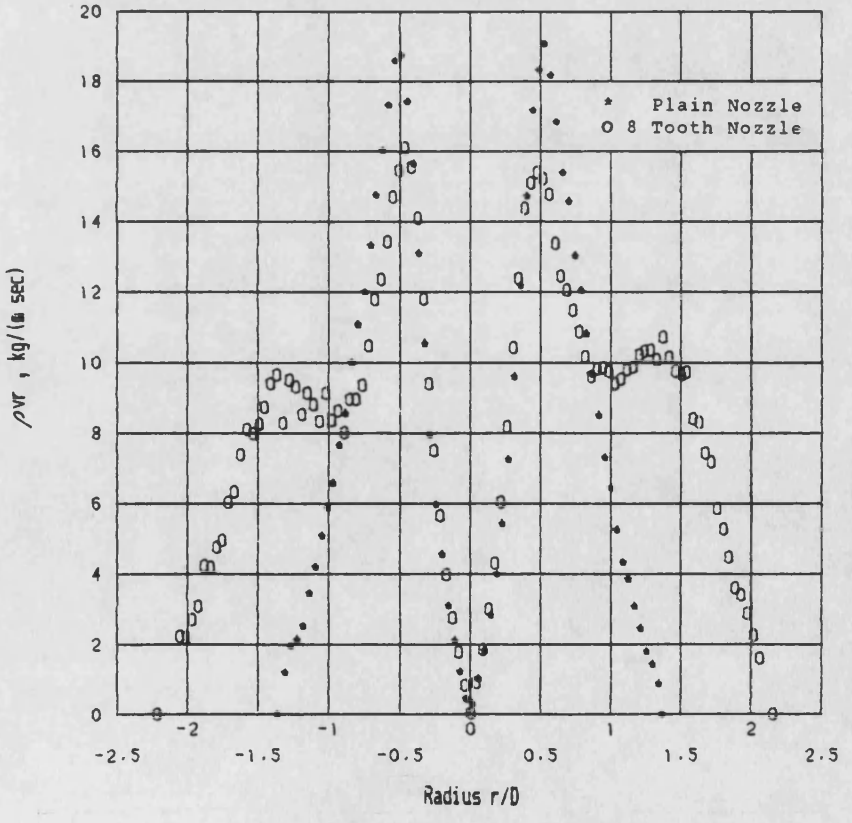

Figure 6.44 Mass Flow at x/D=4 for M=1.0
8 Tooth and Plain Nozzles

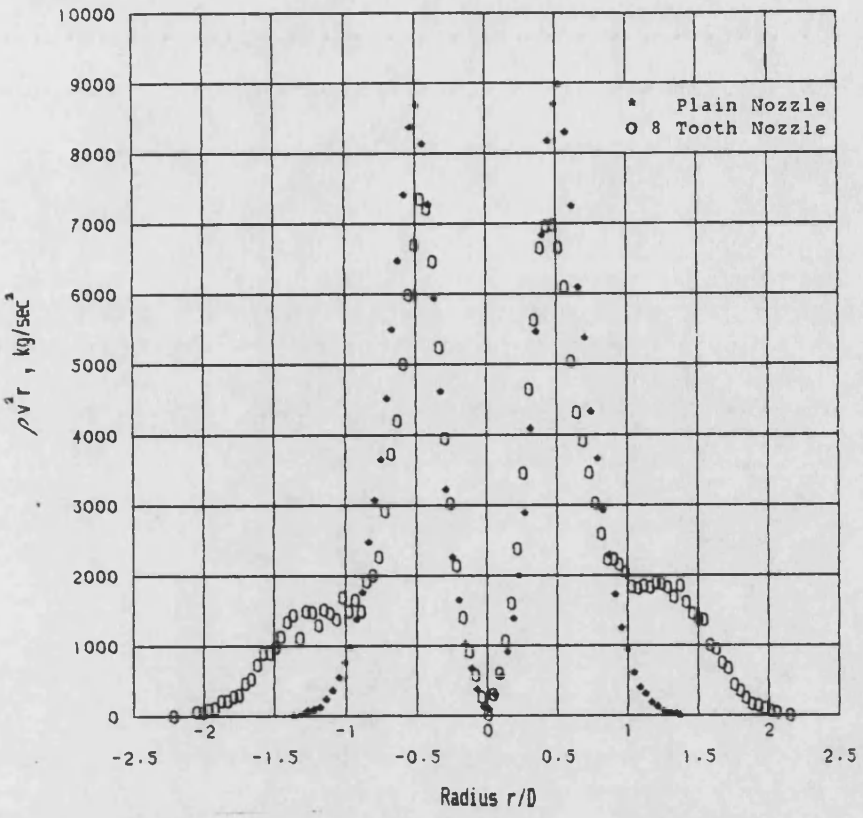

Figure 6.45 Momentum Flux at x/D=4 for M=1.0
8 Tooth and Plain Nozzles

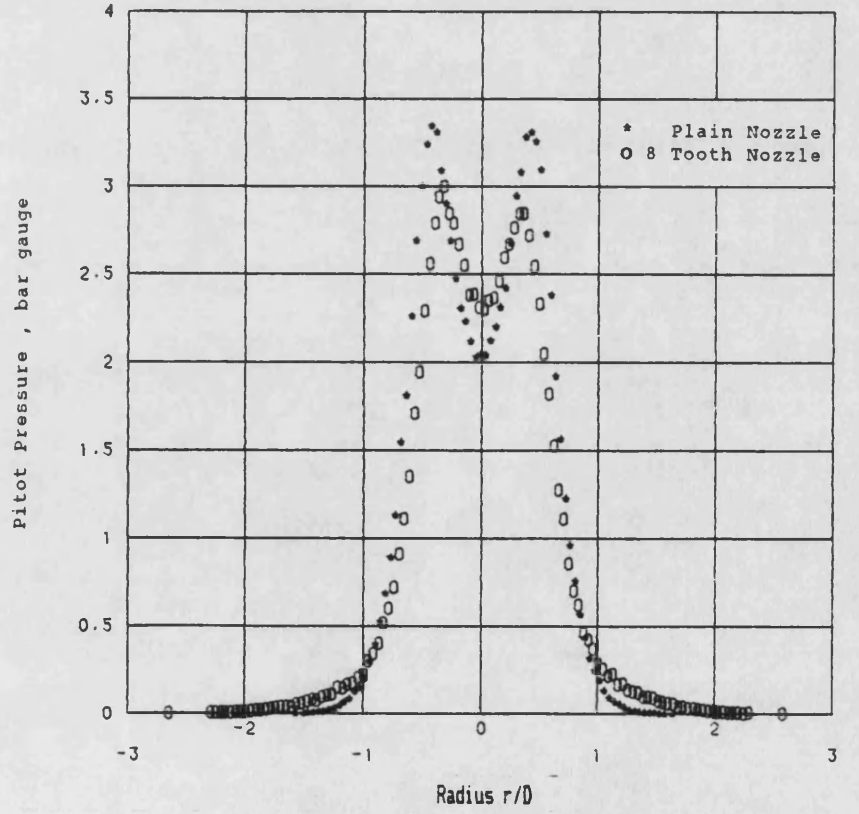

Figure 6.46 Pitot Pressure at x/D=6 for M=1.0
8 Tooth and Plain Nozzles

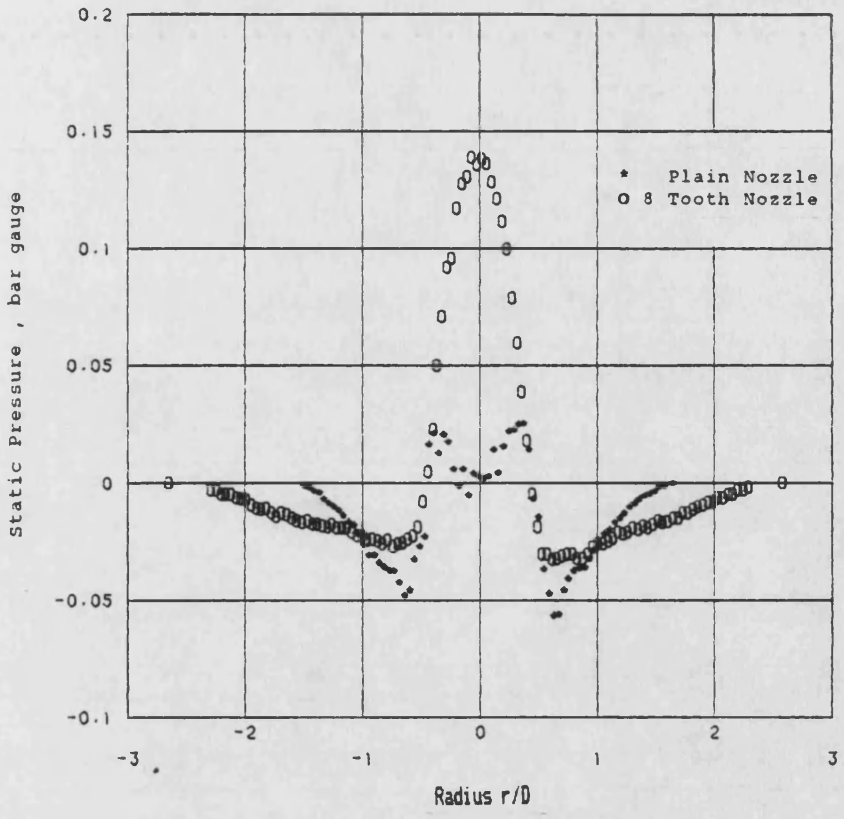

Figure 6.47 Static Pressure at x/D=6 for M=1.0
8 Tooth and Plain Nozzles

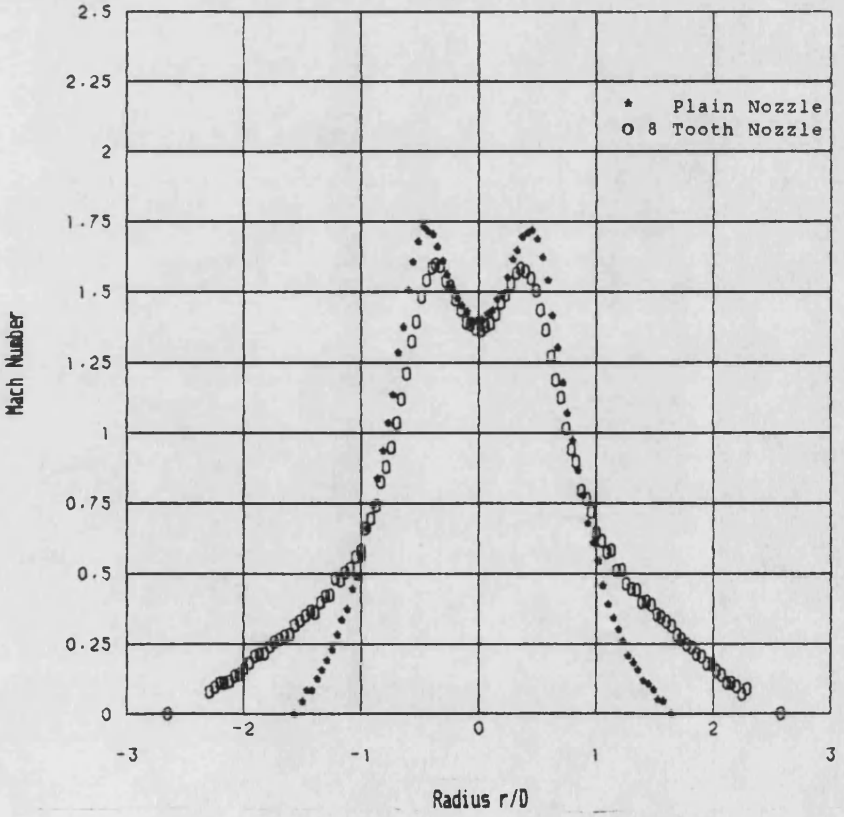

Figure 6.48 Mach Number at x/D=6 for M=1.0
8 Tooth and Plain Nozzles

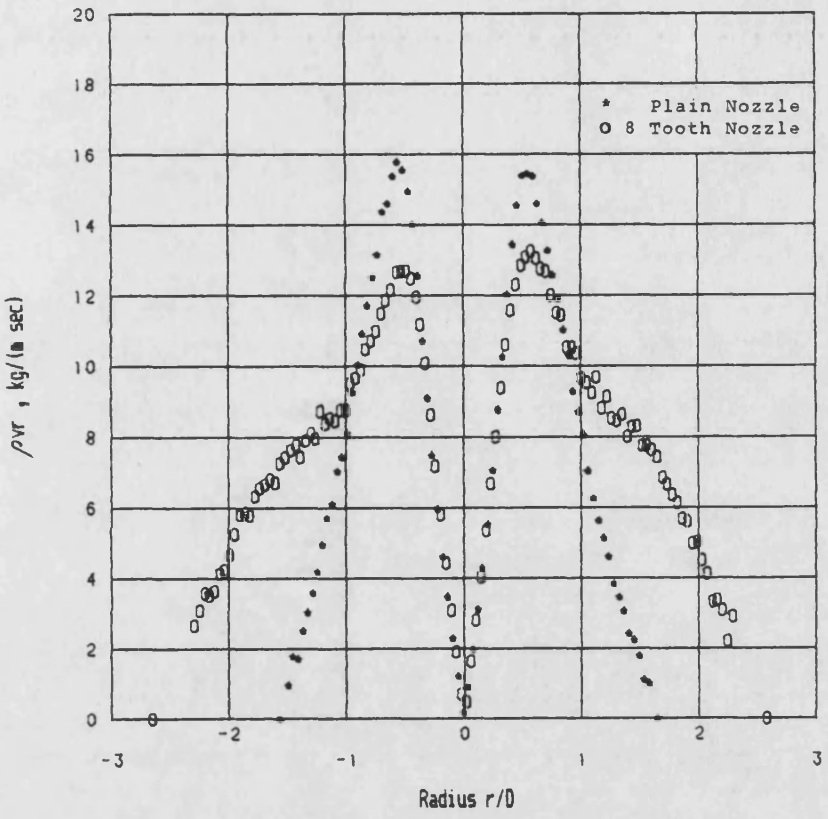

Figure 6.49 Mass Flow at x/D=6 for M=1.0
8 Tooth and Plain Nozzles

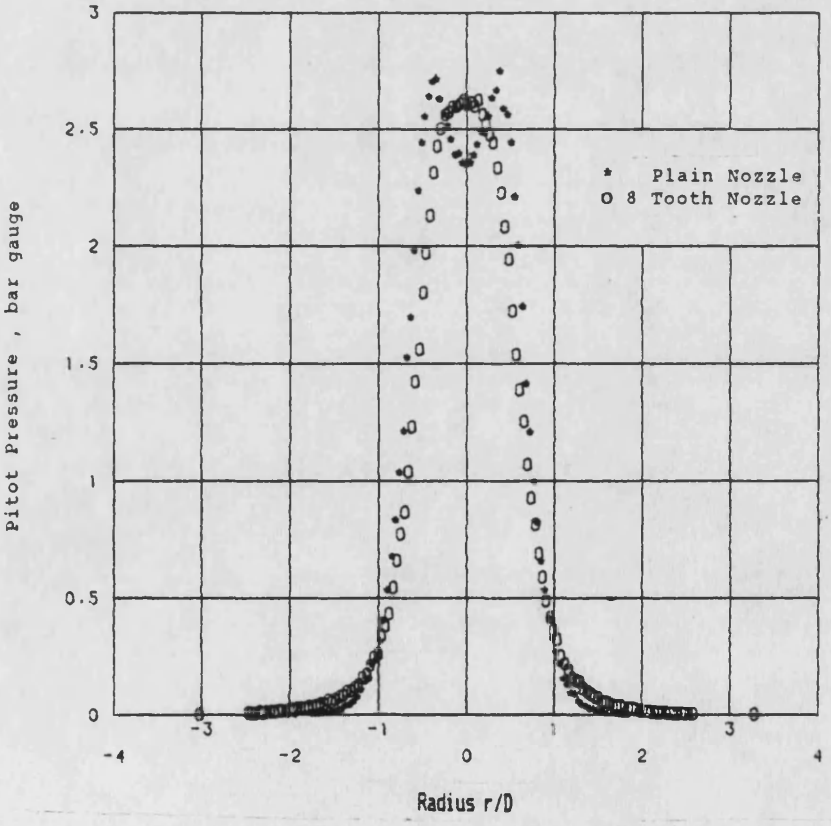

Figure 6.50 Pitot Pressure at x/D=8 for M=1.0
8 Tooth and Plain Nozzles

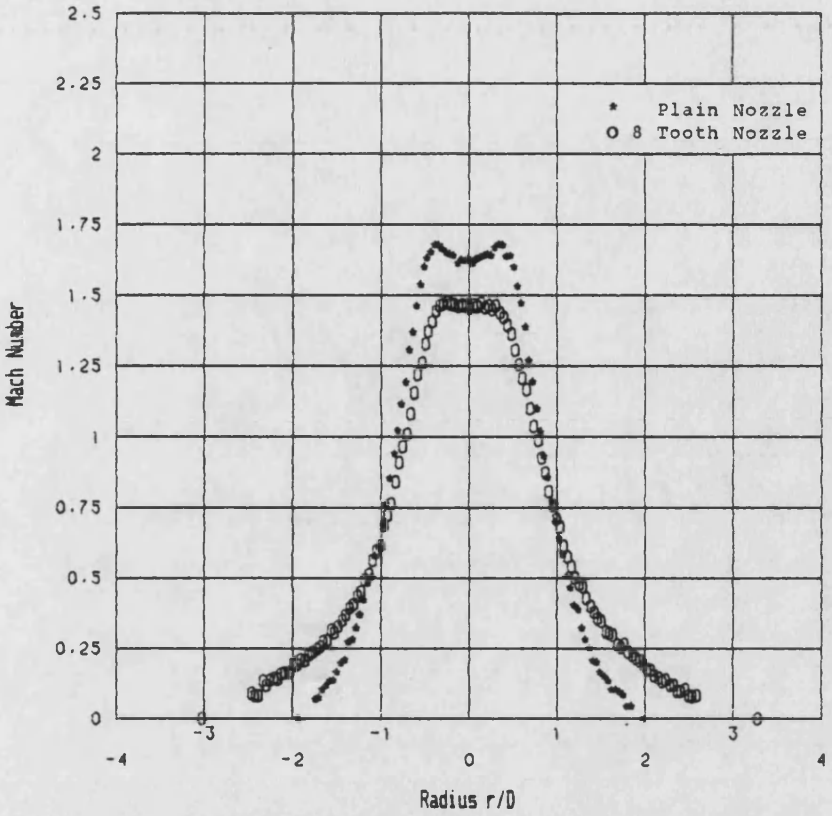

Figure 6.51 Mach Number at x/D=8 for M=1.0
8 Tooth and Plain Nozzles

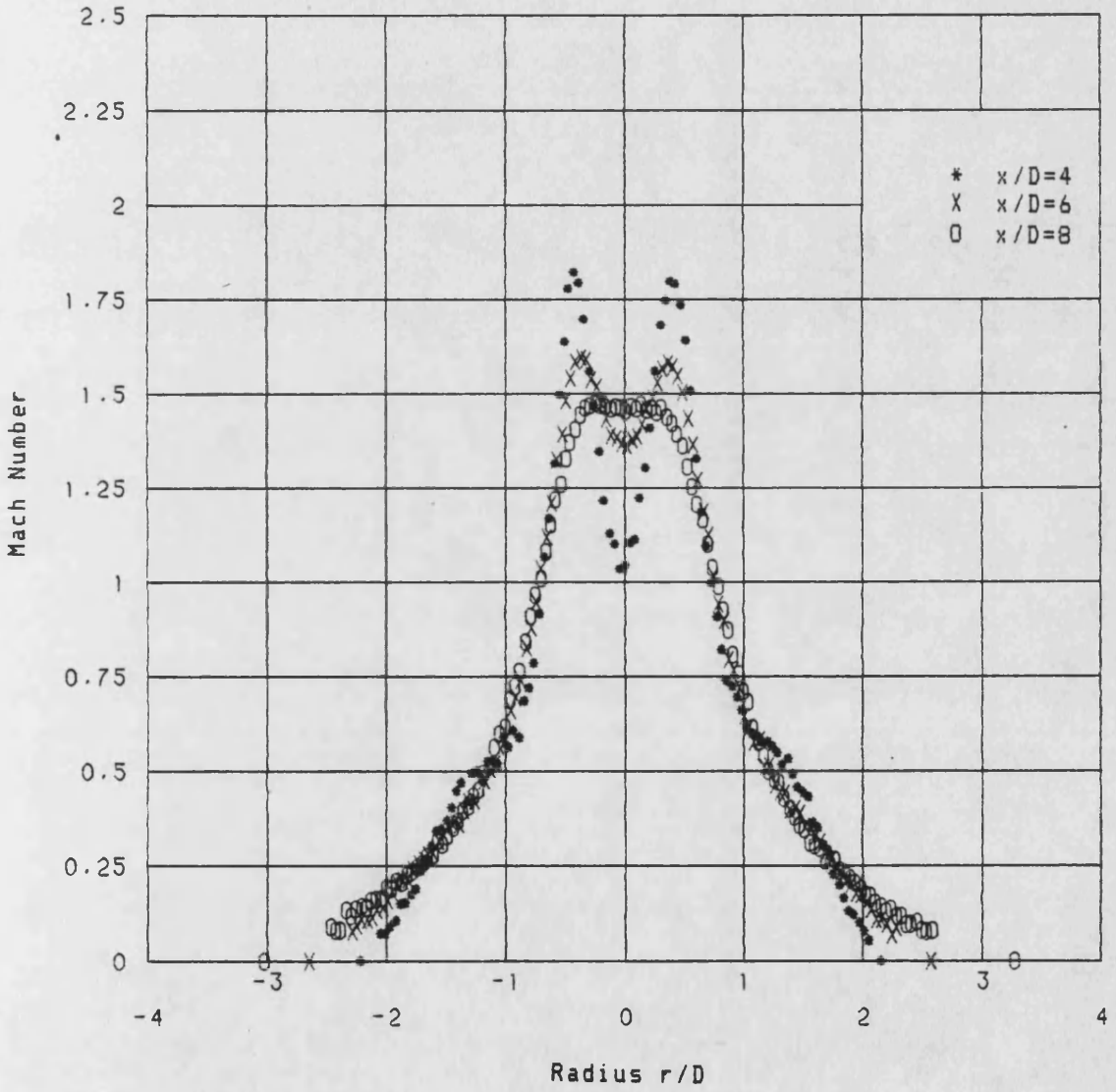

Figure 6.52 Axial variation of Mach Number for M=1.0 8 Tooth Nozzle

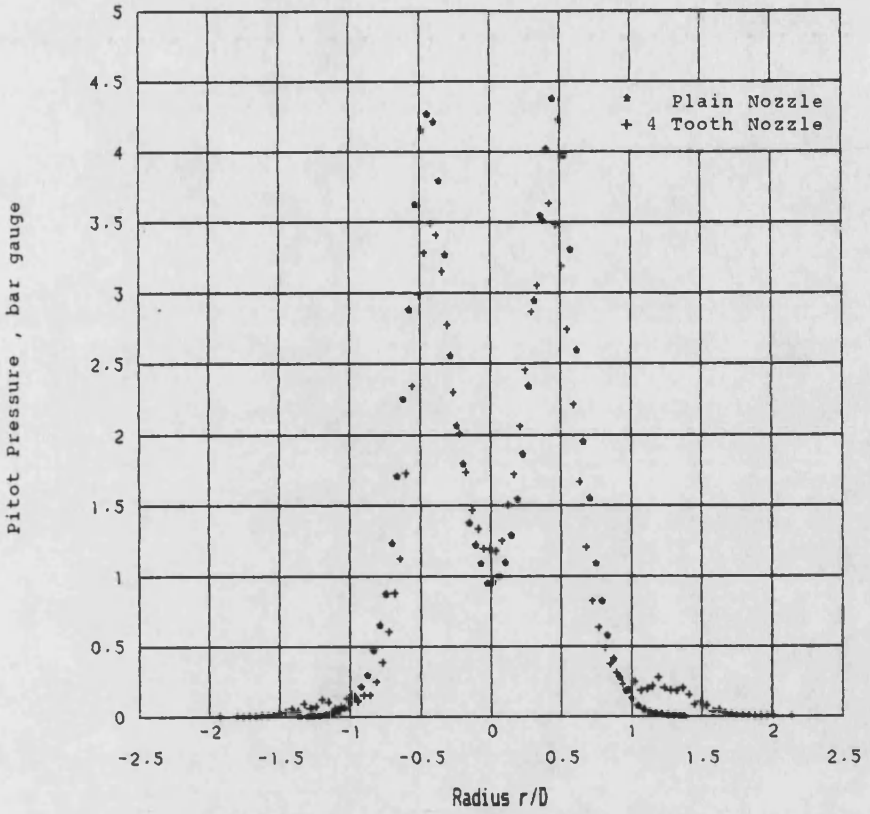

Figure 6.53 Pitot Pressure at x/D=4 for M=1.0
4 Tooth and Plain Nozzles

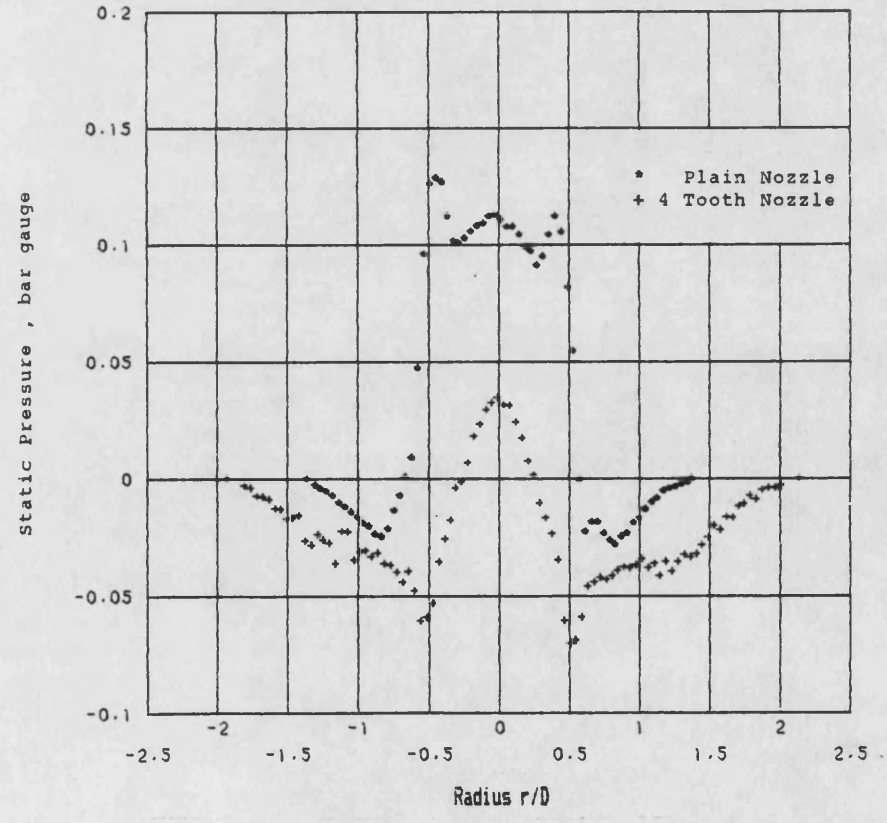

Figure 6.54 Static Pressure at x/D=4 for M=1.0
4 Tooth and Plain Nozzles

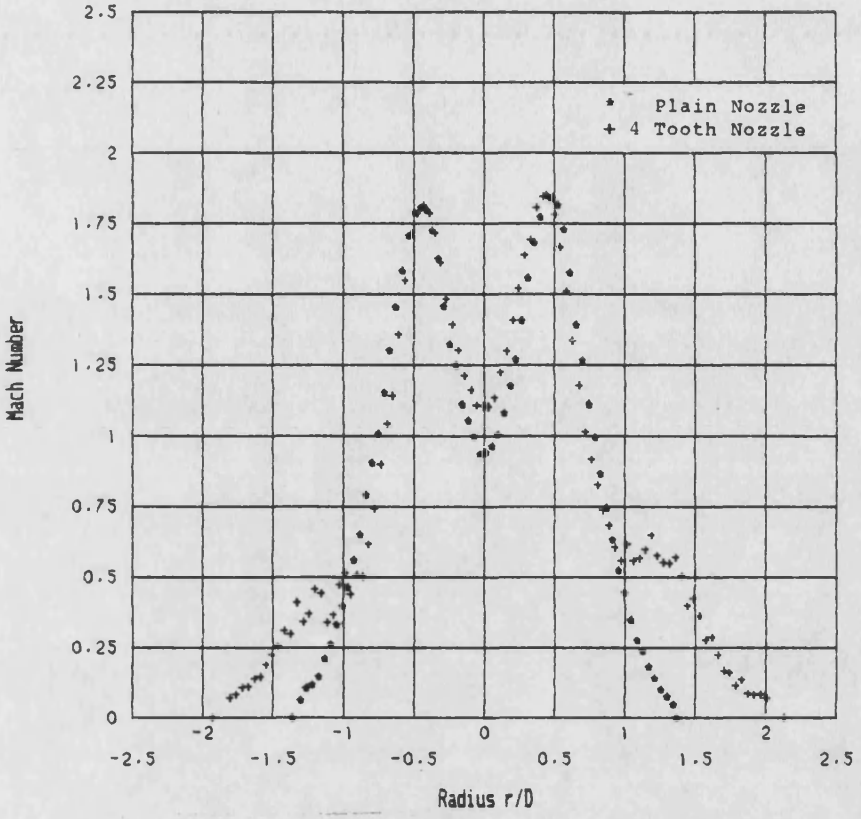

Figure 6.55 Mach Number at x/D=4 for M=1.0
4 Tooth and Plain Nozzles

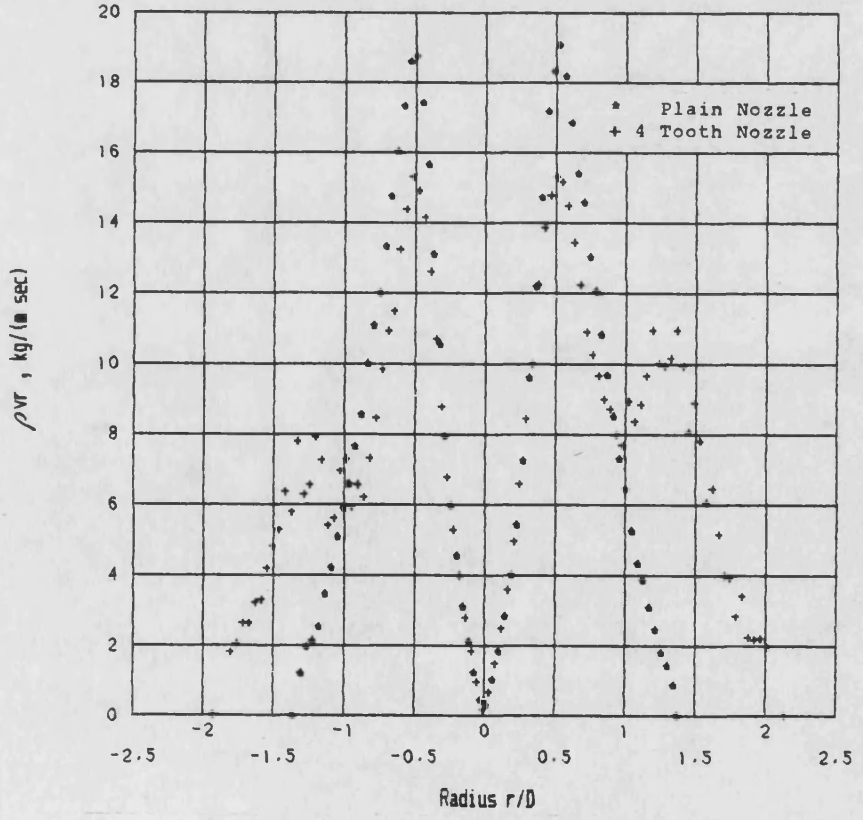

Figure 6.56 Mass Flow at x/D=4 for M=1.0
4 Tooth and Plain Nozzles

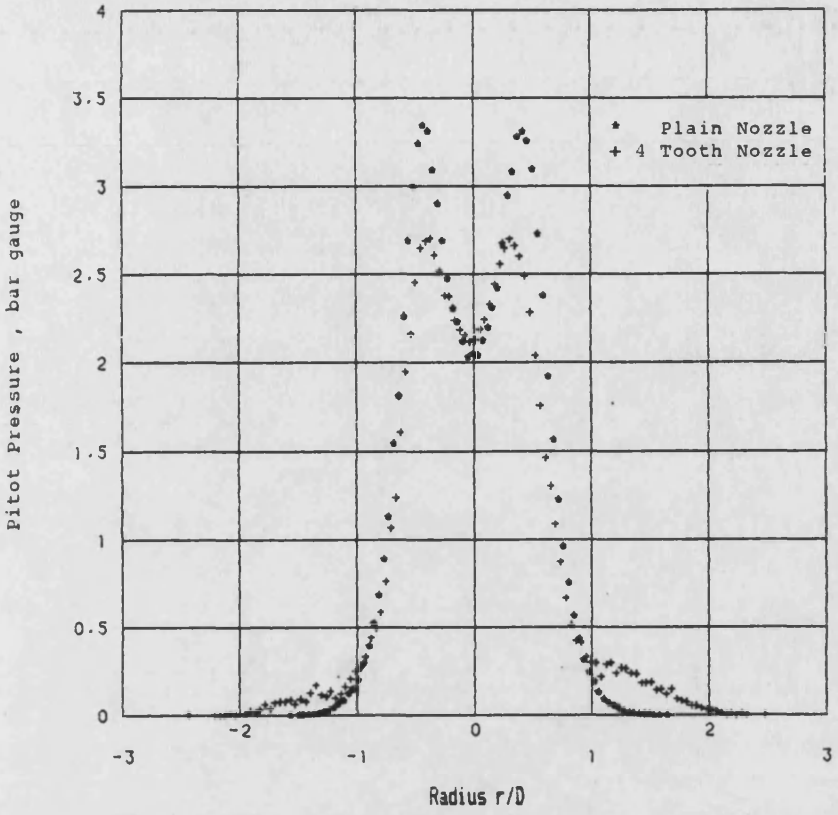

Figure 6.57 Pitot Pressure at x/D=6 for M=1.0
4 Tooth and Plain Nozzles

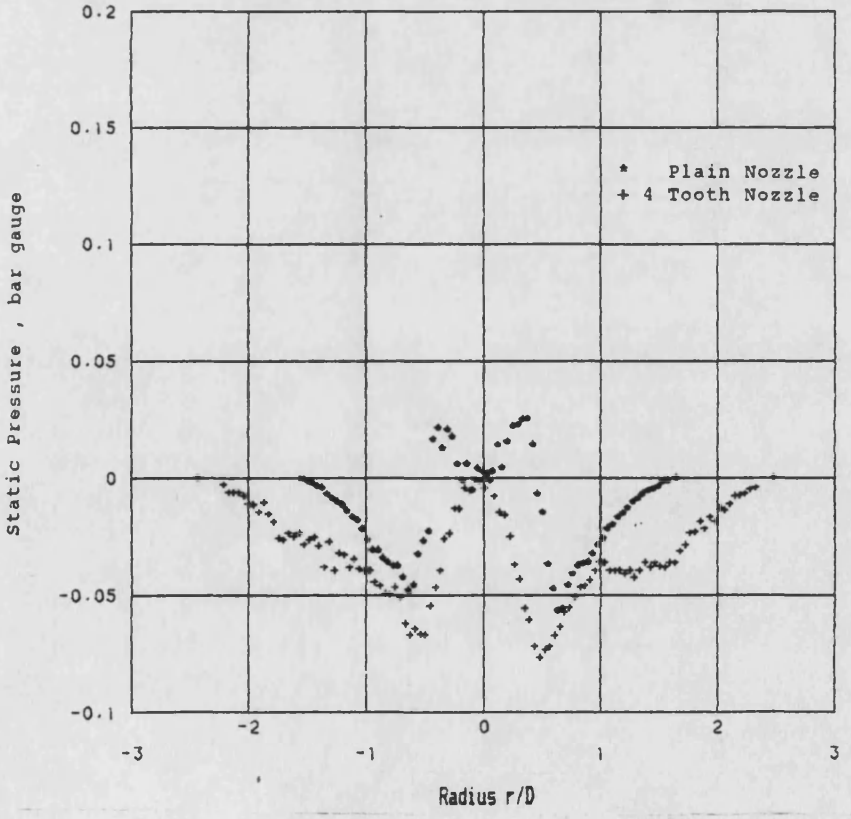

Figure 6.58 Static Pressure at x/D=6 for M=1.0
4 Tooth and Plain Nozzles

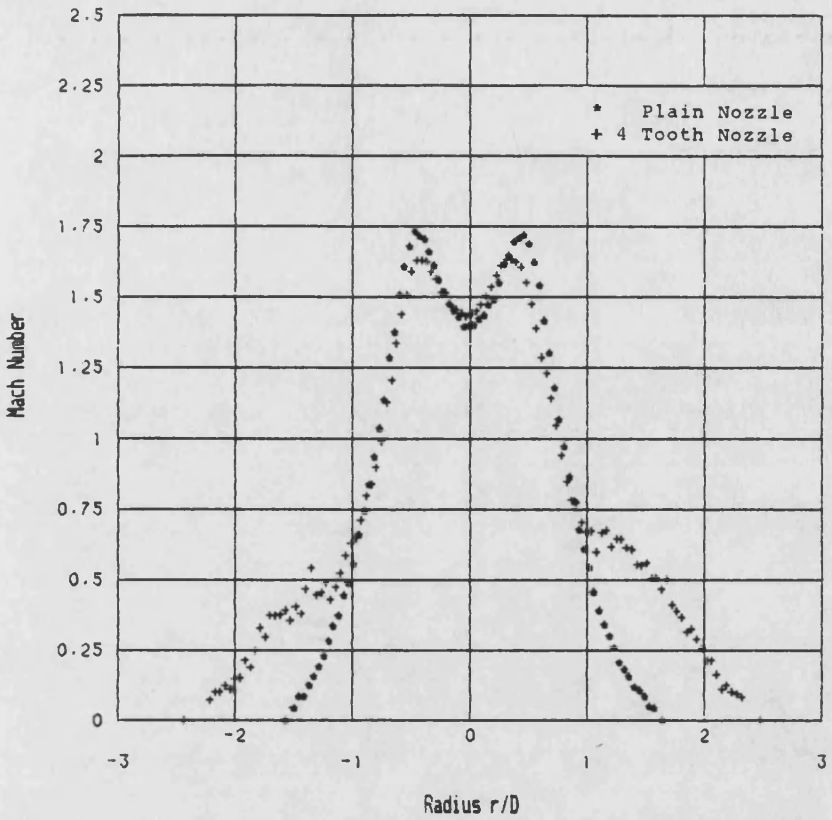

Figure 6.59 Mach Number at x/D=6 for M=1.0
4 Tooth and Plain Nozzles

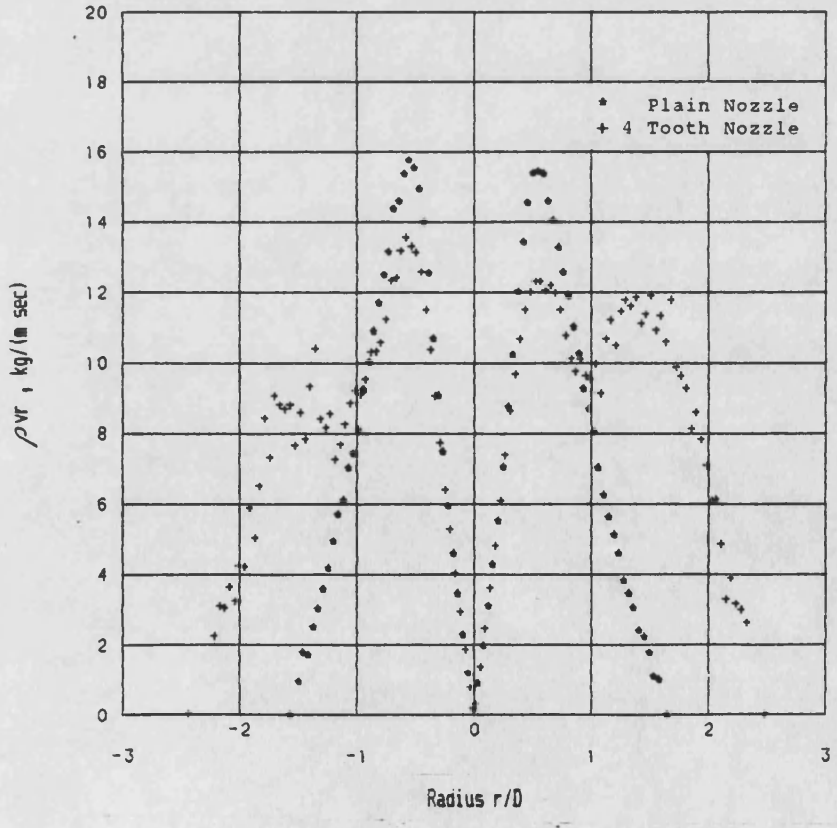

Figure 6.60 Mass Flow at x/D=6 for M=1.0
4 Tooth and Plain Nozzles

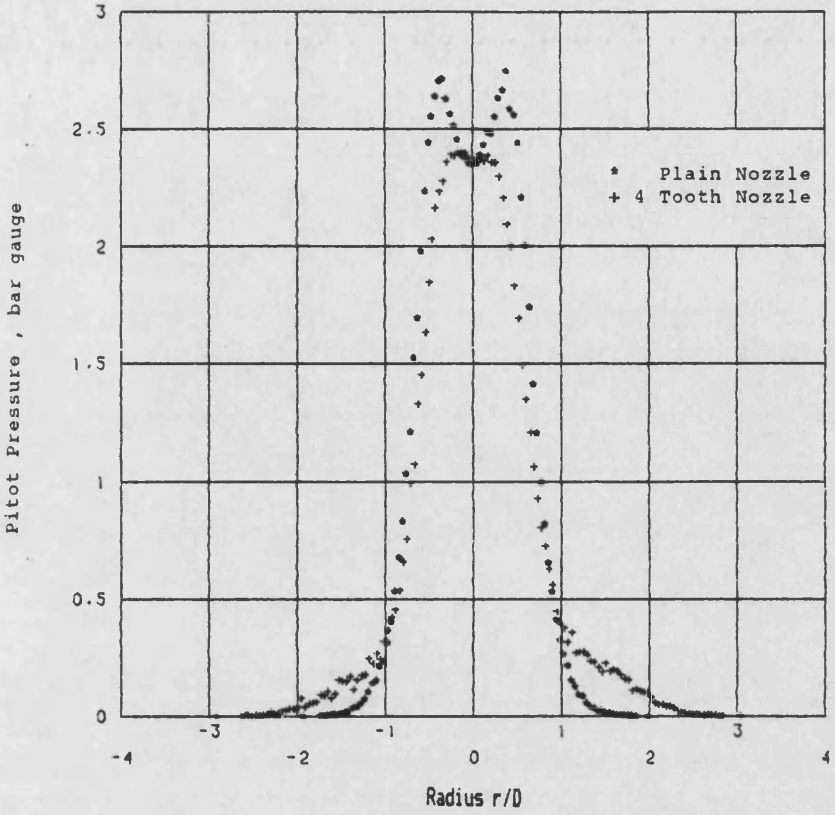

Figure 6.61 Pitot Pressure at x/D=8 for M=1.0
4 Tooth and Plain Nozzles

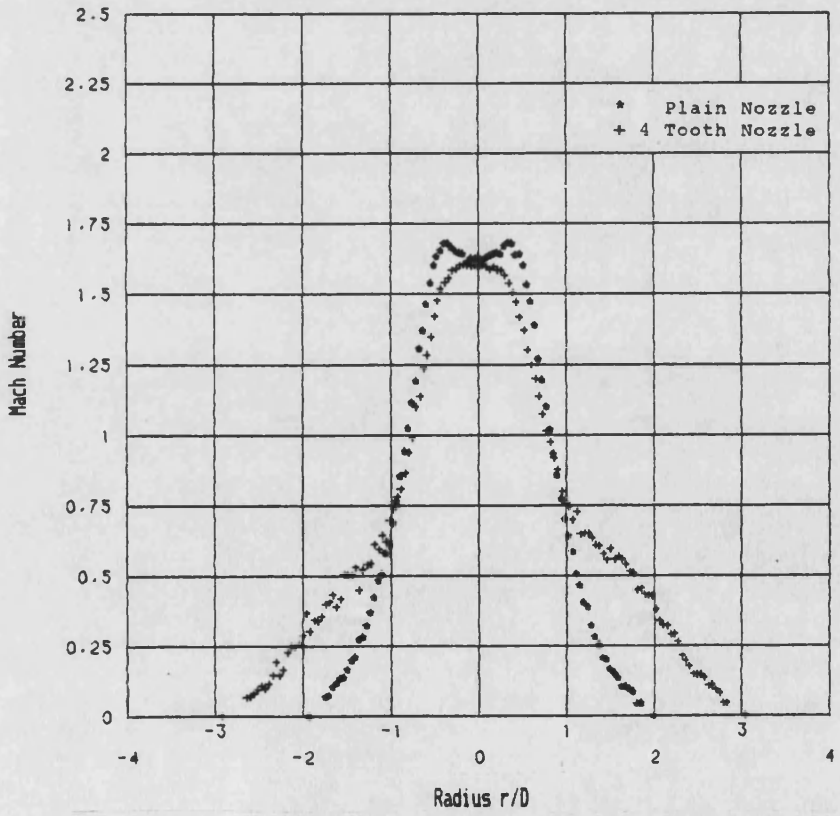

Figure 6.62 Mach Number at x/D=8 for M=1.0
4 Tooth and Plain Nozzles

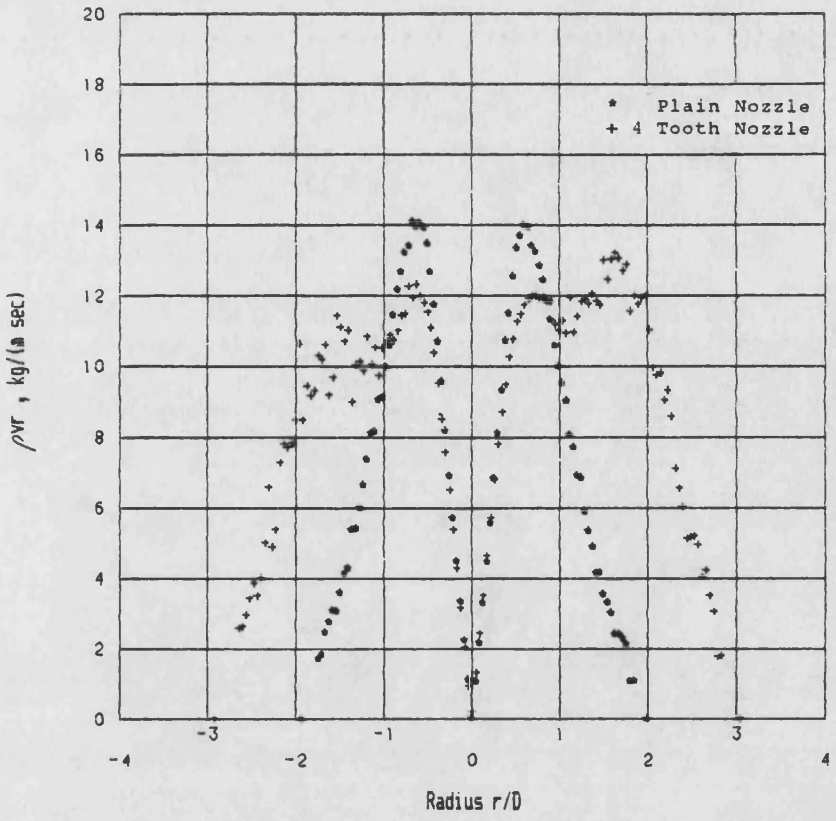

Figure 6.63 Mass Flow at x/D=8 for M=1.0
4 Tooth and Plain Nozzles

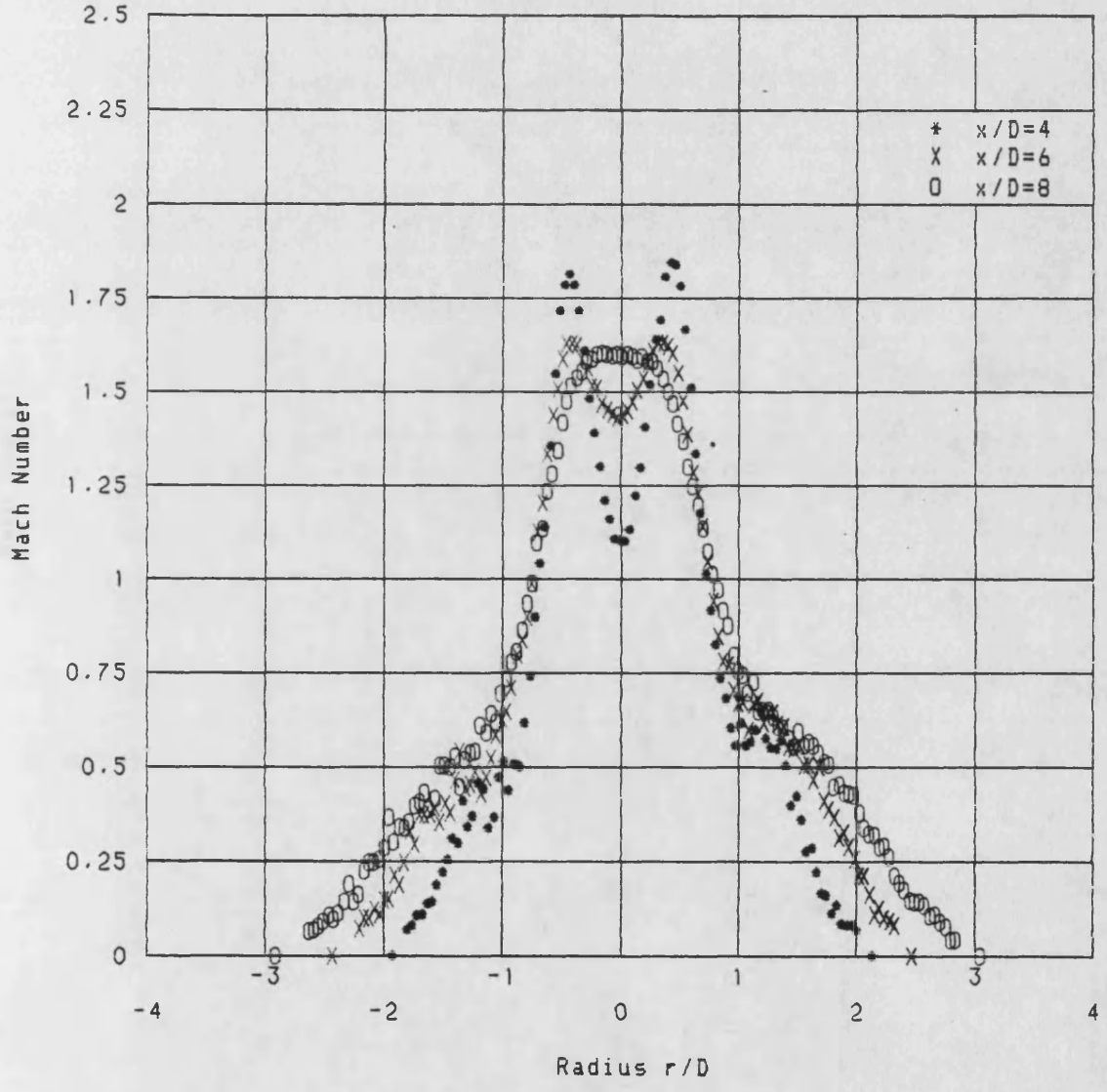

Figure 6.64 Axial variation of Mach Number for M=1.0 4 Tooth Nozzle

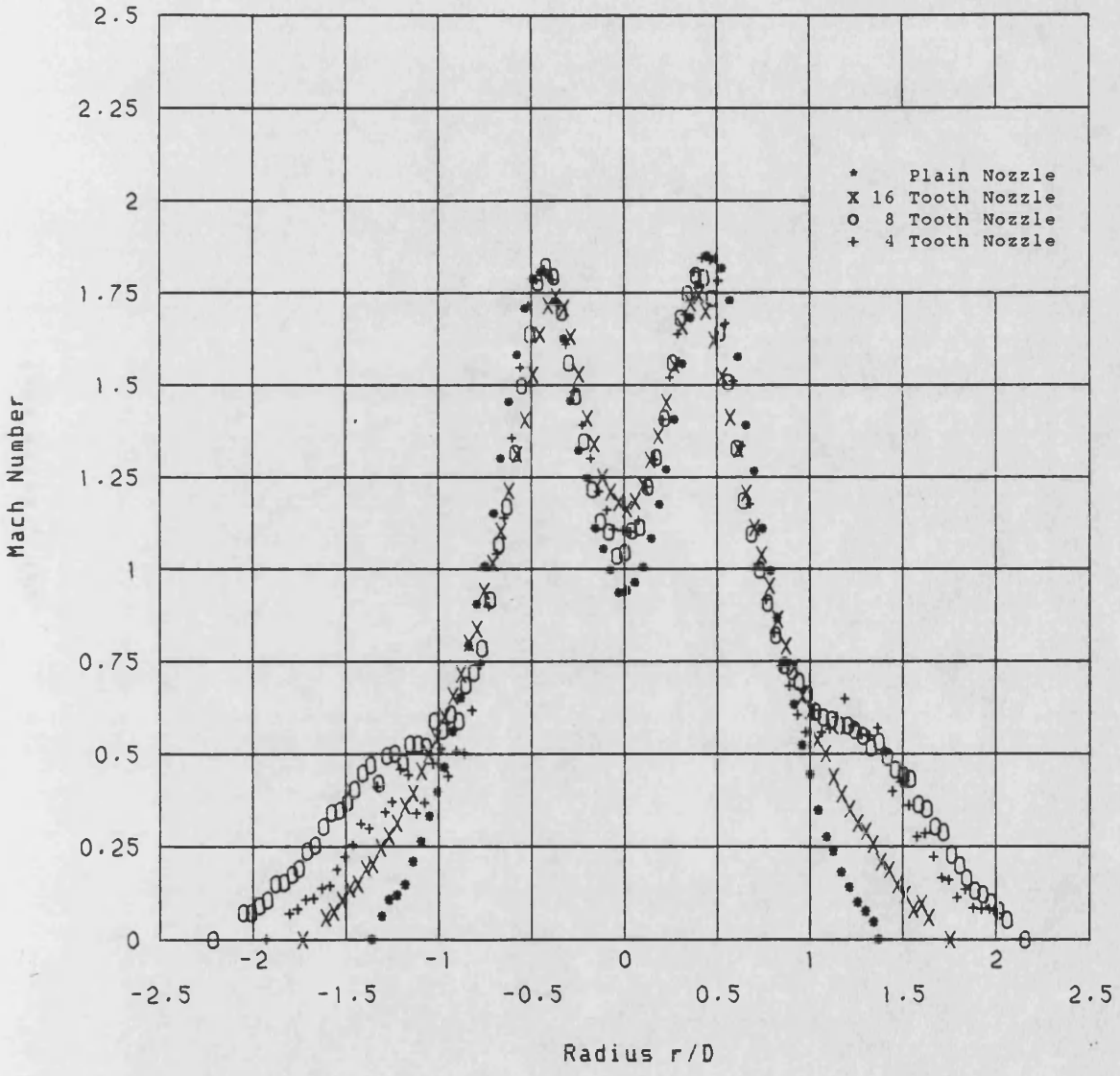

Figure 6.65 Mach Number of M=1.0 Nozzles at x/D=4

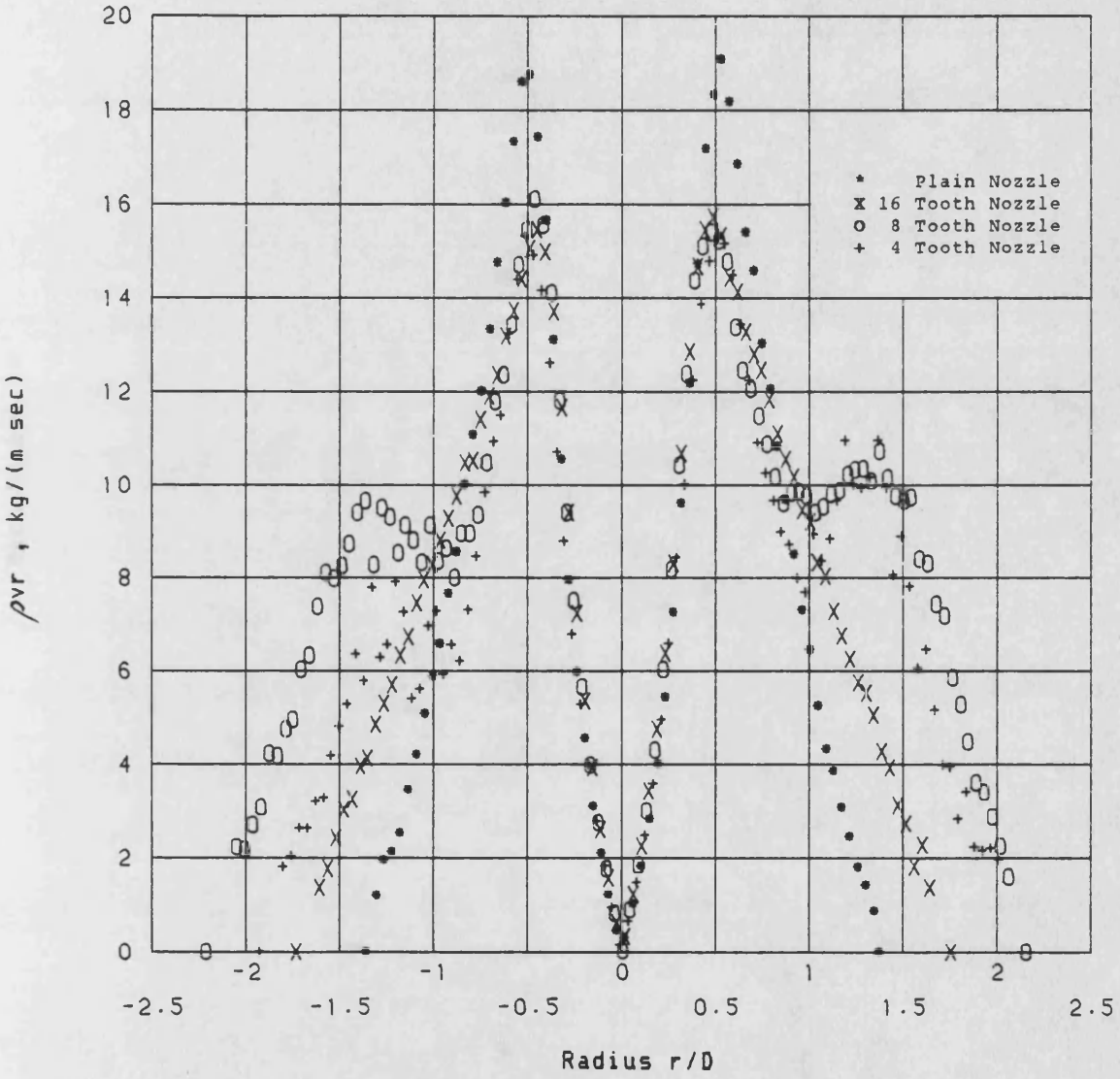

Figure 6.66 Mass Flow of M=1.0 Nozzles at x/D=4

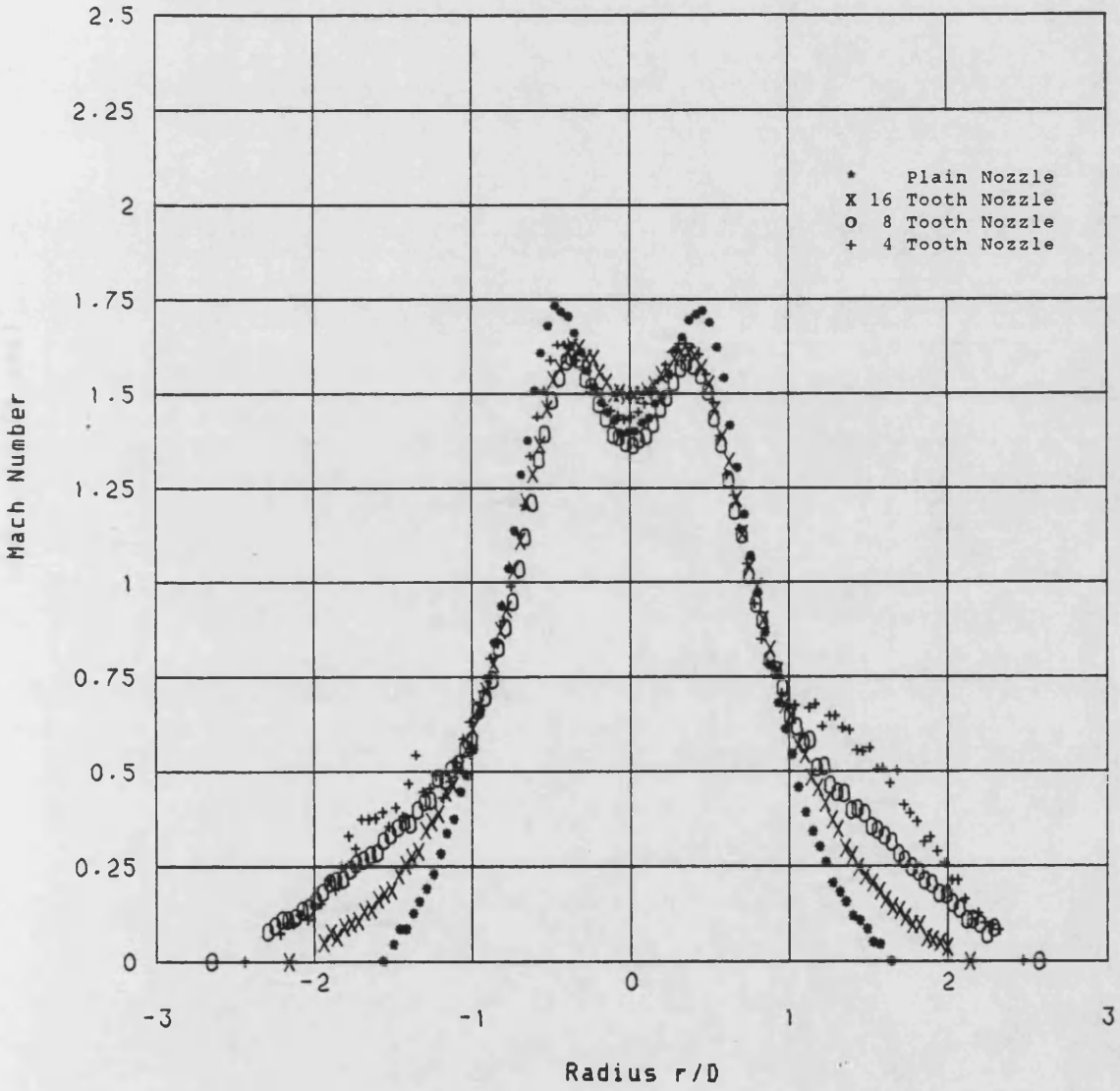

Figure 6.67 Mach Number of M=1.0 Nozzles at x/D=6

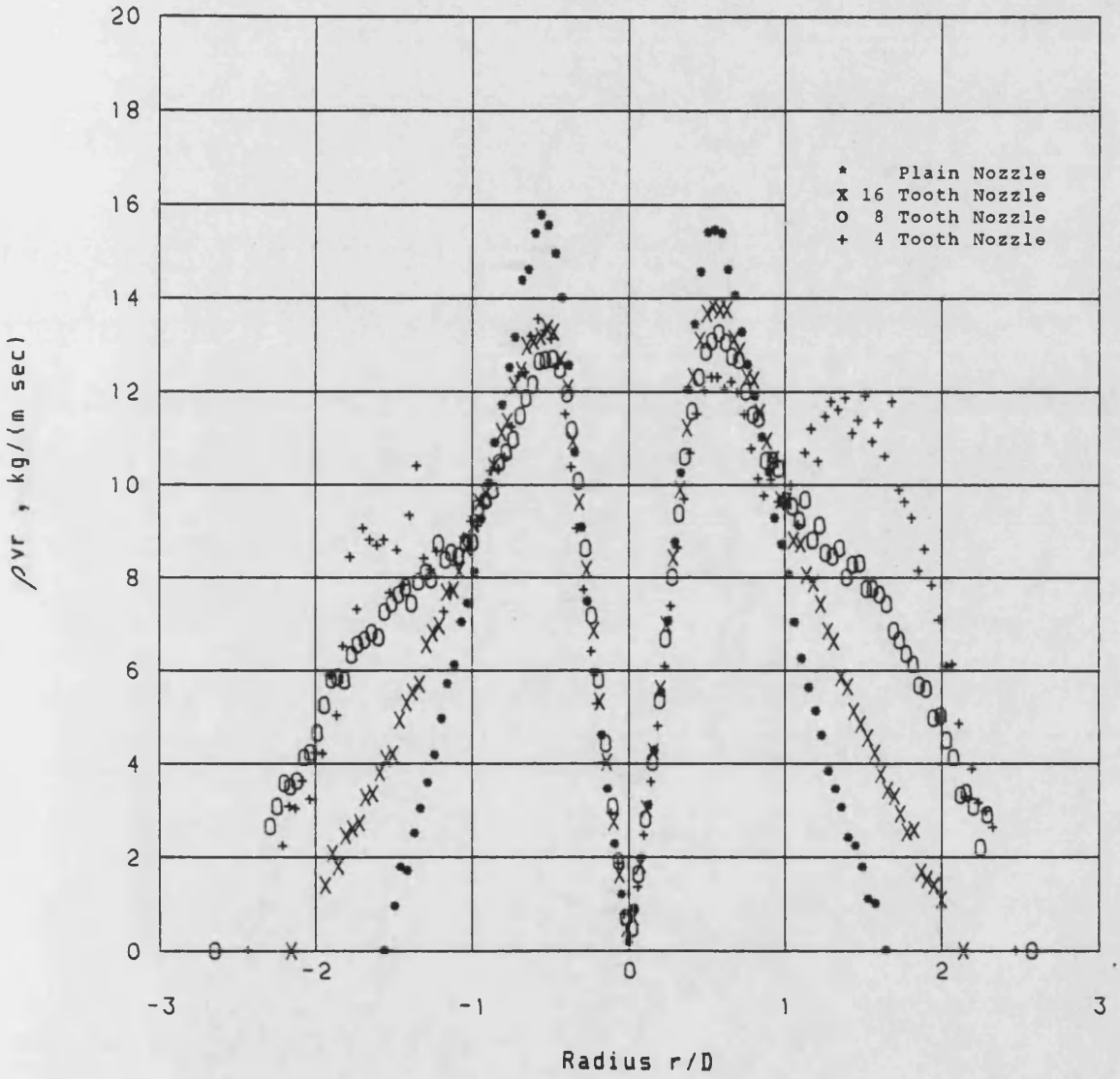

Figure 6.68 Mass Flow of M=1.0 Nozzles at x/D=6

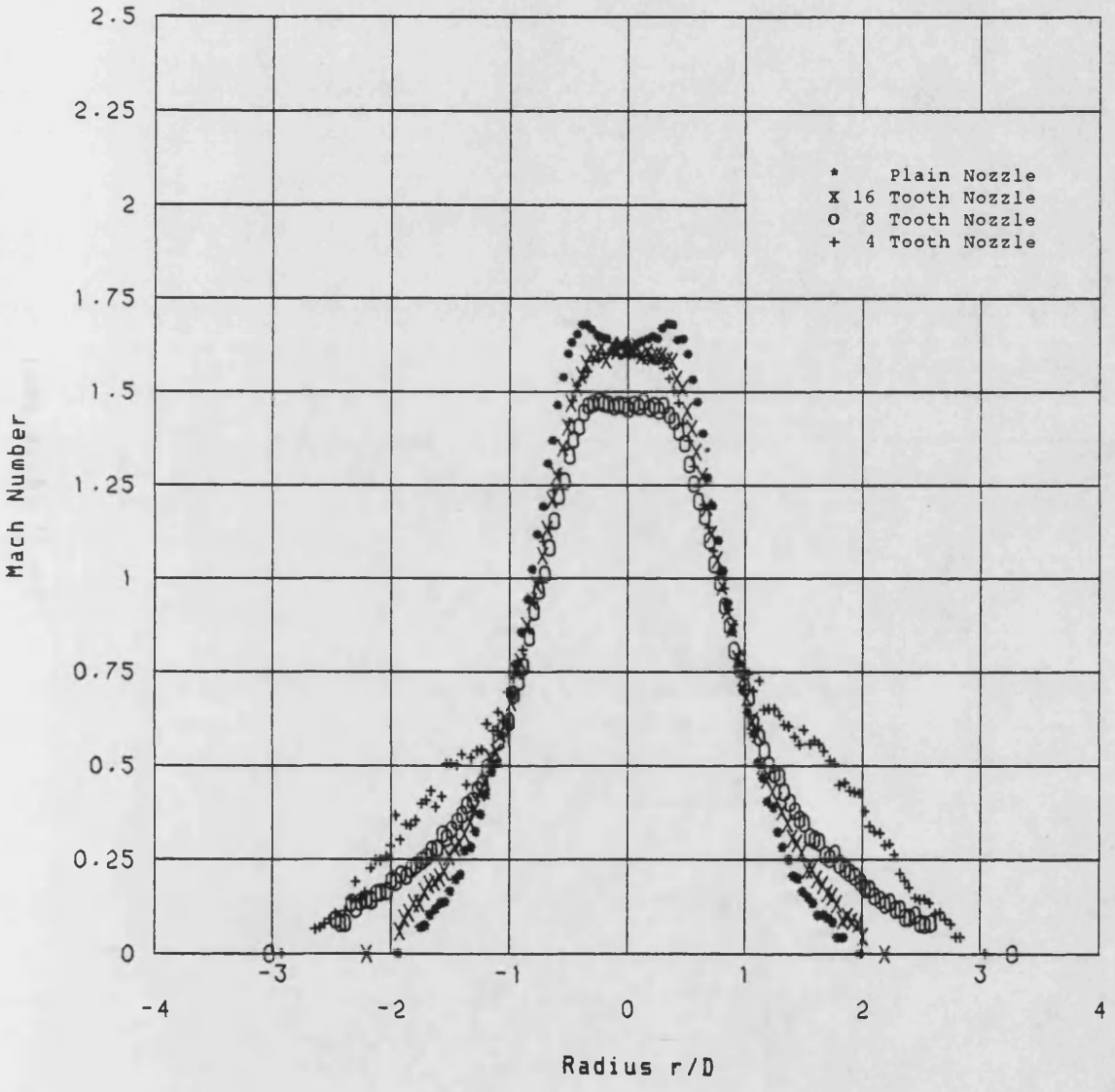

Figure 6.69 Mach Number of M=1.0 Nozzles at x/D=8

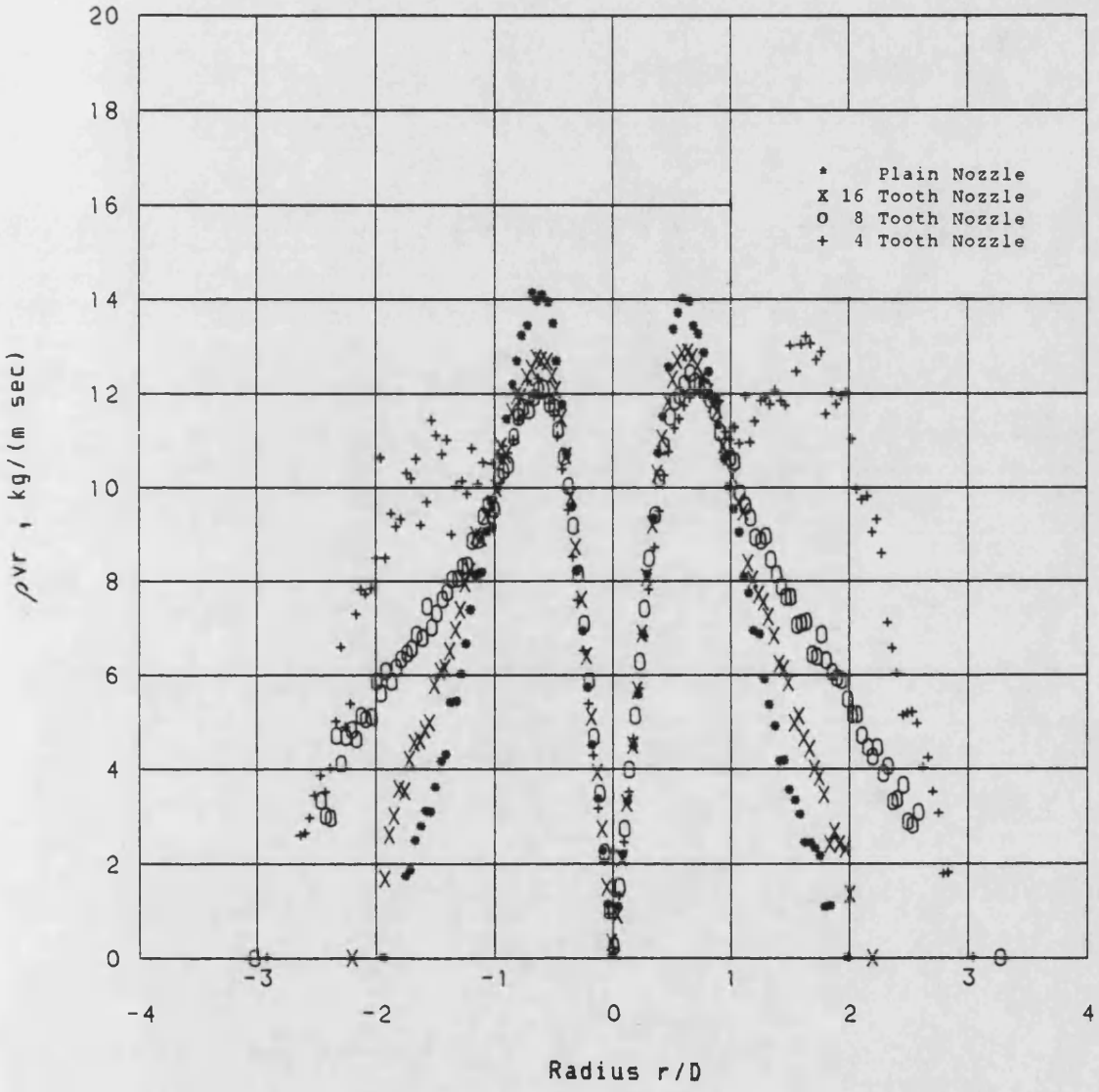

Figure 6.70 Mass Flow of M=1.0 Nozzles at x/D=8

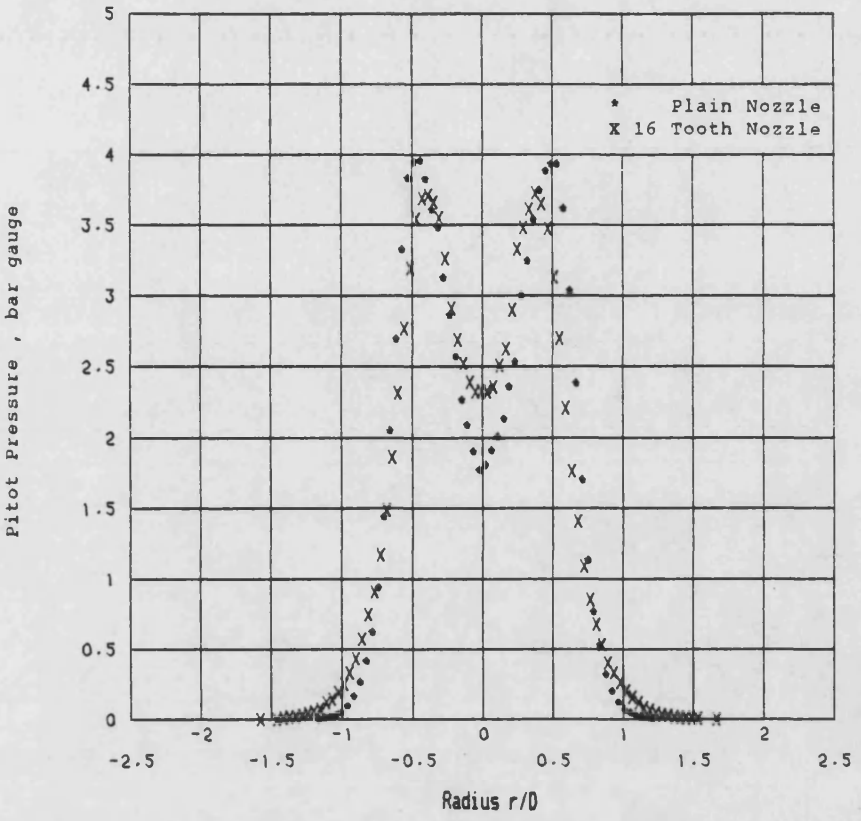

Figure 6.71 Pitot Pressure at x/D=4 for M=1.4
16 Tooth and Plain Nozzles

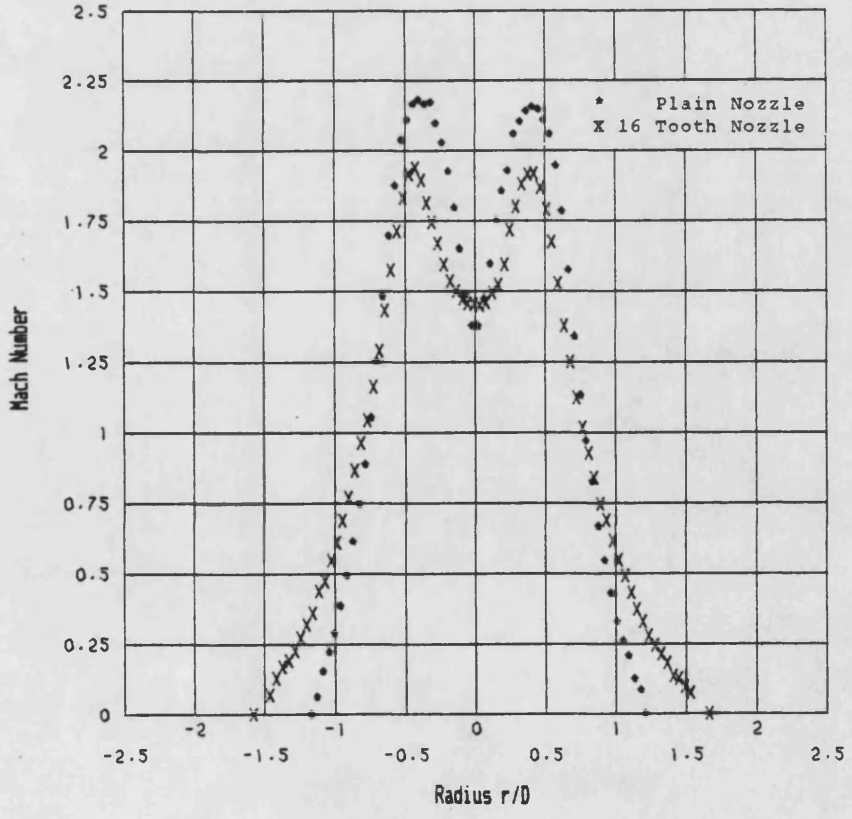

Figure 6.72 Mach Number at x/D=4 for M=1.4
16 Tooth and Plain Nozzles

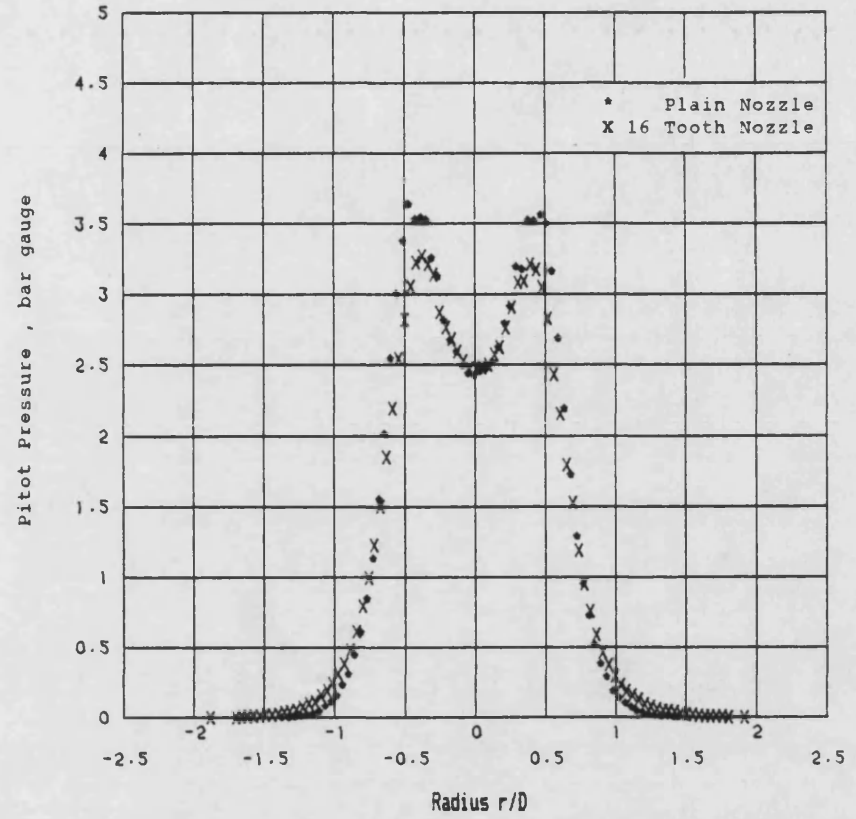

Figure 6.73 Pitot Pressure at x/D=6 for M=1.4
16 Tooth and Plain Nozzles

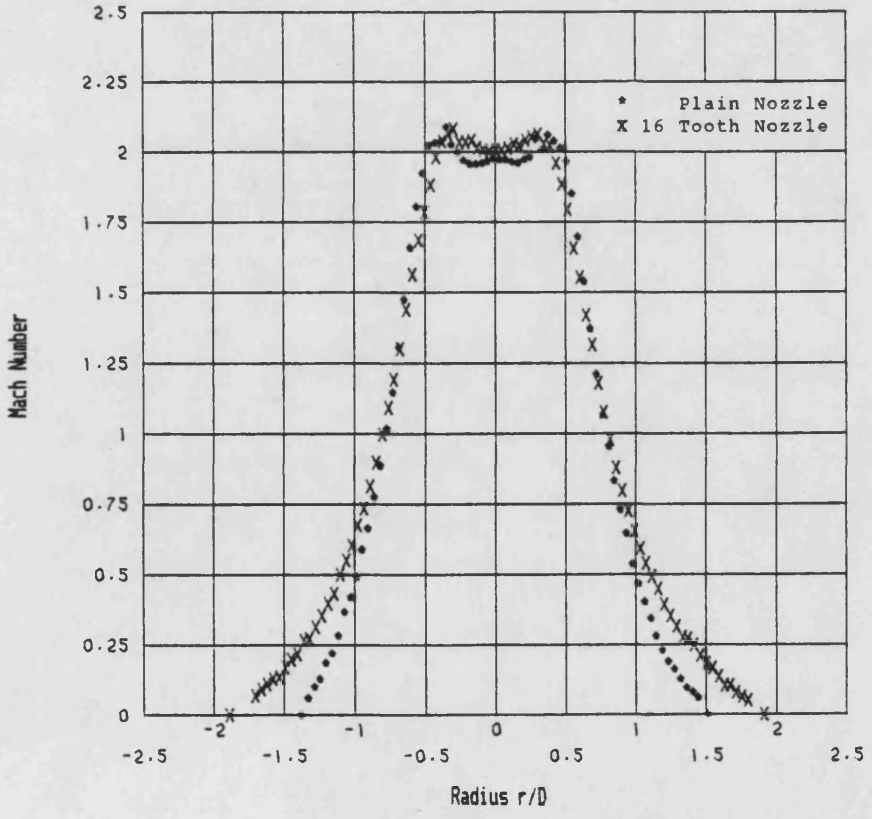

Figure 6.74 Mach Number at x/D=6 for M=1.4
16 Tooth and Plain Nozzles

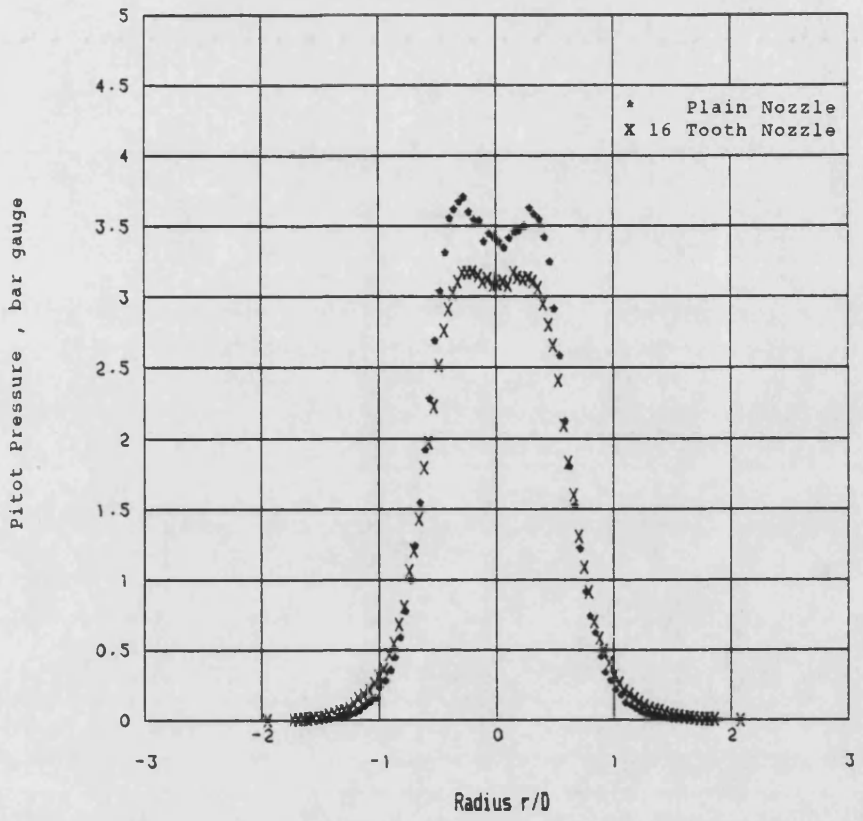

Figure 6.75 Pitot Pressure at x/D=8 for M=1.4
16 Tooth and Plain Nozzles

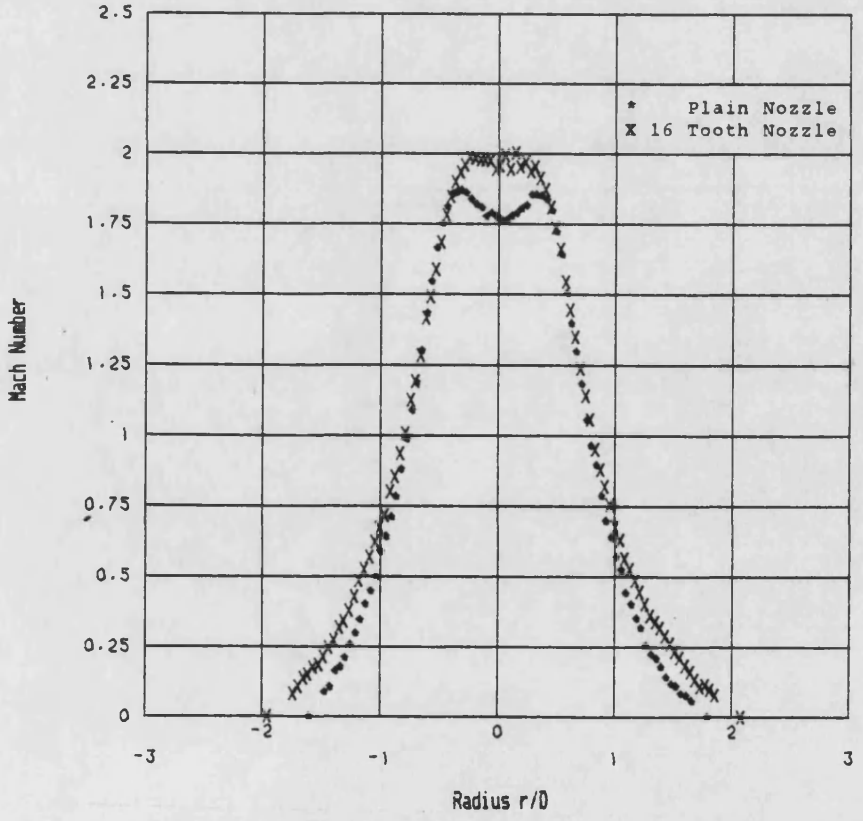

Figure 6.76 Mach Number at x/D=8 for M=1.4
16 Tooth and Plain Nozzles

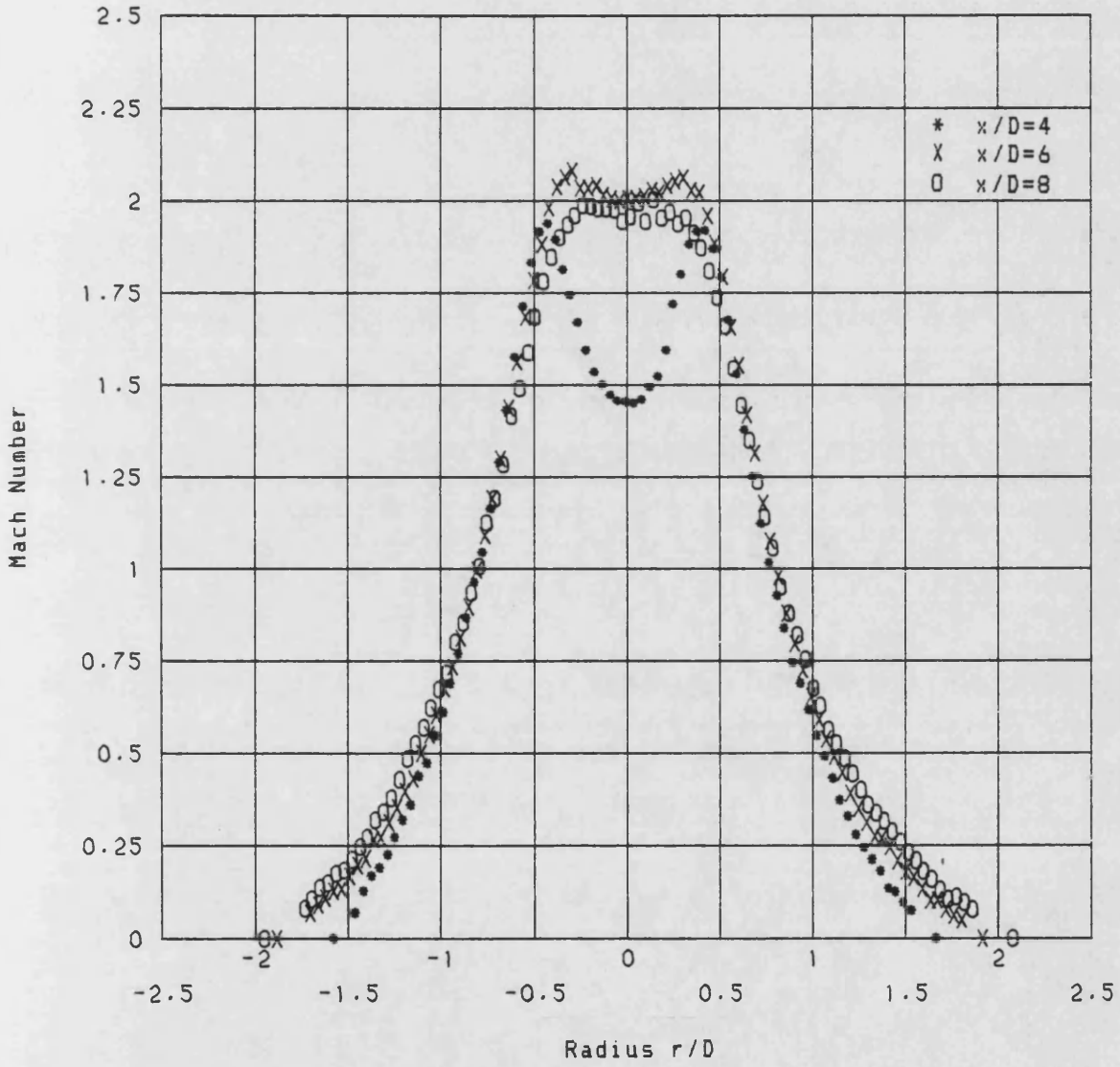

Figure 6.77 Axial variation of Mach Number for M=1.4 16 Tooth Nozzle

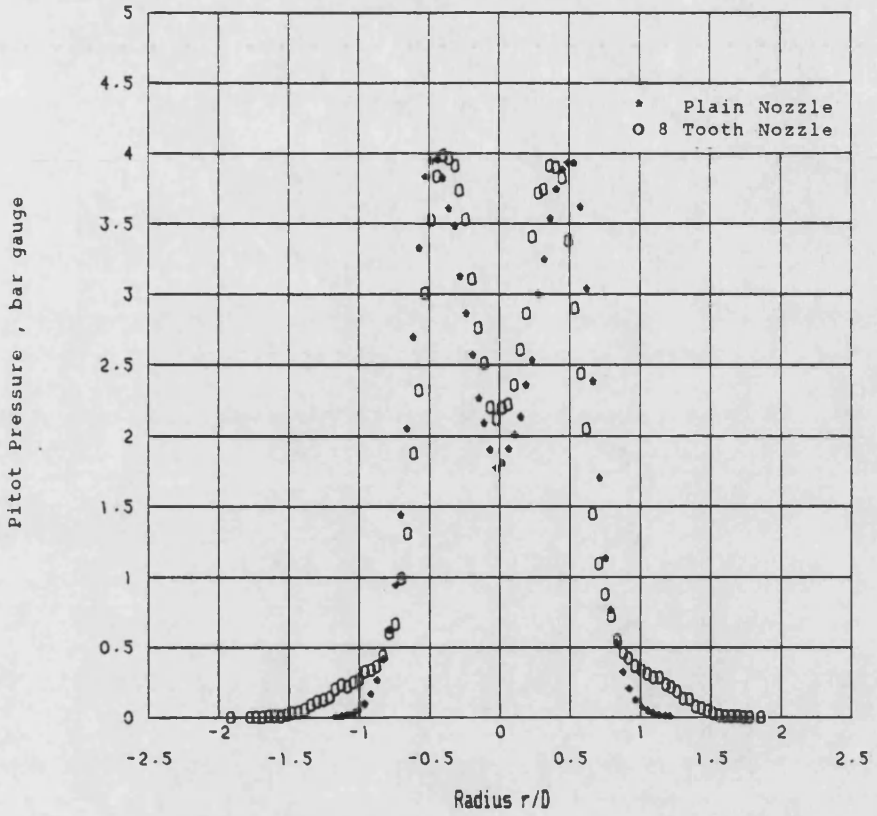

Figure 6.78 Pitot Pressure at x/D=4 for M=1.4
8 Tooth and Plain Nozzles

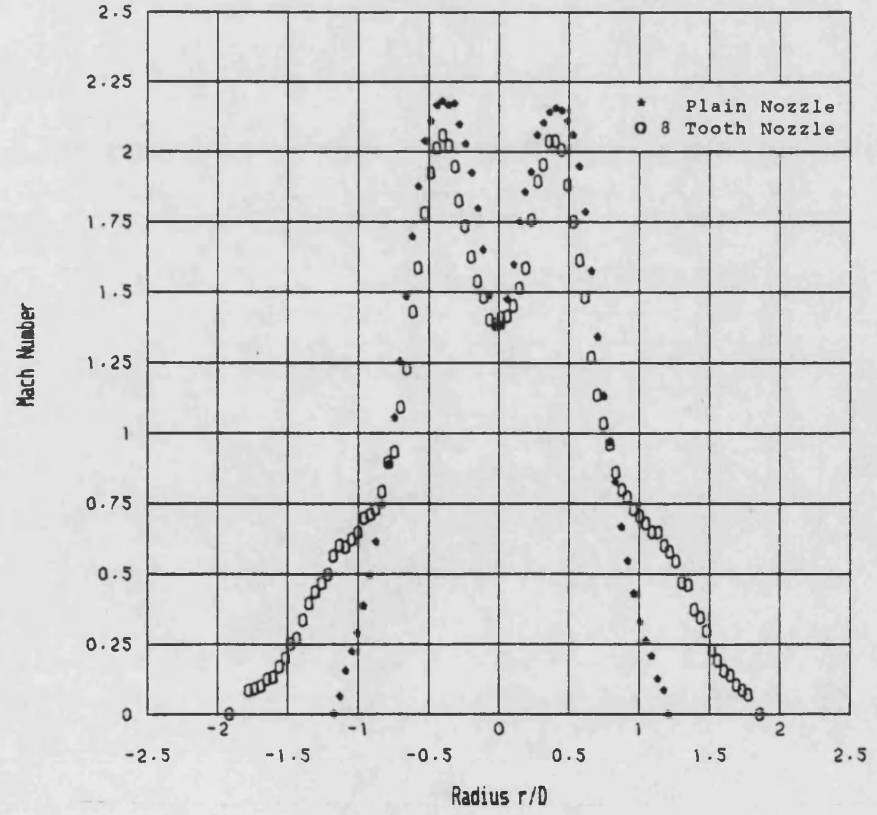

Figure 6.79 Mach Number at x/D=4 for M=1.4
8 Tooth and Plain Nozzles

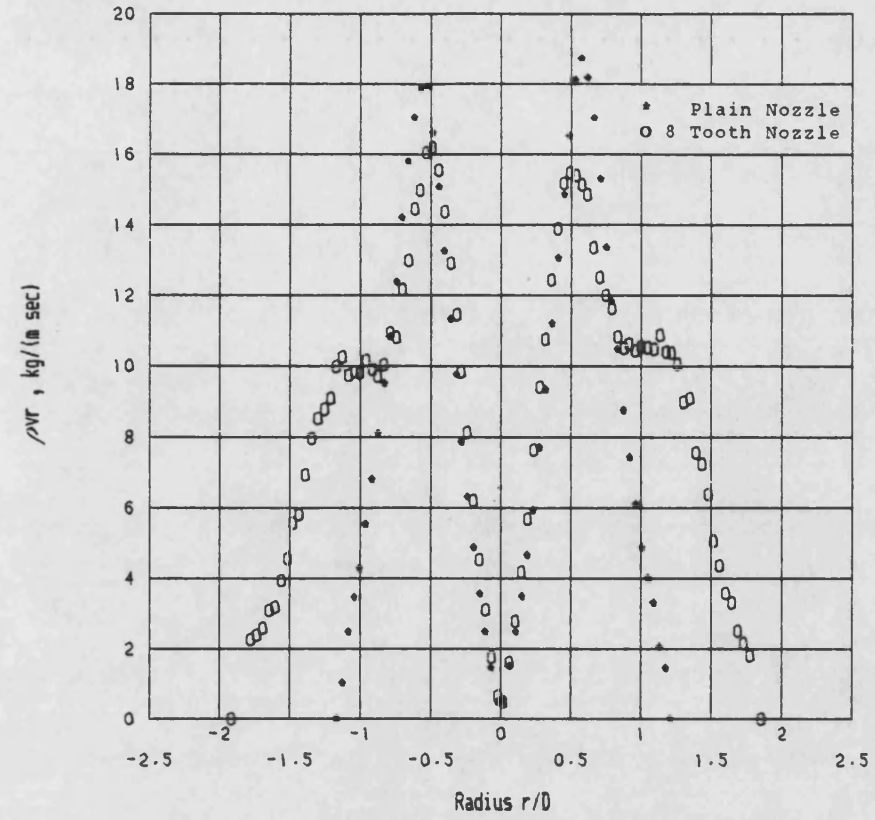

Figure 6.80 Mass Flow at x/D=4 for M=1.4
8 Tooth and Plain Nozzles

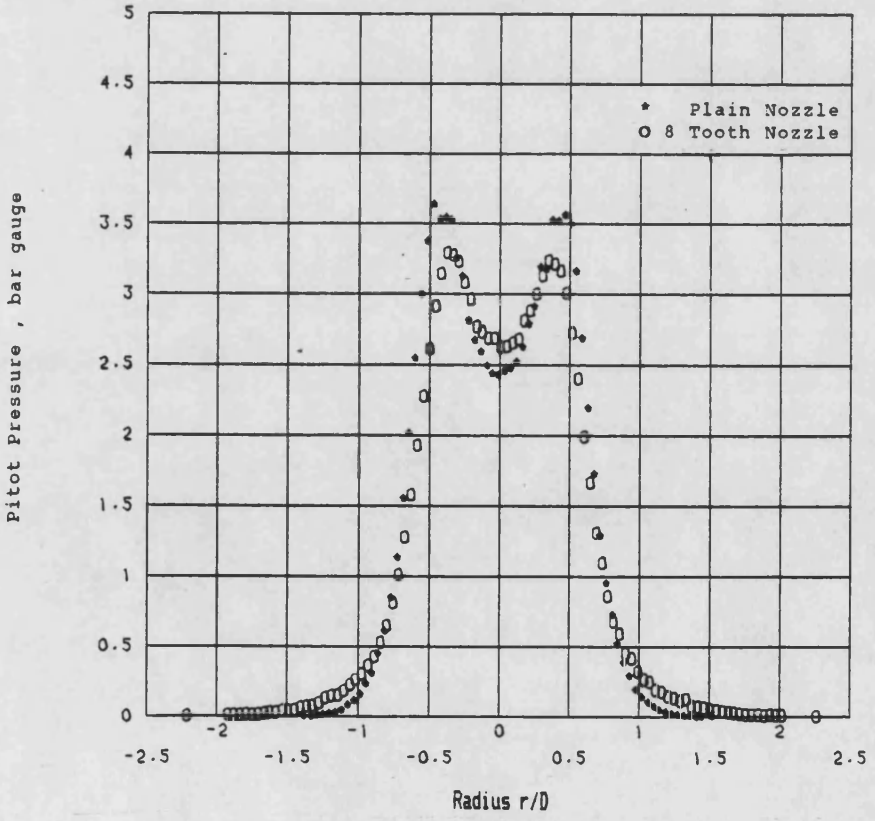

Figure 6.81 Pitot Pressure at x/D=6 for M=1.4
8 Tooth and Plain Nozzles

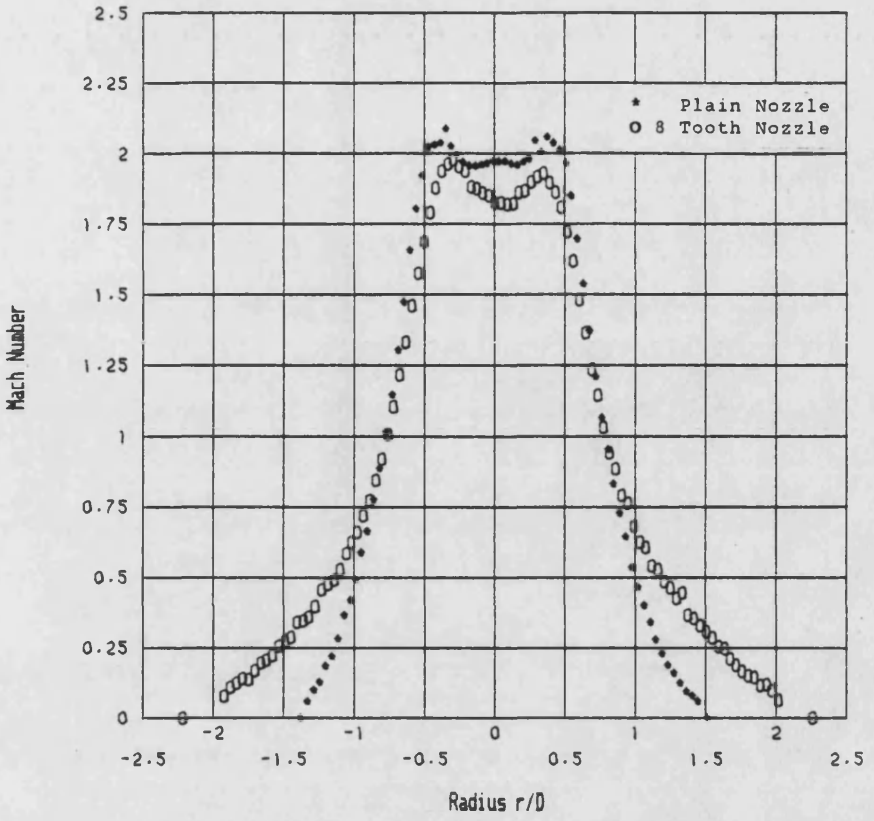

Figure 6.82 Mach Number at x/D=6 for M=1.4
8 Tooth and Plain Nozzles

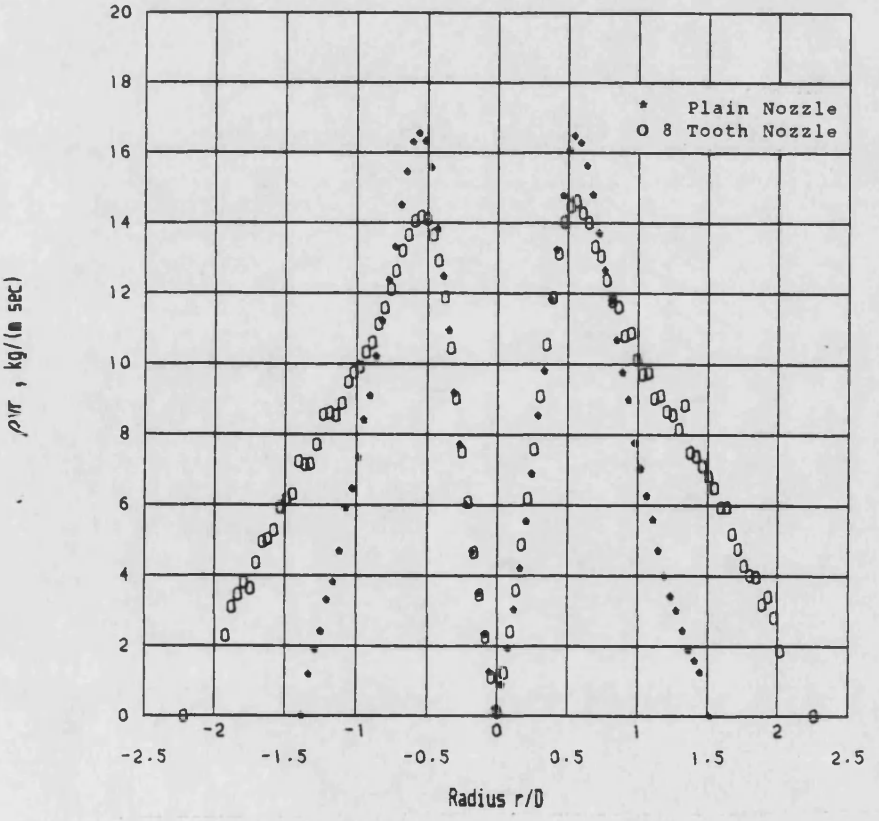

Figure 6.83 Mass Flow at x/D=6 for M=1.4
8 Tooth and Plain Nozzles

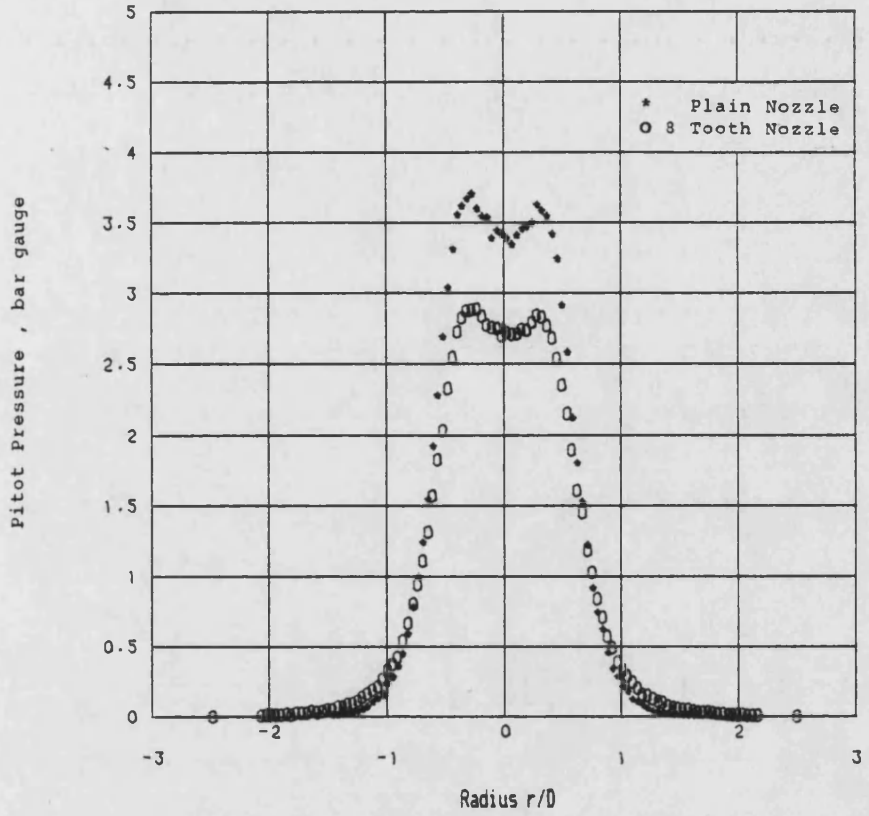

Figure 6.84 Pitot Pressure at x/D=8 for M=1.4
8 Tooth and Plain Nozzles

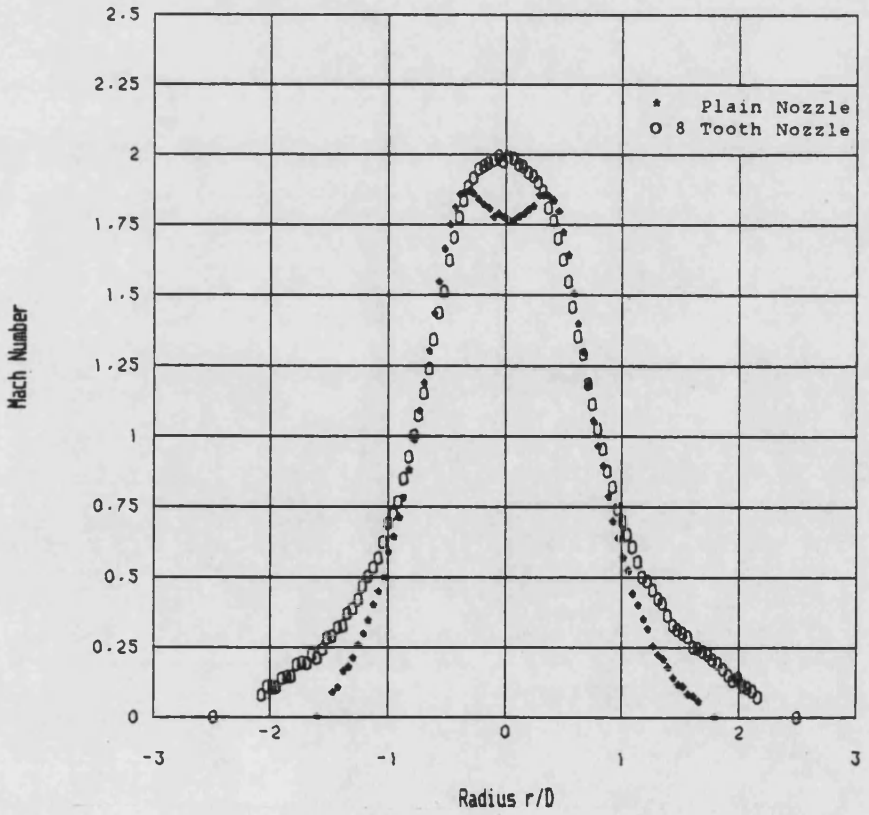

Figure 6.85 Mach Number at x/D=8 for M=1.4
8 Tooth and Plain Nozzles

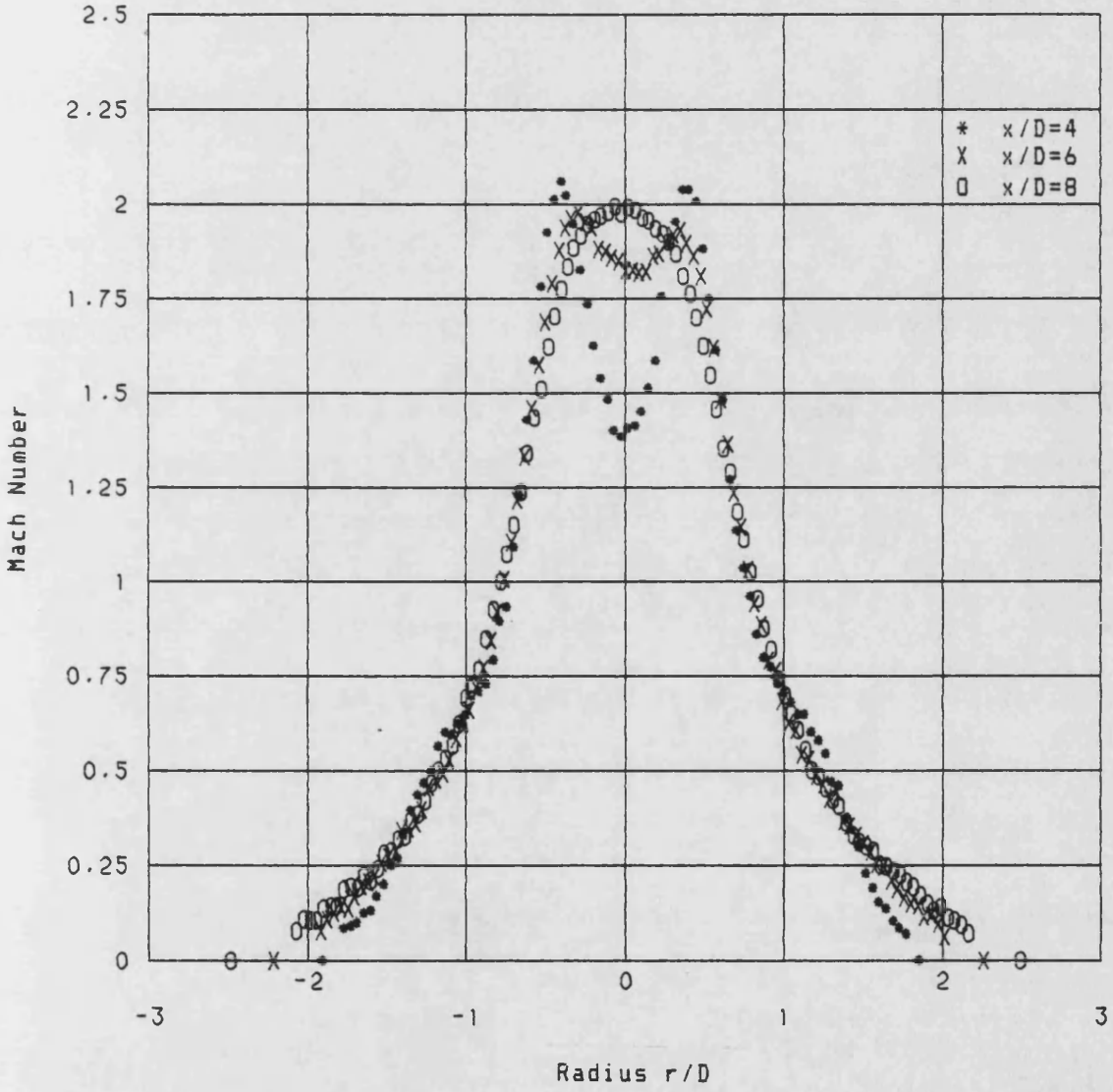

Figure 6.86 Axial variation of Mach Number for M=1.4 8 Tooth Nozzle

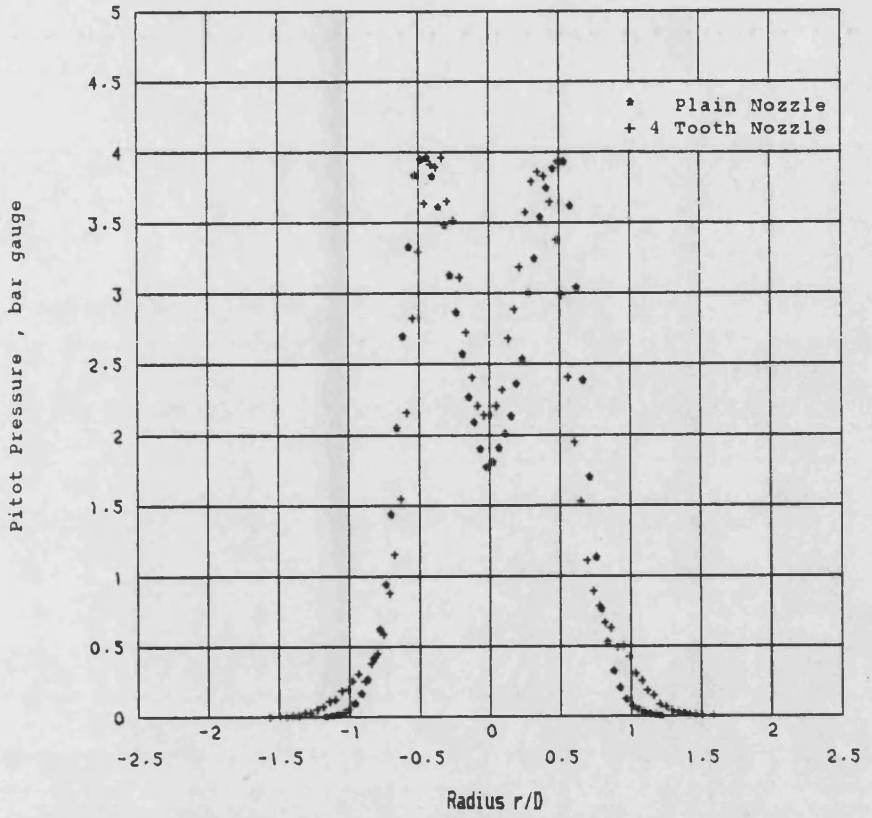

Figure 6.87 Pitot Pressure at x/D=4 for M=1.4
4 Tooth and Plain Nozzles

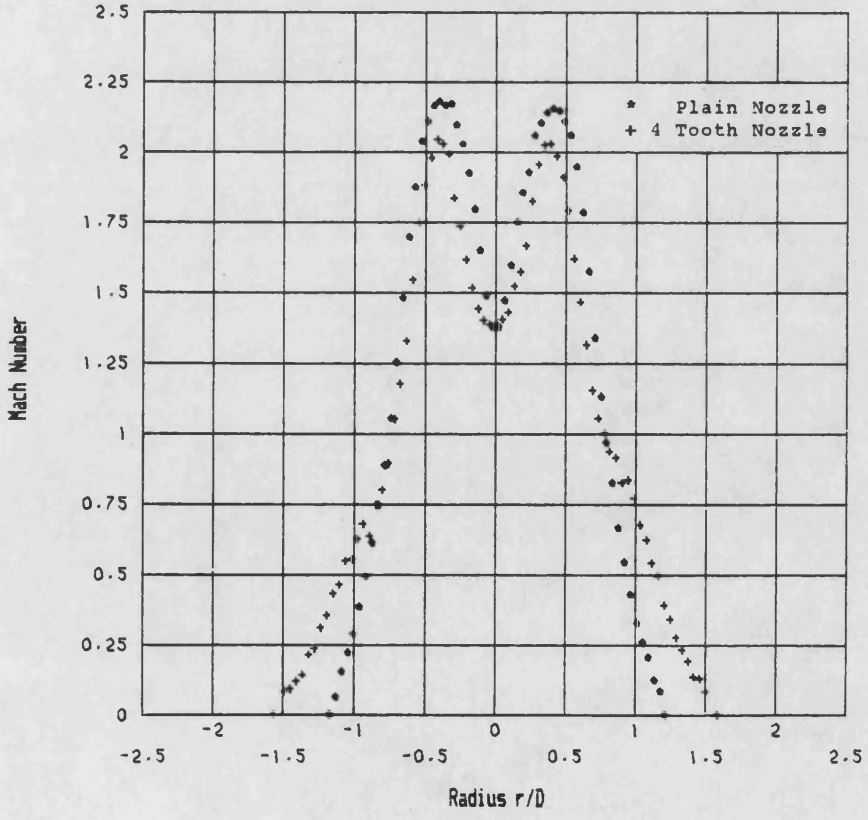

Figure 6.88 Mach Number at x/D=4 for M=1.4
4 Tooth and Plain Nozzles

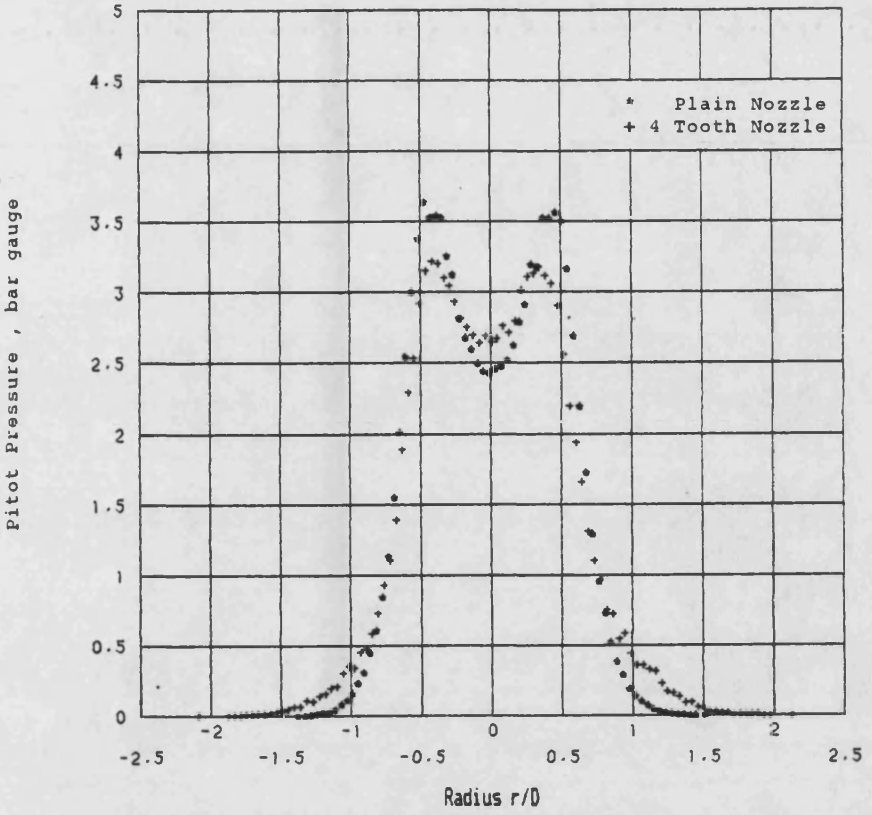

Figure 6.89 Pitot Pressure at x/D=6 for M=1.4
4 Tooth and Plain Nozzles

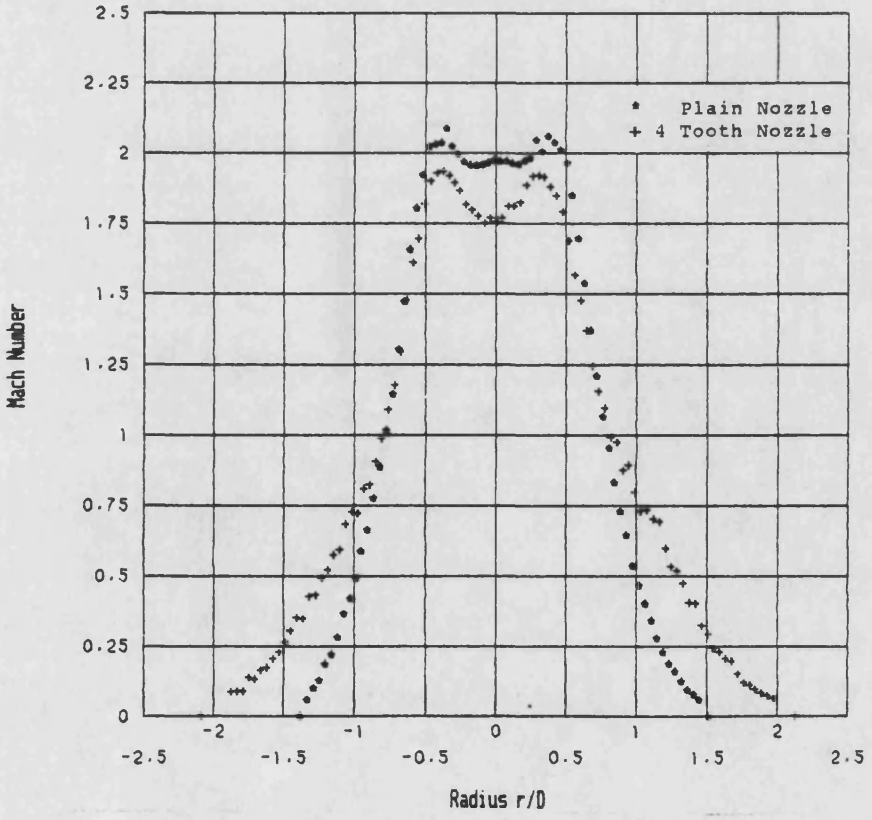

Figure 6.90 Mach Number at x/D=6 for M=1.4
4 Tooth and Plain Nozzles

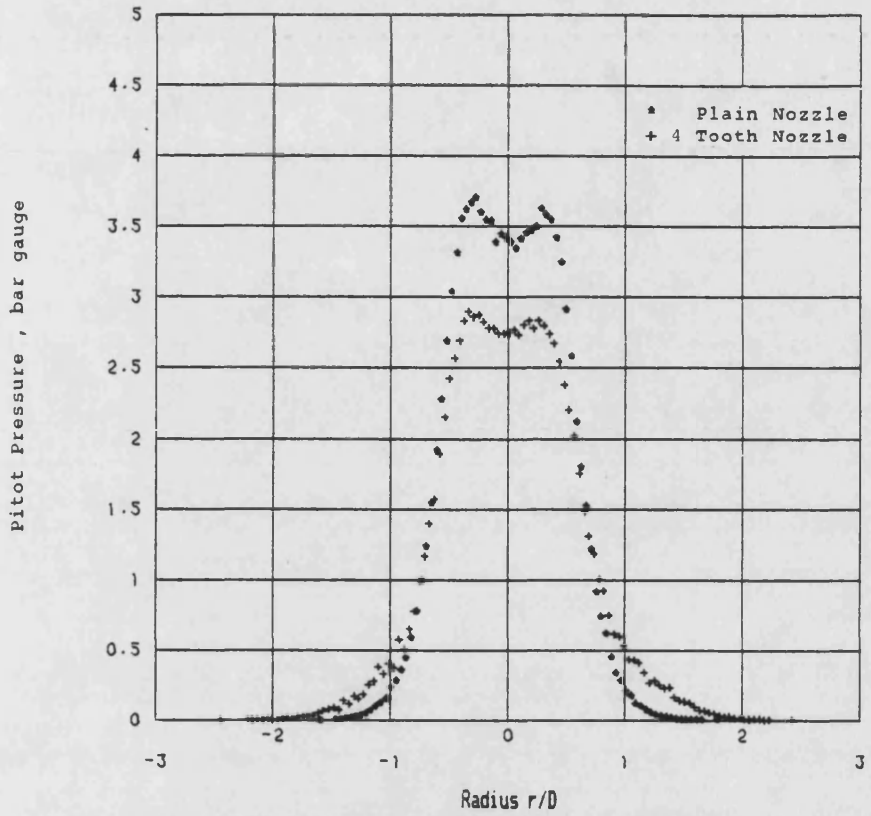

Figure 6.91 Pitot Pressure at x/D=8 for M=1.4
4 Tooth and Plain Nozzles

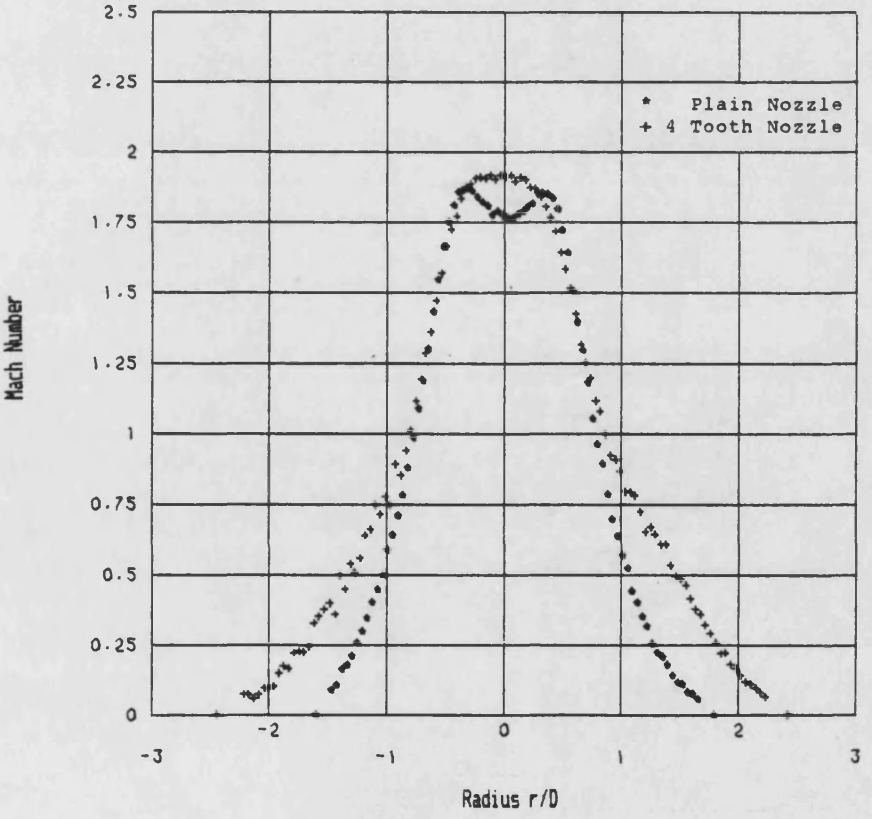

Figure 6.92 Mach Number at x/D=8 for M=1.4
4 Tooth and Plain Nozzles

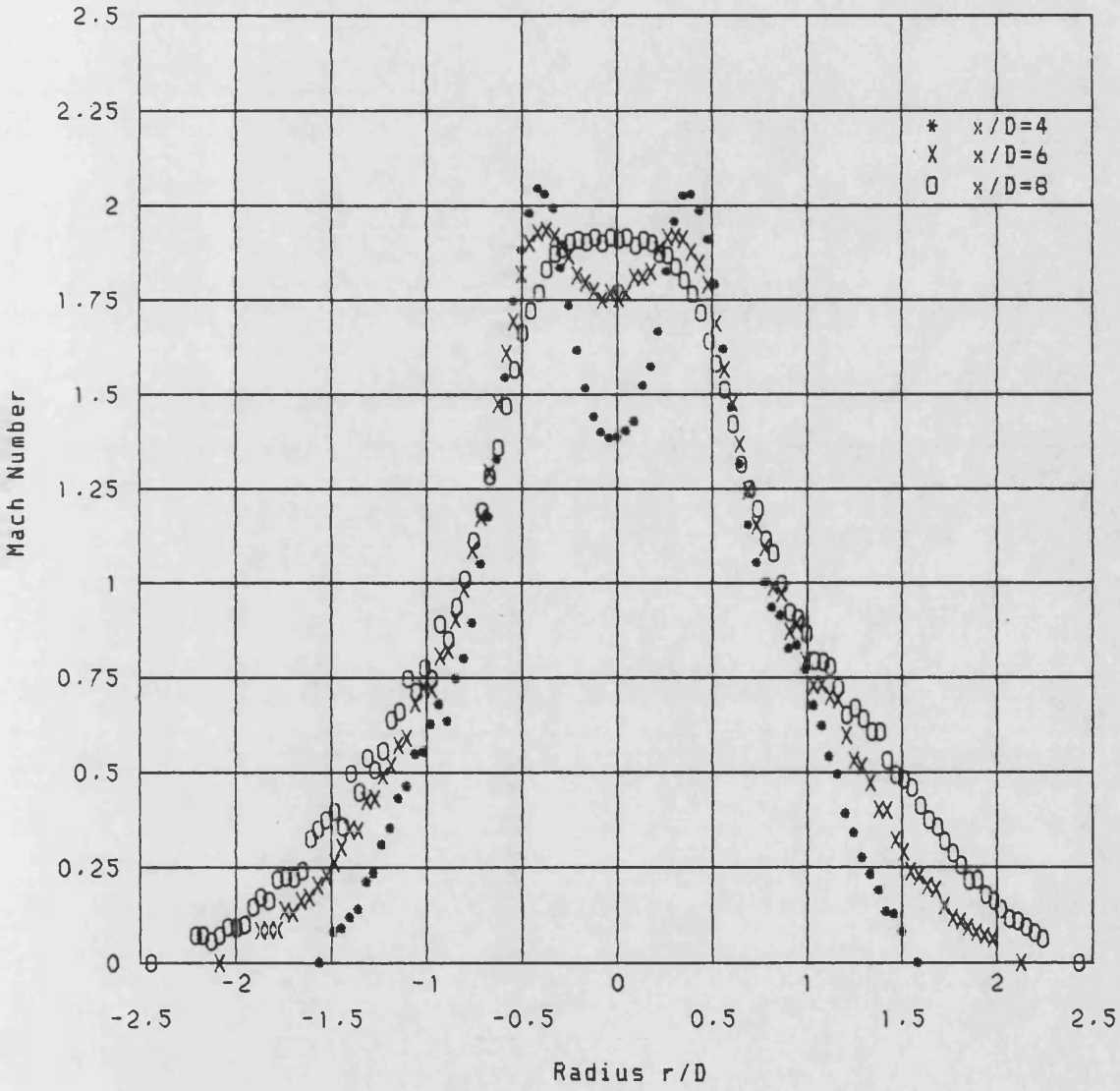

Figure 6.93 Axial variation of Mach Number for M=1.4 4 Tooth Nozzle

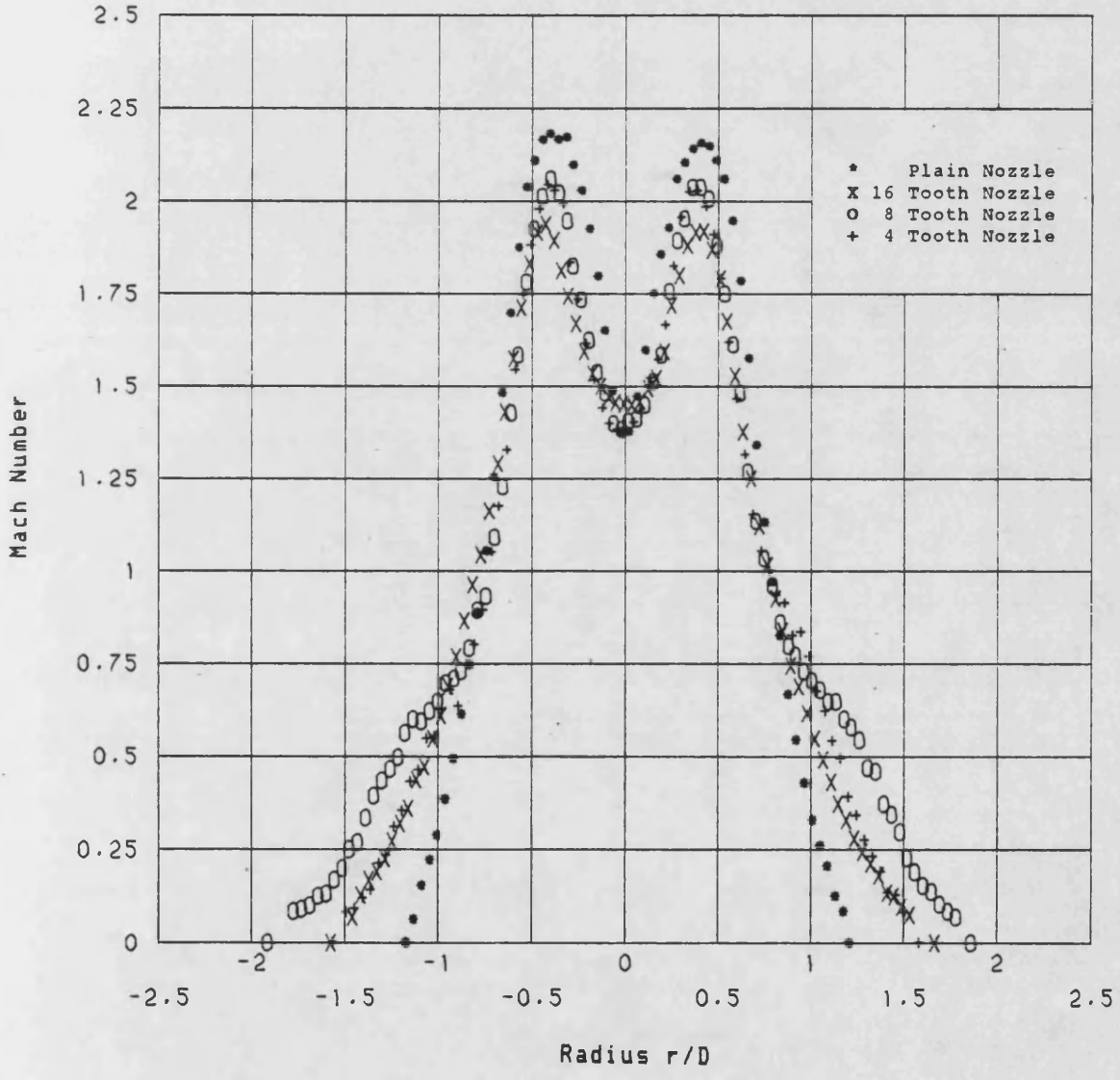

Figure 6.94 Mach Number of M=1.4 Nozzles at x/D=4

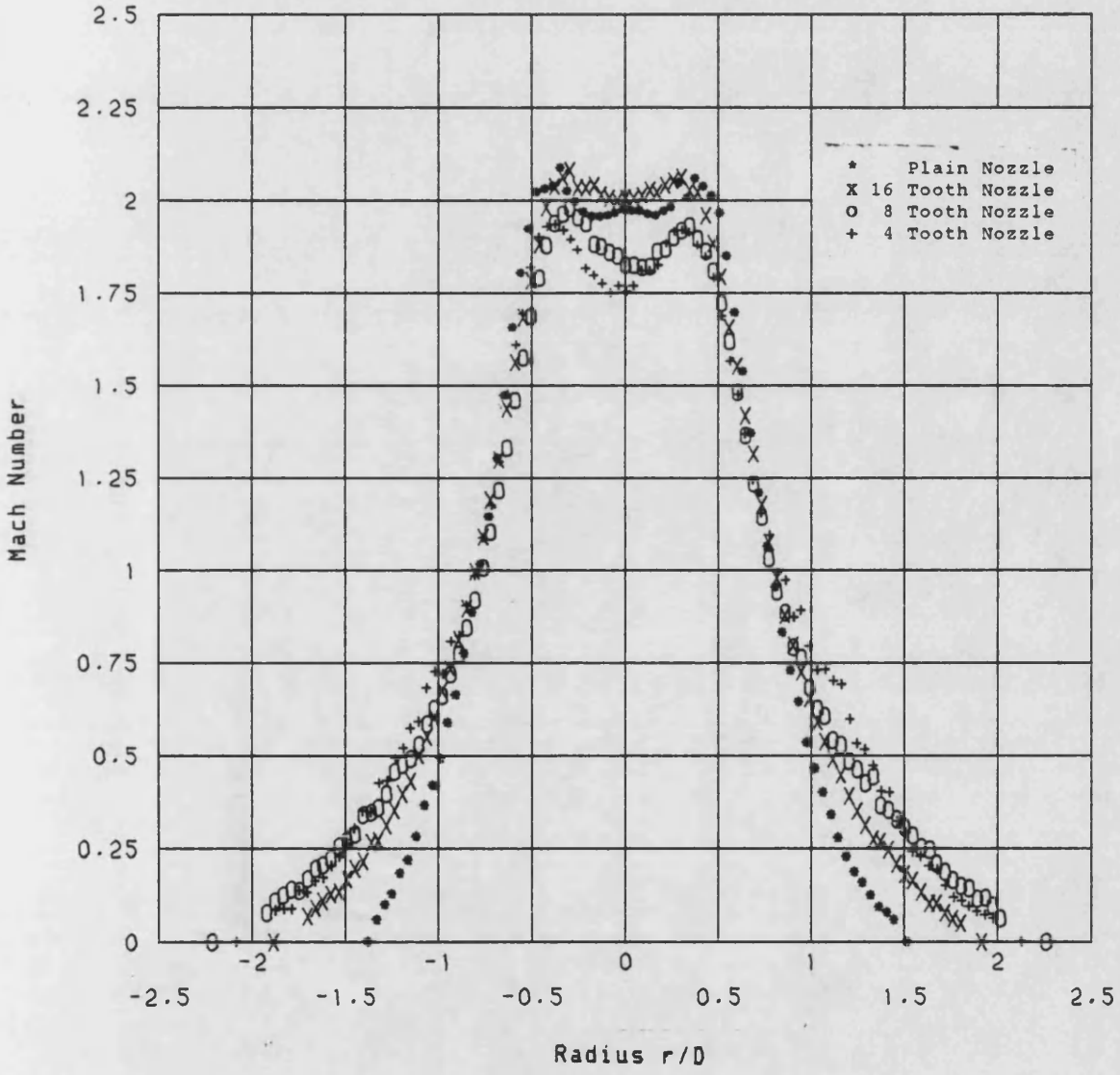

Figure 6.95 Mach Number of M=1.4 Nozzles at x/D=6

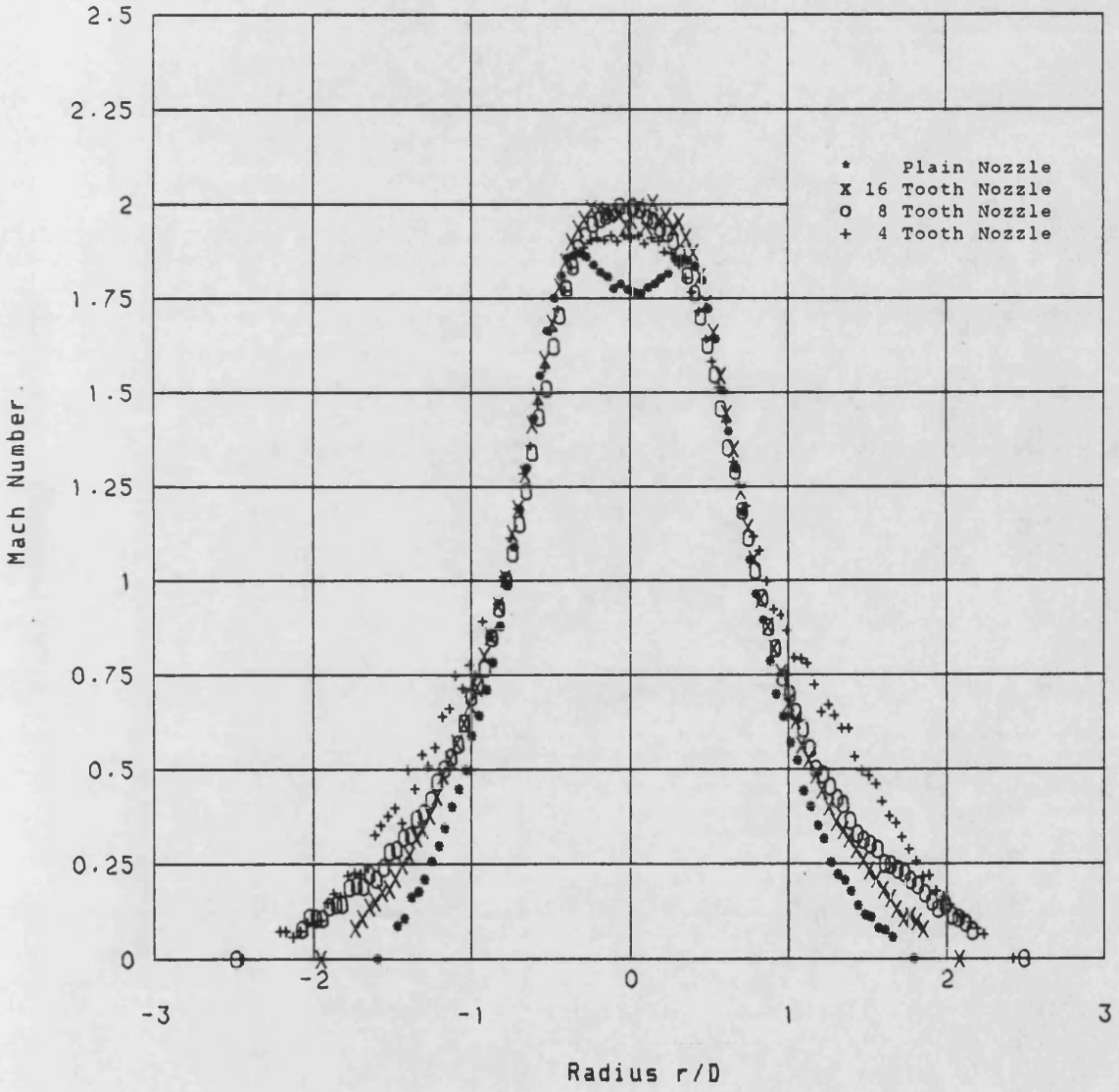

Figure 6.96 Mach Number of M=1.4 Nozzles at x/D=8

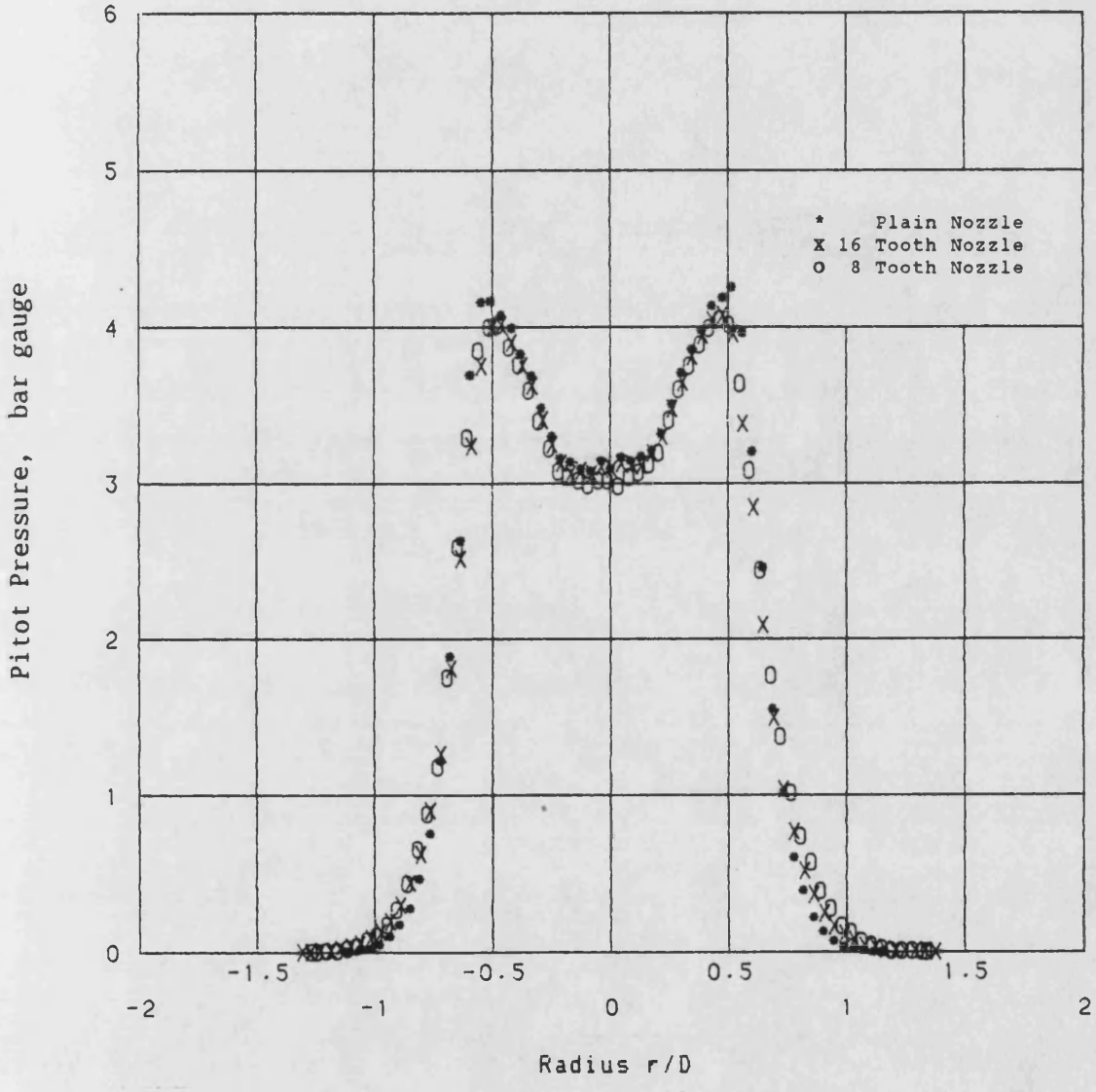

Figure 6.97 Pitot Pressure at x/D=4 for M=1.8 16 Tooth, 8 Tooth and Plain Nozzles

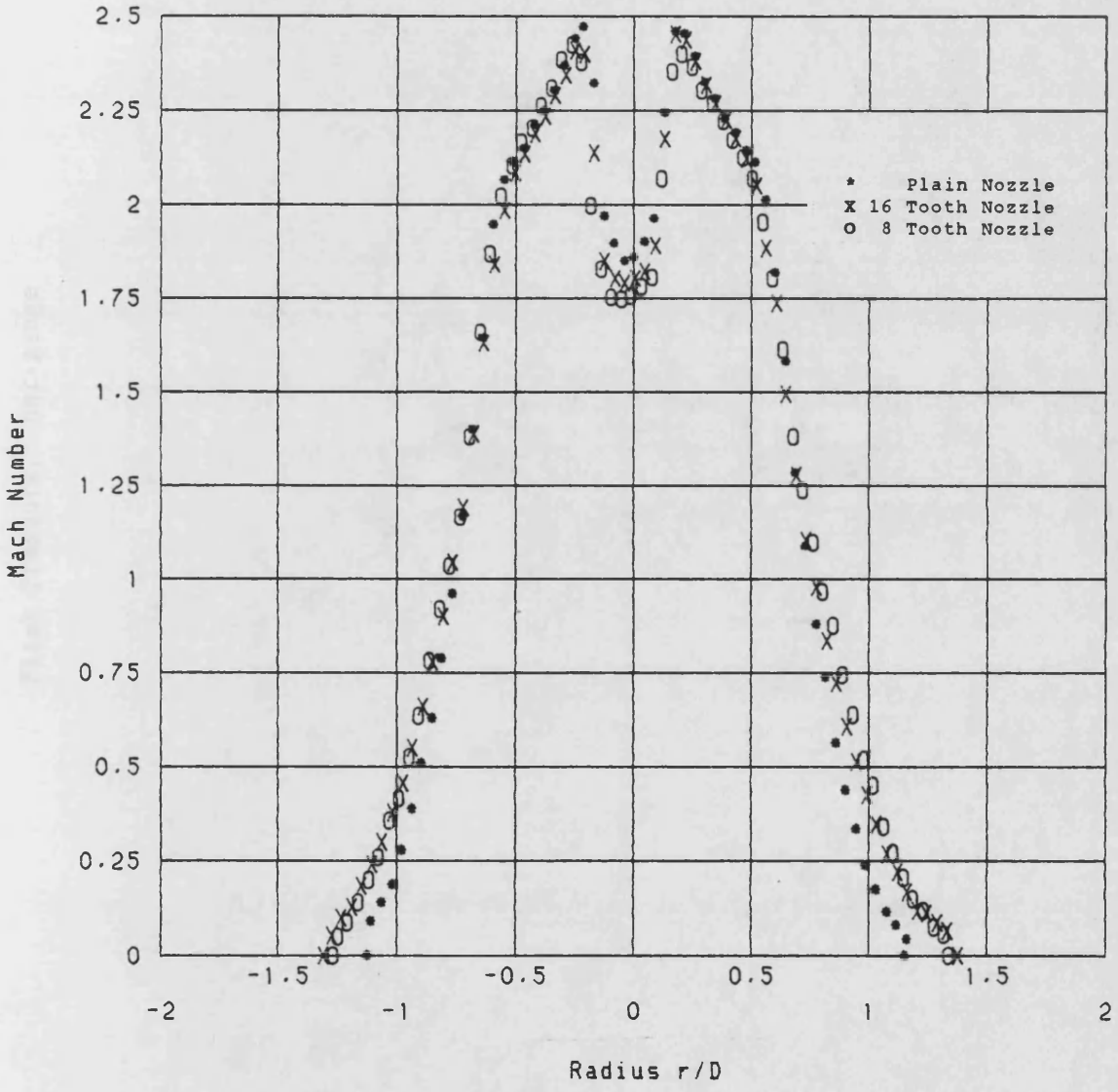

Figure 6.98 Mach Number at x/D=4 for M=1.8 16 Tooth, 8 Tooth and Plain Nozzles

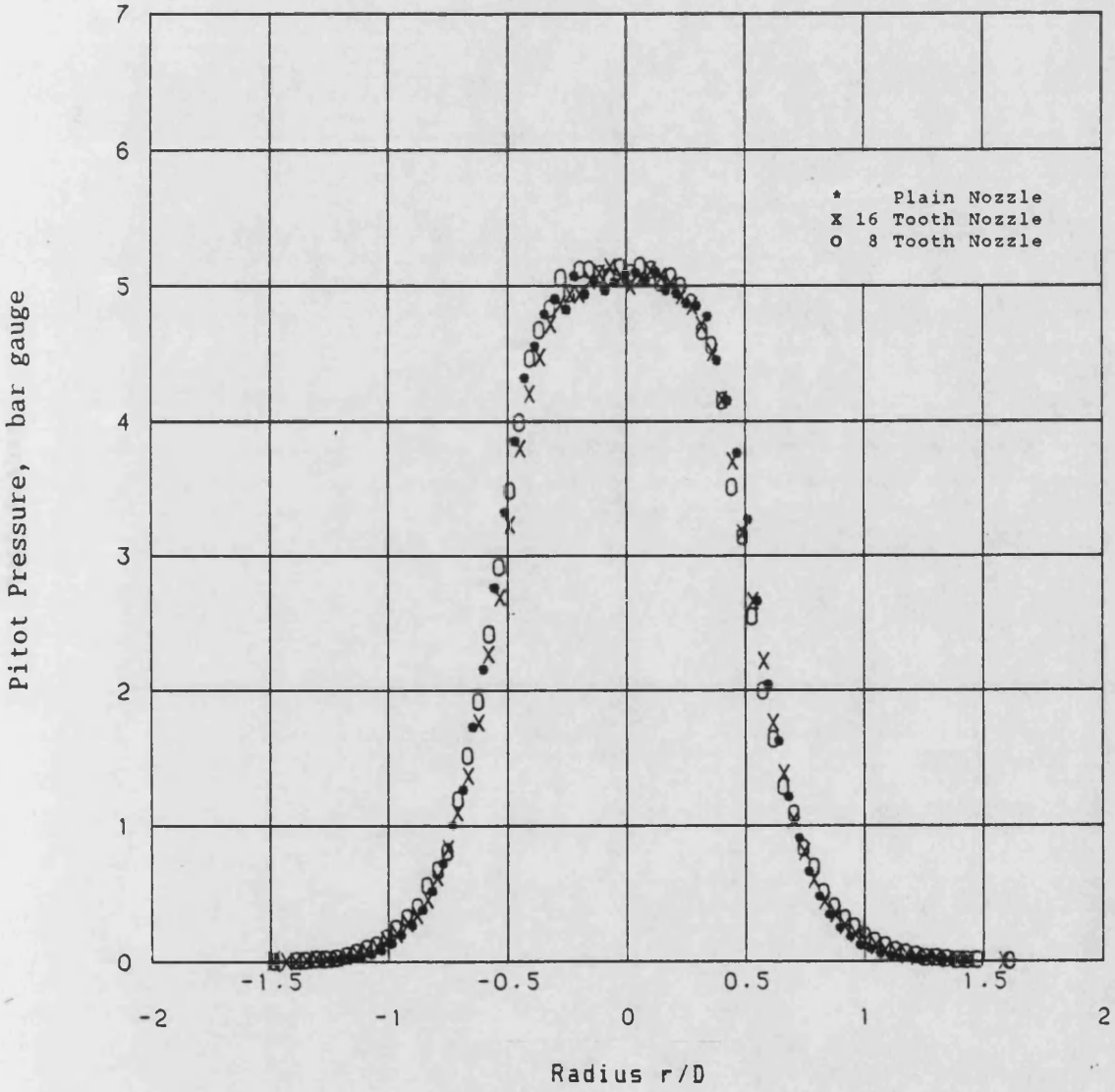

Figure 6.99 Pitot Pressure at x/D=6 for M=1.8 16 Tooth, 8 Tooth and Plain Nozzles

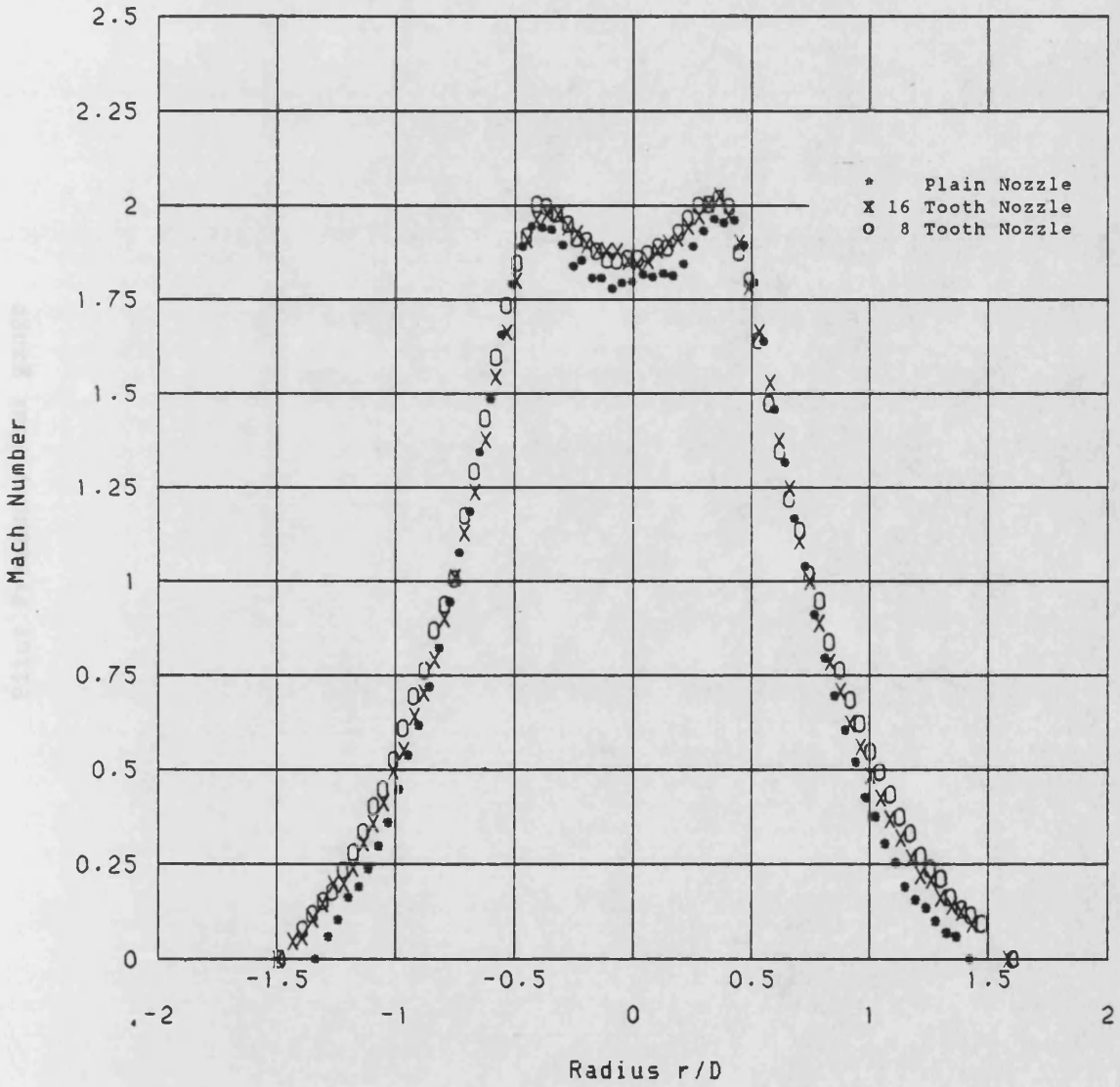

Figure 6.100 Mach Number at x/D=6 for M=1.8 16 Tooth, 8 Tooth and Plain Nozzles

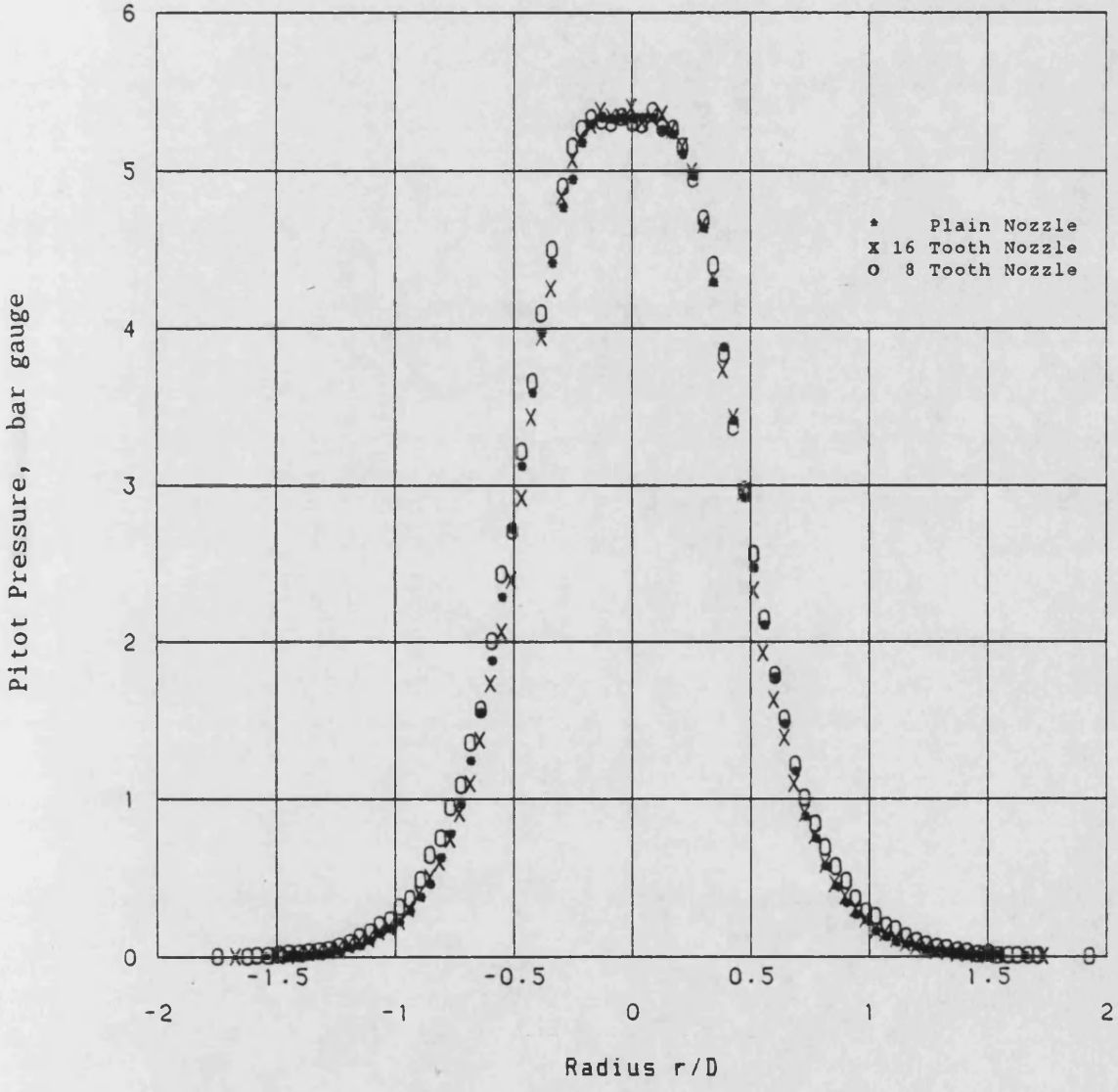

Figure 6.101 Pitot Pressure at x/D=8 for M=1.8 16 Tooth, 8 Tooth and Plain Nozzles

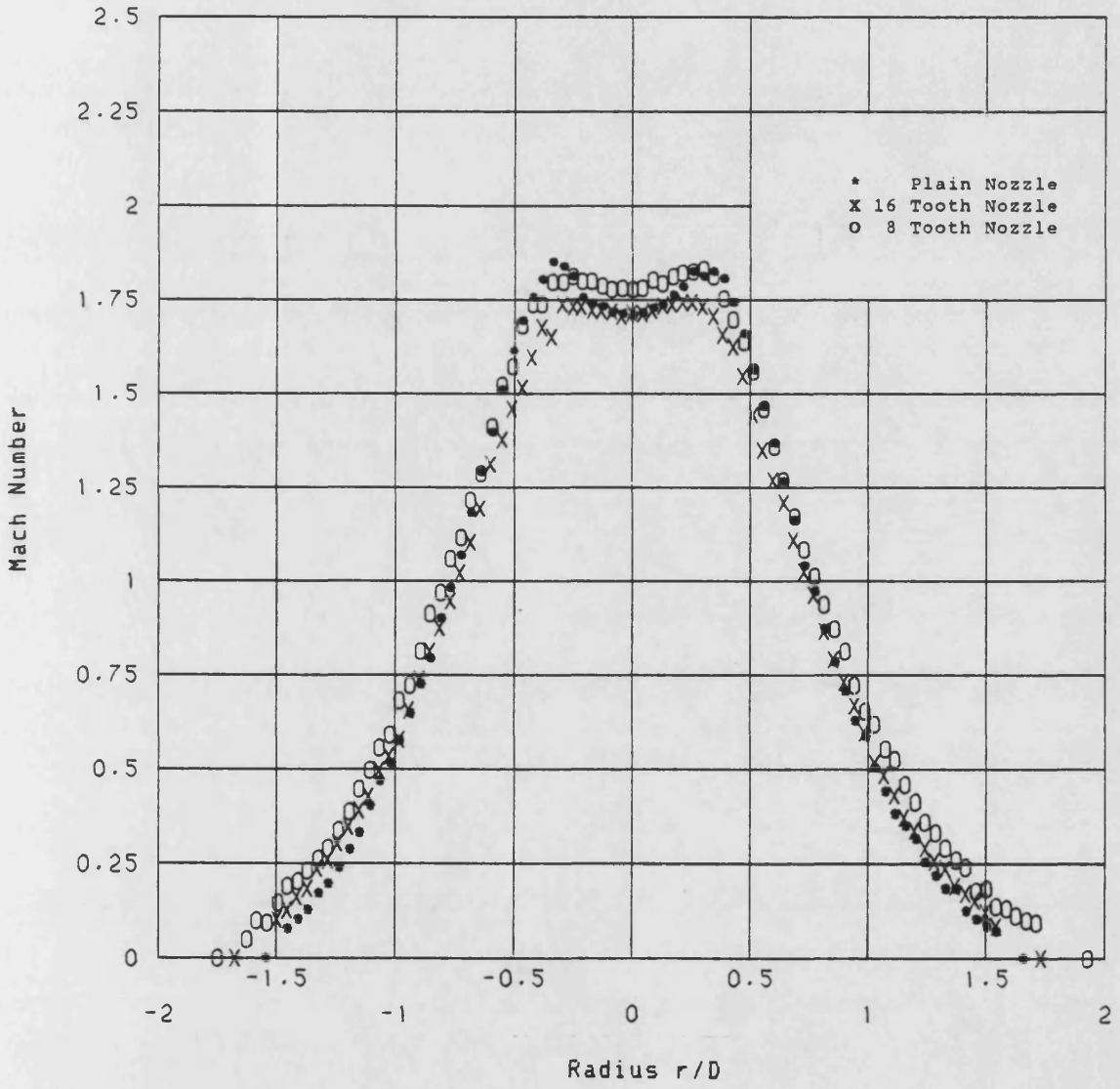

Figure 6.102 Mach Number at x/D=8 for M=1.8 16 Tooth, 8 Tooth and Plain Nozzles

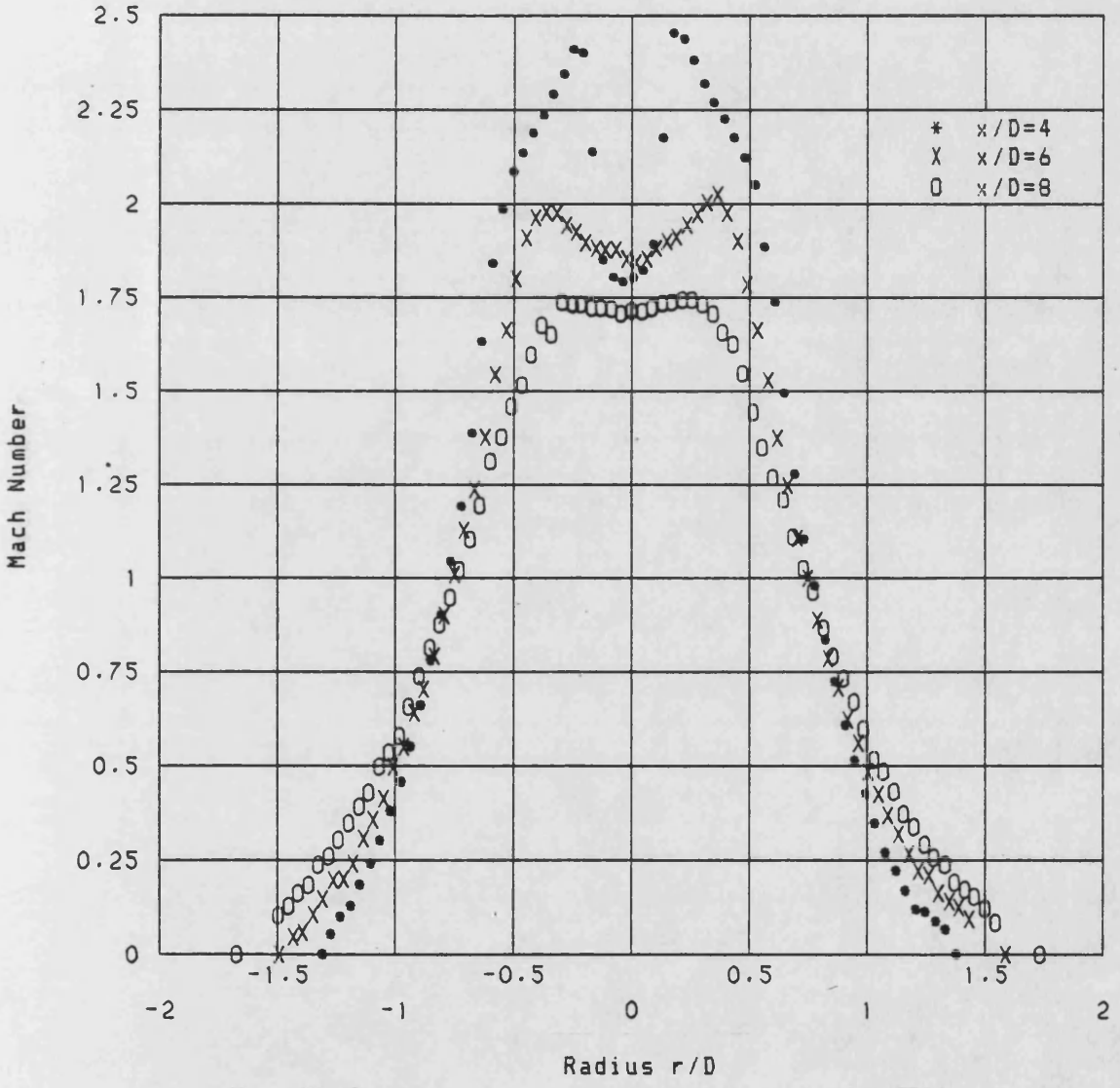

Figure 6.103 Axial variation of Mach Number for M=1.8 16 Tooth Nozzle

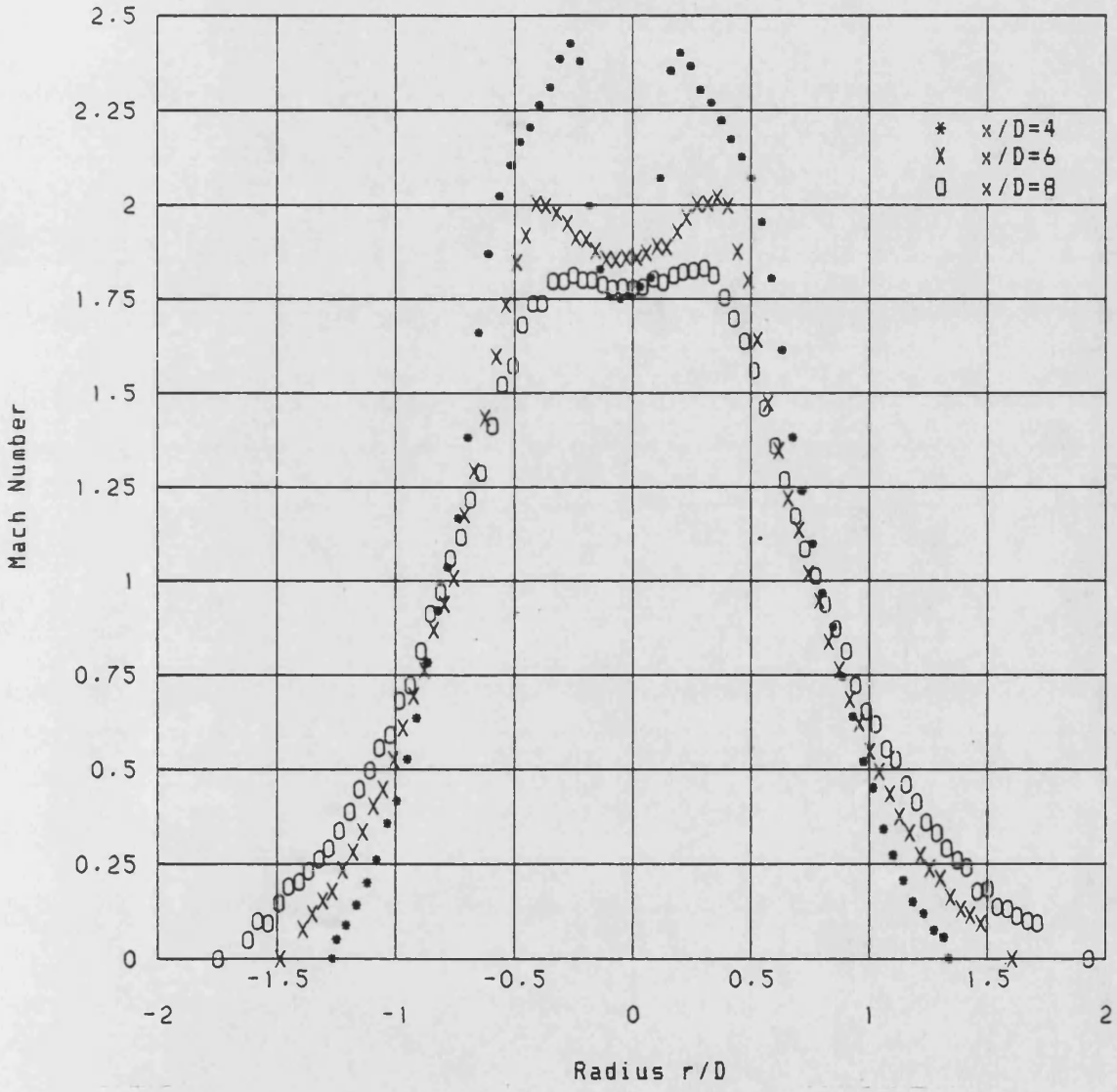

Figure 6.104 Axial variation of Mach Number for M=1.8 8 Tooth Nozzle

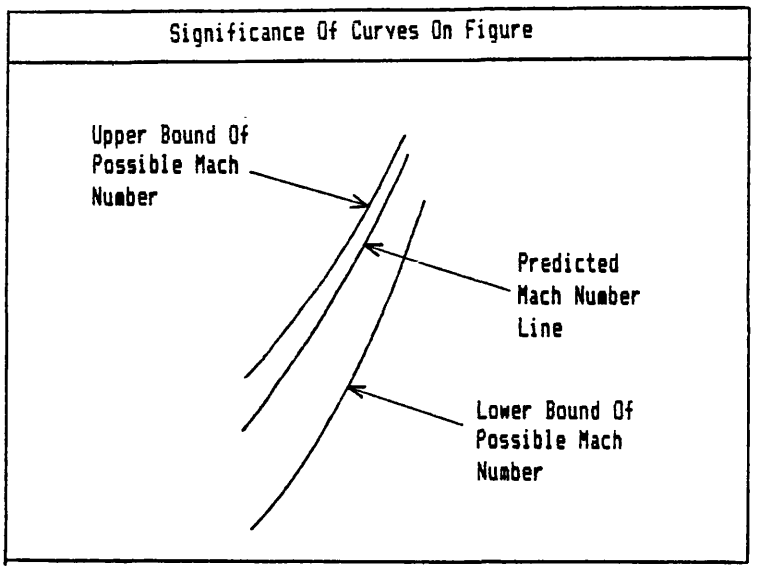

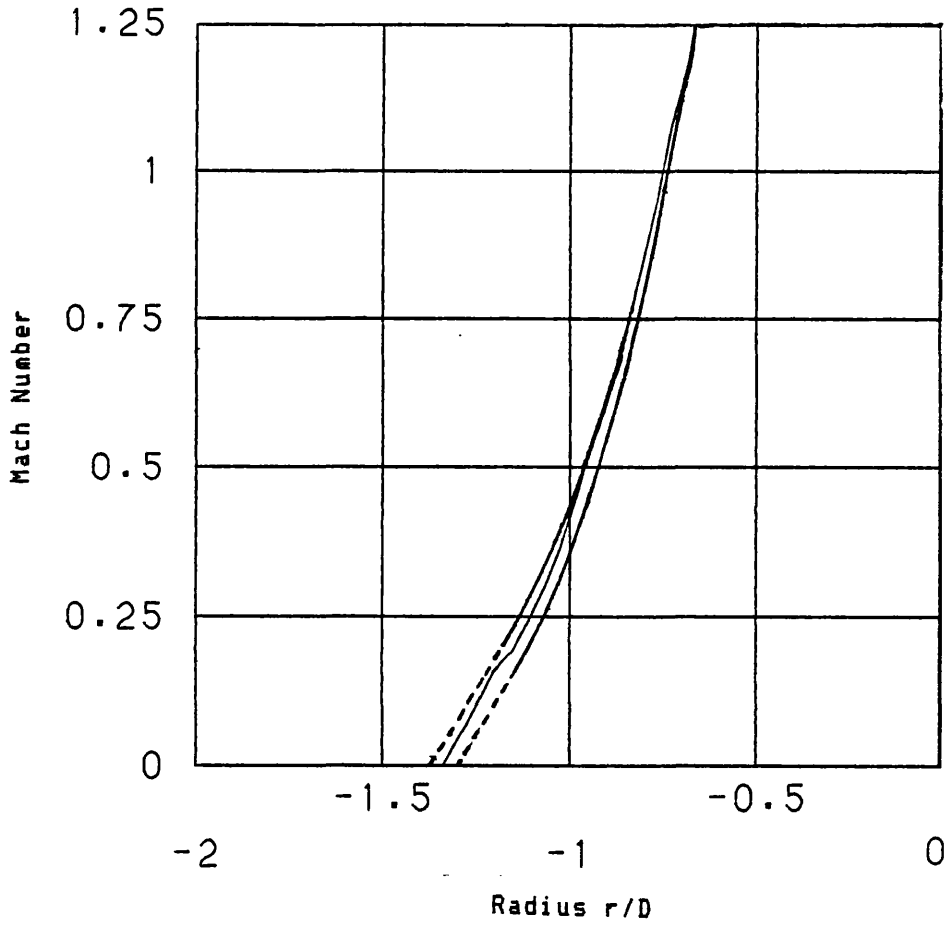

Figure 6.105 Typical Error Limits on Mach Number Profile

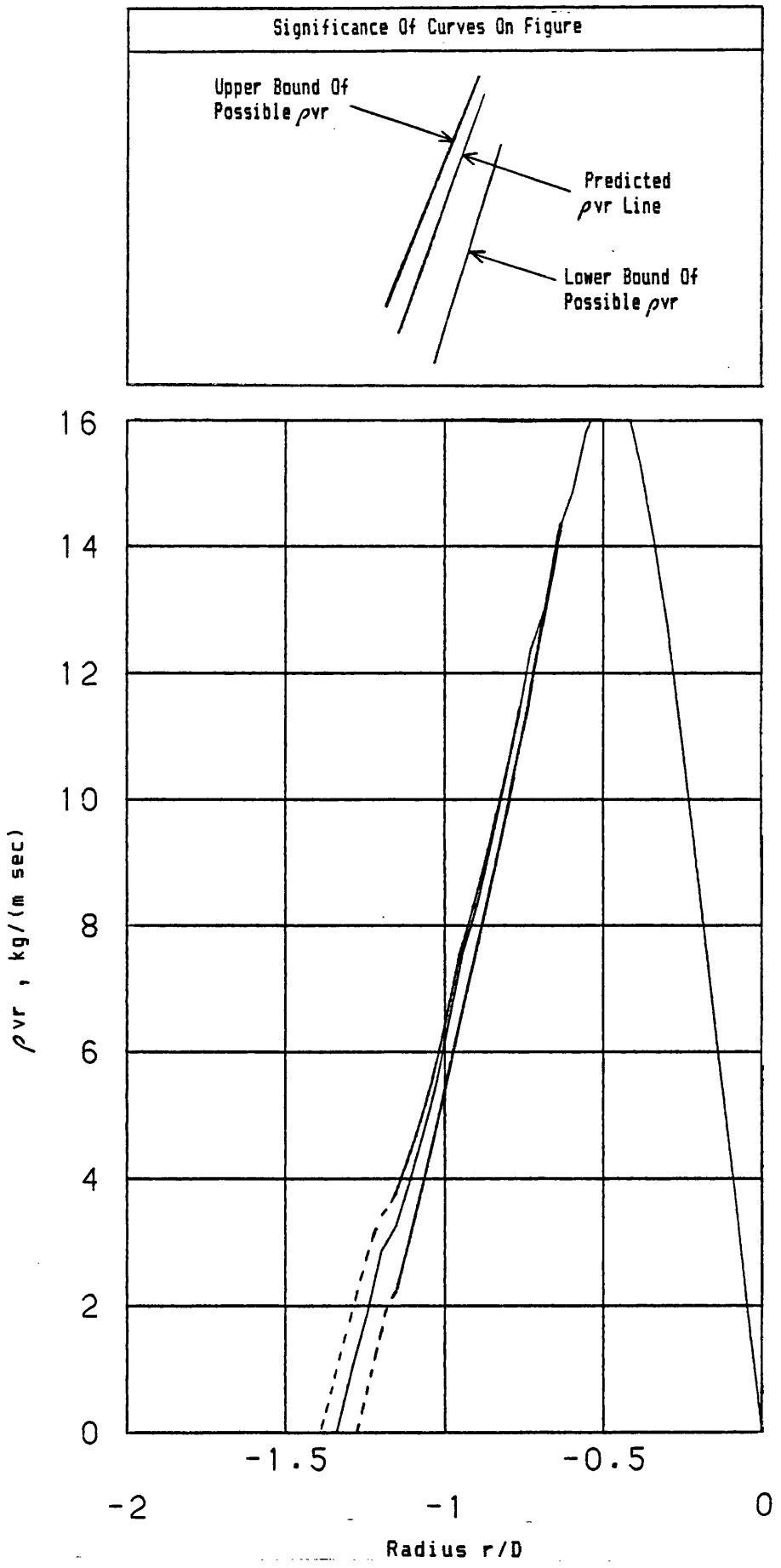

Figure 6.106 Typical Error Limits on ρvr Profile

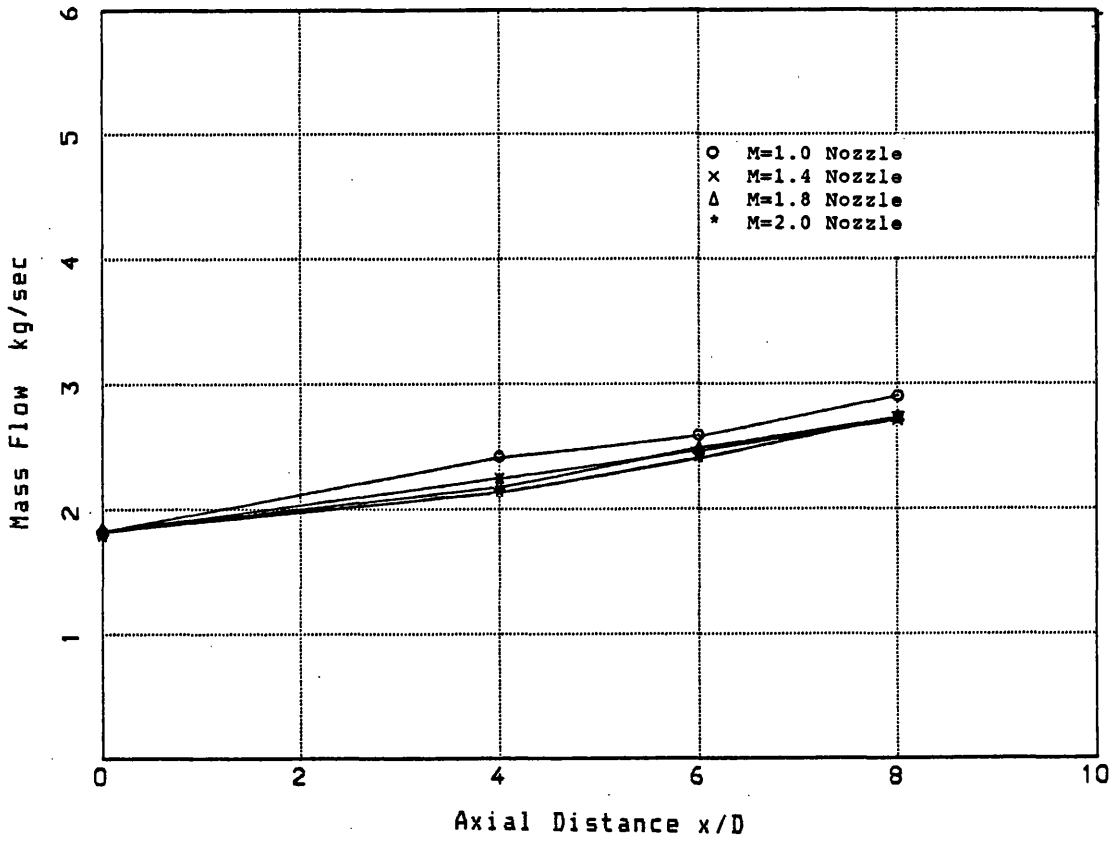

Figure 6.107 Axial variation of Mass Flow for the Plain Nozzles

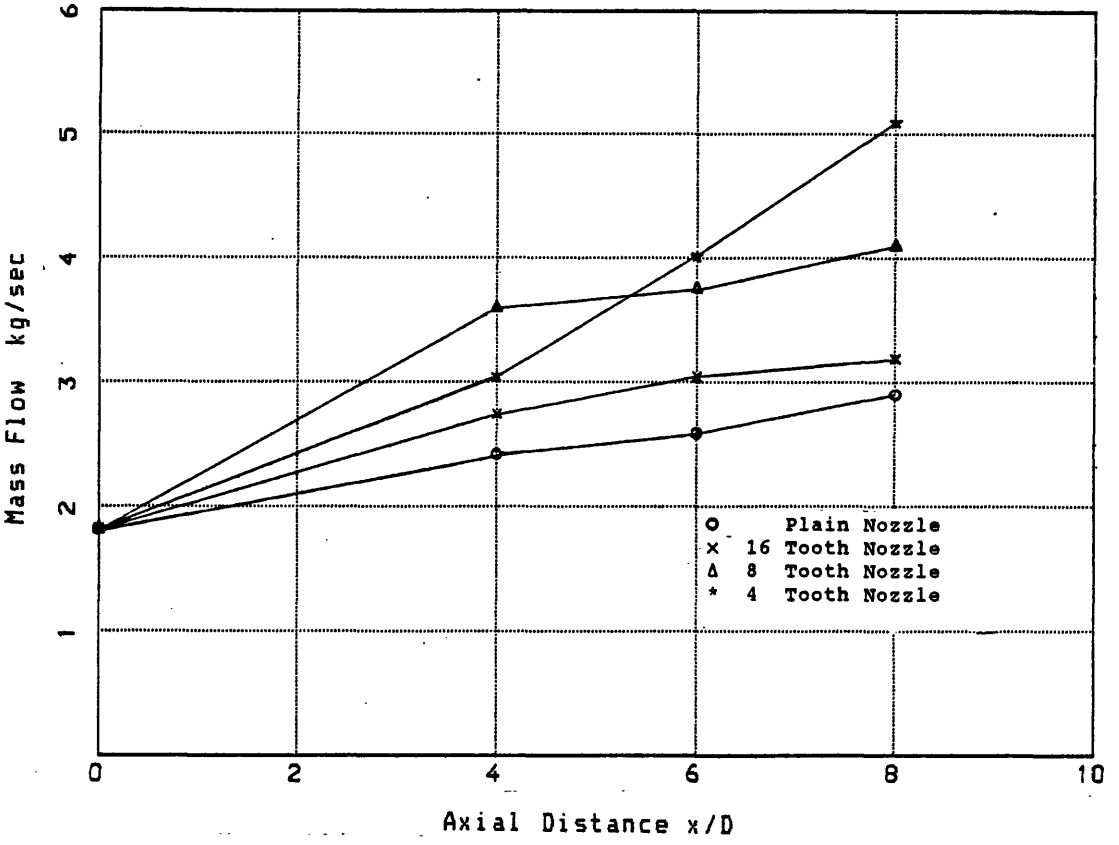

Figure 6.108 Axial variation of Mass Flow for the M=1.0 Nozzles

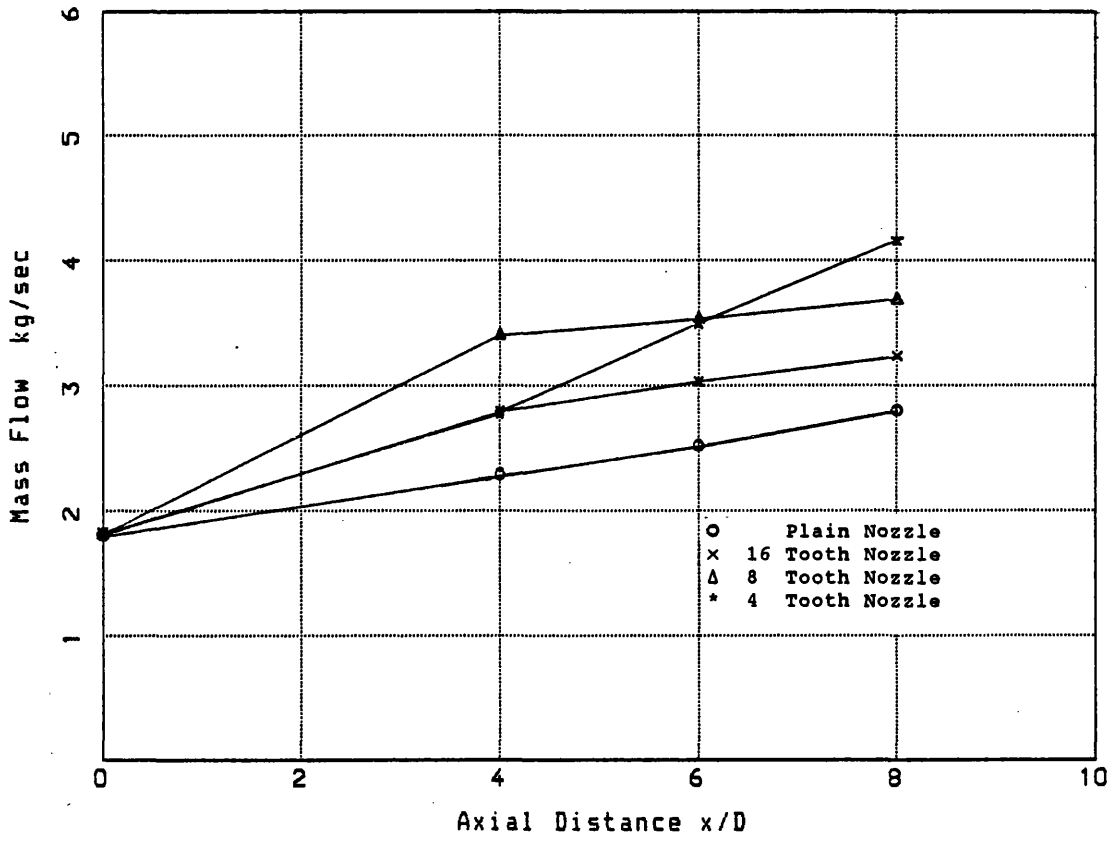

Figure 6.109 Axial variation of Mass Flow for the M=1.4 Nozzles

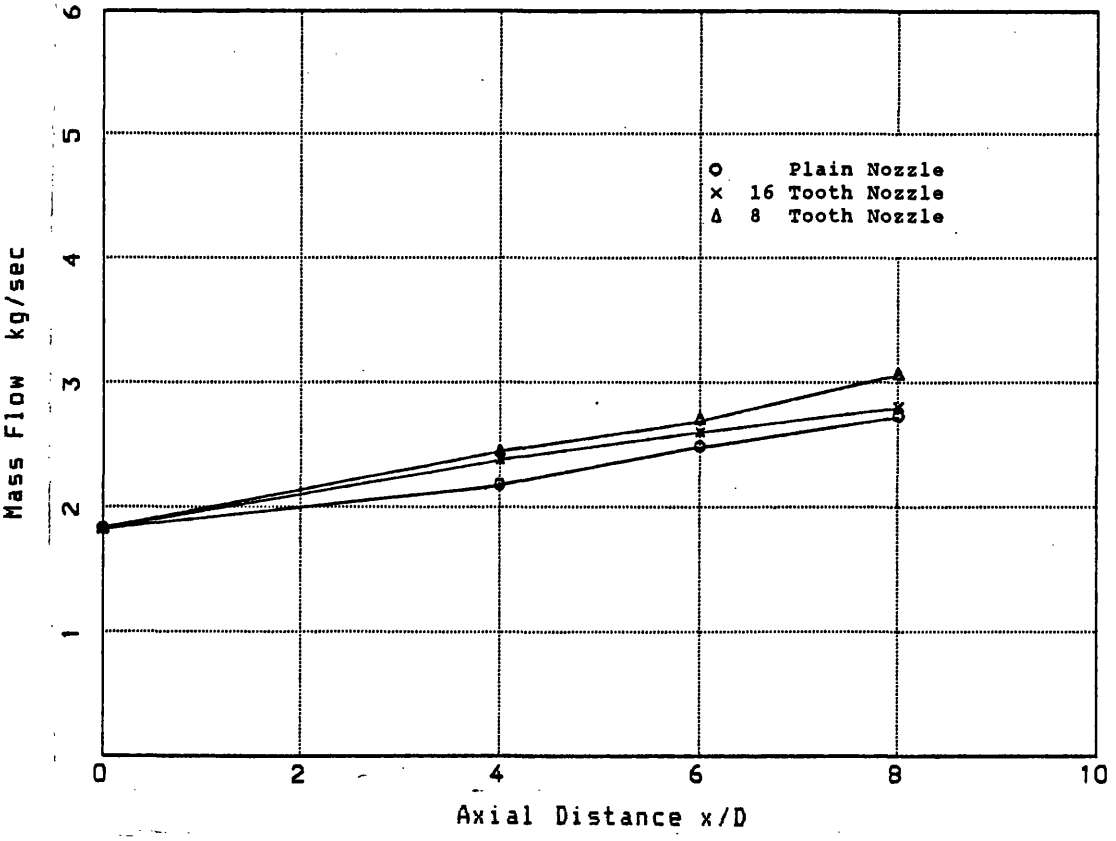

Figure 6.110 Axial variation of Mass Flow for the M=1.8 Nozzles

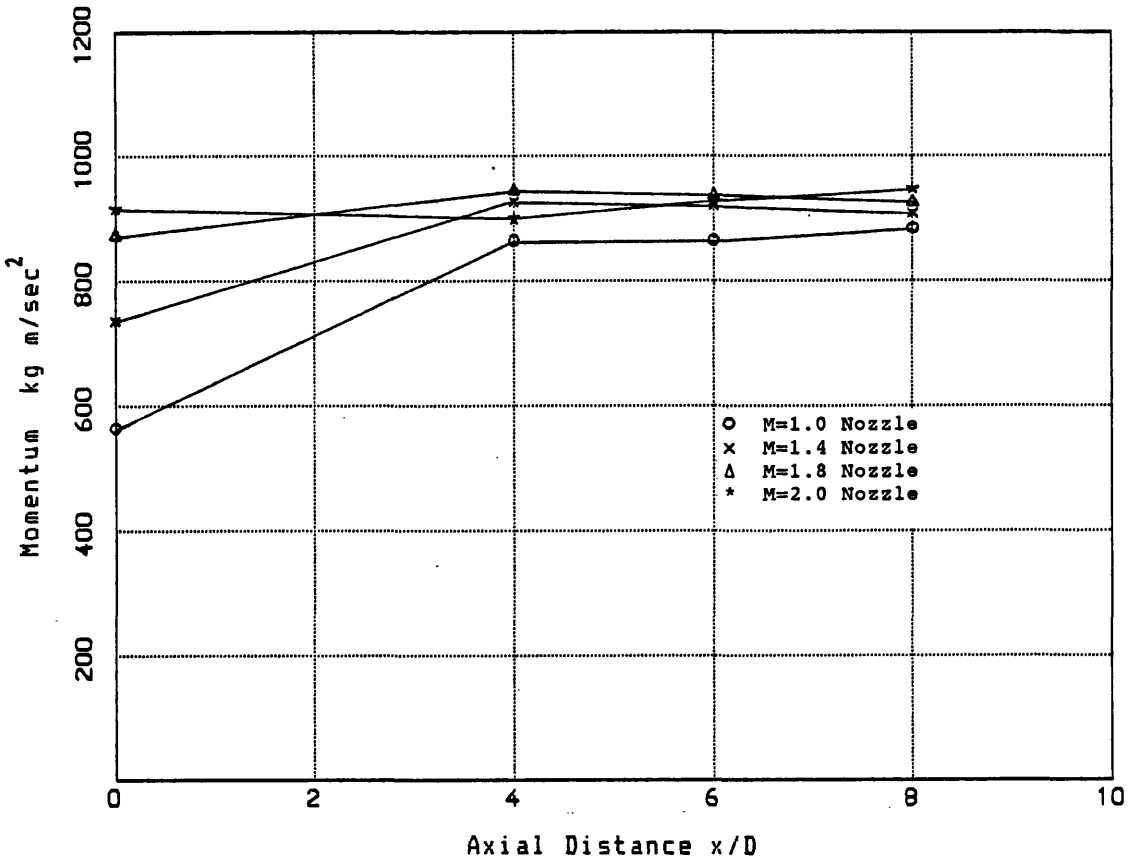

Figure 6.111 Axial variation of Momentum for the Plain Nozzles

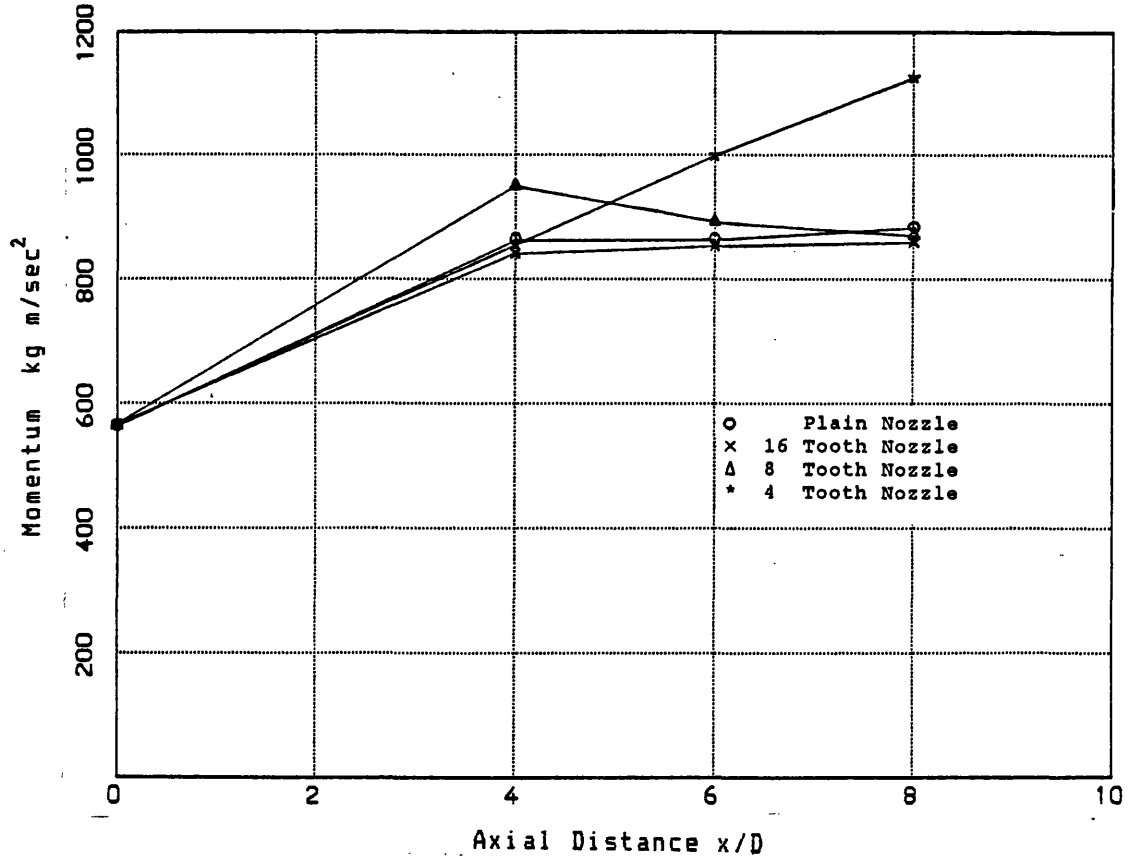

Figure 6.112 Axial variation of Momentum for the M=1.0 Nozzles

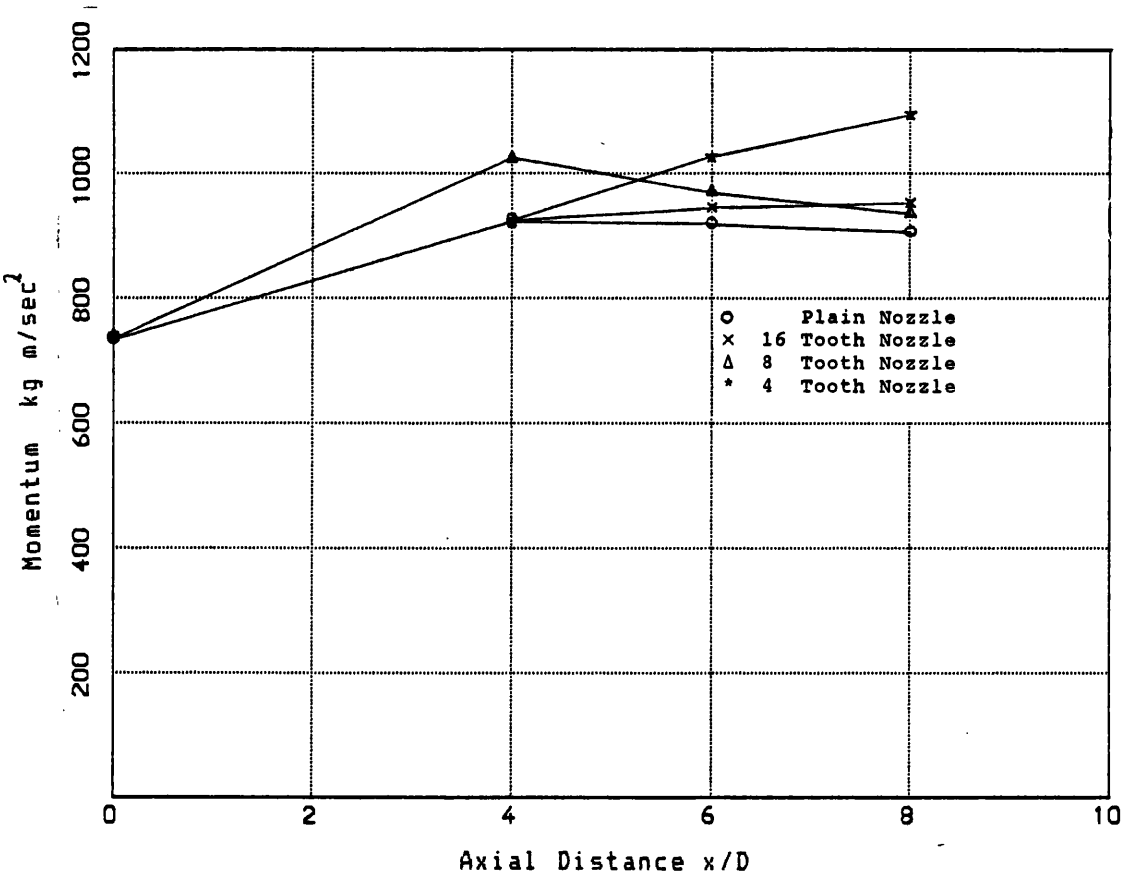

Figure 6.113 Axial variation of Momentum for the M=1.4 Nozzles

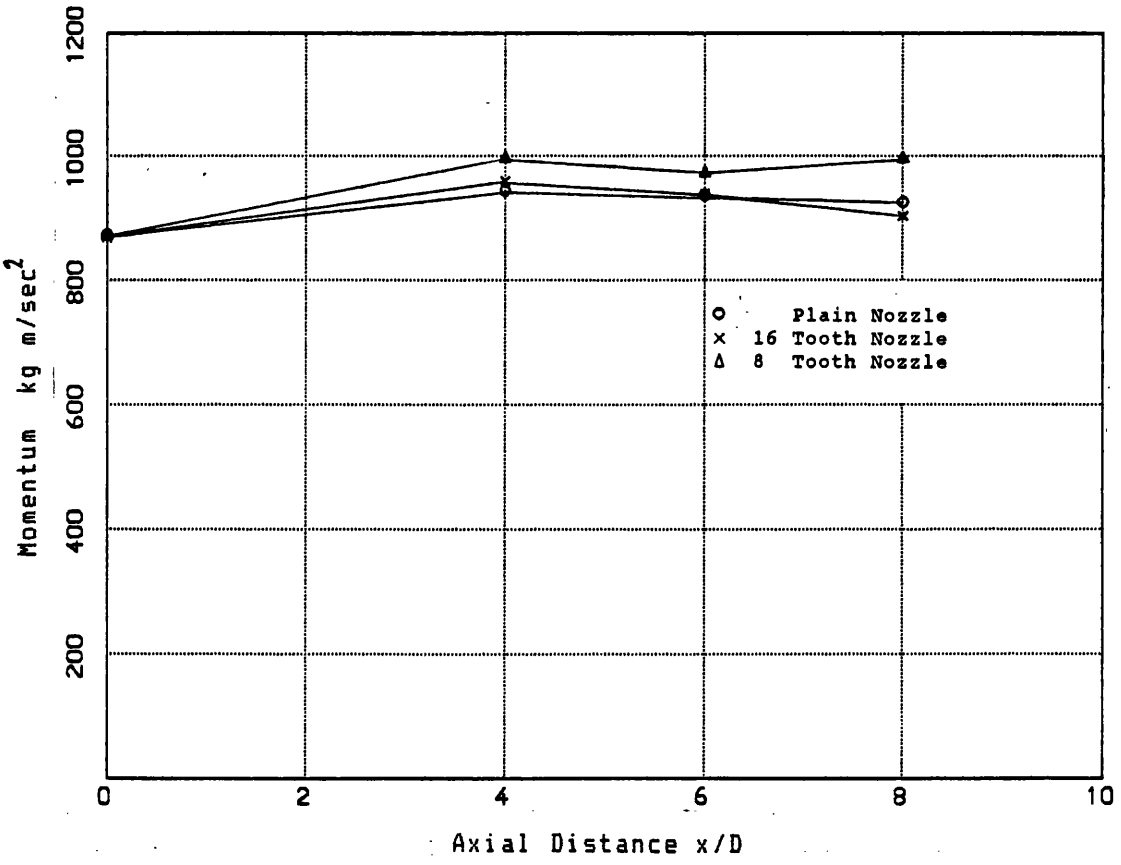

Figure 6.114 Axial variation of Momentum for the M=1.8 Nozzles

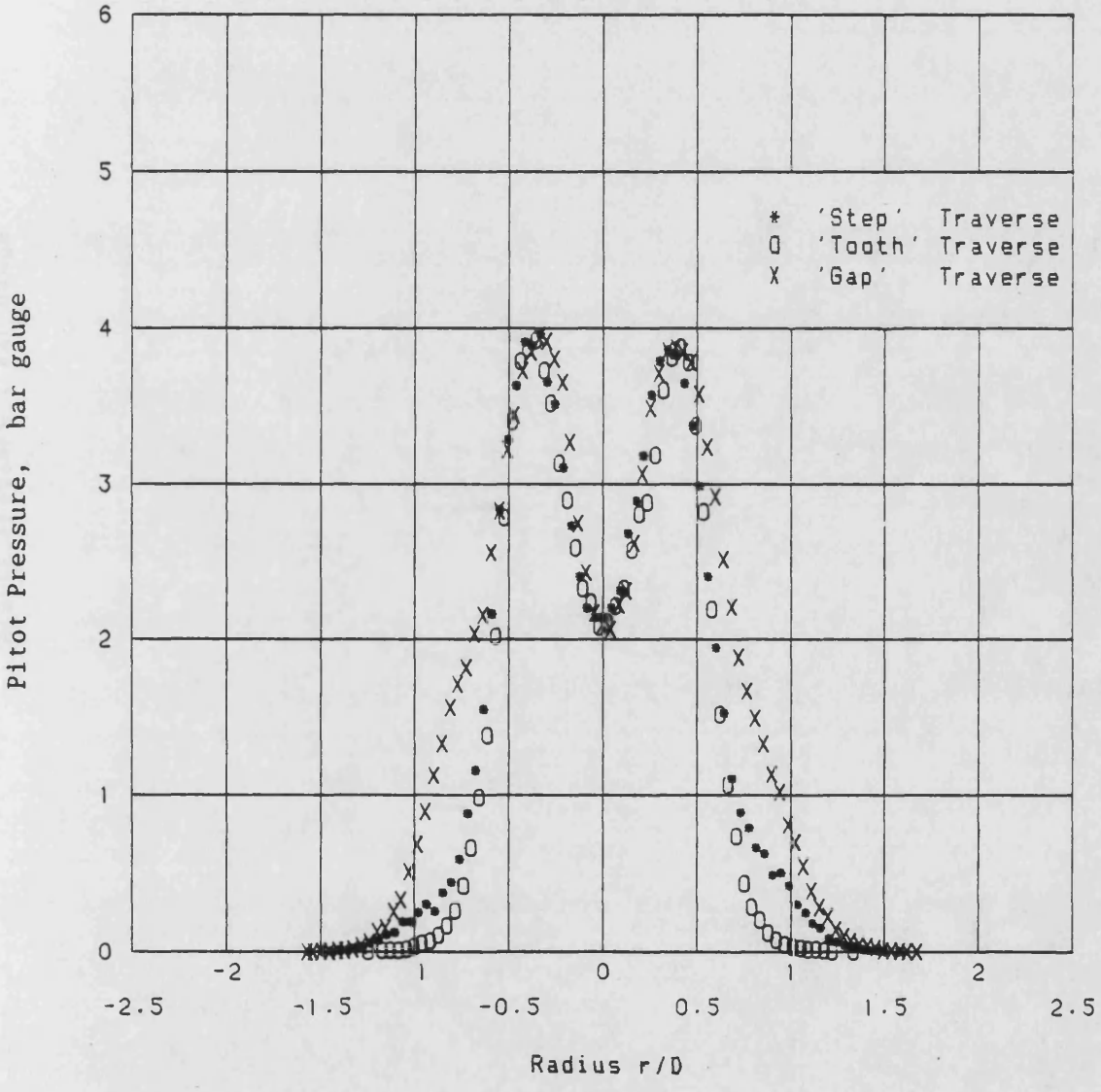

Figure 6.115 Pitot Pressure at x/D=4 for M=1.4 4 Tooth Rotation Test

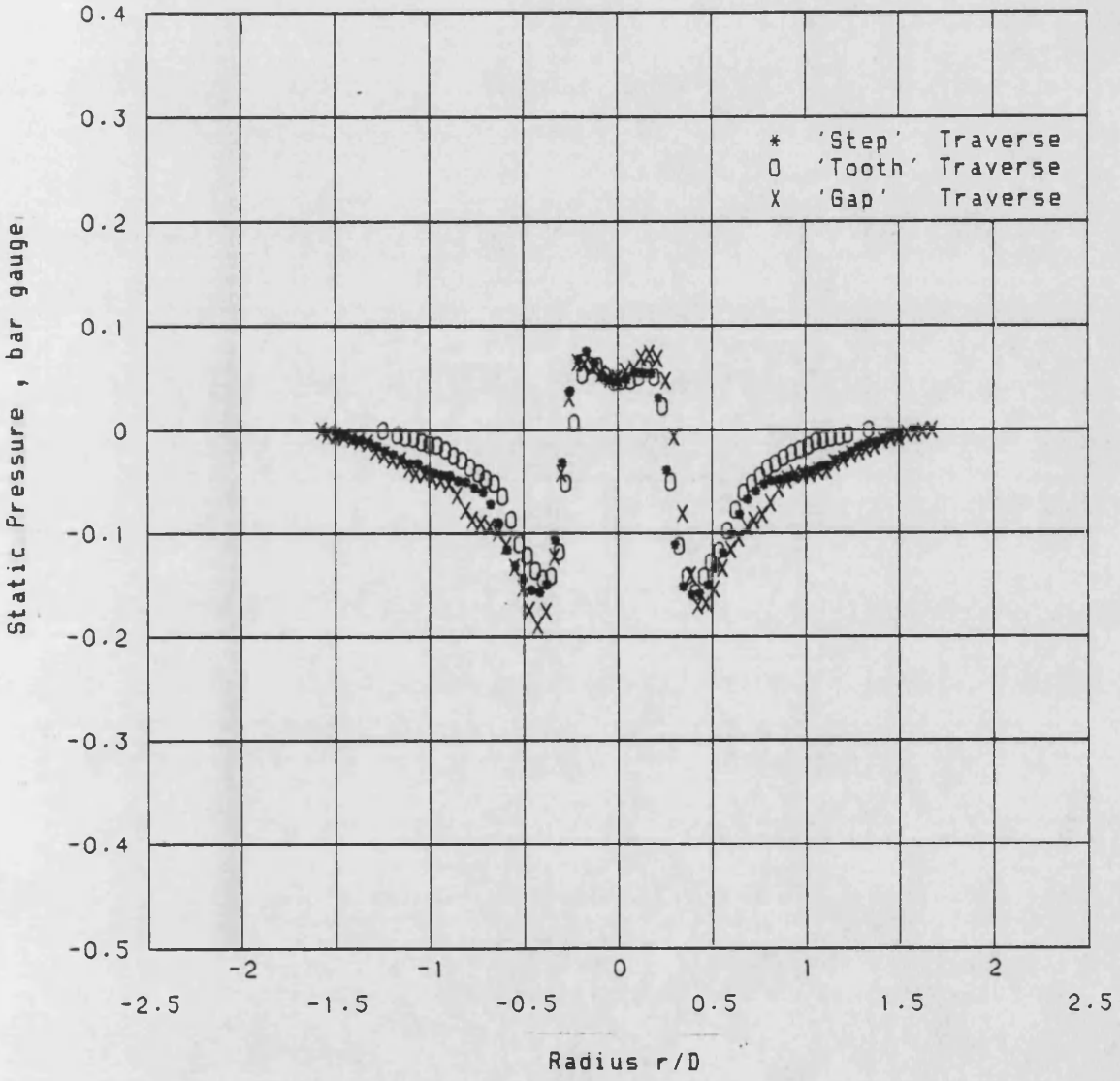

Figure 6.116 Static Pressure at x/D=4 for M=1.4 4 Tooth Rotation Test

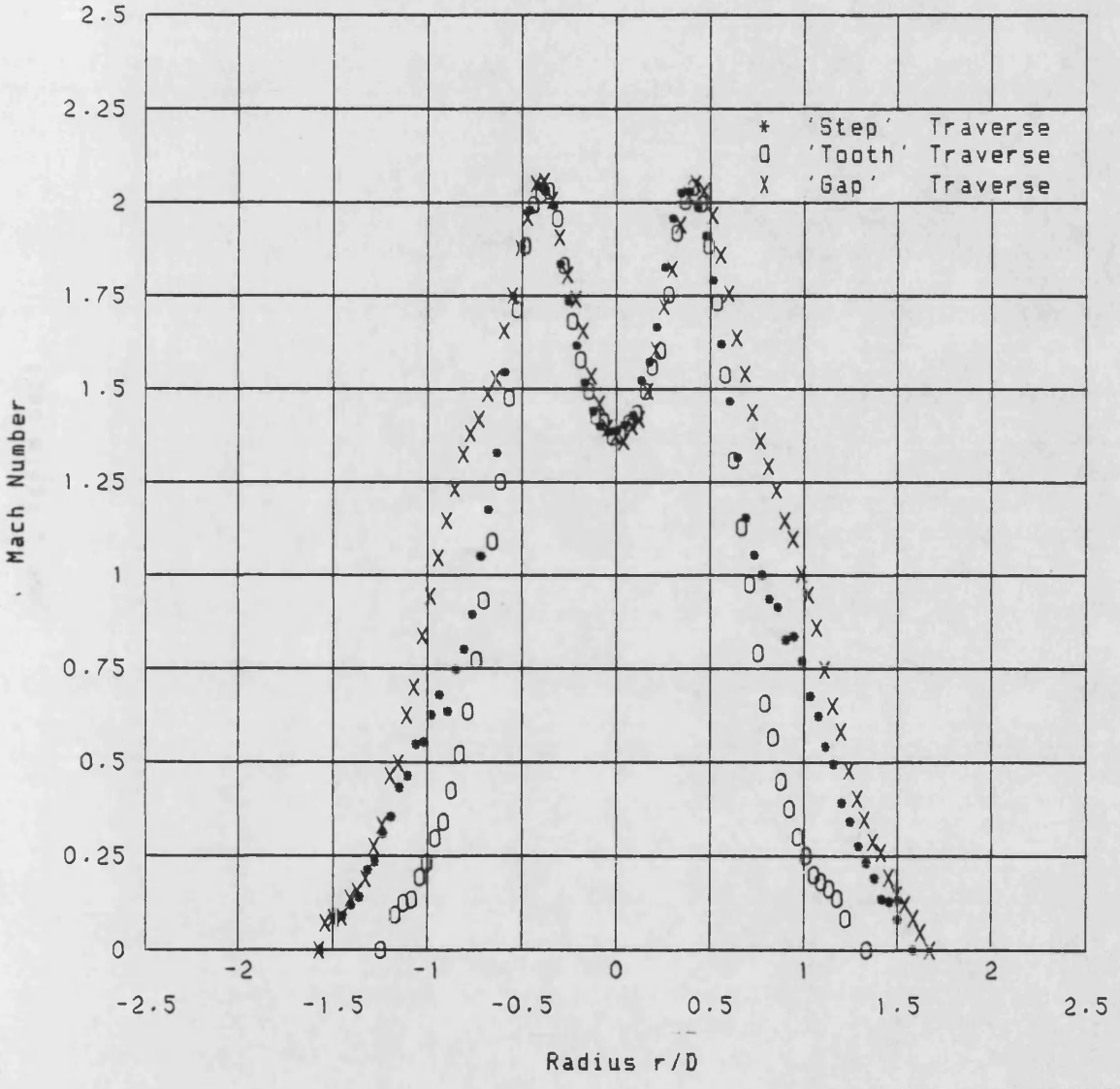

Figure 6.117 Mach Number at x/D=4 for M=1.4 4 Tooth Rotation Test

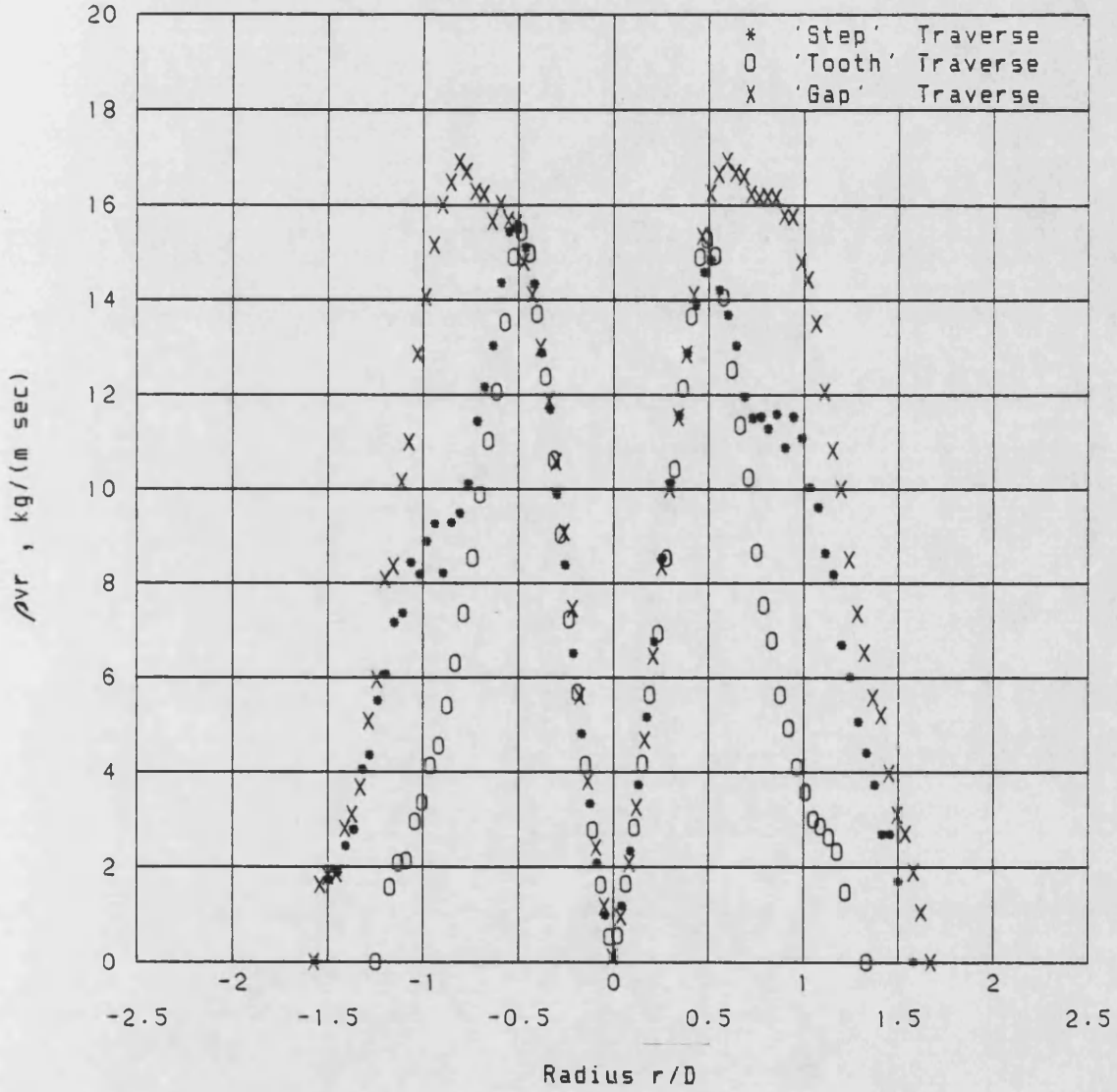

Figure 6.118 Mass Flow at x/D=4 for M=1.4 4 Tooth Rotation Test

Upper Plot

Velocity contours M=1.4 4 Tooth Nozzle

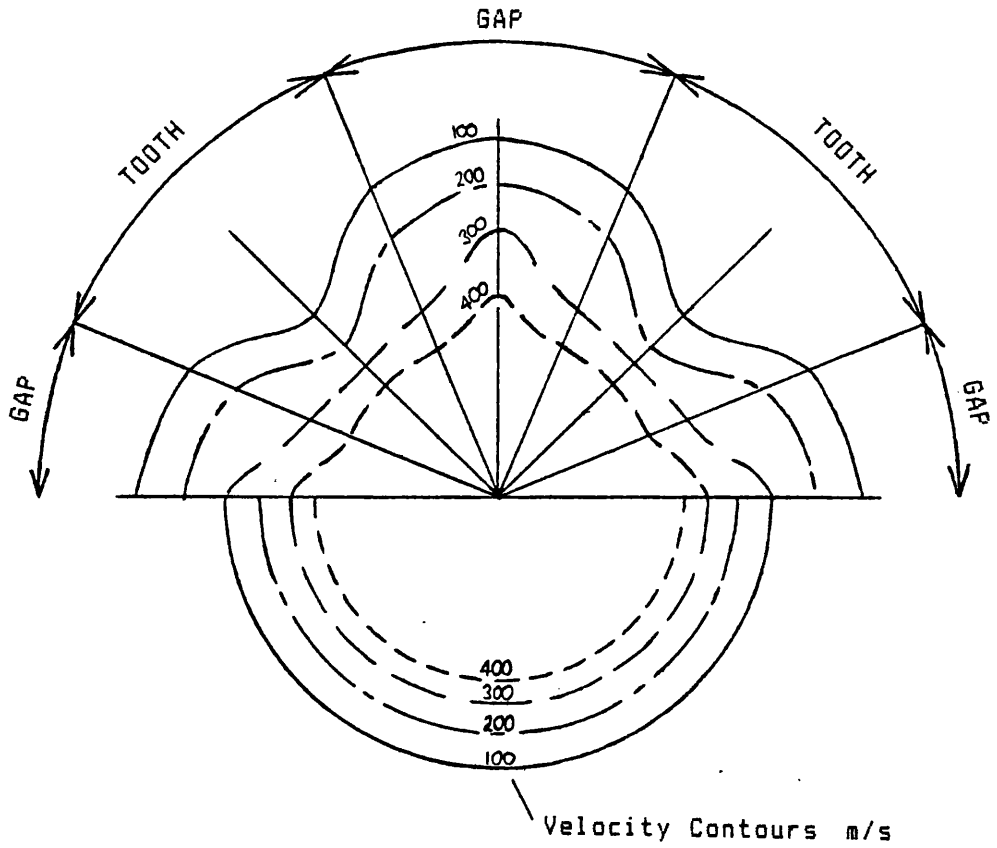

Lower Plot

Velocity contours M=1.4 Plain Nozzle

Figure 6.119 Velocity contours at x/D=4 for M=1.4 4 Tooth and Plain Nozzles

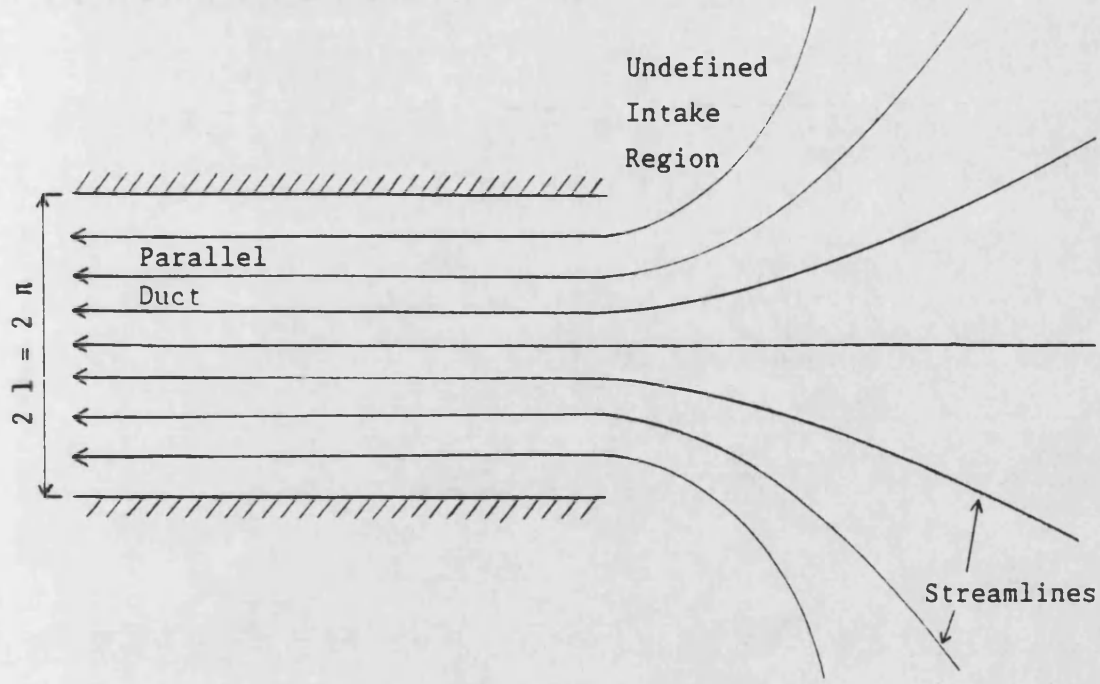

Figure 7.1 Two Dimensional representation of Ejector Inlet

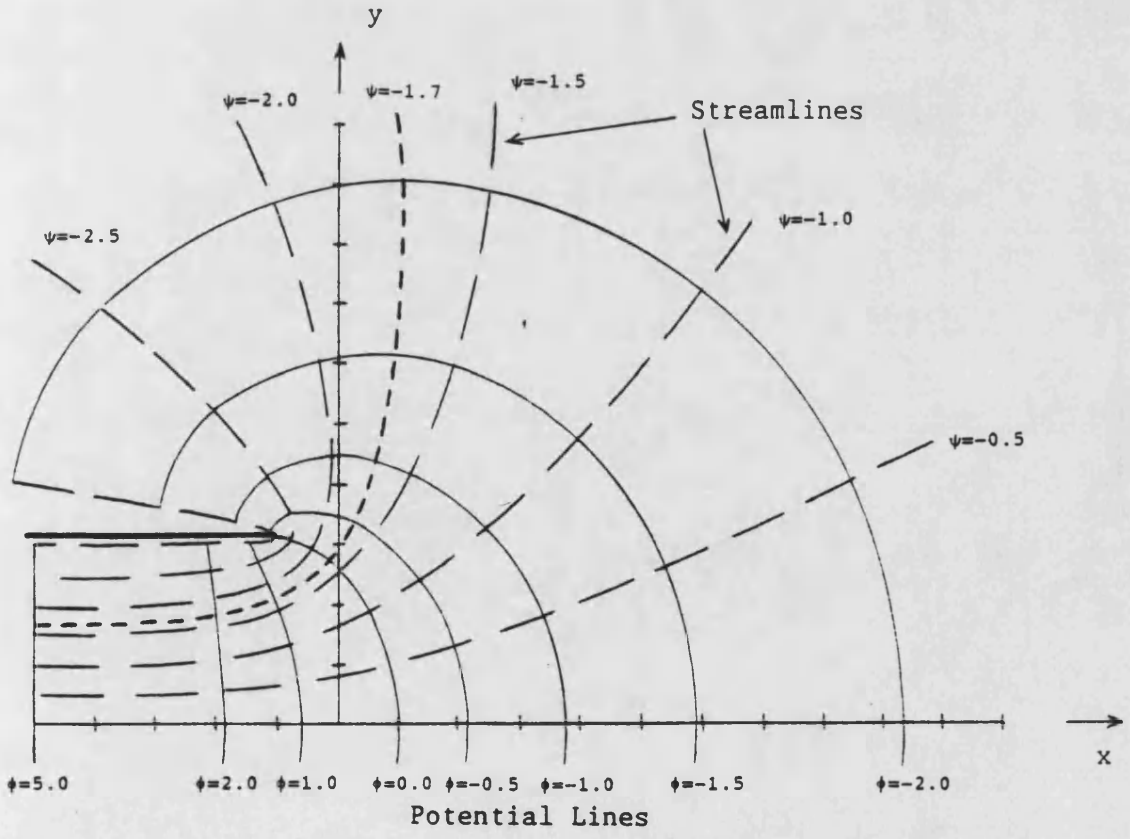

Figure 7.2 Streamline and Potential Line pattern of 2-D Inlet

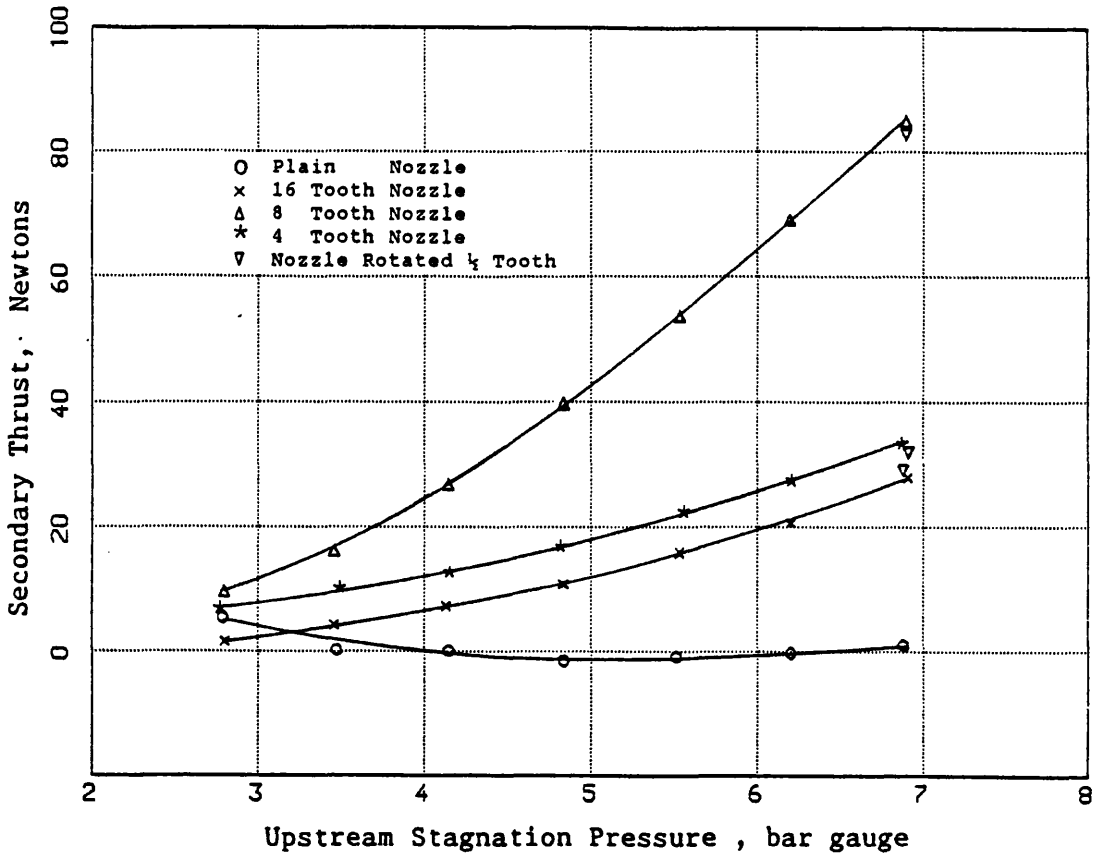

Figure 7.3 Secondary Thrust M=1.0 Nozzle, A_R=15 Duct

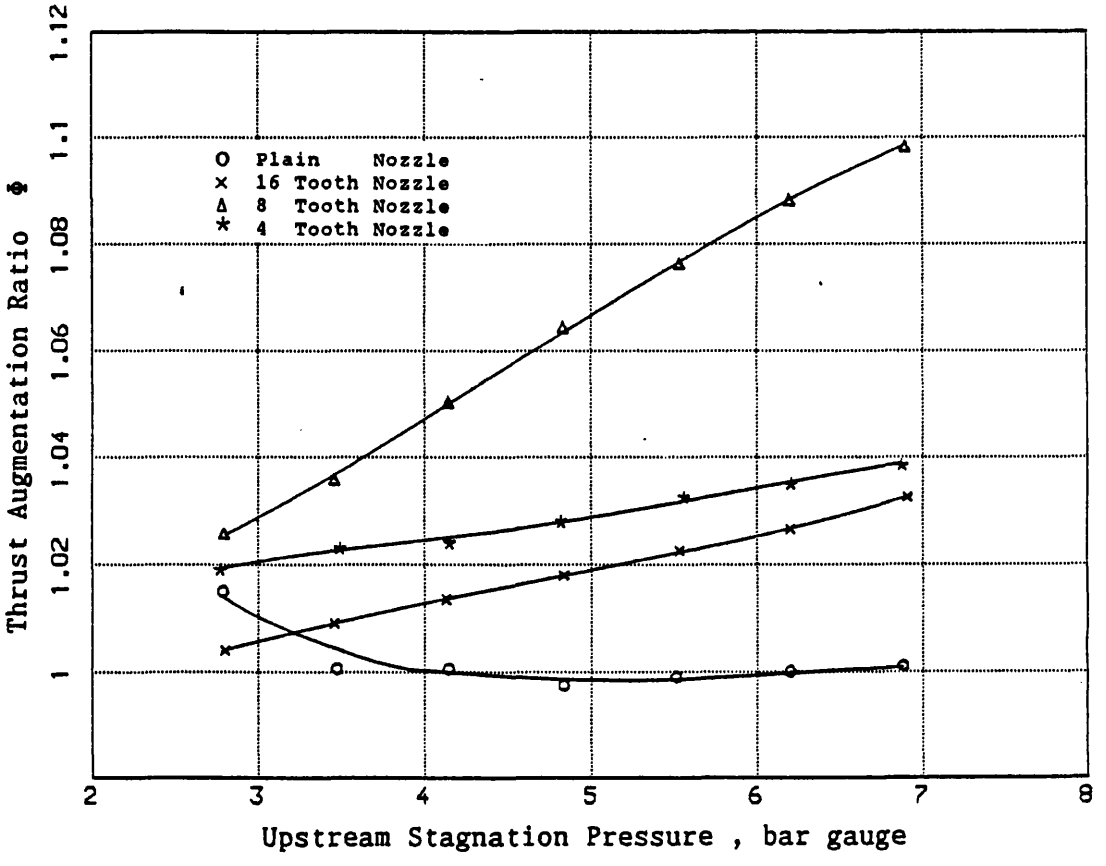

Figure 7.4 Thrust Augmentation Ratio M=1.0 Nozzle, A_R=15 Duct

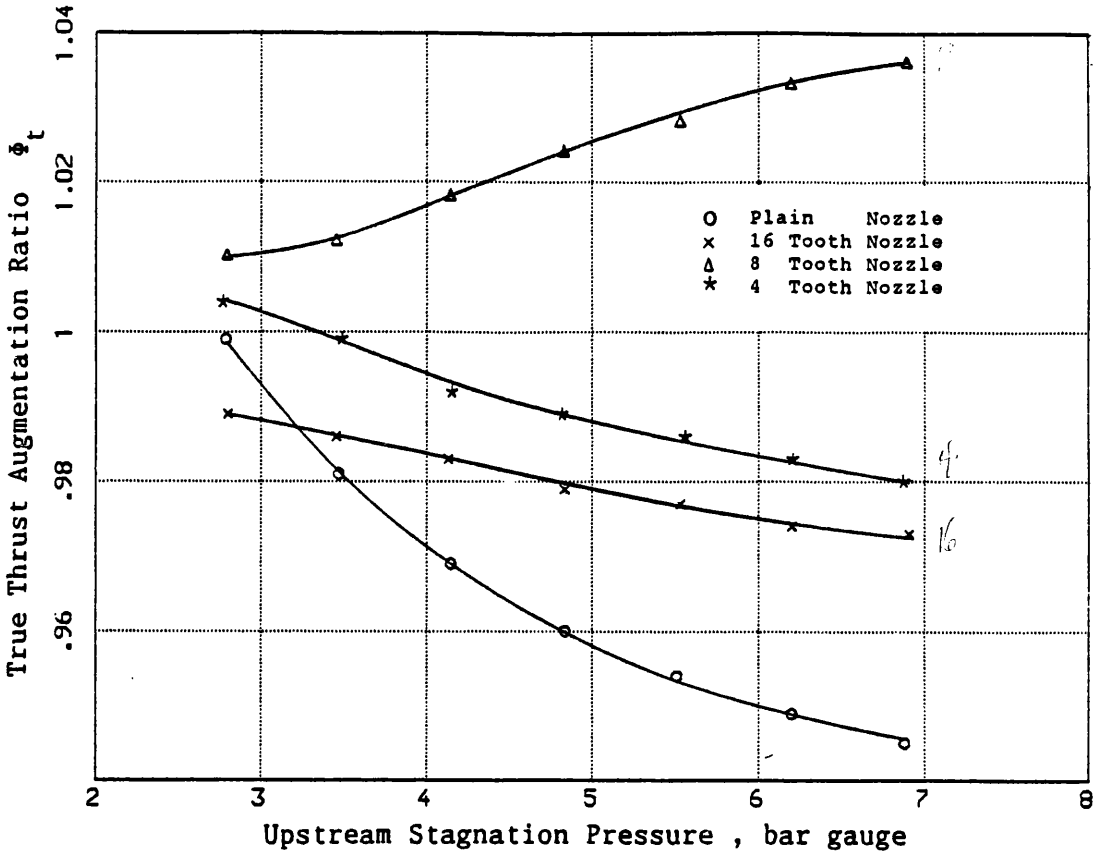

Figure 7.5 True Thrust Augmentation Ratio M=1.0 Nozzle, A_R=15 Duct

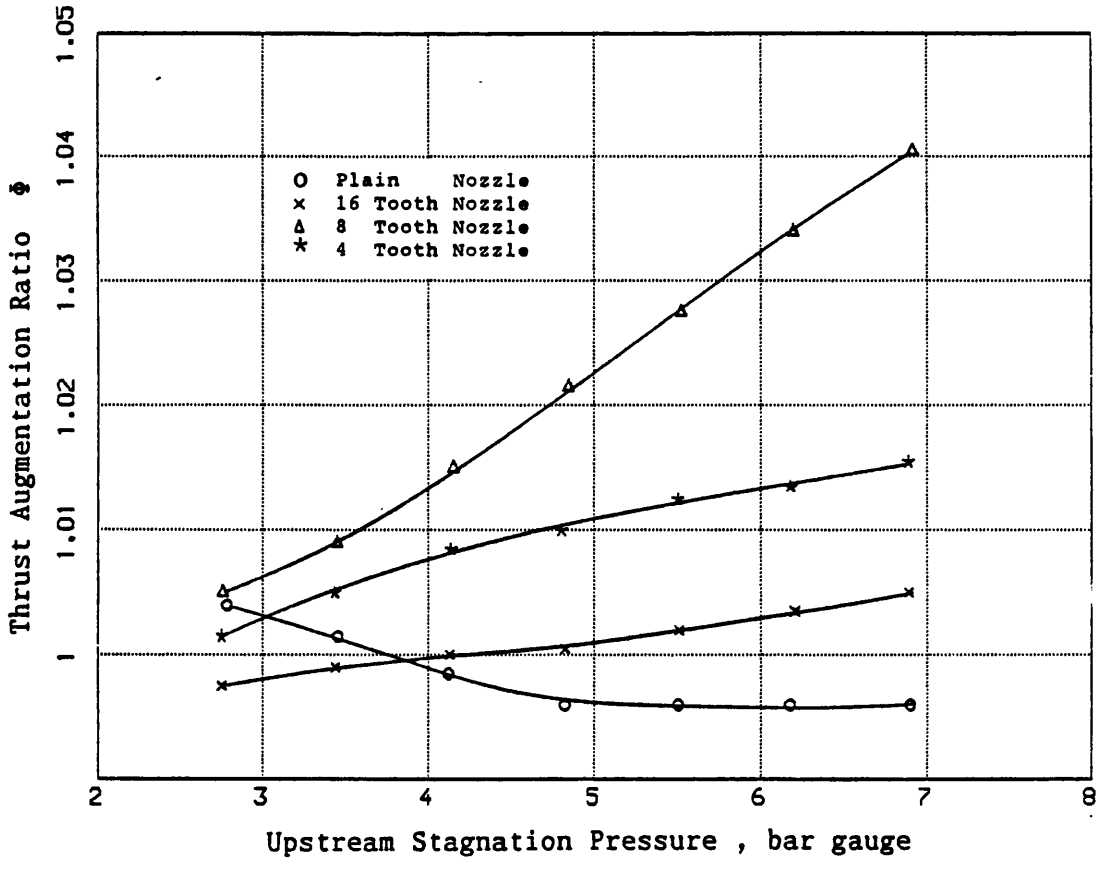

Figure 7.6 Thrust Augmentation Ratio M=1.0 Nozzle, A_R=25 Duct

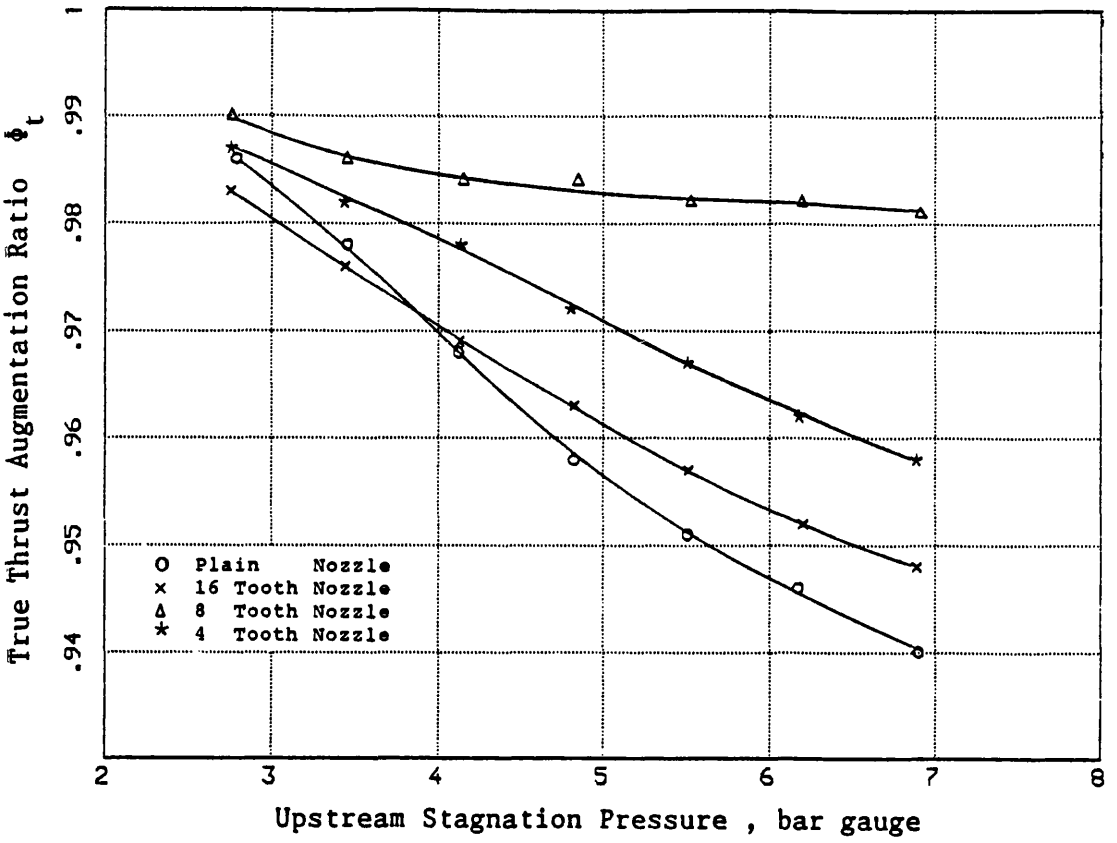

Figure 7.7 True Thrust Augmentation Ratio M=1.0 Nozzle, A_R=25 Duct

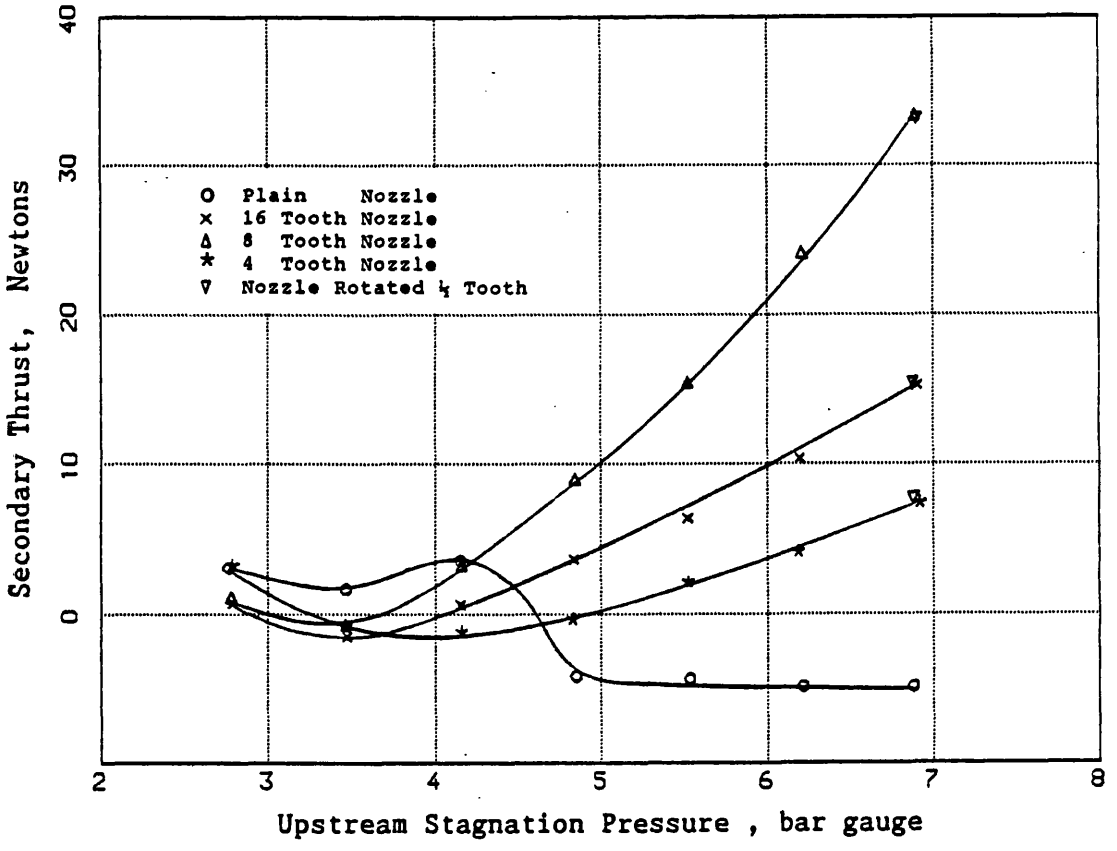

Figure 7.8 Secondary Thrust M=1.4 Nozzle, A_R=15 Duct

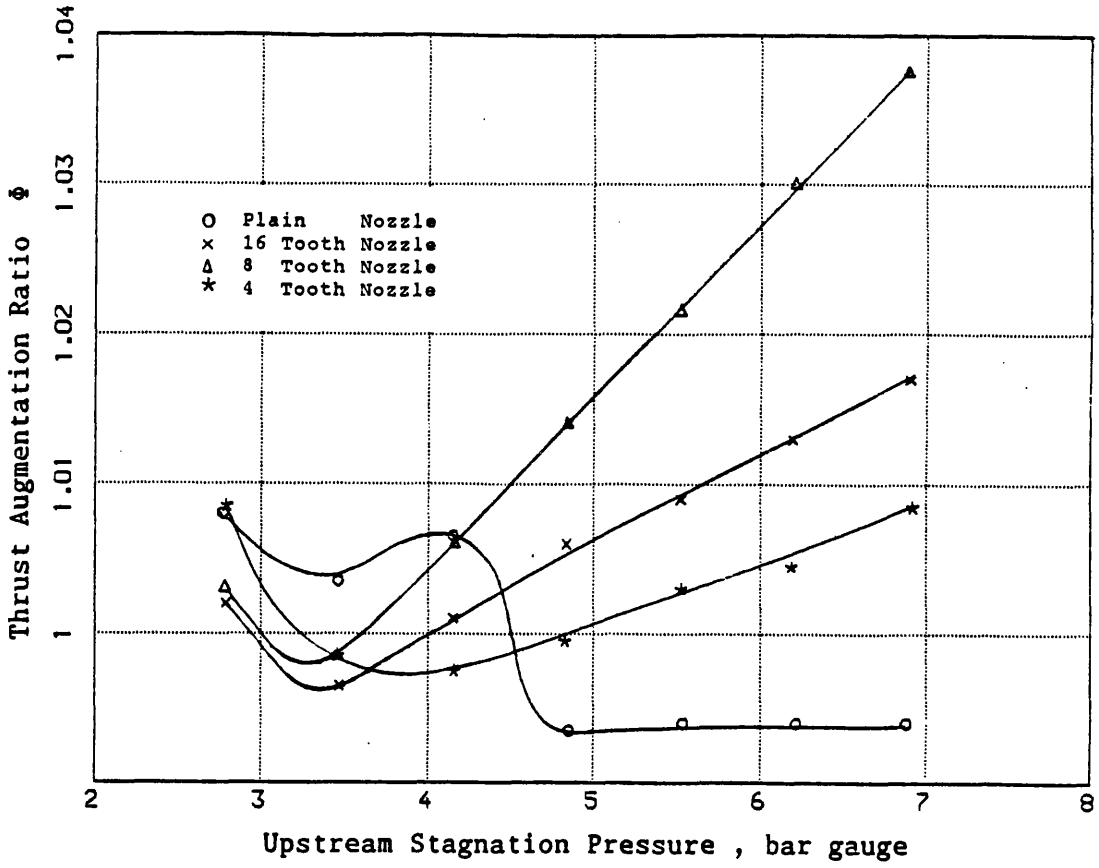

Figure 7.9 Thrust Augmentation Ratio M=1.4 Nozzle, A_R=15 Duct

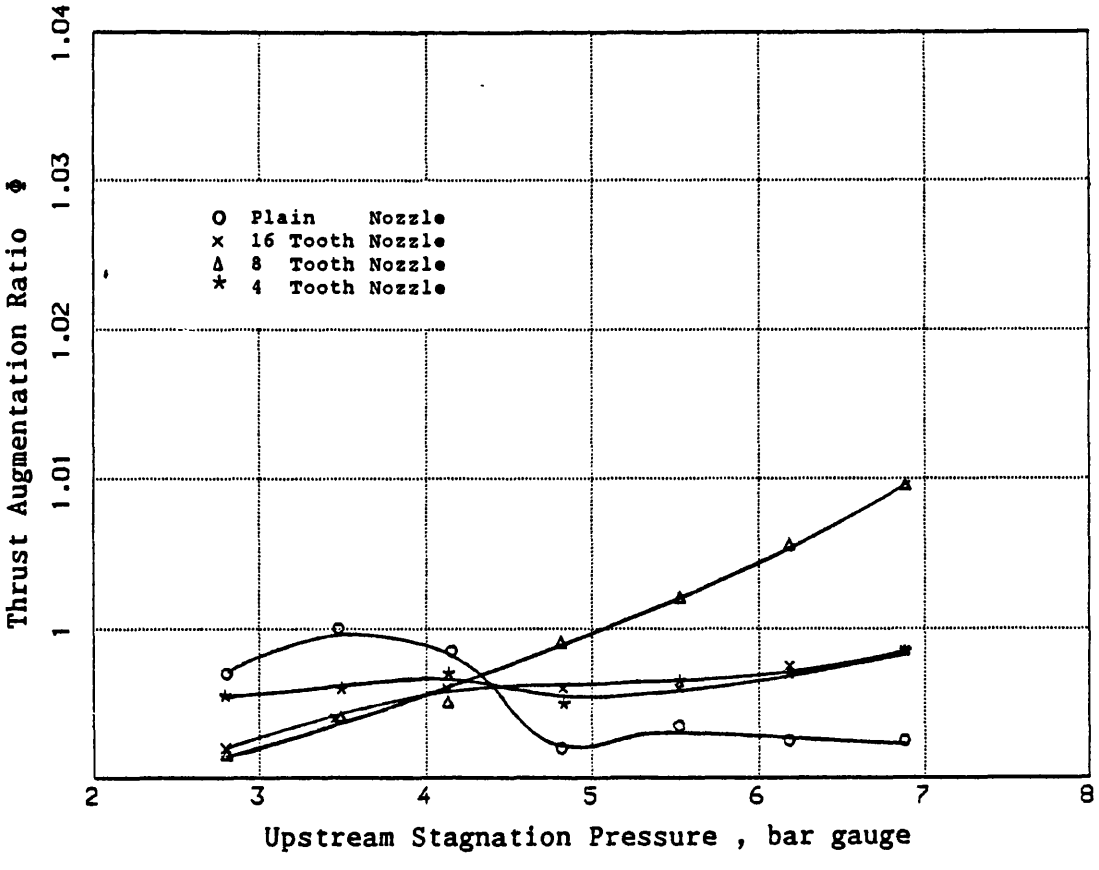

Figure 7.10 Thrust Augmentation Ratio M=1.4 Nozzle, A_R=25 Duct

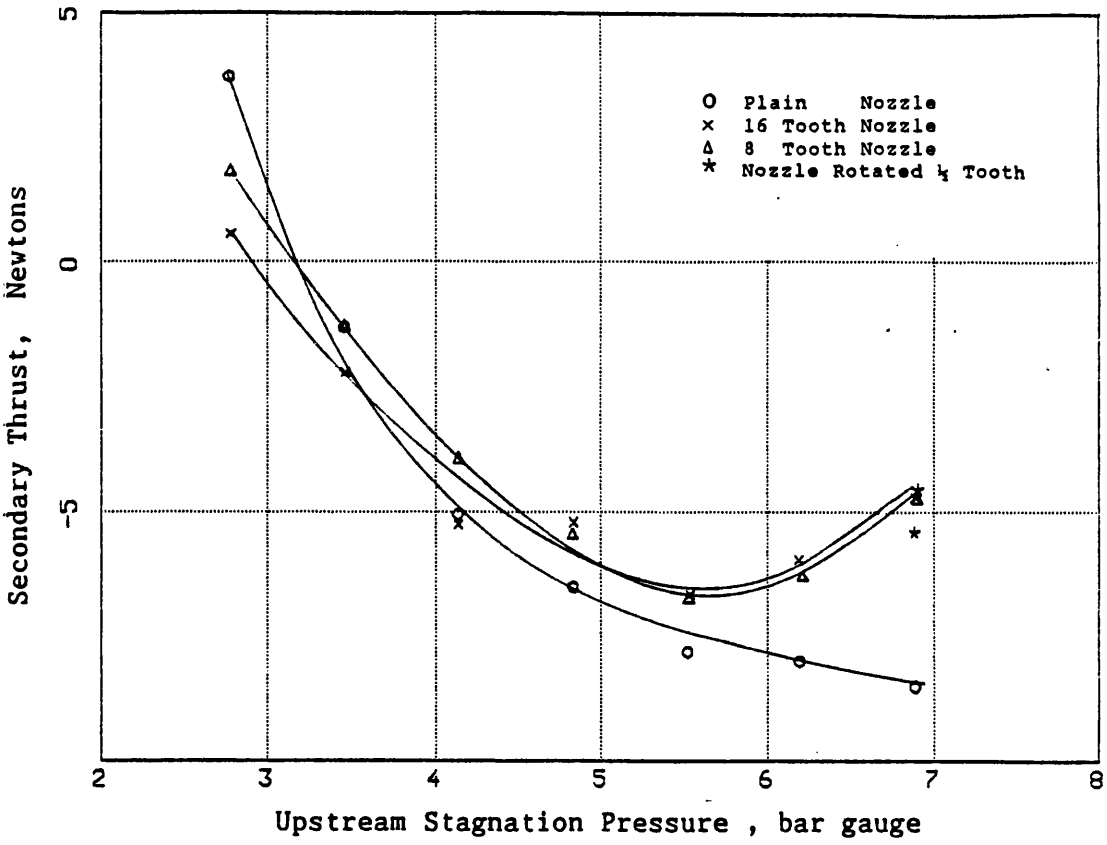

Figure 7.11 Secondary Thrust M=1.8 Nozzle, A_R=15 Duct

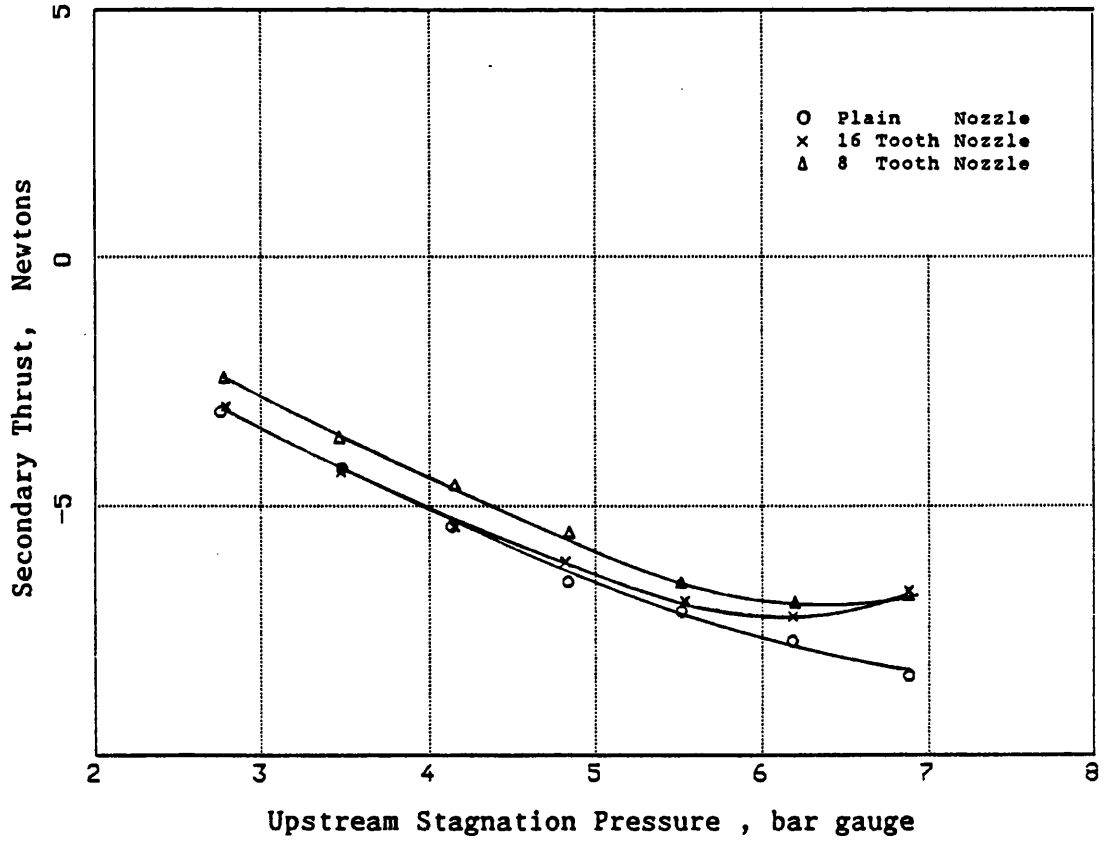

Figure 7.12 Secondary Thrust M=1.8 Nozzle, A_R=25 Duct

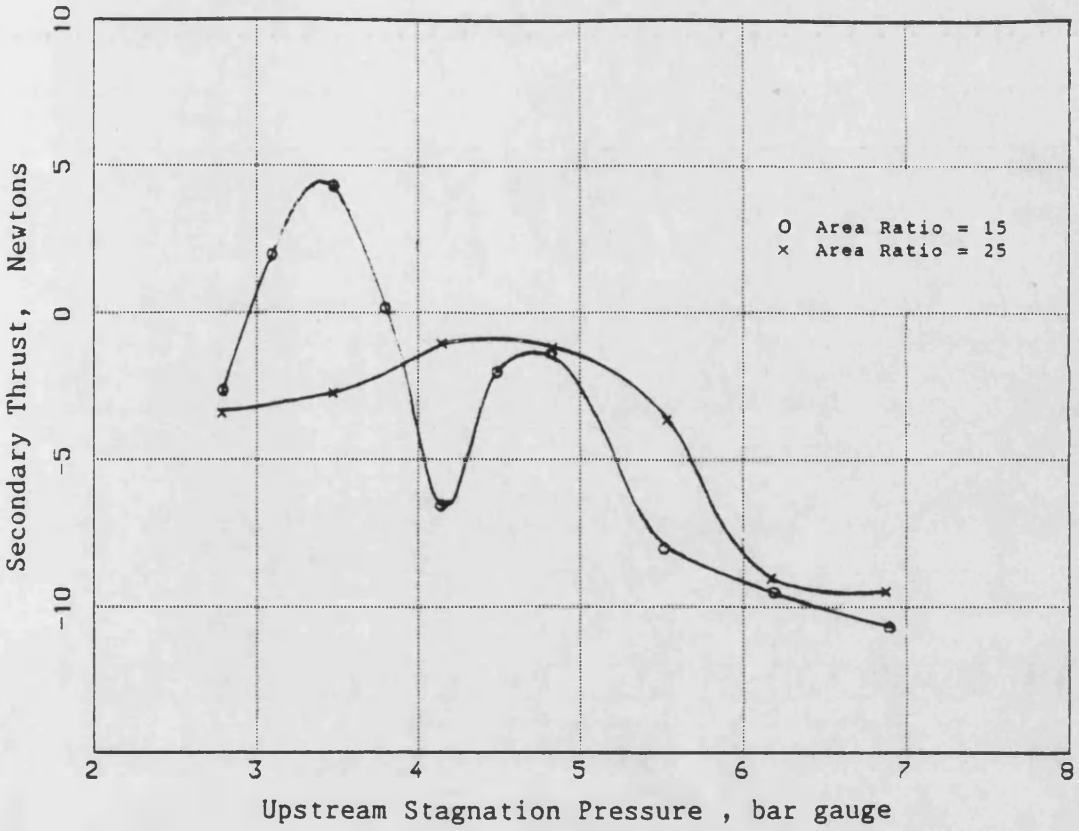

Figure 7.13 Secondary Thrust M=2.0 Nozzle, A_R=15 and A_R=25 Ducts

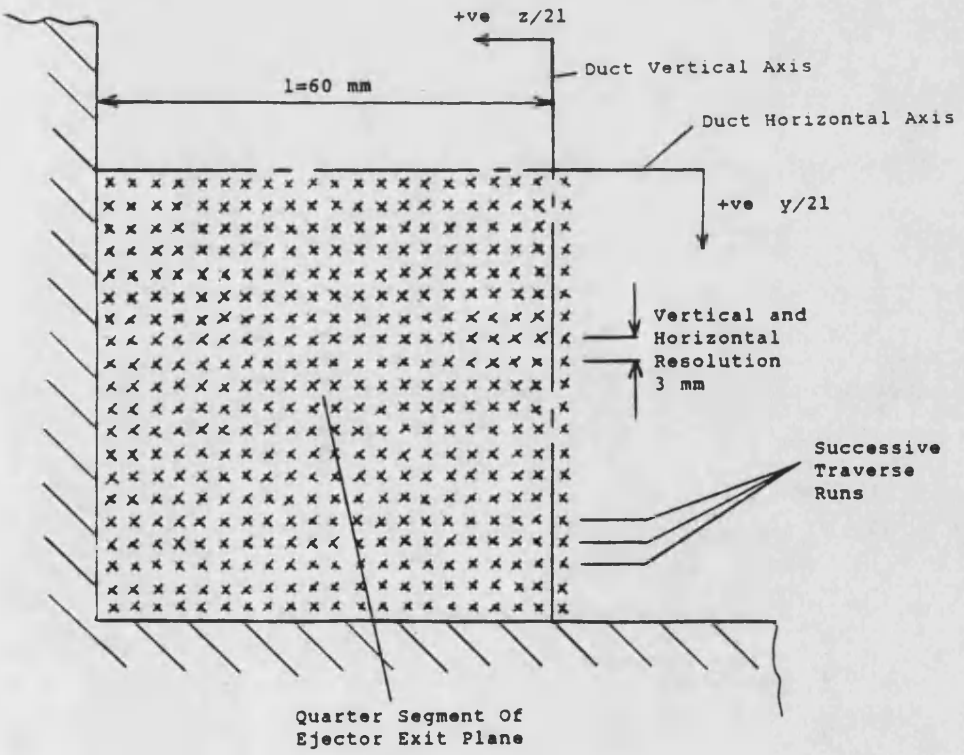

Figure 7.14 Traverse resolution employed in Ducted Jet Tests

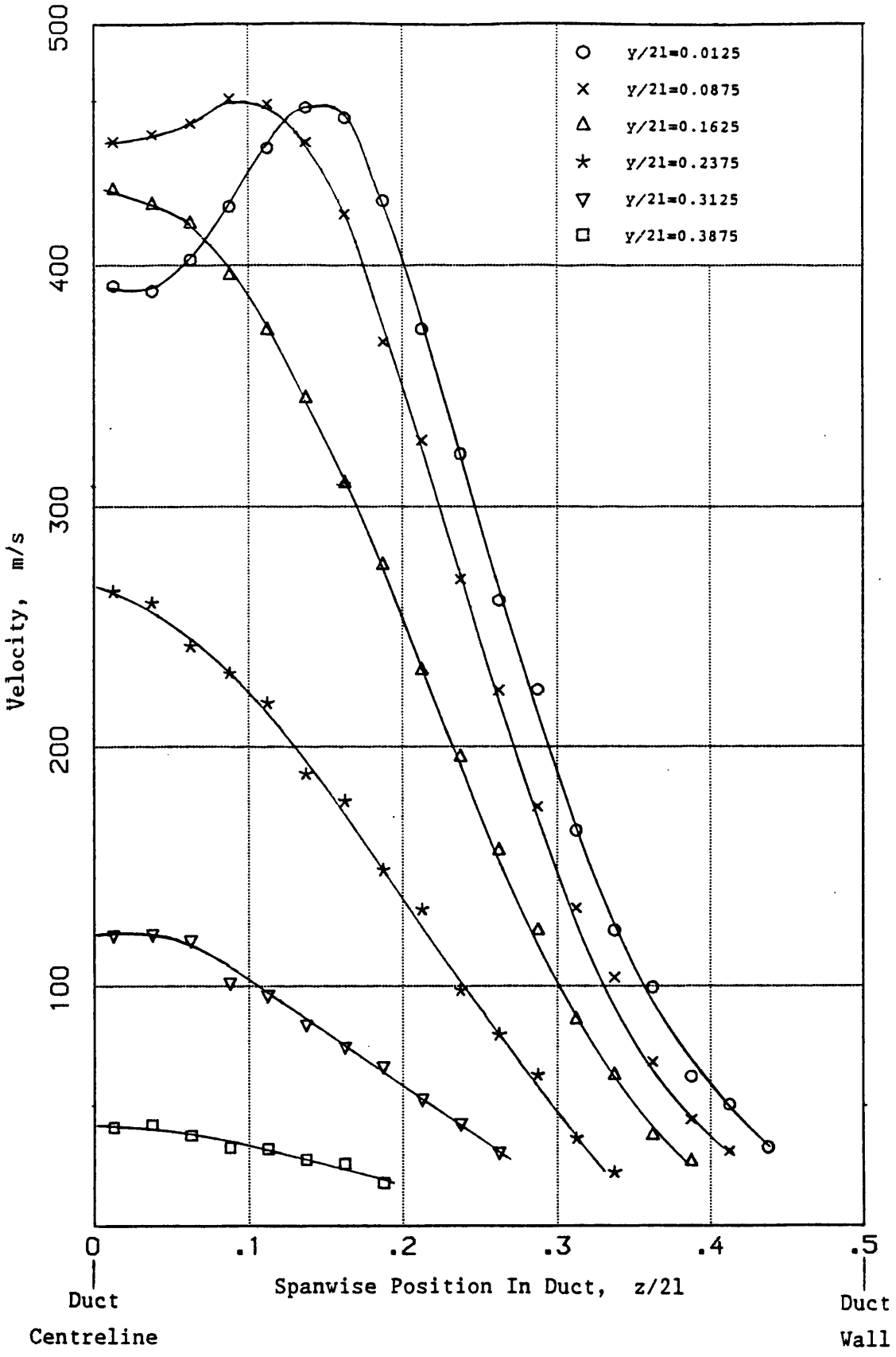

Figure 7.15 Exit Velocity traverses with M=1.0 Plain Nozzle in A_R=15 Duct

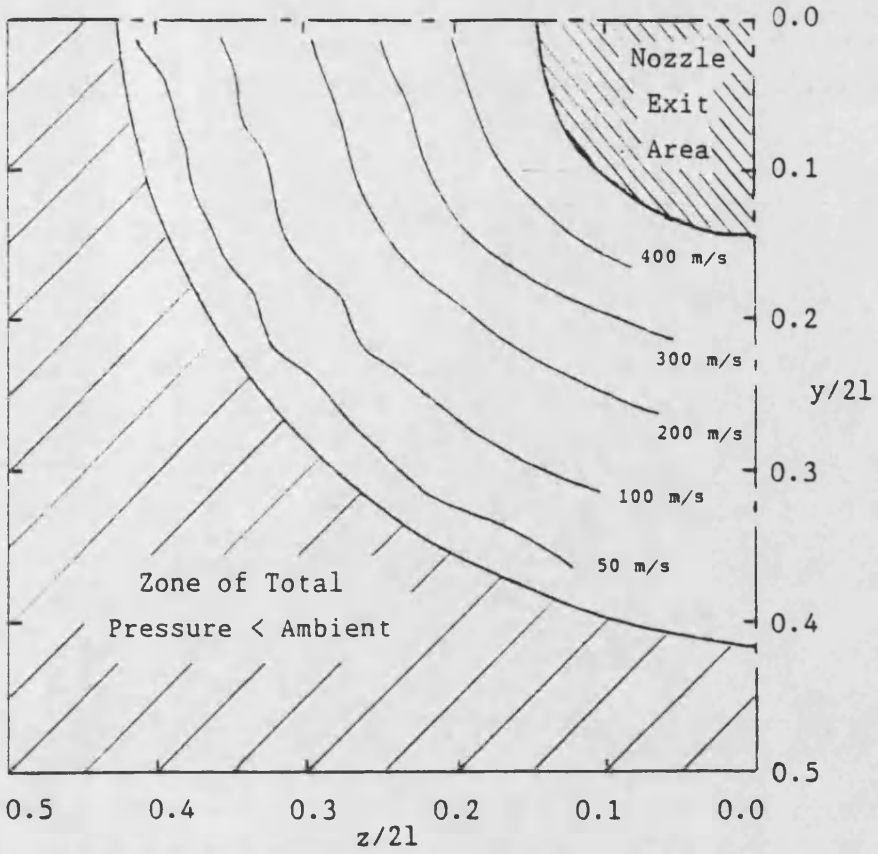

Figure 7.16 Exit Velocity Contours, M=1.0 Plain Nozzle in A_R=15 Duct

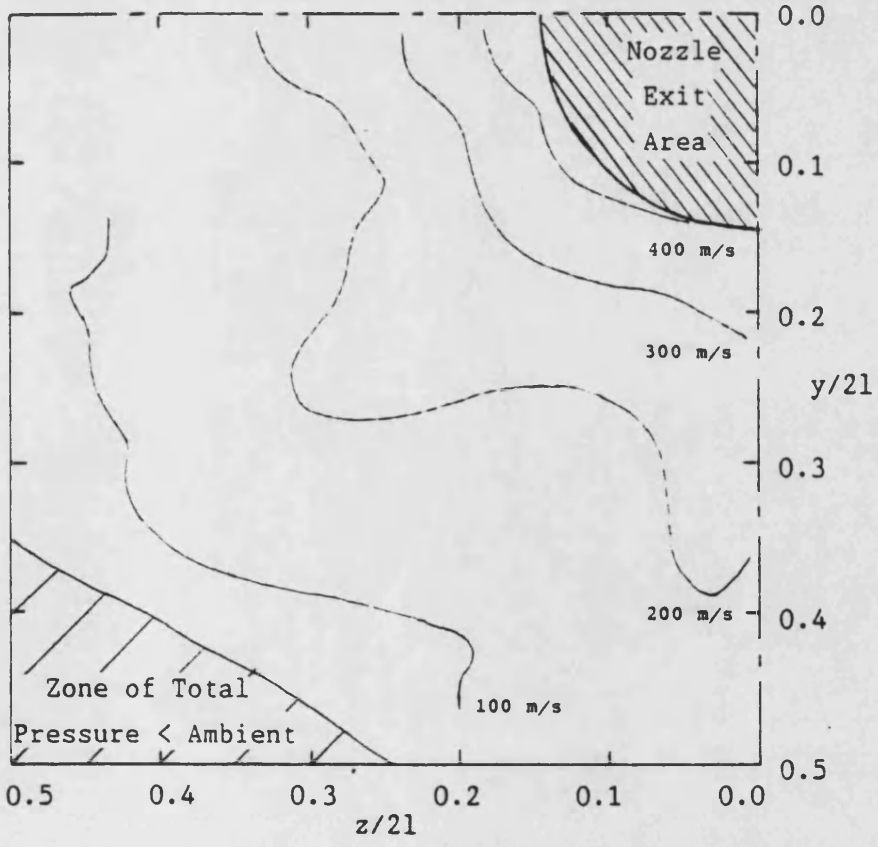

Figure 7.17 Exit Velocity Contours, M=1.0 8 Tooth Nozzle in A_R=15 Duct

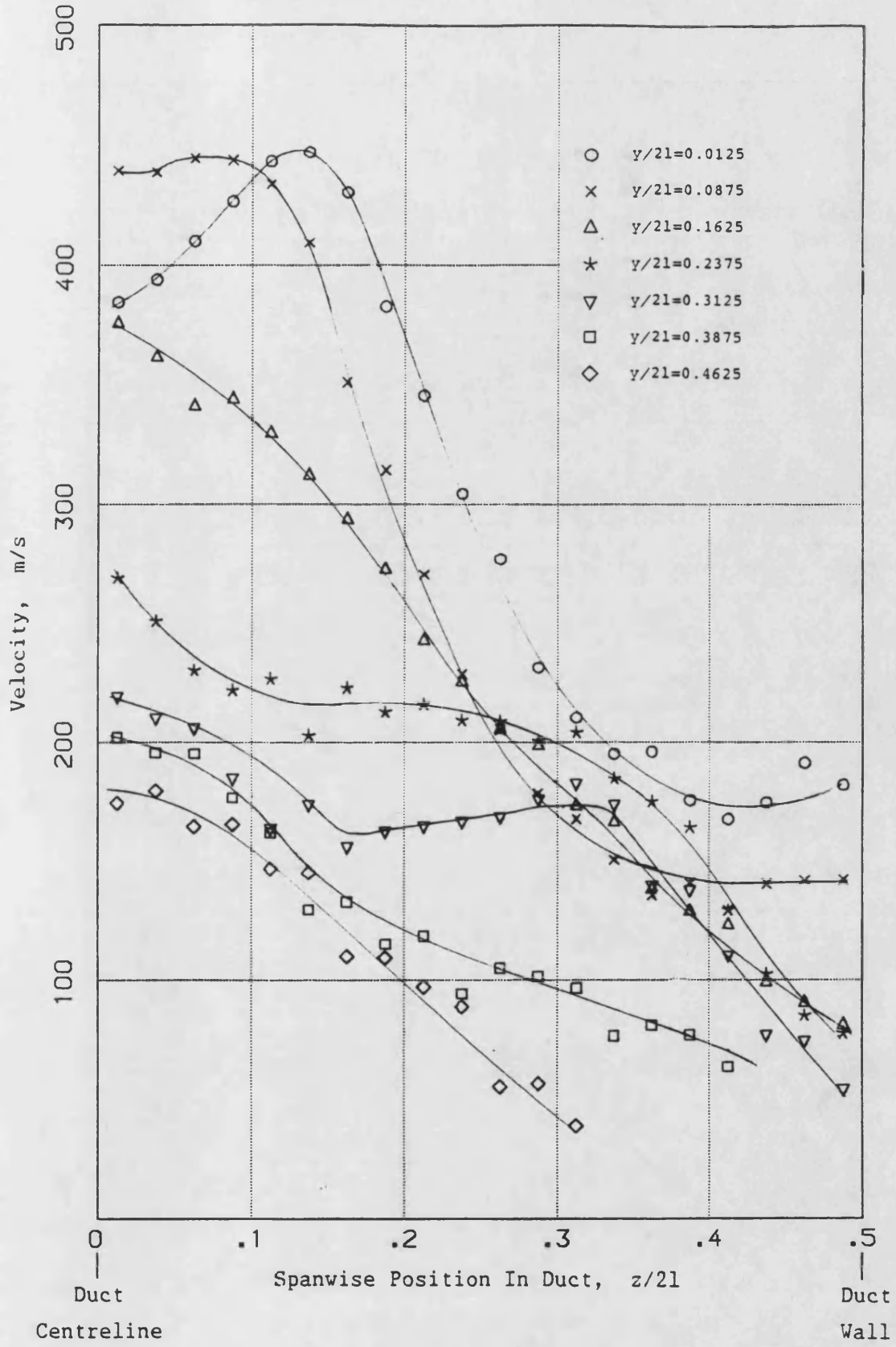

Figure 7.18 Exit Velocity traverses with M=1.0 8 Tooth Nozzle in A_R=15 Duct

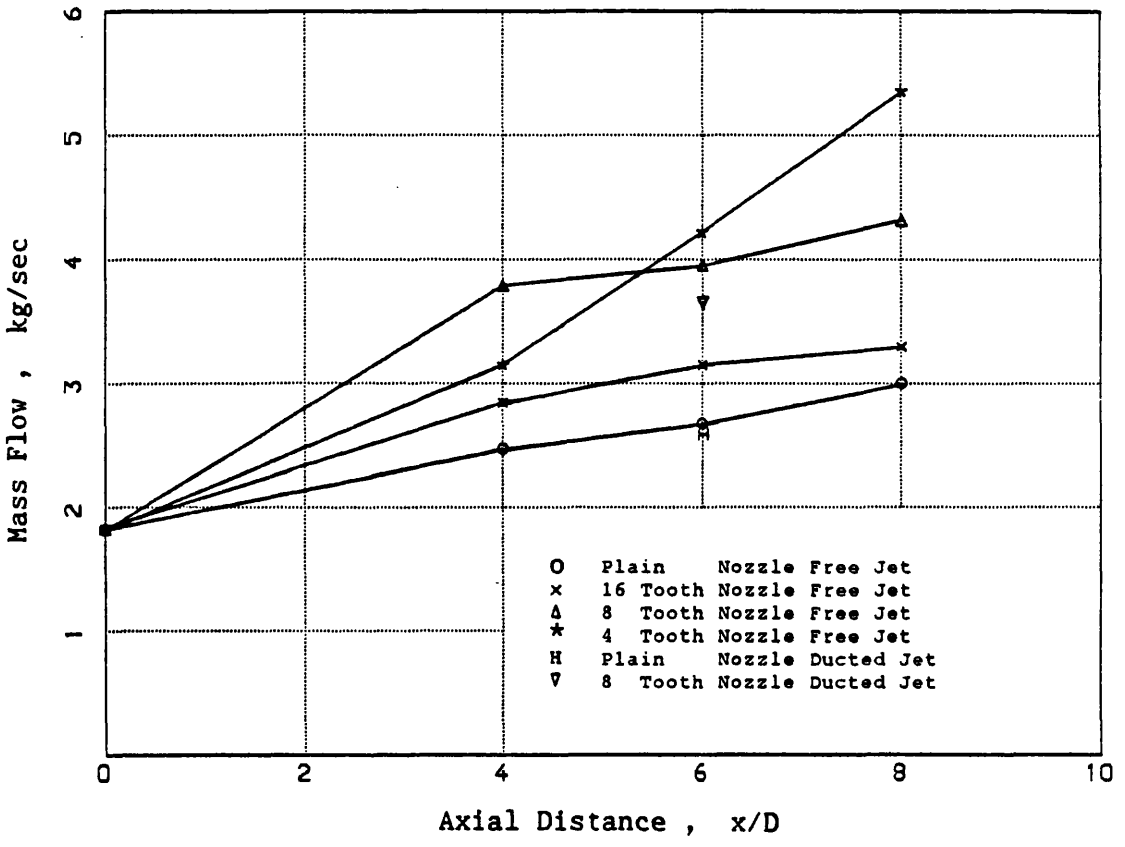

Figure 7.19 Free and Ducted Mass Flows with M=1.0 Nozzles

Figure 7.20 M=1.0 Plain Nozzle A_R=15 Duct

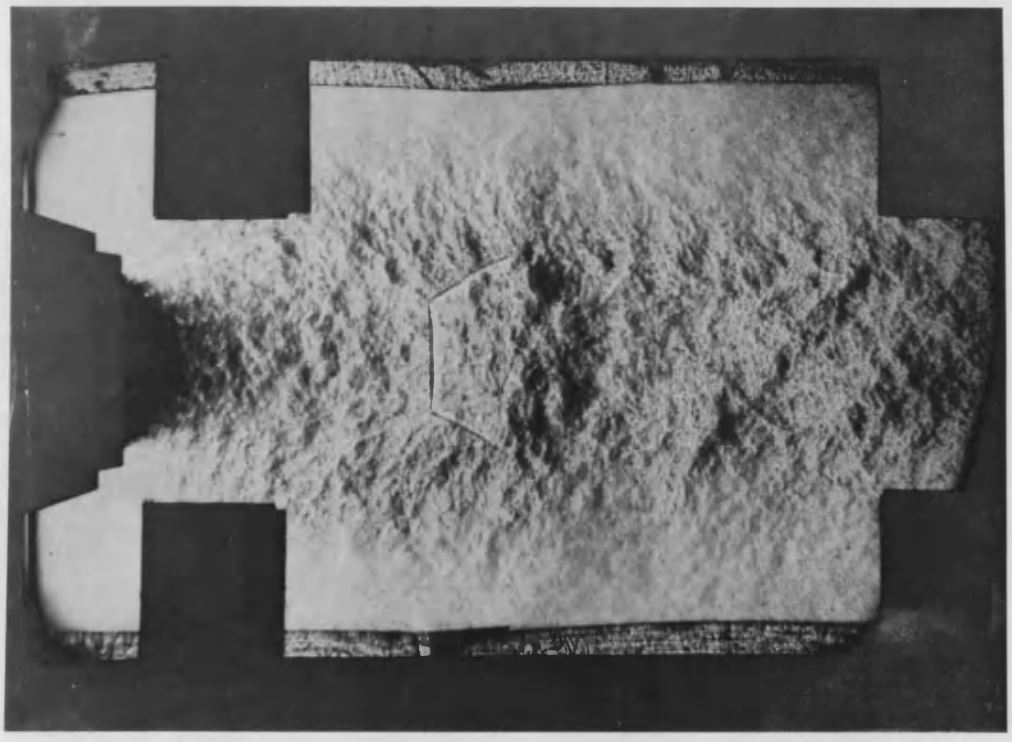

Figure 7.21 M=1.0 16 Tooth Nozzle A_R=15 Duct

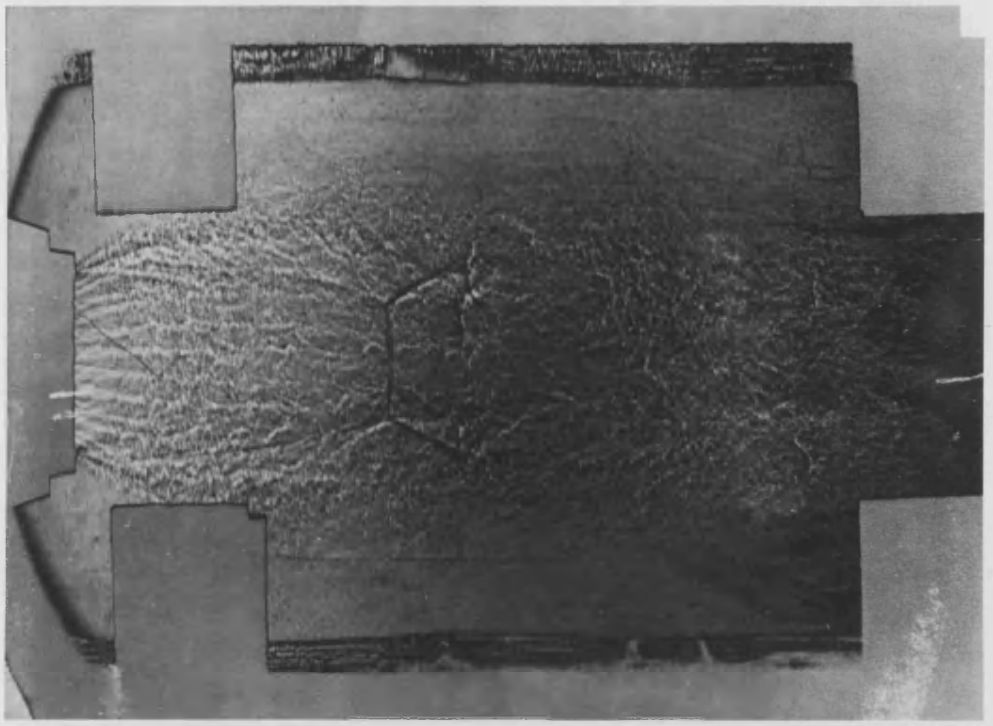

Figure 7.22 Weak schlieren M=1.0 16 Tooth Nozzle A_R=15 Duct

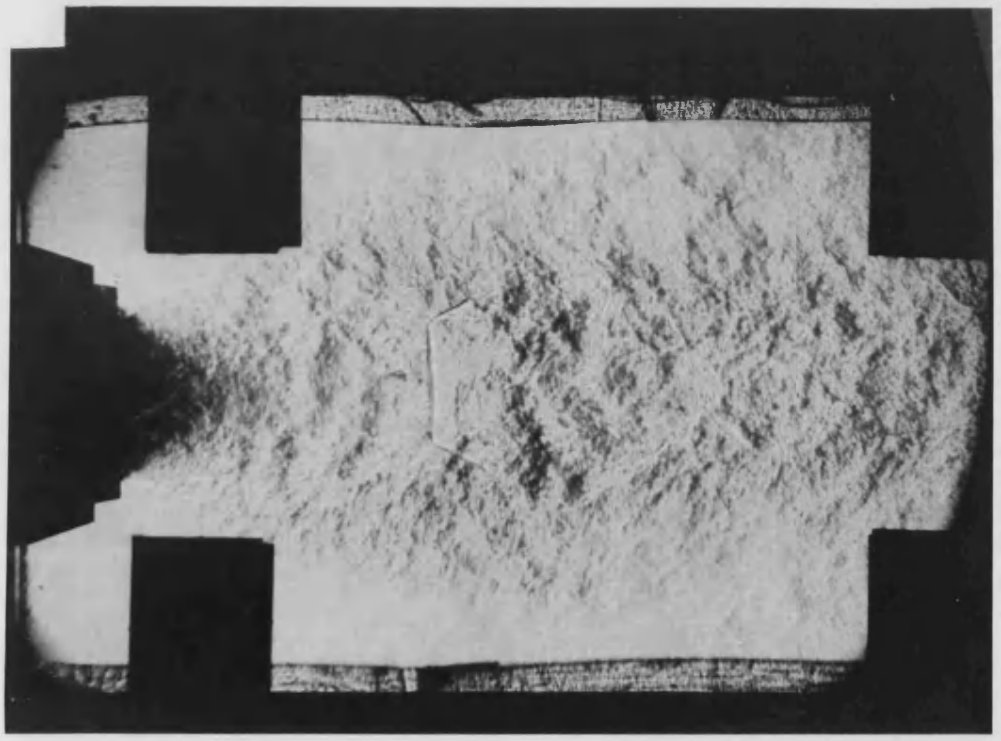

Figure 7.23 M=1.0 8 Tooth Nozzle A_R=15 Duct

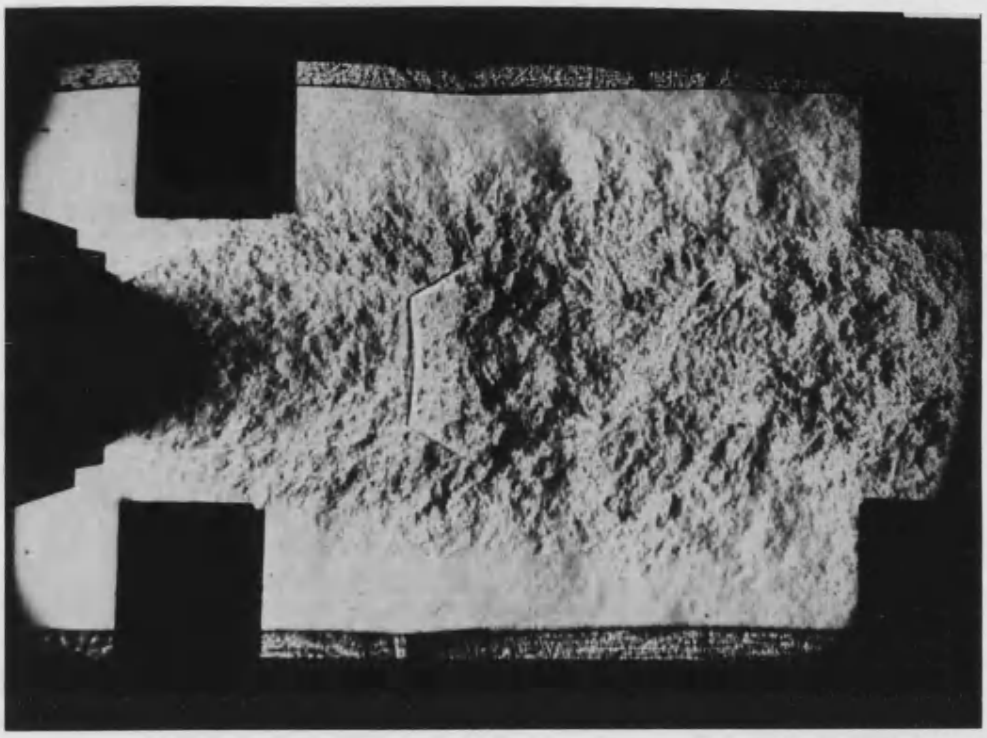

Figure 7.24 M=1.0 4 Tooth Nozzle A_R=15 Duct

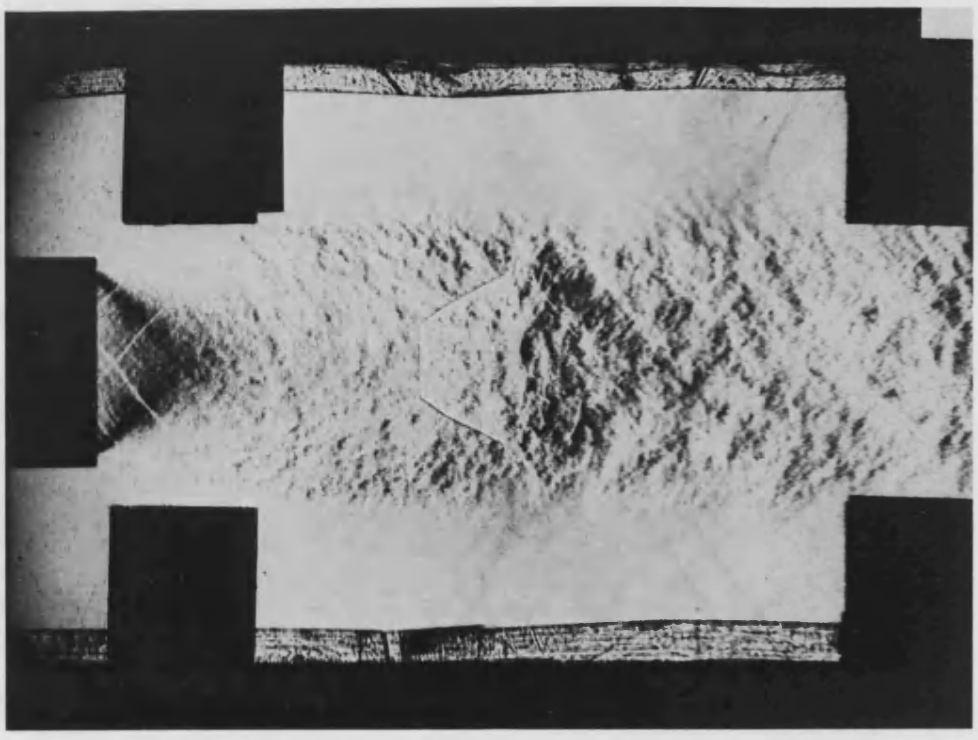

Figure 7.25 M=1.4 Plain Nozzle A_R=15 Duct

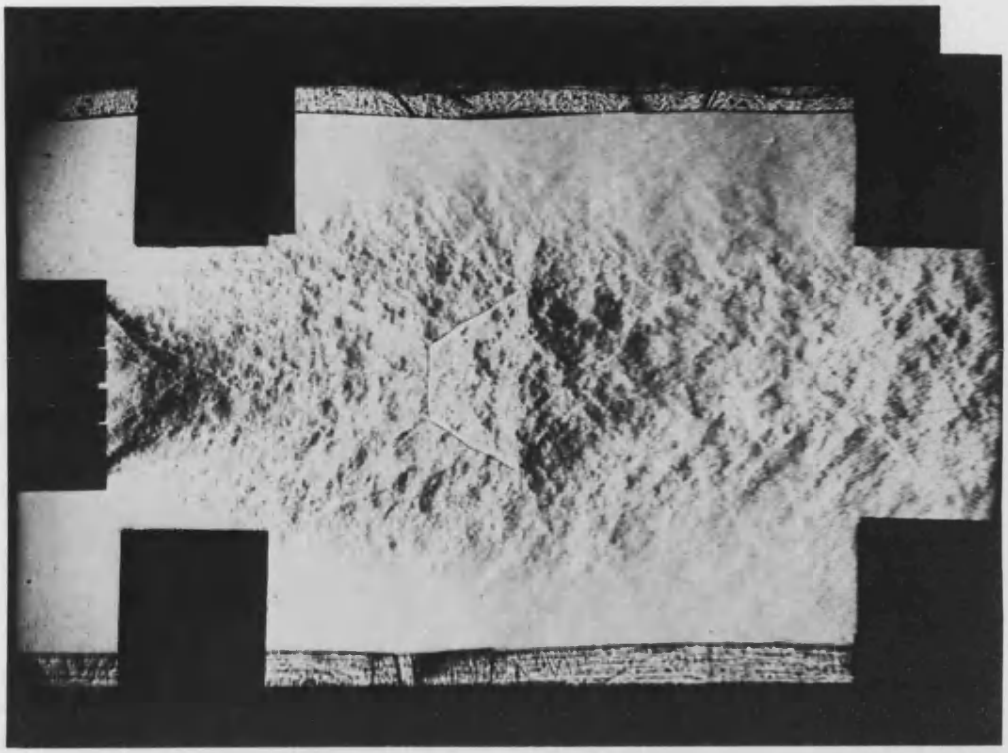

Figure 7.26 M=1.4 16 Tooth Nozzle A_R=15 Duct

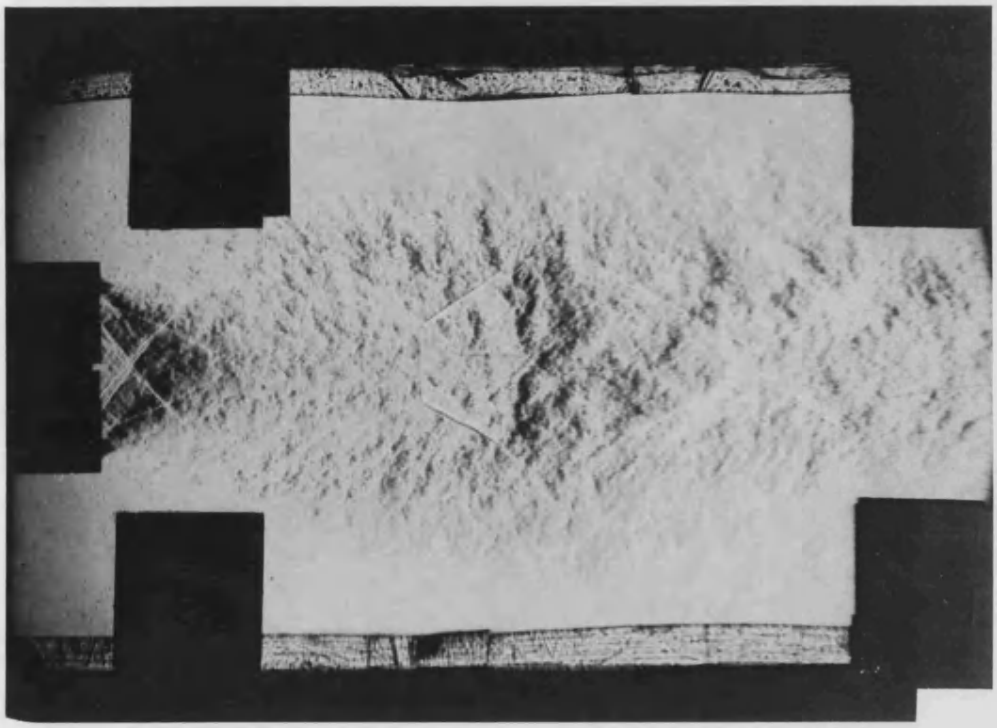

Figure 7.27 M=1.4 8 Tooth Nozzle A_R=15 Duct

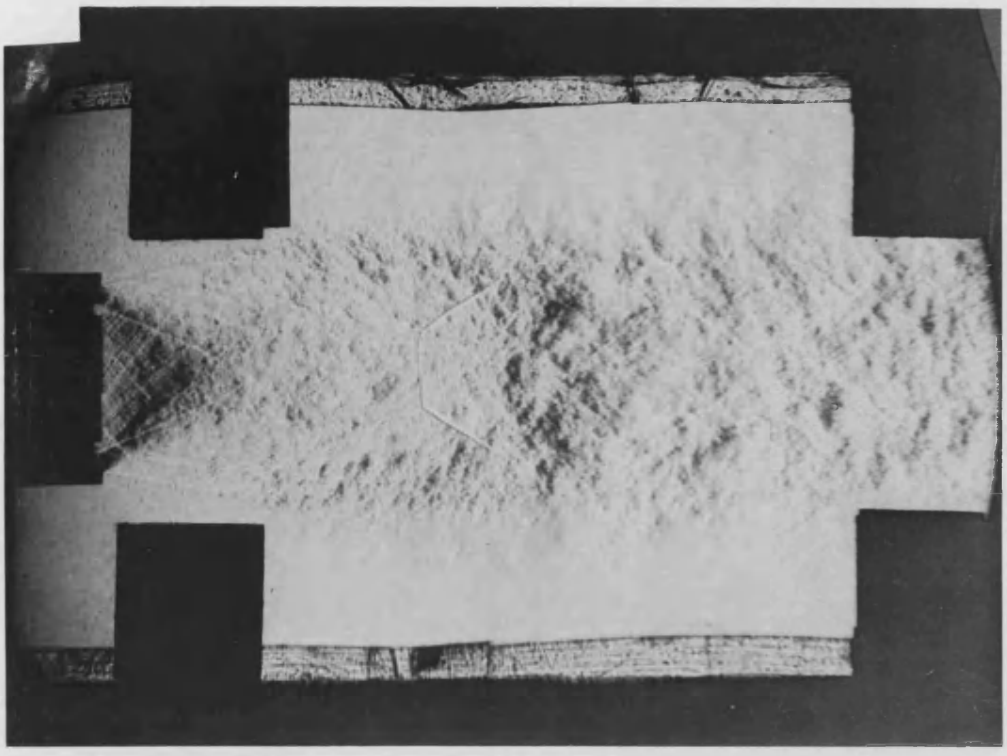

Figure 7.28 M=1.4 4 Tooth Nozzle A_R=15 Duct

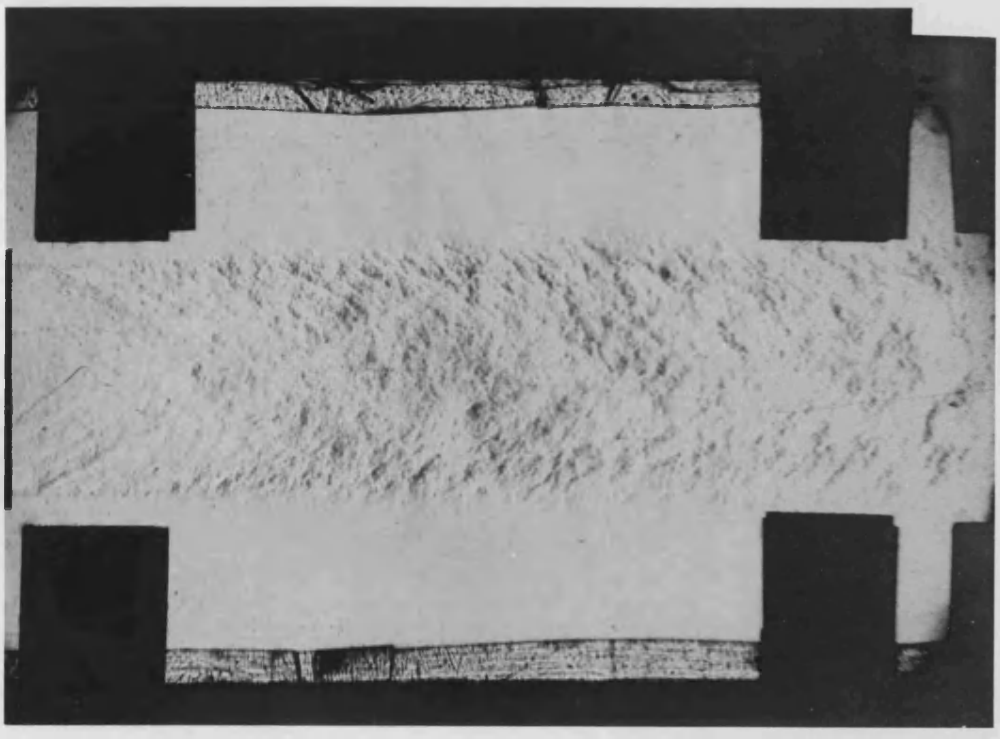

Figure 7.29 M=2.0 Plain Nozzle A_R=15 Duct

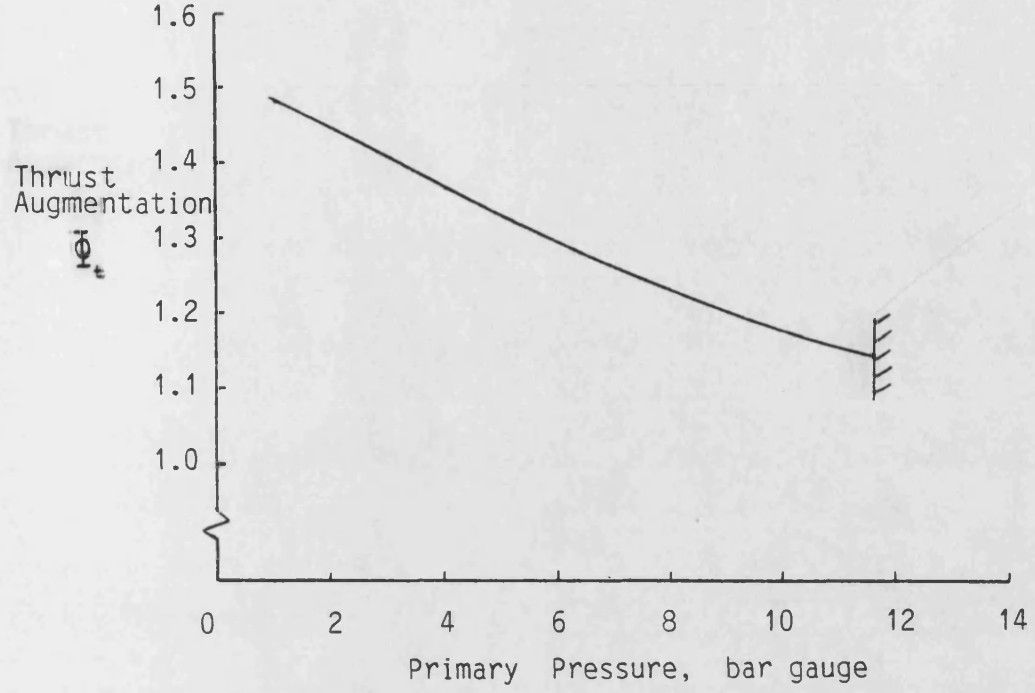

Figure 8.1 The Effect of Primary Pressure on an Area Ratio 13.73 Ideal Ejector

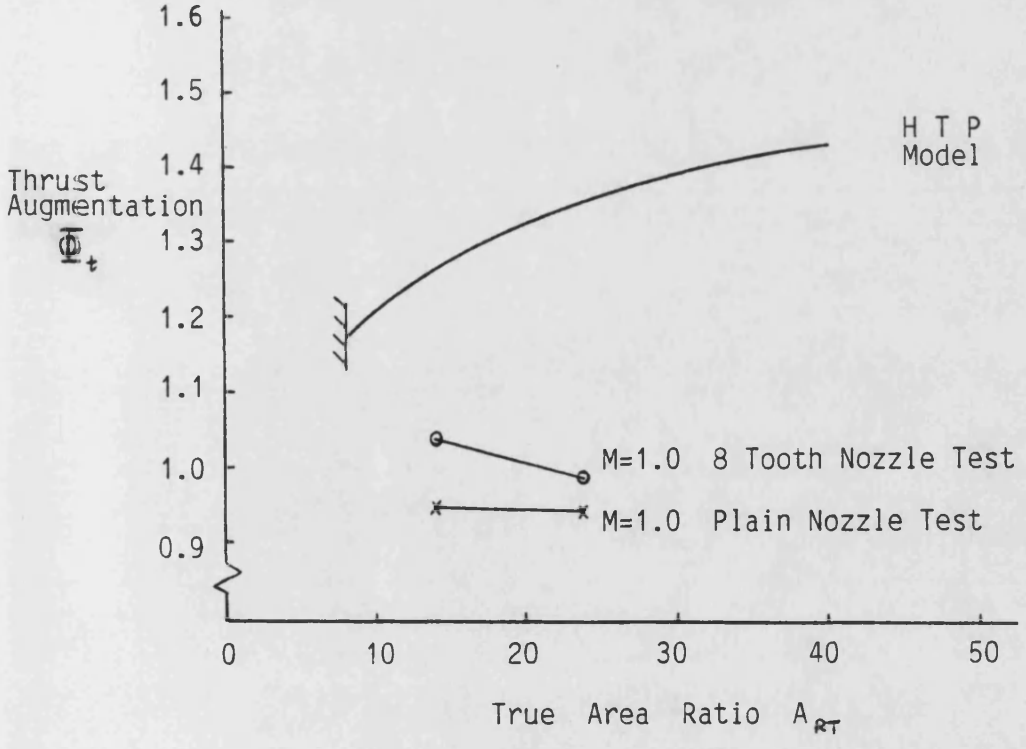

Figure 8.2 The Effect of Area Ratio on a 6.9 bar gauge Ejector

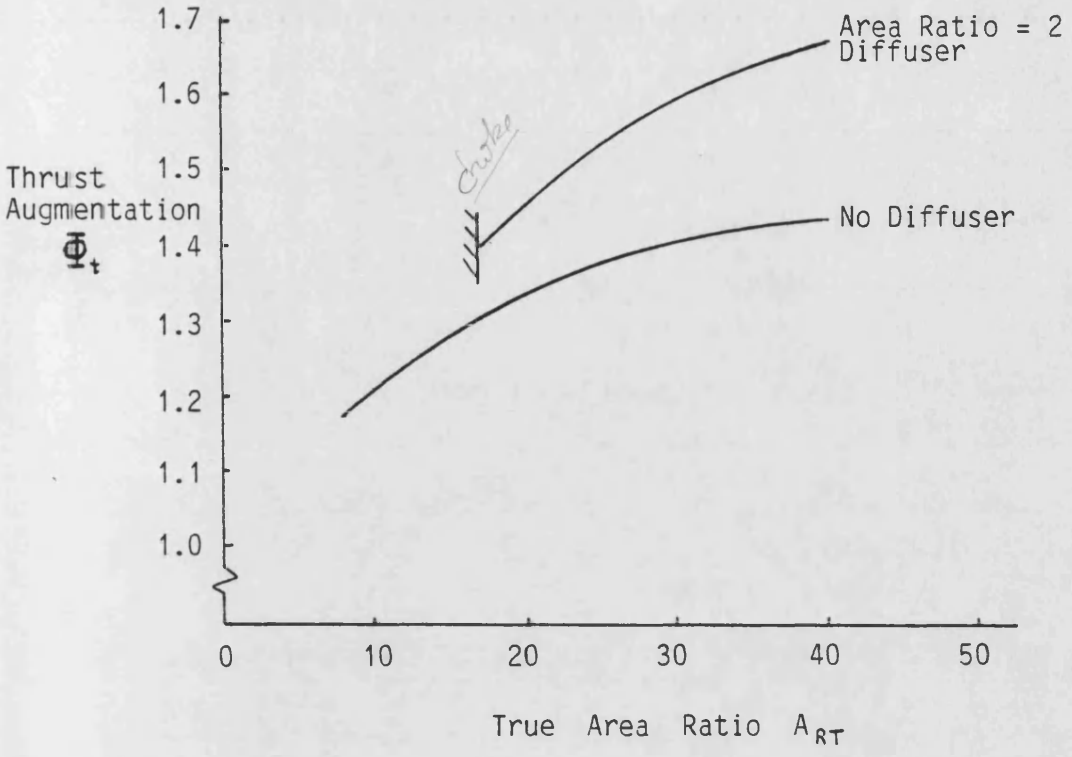

Figure 8.3 The Effect of Diffusion on a 6.9 bar gauge Ideal Ejector

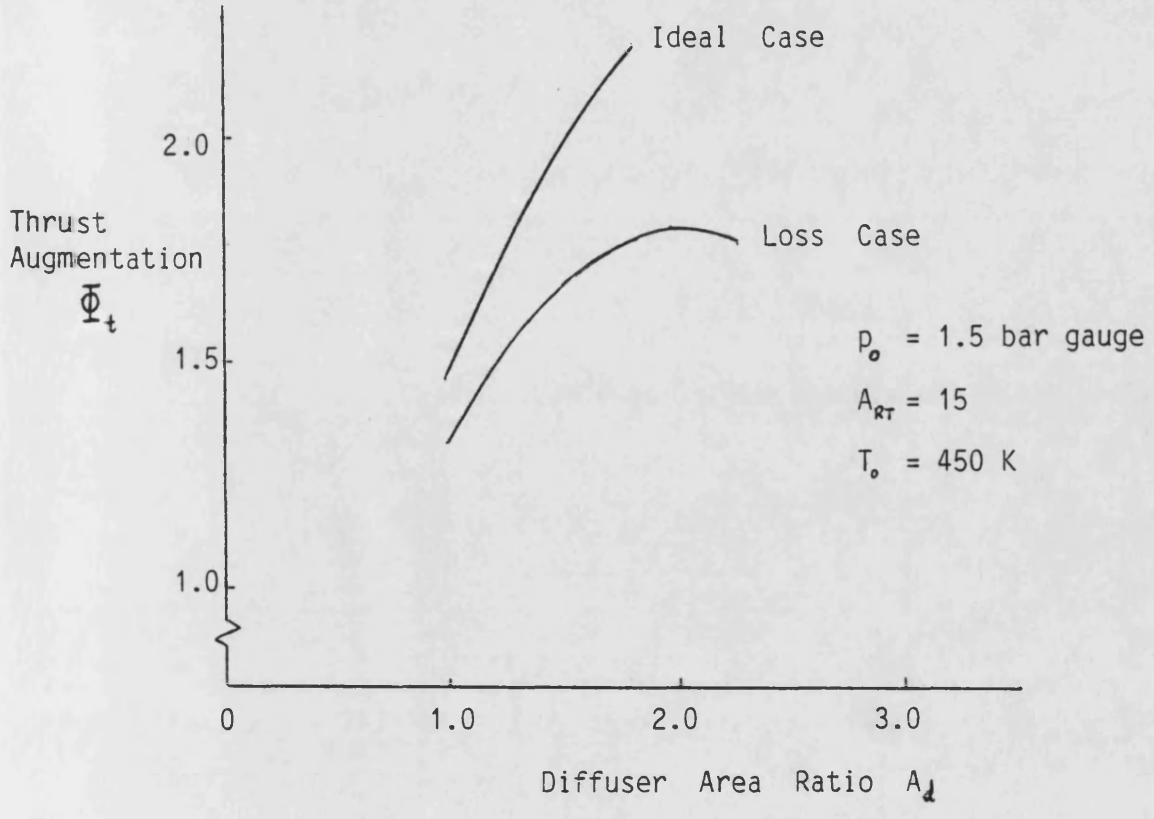

Figure 8.4 The Effect of Diffusion on a 1.5 bar gauge Ejector from Nagaraja, Hammond and Graetch (1973)

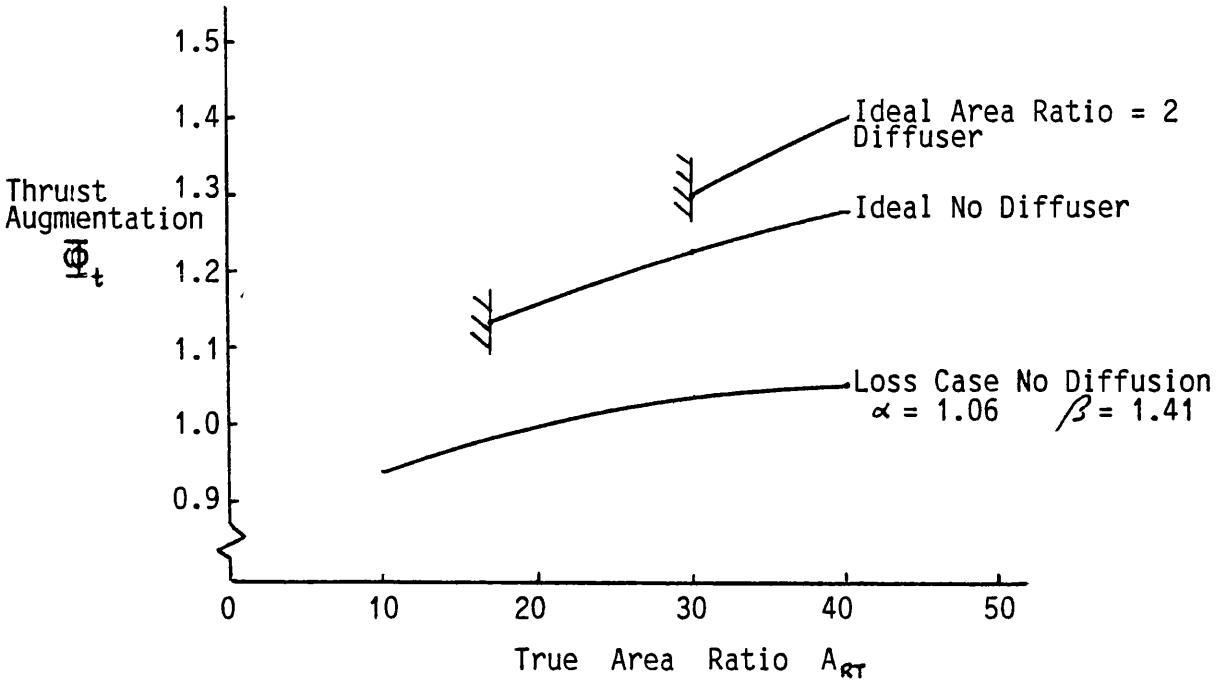

Figure 8.5 Ejector Performance at 14 bar gauge pressure

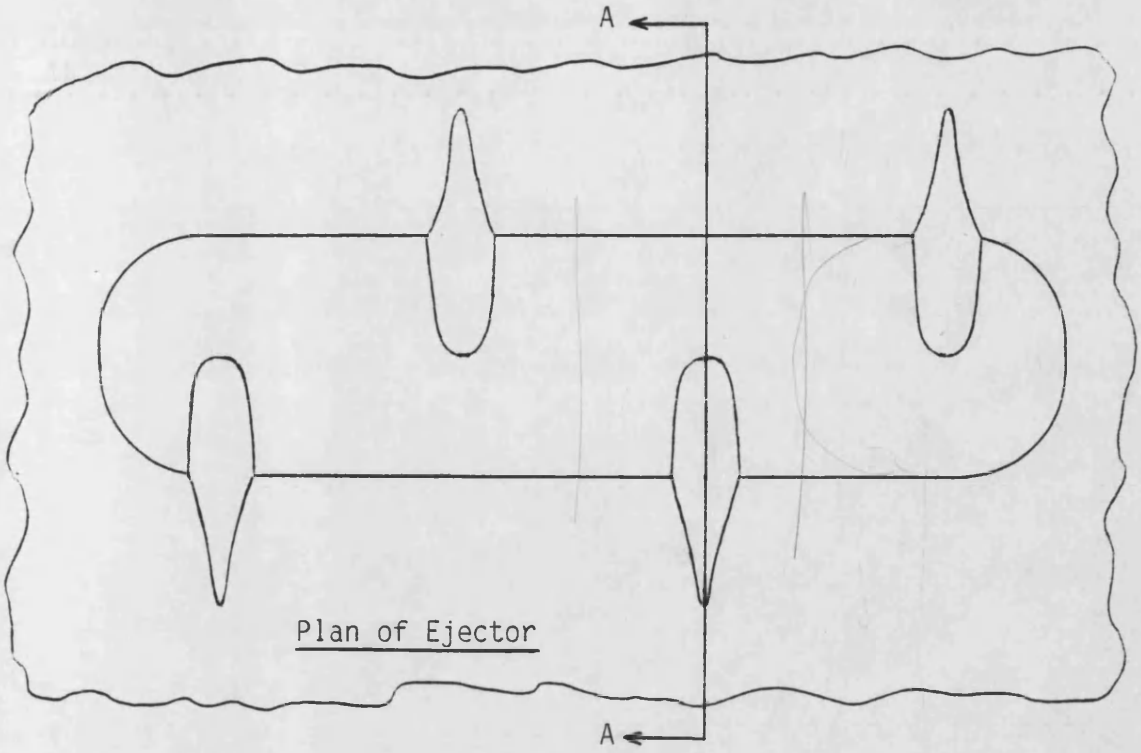

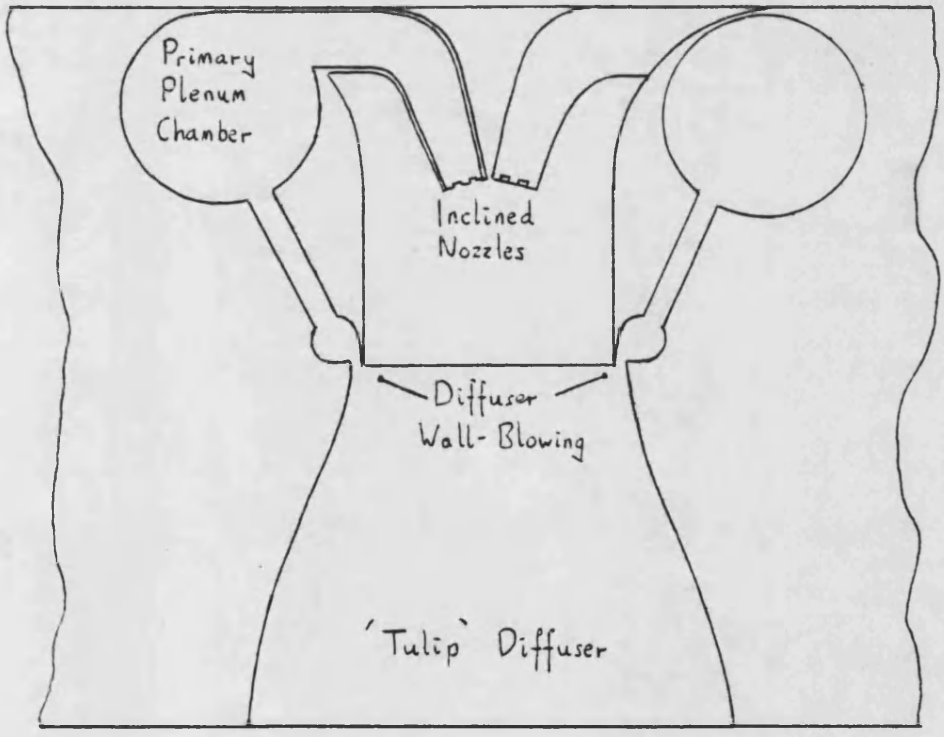

VIEW A-A

Figure 8.6 Two Views of the Proposed 4 Nozzle , 14 bar Ejector

CONFIGURATION TESTED
IN CHAPTER 7:

Area Ratio = 13.73
Aspect Ratio = 1
Achieved $\beta \simeq 1.4$

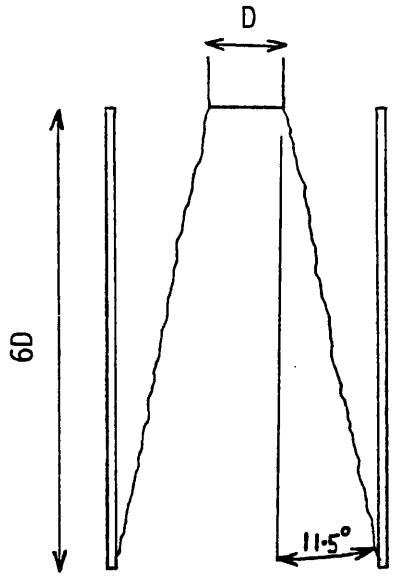

Schematic Side View

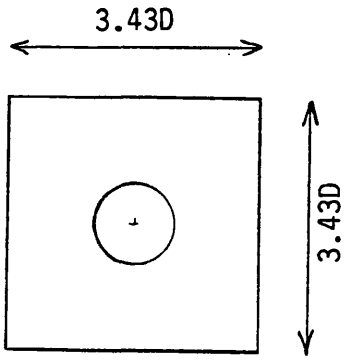

Plan

PROPOSED CONFIGURATION
OF CHAPTER 8:

Area Ratio = 35
Aspect Ratio = 4
Predicted $\beta = 1.4$

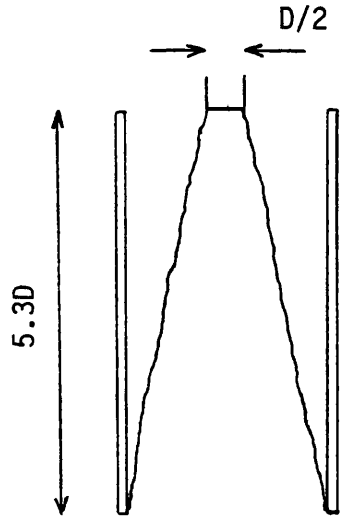

Schematic Side View

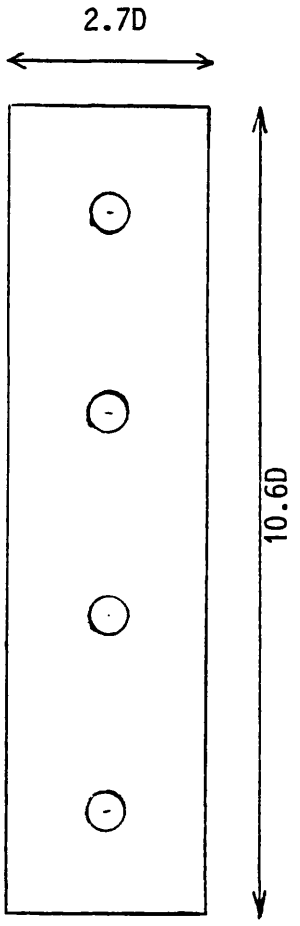

Plan

Figure 8.7 Geometries Required to give Specified Degree of Skewness

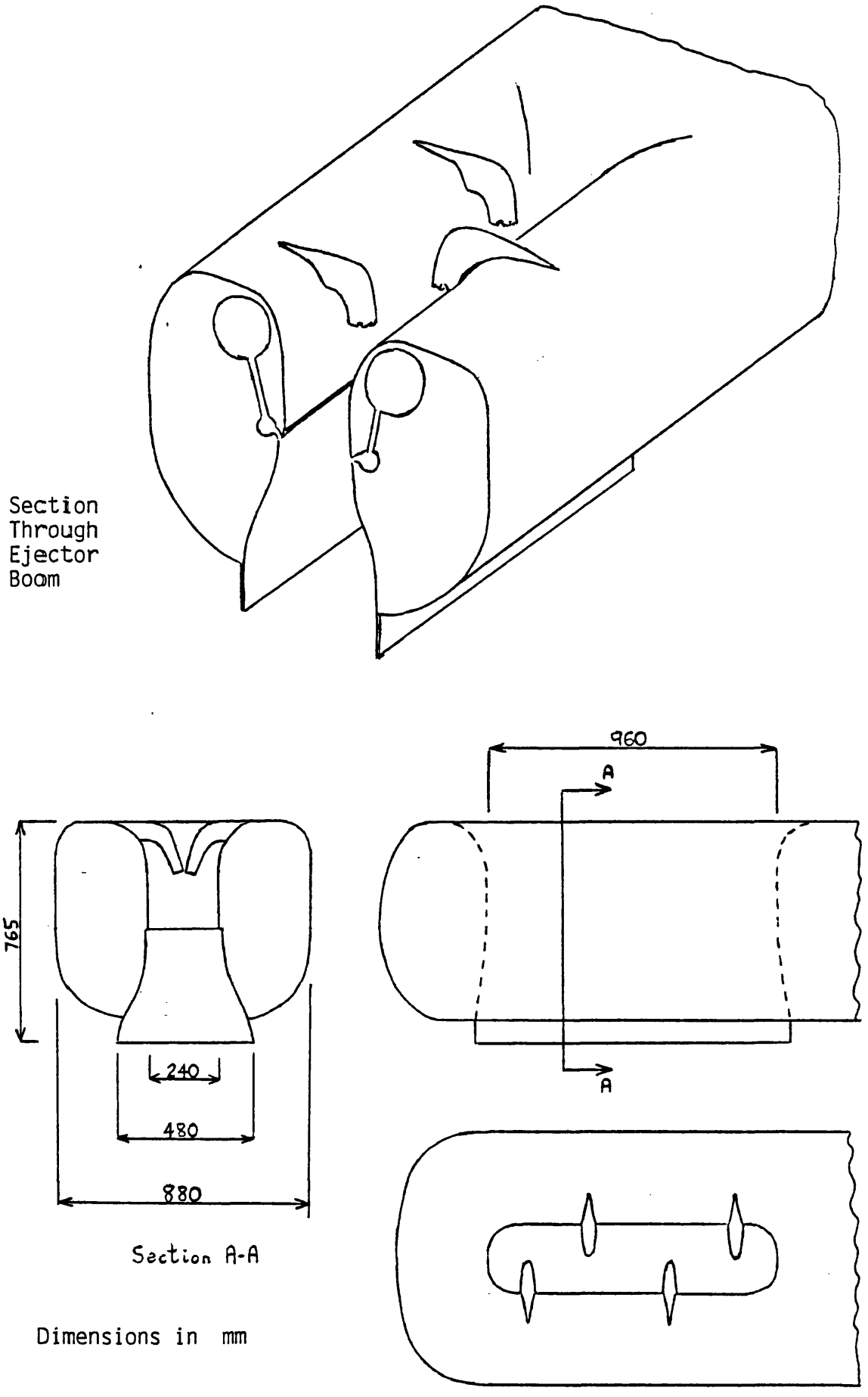

Figure 8.8 Ejector Installation and Representative Dimensions

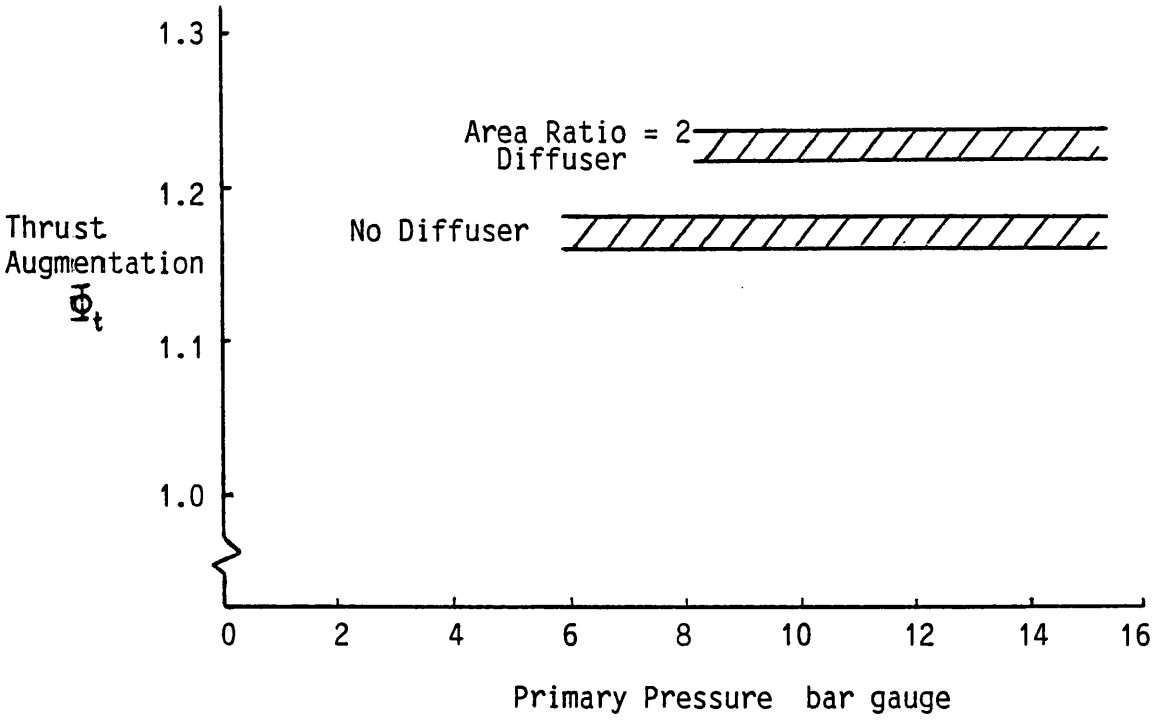

Figure 8.9 The Estimated Performance of the Reaction Control Ejector

u v w Cartesian Velocities

$\underline{i}$ $\underline{j}$ $\underline{k}$ Cartesian Unit Vectors

r θ z Cylindrical Axes

v_r v_θ w Cylindrical Velocities

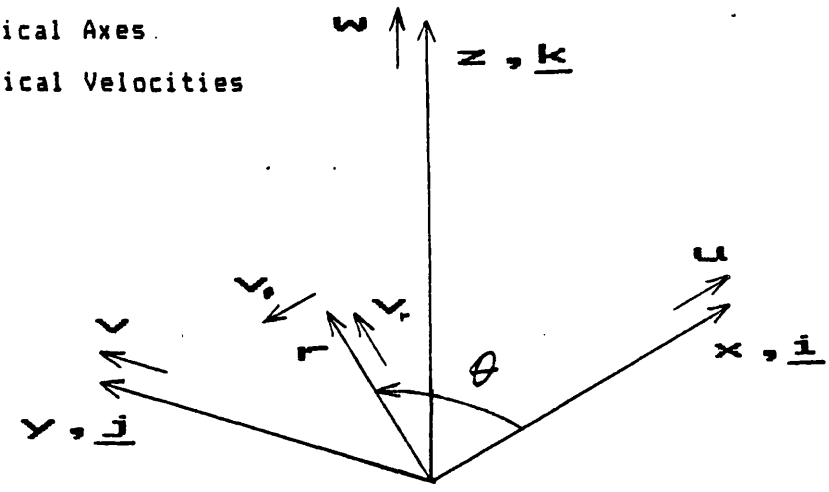

Figure C1 Cartesian And Cylindrical Co-ordinate System

r θ z Cylindrical Axes

$\underline{e_r}$ $\underline{e_\theta}$ $\underline{e_z}$ Cylindrical Unit Vectors

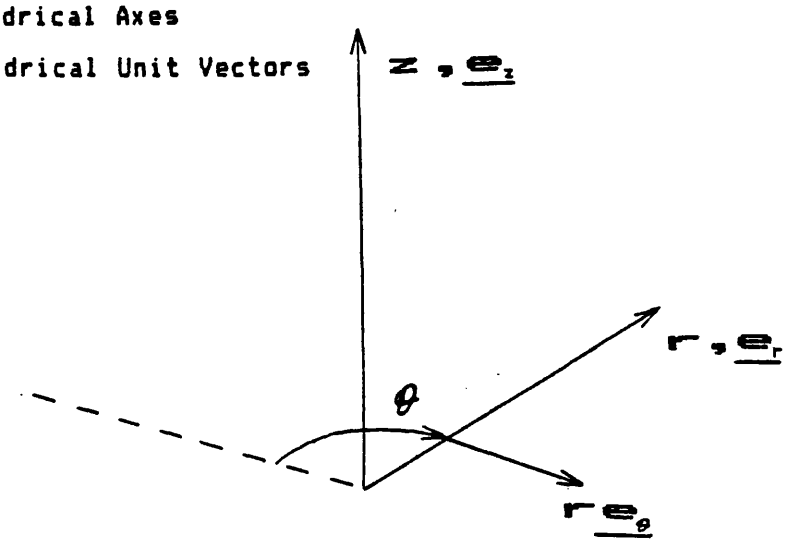

Figure C2 True Cylindrical Co-ordinate System

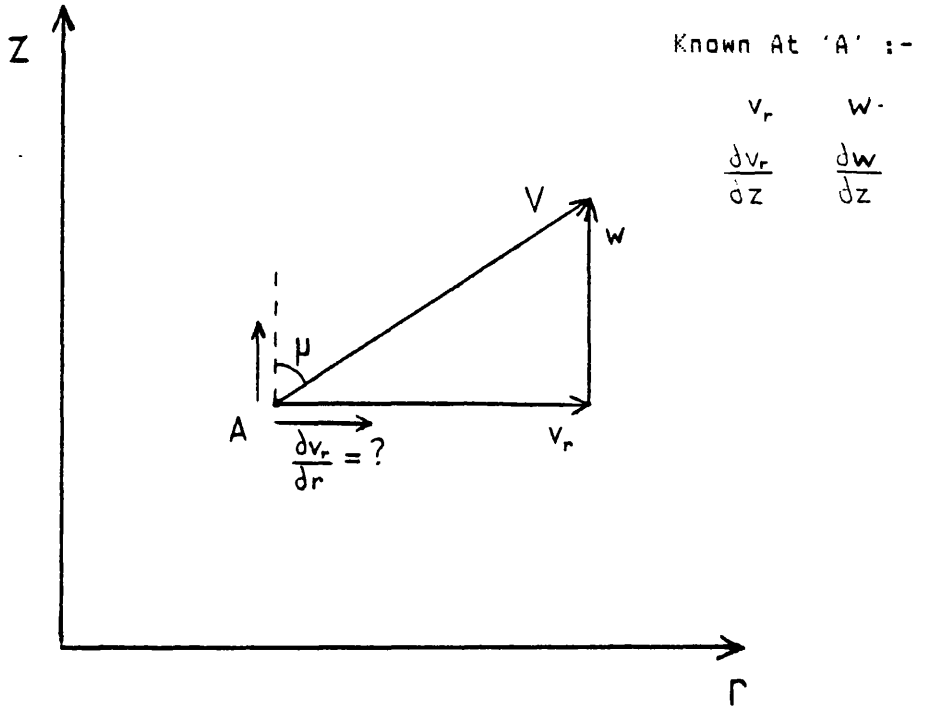

Figure C3 The Characteristic Property

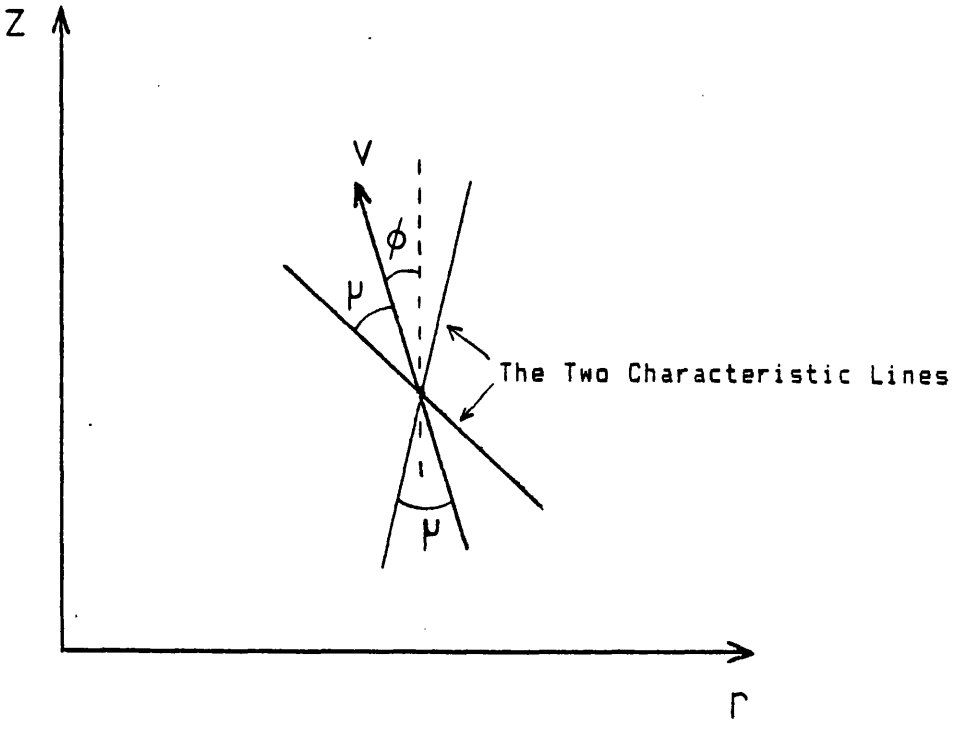

Figure C4 The Local Characteristic Construction

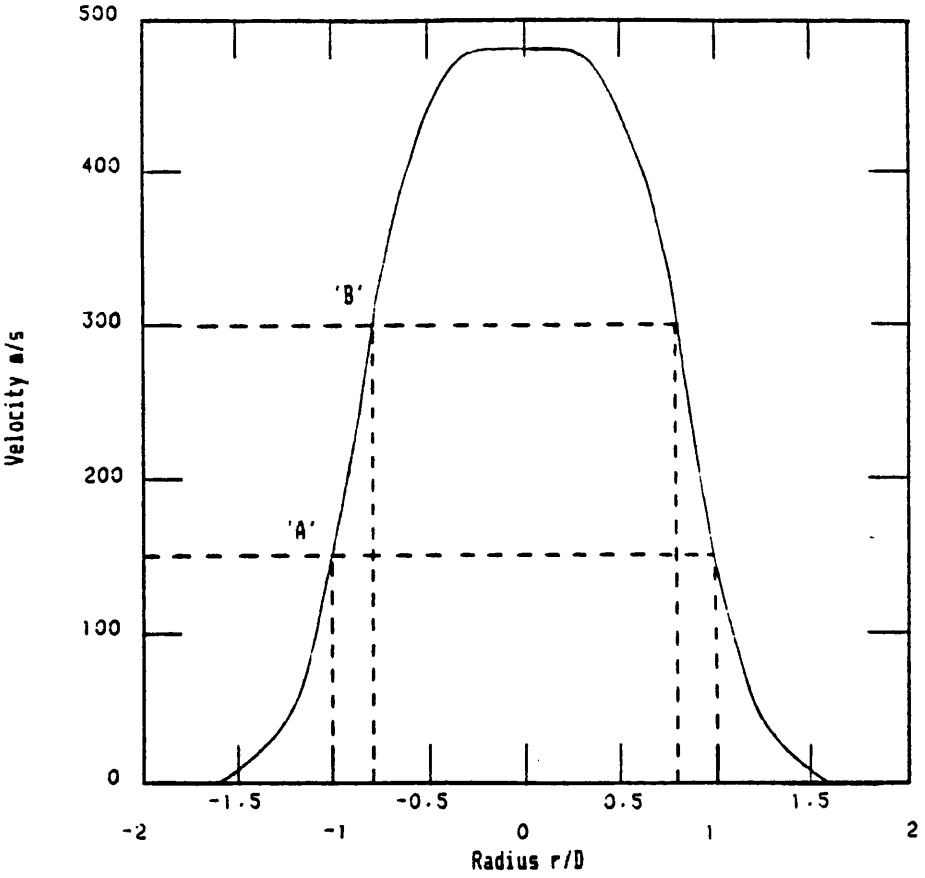

Figure D.1 Typical Velocity Profile with Half-width Details

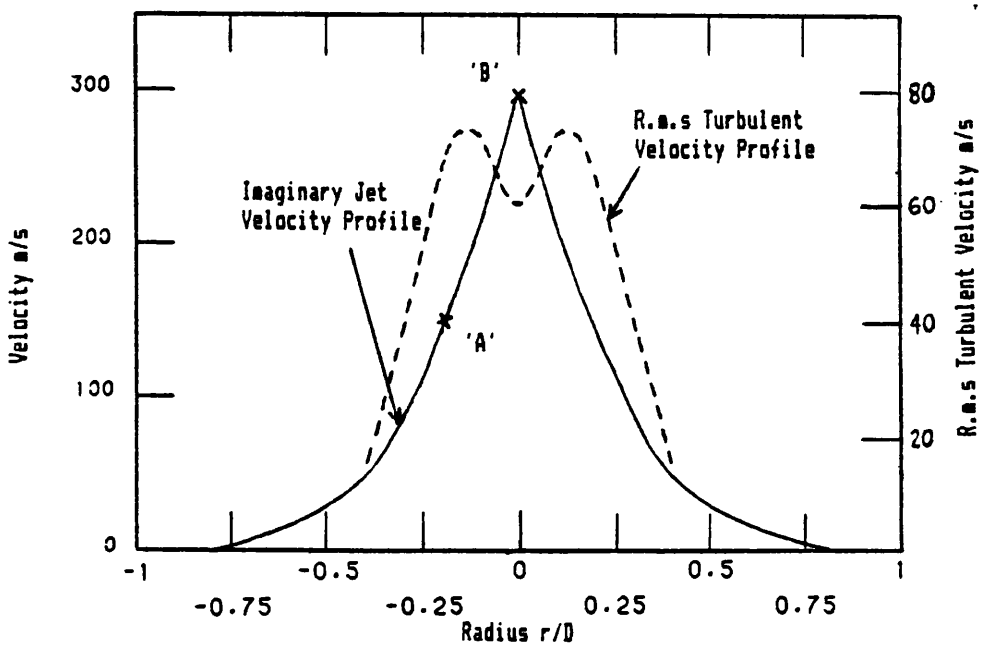

Figure D.2 Imaginary Jet Velocity and Turbulent Velocity Profiles

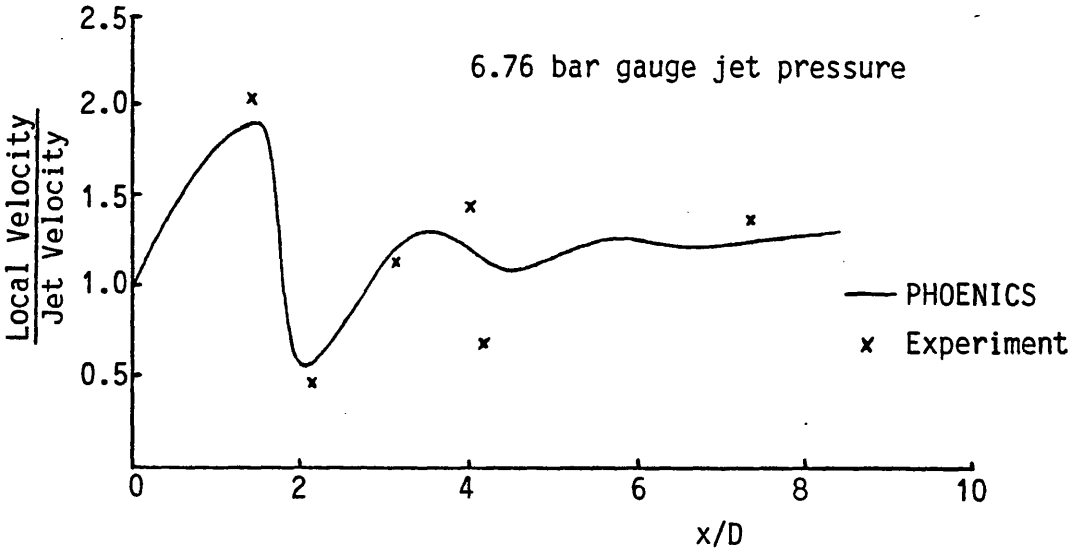

Figure E.1 Centreline Velocity Variation of a 6.76 bar gauge Jet using PHOENICS from Davis, Ludwig and Rhodes (1985)

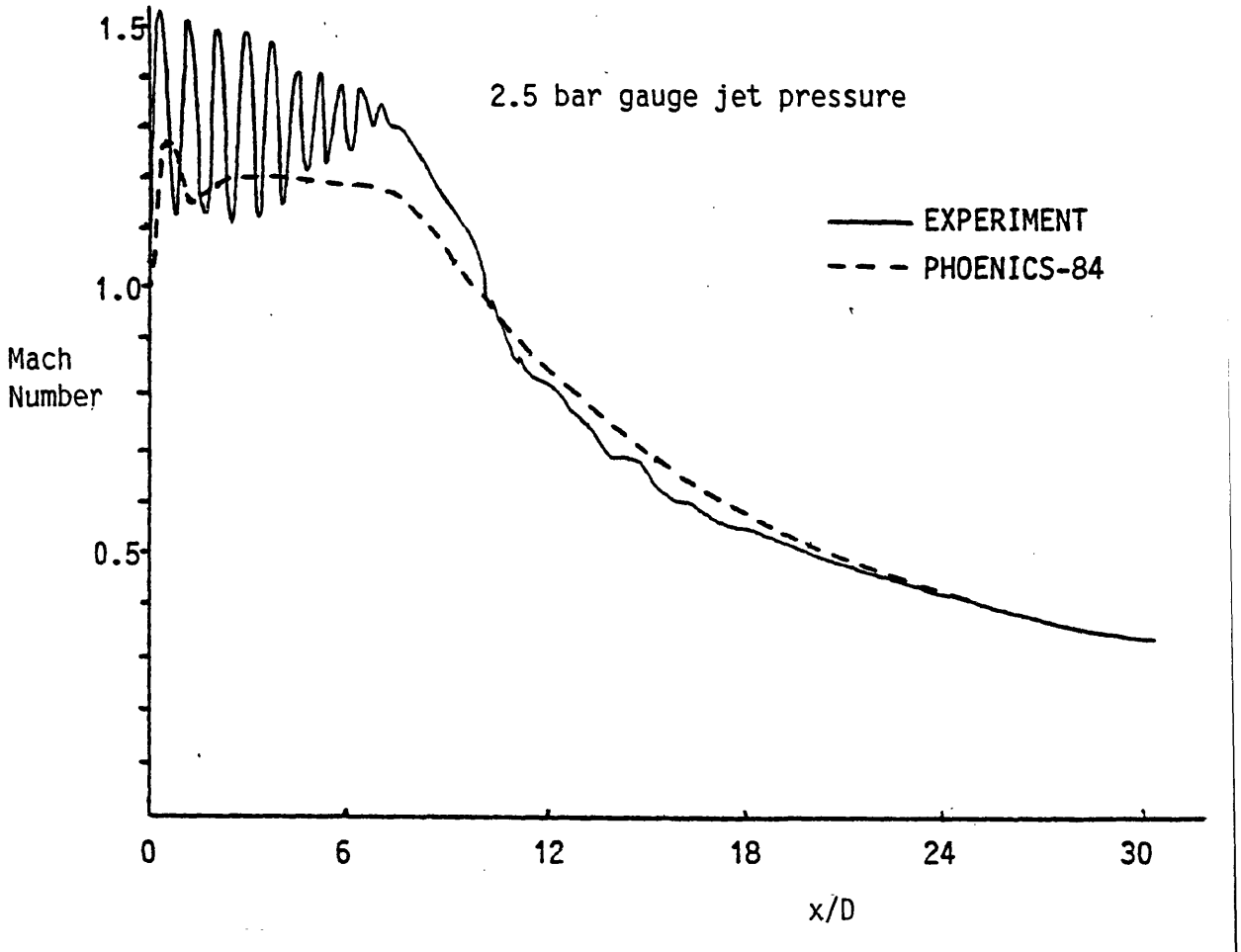

Figure E.2 Centreline Mach Number Variation of a 2.5 bar gauge Jet using PHOENICS from Wilson (1988)

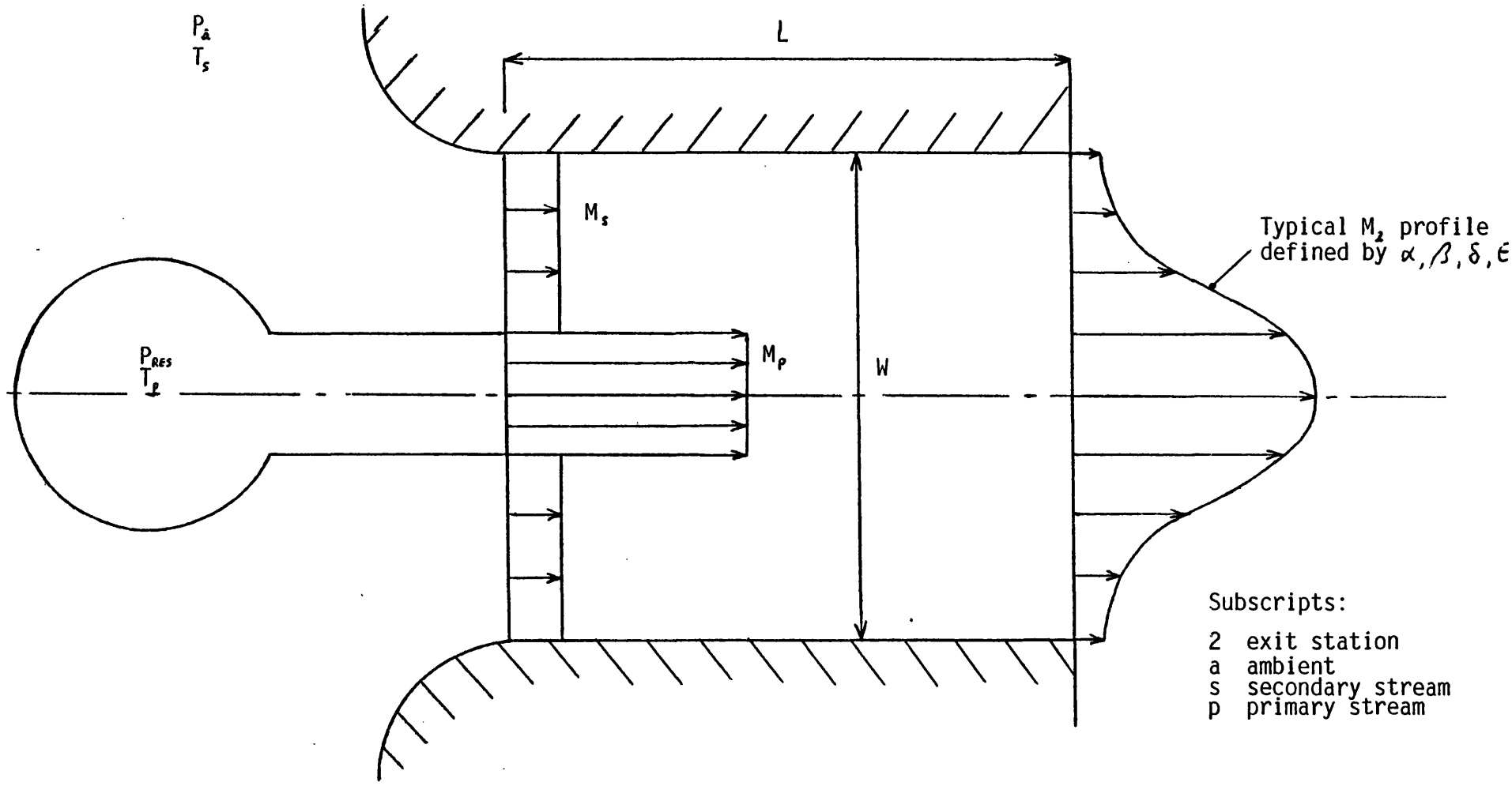

Figure G.1 Notation and Layout of Ejector used in HTP Model